



University
of Glasgow

Davie, Colin Thorpe (2002) *Particulate mechanics framework for modelling multi-physics processes in fracturing geomaterials*. PhD thesis

<http://theses.gla.ac.uk/5537/>

Copyright and moral rights for this thesis are retained by the author

A copy can be downloaded for personal non-commercial research or study, without prior permission or charge

This thesis cannot be reproduced or quoted extensively from without first obtaining permission in writing from the Author

The content must not be changed in any way or sold commercially in any format or medium without the formal permission of the Author

When referring to this work, full bibliographic details including the author, title, awarding institution and date of the thesis must be given

***Particulate Mechanics Framework for
Modelling Multi-Physics Processes in
Fracturing Geomaterials***

A Thesis Submitted to the
University of Glasgow in Fulfilment of the
Degree of Doctor of Philosophy

By
Colin Thorpe Davie
Department of Civil Engineering
University of Glasgow
July 2002



*All knowledge is of itself of some value. There is nothing so minute or
inconsiderable, that I would not rather know it than not.*

Johnson, Samuel (1709 - 1784)
Life of Johnson (J. Boswell), 1775

To My Parents

Acknowledgments

This thesis as taken approximately 1046 days to complete and 3 black pens, 1 red pen, 2 yellow highlighter pens, 2.94m of HB pencil lead, 300 staples, 9 paper clips, 1 bulldog clip, 7080 sheets of paper, 1002 MB of stored data, 3661 cups of coffee, 374 pints of beer, a lot of frustration, a fair amount of stress and an infinite amount of patience, from the following people, have gone into its creation.

Firstly, I would like to thank my supervisor, Professor Nenad Bićanić, most patient of all and forever the optimist, for giving me the chance to undertake this research and sharing his extensive knowledge and experience in helping me through it.

Further thanks to Dr Chris Pearce, for his help and advice and a realistic point of view, and to Mr Ken McColl, without whom a computational project would have been impossible, let alone writing and printing this thesis.

Many thanks must also go to my office mates over the last three years and particular to Hervé Morvan and Gerrit Klemm, who, while sitting next to me, have patiently suffered many of my questions and problems. Further appreciation and gratitude must also be expressed to the other researchers of 76 Oakfield Ave, Lindsay Beevers, Hua Feng Chen, Chris Stirling and Dave Watson, who have tolerantly endured the questions Hervé and Gerrit could not answer. Thanks also to those beyond the bounds of No. 76. and to my many, patient good friends, who have not seen me for the 5 months it has taken me to write up.

Finally, I would like to thank my parents, who have been extremely patient with my extended student status and who have given me limitless support and encouragement over the last three years and for 23 more before that. This thesis is dedicated to them.

A degree, is a first step down a ruinous highway. You don't want to waste it so you go on to graduate work and doctoral research. You end up a thorough-going ignoramus on everything in the world except for one subdivisional sliver of nothing.

Isaac Asimov (The Dead Past)

Abstract

The potential of particulate mechanics was explored with the purpose of developing a single software modelling framework in which to model multi-physics geomechanical problems. Individual particulate models were developed for solid, fluid and granular material phases, building onto the existing Distinct Element Modelling (DEM) environment Particle Flow Code in Three Dimensions (PFC^{3D}), with the intention that they could be combined to represent a geomechanical problem of any configuration. Advantages of utilising PFC^{3D} were firstly, its inbuilt feature allowing inter-particle bonding so that, in the limiting case, solid material could be represented and secondly, its embedded coding language, *FISH*, which allows the creation of user defined variables and functions which may be used to manipulate and modify the basic DEM code.

The Particle Solid Model (PSM) employed a bonded particle assembly with the concept of constructing a determinate lattice to replace a continuum material. Basic particle interactions were handled by the DEM behaviour inherent to PFC^{3D} and complex behaviour, such as fracturing, was realised through additional code written in *FISH*. The Particle Fluid Model (PFM) was created with the concept of developing a macroscopic particle representation of a fluid where the particles moved freely with the flow. Fluid behaviour was implemented by preventing physical contact of the DEM particles through force-separation laws representative of pressure and viscosity fields. These were again realised via *FISH* code. The Particle Proppant Model (PPM) would be implemented simply through the inherent capabilities of the PFC^{3D} DEM code and would be used to represent granular material on a grain for grain basis.

After initial development of the individual models, benchmark tests were carried out to evaluate their basic capabilities. Tests conducted with the PSM showed that, when calibrated through strain energy equivalence, it very accurately reproduced the expected deformation of an equivalent continuum elastic material. Tests conducted with the PFM showed that while it was capable of reproducing static and dynamic fluid behaviour correctly, it proved difficult to calibrate for specific fluid properties.

Nonetheless, accurate static behaviour was shown, and reasonable dynamic solid/fluid interaction behaviour was implied, when the PFM was combined with the PSM in an integrated solid/fluid benchmark model. However, it is accepted that further development work is required, particularly for the PFM.

Following the analysis of its basic behaviour, work continued to expand the capabilities of the PSM to include fracturing behaviour. The progressive development of five failure criteria was undertaken. From examination of the results of benchmark tests carried out on the failure criteria, it was found that the PSM generally dealt well with fracturing behaviour. However, it was also concluded that an elastic-softening plasticity criterion was required in order to ensure mesh (lattice) size objectivity. Furthermore, it was found that for macro-scale PSM meshes, failure criteria based on continuum principles were required in order to develop expected equivalent continuum failure behaviour. However, difficulties were encountered with the implementation of softening behaviour in the models based on continuum principles.

In order to evaluate the overall capabilities and potential of the particulate mechanics framework, parametric studies were conducted on combined solid/fluid models in pseudo-realistic representations of hydraulically driven fractures. Results of these studies showed good behaviour in comparison to theory and to the results of previous studies carried out by other researchers. Furthermore, qualitative results showed excellent promise for the application of the particulate framework to the development of multi-phase models combining solid, fluid and granular material phases.

In conclusion, it was found that the particulate modelling framework shows excellent potential as a simple modelling environment for multi-phase geomechanical problems, in which solid, fluid and granular material phases can be treated simultaneously without the need for separate codes or staggered or iterative techniques. It was further concluded that, provided appropriate principles are applied, this type of framework has potential for modelling in almost any field where computational analyses can be employed and for problems of any size from large-scale (macroscopic) to atomistic (nano-scale) structures. While it is acknowledged that current modelling capacity may be limited by computational requirements, it is noted that considerable possibilities for future research and development are available in this field.

Table of Contents

Acknowledgments	i
Abstract	ii
Table of Contents	iv
List of Figures	viii
List of Tables	xvi
Notation	xvii
Symbols	xvii
Subscripts.....	xxiii
Superscripts.....	xxiii
Abbreviations.....	xxiv
Chapter 1: Introduction	1
1.1. Introduction.....	1
1.2. Geomechanical Test Case.....	3
1.3. Project Aims and Objectives	5
1.4. Numerical Work	6
1.5. Outline of Thesis.....	7
Chapter 2: Review of Modelling Frameworks	9
2.1. Introduction.....	9
2.2. History of Hydraulic Fracturing Research.....	9
2.3. History of Lattice Modelling	25
2.3.1. Background and Development of Lattice Models	25
2.3.2. Lattice Models for Hydraulic Fracturing.....	39
2.3.3. Bonded Particle Assemblies	41
2.4. Alternative Fluid Modelling Techniques.....	46
2.4.1. Current Fracture Fluid Models	46
2.4.2. Particle Fluid Methods.....	48
2.5. Modelling Techniques for Proppant Transport, Proppant Stability and Sand Production.....	54
2.6. Summary.....	61
Chapter 3: Research Proposal and Model Implementation	63
3.1. Introduction.....	63
3.2. Research Proposal.....	63
3.3. An Introduction to Particle Flow Code in Three Dimensions	68
3.4. Theory of the Particulate Mechanics Modelling Framework	72
3.4.1. Cundall & Strack Type Distinct Element Method.....	72
3.4.2. Calculation of Granular Stress State in Particle Models	82
3.4.3. Granular - Continuum Stress Conversion Factors	87
3.5. Proposed Implementation of Particle Solid Model (PSM).....	96

3.6. Proposed Implementation of the Particle Fluid Model (PFM)	98
3.7. Proposed Implementation of the Coupled Solid/Fluid Model (PSM + PFM)....	99
3.8. Proposed Implementation of Particle Proppant Model (PPM)	100
3.9. Proposed Implementation of the Fully Coupled Multi-Physics Framework (PSM + PFM + PPM).....	102
3.10. Summary.....	103
Chapter 4: Numerical Model Development	105
4.1. Introduction.....	105
4.2. The Particle Solid Model (PSM)	105
4.2.1. Development of the PSM.....	105
4.2.2. PSM - Continuum Equivalence	109
4.2.2.1. Hrennikoff's Formulations	109
4.2.2.2. Trial and Error Approaches	113
4.2.2.3. Application of Strain Energy Equivalence Technique to PSM	115
4.2.3. PSM Benchmark Problems.....	124
4.2.3.1. Application of Linear Contact Model in PFC ^{3D}	125
4.2.3.2. Uniaxial Benchmark Model.....	126
4.2.3.2.1. Elastic Deformation Tests.....	126
4.2.3.2.2. Equivalent Continuum Stress Tests	133
4.2.3.3. Cantilever Beam Benchmark Model	137
4.2.4. PSM Conclusions.....	141
4.3. The Particle Fluid Model (PFM)	142
4.3.1. Development History.....	142
4.3.2. Development of the PFM.....	145
4.3.3. Implementation of the PFM.....	150
4.3.4. PFM Benchmark Problems.....	156
4.3.4.1. Pressurised Cylinder Benchmark Model	157
4.3.4.2. Lubrication Flow Benchmark Model.....	163
4.3.5. PFM Conclusions.....	173
4.4. The Coupled Solid/Fluid Model (PSM + PFM)	176
4.4.1. Development of the Coupled Solid/Fluid Model.....	176
4.4.2. Pressurised Notch Coupled Benchmark Problem.....	179
4.4.3. PSM + PFM Conclusions	184
4.5. Summary.....	186
Chapter 5: Failure Criteria for the Particle Solid Model (PSM).....	188
5.1. Introduction.....	188
5.2. Failure Criteria for Lattice Type Models	188
5.3. Development and Implementation of Failure Criteria for PSM	191
5.4. Two-Dimensional Uniaxial Benchmark Model.....	194
5.5. Mark 1 - Failure Criterion.....	197
5.5.1. Theory of the Mark 1 Failure Criterion	197
5.5.2. Implementation of the Mark 1 Failure Criterion	199
5.5.3. Mark 1 Failure Criterion Benchmark Study	201
5.5.4. Mark 1 - Conclusions.....	207
5.6. Mark 2 - Failure Criterion.....	207
5.6.1. Theory of the Mark 2 Failure Criterion	207
5.6.2. Implementation of the Mark 2 Failure Criterion	212

5.6.3. Mark 2 Failure Criterion Benchmark Study	214
5.6.4. Mark 2 - Conclusions.....	219
5.7. Mark 3 - Failure Criterion.....	221
5.7.1. Theory of the Mark 3 Failure Criterion	221
5.7.2. Implementation of the Mark 3 Failure Criterion	227
5.7.3. Mark 3 Failure Criterion Benchmark Study	230
5.7.4. Mark 3 - Conclusions.....	241
5.8. Mark 4 - Failure Criterion.....	242
5.8.1. Theory of the Mark 4 Failure Criterion	242
5.8.2. Implementation of the Mark 4 Failure Criterion	251
5.8.3. Mark 4 Failure Criterion Benchmark Study	255
5.8.4. Mark 4 - Conclusion	261
5.9. Mark 5 - Failure Criterion.....	262
5.9.1. Theory of the Mark 5 Failure Criterion	262
5.9.2. Implementation of the Mark 5 Failure Criterion	264
5.9.3. Mark 5 Failure Criterion Benchmark Study	266
5.9.4. Mark 5 - Conclusions.....	270
5.10. Summary.....	270

Chapter 6: Coupled Hydraulic Fracture Benchmark Models 273

6.1. Introduction.....	273
6.2. Hydraulic Fracture Benchmark Model (PSM)	274
6.2.1. Introduction and Model Set-up	274
6.2.2. Numerical Studies.....	282
6.2.3. Discussion of Results.....	286
6.2.3.1. Introduction.....	286
6.2.3.2. Figures Showing General Fracture Patterns	287
6.2.3.3. Discussion of General Fracture Patterns.....	291
6.2.3.3.1. Introduction.....	291
6.2.3.3.2. Straight Fracture Patterns	291
6.2.3.3.3. Contact Force Patterns for Straight Fractures.....	292
6.2.3.3.4. Deviated Fracture Patterns.....	295
6.2.3.3.5. Random Lattice Mesh Configurations	304
6.2.3.3.6. Application of the Mark 4 and Mark 5 Failure Criteria.....	307
6.2.3.4. Figures Showing Comparative Fracture Propagation Results	311
6.2.3.5. Discussion of Comparative Fracture Propagations.....	317
6.2.4. Conclusions.....	333
6.3. Coupled Hydraulic Fracture Benchmark Model (PSM + PFM).....	337
6.3.1. Introduction and Model Set-up	337
6.3.2. Numerical Studies.....	342
6.3.3. Discussion of Results.....	343
6.3.4. Conclusions.....	360
6.4. Summary.....	362

Chapter 7: Conclusions and Further Work 364

7.1. Introduction.....	364
7.2. Particle Solid Model (PSM).....	365
7.2.1. Summary and Conclusions	365
7.2.2. Suggestions for Further Work	368

7.3. Particle Fluid Model (PFM).....	370
7.3.1. Summary and Conclusions	370
7.3.2. Suggestions for Further Work	371
7.4. Combined Model (PSM + PFM)	371
7.4.1. Summary and Conclusions	371
7.4.2. Suggestions for Further Work	373
7.5. Overall Assessment and Conclusions.....	374
7.6. The Wider Implications for Lattice Type Modelling	379
Appendix IA: References	383
Appendix IB: Bibliography	395
Appendix II: Granular-Continuum Stress Conversion Factors	400
Appendix III: FISH Code	413
AIII.1. Introduction.....	413
AIII.2. Glossary of User Defined Variables.....	413
AIII.3. Glossary of User Defined Functions	416
AIII.4. Particle Fluid Model Code.....	417
AIII.5. Mark 1 Failure Criterion.....	422
AIII.6. Mark 2 Failure Criterion.....	423
AIII.7. Mark 3 Failure Criterion.....	427
AIII.8. Mark 4 Failure Criterion.....	430
AIII.9. Mark 5 Failure Criterion.....	437
Appendix IV: Publications	444
Progressive Fracturing Using Lattice Models	445
Failure Criteria for Quasi Brittle Materials in Lattice Models	451

List of Figures

<i>Fig. 1.1.</i>	Five Main Processes to be Considered by Hydraulic Fracture Simulators	4
<i>Fig. 2.1.</i>	Geometry of CGDD Model Showing Rectangular Cross-Section of Fracture. (After Mendelsohn [56]).....	13
<i>Fig. 2.2.</i>	Geometry of PKN Model Showing Elliptical Cross-Sections (After Mendelsohn [56]).....	14
<i>Fig. 2.3.</i>	Various Fracture Shapes Assumed by Pseudo-Three-Dimensional Models. (After Mendelsohn [57]).....	18
<i>Fig. 2.4.</i>	Example of Three-Dimensional Finite Element Mesh Representing Half Length of Penny-Shaped Fracture (After Advani et al. [2]).....	20
<i>Fig. 2.5.</i>	Diagram Showing Radial, Penny-Shaped Expansion while Fracture remains within Initial Fracturing Layer	21
<i>Fig. 2.6.</i>	Diagram Showing Variation of Fracture Shape as Fracture Enters Bounding Strata with Material Properties and In Situ Stresses Different from those in Initial Layer.....	22
<i>Fig. 2.7.</i>	Examples of a) Triangular Lattice Arrangement, b) Square Lattice Arrangement, c) Hrennikoff's Lattice Arrangement for Arbitrary Poisson's Ratio	26
<i>Fig. 2.8.</i>	Diagram Showing a) Triangular Lattice Overlaid with Idealised Structure of Concrete Aggregate (After Schlangen and van Mier [82]) b) Detail of Lattice Elements Overlapping Areas of Aggregate and Concrete Paste (After van Vliet [95]).....	31
<i>Fig. 2.9.</i>	a) Load-Displacement Curves Showing Non-Linear Behaviour for Experimental Studies and Lattice Simulations of a Felser SEN Beam Test b) Crack Patterns in Lattice Simulations of a Felser SEN Beam Test (After Schlangen and van Mier [80]).....	34
<i>Fig. 2.10.</i>	Diagram of Triangular Lattice as Studied by Schlangen and Garboczi [79] Showing: a) the Intact Lattice and Directions of Applied Strain, b) and c) Directional Bias in Fracturing	37
<i>Fig. 2.11.</i>	Diagram Showing Procedure for Calculation of 'Node Stress' in a Lattice. a) Forces in Lattice Elements b) Resultant Normal and Shear Force Perpendicular to Nodal Cut c) Principal Normal Force d) Cross-Sectional Area of Lattice Elements in Principal Direction e) Nodal Stress (After Schlangen and Garboczi [79]).....	38
<i>Fig. 2.12.</i>	Diagram of Square Lattice with Force Dipole Representing Hydraulic Fracture Fluid Pressure as Used by Tzschichholz et al. [88, 89].....	39
<i>Fig. 2.13.</i>	Example of Fractal Fracture Pattern in a Heterogeneous Square Lattice (After Tzschichholz and Herrmann [88])	40
<i>Fig. 2.14.</i>	Diagram of Particle-Lattice Assembly.....	41
<i>Fig. 2.15.</i>	Diagram Showing Various Types of Inter-Particle Links and their Equivalent Lattice Elements	42
<i>Fig. 2.16.</i>	Diagrams Showing Various Model Representations of Hydraulic Fracturing a) <i>Lattice Model</i> (repeated from Fig. 2.13.) b) <i>Bonded Particle Assembly</i> (after Davie [21]) c) <i>Finite Element Mesh</i> of	

	<i>Penny-Shaped Fracture (repeated from Fig. 2.4.) d) Geometry of PKN Model (repeated from Fig. 2.2.)</i>	45
Fig. 2.17.	Diagram Showing Typical Force-Separation Law for Atomistic Model with Simplified Sinusoidal Approximation (After van Mier [59])	50
Fig. 2.18.	Diagram Showing Overlapping Configuration of DEM Particles Required for Hydrostatic Pressure Distribution (After Zhang et al. [98])	52
Fig. 3.1.	Diagram Showing Particle Pair Moving into Contact	74
Fig. 3.2.	Diagram Showing General Case of a Contacting Particle Pair	76
Fig. 3.3.	Flow Chart Summarising the Calculation Sequence for the Distinct Element Method as Described by Cundall and Strack [18] (Adapted from Trent [86])	81
Fig. 3.4.	Diagram Illustrating Position Vectors of Particle Centroid and Contact Coordinates	85
Fig. 3.5.	Diagram of Simple, Bonded Particle Assembly	88
Fig. 3.6.	Diagram of Development of Contact Forces on the Particle 'p' Experiencing Normal Stress in the x-direction Showing a) the reaction to external loading and b) the total resulting contact forces on the particle	90
Fig. 3.7.	Diagram Showing Alternative Interpretation of Equivalent Continuum Represented by Simple Bonded Particle Assembly	93
Fig. 3.8.	Diagram Showing a) Typical Configuration of Bonded Particle Sheet for PSM and b) a Typical Triangular Lattice Model for Comparison	96
Fig. 3.9.	Detail of Typical Three-Particle Unit of PSM Framework Showing Construction of 'Lattice' Elements	97
Fig. 3.10.	Schematic Diagram of Particle Interaction in PFM	99
Fig. 3.11.	Diagram of Proposed Interaction between PSM and PFM	100
Fig. 3.12.	Diagram of PPM Implementation	101
Fig. 3.13.	Diagram of Final Stage of Proposed Fully Combined Model	103
Fig. 4.1.	Typical Example of Two-Dimensional Bonded Particle Assembly Constructed for PSM	106
Fig. 4.2.	Visualisation of PSM Bonded Particle Assembly as Spring Network	107
Fig. 4.3.	End Elevation of Particle Assembly Showing Contact Spring Position Independent of Particle Size	107
Fig. 4.4.	Diagram of Bonded Particle Pair Showing Equivalent Lattice Element Overlaid	108
Fig. 4.5.	Example of Bonded Particle Assembly Mesh Used for Wellbore Stability Studies (After Davie [21])	113
Fig. 4.6.	Diagram Showing Typical Triangular Unit of Bonded Particle Used for Strain Energy Equivalence Calculation	118
Fig. 4.7.	Diagram Showing Volume Associated with Typical Triangular Lattice Unit for Calculation of Strain Energy Density	119
Fig. 4.8.	Diagram of PSM Mesh for Uniaxial Benchmark Test	126
Fig. 4.9.	Diagram of Finer Mesh PSM for Uniaxial Benchmark Test	130
Fig. 4.10.	Diagram of PSM Mesh for Cantilever Benchmark Problem	138
Fig. 4.11.	Plots of Typical Wellbore Stability Model Meshes a) Before and b) After Fracturing (After Davie [21])	143

Fig. 4.12.	Plots of Hydraulic Fracture Model Meshes a) Before and b) After Fracturing (After Davie [21])	144
Fig. 4.13.	Diagram Showing Radii of Influence Associated with Separation Laws for Fluid Field Properties between dense PFC^{3D} Particles	146
Fig. 4.14.	Diagram Showing Repulsive Forces Applied to Particle Pair	147
Fig. 4.15.	Diagram Showing Drag Forces Applied to Particle Pair	148
Fig. 4.16.	Diagram Illustrating Basis of Calculations for Particle - Particle Interactions and for Particle - 'Wall' Interactions in PFM.....	148
Fig. 4.17.	Diagram Showing Volume of Fluid Associated with Discrete Particles	149
Fig. 4.18.	Flow Chart Summarising the Calculation Sequence for the Distinct Element Method Modified For Inclusion of the PFM Implemented via FISH Code (expanded Fig. 3.3.) (Dashed Outlines Indicate Where Changes were Implemented in the Basic DEM Algorithm)	152
Fig. 4.19.	Flow Chart Summarising FISH Code for Implementation of PFM.....	153
Fig. 4.20.	Flow Chart Summarising FISH Code for Nested Particle Loop Sub-Block of Flow Chart Summarising PFM Code in Fig. 4.19.	154
Fig. 4.21.	Flow Chart Summarising FISH Code for Nested Wall Loop Sub-Block of Flow Chart Summarising PFM Code in Fig. 4.19.....	155
Fig. 4.22.	Diagram Showing Initial Set-up of the Pressurised Cylinder Benchmark Problem for the PFM.....	157
Fig. 4.23.	Plots of Typical Pressurised Cylinder Benchmark Model at a) an Intermediate Stage of Filling and b) Final Steady State Equilibrium (arrows indicate particle velocities).....	158
Fig. 4.24.	Plots of the Final Equilibrium Stages of PFM Pressurised Cylinder Tests under Varying External Pressures of a) 100kPa, b) 200kPa and c) 2000kPa	159
Fig. 4.25.	Plot of Pressure Separation Law for Coefficients of Repulsion of 1×10^4 and 1×10^5	161
Fig. 4.26.	Diagram Showing Overlap of Radii of Influence Around PFM Particles ..	161
Fig. 4.27.	Example Plot of Pressurised Cylinder Model for PFM with 'Fluid Particles' at Equilibrium in 1D Lines, without Lateral Displacement.....	162
Fig. 4.28.	Diagram Showing Initial Set-up of the Lubrication Flow Benchmark Problem for the PFM	164
Fig. 4.29.	Typical Plot of Lubrication Flow Model under Established Steady State Flow Conditions (arrows indicate particle velocities)	164
Fig. 4.30.	Plot of Lubrication Flow Velocity Profiles from PFM and Theory - Run 001 ($\xi = 0.0, Y = 0.0075\text{m}, \frac{dp}{dx} = -1.0, \Rightarrow \mu = 0.0747$).....	167
Fig. 4.31.	Plot of Lubrication Flow Velocity Profiles from PFM and Theory - Run 002 ($\xi = 0.0, Y = 0.0075\text{m}, \frac{dp}{dx} = -2.0, \Rightarrow \mu = 0.0705$).....	168
Fig. 4.32.	Plot of Lubrication Flow Velocity Profiles from PFM and Theory - Run 002 ($\mu = 0.0747$, as predicted by Run 001).....	168
Fig. 4.33.	Plot of Lubrication Flow Velocity Profiles from PFM and Theory - Run 003 ($\xi = 0.7, Y = 0.0075\text{m}, \frac{dp}{dx} = 1.0, \Rightarrow \mu = 0.242$).....	170
Fig. 4.34.	Plot of Lubrication Flow Velocity Profiles from PFM and Theory - Run 004 ($\xi = 0.7, Y = 0.0075\text{m}, \frac{dp}{dx} = 2.0, \Rightarrow \mu = 0.4610$)	171
Fig. 4.35.	Example of a Velocity/Time Plot for a PFM Particle as it Travels Through the Lubrication Flow Model	172
Fig. 4.36.	Diagram Showing Excess Drag Effect of Multiple PSM Particles on Single PFM Particle	177

Fig. 4.37.	Diagram Showing Varying Separations of ‘Visible’ Particles within Radius of Influence of Drag.....	178
Fig. 4.38.	Diagram Showing Situation Where PFM Particles May Fail to ‘See’ the PSM Mesh.....	179
Fig. 4.39.	Diagram Showing Initial Set-up of the Coupled Benchmark Model for PSM + PFM	180
Fig. 4.40.	Plots of Coupled Benchmark Model for PSM + PFM during Fluid Flow into Notched PSM Mesh a) after 4000 time steps and b) after 8000 time steps	181
Fig. 4.41.	Plot of Coupled Benchmark Model for PSM + PFM at Steady State Equilibrium	181
Fig. 4.42.	Plot of Coupled Benchmark Model for PSM + PFM at Equilibrium Showing Forces in Inter-Particle Links	183
Fig. 5.1.	Flow Chart Summarising the Calculation Sequence for the Distinct Element Method Modified For Inclusion of Failure Criteria Implemented via <i>FISH</i> Code (expanded <i>Fig. 3.3.</i>) (Dashed Outlines Indicate Where Changes were Implemented in the Basic DEM Algorithm)	193
Fig. 5.2.	Diagram of PSM Meshes for Uniaxial Benchmark Fracture Model Showing a), b) & c) Coarse, Medium and Fine Meshes for Prescribed <i>x</i>-displacement d), e) & f) Coarse, Medium and Fine Meshes for Prescribed <i>y</i>-displacement	195
Fig. 5.3.	Diagram Showing Simple Linear Elastic Constitutive Model for Mark 1 - Uniaxial Total Strain Failure Criterion for the PSM	198
Fig. 5.4.	Flow Chart Summarising <i>FISH</i> Code for Mark 1 Failure Criterion	200
Fig. 5.5.	Load-Displacement Plots for the Two-Dimensional Uniaxial Benchmark Model with the Mark 1 Failure Criterion and Prescribed Displacement in the <i>x</i>-direction	202
Fig. 5.6.	Load-Displacement Plots for the Two-Dimensional Uniaxial Benchmark Model with the Mark 1 Failure Criterion and Prescribed Displacement in the <i>y</i>-direction	202
Fig. 5.7.	Load-Displacement Plot for Two-Dimensional Uniaxial Benchmark Model Coarse Mesh with the Mark 1 Criterion and Prescribed Displacement in the <i>x</i>-direction, Overlaid with Plot of Number of Failed Elements-Displacement	205
Fig. 5.8.	Load-Displacement Curves for Experimental Studies and Lattice Simulations of a Felser SEN Beam Test (After Schlangen and van Mier [80]).....	206
Fig. 5.9.	Diagram Showing Development of Principal Stresses in the Inter-Particle Link Elements of a PSM Mesh from the Principal Stresses in Particles.....	209
Fig. 5.10.	Diagram Showing Development of Principal Stresses in the Inter-Particle Link Elements of a PSM Mesh from a Average Stress Tensor in the Link Element.....	210
Fig. 5.11.	Flow Chart Summarising <i>FISH</i> Code for Mark 2 Failure Criterion	213
Fig. 5.12.	Load-Displacement Plots for the Two-Dimensional Uniaxial Benchmark Model with the Mark 2 Failure Criterion and Prescribed Displacement in the <i>x</i>-direction	215

Fig. 5.13.	Load-Displacement Plots for the Two-Dimensional Uniaxial Benchmark Model with the Mark 2 Failure Criterion and Prescribed Displacement in the y-direction	215
Fig. 5.14.	Diagram Showing Elastic-Softening Constitutive Model for Mark 3 - Uniaxial Total Strain Failure Criterion for the PSM	222
Fig. 5.15.	Diagram of Elastic-Softening Constitutive Model Showing Increasing Gradient of Softening Slope with Increasing Element Length	223
Fig. 5.16.	Diagram Showing Self Equilibrating Out of Balance Corrective Forces Applied to Particle Pair to Redistribute Relaxation Stress to Other Parts of Bonded Particle Assembly	225
Fig. 5.17.	Flow Chart Summarising <i>FISH</i> Code for Mark 3 Failure Criterion	229
Fig. 5.18.	Load-Displacement Plots for the Two-Dimensional Uniaxial Benchmark Model with the Mark 3 Failure Criterion and Prescribed Displacement in the x-direction (Modified E_s - constant G_f).....	231
Fig. 5.19.	Load-Displacement Plots for the Two-Dimensional Uniaxial Benchmark Model with the Mark 3 Failure Criterion and Prescribed Displacement in the y-direction (Modified E_s - constant G_f).....	231
Fig. 5.20.	Load-Displacement Plots for the Two-Dimensional Uniaxial Benchmark Model with the Mark 3 Failure Criterion and Prescribed Displacement in the x-direction (Constant E_s - non-constant G_f).....	232
Fig. 5.21.	Load-Displacement Plots for the Two-Dimensional Uniaxial Benchmark Model with the Mark 3 Failure Criterion and Prescribed Displacement in the y-direction (Constant E_s - non-constant G_f).....	232
Fig. 5.22.	Diagram Showing Alternative Interpretations of Characteristic Length, h, for Two-Dimensional Uniaxial Benchmark Model Meshes for displacement in a) the x-direction and b) the y-direction.....	235
Fig. 5.23.	Load-Displacement Plot for Two-Dimensional Uniaxial Benchmark Model Coarse Mesh with the Mark 3 Criterion and Prescribed Displacement in the x-direction, Overlaid with Plot of Number of Failed Elements-Displacement	236
Fig. 5.24.	Load-Displacement Curves for Tension Specimen Constructed with a Random Bonded Particle Assembly Model (Bažant et al. [7]).....	237
Fig. 5.25.	Diagram Showing Elastic-Softening Constitutive Model for Modified Mark 3 Failure Criterion with Elastic Unloading Scheme	240
Fig. 5.26.	Diagram Showing Equivalent Continuum ‘Diamond’ Area of PSM Mesh Associated with Individual Link Elements for Mark 4 Failure Criterion	243
Fig. 5.27.	Diagram Showing a) a General Arrangement of Uniaxial Strain Gauges (after Kalu [45]) and b) the Equivalent Arrangement for Inter-Particle Link Elements in a PSM Mesh	244
Fig. 5.28.	Diagram Showing Construction of Averaged Strain Tensors in Intra-Element Triangles and Inter-Particle Link from Uniaxial Strains in Individual Inter-Particle Links.....	246
Fig. 5.29.	Diagram Showing Elastic-Softening Constitutive Model for Mark 4 - Continuum Total Strain Failure Criterion for the PSM	248
Fig. 5.30.	Flow Chart Summarising <i>FISH</i> Code for Mark 4 Failure Criterion	254
Fig. 5.31.	Load-Displacement Plots for the Two-Dimensional Uniaxial Benchmark Model with the Mark 4 Failure Criterion and Prescribed Displacement in the x-direction	256

Fig. 5.32.	Load-Displacement Plots for the Two-Dimensional Uniaxial Benchmark Model with the Mark 4 Failure Criterion and Prescribed Displacement in the y-direction	256
Fig. 5.33.	Load-Displacement Plot for the Two-Dimensional Uniaxial Benchmark Model with the Mark 4 Failure Criterion and Prescribed Displacement in the x-direction Showing Typical Detail of Noise Events in the Post-Peak Behaviour Overlaid with Plot of Number of Failed Elements-Displacement (NB - The Data Points are Marked Every 20th Time Step)	258
Fig. 5.34.	Diagram Showing Application of Out of Balance Nodal Forces to Equivalent Continuum Triangular Elements in Order to Redistribute the Relaxation Stress.....	263
Fig. 5.35.	Flow Chart Summarising <i>FISH</i> Code for Mark 5 Failure Criterion	265
Fig. 5.36.	Load-Displacement Plots for the Two-Dimensional Uniaxial Benchmark Model with the Mark 5 Failure Criterion and Prescribed Displacement in the x-direction	267
Fig. 5.37.	Load-Displacement Plots for the Two-Dimensional Uniaxial Benchmark Model with the Mark 5 Failure Criterion and Prescribed Displacement in the y-direction	267
Fig. 6.1.	Diagram Showing Set-up of Hydraulic Fracture Benchmark Model Mesh.....	275
Fig. 6.2.	Diagram of Initial Hydraulic Fracture Benchmark Model Mesh Showing Only Inter-Particle Link 'Contact Bonds' for Clarity	275
Fig. 6.3.	Plot Showing Net Pressure Profiles along the Length of a Fracture (After Papanastasiou [69]).....	280
Fig. 6.4.	Diagram Showing Detail of Fluid Pressure Application in the Fracture Tip Region in a PSM Mesh.....	281
Fig. 6.5.	Diagrams of Various Fracture and Contact Force Patterns Produced by Numerical Runs during 1st Parametric Study (Test Groups A, B & C) on Hydraulic Fracture Benchmark Model	288
Fig. 6.6.	Diagrams of Various Fracture Patterns Produced by Numerical Runs during 1st Parametric Study (Test Groups D, E & F) on Hydraulic Fracture Benchmark Model	289
Fig. 6.7.	Diagrams of Various Fracture Patterns Produced by Numerical Runs during 2nd Parametric Study (Test Groups G & H) on Hydraulic Fracture Benchmark Model	289
Fig. 6.8.	Diagrams of Various Fracture Patterns Produced by Numerical Runs during 3rd Parametric Study (Test Groups I, J & K) on Hydraulic Fracture Benchmark Model	290
Fig. 6.9.	Diagram Showing Typical Displacement of Hydraulic Fracture Benchmark Model Mesh a) Under Symmetrically Applied Fluid Pressure Forces and Confining Loads b) Under Unbalanced Fluid Pressure Forces and Confining Loads (Arrows Indicate Particle Velocities).....	298
Fig. 6.10.	Typical Contact Force Patterns for Hydraulic Fracture Benchmark Model with Mark 4 and Mark 5 Failure Criteria under Confined Conditions Illustrating High Degree of Distortion in the Mesh Resulting from Overall Displacement in the y-direction.....	309

Fig. 6.11.	Plotted Results from FE Study by Papanastasiou [69] Showing a) Propagating Fracture Width Profiles in an Elastic Medium, b) Propagating Fracture Width Profiles in and Elasto-Plastic Medium & c) Plots of Net Pressure in Wellbore during Fracture Propagation.....	311
Fig. 6.12.	Comparative Results from Test Group A (Runs 001, 002 & 003 - E = 1785.0MPa, $\nu = 0.00$, $\sigma_2 = 0.0\text{MPa}$, $\sigma_3 = 0.0\text{MPa}$) Showing a) Final Fracture Width Profiles, b) Number of Failed Inter-Particle Link Elements in Time during Fracture Propagation and c) Net Wellbore Pressure against Propagating Fracture Length.....	312
Fig. 6.13.	Comparative Results from Test Group B (Runs 004, 005 & 006 - E = 1785.0MPa, $\nu = 0.125$, $\sigma_2 = 0.0\text{MPa}$, $\sigma_3 = 0.0\text{MPa}$) Showing a) Final Fracture Width Profiles, b) Number of Failed Inter-Particle Link Elements in Time during Fracture Propagation and c) Net Wellbore Pressure against Propagating Fracture Length.....	313
Fig. 6.14.	Comparative Results from Test Group C (Runs 007, 008 & 009 - E = 1785.0MPa, $\nu = 0.25$, $\sigma_2 = 0.0\text{MPa}$, $\sigma_3 = 0.0\text{MPa}$) Showing a) Final Fracture Width Profiles, b) Number of Failed Inter-Particle Link Elements in Time during Fracture Propagation and c) Net Wellbore Pressure against Propagating Fracture Length.....	314
Fig. 6.15.	Comparative Results from Test Group D (Runs 010, 011 & 012 - E = 1785.0MPa, $\nu = 0.00$, $\sigma_2 = 9.0\text{MPa}$, $\sigma_3 = 3.7\text{MPa}$) Showing a) Final Fracture Width Profiles, b) Number of Failed Inter-Particle Link Elements in Time during Fracture Propagation and c) Net Wellbore Pressure against Propagating Fracture Length.....	315
Fig. 6.16.	Comparative Results from Test Group E (Runs 013, 014 & 015 - E = 1785.0MPa, $\nu = 0.125$, $\sigma_2 = 9.0\text{MPa}$, $\sigma_3 = 3.7\text{MPa}$) Showing a) Final Fracture Width Profiles, b) Number of Failed Inter-Particle Link Elements in Time during Fracture Propagation and c) Net Wellbore Pressure against Propagating Fracture Length.....	316
Fig. 6.17.	Diagram Showing Typical Fracture Width Profiles for a Propagating Hydraulic Fracture in a PSM mesh.....	318
Fig. 6.18.	Plot Showing Example of Actual Position of Fracture Width Profile Resulting from Overall Displacement of Mesh and Corrected Fracture Width Profile for Comparative Overlay	319
Fig. 6.19.	Diagram Showing Set-up of the Coupled Hydraulic Fracture Benchmark Model.....	339
Fig. 6.20.	Diagram of the Coupled Hydraulic Fracture Benchmark Model Mesh Showing Only Inter-Particle Link 'Contact Bonds' and 'Fluid Particles' for Clarity.....	339
Fig. 6.21.	Diagrams of Various Stages of Fracture Propagation Produced during Run 001 of the Parametric Study on the Coupled Hydraulic Fracture Benchmark Model (Mark 1 Failure Criterion, Zero Confining Pressure, Critical Pressure of 66kPa).....	344
Fig. 6.22.	Diagrams of Various Stages of Fracture Propagation Produced during Run 002 of the Parametric Study on the Coupled Hydraulic Fracture Benchmark Model (Mark 2 Failure Criterion, Zero Confining Pressure, Critical Pressure of 56kPa).....	345
Fig. 6.23.	Diagrams of Various Stages of Fracture Propagation Produced during Run 003 of the Parametric Study on the Coupled Hydraulic Fracture	

	Benchmark Model (Mark 3 Failure Criterion, Zero Confining Pressure, Critical Pressure of 129kPa).....	346
<i>Fig. 6.24.</i>	Diagrams of Various Stages of Fracture Propagation Produced during Run 004 of the Parametric Study on the Coupled Hydraulic Fracture Benchmark Model (Mark 1 Failure Criterion, $\sigma_2 = 75.0\text{kPa}$, $\sigma_3 = 75.0\text{kPa}$, Critical Pressure of 190kPa)	347
<i>Fig. 6.25.</i>	Diagram Illustrating Progression of Fracture Development in Coupled Hydraulic Fracture Benchmark Model under Mark 2 Failure Criterion....	351
<i>Fig. 6.26.</i>	Diagram Showing Deformation of Coupled Hydraulic Fracture Model Mesh after Complete Fracture Propagation	354
<i>Fig. 6.27.</i>	Plots of Number of Failed Inter-Particle Link Elements in Time for the Numerical Runs of the Parametric Study of the Coupled Hydraulic Fracture Benchmark Model	356
<i>Fig. AII.1.</i>	Typical Example of Regular Hexagonally Packed Particle Assembly Employed by the Particle Solid Model.....	400
<i>Fig. AII.2.</i>	Diagram of Simple Loading Case Considered in Order to Derive Granular -Continuum Conversion Factor for Normal Stress in the x -direction	401
<i>Fig. AII.3.</i>	Diagram of Development of Contact Forces on the Particle 'p' Experiencing Normal Stress in the x -direction Showing a) the reaction to external loading and b) the total resulting contact forces on the particle	402
<i>Fig. AII.4.</i>	Diagram of Simple Loading Case Considered in Order to Derive Granular -Continuum Conversion Factor for Normal Stress in the y -direction	404
<i>Fig. AII.5.</i>	Diagram of Development of Contact Forces on the Particle 'p' Experiencing Normal Stress in the y -direction Showing a) the reaction to external loading and b) the total resulting contact forces on the particle	405
<i>Fig. AII.6.</i>	Diagram of Simple Loading Case Considered in Order to Derive Granular -Continuum Conversion Factor for Shear Stress across the y -direction	407
<i>Fig. AII.7.</i>	Diagram of Development of Contact Forces on the Particle 'p' Experiencing Shear Stress across the y -direction Showing a) the reaction to external loading and b) the total resulting contact forces on the particle.....	408
<i>Fig. AII.8.</i>	Diagram Showing Equilibrium Conditions for Particle under Shear Loading Conditions as Shown in <i>Fig. AII.7. b)</i>	411

List of Tables

Table 3.1. Summary of DEM Implementation of Hydraulic Fracture Processes.....	67
Table 4.1. Uniaxial Benchmark Model Input Values for Young's Modulus and Poisson's Ratio and Corresponding Contact Stiffnesses.....	127
Table 4.2. Results of Deformation Analysis for PSM Uniaxial Benchmark Problem.....	129
Table 4.3. Results of Deformation Analysis for PSM Finer Mesh Uniaxial Benchmark Problem	131
Table 4.4. Results of Analysis of Equivalent Continuum Stresses for PSM Uniaxial Benchmark Problem.....	134
Table 4.5. Cantilever Benchmark Model Input Values for Young's Modulus and Poisson's Ratio and Corresponding Contact Stiffnesses.....	139
Table 4.6. Results of Cantilever Benchmark Problem for PSM.....	139
Table 4.7. Results of Pressurised Cylinder Study for the PFM	158
Table 4.8. Results of Lubrication Flow Study for the PFM	166
Table 5.1. Material Properties Applied to Two-Dimensional Uniaxial Benchmark Model.....	196
Table 5.2. Details of Two-Dimensional Uniaxial Model Studies with Mark 1 Failure Criterion.....	201
Table 5.3. Details of Two-Dimensional Uniaxial Model Studies with Mark 2 Failure Criterion.....	214
Table 5.4. Details of Two-Dimensional Uniaxial Model Studies with Mark 3 Failure Criterion.....	230
Table 5.5. Details of Two-Dimensional Uniaxial Model Studies with Mark 4 Failure Criterion.....	255
Table 5.6. Details of Two-Dimensional Uniaxial Model Studies with Mark 5 Failure Criterion.....	266
Table 6.1. Material Properties Applied to Hydraulic Fracture Benchmark Model	276
Table 6.2. Details of Numerical Runs Carried Out for the First, General Parametric Study of Hydraulic Fracture Benchmark Model	284
Table 6.3. Details of Numerical Runs Carried Out for the a) Second and b) Third, Specific Parametric Studies of Hydraulic Fracture Benchmark Model.....	285
Table 6.4. Summary of General Fracture Patterns Produced in Listed Numerical Runs During Parametric Studies on Hydraulic Fracture Benchmark Model.....	287
Table 6.5. Material Properties Applied to the PSM Component of the Coupled Hydraulic Fracture Benchmark Model	338
Table 6.6. Details of Numerical Runs Carried Out for the Qualitative Parametric Study of the Coupled Hydraulic Fracture Benchmark Model	342
Table 6.7. Summary of Critical Pressures Determined in the Numerical Runs Carried out for the Parametric Study of the Coupled Hydraulic Fracture Benchmark Model	343

Notation

Symbols

A	- area
$A_{(bar)}$	- cross-sectional area of a bar element
$A_{(beam)}$	- cross-sectional area of a beam element
$a_{(H)}$	- material constant originally defined as $a = \frac{l}{EA}$ (Herrmann et al. [34])
$A_{(link)}^*$	- apparent cross-sectional area of an inter-particle link element in a PSM mesh
$a^{(p)}$	- acceleration of a particle
[B]	- is the strain matrix for a finite element
$b_{(H)}$	- material constant originally defined as $b = \frac{l}{GA}$ (Herrmann et al. [34])
c	- inter-particle cohesion
$c_{(H)}$	- material constant originally defined as $c = \frac{l^3}{EI}$ (Herrmann et al. [34])
[D]	- is the elasticity matrix fro a finite element
d	- separation between two particles
$\frac{dp}{dx}$	- pressure gradient
E	- Young's Modulus
e	- refers to any inter-particle link element in a PSM mesh
E^*	- apparent Young's Modulus
$E_{(beam)}$	- Young's Modulus of a lattice beam element
$E_{(lattice)}$	- overall Young's Modulus for a lattice of beam elements
e_i	- unit vector between the centres of particles in contact pair
E_s	- Softening Modulus
E_s^*	- apparent Soften Modulus
F	- force acting on a particle

F_{cor}	- corrective forces applied to particle pair to redistribute relaxation stress in Mark 3 and Mark 4 fracture criteria
F_D	- drag force acting on a ‘fluid particle’ pair
F_F	- ‘fluid’ forces acting on a particle, combining repulsion, drag and external pressure forces
$F_{i(beam)}$	- axial force in a lattice beam element
$F_j^{(c)}$	- component of contact force acting on a particle
F_n	- normal force acting on a particle
$F_{P_{ext}}$	- force applied to a particle in representation of externally applied pressure
F_R	- repulsive force acting between a ‘fluid particle’ pair
F_s	- shear force acting on a particle
f_t	- material tensile strength
G	- shear modulus
g_i	- unit vector lying 90° clockwise to e_i
G_f	- specific fracture energy release rate
G_{IC}	- strain energy release rate - equivalent to fracture energy release rate
$G_{(lattice)}$	- overall shear modulus for a lattice of beam elements
h	- lattice element length/characteristic length
$h_{(beam)}$	- height of a lattice beam element
h_{max}	- maximum lattice element length/characteristic length for Mark 3 criterion elastic-softening constitutive model
I	- moment of inertia
$I_{(beam)}$	- moment of inertia of a lattice beam element
$[K]$	- stiffness matrix for a finite element
K_0	- initial lattice element stiffness
K_{IC}	- fracture toughness
K^n	- contact normal secant stiffness
k_n	- normal contact spring stiffness
K^s	- contact shear tangent stiffness
k_s	- shear contact spring stiffness
L	- ratio of overall mesh length to element length in a lattice type model
l	- length
l_0	- original length of a material sample

$l_{0(link)}$	- original length of inter-particle link element in PSM mesh
$l_{(bar)}$	- length of a bar element
$l_{(beam)}$	- length of a lattice beam element
l_f	- fracture length
$l_{(link)}$	- length of inter-particle link element in PSM mesh
M	- moment acting on a particle
m	- mass of a particle
$M_{i,j(beam)}$	- bending moment in a lattice beam element
$m_{(link)}$	- unit vector in the direction an inter-particle link element in PSM mesh
$n_{1(link)}$	- unit vector in the direction of the maximum principal stress in an inter-particle link element in PSM mesh
N_c	- number of contacts on a particle
N_f	- maximum tensile load capacity of a material sample
N_{fail}	- preset maximum number of failed inter-particle link elements
$n_i^{(c,p)}$	- unit vector in the direction from a particle centroid towards a contact
n_k	- unit, outward normal to a surface
N_{link}	- number of broken inter-particle link elements in a PSM mesh
N_p	- number of particles in a volume
P	- applied normal load
P_e	- external pressure on a thick walled cylinder
P_{ext}	- external pressure
P_f	- fracture fluid pressure
P_i	- internal pressure on a thick walled cylinder
Q	- flow rate
Q	- applied shear load
$Q_{i(beam)}$	- shear force in a lattice beam element
$r^{(p)}$	- particle radius
R_D	- radius of influence of drag
r_e	- external radius of a thick walled cylinder
r_i	- internal radius of a thick walled cylinder
r_m	- radius at which measurement is taken on a thick walled cylinder
R_R	- radius of influence of repulsion
S°	- the set of all inter-particle link elements in a PSM mesh

\mathbf{S}_{eff}^o	- the set of inter-particle links considered as <i>candidates for failure</i>
\mathbf{S}_{se}^o	- the set of inter-particle links considered as <i>softening elements</i>
$\mathcal{S}^{(p)}$	- particle surface
[T]	- matrix of coefficients (for calculation of strain tensor from strain gauges)
T_{ij}	- any Cartesian tensor
$t_j^{(p)}$	- surface traction vector
$t_{(plate)}$	- plate thickness
u	- total displacement
u_f	- fluid velocity
$u_{i,j}$	- horizontal nodal displacement of a lattice beam element
V	- volume
v	- velocity of two particles
V_f	- fracture volume
$v_{i,j}$	- vertical nodal displacement of a lattice beam element
v_n	- normal component of closing velocity of two particles
V_o	- strain energy density
$V^{(p)}$	- volume of a particle
$v^{(p)}$	- actual velocity of an individual particle
V_r	- relative velocity of 'fluid particle' pair
v_s	- shear component of closing velocity of two particles
W_{tot}	- total stored strain energy
x_i	- location coordinates
$x_i^{(c)}$	- location of a contact
$x_i^{(p)}$	- location of a particle centroid
Y	- separation of parallel plates
y	- distance to the point of measurement (lubrication flow)
α	- angle between line joining centroids of particle pair and the global x -axis
α_D	- coefficient of drag
$\alpha_{(l,j)}^{G-C}$	- granular-continuum stress conversion factors (general notation)
$\alpha_{(x,x)}^{G-C}$	- granular-continuum stress conversion factor for σ_{xx} component of tensor
$\alpha_{(x,y)}^{G-C}$	- granular-continuum stress conversion factor for τ_{xy} component of tensor

$\alpha(y, x)^{G-C}$	- granular-continuum stress conversion factor for τ_{yx} component of tensor
$\alpha(y, y)^{G-C}$	- granular-continuum stress conversion factor for σ_{yy} component of tensor
α_R	- coefficient of repulsion
β	- average nodal rotation
γ_{xy}	- shear strain
Δf	- equivalent out of balance nodal forces for a finite element
ΔF_n	- increment of normal force on a particle
ΔF_s	- increment of shear force on a particle
δ_{ij}	- Kronecker delta
$\{\delta u\}$	- nodal displacements for a finite element
$\delta_{x,y}$	- change in length of a material sample in x and y -directions respectively
Δn	- relative normal displacement of particles in contact pair
Δs	- relative shear displacement of particles in contact pair
Δt	- length of the time step
$\Delta \sigma_1$	- relaxation stress - in terms of maximum principal stress
$\Delta \sigma_{1(link)}^{\rightarrow}$	- component of relaxation stress acting in direction of the inter-particle link element - in terms of maximum principal stress
$\Delta \sigma_{(link)}$	- relaxation stress - in the direction of an inter-particle link element
$\{\epsilon\}$	- nodal strains for a finite element
$\epsilon_{1(link)}$	- maximum principal strain in an inter-particle link element
$\epsilon_{2(link)}$	- minimum principal strain in an inter-particle link element
$\epsilon_{(1,2)(link)}$	- continuum total strain in and inter-particle link element as defined by the principal strains
$\epsilon_{a,b,c}$	- uniaxial strain in a strain gauge or equivalent inter-particle link element
ϵ_e	- maximum elastic strain
$\epsilon_{ij(\Delta)}$	- averaged strain tensor in a triangle formed by three inter-particle links
$\epsilon_{ij(link)}$	- averaged strain tensor in an inter-particle link element in PSM mesh
$\epsilon_t(link)$	- uniaxial total strain in an inter-particle link element in PSM mesh
ϵ_u	- ultimate strain
$\epsilon_{x,y}$	- strain in the x and y -directions respectively
$\epsilon_{xx,xy,yx,yy}$	- strain tensor components

θ	- angular velocity of a particle
θ	- angle of rotation relative to defined coordinate system
$\theta_{a,b,c}$	- angle between x -axis of coordinate system and axial direction of strain gauge or equivalent inter-particle link element
$\kappa_{(lattice)}$	- overall bulk modulus for a lattice of beam elements
μ	- dynamic viscosity
ν	- Poisson's ratio
$\nu_{(lattice)}$	- overall Poisson's ratio for a lattice of beam elements
ξ	- coefficient of damping
σ	- stress
$\{\sigma\}$	- nodal stresses for a finite element
$\sigma_{1(link)}$	- maximum principal stress in an inter-particle link element in PSM mesh
$\sigma_{(link)}$	- uniaxial stress in an inter-particle link element in PSM mesh
$\sigma_i^{(p)}$	- maximum principal stress in a particle
$\sigma_{(link)}^{pred}$	- elastic predictor stress <i>a.k.a.</i> effective stress <i>a.k.a.</i> elastic response stress
$\sigma_{i(link)}^{pred}$	- principal elastic predictor stress <i>a.k.a.</i> principal effective stress <i>a.k.a.</i> principal elastic response stress
σ_{ij}	- local stress tensor throughout a volume
$\bar{\sigma}_{ij}$	- averaged stress tensor in a volume
$\bar{\sigma}_{ij(link)}$	- averaged stress tensor in an inter-particle link element in PSM mesh
$\bar{\sigma}_{ij}^{(p)}$	- averaged stress tensor in a particle
σ_r	- radial stress
σ_t	- tensile stress capacity of a lattice element
$\sigma_{x,y}$	- stress in the x and y -directions respectively
$\sigma_{xx,xy,yx,yy}$	- stress tensor components
$\sigma_{xx,yy}^G$	- normal components of granular stress tensor
τ_{xy}	- shear stress
$\tau_{xy,yx}^G$	- shear components of granular stress tensor
$\phi_{i,j}$	- rotational nodal displacement of a lattice beam element

-
- ϕ_μ - inter-particle friction angle
 ω - angular acceleration of a particle

Subscripts

- $(A,B,C),..$ - denotes a triangle formed by three the inter-particle links
(bar) - refers to a framework bar element
(beam) - refers to a lattice beam element
(H) - refers to constants originally defined by Herrmann et al. [34]
 i, j, k - vector or tensor indices $\{i, j, k = 1, 2, 3\}$
(lattice) - refers to an overall lattice of beam elements
(link) - refers to an inter-particle link element in PSM mesh
(plate) - refers to a continuous plate
 t_0 - start time
 t_1, t_2, \dots - incremental time steps; $t_1 = t_0 + \Delta t$ etc.
 x, y - with respect to x and y -directions in the relevant coordinate system

Superscripts

- $(A),(B),...$ - denote individual particles in a contact pair
 $(A,B),...$ - denotes a measurement taken between the particles of a contact pair or in the inter-particle link between them
 $(A,B,C),..$ - denotes a triangle formed by three the inter-particle links
(c) - refers to any contact
G - indicates a granular property rather than a continuum property
G-C - indicates the conversion of a granular property to a continuum property
(p) - refers to any particle
(w) - refers to any wall

Abbreviations

- CGDD** - Christianovic, Geertsma, De Klerk & Daneshy Model
DEM - Discrete Element Model / Distinct Element Method
FE - Finite Element
LEFM - Linear Elastic Fracture Mechanics
LGA - Lattice Gas Automata Method
MAC - Marker-and-Cell Method
MD - Molecular Dynamics
PAF - Particle-and-Force Method
PFC^{3D} - Particle Flow Code in Three Dimensions
PFM - Particle Fluid Model
PIC - Particle-in-Cell Method
PKN - Perkins, Kern and Nordgren Model
PPM - Particle Proppant Model
PSM - Particle Solid Model
SPH - Smooth Particle Hydrodynamics
SSF - Single Software Framework

Chapter 1:

Introduction

1.1. Introduction

Geomechanical problems are usually associated with ground works in civil engineering, mining engineering or petroleum engineering and concern mechanical processes naturally occurring or deliberately instigated in geomaterials. Common examples of geomechanical problems include slope stability, wellbore or tunnel stability, fluid flow in the ground and the construction geotechnical structures such as retaining walls, foundation footings and piling.

In analysing geomechanical problems, extensive use is made of numerical modelling. This firstly allows complex and repetitive parametric analyses to be carried out in the design phase of a particular structure, in order to determine, for example, conditions of stability. Secondly, numerical modelling also allows predictions to be made of developing conditions during the construction phase, in a subterranean environment where observations cannot readily be made. In some cases, predictive modelling of this kind may be applied in real time (Hopkins [35]).

Numerical modelling is also applied in researching geomechanical behaviour and related engineering techniques in order to improve understanding and implementation. Particularly in the petroleum industry, this kind of research tends to be driven by a desire to improve efficiency and hence the economy of the techniques employed to aid the commercial extraction of hydrocarbons, the execution of which may account for a significant portion of the overall cost of extraction and processing.

Whatever its purpose, numerical modelling of geomechanical problems can encounter many difficulties. Firstly, the problems themselves are often complex and secondly, they may involve complicated combinations of various material phases. In

their natural situation in the ground, it is common for fluids such as water, oil and gases, occurring naturally or as a result of the actions of man, to be present within a geomaterial. Thus, for a specific problem it may be necessary to employ a coupled multi-physics model that can handle the interactions of solid, liquid and gaseous material phases.

Furthermore, it can be difficult to determine the most appropriate type of model for a specific problem. While for large-scale problems, where the overall material behaviour is of concern, continuum mechanics models may seem appropriate, it can be difficult to justify the description of a geomaterial as a continuous material. Firstly, on a micro-scale, geomaterials generally consist of granular or particulate matter, which may be loose, as in the case of soils, or cemented, as in the case of concrete and rock, and secondly, on a meso- or even macro-scale, cemented geomaterials are usually divided, by sets of joints and fractures, into larger blocks. While continuum mechanics models can represent the properties of granular and fractured material through a smeared approach and similarly allow the introduction of propagating fracture behaviour, such models generally consider localised stress concentrations and strain energy dissipation, for example around a fracture tip, whereas this behaviour tends to be more widely distributed in a granular material (Bruno et al. [11]). Hence, for cases in which micro-scale granular behaviour is of interest or where the representation of meso- and macro-scale fractures as discrete features is important, as, for example, may be the case where the action of a fluid phase must be accounted for, a discrete model may be more suitable. However, a drawback of discrete models is that a large number of individual elements may be required, especially when considering grain-scale phenomena, and this can lead to extensive computational overheads, thereby making it less feasible to model large-scale problems.

As can be seen, finding a numerical method that can represent the contradicting requirements of the processes acting in a given geomechanical problem can be difficult and often a compromise is required that typically results in one or more processes being treated less accurately than others and less accurately than would be ideally desired. These difficulties are further illustrated by the test case described in the following Section.

1.2. Geomechanical Test Case

A typical example of a geomechanical problem, which illustrates the various difficulties discussed above, is the modelling of hydraulically driven fractures. Hydraulically driven fractures are very common and have enormous significance in many geomechanical fields where they can be created both naturally and artificially. Examples of spontaneously occurring hydraulically driven fractures are, the exploitation of pre-existing joint sets by high-pressure ground water, magma intrusions, welling up from deep in the Earth's crust and, in or around man made hydraulic structures, such as unlined, subterranean aqueducts, mass concrete dams (Visser and van Mier [94]) and offshore structures. Instances of deliberately created hydraulic fractures can be found in many fields of engineering. For example, in *geotechnical engineering*, for soil reinforcement, in *environmental engineering*, where the injection of chemical and radioactive waste has been investigated (Wilcock [96]), in *energy generation*, where applications for geothermal reservoirs have been found (Mendelsohn [56]), and in *petroleum engineering*, for the stimulation of hydrocarbon reservoirs, the re-injection of drilling cuttings from wellbores (Papanastasiou [69, 72]) and for the prevention of sanding and formation failure around wellbores.

By way of an example, the modelling of *Hydraulic Fracture Treatments*, as employed extensively by the petroleum industry in order to stimulate production from old and low permeability hydrocarbon reservoirs, is examined in more detail. The treatments involve the development of hydraulically driven fractures initiated from a wellbore, through the pumping of high pressure fluid, and propagated into the hydrocarbon reservoir. Once in place, the fractures provide high permeability pathways through the rock, increasing the effective permeability of the reservoir and subsequently increasing the potential fluid extraction rate, thereby improving the economics and extending the life of the well. In order to maintain the high permeability pathways when extraction of the hydrocarbons begins, proppant material, similar to sand but often synthetic, is packed into the fractures to hold them open.

The modelling of hydraulically driven fracturing in porous materials is considered one of the most complex problems in fracture mechanics (Visser and van Mier [94]) and requires the coupling of fracture mechanics, fluid mechanics and thermodynamics (Clifford [16], Noorishad [66]). Ignoring the additional difficulties of thermodynamics, it can be summarised that there are five coupled processes to be accounted for when modelling a Hydraulic Fracture Treatment. These processes are; deformation of the reservoir rock matrix, propagation of the fracture, viscous fluid flow in the fracture, leak-off of fluid into the porous reservoir rock, and proppant transport in the fracture (Hopkins [35]) (See *Fig. 1.1.*).

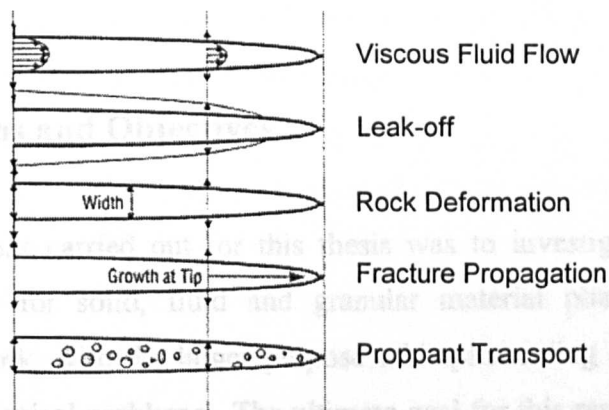


Fig. 1.1. Five Main Processes to be Considered by Hydraulic Fracture Simulators

(After Hopkins [35])

A typical hydraulic fracture, developed during a Hydraulic Fracture Treatment, may be hundreds of metres in length and tens of metres in height and, when considering these dimensions, the five, coupled issues, listed above, may be reasonably described as continuous processes. However, the width of such a fracture is typically only a few millimetres and, in consideration of this scale, it may be more accurate to describe the proppant material as the particulate matter that it is. Furthermore, if the fracture, which must itself be considered as a discrete feature, is propagating in a strong, continuous material, then a continuum mechanics approach may be reasonable, however, if the reservoir material is weak or largely discontinuous, a discrete approach may be required in order to accurately capture the distributed strain energy dissipation behaviour. It can thus be seen that reconciling the behaviour of the five, coupled processes along with

these various considerations of scale and model type can prove very difficult in what is considered a fully three-dimensional problem (Clifford [16]).

The obvious complexities involved in modelling the various material phases involved in Hydraulic Fracture Treatments and the wide ranging significance of the hydraulically driven fracture problem in general, made this a useful geomechanical test case for the work carried out for this thesis. Consequently, while it is hoped that the results of the research presented in this thesis will be generally applicable in modelling geomechanical problems, discussions and benchmark testing focus primarily on the processes involved in hydraulic fracturing.

1.3. Project Aims and Objectives

The aim of the work carried out for this thesis was to investigate the potential for developing models for solid, fluid and granular material phases in a particulate mechanics framework, with the larger purpose of implementing coupled, multi-phase models of geomechanical problems. The ultimate goal for this research was to develop a versatile, single software, multi-physics modelling framework, that could handle both continuous and discrete processes simultaneously, for problems of any scale, without the need for complex coupling or staggered analyses and without the need for compromise in terms of the accuracy or detail with which each separate material phase or process was considered.

The advantages of a particulate mechanics framework such as this, can be argued from the standpoint of providing a highly flexible environment in which complex, coupled phase behaviour could be captured for geomaterials ranging from strong, continuous materials of low ductility, to weak, poorly consolidated, highly deformable materials. Such a framework would naturally handle large deformations and discrete or discontinuous processes commonly encountered in geomechanical problems, such as micro-cracking, propagation of complex fracture patterns, disaggregation and grain movement, without a requirement for remeshing or a loss of numerical accuracy. Furthermore, since the solid, fluid and granular material phases

would be modelled within a single framework, coupling could be achieved without the need for separate meshes, or for staggered or iterative solutions.

1.4. Numerical Work

The computational part of this work involves the creation of several numerical models that represented firstly, the structure and behaviour of solid phase geomaterials, secondly, the behaviour of fluid phase material and finally, the behaviour of granular material. As discussed previously, these models were developed with the intention of combining the individual phase models in any configuration as required in order to investigate multi-physics geomechanical problems.

The models were created using the modelling environment Particle Flow Code in Three Dimensions (PFC^{3D}). This is an existing distinct element modelling (DEM) environment that also allows further development through the addition of user defined routines implemented via a built-in programming language called *FISH* (See Chapter 3, Section 3.3.). The models representing the structure and behaviour of solid geomaterials were created with the concept of constructing a lattice to replace a continuum material. This was similar to the method created by Hrennikoff [36] and more recently explored by Herrmann et al. [34, 19], Schlangen and Garboczi [79], Schlangen and van Mier [80, 81, 82], Tzschichholz et al. [87, 88, 89], van Mier [58, 59] and van Vliet [95]. The models representing the behaviour of fluid phase material were created with the concept of developing a particle representation of a fluid where the particles are free to move with the flow. This was conceived of similar techniques such as Molecular Dynamics (Ercolessi [27, 28]) and Smooth Particle Hydrodynamics (Bonet et al. [10], CSIRO [17], Libersky et al. [49], Lowenstein and Mathews [52], Monaghan [61, 62], Randles et al. [75], SPH at GMU [83]) as well as previously developed discrete particle fluid representations (Harlow and Meixner (1961): cited by Johnson [43]), Zhang et al. [98]). For the modelling of granular material, no additional development work was required beyond the inherent capabilities of the PFC^{3D} DEM code.

1.5. Outline of Thesis

This thesis consists of seven Chapters through which the development of the research work carried out for this project is presented. The content of the Chapters is summarised below.

In *Chapter 2* the histories of research of four fields of computational modelling that were considered during the course of these studies, namely modelling of hydraulic fracturing, lattice modelling, modelling of fluid and modelling of proppant material, are discussed in detail along with reference to their relationships to the work carried out for this thesis.

Chapter 3 begins with a statement of the research proposal for this thesis before discussion is made of the theory underlying the DEM modelling environment Particle Flow Code in Three Dimensions (PFC^{3D}), which was chosen as the basis of the multi-physics particulate modelling framework. Specific proposals are then laid out for the implementation of individual models, within PFC^{3D}, for each of the various material phases to be considered.

In *Chapter 4* the development of the individual models for each of the material phases, the *particle solid model* (PSM), the *particle fluid model* (PFM) and a *combined solid/fluid model* (PSM + PFM), are described in detail. Also described are benchmark tests developed in order to investigate the capacity of each of the models to reproduce basic behaviour for their respective material phases. The results of these benchmark tests are presented and discussed in detail along with the conclusions drawn.

In *Chapter 5* work carried out in order to extend the behaviour of the PSM to include fracturing is described. The evolving development of five failure criteria is discussed in conjunction with the results of tests carried out on a simple benchmark model in which the failure criteria were tested. Results of the tests are discussed in detail and comparisons are drawn both with theoretical results and with the results of similar studies carried out by other researchers. Again, conclusions reached through examination of these results are presented in full.

Chapter 6 contains descriptions of parametric studies carried out with two hydraulic fracture benchmark models. The first of these benchmark models considered a reproduction of a finite element model developed for a previous study of hydraulic fracture propagation behaviour (Papanastasiou [69, 70, 71, 72]). The studies carried out with this model were designed to test the capabilities of the particulate modelling framework to capture the interaction of solid, fluid and fracture propagation behaviour in a pseudo-realistic multi-phase representation of a geomechanical problem. The second benchmark model was of a qualitative nature and the parametric study was designed to evaluate the ultimate potential of the particulate modelling framework. The results of both of these studies are reported and discussed in detail and the conclusions arrive at are presented in full.

In the *final Chapter*, a statement is given of the findings and conclusions reached after examination of the results of the studies presented in the preceding Chapters. This is accompanied by suggestions for the desired progression of this work, beyond that which has been achieved in the course of these studies. A summary of the overall performance of the multi-physics particulate modelling framework is then presented and comparisons are made with possible alternative modelling schemes in order to highlight the advantages and disadvantages of the particulate framework. In the final section of the thesis, a discussion is made of the implications of this work for the overall study and future development of the fields of lattice type modelling and particulate mechanics modelling frameworks.

Chapter 2:

Review of Modelling Frameworks

2.1. Introduction

This chapter presents a summary of modelling methods developed, by various other research groups, for previous investigations into geomechanical problems, with particular reference to the growth behaviour of hydraulically driven fractures and other related research topics. Firstly, the discussion will focus on the general trend in hydraulic fracture model development before moving on to look at the histories of research in three areas of specific interest to the work carried out for this thesis; lattice modelling, modelling of fluid and models concerning proppant transport.

In addition to the presentation of the research histories, discussion will be made of the techniques and findings of these investigations and of their relevance to the work to be undertaken in this project. It may be noted that, for clarity, discussion of this kind appears in italicised text.

2.2. History of Hydraulic Fracturing Research

The mechanisms and growth behaviour of hydraulically driven fractures have been under investigation for some 40 years. Research has been driven primarily by the oil industry and the goal of designing the most economical fracture treatments possible in order to reduce the high costs involved in stimulating hydrocarbon reservoirs (See Chapter 1, Section 1.2.). In order to do this, the best possible understanding of the mechanisms involved in the growth of hydraulically driven fractures is required. With a complete knowledge of this behaviour, it should be possible to optimise the fracture length, the fracture width, the fracturing fluid type and the pumping schedule (Economides and Nolte [26]) so that fracturing is limited to precisely the rock layers in

which it is required, i.e. the reservoir payzone. Precise fracture placement is also critical in other applications such as toxic waste injection where it is highly desirable that the waste does not contaminate aquifers that may be used for drinking water supplies. Furthermore, in civil engineering a complete understanding of hydraulically driven fracture behaviour may lead to more economical designs for hydraulic structures, such as dams, unlined tunnels and offshore structures, where undesired fractures of this kind can significantly reduce stability. Other applications, not necessarily driven by economic motives include the study of magma driven fractures (Lister [50, 51]).

In the field, during the application of hydraulic fracture treatments to reservoir formations the only pieces of feedback information available at the wellhead are, typically, the pump rate and the downhole pressure. In some instances, it has been possible to acquire extra data, either from tilt metres on the surface or by measuring acoustic emissions as the fracture propagates. However, these techniques add to the cost of the treatment and in the field they are often impractical, especially in the offshore environment (Tzschichholz and Herrmann [88]). It is for these reasons that it has become the practice to carry out a numerical simulation of a fracture treatment before it is implemented in the field. As could be expected a great deal of importance has been placed in the development of the fracture simulators and research is focused on modelling the processes associated with hydraulic fracture growth as accurately as possible.

As mentioned in Chapter 1, Section 1.2. it is understood that hydraulically driven fracturing of porous materials is one of the most complex problems in fracture mechanics (Visser & van Mier [94]) and that it is strongly influenced by the interaction of solid and fluid mechanics and by thermodynamic effects (Clifford [16], Noorishad et al. [66]). While the role of solid and fluid mechanics is reasonably obvious, the significance of thermal effects is illustrated by the fact that a 3000m deep reservoir will have a temperature of around 100°C whereas the fracture fluid may be at only 25°C (Clifford [16]). This differential will induce a large thermal stress that may considerably affect the fracture behaviour. Although thermal effects may not be very significant for the relatively fast process of hydraulic fracturing, they become significant when techniques such as waterflooding are employed in order to improve hydrocarbon recovery. While much of the previous numerical modelling research has focused on the

development of a model that coupled these three mechanisms, the complexities of thermodynamics has meant that thermal effects have been ignored by some hydraulic fracture models. This exclusion is probably acceptable in two situations, firstly, if the object of a certain model is to research a specific aspect of hydraulically driven fracture growth behaviour, in which case complex thermal considerations may obscure the results of the study and secondly, if the hydraulically driven fractures develop in a situation where temperature may not be so important, e.g. fractures in structural engineering applications or in shallow, geotechnical applications. However, the significance of thermodynamic effects in stimulating deep hydrocarbon reservoirs, illustrated above, implies that thermal effects should not be left out of a model that attempts to simulate enhanced hydrocarbon recovery operations in this area. Furthermore, thermal effects cannot be ignored in applications such as magma driven fractures and geothermal energy exploitation.

A fundamental assumption of most models, with or without thermal effects, is that the state of stress in a deep reservoir is such that the maximum principal stress is vertical and the minimum principal stress is, therefore, horizontal. The fractures are assumed to open in the direction of least resistance and consequently, are in the form of large vertical, planar structures (Advani et al. [1, 2, 3], Clifford [16], Hopkins [35], Mendelsohn [56, 57], Ouyang et al. [67], Papanastasiou [69, 70, 71, 72]). This is a simplification that allowed earlier models, limited by computational power, to consider just one or two dimensions but can be justified in that for most cases the fractures will indeed be generally vertical and due to the large ratio of fracture length to width any variation across the width has negligible effect on behaviour. In reality, hydraulic fracture propagation is a fully three-dimensional problem. Despite this, early simulators considered only a one-dimensional analysis of fluid flow coupled with a two-dimensional plane strain fracture model. While perhaps giving a general idea of fracture growth in a simple medium, these models were clearly not sufficient to optimise a hydraulic fracture treatment. More recently, the problem has been modelled in two dimensions and indeed, it was two-dimensional models that were most commonly used in industry from the 1960s through to the 1980s. Some of these two-dimensional models still form the basis of more complex models in use today and are still, themselves, used in certain research investigations (Gu and Leung [33], Unwin and Hammond [90]).

Many of the two-dimensional models use the Christianovic, Geertsma, De Klerk & Daneshy (CGDD) Model (Mendelsohn [56]), coupled with fluid flow models of varying complexity. The solid mechanics part of the CGDD model assumes the fracture to be initiated within an infinitely continuous, homogeneous, isotropic, elastic solid that experiences plane strain behaviour in the horizontal planes. These assumptions are obviously limited in terms of a realistic problem. Natural rock formations are certainly not homogeneous or isotropic and such properties have been shown to have a significant effect on hydraulically driven fracture growth behaviour (Advani et al [2, 3], Clifford [16], Gu & Leung [33], Ouyang et al. [67]). Furthermore, reservoir formations are very likely to contain joints, faults and other discontinuities that may cause the rock not to behave as an infinitely continuous material. However, it has been shown that fractures will cross discontinuities without much change in orientation (Lamont and Jessen (1963), Daneshy (1974), Hanson (1975), Zoback et al. (1977): all cited by Mendelsohn [56, 57]) and given the high confining pressures associated with deep hydrocarbon reservoirs, it is unlikely that the discontinuities will be open. The assumption of an infinitely continuous material can therefore be considered reasonable. Additionally, recent work (Papanastasiou [69, 70, 71, 72]) has shown the assumption of purely elastic behaviour to be inadequate. The studies found that elasto-plastic deformation had a significant effect on fracture shape and growth and is therefore a factor that should be considered by hydraulic fracture simulators, particularly when investigating fracture treatments in weak, poorly consolidated rocks.

In terms of realistic hydraulic fracture problems, the assumption of plane strain in horizontal planes by the CGDD model is very inaccurate. Horizontal plane strain implies that the fracture has rectangular vertical cross-sections in both the xz and yz -planes (See *Fig. 2.1* below). This is analogous to the assumption that the fracture does not spread vertically beyond the layer in which it was initiated. While this is a very desirable outcome for a fracture treatment, it has been shown and is now generally accepted that, this is not the case given that the boundaries between rock strata behave as any other discontinuity (See above).

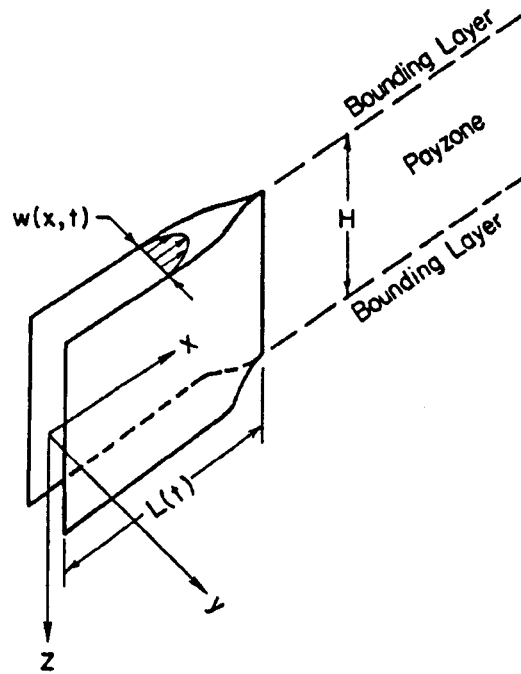


Fig. 2.1. Geometry of CGDD Model Showing Rectangular Cross-Section of Fracture.
(After Mendelsohn [56])

However, although the assumption of horizontal plane strain behaviour may be inaccurate with regard to fractures that have a high length to height ratio, as was typical of fracture treatments until recently, the same assumption can be accepted as reasonable for fractures of low length to height ratio (Mendelsohn [56, 57], Papanastasiou [69, 70]). With the current trend away from long, narrow fractures to short, wide fractures (Papanastasiou [70]) the CGDD model may well be applicable for simulation of new fracture treatments. Furthermore, this type of model can be applicable in certain research applications, where a relatively simple model can be constructed to examine, for example, local behaviour at the fracture tip rather than the overall fracture shape.

This is an approach taken by Papanastasiou [69, 70, 72] and, as discussed in Chapter 6, Section 6.2., it is the simplification applied in the work carried out for this thesis.

The common alternative to the CGDD model is the Perkins & Kern Model, latterly known as the Perkins, Kern and Nordgren (PKN) Model. This also assumes rectangular fractures of constant height but with plane strain behaviour in vertical planes

rather than horizontal. The main difference this produces is that the vertical cross-sections of the fracture in the yz -plane are elliptical (See Fig. 2.2 below).

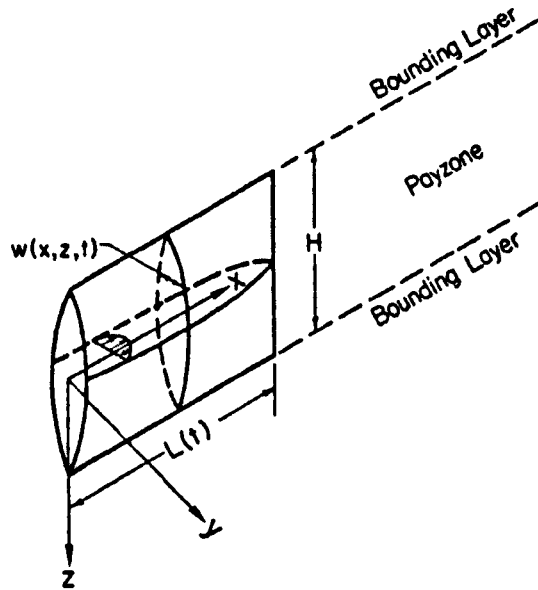


Fig. 2.2. Geometry of PKN Model Showing Elliptical Cross-Sections
(After Mendelsohn [56])

The size of the ellipses varies in time. This approach is far more accurate than the CGDD method in representing the shape and processes involved in hydraulically driven fractures with a high length to width ratio, as discussed above. Geertsma and Haafkens (1976): cited by Mendelsohn [56] suggest that fractures with a length to height ratio above unity should be modelled by vertical plane strain rather than horizontal plain strain. This certainly applies to many hydraulic fracturing treatments designed today. As with the CGDD Model, the assumption of rectangular vertical cross-sections in the xz -plane, implying that the fracture remains within the rock strata in which it was initiated, is a limiting simplification to the modelling of realistic fracture treatments. However, the growing, elliptical nature of the fractures described by the PKN Model would be more easily adapted to multi-layer propagation and so it is a preferable model to the CGDD Model as the basis of a fracture simulator. As mentioned before, the PKN Model still has its place in research where a simplified approach may be sufficient for the investigation of a specific process (Gu and Leung [33], Unwin and Hammond [90]).

The two basic solid phase models, discussed above, have been coupled with various fluid models accounting for fluid flow in one or two dimensions. One-dimensional fluid models consider simple fluid flow along the length of a fracture while two-dimensional models usually consider fluid flow along the length and varying over the height of the fracture. Two-dimensional flow is of more concern in the elliptical PKN fractures than in the CGDD fractures of constant width and it was Nordgren's work (discussed by Mendelsohn [56]) to extended the Perkins and Kern model to include changes in flow behaviour with changing fracture width, that gave the PKN Model its final name. Fluid flow in the third dimension, across the width of the fracture, is usually assumed to have a negligible effect due to the very high length to width and height to width ratios. This assumption may be acceptable for long, narrow fractures, however, in short, wide fractures the width dimension may become more significant. This may be especially true when the short, wide fractures are associated with formation stability and prevention of sanding where fluid pressure gradients are important (See Section 2.4.). Lateral fluid flow and turbulence may also be significant in applications such as proppant transport (Unwin and Hammond [90]) (See also Section 2.5.).

For a full fracture simulation, it is highly desirable to model fluid flow in at least two-dimensions. It is now understood that a fracture will grow beyond the layer in which it is initiated and that this vertical growth, through multiple rock layers with differing properties, results in variation of the width and hence permeability of the fracture over its height. These variations will subsequently cause significant variations in the flow rate and pressure profile over the height of a fracture that cannot reasonably be dealt with by anything less than a two-dimensional flow model.

In addition to the flow regime in the fracture, the fracturing fluid has to be considered and models of simple fluids, obeying Darcy's law and Navier-Stokes law, and complex non-Newtonian fluids have been coupled, in one and two dimensions, with the PKN Model. Fracturing fluids used in practice are often, although not always (Clifford [16]), non-Newtonian, power-law fluids that exhibit complex behaviour such as shear-thinning, where the viscosity decreases with increasing shear-strain rate (Papanastasiou [69]) and viscoelasticity with high normal stresses (Unwin and Hammond [90]). Various studies have considered the inclusion of non-Newtonian fluid

behaviour to be important in fracture growth (Advani et al. [2, 3]), fracture tip processes (Desroches et al. [22], Lenoach [47]) and proppant transport (Ouyang et al [67], Unwin and Hammond [90]), where it was particularly noted that proppant concentration and migration and fluid power-law behaviour were interdependent. It therefore seems reasonable that a fracture simulator should be able to emulate this type of fluid behaviour since it will dramatically affect the development of fluid flow and pressure gradients in a propagating fracture. However, it is understood that this kind of behaviour is complex to describe mathematically and requires sophisticated algorithms that are computationally expensive. As with previous processes, discussed above, it is considered that it may not be necessary to include complex fluid behaviour in every instance, particularly in research concerned with processes not specifically dependent on the fluid flow behaviour or change of pressure.

It was not an objective of the work carried out for this thesis to model complex fluid behaviour in a fracture and so simplifications have been adopted that are consistent with those made by Advani et al. [1] and Papanastasiou [69]. These are discussed in detail in Chapter 6, Section 6.2. and modelling of fluid flow in the fracture is further discussed in Section 2.4..

Several other studies have made additions to the basic PKN and CGDD Models and these include the introduction of heat transfer between the fracture and reservoir fluids, proppant transport (See Section 2.5.) and leak-off of fracture fluid into the porous reservoir rock. Several of these models have been shown to produce good results for their specific purposes (Mendelsohn [56, 57]). Of particular note is the addition of leak-off, a process whereby fluid is lost from the fracture to the porous reservoir rock. Fluid leak-off is considered by some to be a very important factor in hydraulically driven fracture growth behaviour (Bale et al. [6]). Gu and Leung [33], in fact suggest that an accurate estimate of leak-off during a fracture treatment is critical to its success. Furthermore, Lenoach [47] found that, depending on the reservoir permeability, a zone exists, near the fluid front, in which behaviour is dominated by fluid loss. Visser and van Mier [93] also found that parameters describing the interaction of a poroelastic medium with reservoir and fracture fluids strongly affected the initiation and propagation behaviour of hydraulically driven fractures. In a separate study, Visser & van Mier [94] also note that leak-off can affect the efficiency of a fracture treatment by

increasing the pore pressure in the rock, which acts to resist deformation of the material and can counteract the fracture pressure itself. Papanastasiou [72] similarly notes that leak-off can change the effective stress in the reservoir formation and hence change the size of the plastic zones around a propagating fracture tip. However, Papanastasiou also points out that the study in question focuses on the effect of plasticity and not the effect of leak-off, on fracture behaviour.

Once again, from the evidence cited above, it would seem that in order to accurately model a hydraulic fracture treatment, the parameter in question, in this case leak-off of the fracture fluid to the reservoir formation, should be included in a hydraulic fracture simulator. However, when researching specific hydraulic fracturing processes in isolation, it is not necessary, and indeed reduces the clarity of the results of the study, to include leak-off. Several investigations, including Papanastasiou's [72], ignore the effects of leak-off on the grounds that it can be minimised in the field by the inclusion of additives with the fracture fluid that will deposit a filtercake on the fracture boundaries, thereby blocking the flow of fluid from the fracture to the reservoir rock. Given this argument and the evidence presented above, it is perhaps not just leak-off that should be modelled by hydraulic fracture simulators but also the inclusion of additives, their effectiveness in depositing filtercake and the subsequent change in leak-off rate with time. This is the approach originally considered by Carter (1957): cited by Mendelsohn [56]. It should be noted that in order to successfully build up filtercake or, similarly, pack proppant into a fracture (See Section 2.5.) it is necessary that there is a through flow in the fracture. For this to happen leak-off must take place. Therefore, in order to model these processes some account of leak-off must also be made.

The work in this project looks only at simplified hydraulic fracturing situations, mostly based around the work of Papanastasiou, and so it was considered unnecessary to account for leak-off. It is argued that in the case of the hydraulically driven fracture models developed in this work, either filtercake builds up quickly enough to make the effects of leak-off negligible, as proposed above, or that the solid media is of low porosity, which, although not realistic for fracture of hydrocarbon reservoirs, may be applicable to fractures in engineering structures. It is understood, however, that in the case of proppant transport models some account of leak-off will need to be made.

It is now generally accepted that, although desirable, the assumption, by both the PKN and CGDD Models, of a rectangular fracture, fully contained within the layer in which it is initiated, is not correct. If a fracture leaves its original strata then its growth behaviour will be dependent on the material properties of the different layers into which it intrudes and it has been realised that this then becomes a fully three-dimensional problem.

The first step from two-dimensional models towards modelling in three dimensions was the development of models known as pseudo-three-dimensional models (See Fig. 2.3.). These models mostly use the PKN Model as their basis and are a combination of two two-dimensional models, usually coupled iteratively (Mendelsohn [57]). One of these calculates crack growth and fluid flow along the fracture length and the other calculates crack growth and perhaps fluid flow in the vertical direction. The models are coupled at the mid-point cross-section of the fracture both vertically and horizontally so that the maximum height and length are calculated. Despite this, no estimate is made of the overall shape of the fracture between these maxima.

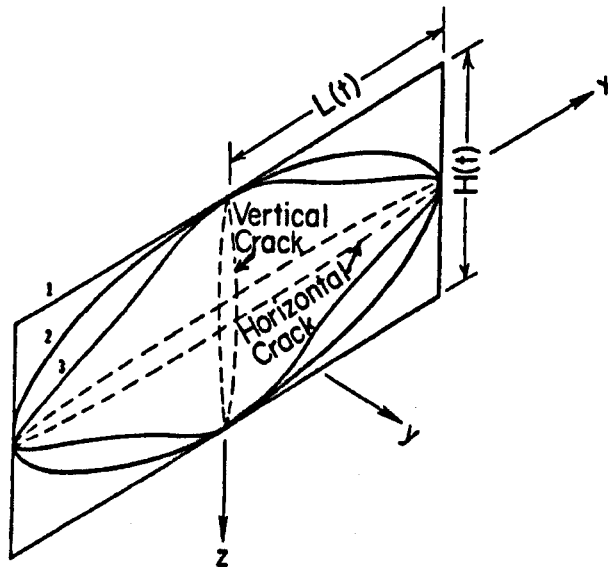


Fig. 2.3. Various Fracture Shapes Assumed by Pseudo-Three-Dimensional Models.
(After Mendelsohn [57]).

Some pseudo-three-dimensional models treat the fracture as rectangular, which would be very similar to the two-dimensional models discussed above, and others assume elliptical shapes. However, the true shape of the fracture may be entirely different and

probably the best estimate by pseudo-three-dimensional models is made by those that are coupled at more than one cross-section in vertical and horizontal directions, thereby calculating several points along the fracture front (See *Fig. 2.3.* above).

Although these models are an improvement over the two-dimensional models, they still make simplifications that are thought to detract from their ability to simulate and facilitate the optimisation of hydraulic fracture treatments. For example, as with the CGDD and PKN Models, on which they are based, pseudo-three-dimensional models assume the fractures are vertical and planar, i.e. the fractures only propagate in the direction in which they are initiated. This is a limitation, as fracture in the ground will tend to deviate around inhomogeneities in the rock. Furthermore, hydraulic fractures are known to turn, shortly after initiation, from opening in the direction of least resistance in the near wellbore stress regime to opening in the direction of least resistance in the far field stress regime. If a model such as this is to be used in the simulation of hydraulic fracture treatments it must be considered to model only the length of fracture beyond any realignment. The planar representation may then be an acceptable approximation of a fracture treatment however, it should be noted that the boundary conditions at the open end of the fracture may not be the same those that prevail in the wellbore. It is, however, doubtful that a pseudo-three-dimensional model would provide the best optimisation possible. It is also hard to see how pseudo-three-dimensional assumptions of fracture shape could really benefit specific aspects of research.

As with the two-dimensional models various assumptions may be made about the fluid behaviour in the fracture. In the case of pseudo-three-dimensional models, these assumptions depend on the assumed fracture shape. Some models assume no pressure variation over the height of the fracture while others use solutions that are more complex. A review of several of these models, based on the PKN and CGDD Models, is given by Mendelsohn [57].

The limitations of the two-dimensional and pseudo-three-dimensional models, described above, and the desire to simulate hydraulic fracture treatments as accurately as possible led to the development of planar-three-dimensional models in the 1980s, in which three-dimensional fracture growth behaviour is considered but in which the

fracture is not considered to turn or rotate out of its initial orientation. More recently, fully-three-dimensional models, in which a single fracture is allowed grow with almost complete freedom, have also been developed. These models have only become of practical use in the field as powerful personal computers have become readily available. As would be expected, these models take into account the elastic response of the solid phase in all directions, but vary in the way that fluid behaviour is dealt with. Three-dimensional fluid behaviour is very complicated and various simplifications, such as laminar fluid flow along the length and possible varying over the height of the fracture, are assumed in order reduce the complexity of the models. This is discussed in more detail in Section 2.4. The simplification of fluid flow in the fracture is probably acceptable for simulation of hydraulic fracture treatments given the typically narrow opening of a fracture and it is probably of more importance to consider an accurate representation of the fracture fluid itself, as discussed previously.

Some three-dimensional models still use the CGDD or PKN Models as their basis. Initially, these models simulated penny-shaped fractures with a radial fluid flow and various developments were made to include the effects of complex processes, such as thermal considerations and fluid leak-off. As the fracture propagated it was assumed to maintain its penny-shape (See *Fig. 2.4.* below).

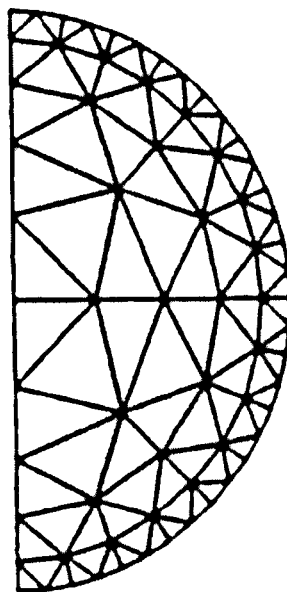


Fig. 2.4. Example of Three-Dimensional Finite Element Mesh Representing Half Length of Penny-Shaped Fracture (After Advani et al. [2])

As with the rectangular fractures simulated by the two-dimensional models it was realised that the simplified penny-shaped fracture was not realistic for the simulation of a full fracture treatment, although it may be suitable for modelling of fractures in their early development, before they leave the bounds of their original rock strata. This is confirmed by Ouyang et al. [67] who found that while the fractures grew within material of uniform properties, they expanded radially and remained penny-shaped (See Fig. 2.5.).

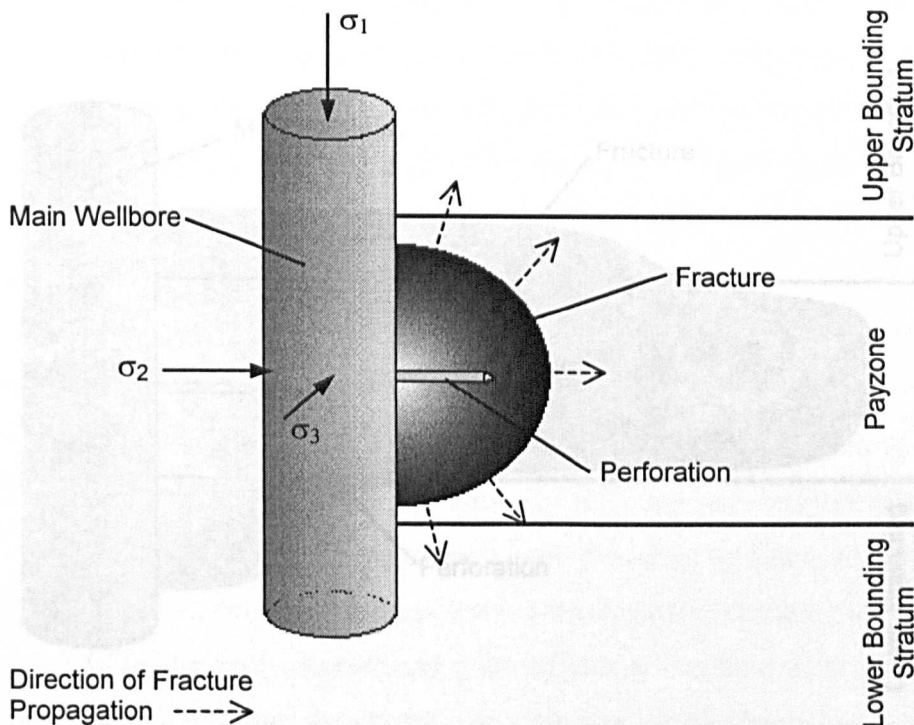


Fig. 2.6. Diagram Showing Variation of Fracture Shape as Fracture Leaves Bounding Strata

Fig. 2.5. Diagram Showing Radial, Penny-Shaped Expansion while Fracture remains within Initial Fracturing Layer

In order to accurately simulate a fracture treatment this research was done. For this reason the penny-shape may also be suitable for certain research applications and this was the approach taken by Clifford [16] where coupling of thermal effects with solid and fluid mechanics was the specific focus of the research and not the developing shape of the propagating fracture. Several variations of the penny-shape were explored such as the elliptical fractures investigated by Advani et al. [2, 3]. These however, remained symmetrical about the horizontal centreline and although closer propagating fracture front these models must employ a remedial scheme or, in the case

approximations of real hydraulic fractures they were still over simplified for the purposes of optimisation.

The height of a fracture in the field is usually governed by the rock strata bounding the payzone, where the in situ stresses and material properties may vary from those of the initial fracturing layer. As the fracture intersects these bounding layers, its penny-shape will be lost and it may develop an essentially arbitrary shape (See Fig. 2.6.).

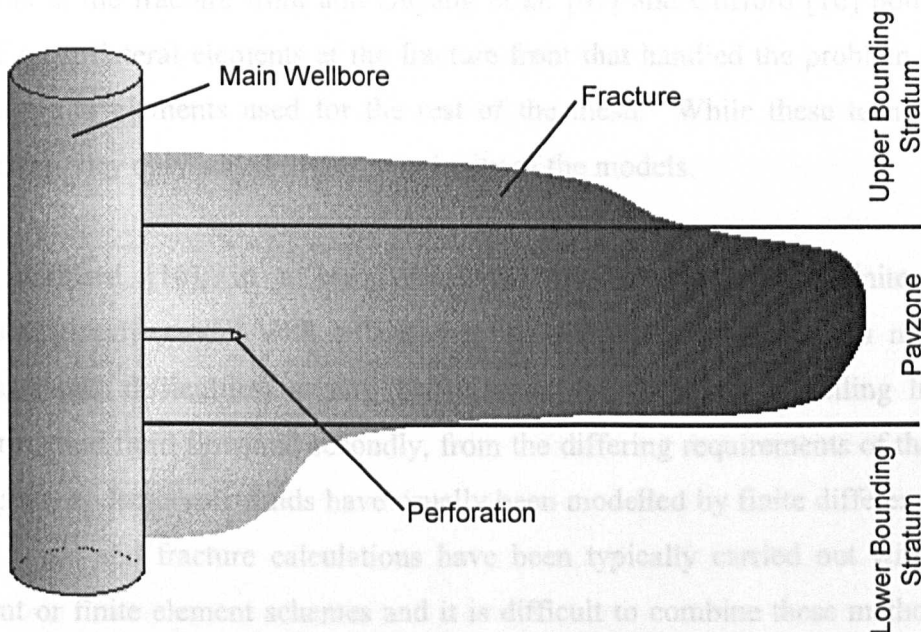


Fig. 2.6. Diagram Showing Variation of Fracture Shape as Fracture Enters Bounding Strata with Material Properties and In Situ Stresses Different from those in Initial Layer

In order to accurately simulate a fracture treatment this arbitrary shape must be reproducible within the model. More complex models such as those developed by Advani et al. [2, 3] and Ouyang et al. [67] deal with these arbitrary shapes quite well and their results illustrate the effects of the differing properties and confining stresses associated with different rock layers. A disadvantage of these finite element (FE) schemes is that they still assume the propagation of the fracture to be linear which, as discussed previously, may not be the case. Furthermore, due to the movement of the propagating fracture front these models must employ a remeshing scheme or, in the case

of Ouyang et al. [67], an adaptive remeshing scheme each time there is a change in the fracture geometry. These schemes can be computationally very expensive, especially for complex fracture shapes. Moreover, a major disadvantage of these models is that they give very poor results when large contrasts exist between the properties of the various rock strata.

A further computational problem commonly noted within three-dimensional models is the presence of a singularity at the fracture tip. In order to deal with this special measures are required. Advani et al. [2, 3] applied special shape functions to elements at the fracture front and Ouyang et al. [67] and Clifford [16] both applied a line of quadrilateral elements at the fracture front that handled the problem better than the triangular elements used for the rest of the mesh. While these techniques were successful, they only added to the complexity of the models.

Clifford [16], in a study involving the coupling of a finite difference fluid/temperature model with a boundary element fracture mechanics model, notes computational difficulties, arising firstly, from the differing modelling histories of fracturing and fluid flow and secondly, from the differing requirements of the solid and fluid phases. Reservoir fluids have usually been modelled by finite difference schemes while stress and fracture calculations have been typically carried out with boundary element or finite element schemes and it is difficult to combine these methods. When they are brought together to model the complex three-dimensional behaviour of hydraulic fractures, further problems arise due to the different meshing requirements for the two phases. Stress would be concentrated at the fracture tip, requiring a fine mesh in this area, while temperature and fluid fronts may be situated elsewhere in the rock medium. The obviously complex mesh involved in catering for all three phases would certainly be computationally expensive to deal with.

Due to the computational effort required it has been felt that pseudo-three-dimensional models are more suited for industry use in the field, as the errors made are acceptable when viewed against their economy. However, three-dimensional models are more accurate and can show the errors made by pseudo- counterparts and furthermore, if computing power continues to increase at present speeds, the three-dimensional modelling will be economic for industrial use very soon. Indeed, Hopkins

[35] mentions the development of pseudo- and planar-three-dimensional simulators that are capable of using real-time feedback from wells during fracture treatments in order to adjust the pumping schedule as fracturing progresses. This kind of analysis must be the ultimate goal in fracture treatment simulation tools although, given that some of these models are still dealing with pseudo-three-dimensional approximations, as discussed above, there clearly remains room for advancement.

While the models discussed above make various reasonable assumptions and approximations of hydraulically driven fracture growth behaviour and have progressed towards solutions capable of facilitating the optimisation of fracture treatments, they have several common disadvantages. Firstly, all of the models described above consider a single, essentially straight fracture, where the model mesh defines the fracture itself while the reservoir is not modelled other than to define the conditions for fracture expansion. With the exception of the models developed by Advani et al. [2, 3] and Ouyang et al. [67] that look at multi-layer formations, none of these models consider the reservoir material as anything but homogeneous and isotropic, leading to a single, straight fracture. However, in reality a fracture may deviate around a harder area of rock, shift latterly as it crosses a discontinuity or develop branching and sub-fractures. Furthermore, as mentioned previously, fractures are known to change direction when going from the near well stress regime to the far field stress regime, but the models discussed would not allow for this. Perhaps a better approach would be to firstly, model a region of reservoir around the wellbore that is to have a fracture treatment applied and then model the treatment itself. It is appreciated that, to use this approach and cater of all of these factors, the models would need to become very complex, certainly fully-three-dimensional and would require greater and greater computing power and time to run. As mentioned above, this not acceptable to companies who are looking to optimise the economics of fracture treatments by modelling. There is no advantage for them in spending more time modelling than actually applying the fracture treatments. For the purposes of researching this subject and developing the understanding of hydraulically driven fracture growth behaviour it seems reasonable to make use of simplified models that are concerned with specific processes rather than using complex models, that take into consideration all of the issues described above.

This is the approach taken for the numerical work in this project, although it is hoped that, in the future, the developed modelling framework could be applied to problems that are more complex.

2.3. History of Lattice Modelling

(with Particular Reference to Hydraulically Driven Fractures)

2.3.1. Background and Development of Lattice Models

In the early 1940s, the framework method was developed by Hrennikoff [36] as a technique to overcome the mathematical complexities in the solution of differential elasticity equations applied to the analysis of continuous mechanics problems. The underlying principle of this technique is the substitution of the continuum with a lattice of bar elements such that the framework behaves, mechanically, exactly as the continuum would. The equations developed for the framework elements, describing the resolution of forces as for a planar truss, are relatively simple and, unlike the differential equations of elasticity theory, can always be solved.

The models developed by Hrennikoff [36] consisted of regular arrangements of simple truss elements that were capable of carrying only axial loads. To calibrate the properties of the truss members, in order to reproduce the behaviour of the continuum material to be represented, Hrennikoff developed various formulations, for various lattice configurations, by rearrangement of the equations of elasticity. These formulations calculated the required cross-sectional area for the truss elements. Hrennikoff concluded that, in order to arrive at a regular, plane stress lattice, Poisson's ratio, ν , had to be fixed at $\frac{1}{3}$ for a triangular lattice configuration. He found the value of $\nu = \frac{1}{3}$ was also required for square and oblong lattice arrangements with diagonal bracing and, finally, that a complex arrangement of concentric squares braced by diagonal members was required in order to reproduce an arbitrary value for ν (See Fig. 2.7. below). (NB - given that Hrennikoff was dealing with frameworks of pin-jointed bar elements, diagonal bracing members would have been required in square type formations in order to ensure stability of the structural configuration).

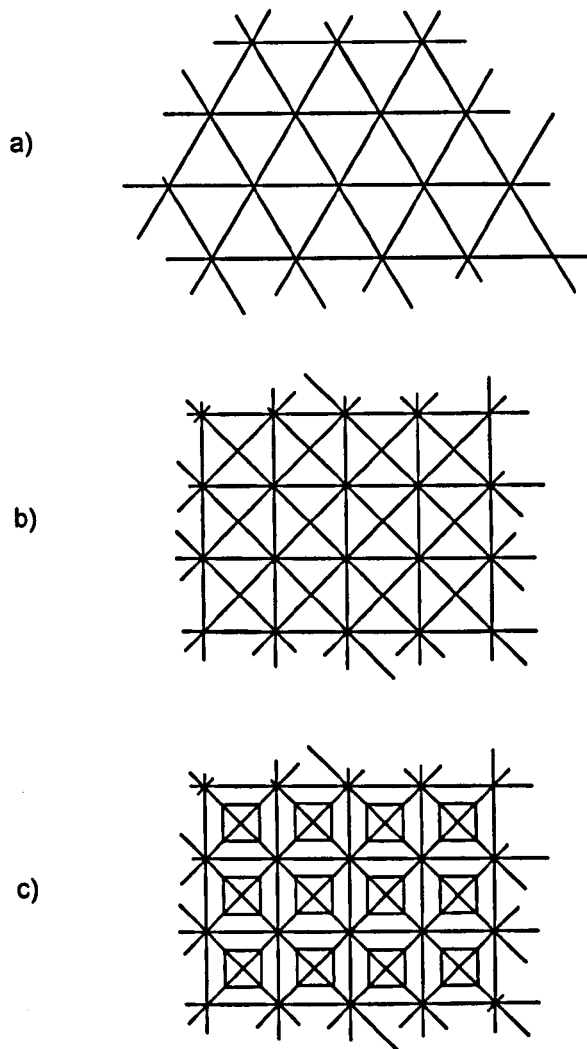


Fig. 2.7. Examples of a) Triangular Lattice Arrangement, b) Square Lattice Arrangement, c) Hrennikoff's Lattice Arrangement for Arbitrary Poisson's Ratio

Hrennikoff successfully applied the framework method to problems of two- and three-dimensional stress and of bending of plates and cylindrical shells, and notes that the fixed value of $\nu = \frac{1}{3}$ is reasonably close to that of the metals in which he was interested. This value is also reasonable for certain rock types and so the simple trusses may be an acceptable approximation for some problems.

In the 1980s, the framework method came back into fashion and found a new application in statistical physics where networks of springs were investigated (Feng et al. [29]). In addition to this, several groups began to look into Hrennikoff's original use for the framework method and applied the technique to various heterogeneous materials,

for example, concrete and rock (Schlangen and Garboczi [79], Schlangen and van Mier [80, 81, 82], Tzschichholz et al. [88, 89], van Vliet [95]). Lattice models were chosen as a new approach to modelling of these materials because of the ease with which material heterogeneity can be reproduced, simply by applying different properties to individual elements or groups of elements during the calibration process. It was also argued that, if the lattice elements are of suitable size, it is possible to pick up even the high degree of heterogeneity associated with concrete at the aggregate scale (Schlangen and van Mier [82]).

Recent studies have tended to use regular, simple lattices, in either triangular or square configurations, consisting of beam elements, although the use of random lattice configurations is also discussed (van Mier [59], van Vliet [95]). Beam elements of three types have been studied, particularly by Schlangen and Garboczi [79], that are capable of transferring, firstly, only axial forces, secondly, normal and shear force and thirdly, normal and shear forces as well as bending moments. The first type of element forms a lattice that is analogous to a simple truss as described by Hrennikoff, or a central force spring network as discussed by Feng et al. [29], and has an overall Poisson's ratio fixed at $\frac{1}{3}$. The second type of lattice is similar to a spring network consisting of linear and shear springs and has a variable value of overall Poisson's ratio up to a maximum of $\frac{1}{3}$, when the shear capacity reaches zero and the lattice becomes identical to the first type described. This is clearly a more suitable and desirable model for materials with a range of values for the Poisson's ratio. Lattices consisting of either of these two element types can be considered as a discretisation of a linear elastic continuum. The third element type produces a lattice with a variable Poisson's ratio, up to a maximum value of $\frac{1}{3}$, similar to the two force element, but can be considered as a discretisation of a higher order, Cosserat continuum. Although these multi force elements are capable of representing more complex materials than the simple truss elements discussed by Hrennikoff [36], they are still limited by the maximum value of Poisson's ratio. As mentioned before, the maximum value of $\frac{1}{3}$ is acceptable for many of the rocks under investigation in connection with hydraulic fracturing and so in most cases a lattice model can be a useful tool. In the event that a material with a higher Poisson's ratio is to be modelled then a lattice will not be sufficient unless the complex configurations mentioned above are adopted.

As mentioned above, the beam lattices must be calibrated in a similar fashion to the truss models developed by Hrennikoff, so that the overall behaviour of the lattice reproduces that of the continuum material that is to be approximated. Two distinct approaches to calibration have been taken by different research groups. The first method (Herrmann et al. [34], Tzschichholz [87], Tzschichholz and Herrmann [88]) defines the equations of elasticity for a beam element as shown below. The assumption is made that, as with any structural beams, they can transmit, axial and shear loading and bending moments (See Eq. 2.1. to Eq. 2.6.). (It can be noted that, unlike Hrennikoff's frameworks, the assumption of structural beam elements with the capacity to transmit bending moments allows the use of frameworks in open configurations such as the square lattice adopted by the researches mentioned above).

$$F_{i(\text{beam})} = \frac{1}{a_{(H)}} (u_i - u_j) \quad \text{Eq. 2.1.}$$

$$Q_{i(\text{beam})} = (b_{(H)} + \frac{1}{12} c_{(H)})^{-1} [v_i - v_j + \frac{1}{2} (\phi_j + \phi_i)] \quad \text{Eq. 2.2.}$$

$$M_{i(\text{beam})} = \frac{b_{(H)}}{c_{(H)} (b_{(H)} + \frac{1}{12} c_{(H)})} (\phi_i - \phi_j) + \frac{1}{2} (b_{(H)} + \frac{1}{12} c_{(H)})^{-1} \left[v_i - v_j + \frac{2}{3} \phi_i + \frac{\phi_j}{3} \right] \quad \text{Eq. 2.3.}$$

$$a_{(H)} = \frac{l_{(\text{beam})}}{E_{(\text{beam})} A_{(\text{beam})}} \quad \text{Eq. 2.4.}$$

$$b_{(H)} = \frac{l_{(\text{beam})}}{G_{(\text{beam})} A_{(\text{beam})}} \quad \text{Eq. 2.5.}$$

$$c_{(H)} = \frac{l_{(\text{beam})}^3}{E_{(\text{beam})} I_{(\text{beam})}} \quad \text{Eq. 2.6.}$$

where, $F_{i(\text{beam})}$, $Q_{i(\text{beam})}$ and $M_{i(\text{beam})}$ are, respectively, the normal force, shear force and bending moment in a beam element, $u_{i,j}$ and $v_{i,j}$ are horizontal and vertical nodal displacements of a beam element and $\phi_{i,j}$ are rotational displacements at the ends of a beam element. $a_{(H)}$, $b_{(H)}$ and $c_{(H)}$ are defined as material dependent constants where $l_{(\text{beam})}$, $A_{(\text{beam})}$, $E_{(\text{beam})}$, $G_{(\text{beam})}$ and $I_{(\text{beam})}$ are, respectively, the length, cross-sectional area, Young's Modulus, shear Modulus and moment of inertia of a beam element. NB - for convenience and consistency in this thesis some of the notation in Eq. 2.1. to Eq. 2.6. has been altered from the original text (Herrmann et al. [34]).

Values for the material constants, $a_{(H)}$, $b_{(H)}$ and $c_{(H)}$ were then chosen arbitrarily to define the behaviour of the lattice. This implies that in order to represent a specific continuum material a trial and error approach would have to be adopted, using a benchmark model, altering the material properties of the beam element until the response of the lattice matched that of expected for an equivalent continuum. This process would probably be lengthy and there would seem to be an opportunity for errors to be included given that there are several variables to set for a given material. A better approach would perhaps be to follow the method applied by Hrennikoff and, assuming the properties of the individual lattice elements to be the same as those of the equivalent continuum material that is to be approximated, rearrange the equations described above in terms of the cross-sectional area of the elements.

The second method for calibrating the properties of lattice beam elements looks in to the elastic energy of a unit cell of the lattice under a uniform strain, from which it is possible to derived formulae for the elastic moduli of the lattice beam elements (Schlangen and Garboczi [79], Feng et al. [29]). The equations for a regular, triangular lattice are shown in Eq. 2.7. to Eq. 2.10. below.

$$\kappa_{(\text{lattice})} = \frac{\sqrt{3}}{2} \frac{E_{(\text{beam})} A_{(\text{beam})}}{l_{(\text{beam})}} \quad \text{Eq. 2.7}$$

$$G_{(\text{lattice})} = \frac{\sqrt{3}}{4} \frac{E_{(\text{beam})} A_{(\text{beam})}}{l_{(\text{beam})}} \left(1 + \frac{12I_{(\text{beam})}}{A_{(\text{beam})} l_{(\text{beam})}^2} \right) \quad \text{Eq. 2.8}$$

$$v_{(lattice)} = \frac{\kappa_{(lattice)} - G_{(lattice)}}{\kappa_{(lattice)} + G_{(lattice)}} = \frac{\left(1 - \frac{12I_{(beam)}}{A_{(beam)}l_{(beam)}^2}\right)}{\left(3 + \frac{12I_{(beam)}}{A_{(beam)}l_{(beam)}^2}\right)} \quad -1 < v_{(lattice)} < \frac{1}{3} \quad \text{Eq. 2.9.}$$

For a rectangular beam element, *Eq. 2.9.* becomes (Schlangen and Garboczi [79]),

$$v_{(lattice)} = \frac{\left(1 - \left(\frac{h_{(beam)}}{l_{(beam)}}\right)^2\right)}{\left(3 + \left(\frac{h_{(beam)}}{l_{(beam)}}\right)^2\right)} \quad \text{Eq. 2.10.}$$

where, $\kappa_{(lattice)}$, $G_{(lattice)}$ and $v_{(lattice)}$ are, respectively, the overall bulk modulus, shear modulus and Poisson's ratio of a lattice of beam elements and $h_{(beam)}$ is the height of a single lattice element.

From the equations above it can be seen that Young's modulus, for the lattice as a whole, $E_{(lattice)}$ can be derived as in *Eq. 2.11.* (van Vliet [95]),

$$E_{(lattice)} = 2\sqrt{3} \frac{E_{(beam)}A_{(beam)}}{l_{(beam)}} \left(\frac{1 + \left(\frac{h_{(beam)}}{l_{(beam)}}\right)^2}{3 + \left(\frac{h_{(beam)}}{l_{(beam)}}\right)^2} \right) \quad \text{Eq. 2.11.}$$

NB - for convenience and consistency in this thesis some of the notation in *Eq. 2.7.* to *Eq. 2.11.* has been altered from the original texts (Schlangen and Garboczi [79], van Vliet [95]).

The equations above provide a quick and easy way of calibrating a triangular lattice to represent any continuous material with a given Poisson's ratio and Young's modulus. It is noted by van Vliet [95], however, that these expressions refer to an infinite continuum in which there are no boundary effects. A study carried out by van Vliet, conducting simple uniaxial load tests with lattice models, showed that, provided the ratio of lattice width to element length is high enough (≥ 20), boundary effects are negligible and the expressions above can be considered an acceptable approximation. As mentioned before, with a calibration technique available, it is easy to model heterogeneous material by applying different material properties to the lattice elements in different areas of the lattice. Schlangen and van Mier [81, 82] implement this idea, using the calibration technique above, by overlaying the lattice with a randomly generated, idealised structure of concrete (See Fig. 2.8. a)).

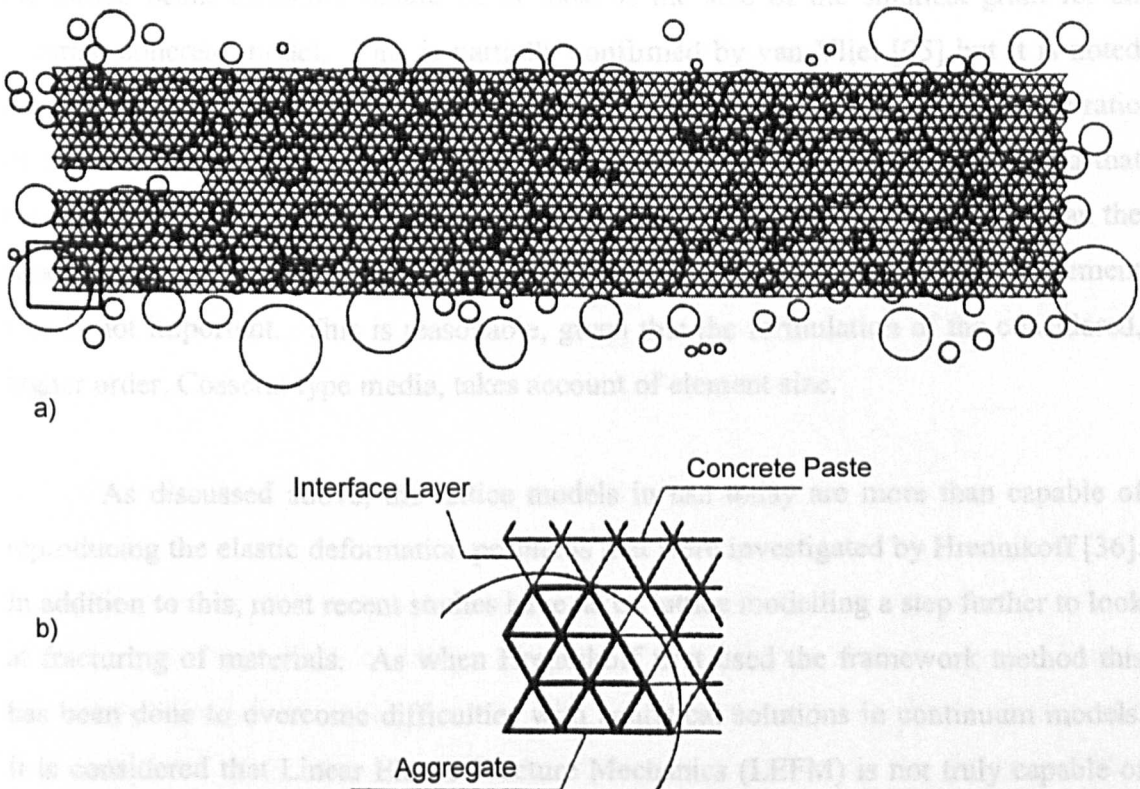


Fig. 2.8. Diagram Showing a) Triangular Lattice Overlaid with Idealised Structure of Concrete Aggregate (After Schlangen and van Mier [82]) b) Detail of Lattice Elements Overlapping Areas of Aggregate and Concrete Paste (After van Vliet [95])

Lattice elements that fall within an aggregate grain are given aggregate properties, different to those given to elements that fall within the concrete paste. This proves to be a very efficient scheme although there are limitations. For example, in applying circular areas, representative of aggregate grains, to a triangular lattice, a perfect match is not possible and some elements will lie between two regions (See *Fig. 2.8. b*). However, various approximations could be developed to overcome this and the problem disappears as the discretisation of the lattice increases. Schlangen and van Mier [81, 82] chose to apply a third material type to elements that overlapped aggregate and concrete paste and define it as an interface layer material.

Obviously, for this differential calibration to be effective the element size has to be sufficiently small in comparison with the material heterogeneities. Following a sensitivity study on lattice element size, Schlangen and van Mier [82] recommend that the lattice beam elements should be at most $\frac{1}{3}$ the size of the smallest grain for an accurate concrete model. This is partially confirmed by van Vliet [95] but it is noted that, although the accuracy of modelling heterogeneities will depend on the chosen ratio of beam length to aggregate size, no optimum value was found. It is concluded that reasonable accuracy will be achieved as long as the lattice elements are smaller than the smallest grain size and it is further implied that for a homogeneous model the element size is not important. This is reasonable, given that the formulation of the considered, higher order, Cosserat type media, takes account of element size.

As discussed above, the lattice models in use today are more than capable of reproducing the elastic deformation problems that were investigated by Hrennikoff [36]. In addition to this, most recent studies have taken lattice modelling a step further to look at fracturing of materials. As when Hrennikoff first used the framework method this has been done to overcome difficulties with analytical solutions in continuum models. It is considered that Linear Elastic Fracture Mechanics (LEFM) is not truly capable of analytically describing the processes associated with fracturing of heterogeneous materials (Schlangen and Garboczi [79]). For example, as with the hydraulic fracture models discussed in Section 2.2., only one fracture is considered by the LEFM model although a heterogeneous material, such as concrete, is likely to experience multiple fractures as branches form, leading away from the main fracture. There is also thought

to be a damaged zone around a fracture caused by micro-crack formation ahead of the main fracture tip that would not be captured by LFM.

When considering fracturing in a lattice model, the lattice beam elements are still considered in the same way a structural beam would be. Pre-failure they are treated elastically according to the material properties assigned to them. In addition to the elastic properties, the elements are also given a failure criterion. This can be chosen depending on the type of behaviour to be modelled, however lattice models are not generally considered to fail in compression. Most recent studies have used a criterion similar to that shown in *Eq. 2.12* where a lattice element is considered to have failed if a combination of axial and bending loads exceed the tensile strength of the beam (Herrmann et al. [34], Schlangen and van Mier [82]). Simpler axial load criteria have also been applied such as that shown in *Eq. 2.13* (Schlangen and Garboczi [79]).

$$\sigma_i < \frac{F_{i(\text{beam})}}{A_{(\text{beam})}} + \frac{\left(|M_{i(\text{beam})}|, |M_{j(\text{beam})}| \right)_{\max}}{I_{(\text{beam})}} \quad \text{Eq. 2.12.}$$

$$\sigma_i < \frac{F_{i(\text{beam})}}{A_{(\text{beam})}} \quad \text{Eq. 2.13.}$$

where, σ_i is the tensile stress capacity of a lattice element.

Whichever failure criteria is applied, once an element is determined to have failed it is removed from the lattice and plays no further part in the analysis. This is consistent with a fully brittle failure. The forces that were transferred through the broken element have to be re-routed through other members in the lattice and this redistribution, and the associated relaxation, is usually assumed to happen fast enough to be complete by the beginning of the next time step (Herrmann et al. [34]). The fully brittle failure criteria and the assumption of an instant stress redistribution take no account of dynamics or of fracture energy distribution. These would seem to be severe limitations for a model of an inherently dynamic problem. However, given the micro-scale of the lattice elements in these investigations ($\sim 1\text{mm}$) and the limitation of

breakage to one element per time step, the small energy release rate could be considered negligible. It is noted by van Vliet [95] that allowing the removal of more than one element per time step reduces computational time significantly but also reduces the realistic possibility of stress redistribution before the beginning of the next time step. It is furthermore argued by van Mier that quasi-brittle materials, such as concrete and rock, exhibit elastic-brittle behaviour at the grain level, while showing overall elastoplastic behaviour, making the lattice model a very accurate representation. In confirmation of this, studies of fracture in concrete and sandstone (Schlangen and van Mier [80, 82]) have shown overall non-linear responses with the application of fully brittle fracture criteria (See Fig. 2.9. a).

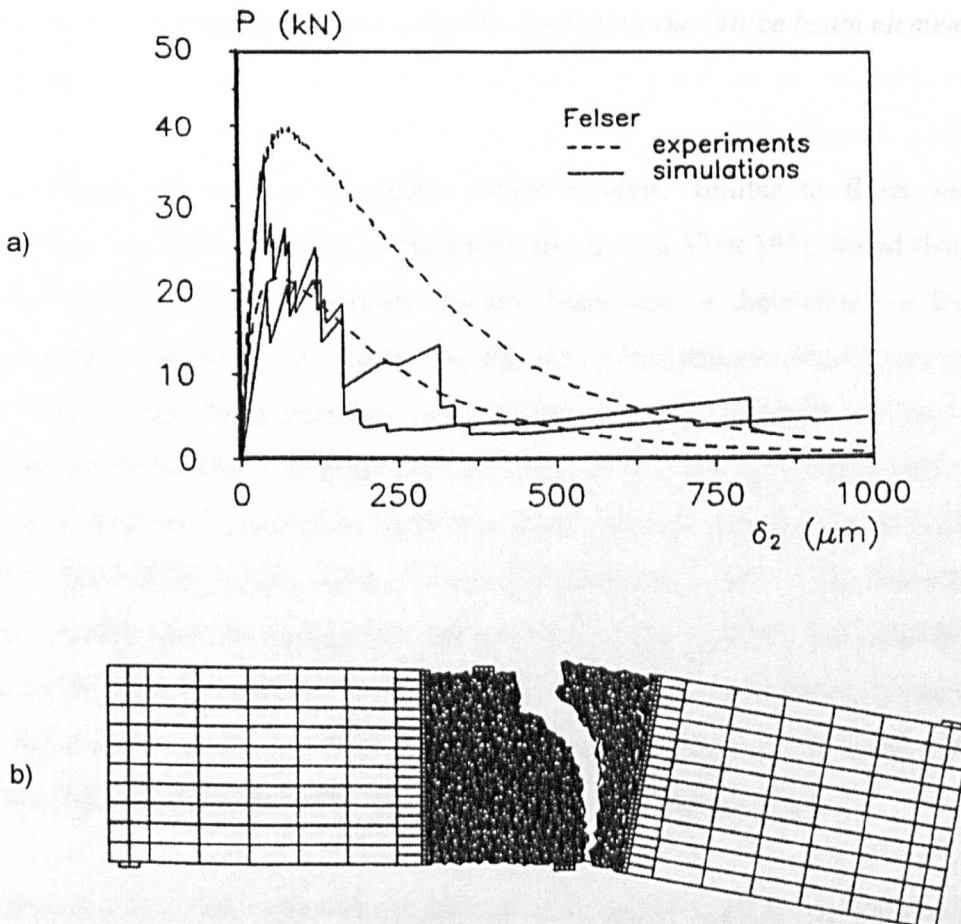


Fig. 2.9. a) Load-Displacement Curves Showing Non-Linear Behaviour for Experimental Studies and Lattice Simulations of a Felser SEN Beam Test b) Crack Patterns in Lattice Simulations of a Felser SEN Beam Test (After Schlangen and van Mier [80])

This was a result also reported by Herrmann et al. [34]. Furthermore, as can be seen in Fig. 2.9. b), the fracture patterns in Schlangen and van Mier's models matched very closely the behaviour of experimental samples and phenomena such as multi-cracking, crack bridging and micro-fracture development were all noted.

It was hoped to be able to reproduce this kind of behaviour in the numerical work carried out for this project. However, differences in the configurations of the lattice models and the scale of the elements meant that more complex failure criteria were required. Furthermore, it was considered appropriate in this work to consider the dynamics of the fracturing process and the fully brittle failure criteria were no longer sufficient. This is discussed in detail in Chapter 5. The scale effect is noted by Chang et al. [14] who suggest that, in order to avoid the use of a very fine mesh, a phenomenological softening criterion could be applied to the lattice beam elements in a courser mesh.

In studies on regular, triangular lattice models, similar to those used by Schlangen and van Mier [80, 82], as discussed above, van Vliet [95], found that, for a lattice with varying element strength, fracture behaviour is dependent on the ratio between stronger and weaker elements. He also found that this produced more realistic fracture shapes than homogeneous, regular lattices where straight fractures were formed. As an alternative to strength variation in a lattice, varying element stiffness can be employed, however, it should be noted that while strength variations do not influence the stress distribution in the lattice, varying stiffnesses would. The concrete and sandstone models used by Schlangen and van Mier were models of a heterogeneous material and as such were given varying strengths and material properties, depending on their location in the mesh, as would seem realistic for a model of this kind. As noted previously, these models produced, qualitatively, very realistic results.

Due to constraints within the modelling environment used for construction of the lattice models in this work, heterogeneity could only be introduced via variation of strength on an individual element basis. It would, however, be possible to vary the stiffness of particular regions of the mesh, for example, in order to model aggregate grains, although with the macro-scale models used in this work, grain scale heterogeneity would not be appropriate. The ability to vary the stiffnesses of lattice

elements is even more applicable when using a non-linear failure criterion where the secant stiffness changes in time. Given that this is not feasible for the models in this work, plasticity must be formulated using initial element stiffness, K_0 .

The finding by van Vliet [95], mentioned above, that homogeneous lattices produce straight fractures rather than the realistic fracture patterns produced by lattices with strength or stiffness variation, has been further considered by other researchers in the field. It is argued by Schlangen and van Mier [82] that the triangular lattice gives the least opportunity for a preferential fracture direction and subsequently straight fractures and for this reason triangular lattices are preferred for the work carried out for this thesis. However, an extensive study of homogeneous lattices with different configurations (Schlangen and Garboczi [79]) found that while triangular lattices showed fewer tendencies than square lattices for a preferential fracture direction and showed a more realistic fracture pattern, different orientations of triangular lattice produced different results, thus showing that some directional preference exists. In addition, they found that the fracture patterns were also heavily affected by the element type. Single force, truss elements produced the least realistic patterns while the three force, Cosserat type, elements produced a good representation of fracture patterns seen in experimental work. However, all types of element were affected, to some extent, by the lattice configuration. The most realistic fracture patterns were seen in a model employing a random lattice configuration with elements of different lengths and orientations. It is commented, however, that, given a fine enough discretisation, a regular, triangular lattice with random element properties or strengths could be expected to produce similar results to the random configuration. On the micro-scale, dealt with by Schlangen and van Mier [1,3] and Schlangen and Garboczi [79], this would seem the most practical approach to a realistic model, given the added difficulties in setting up the mesh and calibrating the properties for a random lattice. Although this is not the main focus of the work in this thesis, the progression to random lattice properties, in a random configuration is a logical one in order to model, as accurately as possible, heterogeneous materials such as concrete and rock. This may be more appropriate for rock than concrete due to the macro-scale of the models employed in comparison with the scale of heterogeneities in the materials.

As mentioned before, the work in this project deals exclusively with triangular lattices of constant stiffness and material properties. However, a rudimentary attempt is made to show the effects of random strength in comparison to complete homogeneity in the lattice (See Chapter 6, Section 6.2.3.3.5.).

Schlangen and Garboczi [79] also note that a directional bias is present in the triangular lattice configuration under uniaxial strain, whereby some elements will carry more load than others will. When the lattice was strained in the y -direction (See Fig. 2.10 below), it was found that a 33% higher stress was reported at fracture than when the lattice was strained in the x -direction. Furthermore, when the lattice was strained in the x -direction, the bonds aligned directly with the x -direction failed, while those at an angle remained intact.

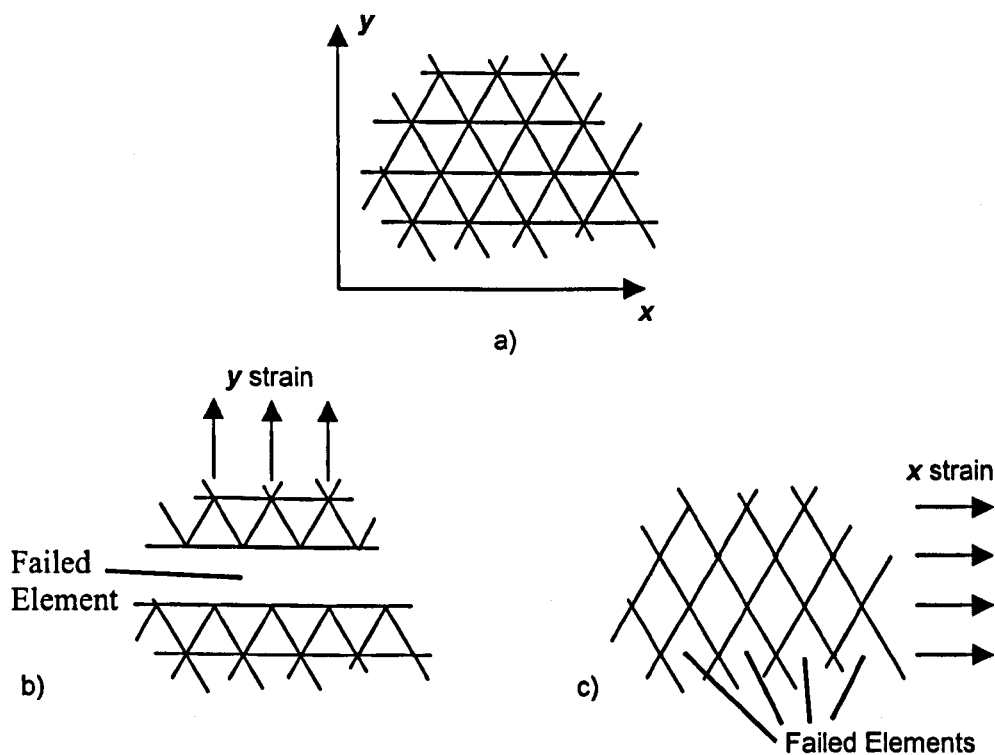


Fig. 2.10. Diagram of Triangular Lattice as Studied by Schlangen and Garboczi [79] Showing: a) the Intact Lattice and Directions of Applied Strain, b) and c) Directional Bias in Fracturing

An inherent lattice anisotropy is also noted by Chang et al. [14] who report that the tensile strength of the modelled concrete is influenced by the underlying lattice

structure. Upon examination of the general deformation and failure processes involved with a triangular lattice, as shown in *Fig. 2.10* above, it is obvious that this directional bias would exist. Similar behaviour was noted in the work carried out for this thesis, where, under prescribed loading, the strain at failure was far greater in the y -direction than it was in the x -direction, consistent with the excess stresses reported by Schlangen and Garboczi [79].

Schlangen and Garboczi overcome the directional bias by implementing what they refer to as the ‘node stress’ for the failure criterion. The ‘node stress’ is calculated from the maximum principal force at a node over the combined cross-sectional area of the beams that lie across the principal direction associated with the force (See *Fig. 2.11*).

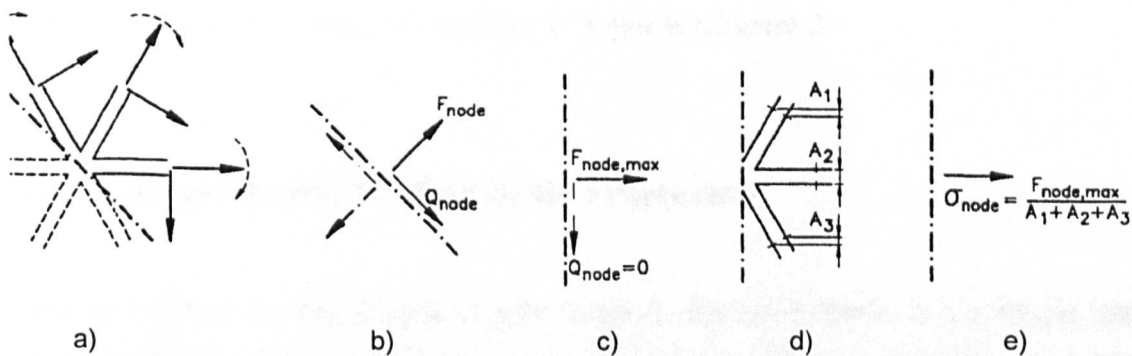


Fig. 2.11. Diagram Showing Procedure for Calculation of ‘Node Stress’ in a Lattice. a) Forces in Lattice Elements b) Resultant Normal and Shear Force Perpendicular to Nodal Cut c) Principal Normal Force d) Cross-Sectional Area of Lattice Elements in Principal Direction e) Nodal Stress (After Schlangen and Garboczi [79])

Applying this homogenisation technique resulted in a clearly defined fracture, at the same level of stress, under strain in either direction, as would be expected for a homogeneous continuum material. However, since the ‘node stress’ defines the stress state at a point, it is no longer possible to implement the more complex failure criteria associated with a structural beam element (See *Eq. 2.12.* above). This was considered a limitation of what should otherwise be seen as a positive advancement of the lattice-continuum equivalence in terms of fracturing and work, discussed in Chapter 5 of this thesis, concentrates on the development of more complex, continuum type fracture

criteria for a lattice model based on a stress and strain homogenisation schemes with similarities to the ‘node stress’ method.

The results of various studies presented above indicate that although lattice modelling is a very versatile technique, that can accurately model complex global behaviour using simple local mechanical models, it has some limitations and inherent inaccuracies relating to mesh dependency. By making use of fine meshes, random variation of material properties and stress homogenisation schemes these dependencies can be overcome to produce apparently realistic fracture behaviour, but care must be taken to ensure that the results represent material behaviour and not model behaviour.

As mentioned, various methods are investigated in this thesis to overcome the problems described above by applying continuum principles to the failure criteria used in the lattice models. These are examined in detail in Chapter 5.

2.3.2. Lattice Models for Hydraulic Fracturing

From the work on fracture of quasi-brittle material, discussed above, it is a simple step to apply forces to a fractured lattice in such a way that they represent the loading that would be experienced by rock during a hydraulic fracturing treatment. Tzschichholz et al. [88, 89] have done exactly this. Their models involved a square lattice from which one element was removed from near its centre. The removed element was replaced with equal and opposite forces acting in directions parallel to the long axis of the removed element (See Fig. 2.12. below).

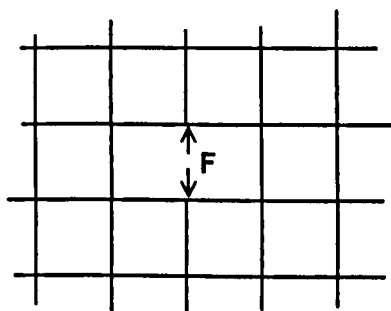


Fig. 2.12. Diagram of Square Lattice with Force Dipole Representing Hydraulic Fracture Fluid Pressure as Used by Tzschichholz et al. [88, 89]

The forces, representing fluid pressure, were increased with time until the strength capacity of one of the adjacent bonds was reached. Fracture behaviour was dealt with as for the lattice models previously discussed and the failed bond was removed. For the purposes of the hydraulic fracture model, it was replaced with a force dipole similar to the original one. This process was then repeated. It was found that in a homogeneous lattice, linear fractures developed and this is consistent with Schlangen and Garboczi's [79] finding that square lattices fail with a strong preferential fracture direction. In contrast to this and again in agreement with the findings of Schlangen and Garboczi, Tzschichholz and Herrmann [88] found that, in a heterogeneous lattice, more realistic fracture patterns developed. The fracture shapes were in fact found to be fractal in nature (See Fig. 2.13. below).

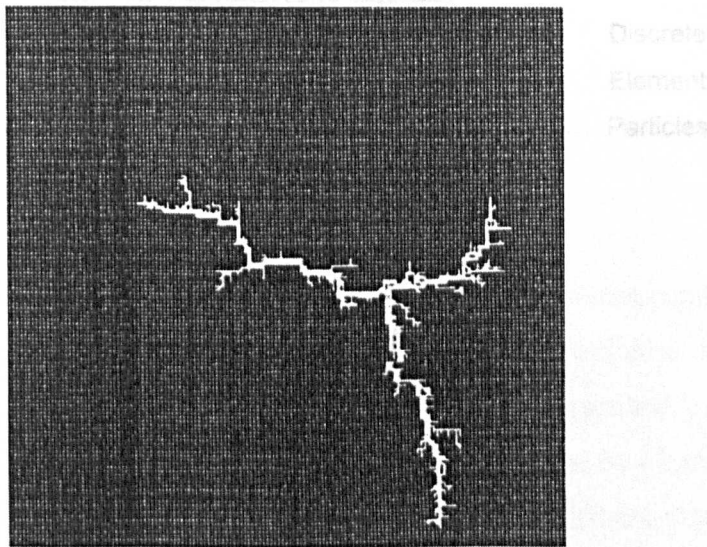


Fig. 2.13. Example of Fractal Fracture Pattern in a Heterogeneous Square Lattice (After Tzschichholz and Herrmann [88])

The hydraulic fracture models developed for this project and discussed in Chapter 6 drew heavily on the work by Tzschichholz et al. and it was hoped to be able to reproduce similar free fracture shapes.

2.3.3. Bonded Particle Assemblies

In a parallel development to the typical lattice models already discussed in this section, several research groups (Bažant et al. [7], Beranek and Hobbelman [8], Chang et al. [14], Bruno et al. [11], Jirásek and Bažant [40, 41], Morikawa and Sawamoto [63]), also realising the difficulties encountered by classical continuum material models and linear elastic fracture mechanics in dealing with fracture of quasi-brittle, heterogeneous materials, such as concrete and rock, have turned to modelling fracture with DEM. In general, the models used in these studies consist of a collection of particles bonded together, thereby producing a structure similar to a lattice model (See *Fig. 2.14* below).

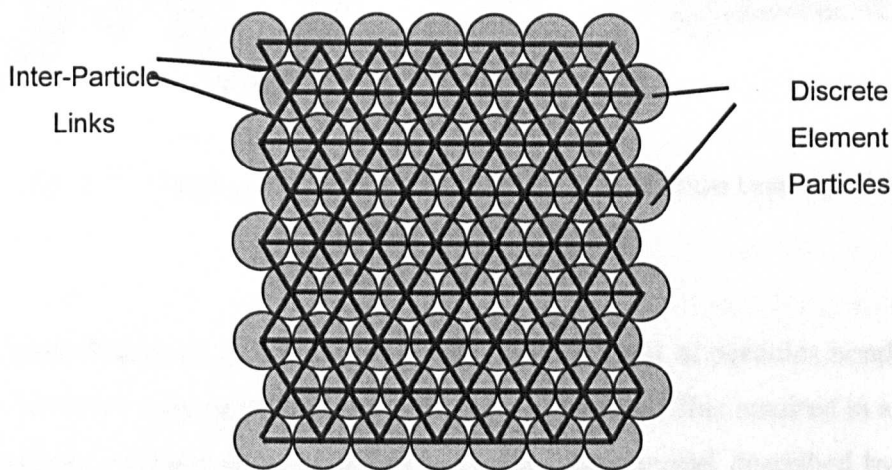


Fig. 2.14. Diagram of Particle-Lattice Assembly

Rather than calibrating the material properties of beam elements in order to reproduce the overall behaviour of an equivalent continuum, here the links between the particles must be given suitable properties. The calibration and the type of material modelled depend on the characteristics of the links. Generally, these links take the form of various combinations of contact springs (See *Fig. 2.15.* below) and these can be related to the different lattice elements, as described previously (See Section 2.3.1.).

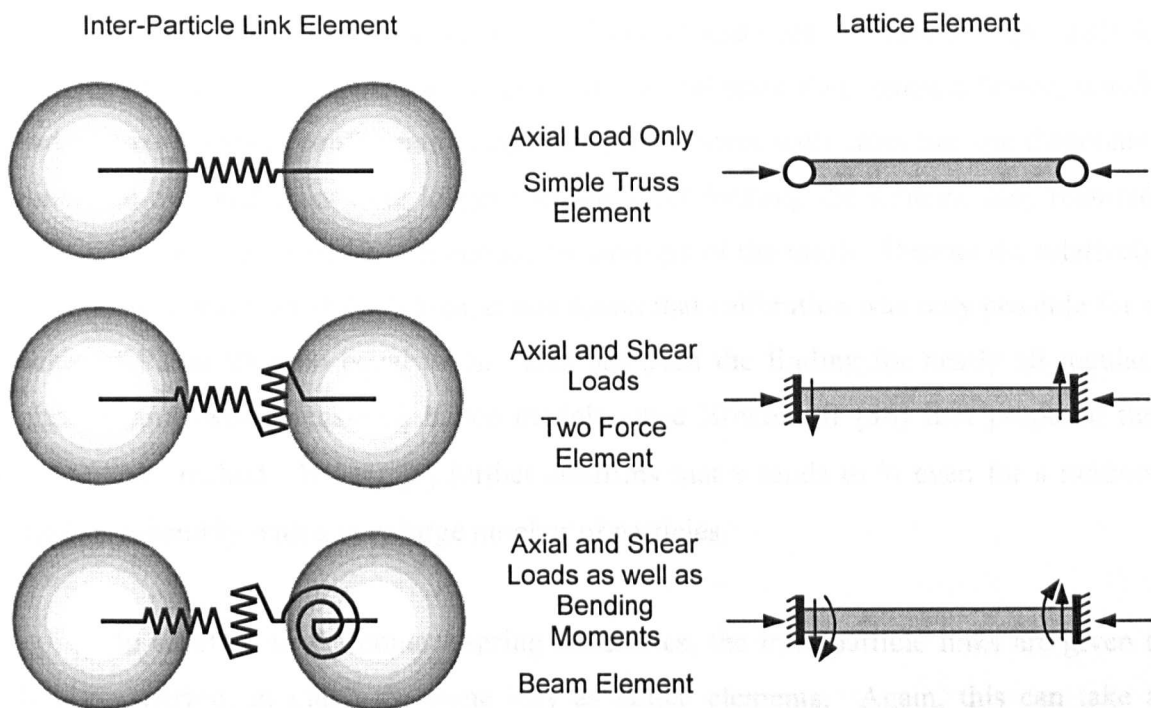


Fig. 2.15. Diagram Showing Various Types of Inter-Particle Links and their Equivalent Lattice Elements

For example, Bažant et al. [7] used a random arrangement of particles bonded together by links that were only capable of transferring axial loads. This resulted in a model that corresponds to a simple truss model or the single force model described by Schlangen and Garboczi [79]. Alternatively, the links in the model developed by Chang et al. [14] consisted of normal, shear and rotational springs. When the stiffness matrix for this kind of link is derived, it is found that, if appropriate spring stiffnesses are chosen, the behaviour will match that of a lattice beam element, as used by Schlangen and van Mier [80, 81], Tzschichholz [87], Tzschichholz and Herrmann [88] and Tzschichholz et al. [89]. Therefore, such a particle model reproduces a Cosserat type continuum.

The calibration of the link properties often follows a similar method to those described by Schlangen and Garboczi [79] and Feng et al. [29], and implemented by Schlangen and van Mier [80, 81, 82] and van Vliet [95], which consider the strain energy equivalence in a typical unit of the lattice. This technique was first proposed for a bonded particle assembly by Morikawa and Sawamoto [63] who developed models with a triangular lattice-type configuration for modelling concrete under impact loading. Their model was similar to the two force lattice, as referred to by Schlangen and

Garboczi [79], where the links consisted of normal and shear contact springs. Jirásek and Bažant [40, 41] followed these principles to calibrate their particle-lattice, which had a more complex configuration, consisting of squares with cross bracing diagonals. Since the diagonal links were longer than the links forming the squares, they required different properties in order to maintain the isotropy of the mesh. Despite the relatively complex construction of the lattice, it was found that calibration was only possible for a value of Poisson's ratio equal to $\frac{1}{3}$. This has been the finding for nearly all regular, plane strain, two-dimensional lattice models since Hrennikoff [36] first proposed the framework method. Bažant [7] further confirms that ν tends to $\frac{1}{3}$ even for a random particle assembly with a very large number of particles.

In addition to the contact spring stiffnesses, the inter-particle links are given a failure criterion, in much the same way as lattice elements. Again, this can take a variety of forms, which can be related to those discussed in Section 2.3.1., for lattice beam elements. Morikawa and Sawamoto [63] used three elastic-perfectly-plastic fracture criteria, for tension, shear and compression, based on the Mohr-Coulomb criteria with a tension cut-off. Failure was assumed to occur at a maximum strain equal to twice the strain at the elastic limit. The Mohr-Coulomb law is a good approximation for concrete and rock behaviour. However, the assumption of elastic-perfectly-plastic behaviour is an obvious simplification of reality. While this may be easier to implement it does not account for the energy dissipation before eventual fracture. Although, Morikawa and Sawamoto [63] reported good results for their model it is felt that a softening model would better represent concrete or rock behaviour. It should also be noted that Morikawa and Sawamoto [63] allow failure of their model in compression. Although this is unusual for a lattice type model however, it is a well known failure mechanism for concrete and so it would seem very desirable to include it. It is not clear, however, how realistic this will be in a particle assembly constructed in a DEM. While the inter-particle links may fail in compression and be removed, the two separated particles, if in contact, will presumably be able to transfer a load in compression.

The models developed for the work carried out for this thesis will not be considered to fail in compression. Simple failure criteria will be applied and tensile fracture will be assumed as the governing failure mechanism.

Bažant et al [7] also applied a plasticity model to the links in their model. In contrast to the model used by Morikawa and Sawamoto, this was an elastic-softening model in which the softening modulus was altered in order to maintain constant fracture energy, G_f (where G_f is the area under the stress-strain diagram multiplied by the inter-particle link length). This is also similar to the constitutive model used by Jirásek and Bažant [40, 41] who note that the parameter having the strongest influence on the overall ductility of the lattice is the fracture energy of the inter-particle links, G_f^* . Given this assertion, it is therefore important that any failure criterion considers the fracture energy. However, Jirásek and Bažant further note that for the fracture energy in a link to be constant the assumption must be made that only one crack forms over its length. Although typical lattice models use fully brittle fracture criteria, they all consider the lattice elements to be either fully intact or completely failed. *This is equivalent to the assumption of single crack formation and this will be the approach used in this work.*

There are several advantages in the use of lattice or bonded particle assembly models for fracture analyses. Firstly, the model mesh represents the rock matrix rather than the fracture as is the case for the finite element models discussed in Section 2.2. (See Fig. 2.16. below). As illustrated in the figure below, this gives the model the freedom to fracture in any direction and open multiple cracks, as determined by the prevailing conditions. There is no need to make assumptions of fracture shape or of propagation direction. Jirásek and Bažant [40, 41] and Bruno et al. [11] also mention the convenience of bonded particle models, especially for the fracture of weak materials where a large fracture process zone develops ahead of the fracture tip and non-local strain-softening damage is inherent in the system. The effects of these processes would be difficult to pick up with the type of continuum models discussed in Section 2.2., however, they are dealt with naturally in a lattice-type model.

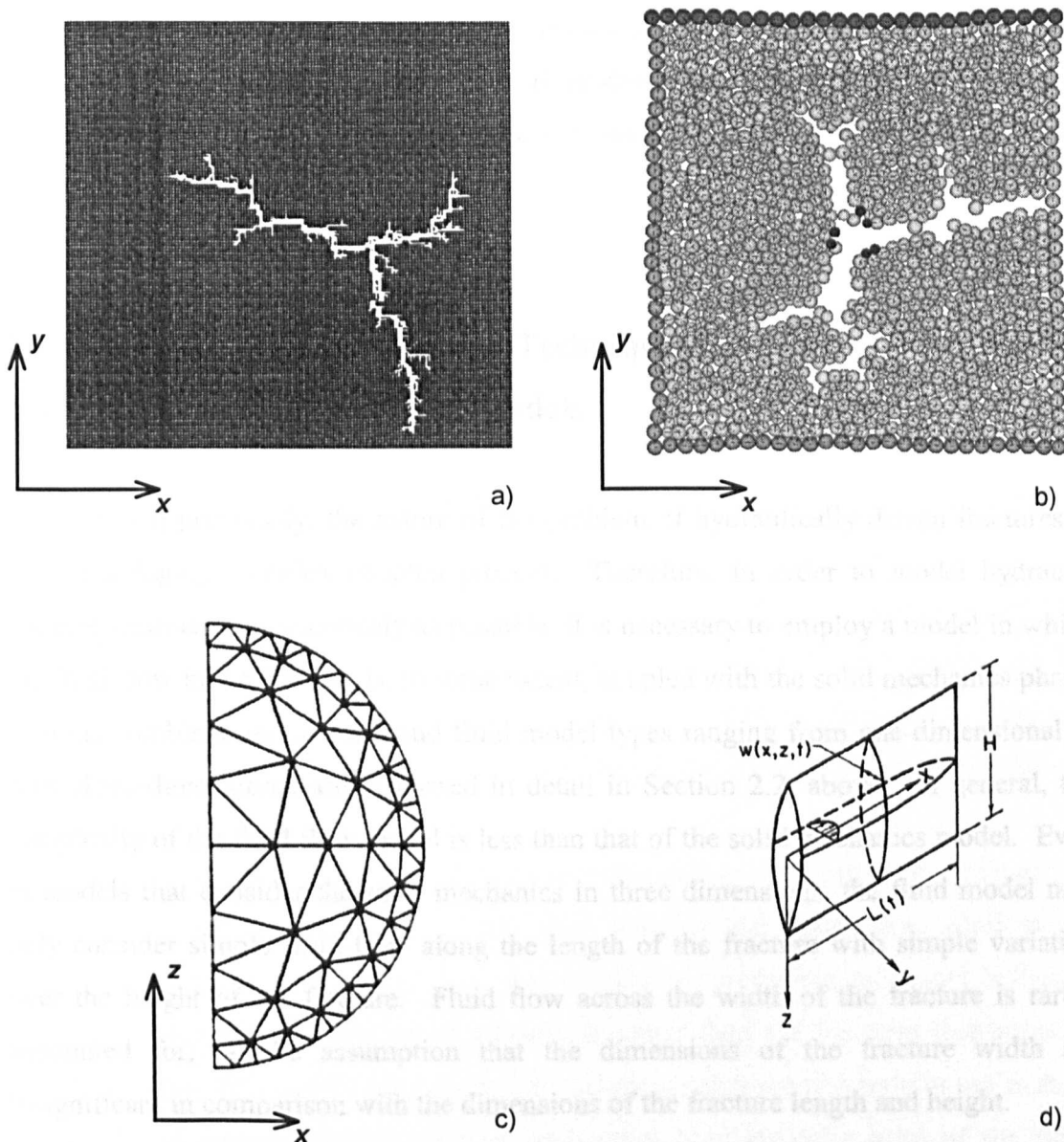


Fig. 2.16. Diagrams Showing Various Model Representations of Hydraulic Fracturing a) Lattice Model (repeated from Fig. 2.13.) b) Bonded Particle Assembly (after Davie [21]) c) Finite Element Mesh of Penny-Shaped Fracture (repeated from Fig. 2.4.) d) Geometry of PKN Model (repeated from Fig. 2.2.)

It is for these reasons that lattice type models were chosen as the basis for the numerical work in this thesis. It is recognised however, that the models discussed here and dealt with in this thesis are all of a two-dimensional format. As such, they can only represent a simple model of hydraulic fracturing, with an assumption of plane strain behaviour in the horizontal plane. As discussed in Section 2.2., this is a simplification of a realistic hydraulic fracture treatment but is adequate for the study of various

specific problems. It is further argued that it should, eventually, be possible to apply all the work carried in this thesis in a fully-three-dimensional version of the considered modelling environment. Although this is well beyond the scope of this project, it is seen as a highly desirable goal.

2.4. Alternative Fluid Modelling Techniques

2.4.1. Current Fracture Fluid Models

As discussed previously, the nature of the problem of hydraulically driven fractures is that of a highly complex coupled process. Therefore, in order to model hydraulic fracture treatments as accurately as possible, it is necessary to employ a model in which the fluid flow in the fracture is, to some extent, coupled with the solid mechanics phase. Various combinations of solid and fluid model types ranging from one-dimensional to fully three-dimensional are discussed in detail in Section 2.2. above. In general, the complexity of the fluid flow model is less than that of the solid mechanics model. Even in models that consider the solid mechanics in three dimensions, the fluid model may only consider simple fluid flow along the length of the fracture with simple variation over the height of the fracture. Fluid flow across the width of the fracture is rarely accounted for, on the assumption that the dimensions of the fracture width are insignificant in comparison with the dimensions of the fracture length and height.

A common assumption for hydraulic fracture models is a lubrication flow regime. Lubrication flow describes steady state, uniform laminar, one-dimensional, flow of an incompressible Newtonian fluid, as would occur between two parallel plates (Douglas et al. [23]). The fluid viscosity is assumed constant and the velocity profile is parabolic with a shear rate of zero at the centre of the flow and increasing towards the edges (Papanastasiou [69]). Although this is accepted as an adequate representation for simple fracture models due to the narrow fracture width and the approximately planar shape of the fracture, studies have shown flow in natural fractures to vary considerably from the parallel plate analogy (Amadei and Illangasekare [4]). This is due to the roughness of the fracture walls and the natural deviation of a fracture through a heterogeneous material, as discussed in Section 2.2. Furthermore, fracturing gels are

often, non-Newtonian, power-law fluids that exhibit complex behaviour such as shear-thinning, where the viscosity decreases with increasing shear-strain rate (Papanastasiou [69]) and viscoelasticity with high normal stresses (Unwin and Hammond [90]). The assumed parabolic velocity profile associated with the lubrication flow model will almost certainly not be an adequate description for a fluid of this type. This kind of fluid may also produce turbulent flow behaviour and this is only examined by a few models specifically designed to test the effects of complex fluids and complex flow regimes. It should be noted that turbulent flow is not a fully understood phenomenon and is an area of concentrated research within the fluid dynamics field. It is by no means simplistic to include its behaviour in a coupled fracturing model. Therefore, a simplified fluid model, such as lubrication flow, is used by fracture treatment simulators in order to reduce the computational effort. Given the difficulties associated with complex fluid models in the context of a coupled hydraulic fracture model and the limitations of the simplified fluid models employed, it may be desirable to look into alternative approaches that may be able to handle complex fluid models more easily.

In addition to the field of hydraulic fracturing, fluid flow in fractures is considered in conjunction with aquifer flow regimes and geothermal applications. Given the assertion, in Section 2.2., that it may be preferable to model hydraulic fractures by modelling a section of a reservoir rather than the fractures themselves it may be appropriate to apply fluid modelling techniques that are currently in use in these fields. Fluid models for this kind of application have typically been of the finite difference type and it is only more recently that they have been combined with finite element methods (Clifford [16]). In this kind of model, flow in the fractures has been dealt with in several different ways. Swenson and Hardeman [84] assume lubrication flow for the fractures in a geothermal reservoir in much the same way as in many hydraulic fracture models, however, Kafritsas [44] assumes the fractures in a rock mass to be a network of line segments, through which, the flow is determined, purely by the fluid head at the nodes of the network. In a third variation, Rouainia et al. [78] assume Darcian flow for the whole rock mass and assign very high values of porosity and permeability to the fractures in contrast to the values for the rock matrix. These models all have some disadvantages. Those assuming lubrication flow or flow through a network of channels, suffer similar limitations to those, discussed above, for hydraulic fracture models. Alternative techniques, such as that used by Rouainia et al., in addition

to applying only a very basic flow model, suffer from the computational expense of recalculating values of porosity and permeability as displacement takes place. This is a similar problem to the remeshing required for FE models when the fluid filled zone changes as is highly feasible in hydraulic fracturing (See Section 2.2.), (Clifford [16]). While these methods are all valid, it seems unlikely that any significant gain would be achieved by applying them to a model for hydraulically driven fracturing. It is therefore considered appropriate to look for a fluid model from an entirely separate field of study.

In contrast to the finite element and finite difference schemes, described above, for fluid flow in fractures and reservoirs, various alternative methods of modelling fluid flow exist and some of these have potential in the field of hydraulic fracturing. These will be discussed in the following Section. Some of these techniques have already been applied to geomechanical problems such as flow through porous media (Jankovic et al. [39]) and debris flows (Rodriguez-Paz et al. [76]) as well as classical hydrodynamic problems such as dam break and hydraulic step problems (Zhang et al. [98]). It is an aim of this project to examine the possibilities of these alternative methods as a more versatile alternative to the continuum methods that are the norm for hydraulic fracturing models.

2.4.2. Particle Fluid Methods

Over the last 45 years, various attempts have been made to solve fluid problems by particle representations. These can take many forms but in general, fluid properties such as density and velocity are carried by the particles and properties such as pressure and viscosity are calculated from the interactions between the particles or by integrating over the region of fluid influence. The advantages of the discrete particle approach are that large movements are dealt with naturally and there is no requirement for remeshing schemes due meshes becoming distorted. While there are other forms of meshless fluid method that do not employ free particles these still require a background grid for the integration of the fluid equations (Bonet et al. [10]).

One of the first particle fluid models was the Particle-in-Cell (PIC) method, which was developed in 1957. This was an Eulerian method that used a combination of particles on a uniform mesh whereby several particles carried mass and position information in each mesh element (Johnson [43]). Field variable could then be calculated by integrating between the particles in each cell. Obviously, this was a very basic code and the background mesh would restrict the model to a predefined region. To avoid this, an adaptive remeshing scheme could be employed but this would obviously revive the problems associated with continuum methods. Nonetheless, the style of this model was still potentially more versatile than a continuum model.

The Marker-and-Cell (MAC) method followed the PIC method in 1965 and is regarded as the first successful technique for modelling incompressible flows (Johnson [43]). The 'marker' refers to particles that are used to locate the material in the mesh and to define the free surface, while the finite difference method is used to solve the hydrodynamic equations. The ability to model free-surface flow is a great advantage and Monaghan [62], writing in 1992, still regards this method as a very flexible and robust model for free surface applications. As with the PIC method, the underlying grid has potential to limit the region of modelling. Furthermore, the MAC method can be difficult to program and, as with the PIC method, can require significant computational effort.

Although the two, early, particle methods described above can accurately and robustly reproduce fluid behaviour the restrictions of the associated background meshes, present in both models, limits their usefulness for a problem such as hydraulic fracturing where the fluid filled domain is likely to vary. For this kind of problem it would be desirable to apply a completely mesh free model. The Particle-and-Force (PAF) method, developed in 1961, was one of the first of this type. It followed similar principles to the PIC method but implemented a Lagrangian scheme and did not require an associated background mesh. The computational points (the particles) were completely free to move. The particles were considered as point masses, of constant magnitude, and interacted with forces that represented fluid like behaviour such as viscous effects. Particles were limited to interact with only their neighbours and their motion was based on the solution of Newtonian equations (Johnson [43]). It can be noted that this scheme is reminiscent of a DEM code and Johnson suggests that it can

also be considered a macroscopic version of Molecular Dynamics (See below). A disadvantage of this type of model is that noise is inherent in flow solutions. For this reason the development team (Harlow and Meixner (1961): cited by Johnson [43]) abandoned the method in favour of more stable techniques.

As mentioned above, Molecular Dynamics (MD) is another meshless method that deals with particle interactions through the application of forces, calculated by means of a certain law, that define the overall behaviour. For atomistic models, this is commonly simplified as a sinusoidal force-separation distribution (van Mier [59]) (See below). In classical molecular dynamics, as with the PAF method, the solution is based on Newton's Second law. Typically, the particle interactions are treated only over a short range, beyond which two particles will not interact.

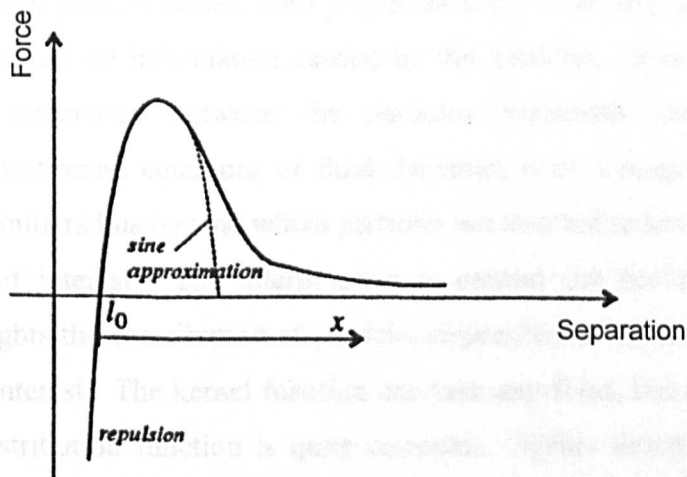


Fig. 2.17. Diagram Showing Typical Force-Separation Law for Atomistic Model with Simplified Sinusoidal Approximation (After van Mier [59])

As with other particle methods, variables associated with the fluid state and thermodynamic variables such as pressure and temperature can be defined and carried by the particles. As the name suggests this method deals with materials at the atomic level and is therefore a micro-scale model in contrast to the macro-scale PAF method. The specific laws describing the particle interaction are therefore associated with behaviour at this scale and are unlikely to be directly appropriate for a larger scale

model. The technique is usually applied in fields such as the study of condensed matter physics, materials science and chemistry (Ercolessi [27, 28]).

One of the most versatile and robust free particle techniques is Smooth Particle Hydrodynamics (SPH). It is a Lagrangian method that was originally designed to study astrophysical phenomena, such as galaxy formation, that involve heat and mass flows (CSIRO [17], Monaghan [61], SPH Group, GMU [83]). Subsequently, it has been extended to model incompressible fluids and free surface flows (Monaghan [62]) as well as mechanical engineering applications such as impact testing (Libersky et al. [49]) and metal forming (Bonet et al. [10]). SPH shares the advantages of other free particles codes in that large movements, complex free surfaces and flow break-up are handled naturally but it has the added advantage of being relatively simple to program.

As with other particle codes, fluid properties such as density, pressure gradients and velocity are based on information carried by the particles. However, rather than looking at the interaction between the particles properties are calculated via interpolation of continuum equations of fluid dynamics over a range of neighbouring particles up to a finite radius beyond which particles are deemed to have no effect on the current volume of interest. The interpolation is carried out according to a kernel function that weights the contribution of particles depending on their distance from the current point of interest. The kernel function can take any form, but a function similar to a Gaussian distribution function is quite common. Spline functions are generally preferred, as they tend to zero at a finite distance. It can be noted that, although any shape of kernel can be used, if the points were fixed in position, the equations would be identical to the finite difference equations.

Given the freedom and versatility of SPH to model free surfaces it may well be suitable for a problem such as the fluid flow in a fracture. However, some technique would have to be developed by which SPH could be coupled to a solid phase model representing the reservoir rock. It may be possible to develop a version of SPH that can itself reproduce solid behaviour, but it is not clear if this will ever be achievable. Alternatively, it may be possible to use SPH to represent solid material as an extremely viscous fluid. However, it is unclear whether fracturing of this type of material would be able to reproduce quasi-brittle material behaviour accurately.

As an alternative kind of Lagrangian particle scheme, Zhang et al. [98] have developed a particle fluid model based on DEM concepts. This is a natural extension of existing DEM models for particle flows and debris slides. Circular two-dimensional discrete element particles were given a mass representative of a square with sides equal in length to the diameter of the element. Fluid behaviour was brought about through particle interaction via contact spring stiffnesses. Although Zhang et al. [98] present a method of relating the DEM dynamic equilibrium equations to Navier-Stokes equation, for the fluid continuum, as the most desirable method of calibrating the particle spring stiffnesses, they calibrate their model with empirical data. Despite this, the DEM contact model would seem to be a reasonable method for fluid modelling and the results of benchmark tests carried out by Zhang et al. [98] look promising. However, it is questionable whether this type of model would be able to deal with a high degree of shear as may be experienced by non-Newtonian, power-law fluids. It is also difficult to imagine this type of contact model successfully dealing with a highly compressible fluid, although this is not likely to be a consideration in a hydraulic fracture model. Furthermore, it is not clear that the model would naturally reproduce a uniform pressure field as would be expected in a near static body of fluid. In the model by Zhang et al., the particles are packed in a regular, square formation and therefore, when a group of these particles is allowed to settle under gravity, they overlap to find an equilibrium position and thus, reproduce a hydrostatic pressure distribution over the depth of the stack. However, in order to develop a hydrostatic pressure distribution in the horizontal direction it is necessary to also overlap the particles in the horizontal direction (See Fig. 2.18. below).

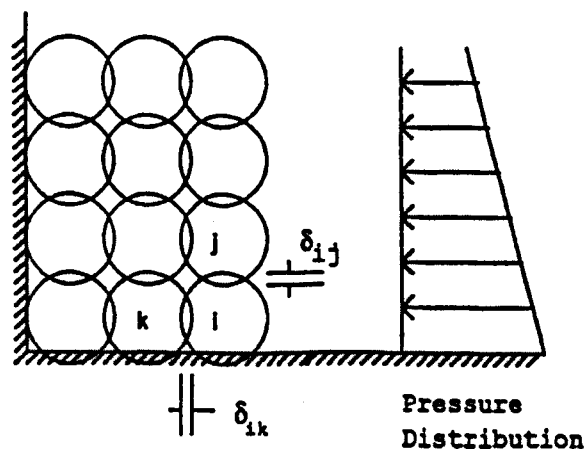


Fig. 2.18. Diagram Showing Overlapping Configuration of DEM Particles Required for Hydrostatic Pressure Distribution (After Zhang et al. [98])

This is not a naturally occurring phenomenon in the model and must be set at the initiation of a problem. Given that the pressure increases with depth, the horizontal overlap must also increase with depth. This results in a stack that is narrower at the bottom than at the top, which may be acceptable for simple benchmark tests but it is difficult to see how the pressure could be transferred to a vertical boundary, as may occur in a coupled problem. Although, in a horizontal plane strain model as used in this work, hydrostatic distributions will not be a consideration, overlaps will need to exist in all directions for a uniform pressure field to be formed. A triangular packing of the particle rather than the square packing used may naturally produce uniform pressure, however, this may affect the behaviour of the model. If these problems proved to be surmountable then, as with the SPH method discussed above, this type of model could be successfully applied to the problem of fluid flow in a fracture. However, again as with the SPH method, a technique would have to be found of coupling the DEM fluid to the solid phase model.

A further variation of the particle fluid method has seen a return to a mesh based method. The Lattice Gas Automata (LGA) method is a statistical model for fluid flow, in which particles move from site to site on a triangular lattice, propagating and colliding with each other according to certain collision rules. The specific rules depend on the type of lattice in use. Although, as with the background meshes associated with other particle methods discussed previously, the lattice would be restrictive in terms of modelling a moving fluid zone, it is possible to rest solid particles on the lattice in addition to the fluid particles and it may be possible to represent the reservoir rock material in this way. The rules for solid-fluid particle collisions would be different to those for fluid-fluid collisions. Furthermore, Jankovic et al. [39 below], in an investigation that applied the LGA technique to the study of moisture transport in concrete, have shown that the LGA method can be used to model flow through porous material. Therefore, the LGA method could equally be applied to the modelling of fluid flow in a reservoir. It may be possible to apply different rules for particle propagation and collision in areas of the lattice where the coupled solid phase model determines fractures to have opened. This would be a similar technique to that used by Rouainia et al. [78] in modelling flow through a porous blocky material (See Section 2.4.1. above). A further advantage of the LGA technique is its stability and robustness. By restricting

particle movements to a lattice the inherent noise associated with methods such as the PAF method is eliminated (Johnson [43]).

In summary it seems that the particle fluid methods described above, and in particular the meshless methods, have significant potential in modelling an advancing fluid front as is consistent with flow in hydraulically driven fractures. While the freedom of these methods would allow fluid flow in multiple fractures in three dimensions simultaneously there are still potential problems with numerical stability and noise in the solutions. Furthermore, a suitable method must be found of coupling the fluid model with whatever model is in place for the solid phase.

2.5. Modelling Techniques for Proppant Transport, Proppant Stability and Sand Production

As mentioned in Chapter 1, Section 1.2. and Section 2.2. above, when a hydraulic fracture treatment is complete, the fracture is often packed with fine grained proppant material in order to prevent the walls of the fracture from closing on each other and to maintain the high permeability pathway through the reservoir to the wellbore. In terms of the success of a fracture treatment in stimulating a hydrocarbon reservoir and increasing the extraction rates, the proppant packing phase is critical and so, as with fracture growth behaviour, significant research has been conducted on the subject. Due to the inaccessible nature of hydraulic fractures in the field, as discussed previously, numerical investigation has formed a large part of the research work.

The proppant material is placed in the fracture by mixing it with the fracture fluid to form a slurry. As the slurry is pumped into the fracture, the fluid phase is lost to the reservoir rock by leak-off (See Section 2.2. above) and the granular proppant material remains in the fracture. When the fracture has been fully packed the pumping process is begun, firstly to remove the fracturing fluid and secondly to begin the extraction of the hydrocarbons.

Two main issues arise at this stage. Firstly, it must be ensured that the proppant material reaches all parts of the fracture and packs it evenly to ensure the most economical use of the fracture. This becomes more important as the fracturing process approaches optimisation, as is the purpose of the research into hydraulic fracture treatment simulation (See Section 2.2.). Secondly, the stability of the proppant after placement is important. When the extraction of the hydrocarbons begins, there is a tendency for proppant material to be dislodged and to travel back up the wellbore with the fluid and as much as 10 - 20% of proppant can be back produced (Asgian et al. [5]). This can cause problems with loss of fracture conductivity, damage to the pumping machinery and downtime, as well as the difficulties associated with separating the granular material from the hydrocarbons (Asgian et al. [5]). There are some wells, however, that despite producing as much as 20% of their proppant do not show significant loss in production. This is thought to be the result of channels forming in certain sections of the fracture, while the fracture remains open due to the stiffness of the rock (Asgian et al. [5]).

Despite the application of various techniques to the prevention of proppant flowback, such as the use of resin coated proppants that bond together in the fracture and the inclusion of fibreglass strands and thermoplastic film strips designed to reinforce the proppant pack, there is still no clear understanding of when to expect flowback or the proppant characteristics that prevent it. There is some evidence, however, that it can be a result of increasing the extraction rate too quickly (Nguyen et al. [65]). Once it starts, proppant flow back can be stopped by reducing production rates or introducing sand control screens downhole. These techniques are undesirable, as they affect the economics of a well. Therefore, a better understanding of the mechanisms associated with proppant flow back is sought in order that other means of preventing it might be found.

A similar problem that can occur in addition to the back production of proppant, especially in low strength reservoir formations, is sand production. This is the out flow of material dislodged from the reservoir rock itself due to tensile or shear failure of the formation, often around the uncased perforations, as the effective stresses change during draw down. As with proppant production this material can damage machinery and needs to be separated from the hydrocarbons. Reducing the draw down in a formation

delays, but cannot prevent its eventual shear failure as reservoir is depleted. As an alternative, it is possible to install screens and gravel packs down hole as in the prevention of proppant flowback. The disadvantage of these screens is that they cause a downhole pressure loss and subsequently affect extraction rates. Both of the discussed measures are economically detrimental to the well and it is therefore important to be able to predict sanding in order to maximise the production rates from the well. Once sanding starts it is often impossible to stop so producers often act conservatively and install sand control mechanisms in wells that may not actually need them. This is obviously not efficient. (General background information on sand production from various referenced sources including Bale et al. [6], Papamichos [68], Papanastasiou [70], Preece et al. [73] and Thallak et al. [85]).

While the three problems described above have separate causes, they are similar in that they all relate to a granular material suspended in a fluid flowing in a fracture. Although the mechanisms resulting in the presence of the granular material are very different, it is argued that the type of model applicable is essentially the same.

The modelling of proppant flow into fractures is often dealt with by continuum based hydraulic fracture models that attempt to simulate the whole course of a fracture treatment in the field (See Section 2.2.). The proppant laden fluid is introduced at some time after fracturing has been initiated and it is essentially modelled as a single phase fluid with smeared properties equivalent to fine grained material suspended in a viscous fluid. The proppant material is not specifically modelled.

Ouyang et al. [67] include proppant transport within their adaptive finite element model with which they have examined the behaviour of fracture growth in layered reservoir formations (See Section 2.2. above). In addition to the propagated shape of the fracture, they look into the distribution of proppant as it penetrates the fracture. This was done by keeping track of the change in the concentration of proppant particles in a unit volume of the slurry based on an initial concentration and depending on various factors such as the change in fracture width, loss of fluid through leak-off and convection flow. A similar technique is applied by Unwin and Hammond [90]. They specifically examined the effects on proppant placement of gravity and convection flow driven by large scale concentration and density differences in different regions of the

fracture and found that proppant settling and convection occur under practical conditions as would be found in the field. Given the critical nature of proppant packing, as discussed above, it is therefore important that the mechanisms of proppant transport and perhaps more importantly fluid flow in the fracture are understood. Although both Ouyang et al. [67] and Unwin and Hammond [90] assume complex, non-Newtonian fluid behaviour (See Section 2.4.1.), they both assume the fracture width effects to be negligible and treat the fluid flow in the fracture, and therefore the proppant transport, in only two dimensions. This could be seen as a limitation given that Unwin and Hammond [90] note the effects of shale layers, where the fracture width will be narrower, as being potential restrictions to even distribution of proppant throughout a fracture in a layered reservoir.

Similarly, Milton-Taylor et al. [60] applied a two-dimensional boundary element method to the study of proppant stability and flowback. In defence of the two-dimensional model, their findings, that channels develop in the fracture pack where proppant flows back leaving bridged, unpropped sections of fracture, matched the findings of experimental tests carried out in the same study. However, in the situation of a packed fracture under in situ confining pressure, in contrast to proppant placement, there is little opportunity for proppant movement across the fracture width, especially given the dominant fluid flow along the length of the fracture as hydrocarbons are extracted to the wellbore.

An alternative method to the continuum techniques described above, is applied by Bruno et al. [11] to look into problems of slurry injection. The slurry particles themselves, along with the reservoir material, are modelled by a DEM model while the fluid, or rather a background pressure field, is modelled by a coupled a FE fluid model. The pressure field, resulting from the updated geometry of the DEM, is converted to drag forces, according to Darcian flow, which then act on the DEM particles in the next time step. A similar technique of applying drag forces to particle based on a pressure gradient is looked at by Asgian et al [5] and by Vangelsten [92], although not for the same application. In addition, a similar, but very basic model, in terms of the fluid behaviour, was developed by Davie [21], initially for the purposes of hydraulic fracture modelling. It is clear that, with the use of a background pressure field and drag forces,

similar to those described above, this model could easily be applied to the modelling of processes such as gravel packing.

Although the model developed by Bruno et al. [11] is not specifically a proppant transport model, the problem is essentially the same and this type of model has applications in many other similar areas of geomechanics, such as sand production problems, gravel packing around wellbores in weak formations, reinjection of contaminated drill cuttings and waste injection. Furthermore, as discussed previously (See Section 2.3.3.), the application of DEM methods to this type of problem is advantageous because, unlike continuum models, they can easily capture processes, which particularly affect weak formations, such as micro-cracking, disaggregation and grain movement. These are all discontinuous failure processes that are distributed over a large area and consequently, continuum methods, which focus on stress singularities and strain energy dissipation at a fracture tip, are not well suited to finding them (Schlangen and Garboczi [79]).

As with the continuum models described previously, the model, applied by Bruno et al. [11], is two-dimensional, although in the horizontal rather than the vertical plane. Despite this, it is obviously capable of capturing particle transport across the width of a fracture and in several fracturing directions at once. The continuum models, discussed above, look at two-dimensional fluid flow in only one fracture (See Section 2.2.) and therefore cannot describe these processes, although these processes may be more significant in problems relating to weak formations and low confining pressures as may be found at shallow depths in the ground. Additionally, it is felt that this kind of coupled DEM model has potential to be applied in three-dimensions in which case it would have the versatility to naturally model the behaviour appropriate for slurry injection under any confining pressure without the need for simplifications.

In addition to the work carried out by Bruno et al. [11], several researchers have chosen DEM techniques for the purposes of specifically modelling proppant stability and sand production, with a view to improving the understanding of the mechanisms that cause these phenomena.

Asgian et al. [5] applied a DEM model to a study of the conditions that would lead to proppant flowback. They modelled a small section of a proppant pack in fracture and, as mentioned above, applied drag forces, based on a background pressure field, to the discrete particles representing both the proppant particles and the reservoir formation. The model was effectively three-dimensional but implemented periodic boundary conditions in order to limit the number of discrete particles required. As with other DEM representations, this was a very adaptable model that naturally captured the dynamic behaviour of a proppant pack, for example, the changing width of the fracture as proppant material was dislodged and the equilibrium of the in situ pressure was re-established.

The model showed reasonable qualitative results and showed behaviour such as arching of the particles and progressive failure of the proppant pack under different draw down rates. However, the results were not entirely consistent with field data that shows proppant packs to be stable under higher pressure gradients than the model results suggested. The differences may come from the effects of capillary forces between the particles or the bonding action of residual fracture gel. Neither of these phenomena would be naturally reproduced by this model but could easily be included. Furthermore, several authors have noted the formation of channels at specific levels in proppant packs, from which almost all proppant flows back, while other sections of the pack are unaffected (Milton-Taylor et al. [60], Goel and Shah [31]). This kind of behaviour could only be captured by a model that considered two-dimensional behaviour in the vertical direction or fully three-dimensional behaviour. For a DEM such as the one used by Asgian et al. [5] a fully three-dimensional model would be required. A difficulty with this would be the computational effort required in dealing with the very large number of particles required to model a fracture several metres in height. This may become reasonable as computational power increases and highly optimised DEM codes are developed.

As discussed above, sand production, as a consequence of formation failure, causes similar problems to proppant flowback. The mechanisms involved in sand production are complex and involve rock and fluid mechanics as well as the coupled interaction of fluid flow and particle motion. It is for these reasons that DEM can be considered the natural choice for modelling sanding (Preece et al. [73]).

To study sand production, Preece et al. used a coupled two-dimensional DEM/fluid model in a similar fashion to the slurry injection model developed by Bruno et al. [11] and discussed above. The sand particles were produced in an existing code, MIMES, and a fixed fluid pressure field was established in the background with a gradient similar to that which would be found in a reservoir under draw down. The fluid effect on the particles was calculated by integrating the pressure field over the particle surface. This resulted in an unbalance force, because of the pressure differential between one side of the particle and the other, which caused the particle to move towards the wellbore perforation. While this is a simple but very effective model, the study in question only deals with the motion of free particles from what would be a void or fracture in the reservoir to the wellbore where they are removed. There is no attempt to model the reservoir material or the production of the sand material from it. Given this simplification, the value of the model is limited in terms of modelling a realistic situation or predicting sanding in a specific well. Having said this, the model shows great potential and if it is possible to apply it to a more complex situation, it could prove to be a very powerful tool indeed.

Thallack et al. [85] have also extensively researched the phenomenon of sanding and provide a comprehensive study of sand production behaviour. As with the other studies discussed above they applied a coupled DEM/fluid model. Their approach to the flow of fluid between the sand particles was based on an equivalent flow network that takes into consideration the particle arrangement. This method has also been applied by Zhai et al. [97] in a study of pore pressure in a DEM model and the technique was originally developed by Hakuno and Tarumi (1988): cited by Thallack et al. [85] and Zhai et al. [97]. Each separate pore space, between the particles, is discretised as a polygon, formed by joining the centroids of the particles surrounding the pore space. Fluid is then assumed to flow in all directions, perpendicular to the polygon edges depending on the calculated pressure gradients. The critical pressure gradient required to dislodge a given particle is then calculated and if the flow passed that particle, from one pore to the next, is sufficient then the particle is disaggregated.

The accuracy of the assumed flow paths from pore to pore is not immediately apparent. However, given the small scale of the material grains in question it is likely to be an acceptable approximation. For a regular packed particle mesh, this question

would not arise, as the flow path would always pass directly through a contact between two particles. This method may then be a practical technique, in the case of bonded particle assemblies applied to hydraulic fracturing (See Section 2.3.3.), in order to take account of reservoir fluids, fluid leak-off and poroelastic effects. Although considered, this application is beyond the scope of this project.

From the studies presented above it seems clear that the DEM would be the preferred choice for modelling the problems of proppant transport, proppant stability and sand production. It was noted however, that the number of particles required to model a full fracture would be unfeasible in terms of computation effort. For this reason these models are probably least appropriate for modelling proppant transport, as this would require a full fracture model. The two other problems could be dealt with, as shown in the previous studies, by models of small sections of a fracture or wellbore perforation. It was, however, also noted that for a complete behavioural accuracy, even in these two problems, a fully three dimensional model should be used and this again may be restrictive due to the number of particles required. However, for modelling in two dimensions in horizontal planes, as is dealt with in the numerical work for this project, the DEM representations can be considered a very useful approach. *For these reasons, a similar technique is the most appropriate for application in this project.*

It should also be noted that once developed for a proppant stability or sand production problem, a model of this kind could easily be adapted and applied to modelling other related geomechanical processes such as gravel packing, waste injection and perhaps even grouting.

2.6. Summary

In this review, a general history of research in the field of hydraulically driven fractures has been presented along with the discussion of several processes that are fundamentally associated with hydraulic fracture treatments in the field. The discussion has particularly focussed on the numerical methods developed for modelling these processes and their various shortcomings, along with some reference to their relevance to the work

in this project. Also presented were similar reviews of alternative modelling methods, some of which have been applied to the study of hydraulic fracturing and others that may have potential applications in this field.

After consideration of the previous investigations and numerical work described and discussed above, decisions were made as to the appropriate aims and objectives for the research in this project. A detailed description of the proposed aims and their planned implementation in the chosen modelling environment is presented in the following Chapter. Also presented is a detailed description of the components and capabilities of the modelling environment, along with a discussion of the numerical theory upon which it is based.

Chapter 3:

Research Proposal and Model Implementation

3.1. Introduction

This Chapter will set out the research work proposed for this project with reference to its relationship to previous investigation work as discussed in Chapter 2. After presenting the evolution of a general proposal and initial direction for the research, discussion will move on to the specific implementation of the various modelling concepts within an existing modelling environment, chosen for its ability to deal with all of the physical processes to be considered, within one, multi-physics modelling framework. A full description will also be given of the modelling environment, including its capabilities and the theory on which it is based.

3.2. Research Proposal

The initial brief of this thesis was to investigate the numerical modelling of geomechanical problems. As discussed in Chapter 1, by way of a geomechanical test case, the work carried out for this thesis was focussed on the processes associated with *Hydraulic Fracture Treatments*, as employed by the petroleum industry for the stimulation of hydrocarbon reservoirs.

After considering work previously carried out in the field of hydraulically driven fracturing it became clear that complex, continuum based, coupled fracture simulators are already in use in the petroleum industry (See Chapter 2, Section 2.2.). It was felt however that even the most complex of these simulators make assumptions about fracture behaviour that, firstly, limit their accuracy in terms of simulating a specific

hydraulic fracture treatment and secondly, limit them to modelling a very specific, single fracture problem in deep hydrocarbon reservoirs.

As discussed in Chapter 2, Section 2.2., an alternative, more general, approach would be to model a reservoir and allow it to fracture rather than modelling a specific fracture itself. In this way, the overall behaviour and processes at work in the reservoir could be taken into account in the simulation of a fracture treatment. Furthermore, the same model would be generally applicable to other problems in the field of geomechanics.

While a model such as this would seem to provide more flexibility for the problem under consideration, it would obviously be complex and require significant computational effort, particularly when dealing with propagating fractures. Furthermore, in a continuum framework such as finite element analysis, discrete fracture pathways would either have to be predefined by interface elements, which would limit the generality of the model, or would require adaptive remeshing to be carried out in order to maintain the numerical stability of the model. This, again, would be computationally expensive.

It is further noted that, as with existing hydraulic fracture simulators, a model such as this would be based on analytical fracture mechanics methods. These fracturing criteria focus on stress singularities and strain energy dissipation at a fracture tip as are characteristic of a low ductility, continuous material. This type of model is therefore not suitable for modelling the essentially discontinuous processes, such as micro-cracking, disaggregation, fracture branching and grain movement, that are especially associated with weaker or unconsolidated formations, as may be found in shallow reservoirs or other situations outside petroleum engineering.

Given the evidence cited above, it would appear that this alternative approach to hydraulic fracture modelling, while requiring even more computational effort than existing fracture models, would be no more generally applicable. However, after considering various other modelling approaches it was found that one possible solution would be the application of lattice models. As seen in Chapter 2, Section 2.3.1., lattice models are capable of dealing with the deformation and fracture of a wide range of

materials, from low ductility, quasi-brittle materials, such as concrete, to low strength, unconsolidated materials, such as weakly cemented sandstones. In a similar fashion to the suggested modelling technique, discussed above, lattice models can be made to represent the continuum material, which is subsequently allowed to fracture. This is in contrast to existing fracture models described, in Chapter 2, Section 2.2., which represent the fracture itself. Lattice models are therefore naturally capable of dealing with the development of multiple fractures and furthermore, do not require predefinition of fracture growth or remeshing.

Extensive studies of fracture in concrete and sandstone have been carried out using lattice modelling techniques (See Chapter 2, Section 2.3.1.) and the numerical results of these have been shown to match well with results of concurrent experimental studies. In addition, some work has been carried out to apply lattice modelling to hydraulic fracturing problems (Tzschichholz and Herrmann [88], Tzschichholz et al. [89]) and, although the studies have been very basic, the results show promise.

A lattice model would therefore seem to be a good choice for a modelling framework with which to advance the study of hydraulically driven fracture growth behaviour and consequently is adopted for the numerical work carried out for this thesis. It should be noted that the lattice models discussed above were two-dimensional, planar representations. It is also proposed to adopt this simplification here, although the ultimate goal of the alternative modelling environment for hydraulic fracture simulators, would be a fully three-dimensional model. The plane strain simplification of hydraulic fracture simulators has been discussed in Chapter 2, Section 2.2., and its limitations are well understood. It is further considered that advances made in two-dimensional plane strain lattice models will be transferable to three-dimensional lattice models in the future.

It must also be reiterated that hydraulic fracturing is a complex problem involving the coupling of several processes. As discussed in Chapter 1, Section 1.2., there are five main aspects to hydraulic fracture treatments that must be addressed by a fracture simulator. These are: viscous fluid flow in the fracture, leak-off of the fluid to the reservoir, deformation of the reservoir formation, fracture propagation and proppant transport. In particular, the interaction between the solid and fluid phases is very

complex since the fracture shape is dependent on the fluid pressure profile and the fluid pressure profile is dependent on the fracture shape. In order to find an equilibrium solution staggered or iterative techniques are often employed. Furthermore, as discussed in Chapter 2, Sections 2.2. & 2.4., the fluid behaviour itself is usually simplified, particularly in commercial fracture simulators.

While the solid phase processes of deformation and fracture could be easily handled by a lattice model, a method would have to be found of coupling it to the fluid flow and proppant transport processes.

After reviewing the numerical study of proppant transport, and other related problems concerning the movement of granular material, it was concluded that discrete element modelling (DEM) was the most appropriate technique and consequently the natural choice for modelling these processes.

In addition to this, it was realised that bonded particle assembly models, discussed in Chapter 2, Section 2.3.3., which can be used to create models that are equivalent to lattice models, are also suited to the DEM framework.

This provided the means to apply a lattice type model to the solid phase, as discussed above, and to implement the modelling of processes such as proppant transport within the same framework. While this might prove very efficient, it was still necessary to find a method of coupling fluid behaviour to both of these DEM models.

A study of fluid modelling techniques showed that it is possible to develop a particle representation of a fluid and that several approaches to this had been investigated in the past (See Chapter 2, Section 2.4.2.). Conveniently, these models are particularly suited to modelling problems of free surfaces flow and flow break up as may occur in a fluid zone of changing size and geometry, such as can be found in a propagating hydraulic fracture. Although, as discussed in Chapter 2, Section 2.4.2., particle fluid models usually work on different principles, it has been shown that it is possible to implement this kind of model within a DEM framework.

By applying this in conjunction with the bonded particle assembly model and the discrete proppant model it was therefore possible to consider all five of the main issues associated with hydraulic fracture treatments within a discrete framework, as shown in Table 3.1. below.

Process	Model Type	Implementation	Model Designation in this Thesis
Viscous Fluid Flow	Particle Fluid Representation	Discrete Element Model (DEM)	Particle Fluid Model (PFM)
Leak-off of Fluid	Particle Fluid Representation	Considered in Fluid Behaviour	PFM
Deformation of Rock	Bonded Particle Assembly	DEM	Particle Solid Model (PSM)
Fracture Propagation	Bonded Particle Assembly	Separation of Inter-particle Links	PSM
Proppant Transport	Discrete Granular Material	DEM	Particle Proppant Model (PPM)

Table 3.1. Summary of DEM Implementation of Hydraulic Fracture Processes

If all of these processes could be implemented within one all encompassing, multi-physics, DEM framework, then a coupled model would be automatically created. A framework of this kind would be extremely versatile and could be applied to many geomechanical problems, such as wellbore stability, gravel packing, grouting, slurry injection, sand production, proppant stability and hydraulic fracturing, without significant changes to the underlying modelling framework. Furthermore, unlike single software frameworks (SSF) based on continuum methods, there would be no necessity for mapping between different meshes for different material phases.

Rather than starting with the development of a new DEM code it was decided to implement the overall modelling framework discussed above in an existing DEM package. The chosen program is a commercial geotechnical DEM code, Particle Flow

Code in Three Dimensions (PFC^{3D}). This was a natural choice for this project as the features of the program included the vital ability to bond discrete particles together, as is required for the Particle Solid Model, and furthermore, includes an embedded coding language, *FISH*, in which additional code can be written to manipulate and alter the basic behaviour of the discrete elements. A full description of the theory and capabilities of PFC^{3D} and the intended implementation of the modelling processes is given in the following Sections.

In summary, it is proposed to develop a two-dimensional, multi-physics, single software modelling framework within a pre-existing discrete element modelling environment, in order to implement coupled models of geomechanical problems such as those related to hydraulic fracture treatments.

The advantages of this framework will be that it can handle complex material behaviour over a wide range of material types and can naturally deal with large deformations and discrete or distributed fracturing behaviour, without the need for remeshing or loss of numerical accuracy. Furthermore, coupling of solid, fluid and particle phases will be achieved without the need for consistency and mapping between separate meshes, or for staggered or iterative solutions, as all of the models will be constructed within the same DEM environment and will be solved simultaneously by the existing dynamic relaxation solver.

Given the relative simplicity of the proppant type model it can be implemented without significant additions to the basic behaviour of the PFC^{3D} DEM code. It is therefore proposed that the work in this project will focus on the development of the solid and fluid phase models and their coupling, in the assumption that the proppant model could be included at any stage.

3.3. An Introduction to Particle Flow Code in Three Dimensions

As mentioned previously (See Section 3.2), the numerical analyses carried out as part of this project will use models formulated in the existing, commercially available, distinct

element modelling (DEM) environment, Particle Flow Code in Three Dimensions (PFC^{3D}) (Itasca Consulting Group [37]).

PFC^{3D} was designed as a geotechnical modelling environment and nominally deals with transient dynamics of particulate media. The basic components of PFC^{3D} models are rigid spherical particles, known simply as 'balls', which interact, when in contact, by way of normal and shear contact springs. The behaviour of these particles is determined by a Cundall and Strack type distinct element method that involves an explicit time stepping scheme during which Newton's Second Law is integrated twice in each time step (See Section 3.4.1. and Cundall and Strack [18]).

In order to create a model, particles can be generated, individually or in groups, at precise co-ordinates or randomly positioned within three-dimensional volumes. The volumes can be defined with boundaries created by rigid, laminar objects known simply as 'walls'. 'Walls' can be generated by defining the co-ordinates of their corners and can be defined as planar or concave. Interactions with 'walls' are dealt with similarly to 'balls', by way of normal and shear contact springs, however 'walls' are generally considered to be fixed and will not move when acted on by a force resulting from a 'wall'-'ball' contact.

The particles can be assigned basic properties such as size and density and these properties may be given to individual 'balls' or to discrete regions defined within the overall model. Furthermore, properties concerning interaction may also be assigned to particles in the same way. These include damping and friction coefficients and the contact spring stiffnesses mentioned previously. The particles are considered rigid but are allowed to overlap and interaction between them is dealt with by assuming a constitutive model at any contact that develops. In its simplest form, this represents linear elastic spring behaviour. 'Walls' are also considered rigid and are similarly assigned stiffnesses and a friction coefficient. The creation of particles and 'walls', in the way described above, allows great freedom for the modelling of non-cohesive granular material such as soil.

Although PFC^{3D} calculates a full dynamic solution at each time step, it allows the calculation of static solutions through the implementation of a dynamic relaxation

solver. Dynamic relaxation is based on the principle that the static solution is the limiting case of a dynamic solution. PFC^{3D} achieves a steady state by applying a local damping coefficient to the contact springs between particles in contact. Over time, this causes the oscillating velocities associated with the dynamic solution for a mass attached to a spring, to reach a steady state. The shorter the time and the fewer the oscillations, the closer the solution is to a static solution. PFC^{3D} uses a default value for the damping coefficient that is as high as possible without compromising the numerical stability of its models. However, by optimally scaling the inertial masses of the particles, a quasi-static solution can be produced after each time step. Although a steady state might be reached eventually in a fully dynamic case, as energy is lost through friction, for example, depending on the specific configuration of a particular model, the process is accelerated considerably by dynamic relaxation.

PFC^{3D} also deals with bonded particulate media by the application of bonds between particles. There are two types of bond available within PFC^{3D}. The first are 'contact bonds' which, as the name suggests, form only where a physical contact exists between particles. These bonds are considered to exist as point contacts. They are assigned values of tensile and shear strength only and therefore have no resistance to bending moments and cannot be failed in compression. The strengths are assigned in terms of the force that a particular bond is able to resist rather than by a general stress capacity.

The second type of bond is known as a 'parallel bond'. They may be applied in addition to the 'contact bonds' and take the form of elastic cylinders that are assigned individual properties of stiffness and strength that act in addition to the properties of the particles. In contrast to the 'contact bond' strength, the tensile and shear strengths of the 'parallel bond' are assigned in terms maximum stress capacities. It may be further noted that, they are also capable of resisting bending and can be used to bond particles that are not in direct contact.

A group of spheres bonded with one or both types of bond will essentially behave as an elastic solid and PFC^{3D} contains extensive built-in logic to deal with this concept. In addition, these 'solids' are capable of fracturing behaviour, as the bonds will cease to act if their strengths are exceeded, i.e. the bonds will 'break'. This means

that there is as much freedom to model solids as there is to model granular materials. PFC^{3D} is therefore ideally suited to model materials such as rock, which consist of cemented grains. Extensive use of these bonded particle ‘meshes’ will be made during the course of the work carried out for this thesis.

Other features of PFC^{3D} allow various external conditions to be applied to meshes, created as described above. Boundary conditions can be applied in terms of either displacements or forces. In the case of displacement boundaries, ‘walls’ or ‘balls’ are given a velocity or rotation that converts to a prescribed incremental displacement over time. In the case of force boundaries, ‘balls’ are directly assigned externally applied forces.

When a model is ‘cycled’, the reaction of each particle and ‘wall’ to the conditions it is subject to is calculated after each time step. This reaction is governed by the constitutive model assumed for each contact that forms during the time stepping process. Although external conditions may also be applied to certain particles or ‘walls’, their influence will also be transferred through the model according to the constitutive law. The constitutive model consists of three parts, a stiffness model, a slip model and a bonding model. If the particles are bonded, with either of the bond types described above, the slip model is superseded. Although models that are more complex are available, this project will use only the simple linear contact model, which is defined by the contact stiffnesses discussed above. If ‘balls’ or ‘walls’ with different properties meet then the average values of properties such as friction and damping are taken. For the linear contact model, spring stiffnesses are treated in series, according to *Eq. 3.1.* and *Eq. 3.2.* below (Itasca Consulting Group [37]), and this has consequences for this work that are discussed further in Chapter 4.

$$K^n = \frac{k_n^{(A)}k_n^{(B)}}{k_n^{(A)} + k_n^{(B)}} \quad \text{Eq. 3.1.}$$

$$K^s = \frac{k_s^{(A)}k_s^{(B)}}{k_s^{(A)} + k_s^{(B)}} \quad \text{Eq. 3.2.}$$

where, \mathbf{K}^n is the contact normal secant stiffness, \mathbf{K}^s is the contact shear tangent stiffness, k_n is a normal spring stiffness, k_s is a shear spring stiffness and the superscripts (A) and (B) denote the particles or particle and 'wall' in contact. (It may be noted that the normal stiffness is a secant stiffness, since it relates the total normal force to the total normal displacement, while the shear stiffness is a tangent stiffness, since it relates the increment of shear force to the increment of shear displacement).

These three parts of the constitutive model are applied within the distinct element method, which is described in more detail below (See Section 3.4.1..).

Due to its time stepping nature, PFC^{3D} is capable of allowing various parameters to be monitored as desired. These include the forces on 'walls', the position or velocity of any 'ball', the diagnostic unbalanced force which is averaged for forces over the whole mesh, the porosity of the mesh and the stresses (See Section 3.4.2. below) and energies present in the mesh. These properties can be logged and plotted against time steps or each other at the end of a run.

A further advantage of PFC^{3D} is that it includes a programming language, known as *FISH*, which allows code to be written so that a model can be manipulated in almost any conceivable way. Furthermore, most of the properties that can be monitored during cycling can have their values called by a *FISH* function and so can be included in calculations. Furthermore, modelling features such as logic to describe whether a bond is broken or intact can also be called and altered by *FISH* functions. These facilities proved very useful in the course of developing our own routines and functions for use in this project (See Chapter 4, Section 4.3.3. and Chapter 5, Section 5.3.).

3.4. Theory of the Particulate Mechanics Modelling Framework

3.4.1. Cundall & Strack Type Distinct Element Method

The distinct element method, as described by Cundall and Strack [18], numerically models the dynamic behaviour of discrete, circular discs with a time stepping algorithm in which the velocities and accelerations of the discs are assumed constant over each

time step. A fundamental assumption of the distinct element method is that the time steps can be so small, that disturbances affecting any disc do not propagate beyond its immediate neighbours. It should be noted that although the distinct element method was originally a two-dimensional method it can easily be applied in three dimensions and this is the case in PFC^{3D} where the two-dimensional discs are exchanged for three-dimensional spherical particles.

The actual calculations for spherical particles in contact consist of an alternation between the application of Newton's Second Law, *Eq. 3.3.*, and a force-displacement law, *Eq. 3.4.*

$$F = m.a \quad \text{Eq. 3.3.}$$

$$\Delta F_n = k_n (\Delta n)_{t_1} = k_n v \Delta t \quad \text{Eq. 3.4.}$$

where, F is the force acting on a particle, m is the mass of the particle and a is the acceleration of the particle. ΔF_n is the increment of normal force on the particle, k_n is the normal contact stiffness, Δn is the relative displacement of the particles in contact, v is the closing velocity of the two particles in contact and Δt is the length of the time step. The subscript t_1 , associated with the displacement, indicates that it refers to time step $t_1 = t_0 + \Delta t$, where t_0 is the start time.

NB - for convenience and consistency in this thesis, some of the notation in this Section has been altered from the original text (Cundall and Strack [18]).

The motion of a particular contacting pair of particles, in a particular time step, is calculated, from the forces applied to them, through Newton's Second Law. The force-displacement law is then used to calculate the forces acting on the pair in the next time step from the motion just calculated. This cycle is repeated for sequential time steps.

Although the particles are considered rigid, they are allowed to overlap at contact points. This overlapping takes the place of deformation of the particles and therefore deformation of the whole mesh. The magnitude of the overlap directly relates to the reaction force between two particles or a particle and a 'wall' in the case of PFC^{3D}.

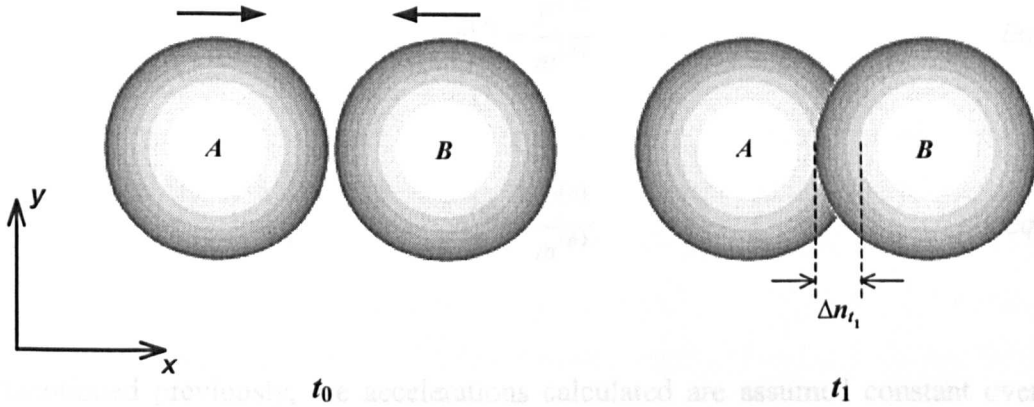


Fig. 3.1. Diagram Showing Particle Pair Moving into Contact

After each time step, the program first determines which particles are in contact. This is done by calculating whether the distance between all pairs of neighbouring particles is less than the sum of their two radii. If a pair of particles is found to be in contact, the overlap is then calculated. This is equivalent to the relative displacement, Δn (See Fig. 3.1.). For each contacting pair, the sum of forces is then calculated from the force-displacement law, Eq. 3.4., so that,

$$F_x^{(A)} = k_n \Delta n_{t_1} \quad \text{Eq. 3.5.}$$

$$F_x^{(B)} = -k_n \Delta n_{t_1} \quad \text{Eq. 3.6.}$$

where, in the case of PFC^{3D} models, the sign convention applies to the Cartesian coordinate system used during the generation of the particle assembly.

The resultant forces calculated are then substituted into Newton's Second Law, Eq. 3.3., which is reorganised to determine the new accelerations on each particle as shown in Fig. 3.8. and Fig. 3.9. below. Obviously, for the example shown in Fig. 3.1., no y-component of force develops between the particles.

$$a_x^{(A)} = \frac{F_x^{(A)}}{m^{(A)}} \quad \text{Eq. 3.7.}$$

$$a_x^{(B)} = \frac{F_x^{(B)}}{m^{(B)}} \quad \text{Eq. 3.8.}$$

As mentioned previously, the accelerations calculated are assumed constant over the time step (in this case $t_1 = t_0 + \Delta t$ to $t_2 = t_0 + 2\Delta t$). Eq. 3.7. and Eq. 3.8. are then integrated to find the velocities, v , for the next time step so that,

$$\left[v_x^{(A)} \right]_{t_2} = \left[\frac{F_x^{(A)}}{m^{(A)}} \right] \Delta t \quad \text{Eq. 3.9.}$$

$$\left[v_x^{(B)} \right]_{t_2} = \left[\frac{F_x^{(B)}}{m^{(B)}} \right] \Delta t \quad \text{Eq. 3.10.}$$

The new value of relative displacement can then be calculated from these velocities as shown below,

$$\Delta n = v_x \cdot \Delta t \quad \text{Eq. 3.11.}$$

$$\therefore \Delta n_{t_2} = \left(v_{t_2}^{(A)} - v_{t_2}^{(B)} \right) \Delta t \quad \text{Eq. 3.12.}$$

$$\therefore \Delta n_{t_2} = \left(\left[\frac{F_x^{(A)}}{m^{(A)}} \right] \Delta t - \left[\frac{F_x^{(B)}}{m^{(B)}} \right] \Delta t \right) \Delta t \quad \text{Eq. 3.13.}$$

where, the relative displacement, Δn , is taken as positive in compression.

The formulae above give only the relative displacement between two particles in a contacting pair, as shown in *Fig. 3.1.* above. If either or both of the particles are in contact with another neighbour then the total relative displacement has to account for these overlaps as well. The vector sum of all the contact forces relating to these displacements gives the resultant force acting on a particle.

Although the calculation process described above is sufficient to model the basic motion of particles, it is desirable to also take into account the rotation of the particles and furthermore the shear forces acting between contacting pairs. This is done by considering the general case of a contacting particle pair (See *Fig. 3.2.*) and developing equations for both normal and shear relative displacements (See *Eq. 3.14.* and *Eq. 3.15.* below).

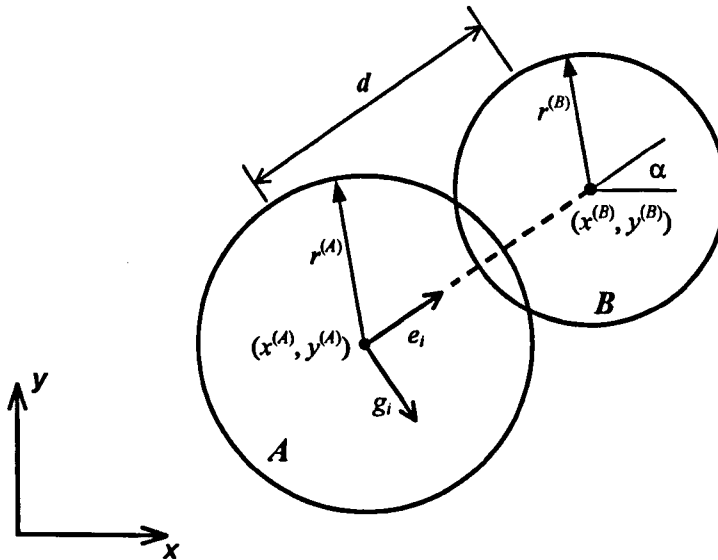


Fig. 3.2. Diagram Showing General Case of a Contacting Particle Pair

$$\Delta n = v_n \Delta t = \left\{ \left(v^{(A)} - v^{(B)} \right) e_i \right\} \Delta t \quad \text{Eq. 3.14.}$$

$$\Delta s = v_s \Delta t = \left\{ \left(v^{(A)} - v^{(B)} \right) g_i - \left(\theta^{(A)} r^{(A)} + \theta^{(B)} r^{(B)} \right) \right\} \Delta t \quad \text{Eq. 3.15.}$$

where, e_i is the unit vector between the centres of the two contacting particles (See Eq. 3.16.), g_i is the unit vector lying 90° clockwise to e_i (See Eq. 3.17.), θ is the angular velocity of a particle and r is the particle radius.

$$e_i = \frac{x_i^{(B)} - x_i^{(A)}}{d} = \begin{bmatrix} \cos \alpha \\ \sin \alpha \end{bmatrix} \quad \text{Eq. 3.16.}$$

$$g_i = \begin{bmatrix} e_y \\ -e_x \end{bmatrix} = \begin{bmatrix} \sin \alpha \\ -\cos \alpha \end{bmatrix} \quad \text{Eq. 3.17.}$$

where, x_i is the location of a particle centroid, d is the separation between the particle centroids, α is the angle between the line joining the particle centroids and the global x -axis and $e_{x,y}$ are the components of the vector e_i parallel to the global axes.

As before, the relative displacements, defined by Eq. 3.14. and Eq. 3.15., are substituted into the force-displacement law, Eq. 3.4., to produce Eq. 3.18. and Eq. 3.19., from which the increments of normal and shear force can be calculated.

$$\Delta F_n = k_n \Delta n = k_n \left\{ (v^{(A)} - v^{(B)}) e_i \right\} \Delta t \quad \text{Eq. 3.18.}$$

$$\Delta F_s = k_s \Delta s = k_s \left\{ (v^{(A)} - v^{(B)}) g_i - (\theta^{(A)} r^{(A)} + \theta^{(B)} r^{(B)}) \right\} \Delta t \quad \text{Eq. 3.19.}$$

where, k_s is the shear stiffness.

At the end of each time step, these force increments are added to the total of all normal and shear force increments, F_n and F_s , calculated in previous time steps (See Eq. 3.20. and Eq. 3.21.).

$$(F_n)_{i_N} = (F_n)_{i_{N-1}} + \Delta F_n \quad \text{Eq. 3.20.}$$

$$(F_s)_{i_N} = (F_s)_{i_{N-1}} + \Delta F_s \quad \text{Eq. 3.21.}$$

At this point, the particle contacts are also checked for frictional slip. This is done by comparing the total shear force from Eq. 3.21. above with the maximum shear capacity as defined by a Coulomb type frictional law (See Eq. 3.22.).

$$(F_s)_{\max} = F_n \tan \phi_\mu + c \quad \text{Eq. 3.22.}$$

where, ϕ_μ is the smaller of the inter-particle friction angles of the particle pair under consideration and c is the smaller of the inter-particle cohesion values.

Thus, the actual shear force at a particle contact will be the minimum of the forces calculated by Eq. 3.21. and Eq. 3.22. This can be written as in Eq. 3.23. below[†].

$$(F_s)_{i_N} = \min((F_s)_{i_{N-1}} + \Delta F_s, (F_n)_{i_N} \tan \phi_\mu + c) \quad \text{Eq. 3.23.}$$

Finally, before the particle motion can be determined, the moments acting on the particles are also calculated, from the forces calculated above, according to Eq. 3.24. and Eq. 3.25. below.

[†] It should be noted that if a particle contact pair are bonded together, as described in the previous Section, the shear strength of the bond overrides the frictional slip law shown in Eq. 3.22. and the shear force at the contact will be determined by Eq. 3.21. However, if the shear strength of the bonds is exceeded the slip law will be invoked.

$$\sum M^{(A)} = \sum F_s r^{(A)} \quad \text{Eq. 3.24.}$$

$$\sum M^{(B)} = \sum F_s r^{(B)} \quad \text{Eq. 3.25.}$$

where, M is the moment acting on a particle.

From the forces and moments calculated as shown above, the resulting motion of the particles can be calculated. As before Newton's Second Law is rearranged to find the normal and angular accelerations as shown below. Eq. 3.26. and Eq. 3.27. are shown in the general form.

$$a^{(p)} = \frac{\sum F^{(p)}}{m^{(p)}} \quad \text{Eq. 3.26.}$$

$$\omega^{(p)} = \frac{\sum M^{(p)}}{I^{(p)}} \quad \text{Eq. 3.27.}$$

where, I is the moment of inertia of the particle, ω is the angular acceleration of the particle and the superscript (p) refers to any particle.

Again assuming the accelerations constant over a time step, Δt from $t_{N-1/2}$ to $t_{N+1/2}$, the velocities are found from Eq. 3.28. and Eq. 3.29. below.

$$v_{t_{N+1/2}}^{(p)} = v_{t_{N-1/2}}^{(p)} + \left[\frac{\sum F^{(p)}}{m^{(p)}} \right]_{t_N} \cdot \Delta t \quad \text{Eq. 3.28.}$$

$$\theta_{t_{N+1}}^{(p)} = \theta_{t_{N-1}}^{(p)} + \left[\frac{\sum M^{(p)}}{I^{(p)}} \right]_{t_N} \cdot \Delta t \quad \text{Eq. 3.29.}$$

Again as discussed above, these velocities can then be used to update the displacements and rotations of the particles, as shown in Eq. 3.30. and Eq. 3.31. below, assuming the velocities constant over Δt from t_N to t_{N+1} .

$$\left(x_i^{(p)}\right)_{t_{N+1}} = \left(x_i^{(p)}\right)_{t_N} + \left(v_{i_{N+1/2}}^{(p)} \cdot \Delta t\right) \quad \text{Eq. 3.30.}$$

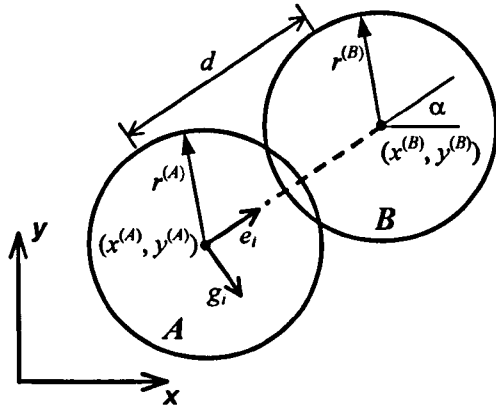
$$\theta_{t_{N+1}}^{(p)} = \theta_{t_N}^{(p)} + \left(\theta_{t_{N+1/2}}^{(p)} \cdot \Delta t\right) \quad \text{Eq. 3.31.}$$

where, θ is the angle of rotation of a particle relative to the global coordinate system.

It should be noted that in PFC^{3D} when the calculation concerns a ‘ball’-‘wall’ contact, calculations are made exactly as described above for a ‘ball’-‘ball’ contact, however the effect of the forces would only be felt by the ‘ball’. ‘Walls’ are either fixed or moving at an assigned velocity. Their velocity cannot be altered by the action of forces resulting from contacts.

It should be further noted that the distinct element model employed by PFC^{3D} is a simplified DEM as it deals only with rigid, spherical particles. Programs such as UDEC (Itasca Consulting Group [38]), MIMES (Preece et al. [73]) and DDA (Rouainia et al. [78]) employ DEM that are capable of dealing with arbitrarily shaped, deformable polygons. However, these programs would not be suitable for the lattice modelling proposed for this work.

The calculation sequence for the Distinct Element Method, as applied to PFC^{3D} models and set out above, can be summarised as shown in the flow chart presented in Fig. 3.3. below.



$$e_i = \frac{x_i^{(B)} - x_i^{(A)}}{d} = \begin{bmatrix} \cos \alpha \\ \sin \alpha \end{bmatrix}$$

$$g_i = \begin{bmatrix} e_y \\ -e_x \end{bmatrix} = \begin{bmatrix} \sin \alpha \\ -\cos \alpha \end{bmatrix}$$

Location of Particle Centroid	Translational Velocity	Angular Velocity
$x_i^{(A)} = (x^{(A)}, y^{(A)})$	$v^{(A)}$	$\theta^{(A)}$
$x_i^{(B)} = (x^{(B)}, y^{(B)})$	$v^{(B)}$	$\theta^{(B)}$

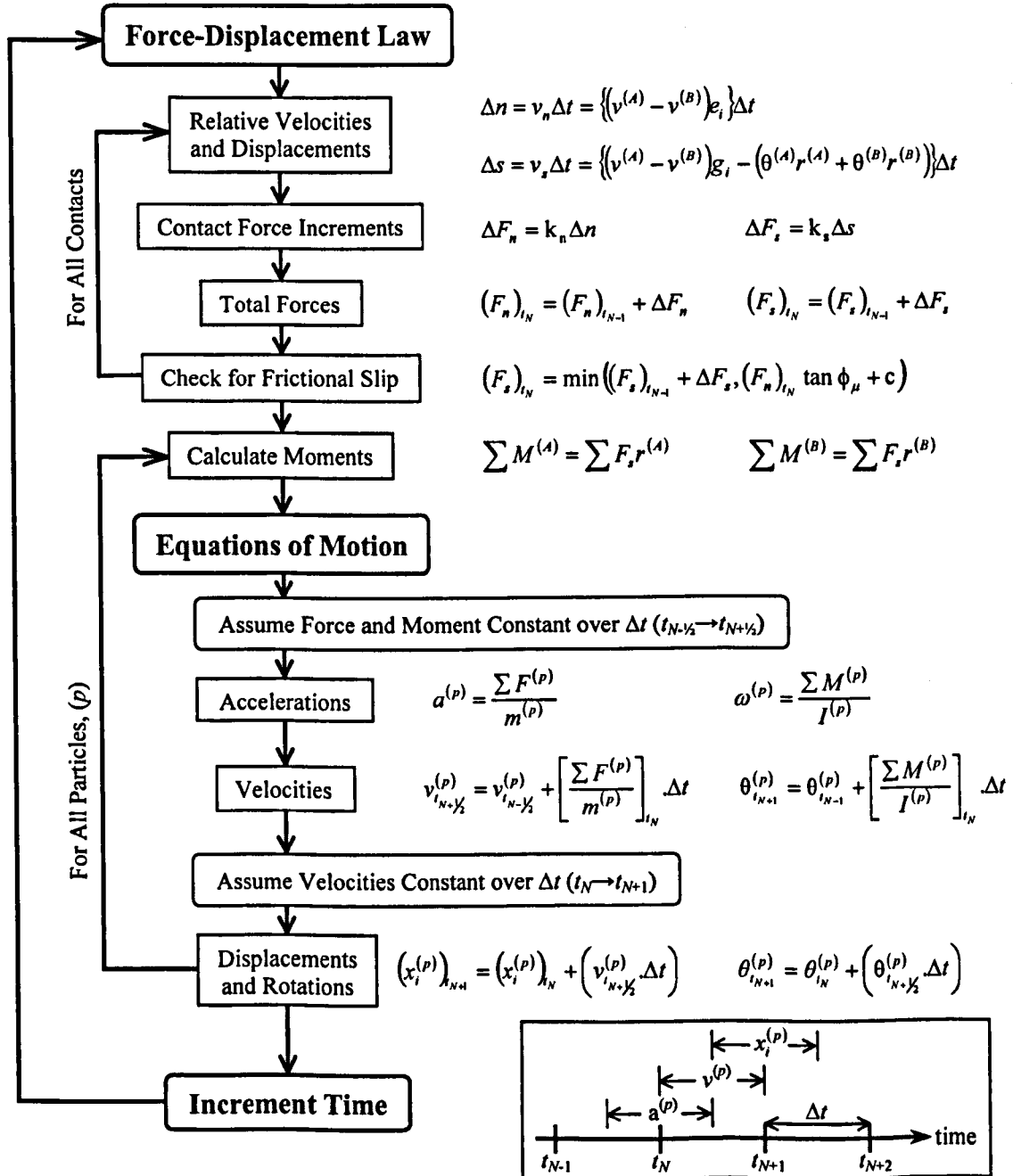


Fig. 3.3. Flow Chart Summarising the Calculation Sequence for the Distinct Element Method as Described by Cundall and Strack [18] (Adapted from Trent [86])

3.4.2. Calculation of Granular Stress State in Particle Models

There are various situations in the modelling and analysis of any mechanical process, in which it is desirable to know the stress field throughout the region of interest. In the case of a continuous body of material the stress state anywhere in that body can be calculated according to the principle laid out by Euler and Cauchy. This says that, on any chosen, closed surface within the body, there exists a stress vector field resulting from the action of the material outside the surface on the material inside the surface. In the limit, as the area of the surface tends to zero, the stress vector is defined as the force acting per unit area of the surface (Fung [30]). This principle is, however, valid only in a continuum where closed surfaces can be defined anywhere. In the case of a particulate material, the medium is discrete, surfaces cannot be defined everywhere and plainly, stress vectors do not exist everywhere. Therefore, in order to calculate stress in a discrete model, such as those considered by PFC^{3D}, it is necessary to apply averaging procedures in order to move from the discrete, micro-scale quantities of particle displacements and contact forces (See Sections 3.4.1. above), to a continuum description. This principle of the homogenisation of a discrete property to a continuum measurement can, in fact, be applied to any quantity on the basis that it is first applied to individual particles, which in turn provide a proportional contribution to a larger averaging volume (Luding et al. [54]). Various strategies have been employed in the application of this procedure to the calculation of stress and while they have subtle differences, they all follow the same general principles in that they take into account the effect of contact forces acting over the volume of individual particles to calculate the average formation stress (Chang and Liao [12], Chang and Ma [13], Christoffersen et al. [15], Cundall & Strack [19], Drescher and de Josselin de Jong [24], Liao et al. [48], Luding et al. [54], Masson and Martinez [55], Rothenburg and Selvadurai [77]).

PFC^{3D} employs a technique that is typical of the methods discussed above where the average stress tensor in a specific volume of particulate material can be calculated according to *Eq. 3.32.*,

$$\bar{\sigma}_{ij} = \frac{1}{V} \int_V \sigma_{ij} dV \quad \text{Eq. 3.32.}$$

where, $\bar{\sigma}_{ij}$ is the averaged stress tensor in the volume and σ_{ij} is the local stress tensor throughout the volume, V .

As mentioned previously, stresses in a discrete medium can only exist in the particles themselves rather than everywhere in the volume. Therefore, the integral in Eq. 3.32. can be replaced with a sum over the total number of particles, N_p , in the volume under consideration, so that,

$$\bar{\sigma}_{ij} = \frac{1}{V} \sum_{N_p} \bar{\sigma}_{ij}^{(p)} V^{(p)} \quad \text{Eq. 3.33.}$$

where, $\bar{\sigma}_{ij}^{(p)}$ is the averaged stress tensor in a particle of volume $V^{(p)}$ and the superscript (p) refers to any particle.

Again, as discussed above, the technique of homogenisation is firstly applied to the individual particles before contributions are made to the whole volume and so, in a similar manner to Eq. 3.32., the average stress in a particle can be calculated according to Eq. 3.34.

$$\bar{\sigma}_{ij}^{(p)} = \frac{1}{V^{(p)}} \int_{V^{(p)}} \sigma_{ij}^{(p)} dV^{(p)} \quad \text{Eq. 3.34.}$$

By applying the tensor identity set out in Eq. 3.35., where, T_{ij} is any Cartesian tensor, δ_{ij} is the Kronecker delta and the notation $,i$ denotes differentiation with respect to x_i , Eq. 3.34. can be rewritten as in Eq. 3.36.

$$T_{ij} = \delta_{ik} T_{kj} = x_{i,k} T_{kj} = (x_i T_{kj})_{,k} - x_i T_{kj,k} \quad \text{Eq. 3.35.}$$

$$\bar{\sigma}_{ij}^{(p)} = \frac{1}{V^{(p)}} \int_{V^{(p)}} \left[(x_i \sigma_{kj}^{(p)})_{,k} - x_i \sigma_{kj,k}^{(p)} \right] dV^{(p)} \quad \text{Eq. 3.36.}$$

Noting that the stresses in a particle are averaged over the volume of the particle and are therefore assumed continuous and in equilibrium throughout that particle, it can be seen that, if there are no body forces present $\sigma_{ij,i} = 0$. Eq. 3.36. then becomes,

$$\bar{\sigma}_{ij}^{(p)} = \frac{1}{V^{(p)}} \int_{V^{(p)}} \left[(x_i \sigma_{kj}^{(p)})_{,k} \right] dV^{(p)} \quad \text{Eq. 3.37.}$$

By applying Gauss's Divergence Theorem the volume integral in Eq. 3.37. can then be rewritten as the surface integral in Eq. 3.38.

$$\bar{\sigma}_{ij}^{(p)} = \frac{1}{V^{(p)}} \int_{S^{(p)}} (x_i \sigma_{kj}^{(p)}) n_k dS^{(p)} \quad \text{Eq. 3.38.}$$

where, n_k is the unit, outward normal to the surface and $S^{(p)}$ is the particle surface.

Eq. 3.38. can be rewritten in terms of a surface traction vector, $t_j^{(p)}$, as in Eq. 3.39.

$$\bar{\sigma}_{ij}^{(p)} = \frac{1}{V^{(p)}} \int_{S^{(p)}} x_i t_j^{(p)} dS^{(p)} \quad \text{Eq. 3.39.}$$

Once again, due to the discrete nature of the medium, the integral above can be replaced with a summation. In this case, the sum is over N_c contact positions where discrete contact forces act on the surface particle rather than a distributed traction field. Eq. 3.39. can then be rewritten as,

$$\bar{\sigma}_{ij}^{(p)} = -\frac{1}{V^{(p)}} \sum_{N_c} x_i^{(c)} F_j^{(c)} \quad \text{Eq. 3.40.}$$

where, $x_i^{(c)}$ is the contact location and $F_j^{(c)}$ is the magnitude of the contact force acting at any contact (c). The sign convention applied in this equation produces compression-negative, tension-positive averaged stresses.

From Fig. 3.4. below it can be seen that the contact location, $x_i^{(c)}$, can be rewritten according to Eq. 3.41.

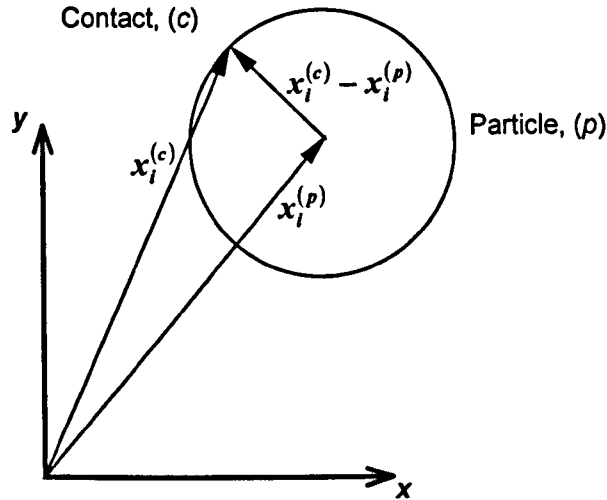


Fig. 3.4. Diagram Illustrating Position Vectors of Particle Centroid and Contact Coordinates

$$x_i^{(c)} = x_i^{(p)} + \underbrace{\left| x_i^{(c)} - x_i^{(p)} \right| n_i^{(c,p)}}_{\text{Branch Vector}} \quad \text{Eq. 3.41.}$$

where, $x_i^{(p)}$ is the location of the particle centroid and $n_i^{(c,p)}$ is the unit vector in the direction from the particle centroid towards the contact. NB - For reference, it can be noted that the second term on the right hand side of the Eq. 3.41. (labelled) is known as the *branch vector* in several of the homogenisation methods referenced above.

Substituting *Eq. 3.41.* into *Eq. 3.40.* gives the expression below for the averaged stress tensor in a particle.

$$\bar{\sigma}_{ij}^{(p)} = -\frac{1}{V^{(p)}} \sum_{N_c} |x_i^{(c)} - x_i^{(p)}| n_i^{(c,p)} F_j^{(c)} \quad \text{Eq. 3.42.}$$

It should be noted that for a particle in equilibrium,

$$\sum_{N_c} F_j^{(c)} \equiv 0 \quad \text{Eq. 3.43.}$$

The average stress tensor in a volume containing N_p particles can now be calculated by substituting *Eq. 3.42.* into *Eq. 3.33.* However, certain complications arise in this calculation. Firstly, pore spaces exist within a volume of particulate material that do not contribute to the stress in the volume and secondly some particles may lie only partially within the volume under consideration. PFC^{3D} deals with this by applying a correction factor based on the porosity of the volume. This correction is not required for the analyses carried out in this project as only average stress tensors for individual particles are considered (See Chapter 4, Section 4.2.3.2.2. and Chapter 5, Section 5.6.). Therefore, the key equation of interest is *Eq. 3.42.*

When considering the stress tensors produced by *Eq. 3.42.* there are several points that should be borne in mind. Firstly, since the equation takes into account the contributions of contact forces acting on a particle at any given time, it calculates Cauchy stress tensors. Secondly, it should be remembered that the stress tensors are averaged over the volume of a spherical particle and for this reason the values of the stresses tend to a true continuum value only as the particle radius tends to zero and the pore space vanishes, i.e. as the granular material tends to a continuum. This issue is addressed in detail, in the context of the work carried out for this thesis, in Chapter 5, Section 5.6.3.

3.4.3. Granular - Continuum Stress Conversion Factors

As discussed in the previous Section, an average stress tensor is calculated internally by PFC^{3D}, for each particle in a model, from the contributions of contact forces acting on the particle (See Eq. 3.42.). These tensors are averaged over the spherical volume of a particle and as such, are a representation of stress in a discrete granular material. Stress throughout each particle is considered uniform and continuous, however, the stress field in a collection of particles representing a granular material cannot be considered continuous, as it would be in a continuum material.

As discussed in Section 3.2. above, it is an aim of this project to develop a two-dimensional representation of a continuum material with a bonded particle assembly. While the average stress tensor will be available for each particle in the assembly, this will be a granular representation, as discussed above, and as such will not be an accurate representation of the stress in an equivalent continuum material.

In order to use the granular stress tensors associated with the particles to describe a two-dimensional, continuum stress field it is first necessary to convert them to continuum stress tensors, as would be found at points, in the same locations as the particle centroids, in an equivalent continuum material, of unit thickness.

This can be achieved by applying simple, controlled load conditions to a two-dimensional particle assembly and determining the ratio between the components of the granular stress tensors, σ_{xx}^G , τ_{xy}^G , τ_{yx}^G and σ_{yy}^G , and the components of a continuum stress tensor that would be expected in an equivalent continuum material under the same loading conditions. It is understood that a certain amount of subjectivity is involved in determining the nature of the equivalent continuum represented by the particle assembly and hence in determining the stress state that would be expected under certain conditions. However, as will be seen below, for any interpretation, as long as consistency is maintained throughout the analysis, a set of reasonably accurate results can be obtained.

Once an equivalent continuum interpretation has been made, then it is possible to determine the ratios between the components of granular stress tensor and the components of the expected continuum stress tensor analytically. This can be done by equating the formula for granular stress (See Eq. 3.42.), via a coefficient, to the equation for continuum stress, which is dependent on the interpretation of the equivalent continuum. Clearly, the coefficient is the ratio between the two values of granular and continuum stress. Once determined, these ratios can subsequently be applied as conversion factors to the components of the granular stress tensor in order to produce an equivalent continuum stress tensor under any loading conditions for the same particle assemble. However, it should be noted that, as will be shown below, the conversion factors are dependent on the configuration of the particles assembly and in particular on the position of the inter-particle contacts. Therefore, in a random particle assembly the conversion factors will be unique to the particles themselves.

The process of determining the granular-continuum stress conversion factors for a bonded particle assembly is illustrated with the simple example shown below.

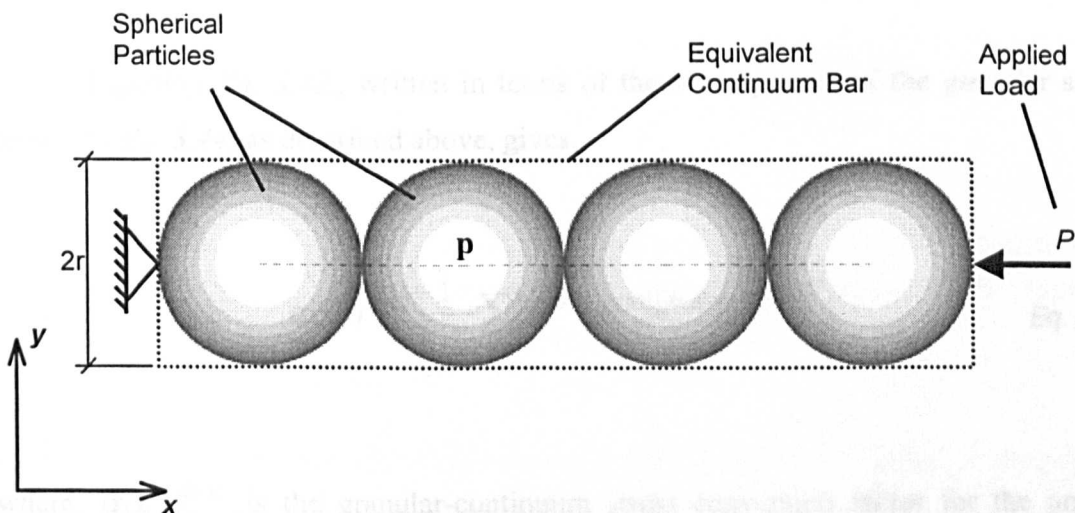


Fig. 3.5. Diagram of Simple, Bonded Particle Assembly

As can be seen above, the simple assembly consists of four particles bonded together. One end of the assembly is fixed and to the other a load, P is applied. The particle

assembly can be considered to represent an equivalent continuum bar of unit thickness, as indicated by the dotted line around the perimeter of the particles.

For the purposes of calculating the granular-continuum stress conversion factors, a typical particle 'p' can be considered. As discussed previously, the granular stress tensor in 'p' can be calculated according to Eq. 3.42. The continuum stress state in the x-direction at the centre of 'p', or in fact, anywhere, in the equivalent continuum bar could be calculated according to Eq. 3.44. It can also be noted that similar expressions could be constructed for the other components of the continuum stress tensor, although, obviously, under the loading conditions shown above, all other stress components are zero.

$$\sigma_x = \frac{P_x}{A_x} \quad \text{Eq. 3.44.}$$

where, σ_x is the continuum stress in the x-direction and A_x is the equivalent continuum cross-sectional area perpendicular to the x-axis.

Equating Eq. 3.42., written in terms of the x-component of the granular stress tensor, to Eq. 3.44. as described above, gives,

$$\alpha_{(x,x)}^{G-C} \cdot \frac{1}{V^{(p)}} \sum_{N_c} |x_i^{(c)} - x_i^{(p)}| n_x^{(c,p)} F_x^{(c)} = \frac{P_x}{A_x} \quad \text{Eq. 3.45.}$$

where, $\alpha_{(x,x)}^{G-C}$ is the granular-continuum stress conversion factor for the normal stress component in the x-direction.

Rearranging Eq. 3.45. in terms of the conversion factor gives,

$$\alpha_{(x,x)}^{G-C} = \frac{P_x V^{(p)}}{A_x \sum_{N_c} |x_i^{(c)} - x_i^{(p)}| n_x^{(c,p)} F_x^{(c)}} \quad \text{Eq. 3.46.}$$

From the model problem shown in Fig. 3.5, it can be seen that the contact forces on the particle 'p', resulting from the external applied load, P , are developed as follows (See Fig. 3.6.).

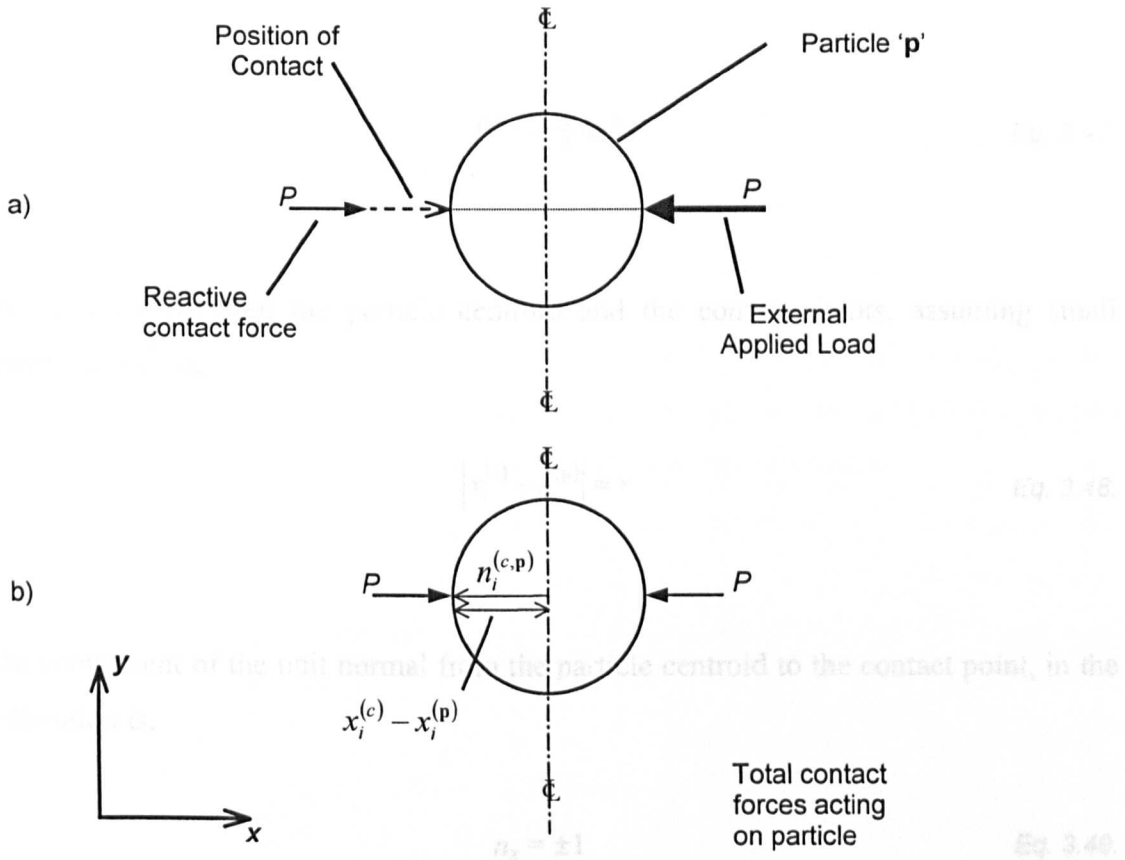


Fig. 3.6. Diagram of Development of Contact Forces on the Particle 'p' Experiencing Normal Stress in the x-direction Showing a) the reaction to external loading and b) the total resulting contact forces on the particle

By examining the components of the reactive contact forces that develop on the particle 'p', in the direction under consideration, and by considering their locations, it is possible to determine the appropriate values of the variables for substitution into Eq. 3.46. For a particle, 'p', in the middle of the assembly, at some distance from the externally applied load, the resulting contact forces, the distance from the particle centroid to the contact positions and the component of the unit vector in the direction under consideration are shown in Fig. 3.6. b). Thus, the following values can be determined and substituted into Eq. 3.46. For a particle, 'p', in the middle of the assembly, at some distance from the externally applied load, the resulting contact forces, the distance from the particle centroid to the contact positions and the component of the unit vector in the direction under consideration are shown in Fig. 3.6. b). Thus, the following values can be determined and substituted into Eq. 3.46.

substituted into Eq. 3.46. in relation to the calculation of the granular continuum stress conversion factor for the normal stress component in the x -direction, $\alpha(x, x)^{G-C}$.

The volume of the spherical particle, 'p', is,

$$V^{(p)} = \frac{4}{3} \pi r^3 \quad \text{Eq. 3.47.}$$

The distance between the particle centroid and the contact points, assuming small deformations[†], is,

$$|x_i^{(c)} - x_i^{(p)}| \approx r \quad \text{Eq. 3.48.}$$

The component of the unit normal from the particle centroid to the contact point, in the x -direction is,

$$n_x = \pm 1 \quad \text{Eq. 3.49.}$$

The component of the contact forces in the x -direction is,

$$F_x = \pm P \quad \text{Eq. 3.50.}$$

[†] Although the initial distance between the centroid of a particle and a contact on the surface of that particle will be equal to the particle radius, this distance will change when the particle assembly deforms. In order to maintain a constant value for the conversion factor it can be assumed that only small deformations occur and that, consequently, the separation between the particle centroid and the contacts remains approximately equal to the particle radius.

The last remaining variable is the equivalent continuum area, A_x . From the equivalent continuum bar that the particle assembly is considered to represent (See Eq. 3.2.) it is clear that the implied width, associated with the applied load, P , is equal to twice the particle radius. Thus, for a bar of unit thickness, the equivalent continuum cross-sectional area in the x -direction is,

$$A_x = 2r.1 \quad \text{Eq. 3.51.}$$

Substituting these values into Eq. 3.46. for the two contact forces acting on the particle, as shown in Fig. 3.6. b), gives the following solution for the granular-continuum conversion factor for the component of normal stress in the x -direction,

$$\alpha_{(x,x)}^{G-C} = \frac{-P \frac{4}{3} \pi r^3}{2r.((r.-1.P)+(r.1.-P))} \quad \text{Eq. 3.52.}$$

which simplifies to give,

$$\alpha_{(x,x)}^{G-C} = \frac{\pi r}{3} \quad \text{Eq. 3.53.}$$

If, by way of example, a compressive load, P , of 1.0N is applied to the particle assembly, as illustrated in Fig. 3.5., in which a particle radius of 0.5m is chosen, then the granular stress tensor in particle 'p', developed by Eq. 3.42., will be as shown below (See Eq. 3.54.).

$$\bar{\sigma}_{ij}^{(p)} = \begin{bmatrix} \sigma_{xx} & \tau_{xy} \\ \tau_{yx} & \sigma_{yy} \end{bmatrix} = \begin{bmatrix} -1.9099 & 0.0 \\ 0.0 & 0.0 \end{bmatrix} \text{N/m}^2 \quad \text{Eq. 3.54.}$$

Under the same loading conditions the expected equivalent continuum stress in the x -direction, according to Eq. 3.44., would be,

$$\sigma_x = \frac{P_x}{A_x} = \frac{-1.0}{2 \times 0.5 \times 1} = -1.0 \text{N/m}^2 \quad \text{Eq. 3.55.}$$

Applying the conversion factor, shown in Eq. 3.53., to the x -component of the granular stress tensor shown in Eq. 3.54. gives,

$$\sigma_{xx} = \bar{\sigma}_{xx}^{(p)} \times \frac{\pi r'}{3} = -1.9099 \times \frac{\pi \times 0.5}{3} = -1.0000 \quad \text{Q.E.D.} \quad \text{Eq. 3.56.}$$

As can be seen above, the conversion factor accurately produces the value of stress that would be expected for an equivalent continuum material. This conversion factor can now be applied for any applied load, P , and for particles of any radius, r .

However, as discussed above, the granular-continuum stress conversion factors are dependent on the interpretation of an equivalent continuum material. This can be further illustrated by considering an alternative interpretation for the continuous bar represented by the particle assembly (See Fig. 3.5. above and Fig. 3.7. below).

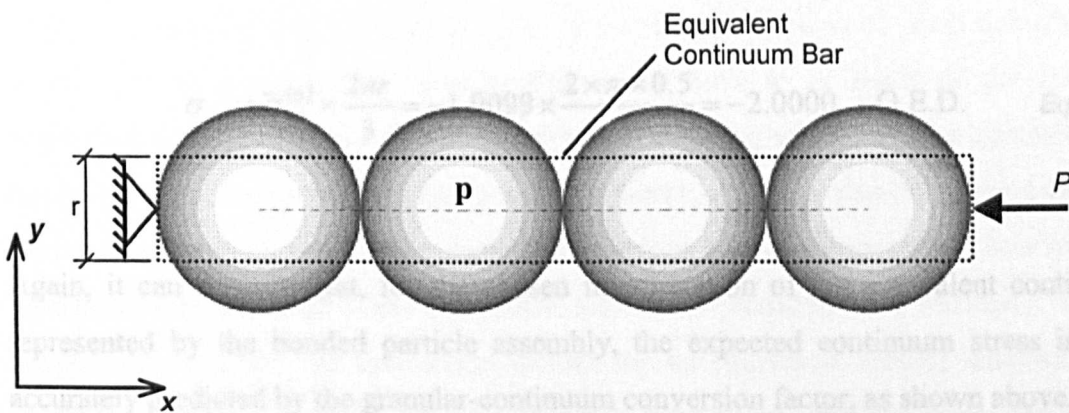


Fig. 3.7. Diagram Showing Alternative Interpretation of Equivalent Continuum Represented by Simple Bonded Particle Assembly

As can be seen, the equivalent continuum area, A_x , previously given by Eq. 3.51., is now given as,

$$A_x = r.1 \quad \text{Eq. 3.57.}$$

Following through the process given above in Eq. 3.46. to Eq. 3.53. it can be shown that the conversion factor is now given as,

$$\alpha_{(x,x)}^{G-C} = \frac{2\pi r}{3} \quad \text{Eq. 3.58.}$$

While the granular stress tensor remains constant, as given in Eq. 3.54., the expected continuum stress, as previously written in Eq. 3.55., is given as,

$$\sigma_x = \frac{P_x}{A_x} = \frac{-1.0}{0.5 \times 1} = -2.0 \text{N/m}^2 \quad \text{Eq. 3.59.}$$

Applying the new conversion factor (See Eq. 3.58.), it can be seen that the predicted continuum stress, previously given in Eq. 3.56., can now be written as,

$$\sigma_{xx} = \bar{\sigma}_{xx}^{(p)} \times \frac{2\pi r}{3} = -1.9099 \times \frac{2 \times \pi \times 0.5}{3} = -2.0000 \quad \text{Q.E.D.} \quad \text{Eq. 3.60.}$$

Again, it can be seen that, for the chosen interpretation of the equivalent continuum represented by the bonded particle assembly, the expected continuum stress is very accurately predicted by the granular-continuum conversion factor, as shown above.

Obviously, the continuous bar represented by a four particle assembly is a very simple example and the continuum interpretation for the particle assembly is almost arbitrary. However, the example serves to emphasise the point that as long as consistency is maintained, accurate predictions can be made for the stress state in the equivalent continuum material. In a larger, two-dimensional particle assembly, the interpretation of the equivalent continuum area will be more restricted, usually to an equal division of the length of a side of the assembly, projected in the axis under consideration. Determining the equivalent continuum area would become more difficult if the overall shape of the assembly is not regular or if the assembly itself consists of randomly distributed particles.

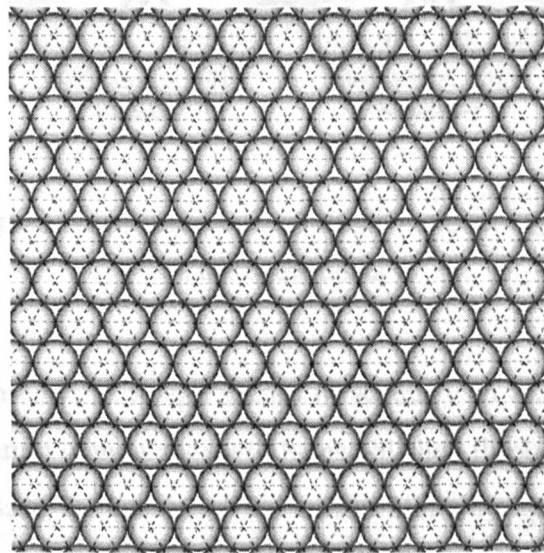
As mentioned previously, the granular-continuum stress conversion factors are dependent on the geometry of the particle assembly, which defines the locations at which the contact forces act. Consequently, they are unique to each particle in an assembly and will vary as the mesh deforms. However, for the purposes of the work carried out for this thesis, it is likely that, for simplicity, a regular configuration will be applied to the bonded particle assembly. If it is further assumed that only small deformations take place (See [†] on page 91), then the conversion factors will be the same for all particles in the assembly and will remain constant at all times.

For a completely general and accurate set of conversion factors, it would be necessary to calculate them individually for each particle in an assembly, at every time step, in order to account for changes in geometry. Obviously, an automatic calculation would be best, however, as can be seen from the description of the technique, shown above, this may be very difficult to code. While the assumption of small deformations would then be unnecessary, consideration would have to be made of the assumed equivalent continuum areas associated with each particle, which are also dependent on the geometry of the assembly. Extending this theory, it should also be possible to apply the development of conversion factors to random particle assemblies, however the determination of an equivalent continuum area would certainly be a difficulty. It may be possible to apply the conversion factors for an equivalent regular assembly to a random assembly, however, this would again involve an approximation and testing would need to be carried out in order to determine the feasibility of this proposal. This was not attempted in the course of this thesis.

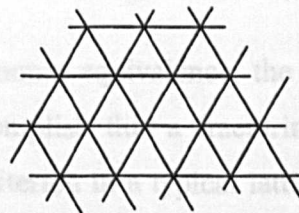
3.5. Proposed Implementation of Particle Solid Model (PSM)

The first part of this project will require the development of a model that will represent the solid phase of the problem, i.e. the reservoir rock formation. As discussed previously this will be developed within the DEM environment PFC^{3D} and will be constructed in a lattice-type configuration.

Rather than the framework of beam or truss elements associated with a typical lattice model, a framework of linked particles will be used. This is similar to bonded particle assembly models as discussed in detail in Section 2.3.3. of Chapter 2. This will be constructed as a two-dimensional sheet of particles packed together in a hexagonal pattern, this being the closest packing possible. The particles will be bonded together, where they touch, using the ‘contact bonds’ available in PFC^{3D} (See Section 3.3.), thereby producing a system analogous to a triangular lattice (See *Fig. 3.8.*).



a)



b)

Fig. 3.8. Diagram Showing a) Typical Configuration of Bonded Particle Sheet for PSM and b) a Typical Triangular Lattice Model for Comparison

In a typical lattice model, the beam elements are given material properties, such as Young's Modulus, E , and Poisson's ratio, ν , so that the overall response of the lattice is the same as the continuum material that is to be represented. In the PSM, the lattice elements are not beams or trusses but consist of two rigid segments, the particles, connected by normal and shear contact springs that are considered to exist over a vanishingly small area (See Fig. 3.9.).

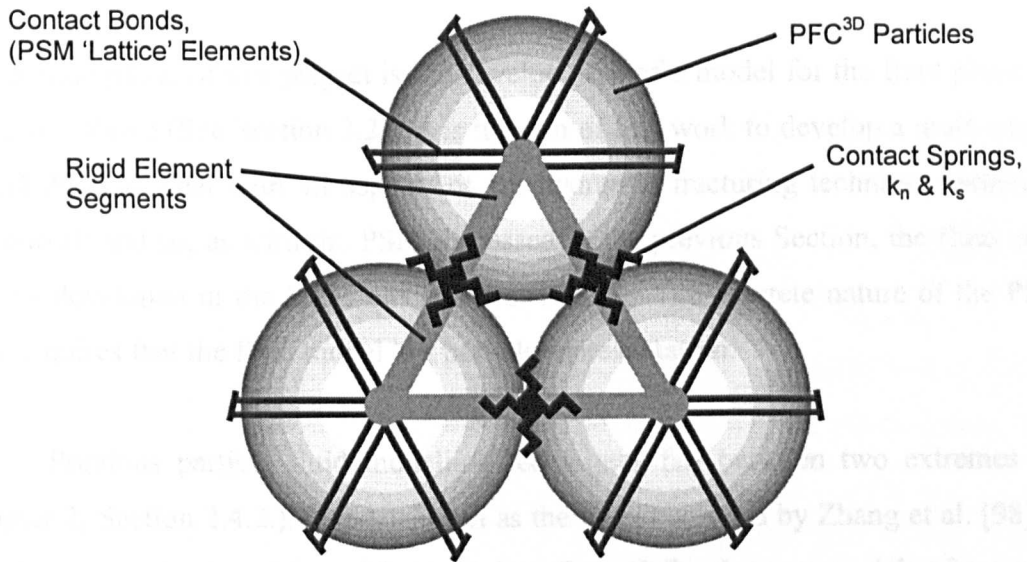


Fig. 3.9. Detail of Typical Three-Particle Unit of PSM Framework Showing Construction of 'Lattice' Elements

It is not, therefore, possible to assign values of E and ν to the 'contact bonds' in the PSM. Instead, continuum equivalence will be established through the normal and shear contact spring stiffnesses, k_n and k_s . This will be done by applying the formulations developed by Morikawa and Sawamoto [63] and Griffiths and Mustoe [32] to the PSM, and will be discussed in detail in Chapter 4, Section 4.2.2.

In addition to the continuum equivalence, the PSM will be required to model fracturing behaviour. To accomplish this a fracturing law must be assigned to the 'contact bonds'. The failure criterion in a typical lattice element is usually based on a combination of critical tensile, shear and bending stresses depending on the exact model in use. Due to the lack of cross-sectional area in the 'contact bonds', it is not possible to directly allocate a maximum stress capacity to the elements of the PSM. Instead,

fracture criteria will be developed by several other means, individually appropriate to the contexts of lattice elements, granular materials and continuum principles. These will be discussed in detail in Chapter 5, and will be implemented by extra code written in the *FISH* language associated with PFC^{3D}.

3.6. Proposed Implementation of the Particle Fluid Model (PFM)

The second phase of this project is the development of a model for the fluid phase. As discussed above (See Section 3.2.), it is the aim of this work to develop a multi-physics model that can deal with all aspects of the hydraulic fracturing technique within one framework and so, as with the PSM discussed in the previous Section, the fluid model will be developed in the DEM environment PFC^{3D}. The discrete nature of the PFC^{3D} code requires that the fluid model is a particle representation.

Previous particle fluid modelling techniques fall between two extremes (See Chapter 2, Section 2.4.2.). Models, such as the one developed by Zhang et al. [98], are based on contact interactions of the particles. Essentially, they are models of a granular material given properties such that it demonstrates fluid behaviour. At the other extreme, techniques such as Smooth Particle Hydrodynamics (SPH) do not involve particle interactions at all. Instead, particles are regarded as moving points at which values of various fluid properties are known. Field quantities are then found by integrating over all points that lie within a kernel of finite radius around each particle.

The PFM will fall between these two extremes. Although it will not be a contact model, it is proposed that the fluid flow behaviour will still be determined by interactions of particles, rather than integration of properties at the particle locations. This will be done by applying repulsive and attractive forces to the discrete particles, representing pressure and viscosity fields, which will maintain a separation between them, disallowing mechanical interaction while causing them to interact with an overall fluid like behaviour. These forces will be a function of the distance between particles within certain radii of influence of each other. Particles out with the radii of influence of a certain particle will have no effect on that particle (See *Fig. 3.10.* below).

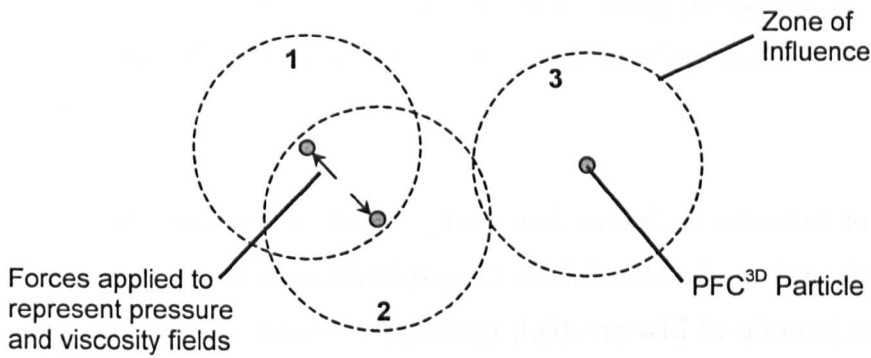


Fig. 3.10. Schematic Diagram of Particle Interaction in PFM

(Particles 1 & 2 interact but particle 3 has no particles within its zone of influence)

This kind of model has similarities to Molecular Dynamics models but is probably most comparable to the Particle and Force (PAF) model (See Chapter 2, Section 2.4.2.). The forces representing the pressure and viscosity fields will be calculated and applied via code written in the *FISH* language associated with PFC^{3D}. The development of the PFM will be discussed in detail in Chapter 4, Section 4.3.

3.7. Proposed Implementation of the Coupled Solid/Fluid Model (PSM + PFM)

As discussed above a main aim of this work is to develop a coupled solid/fluid model within one modelling framework. While the solid phase will be dealt with by the PSM, as described above, two separate approaches will be taken to the fluid modelling.

In the first approach, the PSM will be coupled with a simple fluid model in which forces, representing fluid pressure, will be applied to the discrete particles that represent the walls of the fracture. In the simplest version of this model, the fluid forces will be constant over the full length of the fracture but may vary in time as the volume of the fracture changes resulting in a drop of pressure. The purpose of this model will be to provide a simple framework that is easy to implement and control for the purposes of studying phenomena such as elastoplastic deformation and fracture propagation. In addition to this, it may also be possible to implement a more complex version of this

model in which the fluid pressure forces are varied along the length of the fracture according to an assumed pressure profiles taken from one of several, available hydraulic fracture models.

The second approach to the coupled fluid model is intended to utilise the potential of the single framework, multi-physics model and will combine the PSM with the PFM. The PFM will represent a fracturing fluid and will be allowed to infiltrate a fracture developed within the PSM mesh (See Fig. 3.11. below). Interaction between the two modelling phases will be completely automatic and the PFM will apply pressure to the fracture walls consistent with the fluid it represents, subsequently causing deformation of the solid phase and propagation of the fracture as dictated by the constitutive models. This model will not require independent, iterative or staggered calculation of the fracture shape or of the pressure distributions along the fracture walls.

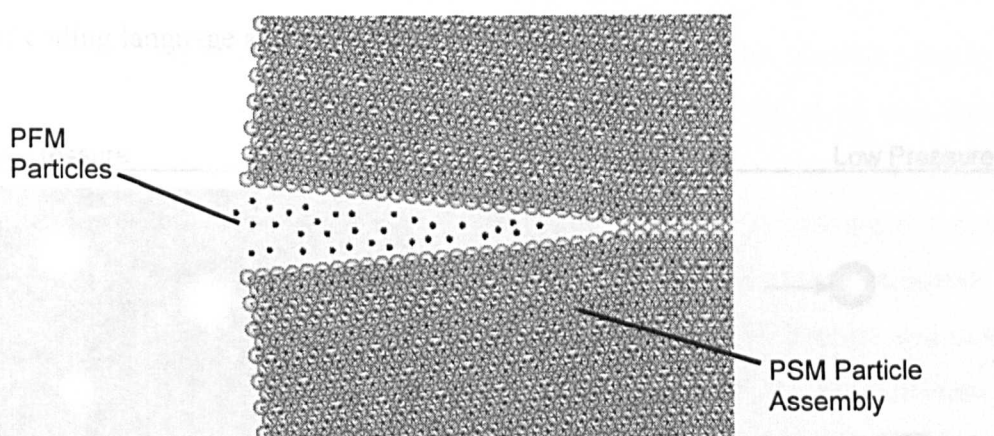


Fig. 3.11. Diagram of Proposed Interaction between PSM and PFM

3.8. Proposed Implementation of Particle Proppant Model (PPM)

Fig. 3.12. Diagram of PPM Implementation

Although this model is referred to as the Particle Proppant Model (PPM), as discussed in Section 2.5. of Chapter 2, all processes associated with the movement of a granular material within a fracture, for example, proppant transport, proppant stability, sand production and gravel packing, are considered similar enough that they necessitate the same modelling concepts. The PPM is therefore designed to handle all of these processes.

The PPM will consist of discrete particles given properties such that they represent the granular material on a grain for grain basis. This will be a simple implementation using the only the standard facilities available in the PFC^{3D} DEM environment and depending on the process being modelled the particles will be generated as free entities or in a closely packed group. Bonding may also be applied between particles in a closely packed group in order to represent the adhesive action of capillary forces or resin.

In addition to the basic particle components, a background pressure field will be implemented in which a gradient will be present (See Fig. 3.12. below). Drag forces, representing the action of fluid flowing passed the particles in a similar fashion to those used by Asgian et al. [5], Bruno et al. [11] and Preece et al. [73], will be applied to the particles on the basis of their position in the pressure field. The pressure field and the drag forces will be implemented and applied to the particles via routines developed in the *FISH* coding language associated with PFC^{3D}.

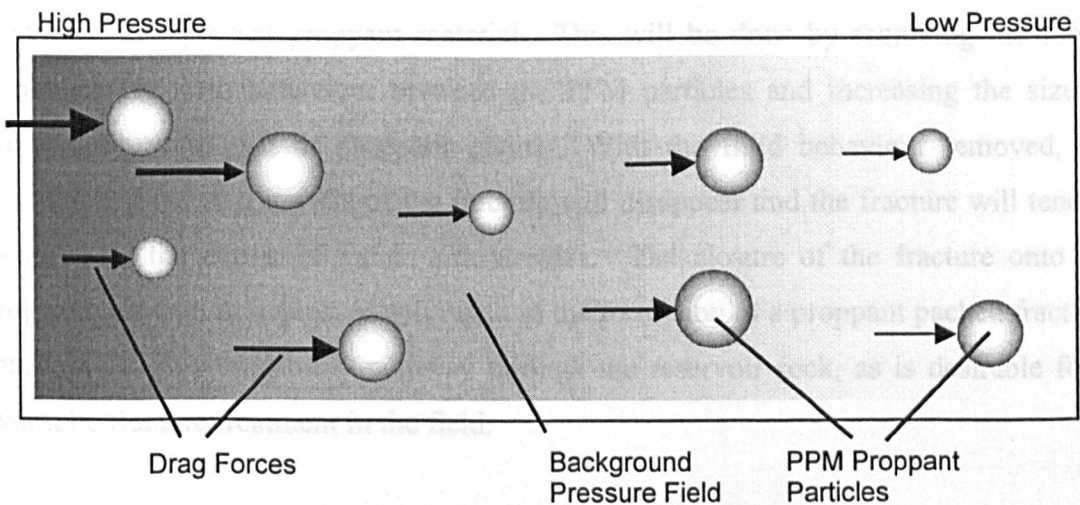


Fig. 3.12. Diagram of PPM Implementation

3.9. Proposed Implementation of the Fully Coupled Multi-Physics Framework (PSM + PFM + PPM)

As the ultimate aim of this project it is proposed to implement a conceptual fully coupled model that will show the full potential of the single framework, multi-physics model by combining the PSM, the PFM and the PPM to model fluid flow and proppant transport within a freely propagating hydraulically driven fracture.

A mesh will be constructed with the PSM to represent the solid phase reservoir formation. As in the coupled solid /fluid model (PSM + PFM), described above, the PFM will be used to represent a fracturing fluid that will be allowed to infiltrate a fracture in the PSM mesh and cause it to further propagate. In addition to the PFM, two approaches will be taken to the inclusion of proppant material within the fracture fluid.

In the first approach, once the fracture has reached the desired length, the infiltration of the PFM fluid will be halted. The particles of the PFM will then be converted to represent proppant material. This will be done by removing the forces implementing fluid behaviour between the PFM particles and increasing the size of these particles to that of proppant grains. With the fluid behaviour removed, the pressure applied to the walls of the fracture will disappear and the fracture will tend to close under the action of the in situ stresses. The closure of the fracture onto the proppant material now present will result in the formation of a proppant packed fracture, forming a high permeability pathway through the reservoir rock, as is desirable for a hydraulic fracture treatment in the field.

The second, alternative and possibly more realistic, approach to the inclusion of the PPM will be to generate, proppant particles within the PFM as it infiltrates the fracture in the PSM mesh. These particles will then be carried along in the fracture as it propagates. Along the fracture walls, particles of the PFM will be removed to simulate the loss of fluid through the process of leak-off and to allow the continued infiltration of the PPM into the fracture. As the proppant particles continue to enter the fracture they will begin to fill it. When the packing process is complete, the remaining PFM particles will be removed. As in the previous approach, the fluid pressure will then disappear

and the walls of the fracture will tend to close, under the in situ stress, onto the proppant pack, leave the high permeability pathway through the reservoir formation (See Fig. 3.13. below).

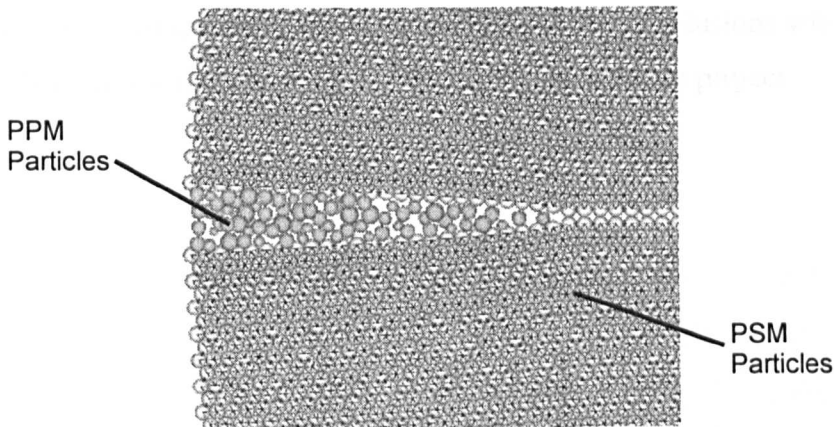


Fig. 3.13. Diagram of Final Stage of Proposed Fully Combined Model

3.10. Summary

In this Chapter, the overall proposal for the research to be conducted in this project has been presented. This outlined a single software framework (SSF), to be constructed within an existing DEM code, for the purposes of modelling multi-phase, geomechanical problems that can be encountered in fields such as civil and petroleum engineering. A particular focus of the research would be the modelling of hydraulic fracture treatments.

Following discussion of the capabilities and theory behind the proposed modelling environment, details have then been presented of the proposed implementations of individual models for each of the solid, fluid and granular components of the framework within the commercial, geotechnical DEM code, Particle Flow Code in Three Dimensions. Also presented were proposed implementations of coupled models consisting of these individual parts.

The following Chapter will discuss the actual development of the solid and fluid phase models and a coupled solid/fluid model created by simple combination of these two single phase models. Evidence for the accuracy of these models in reproducing certain material responses will also be presented through several benchmark studies, the results of which will be discussed in detail. From the results, conclusions will be drawn as to the capabilities of the models and the evolving progress of the project.

Chapter 4:

Numerical Model Development

4.1. Introduction

In this Chapter a full discussion will be made of the development of each of the PSM, PFM and coupled PSM + PFM models as discussed in the previous Chapter. For each of the models a description of the development process and physical interpretation will be given. This will be followed by a description of the methods applied in order to achieve continuum equivalence with the materials that the models are intended to represent. The discussion will then move on to describe benchmark problems with which the validity of each model was tested. The results of these tests are presented and discussed, along with any conclusions. Discussion is also made of the evolution of the research work in this project as it developed from the findings of these model tests.

4.2. The Particle Solid Model (PSM)

4.2.1. Development of the PSM

As proposed in Chapter 3, Section 3.2., the PSM was constructed within the DEM modelling environment PFC^{3D}. The initial purpose of the model was to represent the elastic behaviour of solid materials and, given the nature of the problem under investigation, particularly the behaviour of concrete and rock.

In general, the PSM consists of a two-dimensional bonded particle assembly constructed, in a lattice type configuration, to the appropriate dimensions of the specific problem. In all cases considered in this project, the assembly consisted of a mesh of spherical particles of uniform radius, arranged in triangular formation, in a planar sheet, such that they were packed as closely as possible (See *Fig. 4.1.*).

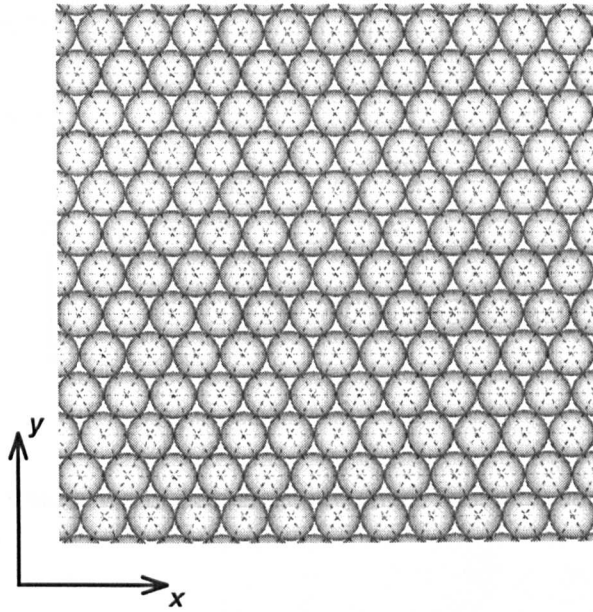


Fig. 4.1. Typical Example of Two-Dimensional Bonded Particle Assembly Constructed for PSM

It should be noted that the triangular mesh is 60° symmetrical and that, therefore, its structure in the x and y -directions not the same. Although the exact orientation of the mesh is arbitrary, the arrangement shown above is applied to all PSM meshes studied in this project. Furthermore, although PFC^{3D} is a fully three-dimensional modelling environment, the particles in a mesh are fixed against displacement in the z -direction and against rotation about the x and y -axes. In this way, only two-dimensional, planar behaviour is considered.

Particle interaction is governed by linear, normal and shear spring stiffnesses that come into effect at each inter-particle contact and the assembly can therefore be visualised as a single layer network of springs (See Fig. 4.2. below). This consequently allows the particle assembly to be regarded as having a unit thickness, no matter what the actual thickness is, as defined by the particle radius.

The inter-particle links are implemented by the inclusion of 'contact bonds' (See Chapter 3, Section 3.3.) that connect particles together where they are in contact in the initial mesh configuration. The 'contact bonds' provide no extra stiffness to the inter-particle contacts and simply allow tensile forces to be transmitted, up to a predefined

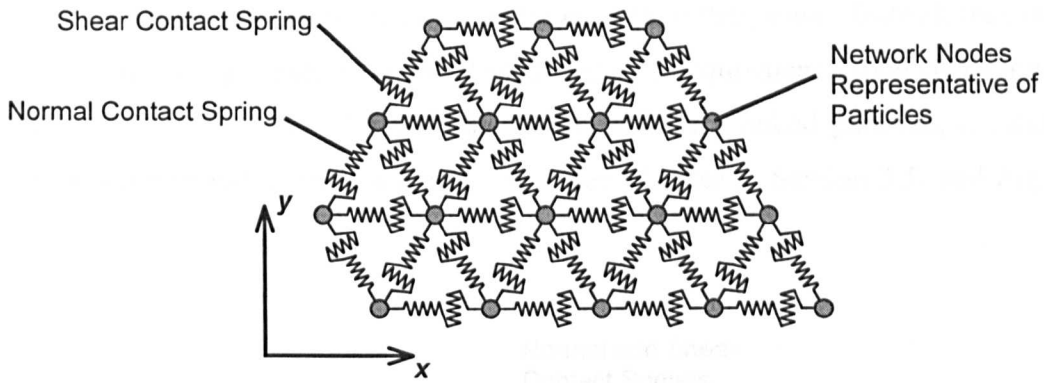


Fig. 4.2. Visualisation of PSM Bonded Particle Assembly as Spring Network

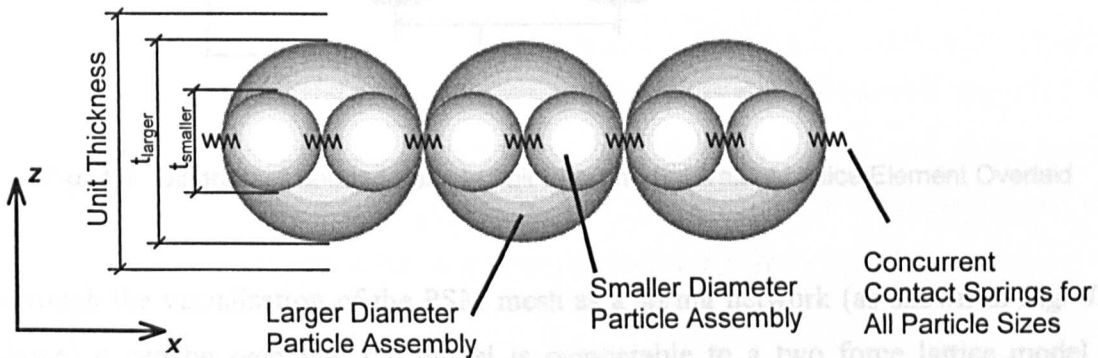


Fig. 4.3. End Elevation of Particle Assembly Showing Contact Spring Position Independent of Particle Size

The actual radius of the particles is, therefore, arbitrary and can be varied as desired in order to ensure an adequate discretisation of the model in question. Model sensitivity to mesh discretisation is studied as part of the benchmark problems discussed in Section 4.2.3. In fact, it should be noted that the mesh dimension of most significance is the inter-particle link length but, obviously, this is directly related to the particle radius.

The inter-particle links are implemented by the inclusion of ‘contact bonds’ (See Chapter 3, Section 3.3.) that connect particles together where they are in contact in the initial mesh configuration. The ‘contact bonds’ provide no extra stiffness to the inter-particle contacts and simply allow tensile forces to be transmitted, up to a predefined

maximum, in the same way as compressive forces. The inter-particle links are not regarded as having any length or cross-sectional area of their own. Instead, they can be thought of as joining together two rigid segments of an equivalent lattice element with a length equal to the distance between the centroids of two linked particles, i.e. initially twice the particle radius in a uniform mesh (See Chapter 3, Section 3.5. and Fig. 4.4. below).

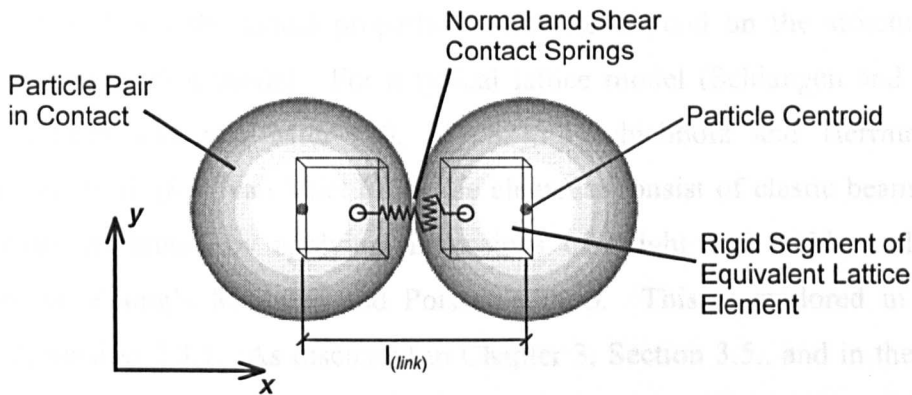


Fig. 4.4. Diagram of Bonded Particle Pair Showing Equivalent Lattice Element Overlaid

Through the visualisation of the PSM mesh as a spring network (as shown in Fig. 4.2. above) it can be seen that the model is comparable to a two force lattice model as described by Schlangen and Garboczi [79] and discussed in Chapter 2, Section 2.3.1. The inter-particle contacts of the PSM are able to transmit normal and shear forces but are not able to support a bending moment. Therefore, in contrast to the lattice models of other researchers (Schlangen and Garboczi [79], Schlangen and van Mier [80, 81, 82], Tzschichholz and Herrmann [88], Tzschichholz et al. [89], van Vliet [95]) that, as discussed in Chapter 2, Section 2.3.1., employed beam elements, the PSM does not reproduce the behaviour of a Cosserat type medium. The exact construction and properties of the inter-particle links is examined in more detail in the following Sections.

It should be also noted that the models developed for this project are considered to be on a macro-scale, with link lengths on the order of metres, as opposed to the micro-scale lattice models of the researchers mentioned above where element lengths were on the order of millimetres.

4.2.2. PSM - Continuum Equivalence

As explored in Chapter 2, Section 2.3.1., the elements of a lattice type model must be given properties such that the overall response of the lattice accurately reproduces the behaviour of the continuum material that it represents. There are various calibration techniques that can be employed in order to develop continuum equivalence and several approaches were investigated in this work. The equivalence techniques applicable to a particular model and the actual properties calibrated depend on the structure of the lattice elements in that model. For a typical lattice model (Schlangen and Garboczi [79], Schlangen and van Mier [80, 81, 82], Tzschichholz and Herrmann [88], Tzschichholz et al. [89], van Vliet [95]), the elements consist of elastic beams and are consequently calibrated by applying dimensions of height and width, and material properties of Young's Modulus and Poisson's ratio. This is explored in detail in Chapter 2, Section 2.3.1. As discussed in Chapter 3, Section 3.5., and in the previous Section of this Chapter, the equivalent lattice elements in the PSM model consist of two rigid segments (the particles) joined where they meet by normal and shear contact springs. Therefore, the only properties that can be varied are the spring stiffnesses and it is through these that continuum equivalence must be found for the PSM.

4.2.2.1. Hrennikoff's Formulations

The first method of element calibration investigated for application to the PSM mesh was the technique originally developed by Hrennikoff [36] (See Chapter 2, Section 2.3.1.), to determine the required properties of bar elements in open frameworks. Hrennikoff developed formulations for the calibration of various framework configurations, one of which was a triangular construction as is equivalent to the PSM mesh and it was hoped that this could be directly applied in this work.

Hrennikoff's original formulations were based on the comparison of various configurations of frameworks with a continuous plate, subject to plane stress conditions. For a particular framework geometry, Hrennikoff calculated the normal strains that it would experience, under an arbitrary external load of P in the x -direction and νP in the

y -direction, and the shear strains it would experience under a uniform shear loading of $P.l_{(bar)}$, where $l_{(bar)}$ is the length of the framework elements. Clearly, for calculation of the normal strains, the value of νP is deliberately chosen in order to produce zero y -strain. These strains were then expressed in terms of parameters specific to the framework, such as the bar element length, the cross-sectional area of the bar elements, the stress in the bar elements and the Poisson's ratio and Young's modulus of the continuum plate material. The expressions derived for the strains in a particular framework were equated to the expressions, shown below, for strain in a plate subject to the same loading.

$$\varepsilon_x = \frac{P(1-\nu^2)}{Et_{(plate)}} \quad \text{Eq. 4.1.}$$

$$\varepsilon_y = 0 \quad \text{Eq. 4.2.}$$

$$\gamma_{xy} = \frac{2(1+\nu)P}{Et_{(plate)}} \quad \text{Eq. 4.3.}$$

where, $\varepsilon_{x,y}$ are strains in the x and y -directions respectively, γ_{xy} is shear strain and $t_{(plate)}$ is the thickness of the continuous plate.

These equalities were then rearranged to solve for the cross-sectional areas of the bar elements. For a framework consisting of isosceles triangles, Hrennikoff found that, due to the symmetry of the framework, the equations were only valid for an equilateral triangular arrangement with a Poisson's ratio fixed at $1/3$. Hence, the required cross-sectional area was shown to be:

$$A_{(bar)} = \frac{\sqrt{3}}{2} l_{(bar)} t_{(plate)} \quad \text{Eq. 4.4.}$$

where, $A_{(bar)}$ is the cross-sectional area of the bar elements.

NB - for convenience and consistency in this thesis some of the notation in *Eq. 4.1.* to *Eq. 4.4.* has been altered from the original text (Hrennikoff [36]).

As mentioned before, the ‘contact bonds’, forming the inter-particle links of the PSM are considered point contacts, existing over a vanishingly small area. From *Eq. 4.4.* it can be seen that a required cross-sectional area is calculated for the framework elements, depending on the framework discretisation and the thickness of the continuum to be replaced. Given that the PSM links have no physical cross-sectional area to alter, a method had to be found of applying properties equivalent to a change in cross-sectional area. As mentioned above this had to be in terms of the normal and shear contact spring stiffnesses. In order to do this the following elastic behaviour relationships were assumed (See *Eq. 4.5.* to *Eq. 4.7.*).

$$k_n = \frac{EA_{(bar)}}{l_{(bar)}} \quad \text{Eq. 4.5.}$$

$$k_s = \frac{GA_{(bar)}}{l_{(bar)}} \quad \text{Eq. 4.6.}$$

$$G = \frac{E}{2(1+\nu)} \quad \text{Eq. 4.7.}$$

where, G is the material shear modulus.

This method was first applied by Davie [21] for a test involving a uniaxially loaded mesh. A parametric study showed that a value of element cross-sectional area approaching twice that calculated by Hrennikoff’s formulation was required in order for the model to reproduce displacements similar to those expected in an equivalent continuum. It was noted at the time that this might have been a systematic difference between the hand calculation applied in the study and the internal calculation of the PFC^{3D} program. Subsequently, this factor of two has been shown to result from

PFC^{3D}'s method of assuming contact spring stiffnesses to act in series (See *Eq. 3.1.* and *Eq. 3.2.* repeated below and Chapter 3, Section 3.3.), which produces internal stiffnesses that are half the value of those input to the model via *Eq. 4.5.* and *Eq. 4.6.*

$$K^n = \frac{k_n^{(A)}k_n^{(B)}}{k_n^{(A)} + k_n^{(B)}} \quad \text{Eq. 3.1.}$$

$$K^s = \frac{k_s^{(A)}k_s^{(B)}}{k_s^{(A)} + k_s^{(B)}} \quad \text{Eq. 3.2.}$$

It could therefore be argued that, if PFC^{3D}'s internal method of calculation were taken into account, Hrennikoff's formulation would give reasonable results when applied directly to a PSM mesh via the assumed elastic relationships shown above (See *Eq. 4.5.*, *Eq. 4.6.* and *Eq. 4.7.*).

However, the study carried out by Davie [21] also showed that the value of ν calculated for the test mesh varied considerably from Hrennikoff's fixed value of $\frac{1}{3}$. When the actual calculated value of ν was applied in the parametric study, the calculated value of required cross-sectional area moved away from that produced by Hrennikoff's formulation. It has been observed by van Mier [59] that, in fact, the value of ν for a lattice type model mesh will depend on both shear stiffness and the normal stiffness of the mesh elements. Hrennikoff's formulation was based only on the contributions of axial loads as transferred by pin-jointed truss elements. Therefore, while the method may be appropriate for the calibration of a PSM mesh consisting of inter-particle links with shear stiffnesses set to zero, it will not be suitable for a mesh with non-zero shear stiffnesses. The presence of shear stiffnesses in the test mesh was thought to account for the discrepancies found in the study discussed above and, for this reason, Hrennikoff's method was abandoned in conjunction with the calibration of continuum equivalence for the PSM.

4.2.2.2. Trial and Error Approaches

An alternative method for establishing continuum equivalence is through a trial and error approach. This technique involves the construction of a suitable benchmark mesh, which represents a continuum problem for which the elastic behaviour is well understood. The model properties, the contact spring stiffnesses in the case of the PSM, are adjusted iteratively until the model response is considered to reproduce the behaviour of an equivalent continuum, with the desired material properties, to a sufficient accuracy.

An example of this approach is the work conducted by Davie [21] in order to establish continuum equivalence for a PSM like mesh, designed to study wellbore stability problems. An example of a bonded particle assembly mesh employed in this numerical study is shown below (See Fig. 4.5.).

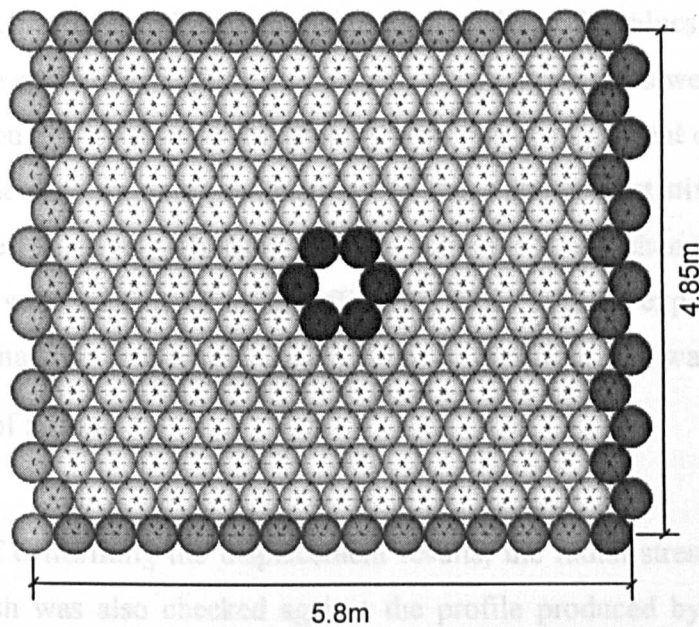


Fig. 4.5. Example of Bonded Particle Assembly Mesh Used for Wellbore Stability Studies

(After Davie [21])

In the search for an appropriate calibration technique, it was noted that the model meshes, as seen above, resembled a thick walled cylinder. Thick walled cylinder behaviour is well understood and can be described by the equations shown below (Dugdale [25]).

$$E.u = \frac{1}{1 - \left(\frac{r_i^2}{r_e^2}\right)} \left\{ P_i \left[(1 - \nu) \frac{r_i^2 r_m}{r_e^2} + (1 + \nu) \frac{r_i^2}{r_m} \right] - P_e \left[(1 - \nu) r_m + (1 + \nu) \frac{r_i^2}{r_m} \right] \right\} \quad \text{Eq. 4.8.}$$

$$\sigma_r = \frac{1}{1 - \left(\frac{r_i^2}{r_e^2}\right)} \left[P_i \left(\frac{r_i^2}{r_e^2} - \frac{r_i^2}{r_m^2} \right) - P_e \left(1 - \frac{r_i^2}{r_m^2} \right) \right] \quad \text{Eq. 4.9.}$$

where, u is the total displacement of a point, σ_r is the radial stress, r_i and r_e are respectively the internal and external radii of the thick walled cylinder, P_i and P_e are respectively the internal and external applied pressures and r_m is the radius between r_i and r_e at which measurement is taken.

For a particular mesh, similar to that shown in *Fig. 4.5.*, values of internal and external radii were approximated, and internal and external pressures were applied. For given values of Young's modulus and Poisson's ratio, the displacement of the mesh was checked against the displacement predicted by *Eq. 4.8.* The contact stiffnesses, k_n and k_s , were then varied iteratively, choosing firstly a value for k_n and then varying k_s , until the displacements were considered to be sufficiently close to those expected for a mesh with the current material properties. In the study in question, this was achieved to a level of accuracy of ± 1 mm.

By way of confirming the displacement results, the radial stress profile over a radius of the mesh was also checked against the profile produced by *Eq. 4.9.* This showed good consistency with the displacements of the mesh for the same conditions. However, it should be noted that the radial stress is only a function of the cylinder size and the pressures applied. It is not a function of material property but is a condition of equilibrium. It is not therefore a good confirmation of the accuracy of the mesh displacement results. Furthermore, it is now thought that an accuracy of ± 1 mm may not be sufficient for the determination of the relatively large contact stiffnesses on the order

of 10^8 N/m. The stiffnesses were only calculated to an accuracy of $\pm 1 \times 10^6$ N/m and it is likely that a wide range and combination of normal and shear stiffnesses will result in the same displacements when measured to this level.

Various alterations could be made in order to improve this calibration technique, for example, the accuracy to which displacements are measured could be increased. However, it is felt that in order to reach a sufficient level of accuracy the time required to calibrate a mesh would also increase excessively. Furthermore, inaccuracies associated with the assumed dimensions of the cylinder, particularly when estimating the radius of a cylinder in a square mesh, would remain. Although a more simple and general benchmark model, such as a uniaxial compression test, could be applied in this technique, the example described above serves to illustrate the inherent difficulties and inaccuracies of the trial and error method. While the results of the study described were considered acceptable for the work for which it was carried out, it is now felt that this particular method is not accurate enough to be pursued in the course of the work carried out for this thesis.

4.2.2.3. Application of Strain Energy Equivalence Technique to PSM

Another method for establishing continuum equivalence for a lattice type model is to look into the strain energy equivalence. This involves the calculation of the stored strain energy in a continuum area equivalent to a typical lattice unit and deriving, analytically, equations relating it to the variables associated with the lattice elements in that unit.

As shown in Chapter 2, Section 2.3.1., this is the approach used by Schlangen and Garboczi [79], Schlangen and van Mier [81] and van Vliet [95], in order to calibrate lattices of beam elements. The general equations derived in order to calculate the two-dimensional elastic moduli for a regular triangular lattice of beam elements can be found in Chapter 2, Section 2.3.1. (See *Eq. 2.7.* to *Eq. 2.9.*). These equations can be rearranged and rewritten specifically for a lattice of rectangular beam elements (See *Eq. 2.10.* and *Eq. 2.11.*) and, for convenience, these are repeated below.

$$v_{(lattice)} = \frac{\left(1 - \left(\frac{h_{(beam)}}{l_{(beam)}}\right)^2\right)}{\left(3 + \left(\frac{h_{(beam)}}{l_{(beam)}}\right)^2\right)} \quad \text{Eq. 2.10.}$$

$$E_{(lattice)} = 2\sqrt{3} \frac{E_{(beam)} A_{(beam)}}{l_{(beam)}} \left(\frac{1 + \left(\frac{h_{(beam)}}{l_{(beam)}}\right)^2}{3 + \left(\frac{h_{(beam)}}{l_{(beam)}}\right)^2} \right) \quad \text{Eq. 2.11.}$$

As can be seen from *Eq. 2.10.*, Poisson's ratio for the lattice is dependent on only the height and length of the lattice elements. It is noted by van Vliet [95] that it is not at all dependent on the thickness of the elements and so the lattice can be considered to have any thickness. For a representation of a continuum model, this is usually taken as unit thickness. The element length is usually chosen in order to achieve an adequate discretisation of the mesh. For the models developed by Schlangen and van Mier [80, 81, 82] and van Vliet [95], the element length was on the order of 1mm in order to capture the heterogeneity of concrete. Since the element length is effectively predetermined by the requirements of the model it is only necessary to adjust the height of the elements to achieve a desired value of Poisson's ratio for the lattice mesh. Rearranging *Eq. 2.10.* in terms of element height gives:

$$h_{(beam)} = \sqrt{\frac{1 - 3v_{(lattice)}}{1 + v_{(lattice)}}} l_{(beam)} \quad \text{Eq. 4.10.}$$

With the height of the beam elements available, it is then possible, from a rearrangement of *Eq. 2.11.*, to calculate a value for the Young's modulus of the beams, in order to reproduce a desired overall Young's modulus for the lattice (See *Eq. 4.11.*).

$$E_{(beam)} = \frac{E_{(lattice)} l_{(beam)}}{2\sqrt{3} A_{(beam)}} \left(\frac{3 + \left(\frac{h_{(beam)}}{l_{(beam)}} \right)^2}{1 + \left(\frac{h_{(beam)}}{l_{(beam)}} \right)^2} \right) \quad \text{Eq. 4.11.}$$

The beam properties given by the equations shown above are derived from the stored strain energy in an equivalent continuum and as such, they reflect the properties of an infinite continuum. It is possible to develop a lattice model with periodic boundary conditions that will hence reproduce an infinite continuum, however, this is not of much practical use as in practice, a model will usually represent a finite domain. A study by van Vliet [95] examined the effect of the boundary conditions, present in a finite model, on the overall material properties of a lattice. This was done by developing simple, square benchmark lattice models in which the properties of the beam elements were calculated as described above. The overall material properties of the lattice models was checked by applying Hooke's Law to the overall mesh deformations under uniaxial loading. The findings of the study showed that if the ratio of overall lattice length to element length was ≥ 20 then this calibration technique was sufficiently accurate. It was also found that the overall Poisson's ratio of the lattice was more sensitive to this ratio than the Young's Modulus.

The strain energy equivalence method has been shown to work well for lattice models consisting of beam elements (See Schlangen and Garboczi [79], Schlangen and van Mier [80, 81, 82], van Vliet [95]) and it was hoped to be able to transfer this method of developing continuum equivalence to the PSM. As with Hrennikoff's method (See Section 4.2.2.1. above) the formulae derived from the stored strain energy required an element cross-sectional area. As explained previously, the inter-particle links of the PSM do not have a physical cross-sectional area and so it would be necessary to find a method by which the material property of Young's modulus related to elements of a certain cross-sectional area could be expressed in terms of the contact stiffnesses, k_n and k_s . This should have been possible through the assumed elastic relationship expressed above in Eq. 4.5. to Eq. 4.7., however, it should be remembered that the beam elements

employed in these lattice models are capable of supporting bending moments as well as the normal and shear forces.

Rather than apply this complex, two stage, calibration procedure to the PSM an alternative method was considered, that directly derives formulae from strain energy equivalence for a bonded particle assembly, consisting of a lattice of contact spring elements, rather than of beam elements. The formulae express the normal and shear contact stiffnesses in terms of the Young's modulus and Poisson's ratio of the continuum material to be represented. These formulations were initially developed by Morikawa and Sawamoto [63] for application in a bonded particle assembly and were further developed by Griffiths and Mustoe [32]. Both of these studies examined a triangularly packed bonded particle assembly very similar to the PSM.

The derivation of these formulae is explained in detail by Griffiths and Mustoe [32] but the principle is based on the calculation of the total strain energy, W_{tot} , stored in a typical, triangular, equivalent lattice unit of the particle assembly, as shown below (See Fig. 4.6.), and the relationship between strain energy density and the stress-strain behaviour of a deformed elastic body.

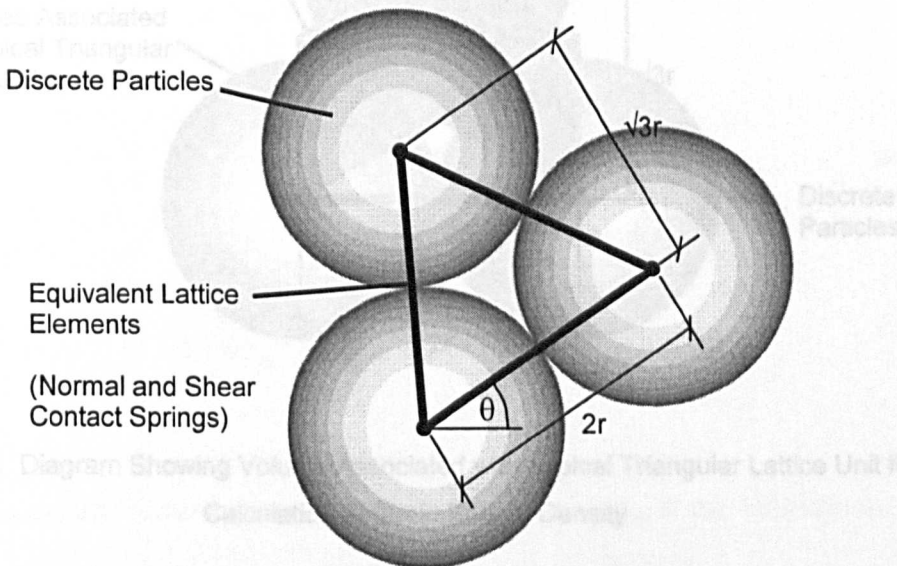


Fig. 4.6. Diagram Showing Typical Triangular Unit of Bonded Particle Used for Strain Energy Equivalence Calculation

It can be shown that the stored strain energy, W_{tot} , in a typical triangular lattice unit, as shown above, can be expressed as Eq. 4.12. and is invariant for any value of the angle θ :

$$W_{tot} = \left[\begin{aligned} & \frac{3r^2(3k_n + k_s)(\epsilon_{xx}^2 + \epsilon_{yy}^2)}{4} + \frac{3r^2(k_n - k_s)(\epsilon_{xx}\epsilon_{yy} + \epsilon_{xy}\epsilon_{yx})}{2} \\ & + \frac{3r^2(k_n + 3k_s)(\epsilon_{xy}^2 + \epsilon_{yx}^2)}{4} + 6r^2\beta k_s(\epsilon_{xy} - \epsilon_{yx}) + 6r^2\beta^2 k_s \end{aligned} \right] \quad \text{Eq. 4.12.}$$

where, r is the particle radius, $\epsilon_{xx,xy,yx,yy}$ are the components of the strain tensor and β is the average nodal rotation.

In order to calculate the strain energy density, an associated volume is assigned to the typical triangular unit, as shown below (See Fig. 4.7.).

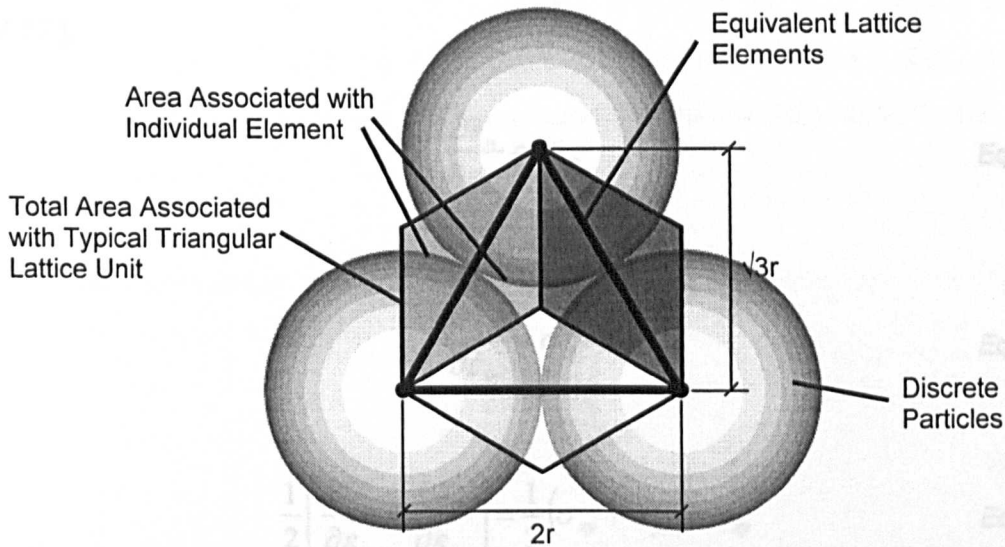


Fig. 4.7. Diagram Showing Volume Associated with Typical Triangular Lattice Unit for Calculation of Strain Energy Density

Each element in the triangular unit is assigned an associated area equal to one third of the triangle on each side of it. Therefore, a typical triangular unit of elements has a total associated hexagonal area equal to twice the enclosed triangular area. As with the PSM,

the particle assembly is assumed to have unit thickness (See Section 4.2.1.) and therefore the volume, V , associated with the lattice unit is equal to:

$$V = 2\sqrt{3}r^2 \quad \text{Eq. 4.13.}$$

The strain energy density in a typical triangular lattice unit can then be expressed as:

$$V_o = \frac{W_{tot}}{V} \quad \text{Eq. 4.14.}$$

By deriving the strain energy density with respect to each of the components of the strain tensor, it is possible to develop the corresponding stress tensor (See *Eq. 4.15.* to *Eq. 4.17.*).

$$\frac{\partial V_o}{\partial \varepsilon_{xx}} = \sigma_{xx} \quad \text{Eq. 4.15.}$$

$$\frac{\partial V_o}{\partial \varepsilon_{yy}} = \sigma_{yy} \quad \text{Eq. 4.16.}$$

$$\frac{1}{2} \left(\frac{\partial V_o}{\partial \varepsilon_{xy}} + \frac{\partial V_o}{\partial \varepsilon_{yx}} \right) = \frac{1}{2} (\sigma_{xy} + \sigma_{yx}) = \tau_{xy} \quad \text{Eq. 4.17.}$$

where $\sigma_{xx,xy,yx,yy}$ are components of the stress tensor and τ_{xy} is the conventional shear stress.

When *Eq. 4.12.* is substituted into equation *Eq. 4.14.* and the derivations described in *Eq. 4.15.* to *Eq. 4.17.* are applied, the following equalities are produced.

$$\sigma_{xx} = \frac{\sqrt{3}}{4}(3k_n + k_s)\varepsilon_{xx} + \frac{\sqrt{3}}{4}(k_n - k_s)\varepsilon_{yy} \quad \text{Eq. 4.18.}$$

$$\sigma_{yy} = \frac{\sqrt{3}}{4}(k_n - k_s)\varepsilon_{xx} + \frac{\sqrt{3}}{4}(3k_n + k_s)\varepsilon_{yy} \quad \text{Eq. 4.19.}$$

$$\tau_{xy} = \frac{\sqrt{3}}{4}(k_n + k_s)(\varepsilon_{xy} + \varepsilon_{yx}) = \frac{\sqrt{3}}{4}(k_n + k_s)\gamma_{xy} \quad \text{Eq. 4.20.}$$

where, γ_{xy} is the ‘engineering’ shear strain, (described as “engineer’s” shear strain by Griffiths and Mustoe).

With the components of the stress tensor available, it is then possible to equate the contact spring formulations in *Eq. 4.18.*, *Eq. 4.19.* and *Eq. 4.20.* directly to solid mechanics formulations, in terms of Young’s modulus and Poisson’s ratio, for both plane stress (See *Eq. 4.21.* to *Eq. 4.23.*) and plane strain (See *Eq. 4.24.* to *Eq. 4.26.*) conditions.

Plane Stress Conditions:

$$\sigma_{xx} = \frac{E}{(1-\nu^2)}\varepsilon_{xx} + \frac{E\nu}{(1-\nu^2)}\varepsilon_{yy} \quad \text{Eq. 4.21.}$$

$$\sigma_{yy} = \frac{E\nu}{(1-\nu^2)}\varepsilon_{xx} + \frac{E}{(1-\nu^2)}\varepsilon_{yy} \quad \text{Eq. 4.22.}$$

$$\tau_{xy} = \frac{E}{2(1+\nu)}\gamma_{xy} \quad \text{Eq. 4.23.}$$

Plane Strain Conditions:

$$\sigma_{xx} = \frac{E(1-\nu)}{(1+\nu)(1-2\nu)} \varepsilon_{xx} + \frac{E\nu}{(1+\nu)(1-2\nu)} \varepsilon_{yy} \quad \text{Eq. 4.24.}$$

$$\sigma_{yy} = \frac{E\nu}{(1+\nu)(1-2\nu)} \varepsilon_{xx} + \frac{E(1-\nu)}{(1+\nu)(1-2\nu)} \varepsilon_{yy} \quad \text{Eq. 4.25.}$$

$$\tau_{xy} = \frac{E}{2(1+\nu)} \gamma_{xy} \quad \text{Eq. 4.26.}$$

In both case these can then be rearranged to solve for k_n and k_s (See Eq. 4.27. & Eq. 4.28. and Eq. 4.29. & Eq. 4.30.).

Plane Stress Condition:

$$k_n = \frac{E}{\sqrt{3}(1-\nu)} \quad \text{Eq. 4.27.}$$

$$k_s = \frac{E(1-3\nu)}{\sqrt{3}(1-\nu^2)} \quad \text{Eq. 4.28.}$$

Plane Strain Conditions:

$$k_n = \frac{E}{\sqrt{3}(1-2\nu)(1+\nu)} \quad \text{Eq. 4.29.}$$

$$k_s = \frac{E(1-4\nu)}{\sqrt{3}(1-2\nu)(1+\nu)} \quad \text{Eq. 4.30.}$$

A number of points can be noted from the equations shown above. Firstly, as mentioned previously, the contact spring stiffnesses are defined only in terms of the Young's modulus and Poisson's ratio of the continuum material that is to be represented. Unlike the properties of the lattice beam elements, defined in *Eq. 2.10.* and *Eq. 2.11.* above, the contact stiffnesses do not depend on the element length. This is because the springs acting at particle contacts, which have no length of their own, are independent of the particle radii.

Secondly, it can be seen from these equations that both the plane stress and plane strain formulations are valid only over a limited range of Poisson's ratio, above which the shear stiffness becomes negative; a meaningless result. In the case of the plane stress formulation this range is between $\nu = 0$ and $\nu = \frac{1}{3}$. This is a well known limitation of triangular lattice models (See Chapter 2, Section 2.3.1.). Similarly, the valid range for the plane strain formulation is between $\nu = 0$ and $\nu = \frac{1}{4}$. In both formulations, when Poisson's ratio is at the maximum value, k_s becomes zero and the bonded particle assembly becomes an axial force lattice, equivalent to a simple pin-jointed truss. When the Poisson's ratio is less than its maximum the assembly behaves as a two force lattice, as described by Schlangen and Garboczi [79] (See Chapter 2, Section 2.3.1.). The limit of this behaviour is when Poisson's ratio reaches zero and k_n and k_s become equal.

Although Morikawa and Sawamoto [63] developed these continuum equivalence equations for a two-dimensional model consisting of cylindrical discrete elements, they can be directly applied to the spherical particles of the PSM. As discussed in Section 4.2.1. above, the fixing of the PSM in the z -direction induces two-dimensional behaviour and both the PSM and Morikawa and Sawamoto's model can be thought of as planar networks of normal and shear contact springs (See *Fig. 4.2.* repeated below).

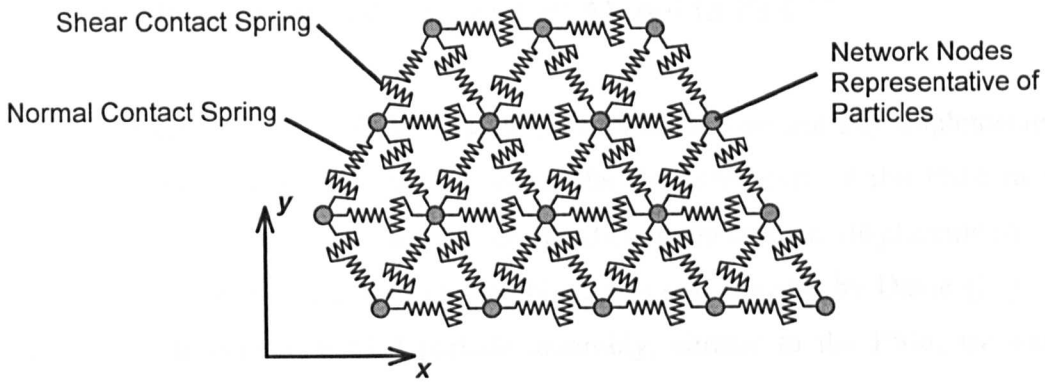


Fig. 4.2. Visualisation of PSM Bonded Particle Assembly as Spring Network
(Repeated from page 107)

The following Sections concern benchmark problems used to verify the behaviour of the PSM with continuum equivalence developed by the equations described here.

4.2.3. PSM Benchmark Problems

The method of finding lattice-continuum equivalence through strain energy equivalence described in the Section 4.2.2.3. above, is easily applicable to the PSM. Furthermore, a similar technique employed by Schlangen and van Mier [80, 81, 82] and van Vliet [95] is seen to produce highly satisfactory results in lattice models consisting of beam elements even with the inclusion of complex heterogeneity. Despite this, it was necessary to assess the validity of the approach in the PSM.

In order to do this several benchmark models were constructed for which the elastic behaviour is well understood and for which the expected response of an equivalent continuum material could be easily calculated. Various benchmark models were suitable for this purpose and the problems used by Griffiths and Mustoe [32] in a validation of the same continuum equivalence technique were adopted. The first of these problems considered the deformation of an almost square mesh under uniaxial loading. The second problem considered the tip displacement of a long, narrow mesh loaded as a cantilever. The construction and testing of these benchmark models is described in the following Sections, along with discussion of the presented results.

4.2.3.1. Application of Linear Contact Model in PFC^{3D}

It should be noted that when these benchmark problems were initially implemented, a common problem was experienced in which the displacements of the PSM meshes tended towards a value twice that of the predicted, theoretical displacements. As discussed in Section 4.2.2.2., a similar problem was encountered by Davie [21] when attempting to calibrate a bonded particle assembly, similar to the PSM, by way of Hrennikoff's formulations.

After examination of the linear contact model employed by PFC^{3D}, it was found that the discrepancy in the deformations was due to the assumption, made within PFC^{3D}, that when two particles meet, their contact springs act in series. This assumption leads to the contact normal secant stiffness, given by Eq. 3.1., and the contact shear tangent stiffness, given by Eq. 3.2. (See Chapter 3, Section 3.3. and equations repeated below for convenience) (See also Itasca Consulting Group [37]).

$$K^n = \frac{k_n^{(A)}k_n^{(B)}}{k_n^{(A)} + k_n^{(B)}} \quad \text{Eq. 3.1.}$$

$$K^s = \frac{k_s^{(A)}k_s^{(B)}}{k_s^{(A)} + k_s^{(B)}} \quad \text{Eq. 3.2.}$$

As can be seen from these formulae, given uniform stiffness in the mesh, as is the case in the PSM, this formulation results in contact stiffnesses equal to half that of the input values. This factor had not been accounted for in the initial implementations of the benchmark problems and consequently the mesh deformations were twice those expected. In order to allow for this the input stiffnesses, calculated from the formulations of Morikawa and Sawamoto [63] (See Eq. 4.27. to Eq. 4.30.) were simply doubled. The results of the studies conducted after this correction can be seen in the following Sections.

4.2.3.2. Uniaxial Benchmark Model

4.2.3.2.1. Elastic Deformation Tests

This benchmark study looks into the elastic deformation of an almost square PSM mesh and compares the findings with the deformations predicted by simple elastic plane strain theory for an equivalent continuum. The test was carried out in order to check the validity of the strain energy equivalence formulations, developed by Morikawa and Sawamoto [63] and further derived by Griffiths and Mustoe [32], when applied to the PSM.

For the purposes of this study, a regular, PSM mesh was constructed, as shown in *Fig. 4.8.* below, to approximately square dimensions, with two force boundaries and two boundaries fixed to produce a double symmetry condition. The particle radius was 0.5m and the equivalent lattice element length was therefore 1.0m. The construction of this model followed as closely as possible the construction of a benchmark model developed by Griffiths and Mustoe [32]. As in the original test the mesh was assumed to experience plane strain behaviour and the contact spring stiffnesses were calculated from the appropriate formulae, as developed by Morikawa and Sawamoto [63] (See *Eq. 4.29.* and *Eq. 4.30.* repeated below).

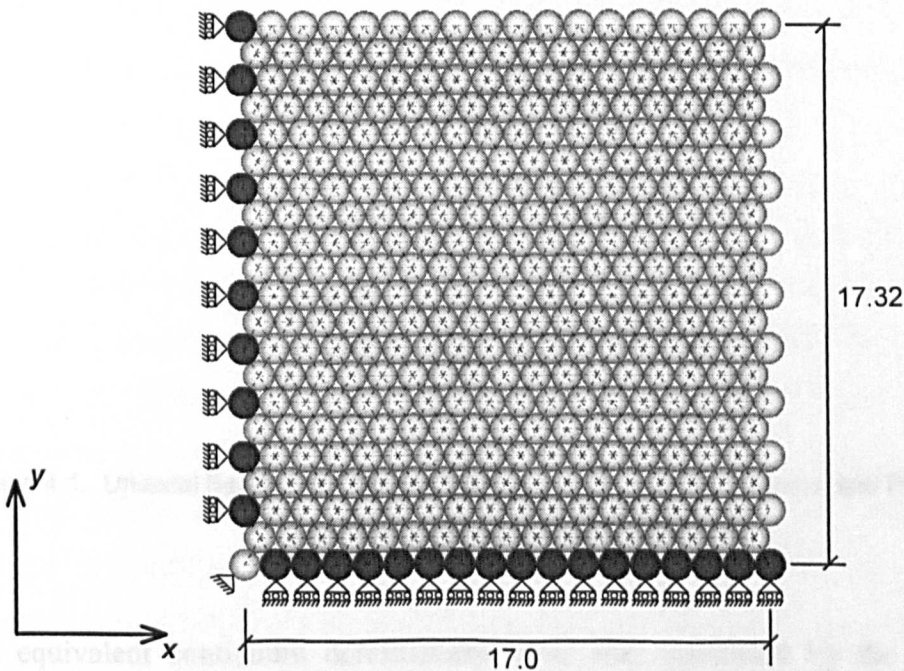


Fig. 4.8. Diagram of PSM Mesh for Uniaxial Benchmark Test

$$k_n = \frac{E}{\sqrt{3}(1-2\nu)(1+\nu)} \quad \text{Eq. 4.29.}$$

$$k_s = \frac{E(1-4\nu)}{\sqrt{3}(1-2\nu)(1+\nu)} \quad \text{Eq. 4.30.}$$

Several studies were conducted, loading the mesh in both the x and y -directions, in both tension and compression. In each case, a load of 1.0N was applied to each particle on the force boundary under consideration, however, in order to maintain symmetry conditions, half loads were applied to the particles at the edges of the mesh. Thus, a total load of 17.0N was applied in the y -direction and 20.0N in the x -direction.

The deformations measured in the mesh and their implications for the material properties of the model were compared with those expected of an equivalent continuum material. The values chosen for the Young's modulus and Poisson's ratio of the model were equivalent to those used by Griffiths and Mustoe and corresponded to certain ratios of k_n to k_s (See Table 4.1. below).

E ($\times 10^6$)	ν	k_n ($\times 10^6$)	k_s ($\times 10^6$)	$\frac{k_n}{k_s}$
1.732	0.00	1.0	1.0	1.0
1.460	0.13	1.0	0.5	2.0
1.076	0.25	1.0	0.0	∞

Table 4.1. Uniaxial Benchmark Model Input Values for Young's Modulus and Poisson's Ratio and Corresponding Contact Stiffnesses

The equivalent continuum deformations were also calculated by the same method applied by Griffiths and Mustoe [32], who showed that the Young's modulus and

Poisson's ratio of a material can be related to deformations under certain loading through rearrangements of the plane strain equations given in Section 4.2.2.3. (See Eq. 4.24. to Eq. 4.26. above) such that:

$$E = \sigma_{x,y} (1 - \nu^2) \varepsilon_{x,y} = \sigma_{x,y} (1 - \nu^2) \frac{l_{0(x,y)}}{\delta_{x,y}} \quad \text{Eq. 4.31.}$$

$$\nu = \frac{-l_{0(x,y)} / l_{0(y,x)}}{\delta_{x,y} / \delta_{y,x} - l_{0(x,y)} / l_{0(y,x)}} \quad \text{Eq. 4.32.}$$

where, $\sigma_{x,y}$ is the stress, $l_{0(x,y)}$ is the original length of the material sample, $\delta_{x,y}$ is the change in length of the material sample and x,y indicates the self perpendicular axes in which the relevant measurement is taken.

These equations were applied in two ways. Firstly, using the Young's modulus and Poisson's ratio of the continuum material, the expected displacements in the x and y -directions were calculated. Secondly, the equations were used in reverse by entering the actual model displacements to return values of Young's modulus and Poisson's ratio for the model mesh.

The results of these tests are shown below in Table 4.2. As can be seen from the table, the deformations of the model mesh in the y -direction, under both compressive and tensile loading, are in very good agreement with the predicted deformations according to Eq. 4.31. and Eq. 4.32. above, and the maximum difference is only -0.31%. Consequently, the inferred material properties for the mesh also match very well with the input values and the maximum variation between input and implied Young's modulus is again only -0.31%. In addition, the lateral deformation and hence the Poisson's ratio, of the PSM mesh show excellent agreement with the continuum values in all cases. It can be further noted that the mesh behaved identically in tension and compression.

Loading Dir. + Tens. - Comp.	E ($\times 10^6$)	ν	Predicted Continuum Deformations		Measured Deformations of PSM Mesh		Implied Properties of PSM Mesh	
			y ($\times 10^{-6}$)	x ($\times 10^{-6}$)	y ($\times 10^{-6}$)	x ($\times 10^{-6}$)	E ($\times 10^6$)	ν
-y	1.732	0.00	-10.00	0.00	-10.00	0.00	1.732	0.00
-y	1.460	0.13	-11.66	1.71	-11.66	1.75	1.460	0.13
-y	1.076	0.25	-15.09	4.94	-15.14	5.16	1.073	0.26
+y	1.732	0.00	10.00	0.00	10.00	0.00	1.732	0.00
+y	1.460	0.13	11.66	-1.71	11.66	-1.75	1.460	0.13
+y	1.076	0.25	15.09	-4.94	15.14	-5.16	1.073	0.26
-x	1.732	0.00	0.00	11.33	0.00	11.16	1.760	0.00
-x	1.460	0.13	-1.94	13.22	-1.99	13.06	1.478	0.13
-x	1.076	0.25	-5.60	17.10	-5.78	17.18	1.071	0.25

Table 4.2. Results of Deformation Analysis for PSM Uniaxial Benchmark Problem

Under loading in the x -direction, it can be seen that the discrepancy between the input and implied properties is slightly larger than that for the y -direction. However, the maximum difference between predicted and actual deformation is 1.57% and the maximum difference between input Young's modulus and implied Young's modulus is 1.59%. These discrepancies are considered acceptable. Furthermore, as with tests that applied load to the mesh in the y -direction, the lateral deformation, and hence the Poisson's ratio, of the PSM mesh are in good agreement with the continuum values for all cases.

It can also be noted that, when loaded in the y -direction, although the model shows only small deviations from theoretical results, the differences between predicted and model values, and in particular of lateral deformations, increase with increasing Poisson's ratio. The sensitivity of the overall Poisson's ratio of a lattice model to the discretisation of the mesh was also noted by van Vliet [95] and this is discussed in more detail below.

The results of the studies discussed above were further confirmed by the results of an additional, brief, study that was carried out on a mesh with the same dimensions as the one shown above (See *Fig. 4.8.*) but with an equivalent lattice element length of only 0.5m (See *Fig. 4.9.* below).

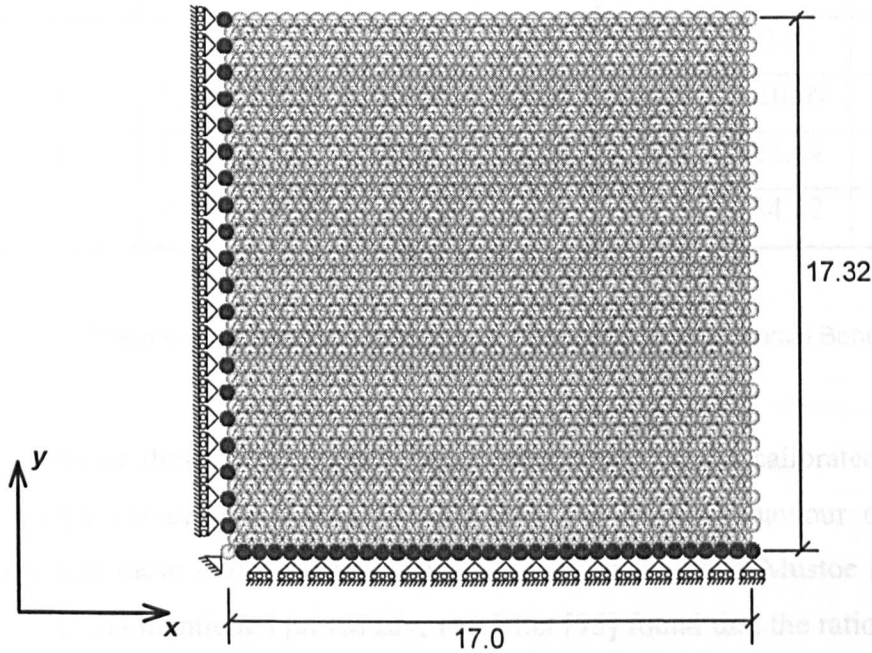


Fig. 4.9. Diagram of Finer Mesh PSM for Uniaxial Benchmark Test

In this, finer mesh, study measurements were taken as in the previous study and the results are shown in Table 4.3. below. As for the coarse mesh, a load of 1.0N was applied to each particle on the force boundary, resulting in a total applied load of 34.0N in the y -direction and 40.0N in the x -direction.

As can be seen from the table below, the results of deformation in the finer mesh model showed even closer agreement with the continuum values than in the previous study. The maximum percentage difference between predicted and actual extension of the mesh is less than 0.19% under loading in the y -direction and 1.00% under loading in the x -direction. This improvement was as would be expected for a mesh of higher discretisation and it was not deemed necessary to repeat all of the tests from the first study. Again, the discrepancy between predicted and actual mesh extension in the y -direction increased with increasing Poisson's ratio.

Loading Dir. + Tens. - Comp.	E ($\times 10^6$)	ν	Predicted Continuum Deformations		Measured Deformations of PSM Mesh		Implied Properties of PSM Mesh	
			y ($\times 10^{-6}$)	x ($\times 10^{-6}$)	y ($\times 10^{-6}$)	x ($\times 10^{-6}$)	E ($\times 10^6$)	ν
+ y	1.732	0	20.00	0.00	20.00	0.00	1.732	0.00
+ y	1.076	0.25	30.18	-9.87	30.24	-10.09	1.074	0.25
+ x	1.732	0	0.00	22.67	0.00	22.44	1.750	0.00
+ x	1.076	0.25	-11.19	34.21	-11.58	34.22	1.076	0.25

Table 4.3. Results of Deformation Analysis for PSM Finer Mesh Uniaxial Benchmark Problem

The results of these studies show that a lattice type model calibrated through strain energy equivalence can accurately reproduce the elastic behaviour of a continuous material and these findings agree with those of Griffiths and Mustoe [32] and of van Vliet [95]. As mentioned previously, van Vliet [95] found that the ratio of mesh length to element length, L , should be ≥ 20 in order for the properties, calibrated through strain energy equivalence, to be accurately reproduced by a lattice model. The ratio, L , in the first study is approximately 17 in both directions. Obviously, this discretisation is a little coarser than van Vliet would suggest is sufficient and, as illustrated above, there are small differences between the theoretically predicted deformations and those actually produced by the mesh. However, these are considered acceptable for the purposes of this study and to confirm the suitability of the strain energy equivalence formulations, developed by Morikawa and Sawamoto [63], for calibrating the PSM. The ratio, L , of the finer mesh, used in the second study, is approximately 34 and, as implicit in van Vliet's findings, the accuracy of the mesh reproduction of continuum behaviour is increased over that of the first study.

The study conducted by van Vliet also showed that the difference between the input value of Poisson's ratio and that implied by the deformation of the mesh was very sensitive to the discretisation of the mesh and hence, to the ratio L , especially when loading the mesh in the x -direction in order to establish Poisson's ratio of the y -direction. Furthermore, van Vliet found that for a given mesh the lateral responses, and

hence the implied Poisson's ratios, would be different in the x and y -directions. Essentially the lattice mesh was showing a degree of anisotropy.

As can be seen from the results in Table 4.2. and Table 4.3., the PSM mesh does not show significant anisotropy in this way, although it is realised that, as discussed above, the meshes used in these studies were of reasonably fine discretisation. A coarser mesh may show similar results to those found by van Vliet. Furthermore, it can be noted in the results of the PSM benchmarks that the agreement between predicted and actual deformations, and consequently between input and implied material properties, decreases with increasing Poisson's ratio. This is particularly noticeable in the case of lateral deformations where the difference between the predicted, theoretical values for lateral deformation and the actual lateral deformations of the mesh range from 0.00% with a Poisson's ratio of 0.0 to 4.58% with a Poisson's ratio of 0.25. Despite the reasonably high percentage differences, the physical differences between the predicted and actual values of deformation are very small and the consequent variations between implied values of Poisson's ratio and input values are almost insignificant when measured to two decimal places (See Table 4.2. and Table 4.3.). However, this phenomenon may be associated with the sensitivity also noticed by van Vliet. The explanation presented by van Vliet concerns the boundary conditions and the fixity of the triangularly configured lattice mesh and this may well be the cause of the similar results in the PSM. As with van Vliet's lattice, the fixed boundaries of the PSM are different in the x and y -directions due to the triangular configuration of the mesh. As can be seen from *Fig. 4.8.* and *Fig. 4.9.* above, the bottom boundary of the mesh, fixed against displacement in the y -direction, consists of a smooth row of particles. However, the left-hand boundary, fixed against displacement in the x -direction, consists of a staggered row of particles. In fact, only the outermost particles, marked in the figures, are fixed and the inner particles of the boundary remain free. Obviously, as the discretisation becomes finer the staggered boundary becomes a closer approximation on a smooth boundary. However, in coarser discretisations the staggered boundary becomes very different to the smooth bottom boundary and this may produce a discrepancy between the x and y deformation of the lattice in comparison with those expected from an equivalent continuum material. A test was conducted with the inner and outer particles of the left-hand boundary fixed against displacement in the x -direction, but it was found that this significantly altered the overall stiffness of the mesh

and the results moved away from those predicted by the theory. It is considered by van Vliet that, given a mesh discretisation ratio, $L \geq 20$, the inaccuracy associated with Poisson's ratio under y extension becomes small enough that it is well within the limits of experimental measurement on real materials. This is the argument adopted in the work carried out for this thesis and, provided that model meshes are suitably discretised, the discrepancy in lateral behaviour of the PSM is considered to be acceptable.

4.2.3.2.2. Equivalent Continuum Stress Tests

In addition to the studies of mesh deformation carried out in the previous Section, studies were also carried out in order to test the ability of the granular-continuum stress conversion factors (See Chapter 3, Section 3.4.3.) to accurately predict the expected stress state for an equivalent continuum material, as represented by the PSM mesh, under various loading conditions. To do this the components of the granular stress tensor in a particle near to the centre of a PSM mesh, where it was considered that boundary effects would be minimised, were recorded under various loading conditions. These granular stress components were then multiplied by the stress conversion factors, as calculated for the hexagonal PSM mesh configuration according to the method set out in Section 3.4.3. of Chapter 3. The resulting continuum stresses were compared to the values of stress that would be expected in an equivalent continuum material under the same loading conditions.

The tests were carried out during a representative sample of the numerical studies carried out in the previous Section, under loading in both the x and y -directions, with varying Poisson's ratio and in both the coarse and fine meshes. Four additional runs were also carried out, firstly in order to load the PSM mesh in both the x and y -directions simultaneously and secondly, in order to load the PSM mesh under pure shear conditions. The details of the numerical studies are given in Table 4.4. below.

Loading Dir.	Mesh Type	Young's Modulus E	Poisson's Ratio ν	Granular Stress Tensor Components				Converted Continuum Stress Tensor Components				Expected Continuum Stress Tensor Components				
				σ_{xx}	τ_{xy}	τ_{yx}	σ_{yy}	σ_{xx}	τ_{xy}	τ_{yx}	σ_{yy}	σ_{xx}	τ_{xy}	τ_{yx}	σ_{yy}	
y	Coarse	1.732	0.00	-0.002	0.000	0.000	1.656	-0.001	0.000	0.000	1.001	0.000	0.000	0.000	0.000	1.000
y	Coarse	1.076	0.25	0.019	-0.001	-0.001	1.670	0.012	-0.001	-0.001	1.010	-0.001	0.000	0.000	1.000	1.000
x	Coarse	1.732	0.00	1.814	0.004	0.004	-0.022	1.140	0.003	0.003	-0.013	0.003	0.000	0.000	0.000	0.000
x	Coarse	1.076	0.25	1.792	0.017	0.017	-0.043	1.126	0.010	0.010	-0.026	0.010	0.000	0.000	0.000	0.000
y	Fine	1.732	0.00	0.040	-0.003	-0.003	6.650	0.012	-0.001	-0.001	2.010	-0.001	0.000	0.000	0.000	2.000
y	Fine	1.076	0.25	-0.002	0.000	0.000	6.618	-0.001	0.000	0.000	2.001	0.000	0.000	0.000	0.000	2.000
x	Fine	1.732	0.00	7.291	0.005	0.005	-0.044	2.290	0.002	0.002	-0.013	0.002	0.000	0.000	0.000	0.000
x	Fine	1.076	0.25	7.251	0.031	0.031	-0.097	2.278	0.009	0.009	-0.029	0.009	0.000	0.000	0.000	0.000
x+y	Coarse	1.732	0.00	1.812	0.005	0.005	1.634	1.139	0.003	0.003	0.988	0.003	0.000	0.000	1.000	1.000
x+y	Coarse	1.076	0.25	1.811	0.015	0.015	1.627	1.138	0.009	0.009	0.984	0.009	0.000	0.000	1.000	1.000
xy	Coarse	1.732	0.00	0.000	1.654	1.654	0.000	0.000	1.000	1.000	0.000	1.000	0.000	1.000	0.000	0.000
xy	Coarse	1.076	0.25	0.000	1.654	1.654	0.000	0.000	1.000	1.000	0.000	1.000	0.000	1.000	0.000	0.000

NB - x+y under 'Loading Direction' indicates that loads were applied in both directions simultaneously

- xy under 'Loading Direction' indicates that self equilibrating shear loads were applied

Table 4.4. Results of Analysis of Equivalent Continuum Stresses for PSM Uniaxial Benchmark Problem

As mentioned above, the recorded components of the granular stress tensor were multiplied by the granular-continuum stress conversion factors as shown below (See Eq. 4.33.).

$$\alpha(i, j)^{G-C} = \begin{bmatrix} \alpha(x, x)^{G-C} & \alpha(x, y)^{G-C} \\ \alpha(y, x)^{G-C} & \alpha(y, y)^{G-C} \end{bmatrix} = \begin{bmatrix} \frac{2\pi r}{3\sqrt{3}} & \frac{2\pi r}{3\sqrt{3}} \\ \frac{2\pi r}{3\sqrt{3}} & \frac{2\pi r}{3\sqrt{3}} \end{bmatrix} \quad \text{Eq. 4.33.}$$

where, $\alpha(i, j)^{G-C}$ is a matrix of the scalar granular-continuum stress conversion factors for multiplication with the granular stress tensor.

As can be seen, the conversion factors for the hexagonal mesh configuration were found to be the same for all components of the granular stress tensor. The conversion factors were calculated according to the methods detailed in Section 3.4.3. of Chapter 3 and a full derivation can be found in Appendix II.

From the results shown in Table 4.4 above, it can be seen that, in general, the expected stress state for an equivalent continuum material is very accurately predicted. Detailed examination of the results shows that when the PSM mesh is loaded in the y -direction the predicted y -component of normal stress is accurate to within 1% of the expected values for an equivalent continuum material. However, under loading in the x -direction the predicted x -component of normal stress is slightly less accurately predicted with an error in the region of 1 to 2%. This discrepancy is possibly a result of the assumptions made in conjunction with the distribution of contact forces, in determining the conversion factor for this component of the stress tensor (See Appendix II). However, this seems unlikely given that the conversion factor found using these assumptions is the same as for all the other components of the stress tensor. A more likely explanation is that round off errors lead to a slightly different physical distribution of contact forces in the mesh to that which would be suggested analytically and this consequently leads to a small error in the construction of the stress tensor. For the purposes of the work carried out for this thesis, the measured results are considered sufficiently accurate.

It can further be seen that the results of the predicted normal continuum stress components, under loading in both the x and y -directions, increase in accuracy when a finer mesh is employed. This finding is as would be expected from the elastic displacement results discussed in the previous Section.

As mentioned above, four additional tests were carried out with alternative loading conditions. In the first set of two tests the mesh was loaded in both the x and y -directions at the same time as is likely to occur in a realistic situation. Examination of the results presented in Table 4.4 shows that both the components of normal stress are predicted with an accuracy of 1 - 1.5% in comparison to the expected values for an equivalent continuum material. Again, this is considered reasonable for the purposes of this work. In the second set of two tests, loads were applied laterally to the edges of the PSM mesh in order to apply conditions of pure shear and evaluate the predicted continuum shear stress components. As can be seen from the results above, these were predicted with a very high degree of accuracy and an error of less than 0.01%.

Each of the tests described above was developed in order to evaluate a particular component of the predicted continuum stress tensor. Under the loading conditions applied, the remaining stress components should have shown zero stress. Again examining the results shown in Table 4.4 it can be seen that this is largely the case. Although some non-zero values of stress are predicted, it can be seen that, in all cases, they are very small. These minor inaccuracies can again be attributed to round off errors in the basic PFC^{3D} DEM code.

A further point of note was that, although the predicted continuum stresses under all conditions showed reasonable accuracy, they were generally more accurate when Poisson's ratio was zero than when it was set to 0.25. Although varying Poisson's ratio alters the ratio of the normal and shear spring stiffnesses in the PSM mesh (See Section 4.2.2.3.), and therefore alters the composition of the contact forces reacting to a specific applied load on a particle, the component of the contact forces in the direction of the applied load must always be the same in order to reach equilibrium. Therefore, the granular stress tensor in a particle is only dependent on the externally applied load. Thus, any variation in the predicted stress results between meshes with different material properties can once again be attributed to numerical round off in the DEM.

As discussed above, the values of the equivalent continuum stresses predicted by the granular-continuum stress conversion factors are seen to be reasonably accurate under all the applied loading conditions. However, as discussed in Chapter 3, Section 3.4.3., the constant conversion factors applied in this work are based on the inherent assumption that the configuration of the PSM remains constant at all times and that therefore, only small deformations occur. Given the results reported above, this can be considered an acceptable assumption, however, it is noted that under larger deformation or if the mesh configuration changes, the results may not be so accurate.

4.2.3.3. Cantilever Beam Benchmark Model

This benchmark study considers the ability of the PSM, calibrated with the strain energy equivalence formulations developed by Morikawa and Sawamoto [63] and further derived by Griffiths and Mustoe [32], to model a problem in bending. As with the Uniaxial Benchmark Test, considered in the previous Section, this test is a reproduction of a similar problem considered by Griffiths and Mustoe [32]. The elastic deformation at the tip of a cantilever, constructed of a PSM mesh, is compared with the deformations predicted by slender beam theory. As with the previous benchmark problem, this test was carried out in order to check the validity of the strain energy equivalence formulations, when applied to the PSM.

For the purposes of this study, a regular PSM mesh was constructed, as shown in *Fig. 4.10.* below. One end of the cantilever was fixed against displacement in both the x and y -directions, as shown below. The particle radius was 0.0833m (1/12) and the equivalent lattice element length was therefore 0.167m (1/6). The particle radius was chosen in order to reproduce the dimensions of the model employed by Griffiths and Mustoe [32] while decreasing the discretisation of the mesh in order to reduce the computational effort required in running the model. Although this is a coarser mesh than the original, the ratio of mesh length to equivalent element length, L , is well above the value of 20 suggested by van Vliet [95] (See Section 4.2.3.2.1.). As in the original test, conducted by Griffiths and Mustoe [32], the cantilever was considered as a plane

stress problem and the contact spring stiffnesses were calculated from the appropriate formulae, as developed by Morikawa and Sawamoto [63] (See Eq. 4.27. and Eq. 4.28. repeated below).

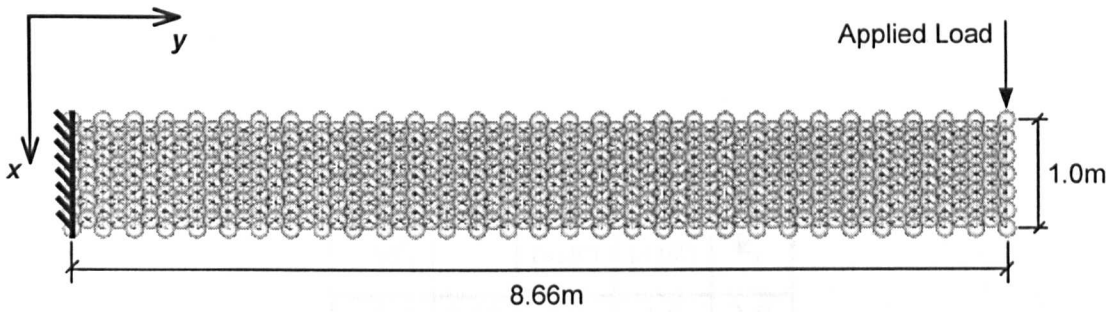


Fig. 4.10. Diagram of PSM Mesh for Cantilever Benchmark Problem

$$k_n = \frac{E}{\sqrt{3}(1-\nu)} \tag{Eq. 4.27.}$$

$$k_s = \frac{E(1-3\nu)}{\sqrt{3}(1-\nu^2)} \tag{Eq. 4.28.}$$

Several studies were conducted, during which a unit point load was applied to the tip of the cantilever, as shown in Fig. 4.10. above. In a repeat of the procedure followed by Griffiths and Mustoe [32] the final tip displacement of the cantilever was measured and compared with the tip displacement predicted by the slender beam theory. This was calculated according to Eq. 4.34. below.

1.485	0.14	1.750	1.791	1.859
1.155	0.33	2.249	2.470	2.346

$$\delta_x = \frac{Pl^3}{3EI} \tag{Eq. 4.34.}$$

Table 4.8. Results of Cantilever Benchmark Problem for PSM

where, P is the applied load at the tip of the cantilever, l is the length of the cantilever and I in the inertial moment of the cantilever.

As in the Uniaxial Benchmark Model, discussed in the previous Section, the values chosen for the Young's modulus and Poisson's ratio of the model were equivalent to those used by Griffiths and Mustoe and corresponded to certain ratios of k_n to k_s (See Table 4.5. below).

E ($\times 10^6$)	ν	k_n ($\times 10^6$)	k_s ($\times 10^6$)	$\frac{k_n}{k_s}$
1.732	0.00	1.0	1.0	1.0
1.485	0.14	1.0	0.5	2.0
1.155	0.33	1.0	0.0	∞

Table 4.5. Cantilever Benchmark Model Input Values for Young's Modulus and Poisson's Ratio and Corresponding Contact Stiffnesses

The results of these studies are shown below in Table 4.6. along with the results of Griffiths and Mustoe's study for comparison.

E ($\times 10^6$)	ν	Predicted Slender Beam Deformations ($\times 10^{-3}$)	Measured Deformations of PSM Mesh ($\times 10^{-3}$)	Measured Deformations from Griffiths and Mustoe [32]
1.732	0.00	1.500	1.522	1.441
1.485	0.14	1.750	1.791	1.859
1.155	0.33	2.249	2.470	2.346

Table 4.6. Results of Cantilever Benchmark Problem for PSM

As can be seen from the table above, the deformations produced by the PSM mesh were in very good agreement with those predicted by slender beam theory. In the first two

tests, the results produced by the PSM were in fact better than those produced by Griffith and Mustoe's model. However, this situation reversed in the case of the third test, where the results of the PSM showed a 9.83% deviation from the predicted deformation.

It can be noted, in fact, that in all cases the PSM over predicts the cantilever tip displacement. It is considered probable that this excess displacement is due to shear deformation that is not accounted for by the slender beam theory. Consequently the deformation predicted by *Eq. 4.34.* is less than the actual deformation of the model mesh. This hypothesis is further substantiated by the fact that the excess displacement increases as the shear stiffness of the inter-particle links decreases. As can be seen from *Eq. 4.28.* this occurs as a consequence of increasing Poisson's ratio. The largest over estimation of displacement by the PSM cantilever model, cited above, occurs when Poisson's ratio is set to the maximum possible value for under plane stress conditions, $\nu = \frac{1}{2}$. In this situation, the shear stiffness of the inter-particle links is set to zero.

This behaviour may be an indication that the PSM becomes less efficient at capturing shear behaviour as the Poisson's ratio of the material increases and the mesh tends from a two force lattice to a truss representation. However, similar results were reported for the uniaxial benchmark model described in the previous Section, where the accuracy of mesh deformations in comparison to predicted, theoretical deformations decreased with increasing Poisson's ratio. This was attributed to the sensitivity of lateral deformations in lattice type models to boundary effects, particularly at coarser discretisations. As suggested by van Vliet [95], it was considered that this effect would diminish with increasing ratio of overall mesh length to lattice element length, L . It can be seen that although the ratio, L , for the cantilever mesh is >50 in the y -direction, it is only 6 in the x -direction and this is well below the value of 20 suggested by van Vliet [95]. This may also contribute to the discrepancy between the slender beam theory and the actual displacements of the PSM cantilever.

Despite the relatively large inaccuracy between the predicted and actual deformation of the PSM cantilever with larger values of Poisson's ratio, the results of this study can be considered acceptable for work in this thesis given two qualifying

conditions. Firstly, deformation of a primarily bending nature, as seen in this model, is unlikely to occur in a hydraulic fracture model and secondly, it can be ensured that the PSM meshes applied to hydraulic fracture modelling have a ratio, $L > 20$ in both the x and y -directions.

4.2.4. PSM Conclusions

From the results of the studies shown above, it can be concluded that, when continuum equivalence is applied through the strain energy equivalence formulations developed by Morikawa and Sawamoto [63], the PSM can be used to accurately model the elastic deformation of continuum materials. The findings of the benchmark problems are in agreement with the findings of benchmark studies conducted by Griffiths and Mustoe [32] and in some instances the PSM produces better results than the original Griffiths and Mustoe model.

A phenomenon of particular note, that was common to all of the benchmark studies discussed in the preceding Sections, was the tendency for the PSM to reproduce predicted theoretical deformations less accurately with increasing values of Poisson's ratio. As the Poisson's ratio increases the PSM tends from a two force lattice, with equal normal and shear stiffnesses at a Poisson's ratio of zero, to an axial force, simple truss representation, with a shear stiffness of zero at the maximum value for Poisson's ratio ($\nu = \frac{1}{3}$ in plane stress conditions and $\nu = \frac{1}{4}$ in plane strain conditions).

Two possible causes were suggested for this loss of accuracy. Firstly, it may be related to the sensitivity of lattice type models, and in particular, their lateral displacements, to mesh discretisation. This effect would be similar to behaviour reported by van Vliet [95]. Secondly, it may be that, as a consequence of the reduction in shear stiffness, the model is less able to capture the effects of shear behaviour in materials with higher values of Poisson's ratio.

However, lateral deformation would have been more significant under the loading regime in the Uniaxial Benchmark Model than in the cantilever Benchmark

Model. Conversely, even a small amount of shear deformation in the Cantilever Benchmark Model would have been significant since no account is made of it by slender beam theory. Therefore, it can be concluded that the loss of accuracy associated with increasing Poisson's ratio may be partially due to both of the causes suggested above.

The numerical models in this project consist of mesh configurations more closely resembling that employed in the Uniaxial Benchmark Model than that used in the Cantilever Benchmark Model. Furthermore, the mechanism of deformation in the hydraulic fracture models developed in this work is more likely to approximate uniaxial loading than the bending or shear experienced by a cantilever. As shown in Section 4.2.3.2.1., the inaccuracies developed by the Uniaxial Benchmark Model mesh are smaller than those developed by the Cantilever Benchmark Model mesh and, additionally, work by van Vliet [95] suggests that these can be reduced further, by increasing the discretisation of the mesh. The findings of the Uniaxial Benchmark Model study conducted with a finer mesh agreed with this suggestion.

A further point of note is that the model employed by Griffiths and Mustoe did not show a decrease in accuracy, in either of the benchmark models, that could be connected to an increase in Poisson's ratio. It is not clear why their model results should differ from those of PSM.

4.3. The Particle Fluid Model (PFM)

4.3.1. Development History

As discussed in Chapter 3, in order to create fully coupled hydraulic fracture models without the need for complex techniques working between multiple codes, it was proposed to develop a fluid phase model within the same modelling framework as the solid phase model (PSM), discussed in the previous Sections. Preliminary work in this area was previously carried out by Davie [21] and two distinct approaches were developed during the course of that research. In the first, largely qualitative approach,

mainly applied in a Wellbore Stability Model (See Fig. 4.11. below), forces, representing fluid pressures, were applied to particles forming the walls of fractures.

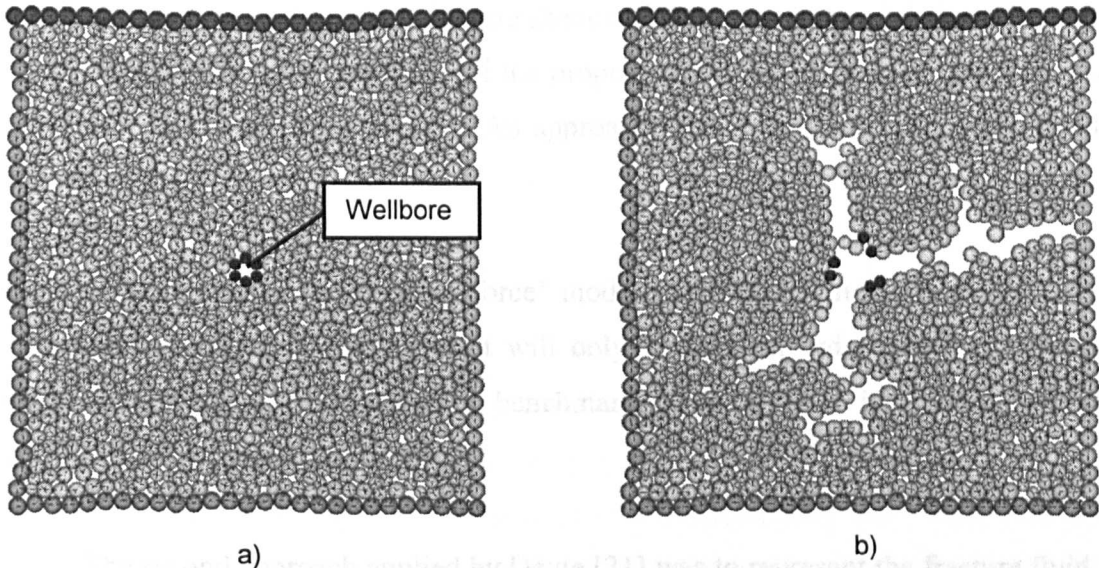


Fig. 4.11. Plots of Typical Wellbore Stability Model Meshes a) Before and b) After Fracturing (After Davie [21])

The model shown above represented a horizontal cross-section through a wellbore. ‘Fluid forces’ were initially applied in a radial pattern to the wall of the wellbore at the centre of the mesh (marked as dark particles) and were increased linearly so that fractures were initiated. As the fractures propagated and lattice elements were removed, ‘fluid force’ dipoles were applied in their place to represent the flow of fluid into the newly opened fracture. This technique is similar to the method applied by Tzschichholz and Herrmann [88] and Tzschichholz et al. [89] and discussed in Chapter 2, Section 2.3.2.

In terms of modelling fluid behaviour, this was a very simple representation, as a constant pressure profile was assumed over the length of the fractures and furthermore, the fluid was assumed to flow instantly along the propagating fracture. In reality, fluid would take a finite time to flow into newly opened sections of a fracture and the pressure would generally decrease with increasing distance from the wellbore. Both of these phenomena would depend on the flow regime and the fluid properties. While it

would be possible to improve this model in order to account for more realistic fluid flow behaviour and pressure distributions this would probably require a separate, dedicated fluid code to accurately compute the pressure field underlying the solid phase material, especially in the case of complex fracture shapes as shown in the model above (See Fig. 4.11.). This would not therefore fulfil the proposal of a single software, multi-physics framework, as discussed previously. An approach of this kind has been developed by Bruno et al. [11].

Although this type of ‘fluid force’ model may feature in the numerical work within this project, it is likely that it will only be used in order to apply an easily controllable pressure distribution in benchmark problems. It is not likely to be developed as a fully coupled model.

The second approach applied by Davie [21] was to represent the fracture fluid in a hydraulic fracture model with fine grained discrete particles (See Fig. 4.12. below).

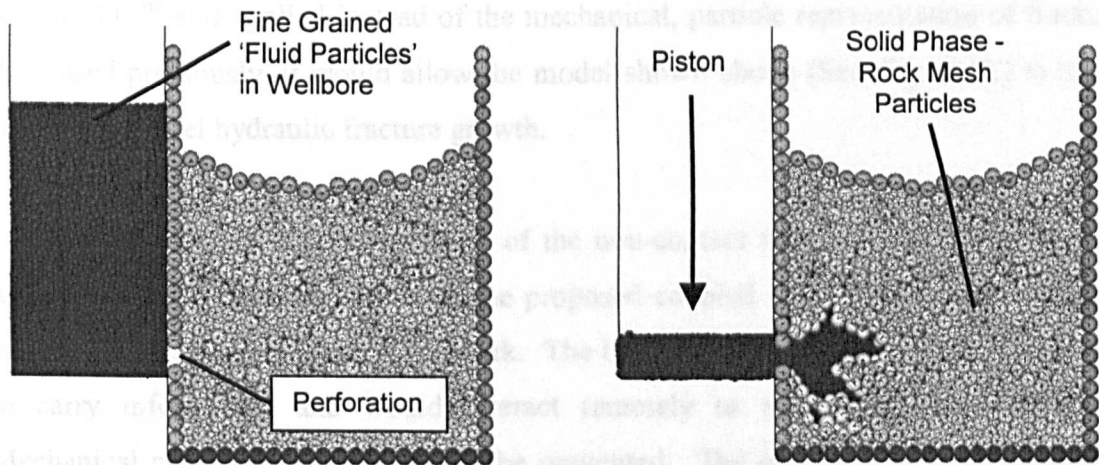


Fig. 4.12. Plots of Hydraulic Fracture Model Meshes a) Before and b) After Fracturing
(After Davie [21])

The hydraulic fracture model, shown above, represented a vertical cross-section through a wellbore. The particles representing the fracturing fluid were pushed down the wellbore by a piston and as the pressure increased, they were forced through a perforation, into the rock matrix. The results above are typical of those produced by the model. The particles were simple, discrete element particles, as are fundamental to the

PFC^{3D} DEM environment. Although their relatively small diameter gave them some tendency to fluid like behaviour when moving en masse, the particles interacted on a purely mechanical basis and consequently the model was more representative of gravel particles being forced into a rock matrix than of a fluid. While this in itself, may have applications in the modelling of geomechanical problems such as gravel packing operations, associated with prevention of sanding and stabilisation of weak formations around wellbores (See Chapter 2, Section 2.5.), it did not represent the behaviour of a pressurised fluid with sufficient accuracy to be used directly in this work. DEM fluid models have been developed, for example by Zhang et al. [98], where the particles are given contact properties such that they more closely represent fluid behaviour for certain benchmark problems and these models show some promise. However, potential difficulties with these DEM contact fluid models are discussed in Chapter 2, Section 2.4.2., and attention is turned to the possibility of representing fluid behaviour with particles that interact at a distance via fluid field properties rather than mechanical properties. This type of model is also discussed in Section 2.4.2. of Chapter 2. It was considered that if this kind of non-contact particle fluid representation was implemented within PFC^{3D} and applied instead of the mechanical, particle representation of fracture fluid used previously, it would allow the model shown above (See *Fig. 4.12.*) to more accurately model hydraulic fracture growth.

A particle fluid representation, of the non-contact type, is therefore developed within the PFC^{3D} in order to create the proposed coupled solid/fluid models within a single software multi-physics framework. The basic DEM particles would be used only to carry information and would interact remotely to reproduce fluid behaviour. Mechanical contact interaction would be prevented. The proposed implementation of such a model within the PFC^{3D} framework is discussed in detail Chapter 3, Section 3.6. and its development and verification is discussed in the following Sections.

4.3.2. Development of the PFM

As discussed in the previous Section, the PFM was constructed within the DEM modelling environment PFC^{3D}. The principle behind the model was to represent fluid

material with a cloud of discrete particles that interacted remotely by way of forces calculated from interaction laws describing the fluid field properties. It was necessary to maintain a separation between particles at all times in order to prevent contact and mechanical interaction of the particles that would lead to erroneous behaviour.

Two force fields were developed, firstly, to represent a pressure field in the fluid and secondly to represent viscous effects. These fields were implemented by forces that were applied to the PFC^{3D} particles as they came within certain radii of influence assigned to each particle. These radii of influence were associated with the separation laws and corresponded to a maximum separation, beyond which a particle would have no influence on another (See Fig. 4.13.). When a particle was within the radii of influence of another then forces were developed, according the separation laws, and applied to the particles by means of code written in the *FISH* programming language associated with PFC^{3D}. Although particles interacted such that forces were calculated for pairs of particles, the effect of all particles within another's radii of influence were taken into consideration by superposition.

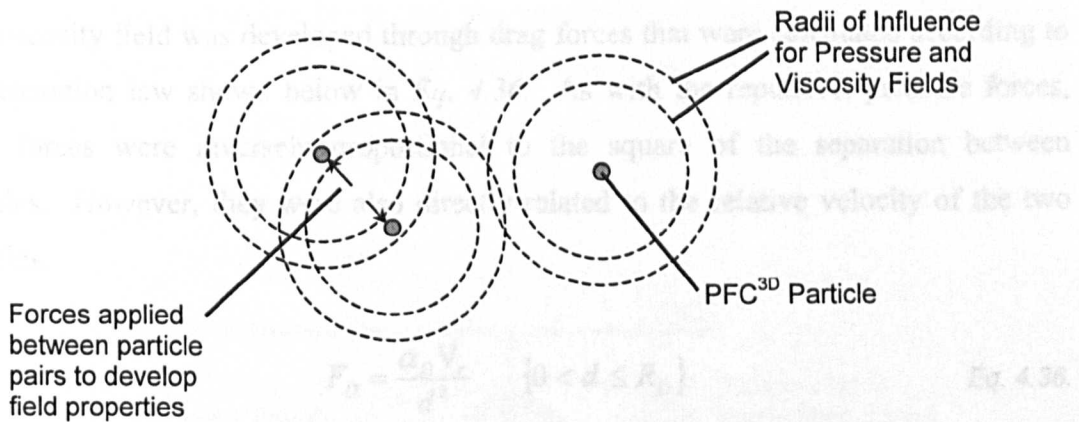


Fig. 4.13. Diagram Showing Radii of Influence Associated with Separation Laws for Fluid Field Properties between dense PFC^{3D} Particles

The pressure field was developed through repulsive forces that were calculated according to the inverse square separation law shown below in Eq. 4.35.

$$F_R = \frac{\alpha_R}{d^2} \quad \{0 < d \leq R_R\} \quad \text{Eq. 4.35.}$$

where, F_R is the repulsive force, α_R is a coefficient of repulsion, d is the separation between two particles and R_R is the radius of influence of repulsion.

These repulsive forces were applied as an equal and opposite force dipole and acted to maintain the separation between two particles and, under zero external pressure, keep them at the maximum radius of influence (See Fig. 4.14.).

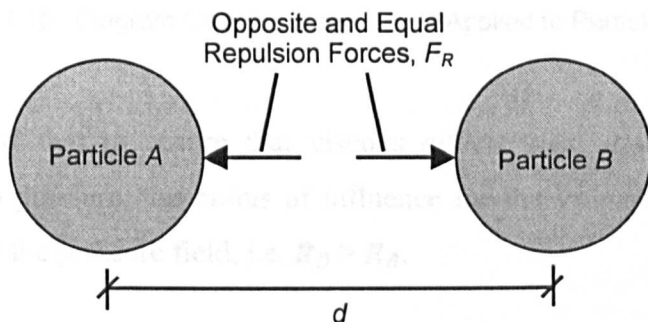


Fig. 4.14. Diagram Showing Repulsive Forces Applied to Particle Pair

The viscosity field was developed through drag forces that were calculated according to the separation law shown below in Eq. 4.36. As with the repulsive, pressure forces, these forces were inversely proportional to the square of the separation between particles. However, they were also directly related to the relative velocity of the two particles.

$$F_D = \frac{\alpha_D V_r}{d^2} \quad \{0 < d \leq R_D\} \quad \text{Eq. 4.36.}$$

$$V_r = v^{(A)} - v^{(B)} \quad \text{Eq. 4.37.}$$

where, F_D is the drag force, α_D is a coefficient of drag, V_r is the relative velocity of a particle pair with individual velocities, $v^{(p)}$ and R_D is the radius of influence of drag.

These drag forces were also applied as an equal and opposite force dipole and acted to bring a pair of particles to the same velocity (See Fig. 4.15.).

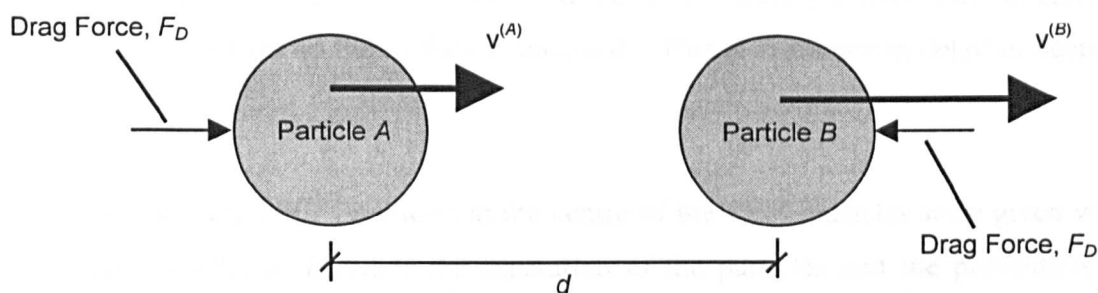


Fig. 4.15. Diagram Showing Drag Forces Applied to Particle Pair

It should be noted that to ensure that viscous effects were developed even under conditions of zero pressure, the radius of influence for the viscosity field was always larger than that for the pressure field, i.e. $R_D > R_R$.

Furthermore, when the particles encountered an object that was not a 'fluid particle', for example a wall or PSM particle, forces were applied as described above for a 'fluid particle' pair, in order to transfer the fluid pressure and viscous drag forces to the solid material. However, in the case of a wall the forces were only calculated on the basis of the perpendicular separation of 'fluid particle' and wall rather than the distance between the centroids of the objects (See Fig. 4.16.).

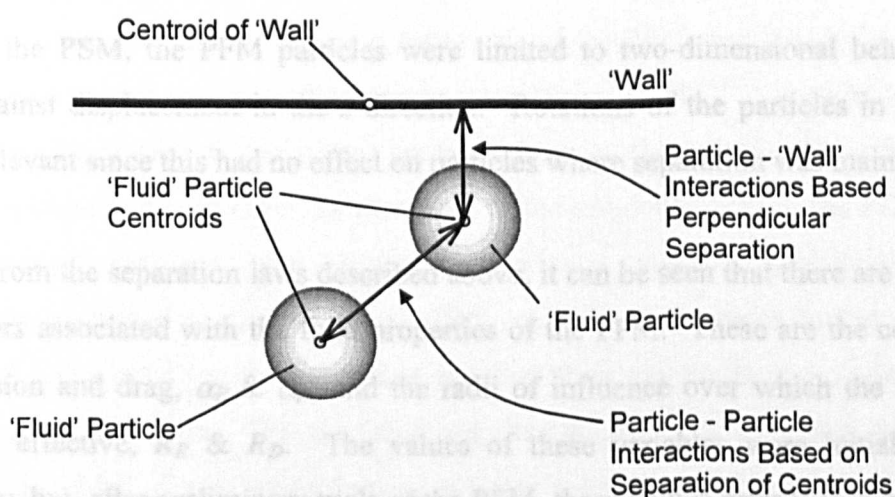


Fig. 4.16. Diagram Illustrating Basis of Calculations for Particle - Particle Interactions and for Particle - 'Wall' Interactions in PFM

In the case of a fluid interacting with a PSM mesh, the ‘fluid particles’ only interacted with the PSM particles on the surface of the mesh. This is discussed in detail in Section 4.4.1. below.

The discrete PFC^{3D} particles at the centre of the PFM particles were given very small radii in order to facilitate the separation of the particles and the prevention of inter-particle mechanical contact. The particle density was relatively high and set so that the mass of the particles represented a cylinder of fluid with radius equal to half the radius of influence of the pressure field and with a unit height. As can be seen from Fig. 4.17. below, this was considered to be the volume of fluid associated with each particle when at rest under zero pressure.

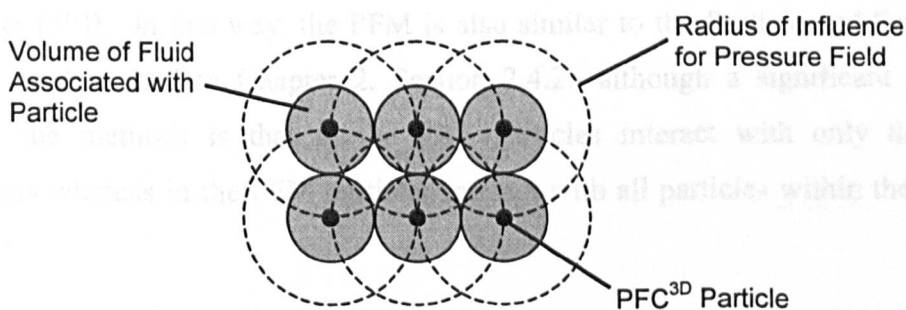


Fig. 4.17. Diagram Showing Volume of Fluid Associated with Discrete Particles

As with the PSM, the PFM particles were limited to two-dimensional behaviour by fixity against displacement in the z -direction. Rotations of the particles in any plane were irrelevant since this had no effect on particles where separation was maintained.

From the separation laws described above, it can be seen that there are four main parameters associated with the fluid properties of the PFM. These are the coefficients of repulsion and drag, α_R & α_D , and the radii of influence over which the separation laws are effective, R_R & R_D . The values of these variables were initially chosen arbitrarily, but, after preliminary trials of the PFM, these values were then tuned by trial and error in order to allow the model to develop fluid behaviour. It was hoped to be able to further tune these variables as required to reproduce the behaviour of fluids with specific properties. This is further discussed in the following Sections. A fifth

parameter, that can be associated with the loss of energy in a fluid through the friction associated with viscosity, is the coefficient of mechanical damping, ξ , which is a basic component of the PFC^{3D} DEM code. This was also varied by trial and error in conjunction with the coefficient of drag so that, while the viscosity of the modelled fluid was altered, the overall fluid behaviour was controlled. Again, this is further discussed in the following Sections.

This method of applying interaction laws based on the separation of particles is similar to the approach of Molecular Dynamics, as discussed in Chapter 2, Section 2.4.2. If applied on a small enough scale the PFM could represent molecular interactions, however the separation laws for molecular scale problems would not be the same as for those in the macro-scale problems to which the PFM is applied in this work (van Mier [59]). In this way, the PFM is also similar to the Particle-and-Force (PAF) method, as discussed in Chapter 2, Section 2.4.2., although a significant difference between the methods is that in the PAF particles interact with only their direct neighbours whereas in the PFM particles interact with all particles within their radii of influence.

4.3.3. Implementation of the PFM

As mentioned above, the fluid behaviour of the PFM was largely implemented through code written in the *FISH* language associated with PFC^{3D}. In order to compute the repulsion and drag forces acting between particles that came within the relevant radii of influence of each other, as discussed in the previous Section, the *FISH* routine examined each particle in turn. While considering a particular particle, all particles were again examined in turn and their effect on the particle under consideration was calculated. The effect on the particle in question from any walls in a model was also taken into consideration. The repulsion and drag forces were superimposed for each particle and added to any forces applied in order to represent external fluid pressures. The combined ‘fluid forces’, F_F , were then added to the total force acting on a particle, $F^{(p)}$, and thus, subsequently affected the particle’s acceleration, as defined by Eq. 3.26. Therefore, in consideration of the PFM, Eq. 3.26. (repeated below) can be rewritten as

in Eq. 4.38. and Eq. 4.39. below. It may be noted that all other equations of the distinct element calculation remained unaltered.

$$a^{(p)} = \frac{\sum F^{(p)}}{m^{(p)}} \quad \text{Eq. 3.26.}$$

$$a^{(p)} = \frac{\sum F^{(p)} + (\sum F_R + \sum F_D + \sum F_{P_{\text{ext}}})}{m^{(p)}} \quad \text{Eq. 4.38.}$$

$$= \frac{\sum F^{(p)} + F_F^{(p)}}{m^{(p)}} \quad \text{Eq. 4.39.}$$

where, $F_{P_{\text{ext}}}$ are forces applied to particles in order to represent external fluid pressure and F_F are the combine repulsion, drag and external 'fluid forces' acting on a particle.

The PFM *FISH* routine was executed in every time step of the model analyses, just before the motion calculation of the basic distinct element method calculation cycle employed in PFC^{3D} (See Chapter 3, Section 3.4.1.). The amendments made to the basic calculation cycle by the PFM *FISH* routine are illustrated in Fig. 4.18. below (in comparison to Fig. 3.3.) and the additional steps in the process are highlighted for clarity. As mentioned above, where 'fluid forces' were applied to a particle, they affected the particle's acceleration, as defined by Eq. 3.26., which is also highlighted in Fig. 4.18. below.

The PFM *FISH* routine itself can be summarised as shown in Fig. 4.19., Fig. 4.20. and Fig. 4.21. Detailed examination can also be made of the actual *FISH* code, which is presented in Section AIII.4. of Appendix III. Where possible, variable names employed in the code, are shown beside the relevant processes in the flow charts presented below.

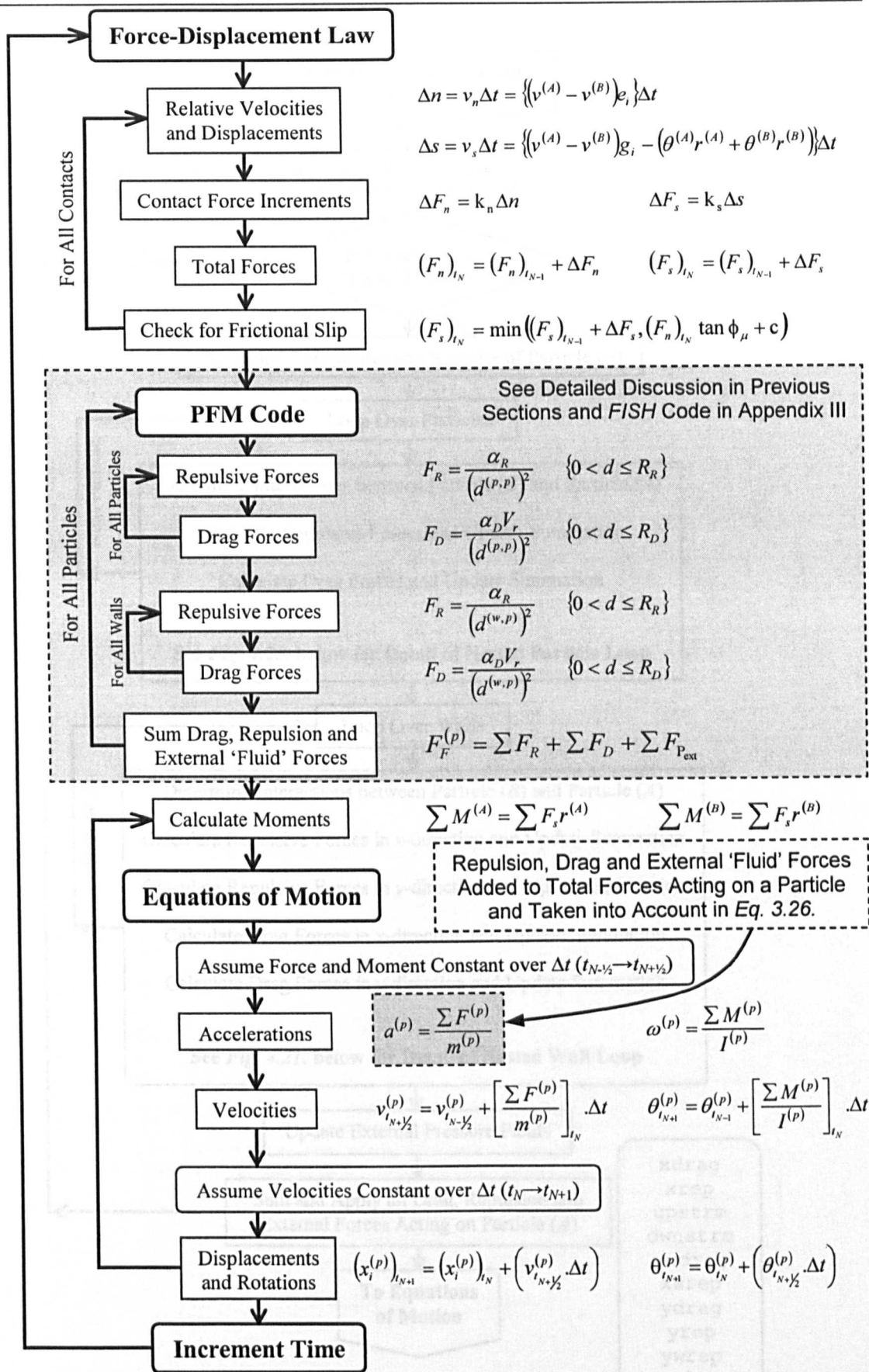


Fig. 4.18. Flow Chart Summarising the Calculation Sequence for the Distinct Element Method Modified For Inclusion of the PFM Implemented via FISH Code (expanded Fig. 3.3.) (Dashed Outlines Indicate Where Changes were Implemented in the Basic DEM Algorithm)

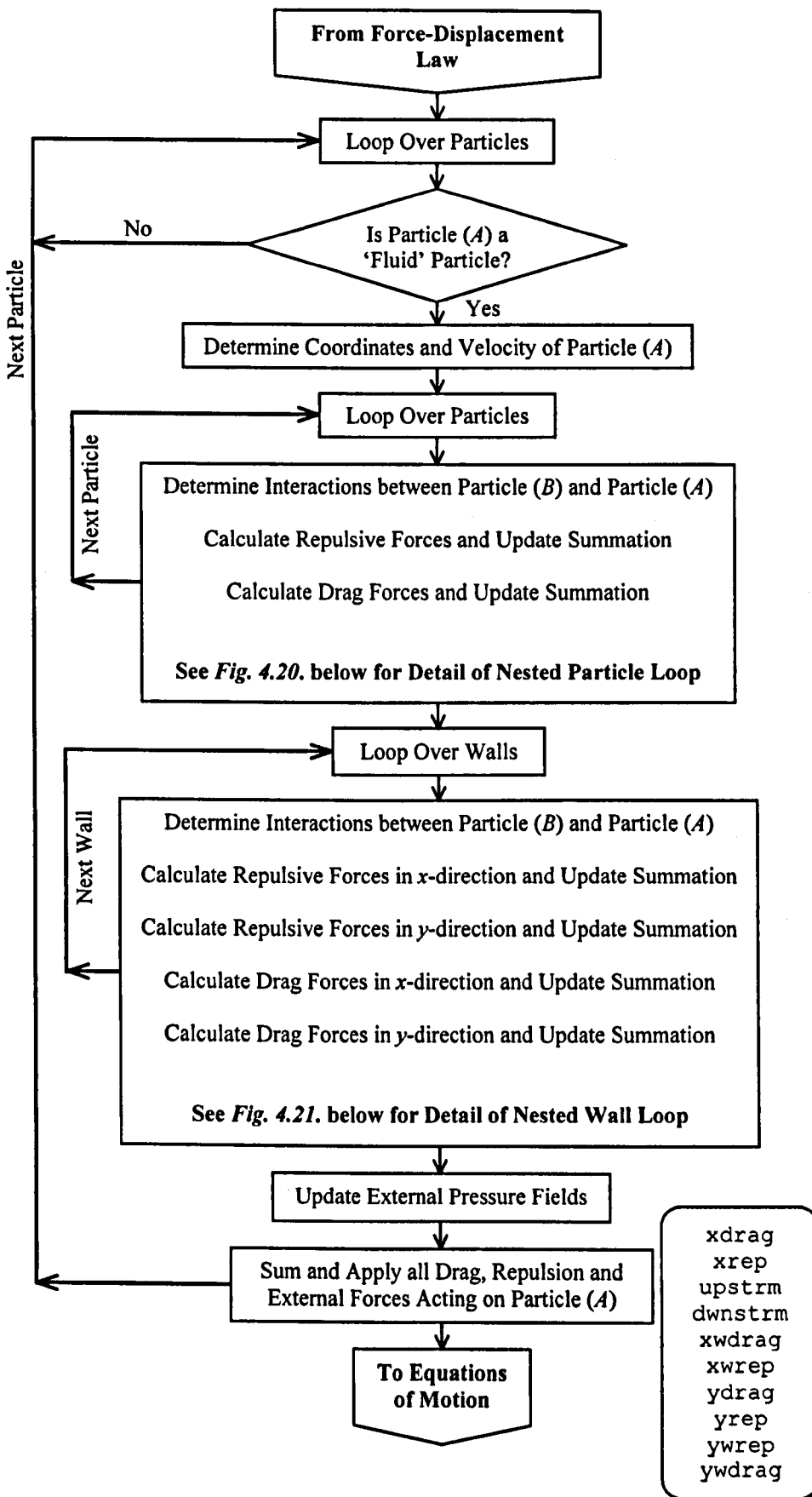


Fig. 4.19. Flow Chart Summarising FISH Code for Implementation of PFM

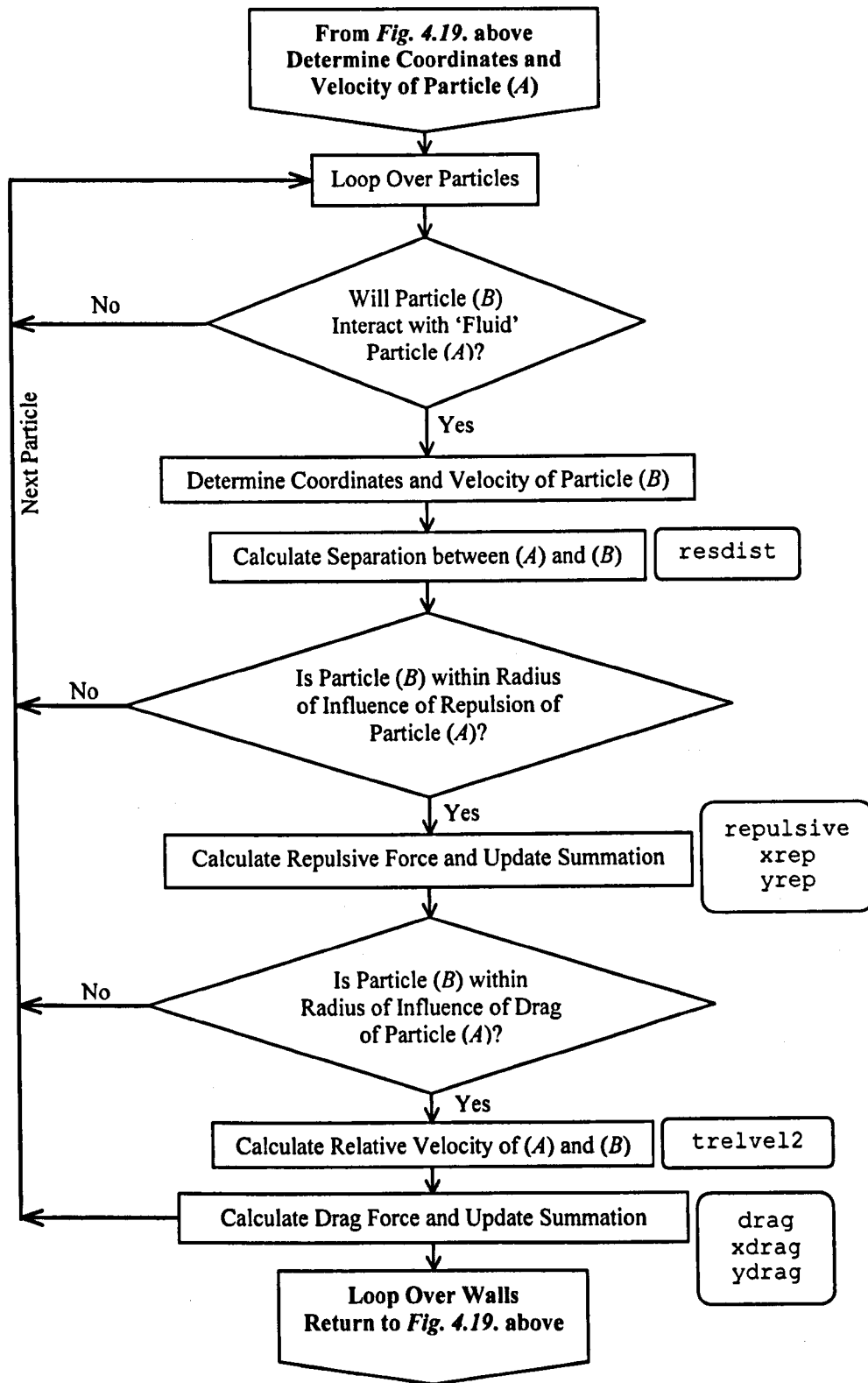


Fig. 4.20. Flow Chart Summarising FISH Code for Nested Particle Loop Sub-Block of Flow Chart Summarising PFM Code in Fig. 4.19.

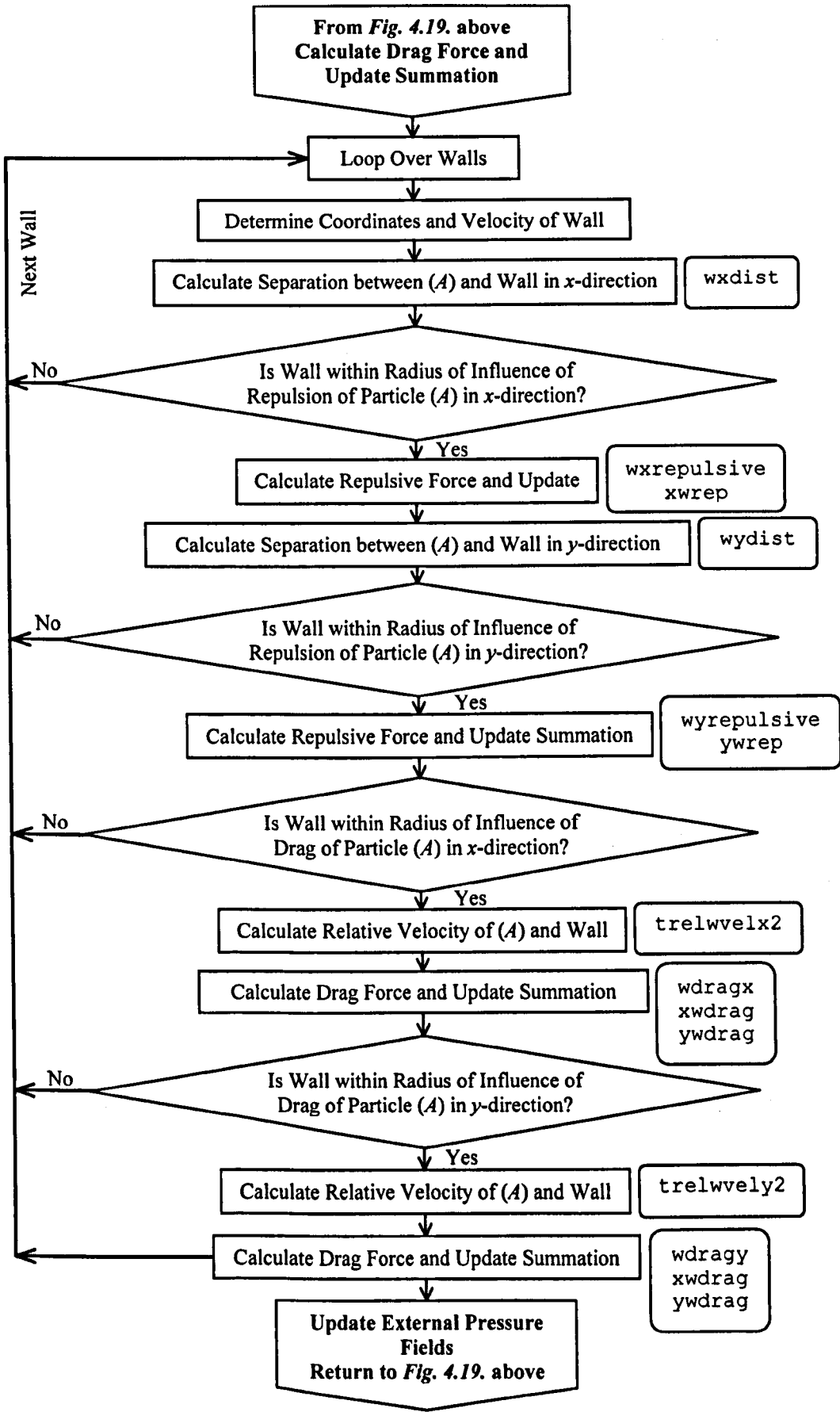


Fig. 4.21. Flow Chart Summarising FISH Code for Nested Wall Loop Sub-Block of Flow Chart Summarising PFM Code in Fig. 4.19.

It may also be noted that, while the PFM *FISH* code worked as required, it was inefficient in its execution due to limitations of the language. For example, it was necessary to search through all 'fluid particles' in order to check whether or not they were within a certain particle's radii of influence and hence whether or not they needed to be considered further. Despite the visibly slow running of the code, this method was acceptable for a limited number of PFM particles as utilised within these studies. However, if a model was to be applied to a problem with a large number of particles, as would be required in a hydraulic fracture simulation, then the code would become too slow for practical purposes. Many, more efficient, schemes can be implemented for searching through particles in DEM codes and while some of these may be realised within *FISH* it was not thought to be worthwhile for the purposes of this project.

4.3.4. PFM Benchmark Problems

As with the PSM it was necessary to conduct benchmark studies with the PFM in order to verify that it could reproduce the desired fluid behaviour. As mentioned previously the calibration of this model was essentially by trial and error variation of the main model parameters; the coefficients of repulsion and drag, the radii of influence over which repulsion and drag were effective and the mechanical damping of the system. The benchmark studies described below were useful in determining the basic behaviour of the model and allowing controlled alterations to be made to these variables.

The first study was concerned with the development of a uniform pressure field in the PFM when confined under a constant external pressure. The second benchmark study looked into the dynamic behaviour of the PFM and its ability to reproduce simple fluid flow regimes that are often assumed for flow in hydraulic fractures. The construction and testing of these benchmark models is described in the following Sections, along with discussion of the presented results.

4.3.4.1. Pressurised Cylinder Benchmark Model

This benchmark test looks at the static pressure distribution along the walls of a pressurised cylinder filled with PFM particles. The problem was set up as shown below in *Fig. 4.22*.

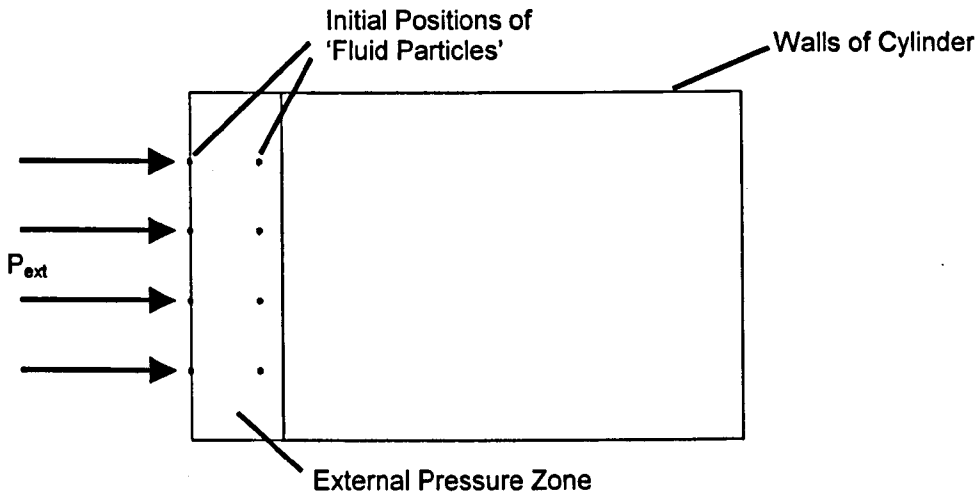


Fig. 4.22. Diagram Showing Initial Set-up of the Pressurised Cylinder Benchmark Problem for the PFM

PFM particles were initially positioned as shown above. Forces were applied to the particles within the external pressure zone such that the total force applied to all particles within the zone was equivalent to a certain predefined external pressure, P_{ext} , for the open end of the cylinder. As the particles moved out of the external pressure zone and into the cylinder, more particles were positioned in their place and were subjected to the same external pressure. This continued until the cylinder filled with particles such that they could no longer move out of the external pressure zone. At this point, the PFM had found a steady state equilibrium. Typical example plots of this process are shown below (See *Fig. 4.23*).

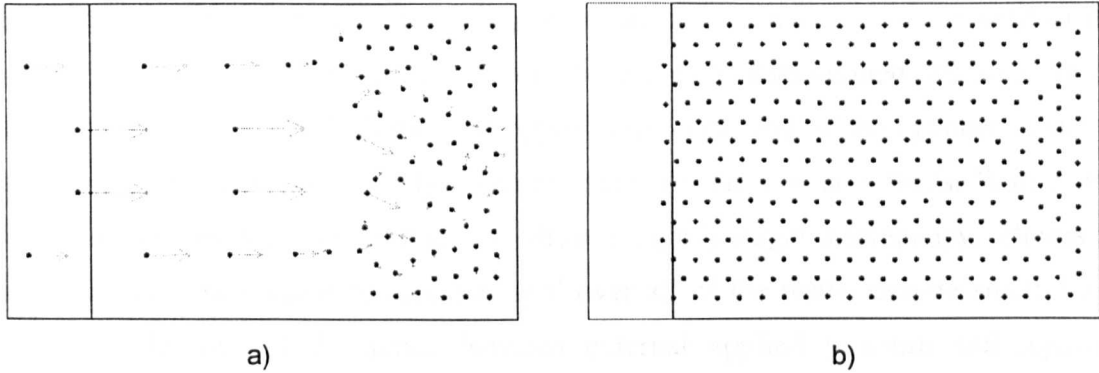


Fig. 4.23. Plots of Typical Pressurised Cylinder Benchmark Model at a) an Intermediate Stage of Filling and b) Final Steady State Equilibrium (arrows indicate particle velocities)

Several studies were conducted with varying external pressure. When the cylinder was full and the PFM particles were in equilibrium the total force on each of the cylinder walls was calculated. This was done simply by calculating the repulsive forces, according to the pressure separation law, for all particles for which a wall of the cylinder was within their radius of influence of repulsion. The total force on each wall was divided by the length of that wall in order to calculate the applied pressure. The results of these studies are shown in Table 4.7. below and additionally, plots of the final equilibrium stages of the three studies listed are shown in Fig. 4.24. below.

P_{ext} (kPa)	α_R	Total Pressure	Total Pressure	Total Pressure	Av. Pressure on Cylinder Walls (kPa)
		Wall 1*	Wall 2*	Wall 3*	
		(kPa)	(kPa)	(kPa)	
100	1×10^4	105	98	109	104
200	1×10^4	209	199	199	202
2000	1×10^5	2098	2006	1968	2024

*Walls labelled according to Fig. 4.22.

Table 4.7. Results of Pressurised Cylinder Study for the PFM

Fig. 4.24. Plots of the Final Equilibrium Stages of PFM Pressurised Cylinder Tests under Varying External Pressures of a) 100kPa, b) 200kPa and c) 2000kPa

As can be seen from the table above, in general the pressures acting on the walls of the cylinder due to the PFM correlate very well with the external applied pressure. In all cases, the pressure on Wall 2, the wall opposite the open end of the cylinder, matches the external pressure most closely. The pressures on the two side walls, Wall 1 and Wall 3, also match very well but tend to show a slightly larger discrepancy. However, as can be seen from the pressures averaged over all of the walls, despite small, local variations, the overall difference between external applied pressure and reported pressure is never more than 4%. It can be further noticed that the largest error occurs under the lowest external pressure. An explanation for this may be found upon examination of the plots shown in *Fig. 4.24.* below.

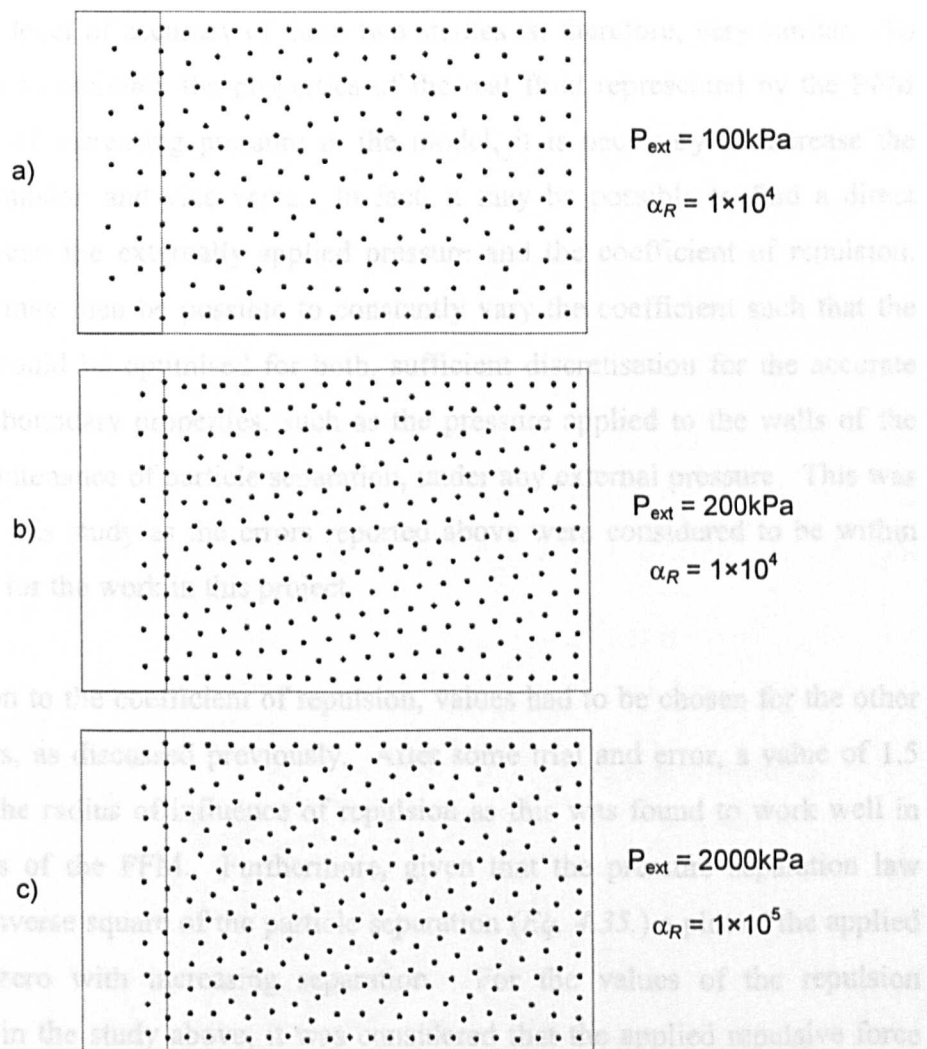


Fig. 4.24. Plots of the Final Equilibrium Stages of PFM Pressurised Cylinder Tests under Varying External Pressures of a) 100kPa, b) 200kPa and c) 2000kPa

It can be seen that the particles pack into the cylinder to a reasonably uniform spacing under any external pressure and that the higher the pressure, the closer the particle spacing. This is as would be expected for the pressure separation law as described in the previous Section. Since relatively few particles are packed into the cylinder in the case of the lowest external pressure (See *Fig. 4.24. a*), the discretisation of points, at which the force applied on the walls of the cylinder is measured, is quite coarse. This may be responsible for the discrepancy between the reported pressure on the walls and the applied external pressure. Consequently, the accuracy of the results improves under higher pressures although it can be noticed that the plot for an external pressure of 200kPa is very similar to that for 2000kPa. This is because the coefficient of repulsion, α_R , was increased from 1×10^4 to 1×10^5 in order to ensure that particle separation was maintained. The level of accuracy of these two studies is, therefore, very similar. To reiterate, in order to maintain the properties of the real fluid represented by the PFM under conditions of increasing pressure in the model, it is necessary to increase the coefficient of repulsion and vice versa. In fact, it may be possible to find a direct relationship between the externally applied pressure and the coefficient of repulsion. Consequently, it may then be possible to constantly vary the coefficient such that the PFM behaviour could be optimised for both, sufficient discretisation for the accurate measurement of boundary properties, such as the pressure applied to the walls of the cylinder, and maintenance of particle separation, under any external pressure. This was not attempted in this study as the errors reported above were considered to be within acceptable limits for the work in this project.

In addition to the coefficient of repulsion, values had to be chosen for the other model parameters, as discussed previously. After some trial and error, a value of 1.5 was chosen for the radius of influence of repulsion as this was found to work well in preliminary trials of the PFM. Furthermore, given that the pressure separation law varies with the inverse square of the particle separation (*Eq. 4.35.*) a plot of the applied force tends to zero with increasing separation. For the values of the repulsion coefficient used in the study above, it was considered that the applied repulsive force developed beyond a separation of 1.5 was insignificant (See *Fig. 4.25.*).

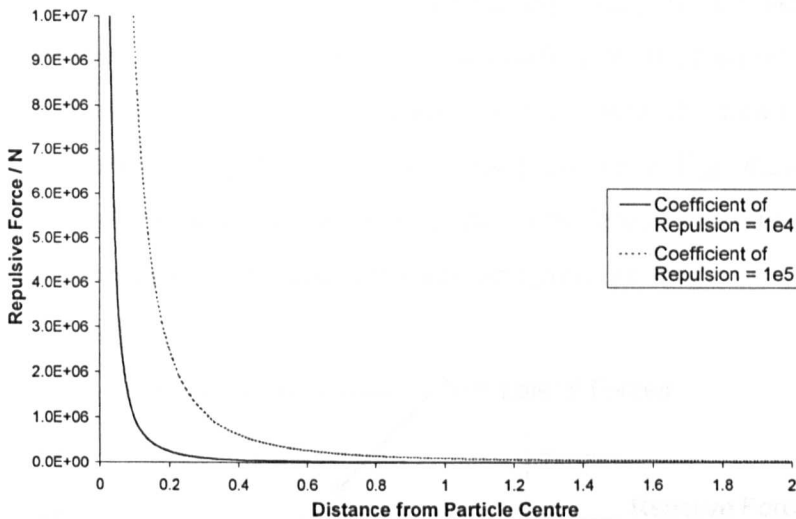


Fig. 4.25. Plot of Pressure Separation Law for Coefficients of Repulsion of 1×10^4 and 1×10^5

Due to the static nature of the pressurised cylinder problem, the viscosity of the fluid was not important and an arbitrary value of 1×10^3 was therefore chosen for the coefficient of drag, α_D . Similarly, an arbitrary value was chosen for the radius of influence of drag. As mentioned previously this had to be larger than the radius of influence of repulsion so that, in a dynamic problem, viscous effects could be modelled even at zero pressure. A value of 2.2 was chosen since this is approximately 50% larger than the radius of influence of repulsion and furthermore, this allowed a particle in the initially square arrangement used in PFM trials (See Fig. 4.26. below) to ‘see’ all eight of its direct neighbours in terms of drag.

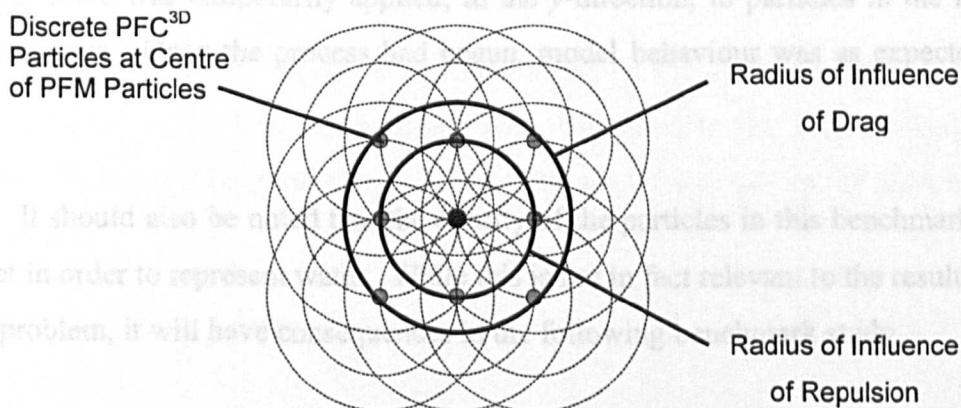


Fig. 4.26. Diagram Showing Overlap of Radii of Influence Around PFM Particles

An additional potential problem with the PFM, especially in a model such as the Pressurised Cylinder Problem, occurs when the configuration of particles entering the model remains planar, and a steady state equilibrium is found through repulsive forces, without the particles moving from their original plane (See Fig. 4.27.). When this happens the model consists of what can be considered separate, parallel, one-dimensional models and does not produce a uniform pressure field.

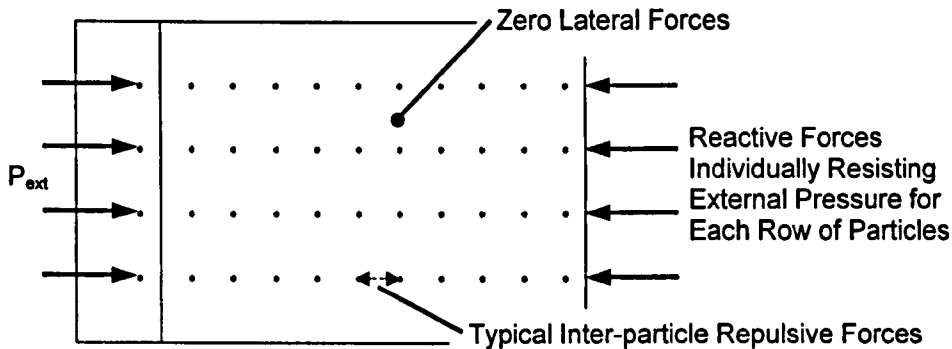


Fig. 4.27. Example Plot of Pressurised Cylinder Model for PFM with 'Fluid Particles' at Equilibrium in 1D Lines, without Lateral Displacement

In most cases a numerical instability or rounding error will ensure that the particles are perturbed and move laterally, filling the cylinder and reaching equilibrium with a uniform pressure field as shown in the examples above (See Fig. 4.24.). In some instances however, this does not happen and it is necessary to induce the desired behaviour. Where this occurred in models applied in these studies, a relatively small 'stirring' force was temporarily applied, in the y -direction, to particles in the External Pressure Zone. Once the process had begun, model behaviour was as expected for a fluid.

It should also be noted that the density of the particles in this benchmark model was set in order to represent water. While this is not in fact relevant to the results of this static problem, it will have consequences in the following benchmark study.

4.3.4.2. Lubrication Flow Benchmark Model

This benchmark problem looks into the development of a lubrication flow regime with the PFM. Lubrication flow, as described by Eq. 4.40. and Eq. 4.41., represents incompressible, one-dimensional, steady, uniform, laminar flow between two parallel plates and is often the assumed flow behaviour in hydraulic fracture models. This is further discussed in Chapter 2, Section 2.4.

$$Q = \frac{Y^3}{12\mu} \frac{dp}{dx} \quad \text{Eq. 4.40.}$$

$$u_f = \frac{1}{-2\mu} \frac{dp}{dx} (Yy - y^2) \quad \text{Eq. 4.41.}$$

where, Q is the fluid flow rate between the plates, Y is the separation of the plates, μ is the dynamic viscosity of the fluid, $\frac{dp}{dx}$ is the pressure gradient, u_f is the fluid velocity and y is the distance to the point of measurement from the plate considered to be the origin ($Y = 0$).

NB - for convenience and consistency in this thesis some of the notation in Eq. 4.41. has been altered from the original text (Douglas et al. [23]).

In order to verify the behaviour developed by the PFM, the velocities of the ‘fluid particles’ in the benchmark model were compared to the fluid velocity profile predicted by lubrication flow theory. The PFM model was set up, as shown in Fig. 4.28. below.

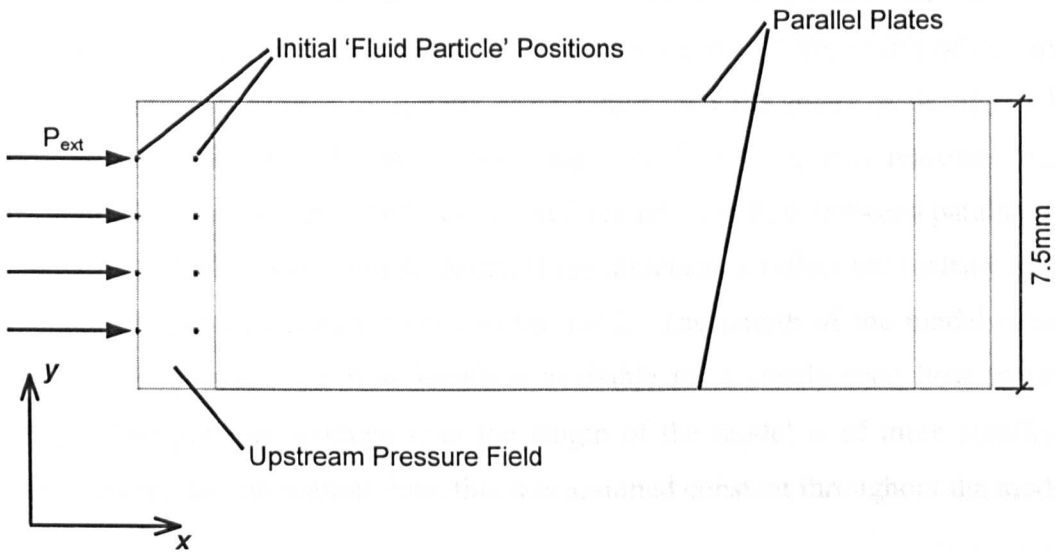


Fig. 4.28. Diagram Showing Initial Set-up of the Lubrication Flow Benchmark Problem for the PFM

The initial configuration of this problem was very similar to that of the Pressurised Cylinder Benchmark Problem, discussed in the previous Section. PFM particles were initially positioned as shown above and forces were applied to represent an external pressure. As the particles moved out of the Upstream Pressure Field, new particles were created in their place. In contrast to the Pressurised Cylinder Model, the downstream end of this model was open. As particles moved through the model and out of the downstream end, they were deleted. In this way, a continuous flow of particles was maintained between the plates. A typical example of steady state flow conditions in the Lubrication Flow Model is shown below in Fig. 4.29.

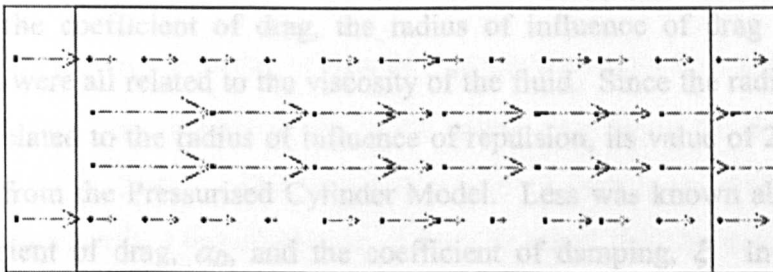


Fig. 4.29. Typical Plot of Lubrication Flow Model under Established Steady State Flow Conditions (arrows indicate particle velocities)

Although the actual dimensions of this model are not important, as long as the consistency of the units is maintained, it may be noticed that the width of this model was considered to be on a millimetre scale rather than the metre scale of the PSM discussed earlier in this Chapter. This scale was chosen for two reasons. Firstly, lubrication flow theory can only be considered realistic for flow between parallel plates at a relatively close spacing and secondly, these dimensions reflect the realistic scale of a hydraulic fracture as it might exist in the field. The length of the model is not of concern as long as enough flow length is available for a steady state flow regime to develop. The pressure gradient over the length of the model is of more significance and, as required for lubrication flow, this was assumed constant throughout the model.

In order to assess the behaviour of the PFM in this benchmark model and the effects of the five main variables, previously discussed above, several studies were carried out with variation of these parameters and the model boundary conditions. However, before the tests could be run, consideration had to be made of the initial values assigned to the model parameters. As mentioned in Section 4.3.4.1., a value for the radius of influence of repulsion of 1.5 (mm in this case) had previously worked well. As can be seen from *Fig. 4.25.*, increasing this value had little effect on interacting particles due to the relatively small forces invoked at greater separations. Reducing the radius of influence of repulsion by only a small amount resulted in mechanical contact between particles, which was an unacceptable occurrence for the PFM. For these reasons the value used in the Pressurised Cylinder Problem (See Section 4.3.4.1.) was preserved for these studies. The value of the coefficient of repulsion applied in the Pressurised Cylinder Problem was also kept since, as discussed previously, suitable values were directly related to the external applied pressure. The three remaining variables, the coefficient of drag, the radius of influence of drag and the damping coefficient were all related to the viscosity of the fluid. Since the radius of influence of drag was related to the radius of influence of repulsion, its value of 2.2 (mm) was also preserved from the Pressurised Cylinder Model. Less was known about the effects of the coefficient of drag, α_D , and the coefficient of damping, ξ . In summary, it was therefore decided that while the other parameters would be held constant the effects of these coefficients would be investigated as part of a general study carried out to verify the ability of the PFM to reproduce a lubrication flow regime.

As mentioned before, in order to compare the behaviour of the PFM to the theoretical description of lubrication flow (See Eq. 4.40. and Eq. 4.41.) the average steady state velocities of the particles were assessed as they passed through the model. These values were then plotted against their y -position, across the flow between the plates. A comparison plot was also made of the theoretical, parabolic velocity profile defined by Eq. 4.41. The only unknown for the model in this equation was the dynamic viscosity of the fluid, μ . By varying this, it was possible to find a 'best fit' theoretical velocity profile for the results produced by the model.

The numerical results of the studies can be seen in Table 4.8. and graphical representations of the velocity profiles, as discussed above, can be found further below, along with discussion of the results (See Fig. 4.30. to Fig. 4.34.).

Run No.	Coefficient of Damping, α_D	Applied Pressure Gradient, $\frac{dp}{dx}$ (N/m ² /m)	Implied Dynamic Viscosity, μ (Nsm ⁻²)	Max. Velocity, $u_{f(max)}$ (from Eq. 4.41.) (m/s)
001	0.0	-1.0	0.0747	0.0000941
002	0.0	-2.0	0.0705	0.0001994
003	0.7	-1.0	0.242	0.0000291
004	0.7	-2.0	0.461	0.0000305

Table 4.8. Results of Lubrication Flow Study for the PFM

As can be seen from the results of Run 001, given above, for a pressure gradient, $\frac{dp}{dx} = 1.0$, the 'best fit' line, shown in Fig. 4.30. below, was found for an implied dynamic viscosity of 0.0747Nsm⁻². This value is consistent with a reasonably high viscosity fluid such as an oil[†]. For comparison, it may be noted that the dynamic viscosity for water is approximately 0.0010Nsm⁻² (Douglas et al. [23]) and Papanastasiou [69] quotes

[†] It is understood that the fluid property of dynamic viscosity varies with temperature. For simplicity, it is assumed that all numerical studies conducted with the PFM in this work are carried out at a constant temperature of approximately 20°C.

a value of 0.100 Nsm^{-2} for a hydraulic fracture gel. The results shown below were considered to be very promising and clearly showed that the PFM was capable of accurately reproducing lubrication flow behaviour.

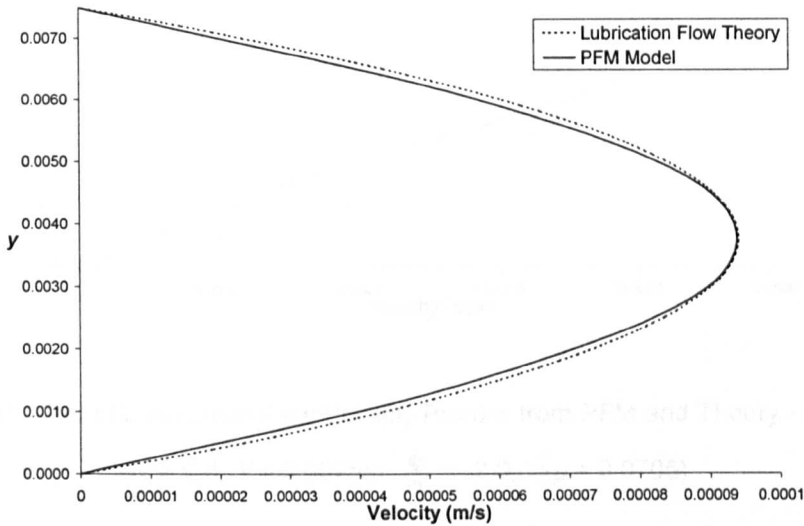


Fig. 4.30. Plot of Lubrication Flow Velocity Profiles from PFM and Theory - Run 001

$$(\xi = 0.0, Y = 0.0075\text{m}, \frac{dp}{dx} = -1.0, \Rightarrow \mu = 0.0747)$$

As discussed, it was hoped that by tuning the PFM parameters, it would be possible to model a fluid of any viscosity. Ideally, especially given the quality of the results, the Lubrication Flow Model would become a useful tool in determining a precise understanding of the behaviour of the PFM and allow calibration to take place before the PFM was applied to a model simulation.

For Run 002 the parameters of the PFM were kept as they had been for Run 001, however the pressure gradient over the model was increased from -1.0 to -2.0. As can be seen from the results shown in Table 4.8. the maximum fluid velocity, predicted by Eq. 4.41. for the centre of the flow, is approximately double that predicted for Run 001, while the implied dynamic viscosity is approximately the same. This is as would be expected for the described increase in pressure gradient and again confirms the ability of the PFM to accurately model fluid behaviour. The slight under prediction of dynamic viscosity and consequent over prediction of velocity can be understood on examination of the velocity profiles plotted in Fig. 4.31. below.

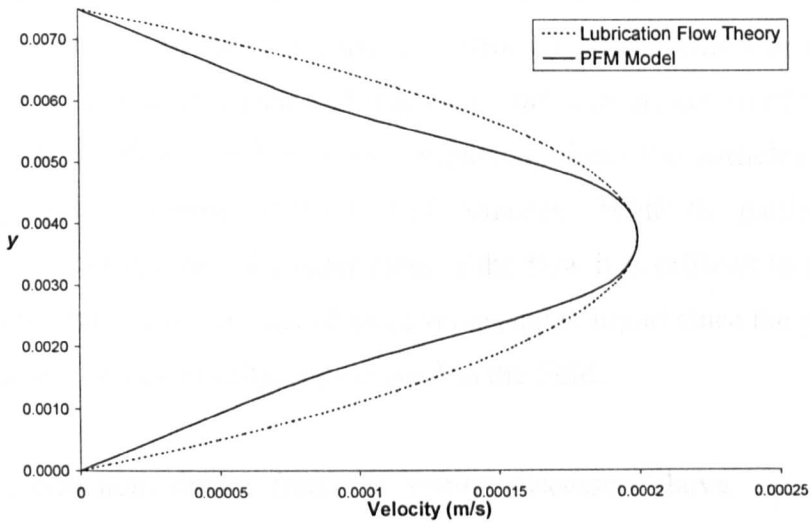


Fig. 4.31. Plot of Lubrication Flow Velocity Profiles from PFM and Theory - Run 002

$$(\xi = 0.0, Y = 0.0075\text{m}, \frac{dp}{dx} = -2.0, \Rightarrow \mu = 0.0705)$$

As can be seen, the velocity profile produced by the model was no longer parabolic. The centre of the flow is moving faster than Lubrication Flow Theory would suggest and consequently, the ‘best fit’ line is no longer an accurate prediction of the actual behaviour. This effect is clearly seen in Fig. 4.32. where the theoretical velocity profile is plotted for a dynamic viscosity of 0.0747Nsm^{-2} , as predicted by Run 001.

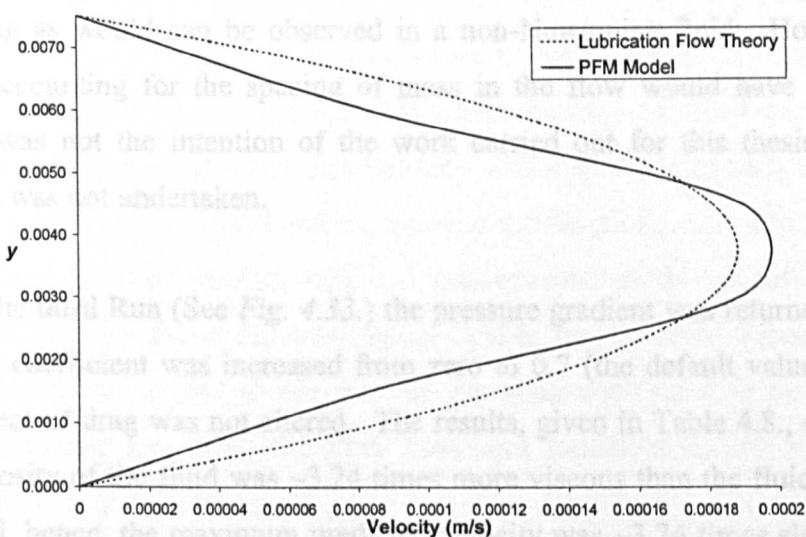


Fig. 4.32. Plot of Lubrication Flow Velocity Profiles from PFM and Theory - Run 002

$$(\mu = 0.0747, \text{ as predicted by Run 001})$$

The velocity profile produced above by the PFM is indicative that the coefficient of drag in the model was not large enough to control the flow. This was confirmed by inspection of the model, which showed that the particles in the centre of the flow were at a steady state condition such that their separation from the particles in front and behind was greater than either of the radii of influence. While the particles were still experiencing drag forces from the outer parts of the flow it is difficult to argue that the behaviour along the centre was that of an incompressible liquid since the particles were moving separately and essentially, gaps existed in the fluid.

The conclusion, drawn from the results discussed above, was that, as the required value for the coefficient of repulsion was directly related to the external pressure on the fluid, so the required value for the coefficient of drag was directly related to the velocity of the fluid. In order to maintain the properties of the real fluid represented by the PFM under conditions of increasing velocity in the model, the coefficient of drag would have to be increased. As with the coefficient of repulsion, discussed in Section 4.3.4.1., it may be possible to find a relationship between the fluid velocity and coefficient of drag such that it can be constantly varied for optimised behaviour. This was not pursued further in the course of this thesis.

Additionally, although this was not the intended behaviour of this model, the result above does hint at the possibility of developing complex fluid behaviour such as shear-thinning as would can be observed in a non-Newtonian fluid. However, some method of accounting for the spacing of mass in the flow would have to be found. Again, this was not the intention of the work carried out for this thesis and further investigation was not undertaken.

For the third Run (See *Fig. 4.33.*) the pressure gradient was returned to -1.0 but the damping coefficient was increased from zero to 0.7 (the default value for PFC^{3D}). The coefficient of drag was not altered. The results, given in Table 4.8., show that the implied viscosity of the fluid was ~3.24 times more viscous than the fluid modelled in Run 001 and, hence, the maximum predicted velocity was ~3.24 times slower. Again, this was the expected modification as the increased damping coefficient increases the rate of energy loss in the model fluid, which, in a real fluid is related to its viscosity. The actual implied value is obviously quite high for a realistic fluid, however, it is

understood that the value of 0.7 for the coefficient of damping was also very high and this Run was intended to be qualitative rather than quantitative.

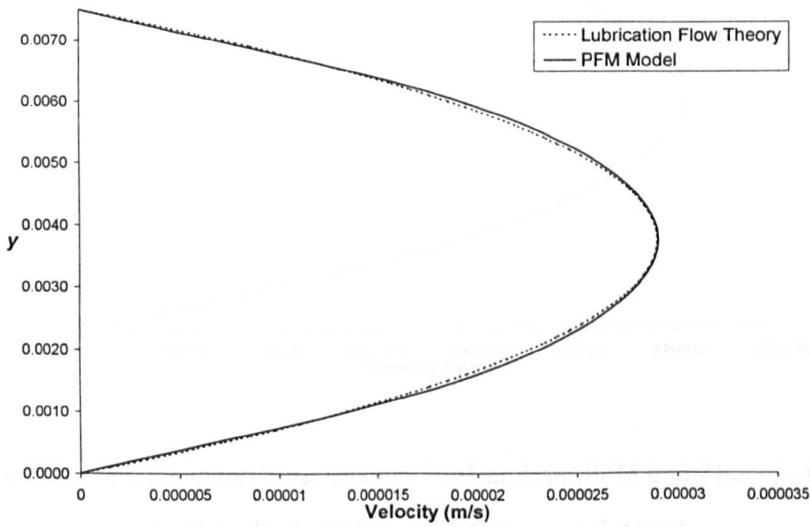


Fig. 4.33. Plot of Lubrication Flow Velocity Profiles from PFM and Theory - Run 003

$$(\xi = 0.7, Y = 0.0075\text{m}, \frac{dp}{dx} = 1.0, \Rightarrow \mu = 0.242)$$

It was hoped that further model runs with the non-zero values for the damping coefficient would show a pattern relating it to the implied dynamic viscosity of the fluid. However, the final run in this study did not show the expected results. As can be seen in Table 4.8., the damping coefficient was again set to 0.7 and the pressure gradient was increased to -2.0. It was expected to see a change in results similar to those shown between Run 001 and Run 002 where the implied viscosity would remain constant while the predicted maximum velocity would double. In fact, it can be seen that the velocity barely increased and the velocity profile plots, shown in Fig. 4.34, are almost identical to those in Fig. 4.33. A consequence of this is that the dynamic viscosity predicted by Eq. 4.41, was almost double the expected value. This is an anomalous result but it also shows that the damping coefficient is by far the most dominant parameter governing the fluid behaviour modelled by the PFM and care should be taken in its application.

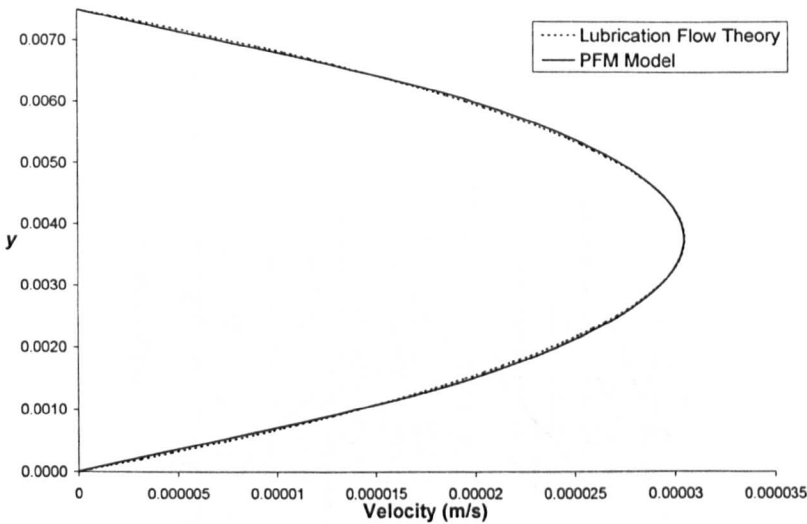


Fig. 4.34. Plot of Lubrication Flow Velocity Profiles from PFM and Theory - Run 004

$$(\xi = 0.7, Y = 0.0075\text{m}, \frac{dp}{dx} = 2.0, \Rightarrow \mu = 0.4610)$$

Additionally, the difference between the velocity profiles of Run 002 (Fig. 4.31. and Fig. 4.32.) and Run 004 (Fig. 4.34.) also shows the favourable effect that the damping coefficient has on the model fluid viscosity. The velocity profile from Run 004 is very close to parabolic, as predicted by lubrication flow theory, and there is no evidence of the shearing in the centre of the flow that was present in Run 002.

As discussed previously, the PFM follows similar principles to the PAF method developed at Los Alamos National Laboratory in the 1960s (Johnson [43]). After some investigation, this method was abandoned by the developers due to inherent noise in the model flow, which was put down to particles interacting with different particles as their direct neighbours changed in time. Although the PFM interacts with all particles within its radii of influence, and consequently may interact with more or less particles at any one time than the PAF particles, the solution also shows a lot of noise. This can particularly be seen in a plot of particle velocity in time (See Fig. 4.35. below).

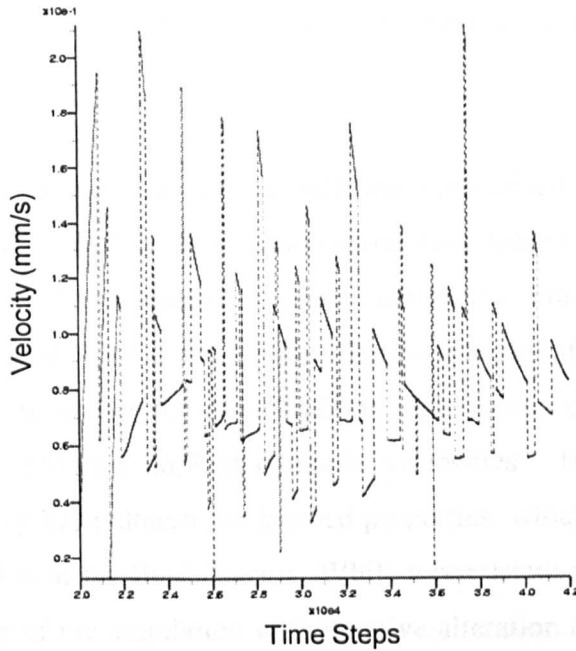


Fig. 4.35. Example of a Velocity/Time Plot for a PFM Particle as it Travels Through the Lubrication Flow Model

It was found that the oscillations of the velocity/time plot were consistent with compression waves that travelled up and down the Lubrication Flow Model as the flow progressed. This was the result of each particle oscillating between the repulsion of a particle downstream of itself and a particle upstream of itself and this process can be likened to the neighbour connection process discussed above for the PAF. It is felt that this effect could be minimised through optimisation of the five main variables and in particular, the coefficients of repulsion and damping however this would have a knock on effect to the fluid behaviour represented by the model. A benefit of the noise in the flow was the confirmation that the 'fluid particles' were interacting through the repulsive and drag forces and that the spacing effects observed in the high velocity flows were not present. As this suggests, less noise was noticed in velocity/time plots from runs featuring flow shear effects. An alternative method of minimising the noise would be to increase the discretisation of the PFM, which should reduce the relative motion of the particles.

Despite the noise in the flow, the overall behaviour produced by the PFM in the Lubrication Flow Problem was considered satisfactory for the initial development of the model.

A further point of note is that, as with the Pressurised Cylinder Model, the density of the particles in all of the Lubrication Flow Runs was set in order to represent water. Given that the fluid properties were determined from the results of the simulations, it was clear that the assumed fluid density was not always appropriate and it would be desirable to repeat these simulations with values of fluid density more appropriate to fluids with the implied dynamic viscosities. However, altering the density of the fluid may have altered the implied properties, which would subsequently require further alteration of the fluid density. While a consistent set of parameters may be found by repetition of the simulation with iterative alteration of the fluid density, it would certainly be time consuming and an analytical solution would be preferable. This is discussed further in the following Section.

4.3.5. PFM Conclusions

From the results of the benchmark studies presented above, it can be concluded that the PFM can accurately reproduce both static fluid behaviour, such as a uniform pressure field, as well as dynamic behaviour, such as the parabolic velocity profile associated with lubrication flow. It is also clear, however, that there are complex relationships governing the effects of the five main model parameters, the coefficients of repulsion and drag, the radii of influence of repulsion and drag and the damping coefficient, on the behaviour of the PFM. These relationships are far from fully understood and while, as shown above, the properties of the fluid represented by the PFM can be determined by comparison with theory, more investigation will be required before the model parameters can be set prior to simulation.

Even given further study it may not be possible to find empirical relationships for these variables and it may be desirable to find an analytical method of calculating them. While the PSM was calibrated through a strain energy equivalence technique

(See Section 4.2.2.3.), no comparable equivalence strategy is apparent for the PFM, however, it may be possible to derive a relationship between the model separation laws and the Navier-Stokes equations for a fluid, as suggested by Zhang et al. [98] for their DEM fluid model. Account would also have to be made of the mechanical damping of the system, since, as noted above, this was found to have a very significant effect on the fluid behaviour of the PFM. Furthermore, it was also noted in the previous Sections, that in order to maintain the properties of the real fluid represented by the PFM as conditions in the model varied, it was necessary to alter the coefficients of repulsion and drag in correspondence to changes in the fluid pressure and velocity fields respectively. As suggested, it may be desirable to develop an automatically varying algorithm for these parameters and, ideally, this would also be related to the Navier-Stokes equation.

Additionally, it may be desirable to vary the mass associated with a particle. Currently, in an approach consistent with that employed in the PAF method, the mass associated with the PFM particles is constant and represents a volume of fluid enclosed by a cylinder half the diameter of its radius of influence of repulsion (See *Fig. 4.17.*). However, it would seem that, when particles move closer together under pressure or dynamic effects, the mass per unit area increases and thus the overall fluid density increases. While this may be representative of a compressible fluid, it cannot be accepted for incompressible or near incompressible fluids such as should be considered in hydraulic fracture problems. In general, this is not thought to significantly affect the results of the benchmark models, discussed in the previous Sections, as the particles do not become highly packed. However, as discussed for Run 002 of the Lubrication Flow Problem, there are instances where particle spacing can increase beyond the radius of influence of repulsion and hence reduce the overall density. A method of varying the density of a particle in relation to the proximity of its neighbours would resolve this problem and allow a constant fluid density to be maintained. This was not attempted during the course of the work carried out for this thesis as it was considered overly complex to implement within the current code.

Also mentioned in Section 4.3.4.2., above was the possibility that the PFM could be applied to the simulation of complex, non-Newtonian fluids. If this were to be possible, it would certainly require the constant variation of the model parameters since, by definition, the dynamic viscosity of a non-Newtonian fluid is not constant. While

this would ultimately be desirable for the purposes of modelling hydraulic fracture treatments where the fracture gels are often non-Newtonian (See Chapter 2, Section 2.4.1.), it is well beyond the current scope of this work. However, given an analytical relationship between the model parameters and the Navier-Stokes equations it should be possible to implement constant variation of the parameters.

It may also be noted from the results of the Lubrication Flow benchmark study, discussed in the previous Section, that the PFM was only seen to model fluids of relatively high viscosity. In fact, although not documented in detail, further trials of the Lubrication Flow Problem had shown great difficulty in reducing the viscosity while maintaining reasonable fluid behaviour. It was felt that these difficulties might have been due to the discretisation of the PFM model. With more particles and therefore more information per unit area, it might be possible to capture fluid behaviour over a larger range of properties. This would probably also be required in order to capture complex flow behaviour such as turbulence, especially in a model of a fracture with a width of only a few millimetres. As stated previously, a finer discretisation may also minimise certain effects such as noise in the flow. A disadvantage of a finer discretisation would be the increased computational effort required to run what is already a slow code.

Despite the problems discussed above, it is felt that the results shown in the previous Sections were very promising and that, with further study, the PFM could be developed into a rigorous fluid modelling tool. However, the aim of this work was to develop a coupled modelling framework and hence, the existing capabilities of the PFM were considered sufficient and further study was temporarily discontinued in order to allow the development of a coupled model (as discussed in the following Section) and the study of fracturing behaviour in the PSM (See Chapter 5).

4.4. The Coupled Solid/Fluid Model (PSM + PFM)

4.4.1. Development of the Coupled Solid/Fluid Model

As discussed previously, an ultimate aim for this work was to create a coupled solid/fluid model within a single software DEM framework. The development of the separate solid and fluid phase models, the PSM and PFM, is described and discussed in detail in Sections 4.2. and 4.3. above. It was the principle of the proposed coupled modelling framework that these models could be very simply integrated to create a coupled solid/fluid model without the need for further modification or other procedures usually associated with coupled models, such as mapping and consistency between different meshes. The benchmark model, described in the following Section, was an initial attempt to do this, however, some minor modifications were required before the coupled benchmark model could be run.

In order for the PFM particles to be able to interact with the PSM mesh it was necessary for them to be able to 'see' PSM particles within their radii of influence. Obviously, since the PFM represents a fluid phase entirely separate from the solid phase material only the surface of the solid material should interact with the fluid in terms of the repulsion and drag forces associated with pressure and viscosity. To implement this, the PSM particles, on the outside of the mesh, that were likely to encounter the fluid were assigned a flag, making them 'visible' to the PFM (This is illustrated in *Fig. 4.36.* below). Thus, as the PFM particles passed by the PSM mesh they would experience drag and repulsion from the solid. Equal and opposite forces would also be applied back to the PSM particles. In this way fluid pressure could be applied to a solid surface and although it is unlikely that a large solid body would be dragged along by viscous effects, smaller bodies, as might be present with the future development of the Particle Proppant Model (PPM), could be dragged along in a fluid flow.

For a real fluid interacting with a real solid, the drag effect of the solid would be different to the drag effects internal to the fluid. Although it would have been quite possible to set the model interaction such that the drag effect of the 'solid particles' on a 'fluid particle' was different to the drag effect of another 'fluid particle', for simplicity in this work drag effects were kept the same throughout.

Initial tests on the coupled PSM + PFM showed that despite only the surface of the solid mesh being 'visible' to the PFM, the 'fluid particles' experienced far more drag than was expected. Obviously, this severely altered the behaviour of the fluid. The effect was found to be due to each PFM particle encountering several of the PSM surface particles within its radius of influence of drag as the PFM particle approached the PSM mesh (See *Fig. 4.36.*).

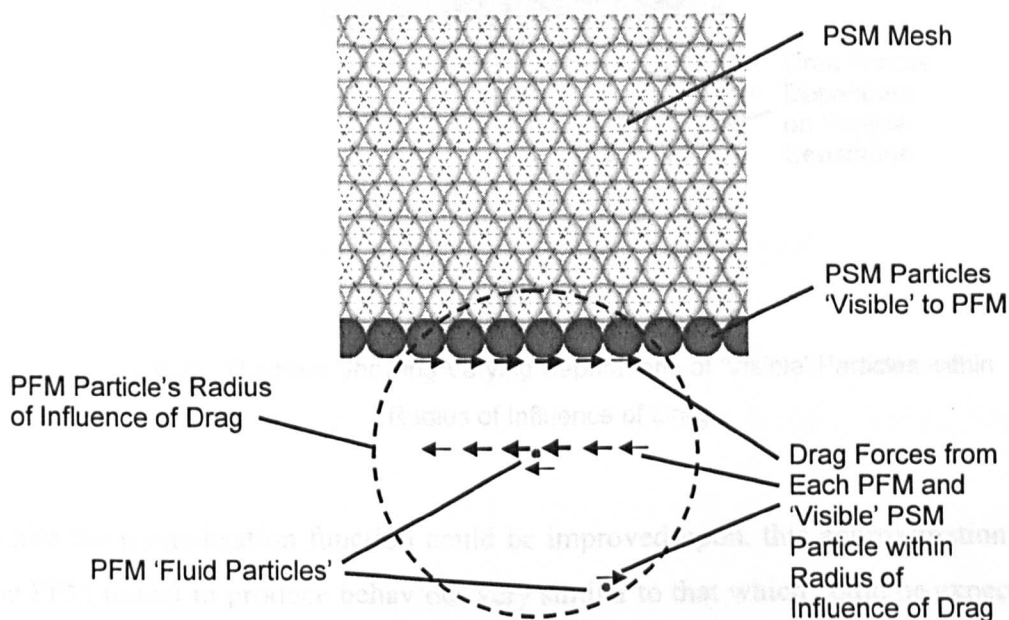


Fig. 4.36. Diagram Showing Excess Drag Effect of Multiple PSM Particles on Single PFM Particle

To combat this, a simple normalisation function was introduced whereby the total drag on a PFM particle was divided by the number of PSM particles within its radius of influence of drag. It was, however, understood that this was an over simplification. Firstly, the total drag force derived from the interaction with the PSM particles would not have an equal contribution from each one due to the differing separations and, secondly, the function did not make a distinction between PSM and other PFM particles within the first particles radius of influence of drag (See *Fig. 4.37.* below).

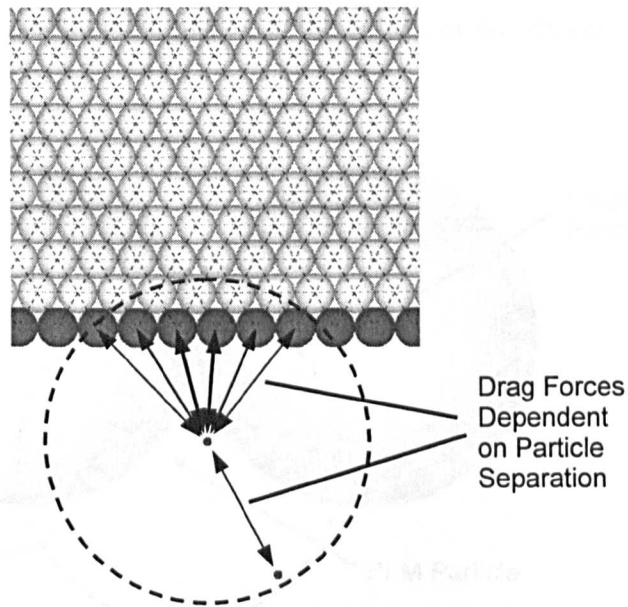


Fig. 4.37. Diagram Showing Varying Separations of 'Visible' Particles within Radius of Influence of Drag

While the normalisation function could be improved upon, this approximation allowed the PFM model to produce behaviour very similar to that which could be expected from the results of the benchmark models discussed in the previous Sections. For this reason the development of the normalisation function was not pursued further in the work carried out for this thesis.

Furthermore, this excess force effect was not noticed in the case of repulsive forces. This was probably a chance occurrence that the discretisation of the PSM was such that only one or two particles fell within a PFM particles radius of influence of repulsion at one time. If the discretisation of the PSM was to increase then it is likely that a normalisation function similar to that employed for the drag forces would also be required for the repulsive forces. Similarly, if discretisation of the PSM were to decrease then normalisation may not be required for either of the force fields. However, if discretisation were to decrease to such an extent that the radius of the PSM particles was greater than the radii of influence of the PFM particles, then a situation is conceivable, whereby 'fluid particles' could fall between the 'visible' PSM particles at the surface of a mesh, without feeling the effects of repulsion or drag (See Fig. 4.38.).

If this were to be the case then some kind of normalisation factor less than one, might be required. Again, this was not pursued further in the course of this thesis.

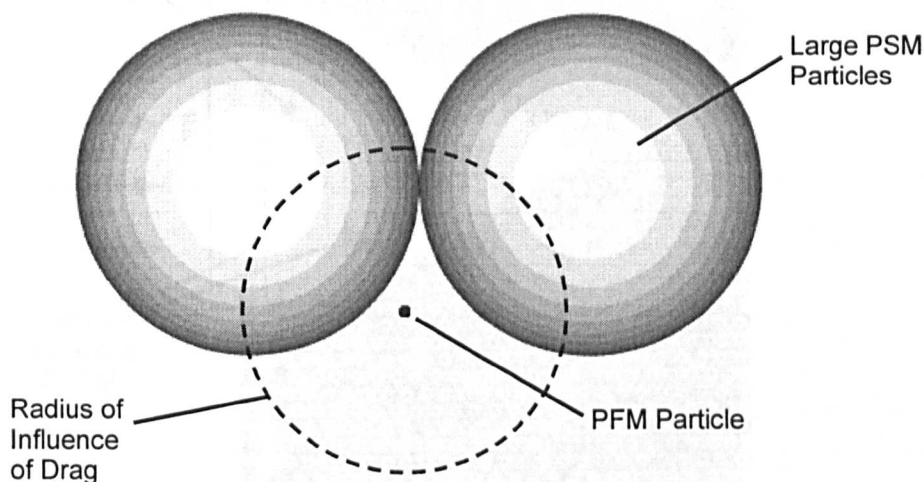


Fig. 4.38. Diagram Showing Situation Where PFM Particles May Fail to 'See' the PSM Mesh

4.4.2. Pressurised Notch Coupled Benchmark Problem

This benchmark problem looks into the elastic deformation of a solid, represented by a PSM mesh under loading from 'fluid particles' of the PFM to which an external pressure is applied. Although, as will be seen, the problem involved very simple interaction it was intended to be representative of the type of interaction that is likely to occur in a hydraulic fracture treatment. The notched PSM mesh can be considered to represent rock reservoir material at the end of an existing fracture or perforation in the wall of a wellbore. The PFM particles can be considered to represent a fracture fluid that infiltrates the notch and applies pressure to the rock. The coupled model was set-up as shown below (See Fig. 4.39.).

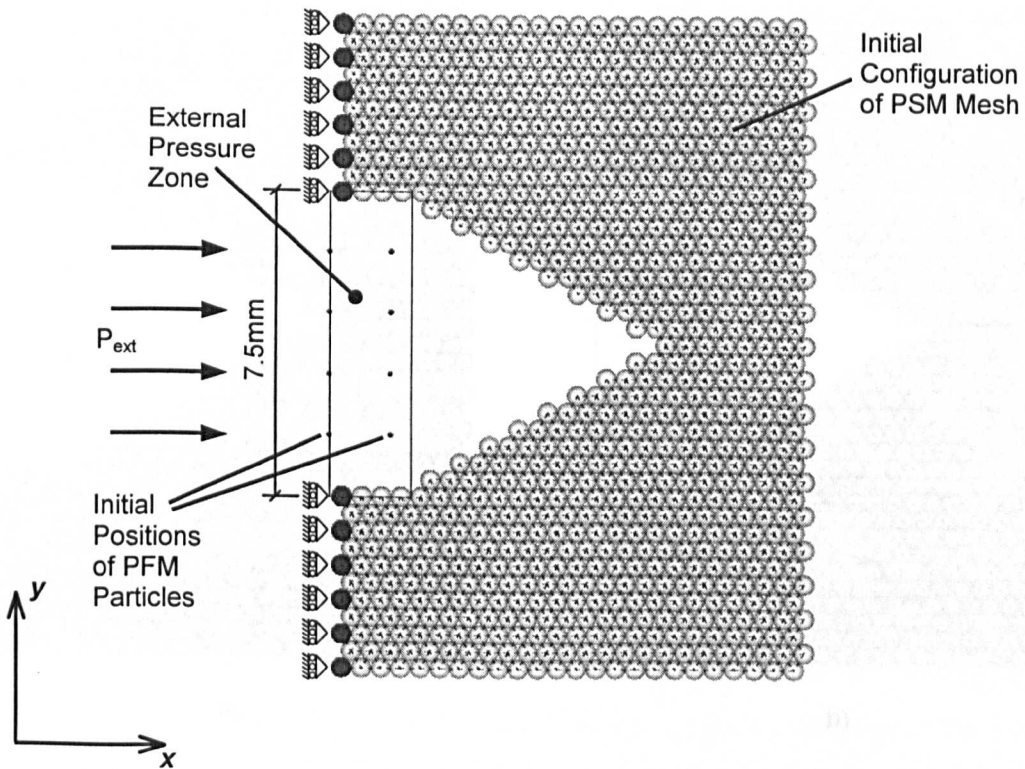


Fig. 4.39. Diagram Showing Initial Set-up of the Coupled Benchmark Model for PSM + PFM

As with the Pressurised Cylinder Benchmark Model, discussed in Section 4.3.4.1., ‘fluid particles’ were created within an External Pressure Zone where forces were applied such that the particles moved into the notch. As before, when particles left the External Pressure Zone, more particles were created in their place. This process continued until the notch was filled and static equilibrium was reached between the walls of the notch and the externally applied pressure (See Fig. 4.40. and Fig. 4.41. below). Obviously, in contrast to the fixed boundaries of the Pressurised Cylinder Model the notch boundaries formed by the PSM mesh were deformable. In order to resist the applied pressure, stress would have to develop within the solid mesh. A discussion of the mechanism by which this occurs can be found in Section 4.2.1. of this Chapter. It should be remembered that, at no time would the PFM ‘fluid particles’ come into mechanical contact with the PSM particles.

Fig. 4.41. Plot of Coupled Benchmark Model for PSM + PFM at Steady State Equilibrium

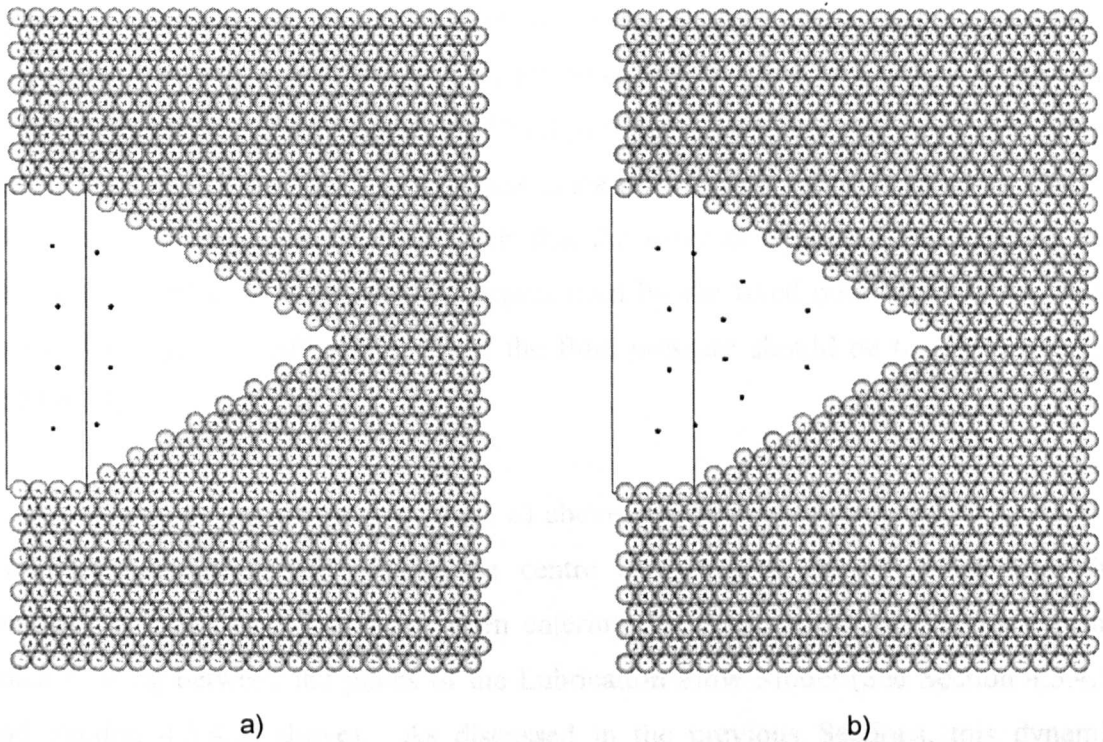


Fig. 4.40. Plots of Coupled Benchmark Model for PSM + PFM during Fluid Flow into Notched PSM Mesh a) after 4000 time steps and b) after 8000 time steps

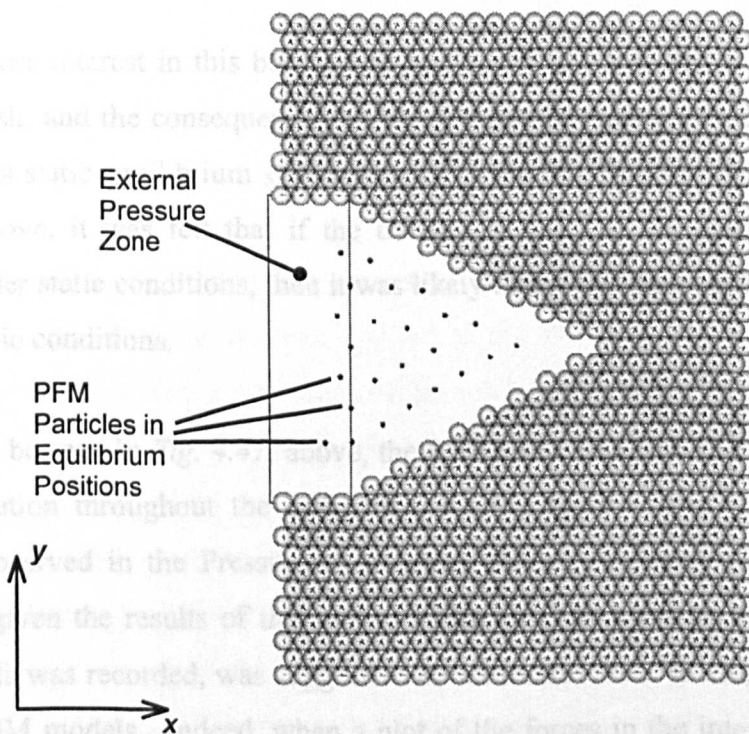


Fig. 4.41. Plot of Coupled Benchmark Model for PSM + PFM at Steady State Equilibrium

By way of verifying the interaction behaviour of the solid and fluid phases, two studies were made. Firstly, a qualitative examination of the dynamic interaction of the solid and fluid phases was carried out as the 'fluid particles' flowed into the notch in the PSM mesh. Secondly, a quantitative study was made of the static equilibrium state, reached when the notch was full of fluid, such that the external applied fluid pressure was compared to the total reactive force experienced by the fixed boundaries of the PSM mesh. Clearly, for equilibrium, all of the fluid pressure should be transferred to the PSM mesh.

As can be seen from *Fig. 4.40. a)* above, the PFM was observed to develop a parabolic velocity profile, where the centre of the flow moved faster than the extremities, much as it had done when entering the Pressurised Cylinder Model and when flowing between the plates of the Lubrication Flow Model (See Section 4.3.4.1. and Section 4.3.4.2. above). As discussed in the previous Sections, this dynamic behaviour was found to accurately reproduce the parabolic velocity profile predicted by Lubrication Flow theory. It was therefore considered that the flow behaviour of the PFM particles into the notch in the PSM mesh was sufficiently representative of fluid behaviour to be of continued use in this project.

Of more interest in this benchmark model was the transfer of fluid pressure to the solid mesh, and the consequent build up of stress in reaction to it, when the notch was full and a static equilibrium state reached. Given the observed dynamic behaviour, discussed above, it was felt that if the transfer of load to the mesh was accurately achieved under static conditions, then it was likely that it was also accurately transferred under dynamic conditions.

As can be seen in *Fig. 4.41.* above, the PFM particles reached a state of relatively even distribution throughout the notch in the PSM mesh. This was similar to the behaviour observed in the Pressurised Cylinder Model, discussed in Section 4.3.4.1. above and, given the results of that study, where an even pressure distribution on the cylinder walls was recorded, was suggestive of successful static interaction between the PFM and PSM models. Indeed, when a plot of the forces in the inter-particle links of the PSM mesh is examined (See *Fig. 4.42.* below) it can be seen that an evenly distributed and symmetrical stress field was built up in the PSM mesh.

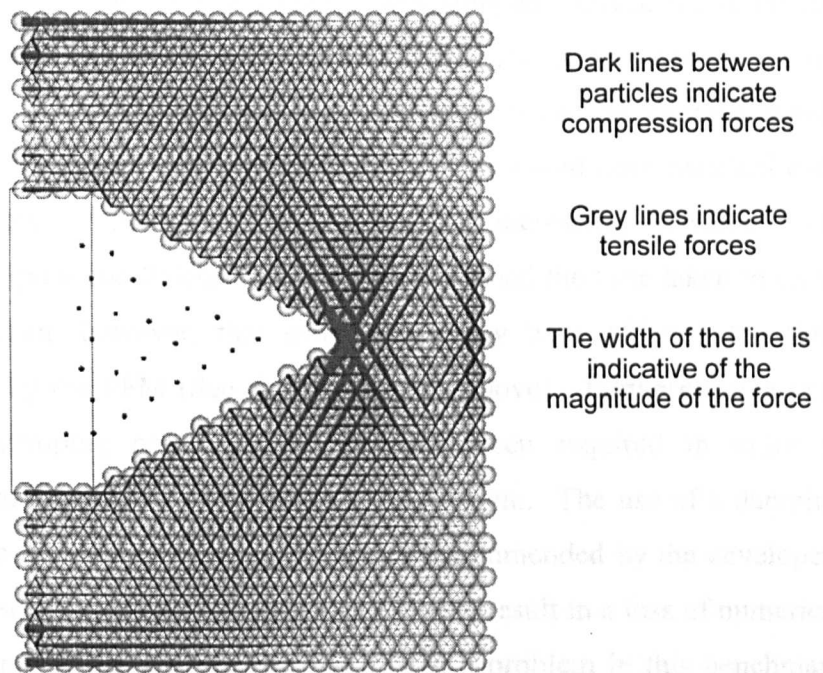


Fig. 4.42. Plot of Coupled Benchmark Model for PSM + PFM at Equilibrium Showing Forces in Inter-Particle Links

As can be seen above, a tensile stress regime dominates at the tip of the notch and at the fixed boundaries, in reaction to the applied external pressure, while compressive stresses dominate in the region near the walls of the notch, where pressure forces are transferred from the PFM to the PSM. Qualitatively, this is precisely the behaviour that would be predicted.

Additionally, as mentioned previously, the transfer of pressure was measured quantitatively. The external pressure applied to the PFM during this benchmark test was 20kPa, which, given the dimensions of the notch, resulted in a total applied force of 150N in the x -direction. When measured at the fixed boundaries of the mesh, the total reactive force was found to be 146.46N in the x -direction. No y -force could be supported by the mesh boundaries. This result was considered acceptable and the small discrepancy between the applied force and the reaction was thought to be the result of some residual movement of the PFM particles. Essentially, they were not quite at steady state equilibrium. However, after the particles had reached their approximate equilibrium locations quite quickly, there was a long period of 'settlement', during which they oscillated about these positions, and it had taken a considerable length of

time for the model to reach the state at which it was stopped. Given the obviously accurate interaction behaviour of the solid and fluid models, it was not considered necessary to continue. It seemed apparent that with more time, the particles would eventually have come to complete rest and the reaction load would have matched even more closely with the applied pressure. Tests showed that increasing the value of the overall mechanical damping coefficient, ξ , would have reduced the time taken to reach precise static equilibrium, however, this would obviously have affected the fluid properties represented by the PFM (See Section 4.3.4.2. above). Furthermore, a very high value for the damping coefficient would have been required in order to significantly shorten the time taken to reach static equilibrium. The use of a damping coefficient greater than the default value of 0.7 is not recommended by the developers of the PFC^{3D} code (Itasca Consulting Group [37]) as it may result in a loss of numerical stability in the solution. While this may not have been a problem in this benchmark model, it may prove to be in more complex models where dynamic interactions of the PFM and PSM are specifically of interest.

4.4.3. PSM + PFM Conclusions

It can be concluded from the results of the benchmark study described in the previous Section that it was possible to successfully integrate the PFM and PSM to create a coupled solid/fluid model without significant additional complications.

It was found that the PFM successfully interacted with the PSM mesh to reach a coupled state of static equilibrium with reasonable accuracy and it can therefore be said that the PSM and PFM display correct coupled behaviour. Furthermore, while the dynamic behaviour was not specifically measured, the PFM ‘fluid particles’ were observed to flow, under an external pressure gradient, in a fluid like manner, passed a PSM mesh. It can therefore be concluded that the model also showed qualitatively accurate, coupled dynamic behaviour and, given the quantitative accuracy of the static equilibrium state, it seems likely that the dynamic interactions were also quantitatively accurate.

While the results produced by the benchmark model discussed above were considered to show an acceptable level of accuracy for this initial attempt at coupling the solid, PSM, and the fluid, PFM, models, it was clear that a number of areas could be improved on. Firstly, as discussed in Section 4.4.1. above, problems were encountered with the pressure and viscosity interactions of the solid and fluid models whereby excessive forces were applied to 'fluid particles' encountering a solid body. These were overcome with the introduction of a normalisation function. However, this function was considered an over simplification and a more rigorous method of accounting for these excessive forces would be required for complete accuracy. Secondly, again as discussed above, in order for the PFM to interact with the PSM mesh it was required to make the PSM particles at the surface of the mesh 'visible' to the PFM. The method by which this was achieved was essentially a brute force, fixed coding method and as such was entirely model specific. A more efficient, perhaps automatic method of implementing the solid/fluid interaction would be sought for a completely general code.

A further consideration for the coupled PSM + PFM model is the discretisation of the two phases. This is partially dependent on the scale of the problem to be modelled. As discussed in the previous Section, the coupled benchmark model considered an area of material only a few millimetres wide. However, for hydraulic fracture simulations it would be required to model a fracture at least 10s of metres in length. This combination of metre scale length with millimetre scale width is a well known problem in the field of hydraulic fracture modelling (See Chapter 2, Section 2.2.).

To model a sample of solid material metres in length with the PSM would require millions of particles if the discretisation applied in the Pressurised Notch Coupled Benchmark Model were to be used. The obvious solution is to use PSM particles that are very much larger, as were considered in the PSM benchmark models, discussed in Section 4.2.3.2. of this Chapter. However, in order for the accuracy of the fluid model to be maintained in a fracture only a few millimetres wide it would be necessary for the PFM particles to have radii perhaps 1000s or 10000s of times smaller than PSM particles. While this is possible, it would result in a number of problems. Specifically, it would cause problems with the interaction of the PFM and PSM, however, it is felt that these could be overcome. More generally, it would obviously

again lead to a requirement for a large number of particles and this is not considered practical with the computational facilities currently available. However, it is conceivable that a purpose written, optimised code, run on a powerful, perhaps parallel, machine could execute a model of this kind. Certainly, if computing technology continues to advance at current rates than it will not be long before this kind of model is practical for all users.

4.5. Summary

In this Chapter has been presented the development of the solid phase Particle Solid Model and the fluid phase Particle Fluid Model. The implementation of both these models was described in detail along with discussion of the mechanics involved in developing the desired solid and fluid behaviours. Discussion was also made of techniques through which the model parameters could be calibrated in order to reproduce the behaviour of a material with specific properties.

In order to verify the behaviour of these models benchmark problems were carried out. The construction of these problems was discussed in detail, together with presentation of the results. From these results, conclusions were drawn as to the accuracy of the model behaviour and the desired evolution and advancement of the work.

In addition to the work discussed above, presentation was also made of a coupled model constructed, as proposed in Chapter 3, by integrating the PSM and PFM within one modelling framework. As with the separate models the development of this coupled model was described in detail before a verification of behaviour was made through the application of a benchmark problem. Once again, the results of this problem were presented and discussed in detail before conclusions were drawn.

In general, it was concluded that both the PSM and PFM were able to adequately reproduce the desired behaviours of solid and fluid materials respectively. However, difficulty was found in calibrating the PFM for a specific fluid of given properties.

Despite this, it was also concluded that these models could be successfully coupled, without significant additional complications, and that they interacted to accurately reproduce expected behaviour.

In the following Chapter, the advancement of the Particle Solid Model to develop fracturing behaviour will be described. Methods, by which fracture criteria can be implemented in lattice type models, will be presented along with discussion of their relationships to fracturing in the PSM. Further presentation will then be made of five failure criteria specifically developed for the PSM along with results of a benchmark model used to test the behaviour of these criteria. From these results, conclusions will be drawn as to proficiency of the criteria and the implications for the project as a whole.

Chapter 5:

Failure Criteria for the Particle Solid Model (PSM)

5.1. Introduction

This Chapter continues the discussion concerning the development of the Particle Solid Model (PSM) that was begun in the last Chapter. Discussion in Section 4.2. of Chapter 4 centred on the initial development of the PSM and its ability to model the elastic behaviour of a solid material. The following Sections deal with the further development of the PSM and its capacity to model more complex behaviour with particular attention to fracture development within the bonded particle assembly.

After discussing the requirements for fracture criteria in a lattice type model, presentation will be made of five failure criteria that were developed for the PSM. The discussion will follow the evolution of these criteria, which was based on the conclusions drawn from the results of a benchmark model in which each consecutive fracture criterion was tested. For each test, the results are presented and discussion is made. Comparison is also made to similar work by other researchers.

5.2. Failure Criteria for Lattice Type Models

As discussed in Chapter 2, many studies have been carried out, by various researchers, into the fracture of quasi-brittle material using typical lattice models (Schlangen and Garboczi [79], Schlangen and van Mier [80, 81, 82], Tzschichholz and Herrmann [88], Tzschichholz et al. [89], van Vliet [95]) or bonded particle assemblies (Bažant et al. [7], Beranek and Hobbelman [8], Chang et al. [14], Bruno et al. [11], Jirásek and Bažant [40, 41], Morikawa and Sawamoto [63]). Obviously, for the parts of

this work concerned with the propagation of hydraulically driven fractures, it is necessary to follow the work of these researchers in order to develop fracturing behaviour for the PSM.

The common representation, in all of the studies cited above, of fracture propagation in a lattice type model is by the sequential removal of lattice elements or inter-particle links, when a predefined element failure criterion is exceeded due to the action of externally applied loads or displacements. The breakage of elements or links is irreversible and once removed they are never allowed to return or reconnect. It is also generally assumed that a lattice element is either completely undamaged or completely failed. Fracture propagation is not considered below the individual element level. Detailed discussion of this subject is presented in Chapter 2, Section 2.3.1.

It is suggested by van Mier [59] that the ideal for a lattice representation is to model a material at the atomic level and employ stress-separation laws to describe its deformation and fracture. However, it is accepted that a model of this kind is computationally unfeasible with current technologies and instead, it is necessary to develop micro- and meso-scale lattice models, with elements of the order of a few millimetres in length, and employ phenomenological models such as Rankine, von Mises or Mohr-Coulomb criteria to determine failure of the elements.

For a typical lattice model, consisting of beam or truss elements that can be considered in the same way as a structural members and consequently have a cross-sectional area, these phenomenological models are often implemented through values of critical tensile stress assigned to each lattice element. Common examples of these criteria take into account simple axial loads and, when available, the bending capacity of the elements (See *Eq. 2.12.* and *Eq. 2.13.* repeated below).

$$\sigma_t < \frac{F_{i(\text{beam})}}{A_{(\text{beam})}} + \frac{\left(|M_{i(\text{beam})}|, |M_{j(\text{beam})}| \right)_{\max}}{I_{(\text{beam})}} \quad \text{Eq. 2.12.}$$

$$\sigma_t < \frac{F_{i(\text{beam})}}{A_{(\text{beam})}} \quad \text{Eq. 2.13.}$$

It is noticeable that another commonality of lattice type models is that they tend not to consider failure of the elements in compression. Some work has been carried out with compressive failure in lattice type models (Morikawa and Sawamoto [63]) but this has usually been with bonded particle assemblies rather than beam or truss frameworks.

The implementation of failure criteria for bonded particle assemblies is dependent on the composition of the inter-particle links (See Chapter 2, Section 2.3.3.) but is often similar to the methods applied in typical lattice models, as discussed above. For example, Beranek and Hobbelman [8] developed a bonded particle assembly in which the bonds consisted of discs of extra material between the particles that were assigned maximum stress capacities in a similar fashion to a lattice beam element. Beranek and Hobbelman's model in fact considered the normal and shear stresses in the bonds for a Mohr-Coulomb failure criterion.

If, however, the inter-particle links are not of suitable configuration and do not have a determinable cross-sectional area, then the application of a critical stress criterion is not possible. This was the case in a previous attempt to model fracturing with a bonded particle assembly similar to the PSM (Davie [21]). As with the PSM this particle assembly was constructed within the DEM code PFC^{3D} and consisted of particles linked together with 'contact bonds', which are a basic component of PFC^{3D} (See Chapter 3, Section 3.3.). These bonds are considered to act over a point contact and consequently have no physical cross-sectional area. Instead of maximum stress capacities, they are assigned maximum tensile and shear strength capacities, expressed in units of force. When the tensile or shear force in the bond exceeds these defined maxima, the bond is removed. The previous work, cited above, attempted to model fracturing by making use of this inbuilt criterion but found great difficulty in calibrating the strength of the 'contact bonds' for a given material strength.

Since the PSM is constructed using the same 'contact bonds' for inter-particle links, it was hoped to apply this method and find a reliable technique with which to calibrate the 'contact bond' strength. Given the difficulties encountered in attempts to calibrate the material properties of such an assembly via trial and error techniques (See Chapter 4, Section 4.2.2.2.), it was felt that a more rigorous approach would be appropriate for application in this work.

5.3. Development and Implementation of Failure Criteria for PSM

As discussed in the previous Section, although typical lattice models assign material strengths to their elements in terms of maximum stress capacities, it was not possible to employ this approach in the PSM due to the lack of physical cross-sectional area associated with the inter-particle links (See Chapter 4, Section 4.2.1.). Furthermore, previous investigation had encountered difficulties in calibrating the existing, force based ‘contact bond’ failure criterion, built in to PFC^{3D}, for a given material strength.

Consequently, it was necessary to look for alternative methods of implementing failure criteria for the PSM. The evolving development of five failure criteria, based on various lattice and continuum principles, is detailed in the following Sections. As with previous models detailed in this work, that extended the model beyond the basic DEM behaviour of PFC^{3D}, these failure criteria were realised through code written in the associated *FISH* language.

The failure criteria were generally implemented in the PSM by examining each ‘contact bond’ in turn, and testing for yield and failure conditions, where ‘yield’ refers to the elastic limit and ‘failure’ refers to the ultimate limit, as appropriate to the particular failure criterion in use. Obviously, in cases where elastic-brittle behaviour was considered, conditions of yield and failure were coincident. All of the inter-particle link elements in which failure conditions were found to have been exceeded were marked as *candidates for failure*. Link elements in which failure conditions had not been reached but in which yield conditions had been exceeded were marked as *softening elements*. Having examined all of the inter-particle link elements within the PSM mesh, self-equilibrating, out of balance forces were applied to all of the *softening elements* in order to simulate the redistribution of stress. Furthermore, from the *candidates for failure*, the ‘worst case’ link element was removed. This process was repeated during each model time step.

What constituted the ‘worst case’ link element from all of the *candidates for failure*, differed from criterion to criterion and the precise determination is discussed in detail in the following Sections. However, it can be noted that in this way, only one link

was removed from the PSM mesh per time step. This is the approach adopted by various other researchers such as Schlangen and Garboczi [79], Schlangen and van Mier [80, 81, 82], Tzschichholz and Herrmann [88], Tzschichholz et al. [89] and van Vliet [95]. As discussed in Section 2.3.1. of Chapter 2, it is suggested that this restriction allows stress redistribution to take place between time steps. However, it is noted that the typical lattice models, employed by all the authors cited above, are subjected to a series of static analyses whereas the PSM is constructed within PFC^{3D}, which employs a dynamic relaxation solution scheme. Consequently the assumption of stress relaxation between time steps may be a natural effect in typical lattice models, however, unless care is taken to ensure that dynamic effects in the PSM meshes are minimised, complete stress relaxation may not take place between time steps. It is arguable that fracturing is in fact a dynamic process and therefore stress relaxation should not be assumed to take place between fracture propagation events and, therefore, multiple instances of element failure per time step should be allowed in lattice type models. However, to realistically account for dynamic effects, very precise control of the boundary conditions and material properties would be required and so, for practical purposes in this work, the analyses were treated as quasi-static problems and consideration of failure was limited to one element per time step.

The *FISH* routines, through which the failure criteria were developed, were executed in every time step of the model analyses, just before the motion calculation of the basic distinct element method calculation cycle employed in PFC^{3D} (See Chapter 3, Section 3.4.1.). The amendments made to the basic calculation cycle are illustrated in *Fig. 5.1.* below (in comparison to *Fig. 3.3.*) and the additional steps in the process are highlighted for clarity. Where out of balance forces were applied to account for softening behaviour, they supplemented the total forces acting on a particle, and subsequently affected the acceleration of the particle, as defined by *Eq. 3.26.*, which is also highlighted in *Fig. 5.1.* below. The precise details of this process will be discussed in relation to the relevant failure criteria in the following Sections.

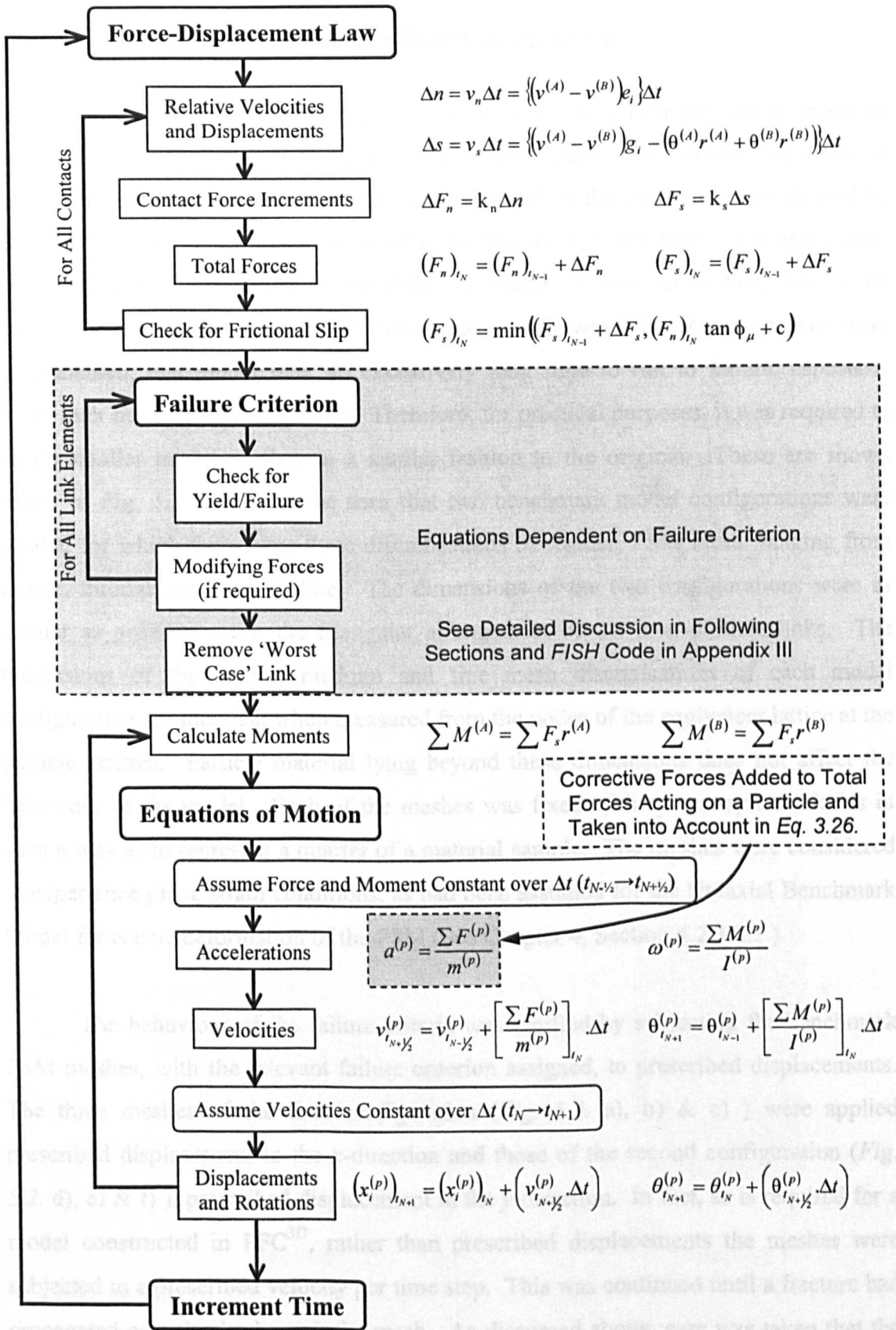


Fig. 5.1. Flow Chart Summarising the Calculation Sequence for the Distinct Element Method Modified For Inclusion of Failure Criteria Implemented via FISH Code (expanded Fig. 3.3.) (Dashed Outlines Indicate Where Changes were Implemented in the Basic DEM Algorithm)

5.4. Two-Dimensional Uniaxial Benchmark Model

In order to test the behaviour of the failure criteria developed for the link elements of the PSM it was necessary to construct a benchmark model. For this purpose, a simple uniaxial model is considered, similar to the one based on the benchmark model used by Griffiths and Mustoe [32] and discussed in Section 4.2.3.2. of Chapter 4 in association with the elastic deformation of the PSM. However, it was found that, due to the complexity and inefficiencies of the *FISH* code through which the fracture criteria were implemented, this model took an excessively long time to run to failure, especially when finer meshes were employed. Therefore, for practical purposes, it was required to create smaller model meshes in a similar fashion to the original. These are shown below in *Fig. 5.2.* and it can be seen that two benchmark model configurations were created for which there were three discretisations of regular, PSM mesh, ranging from coarse, through medium, to fine. The dimensions of the two configurations were as similar as possible given the triangular arrangement of the inter-particle links. The dimensions of the coarse, medium and fine mesh discretisations of each model configuration are identical when measured from the nodes of the equivalent lattice at the particle centres. Particle material lying beyond these dimensions does not affect the behaviour of the model. Each of the meshes was fixed with symmetry boundaries in such a way as to represent a quarter of a material sample. The meshes were considered to experience plane strain conditions, as had been assumed for the Uniaxial Benchmark Model for elastic deformation of the PSM (See Chapter 4, Section 4.2.3.2.1.).

The behaviour of the failure criteria was verified by subjecting the benchmark PSM meshes, with the relevant failure criterion assigned, to prescribed displacements. The three meshes of the first configuration (*Fig. 5.2. a), b) & c)* were applied prescribed displacement in the x -direction and those of the second configuration (*Fig. 5.2. d), e) & f)*, prescribed displacement in the y -direction. In fact, as is required for a model constructed in PFC^{3D}, rather than prescribed displacements the meshes were subjected to a prescribed velocity per time step. This was continued until a fracture had propagated completely through the mesh. As discussed above, care was taken that the applied velocity was sufficiently slow that dynamic effects were minimised in the models. Additionally, PFC^{3D}'s internal function of differential density scaling was employed to develop quasi-static analysis.

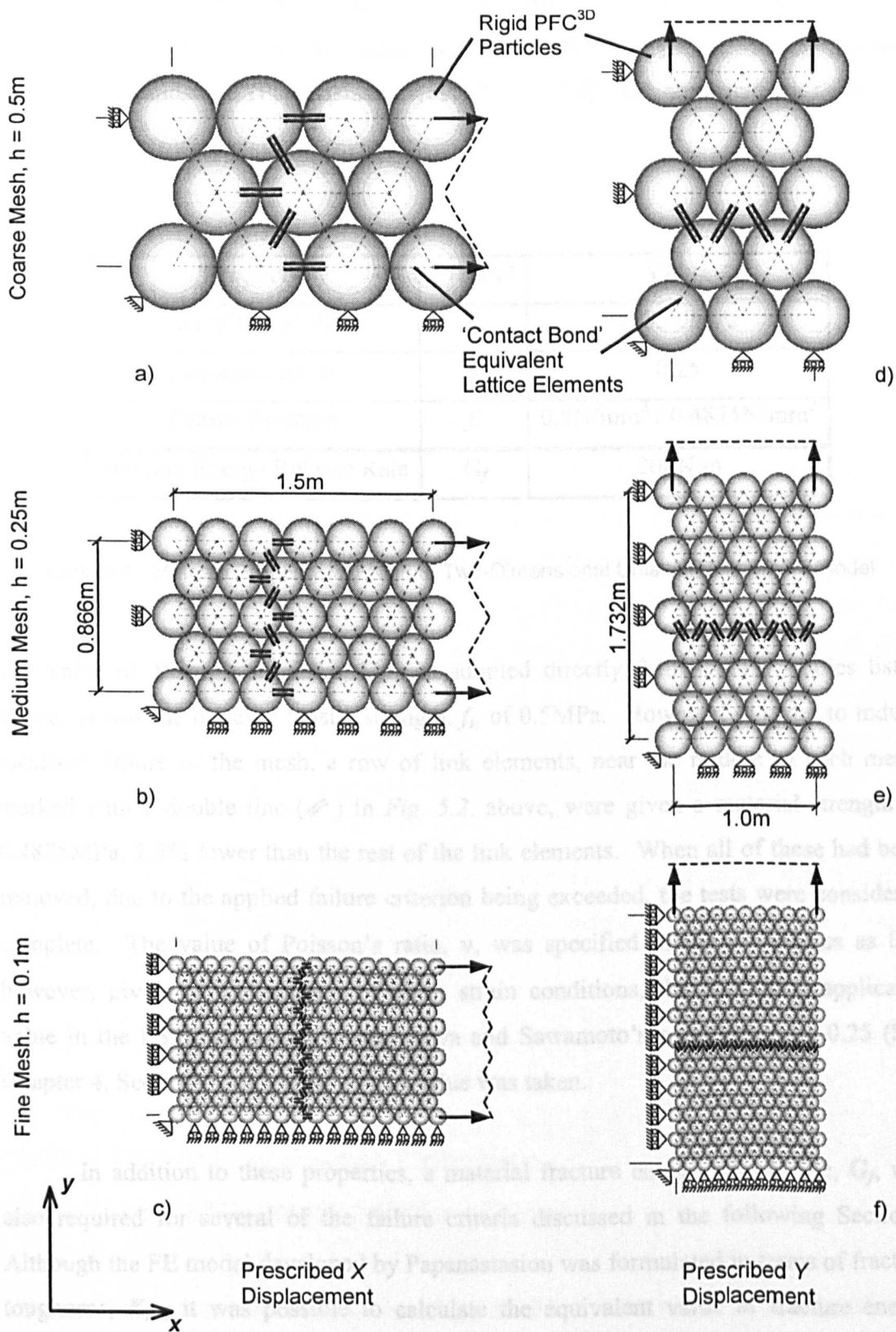


Fig. 5.2. Diagram of PSM Meshes for Uniaxial Benchmark Fracture Model Showing a), b) & c) Coarse, Medium and Fine Meshes for Prescribed x-displacement d), e) & f) Coarse, Medium and Fine Meshes for Prescribed y-displacement

The material properties applied in all of the tests carried out with this benchmark model were taken from finite element studies of hydraulic fracture propagation in a poorly consolidated sandstone (Papanastasiou [69, 70, 71, 72]) and are listed in Table 5.1. below.

Property	Symbol	Value
Young's Modulus	E	1785.0MPa
Poisson's Ratio	v	0.25
Tensile Strength	f_t	0.5N/mm ² / 0.4875N/mm ²
Fracture Energy Release Rate	G_f	200N/m

Table 5.1. Material Properties Applied to Two-Dimensional Uniaxial Benchmark Model

The value of Young's modulus, **E**, was adopted directly from the FE studies listed above, as was the material tensile strength, f_t , of 0.5MPa. However, in order to induce localised failure of the mesh, a row of link elements, near the middle of each mesh, marked with a double line (\parallel) in Fig. 5.2. above, were given a material strength of 0.4875MPa, 2.5% lower than the rest of the link elements. When all of these had been removed, due to the applied failure criterion being exceeded, the tests were considered complete. The value of Poisson's ratio, **v**, was specified in the FE studies as 0.3, however, given the assumption of plane strain conditions, the maximum applicable value in the PSM, according to Morikawa and Sawamoto's equations, was 0.25 (See Chapter 4, Section 4.2.2.3.) and so this value was taken.

In addition to these properties, a material fracture energy release rate, **G_f**, was also required for several of the failure criteria discussed in the following Sections. Although the FE model developed by Papanastasiou was formulated in terms of fracture toughness, K_{IC} , it was possible to calculate the equivalent value of fracture energy release rate through the relationship shown below (See Eq. 5.1.) (Kanninen and Popelar (1985): cited in Papanastasiou [69]).

$$K_{IC}^2 = \frac{G_{IC}E}{1-\nu^2} \quad \text{Eq. 5.1.}$$

where, K_{IC} is the fracture toughness and G_{IC} is the strain energy release rate and is directly equivalent to the fracture energy release rate, G_f .

When this was done, it was found that a value of 510N/m would be required to reproduce the material properties of the FE model. For reasons of practicality, associated with the time required to run numerical studies with the Two-Dimensional Uniaxial Benchmark Model, as will be seen in the following Sections, this value was considered to be too large and the material too ductile for the purposes of this work. A value of 100N/m was then chosen as being representative of a quasi-brittle material such as concrete. However, initial tests found this value to be too brittle and impractical due to the very slow loading rate required in the Two-Dimensional Uniaxial Benchmark Model, particularly for the coarse mesh, in order to capture the true behaviour of the failure criteria. In order to reduce the required load rate a more ductile model material was sought and a value of 200N/m was considered a reasonable compromise.

During each test, overall load-displacement data for the mesh was recorded. Plots of this data are given in the following Sections in order that comparison can be made between the behaviours of the failure criteria.

5.5. Mark 1 - Failure Criterion

(Brittle, Uniaxial Total Strain Criterion)

5.5.1. Theory of the Mark 1 Failure Criterion

The first failure criterion to be developed for the PSM was a very simple uniaxial total strain model. This compared the uniaxial total strain in each inter-particle link element, $\epsilon_{(link)}$, to a simple linear elastic constitutive model as shown in *Fig. 5.3.* below.

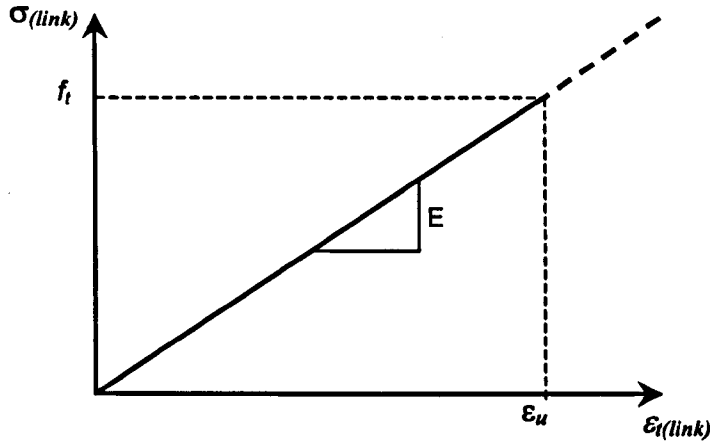


Fig. 5.3. Diagram Showing Simple Linear Elastic Constitutive Model for Mark 1 - Uniaxial Total Strain Failure Criterion for the PSM

The uniaxial total strain in each inter-particle link of the PSM mesh was calculated, according to Eq. 5.2. below, by comparing of the updated overall element length, taken as the distance between the centroids of the particles at each end of the element, with the original length of the element, which was equal to twice the particle radius (See Chapter 4, Section 4.2.1.).

$$\varepsilon_{i(link)} = \frac{l_{(link)} - l_{0(link)}}{l_{0(link)}} \quad \text{Eq. 5.2.}$$

The link elements were considered as *candidates for failure* when the uniaxial total strain exceeded a critical value such that, through Young's modulus, E , for the equivalent continuum material, the equivalent continuum material strength, f_t , was exceeded. From the set of all the *candidates for failure*, the link with the highest strain was removed. This can be stated as shown below (See Eq. 5.3. and Eq. 5.4.).

$$\max \varepsilon_{i(link)}^{\circ} \quad \text{for } e \in \{\mathbf{S}_{eff}^{\circ}\} \quad \text{Eq. 5.3.}$$

$$\{\mathbf{S}_{eff}^{\circ}\} = \left\{ e : \varepsilon_{i(link)}^{\circ} \geq \varepsilon_u = \frac{f_t}{E} \right\} \subset \{\mathbf{S}^{\circ}\} \quad \text{Eq. 5.4.}$$

where, e is any inter-particle link element, ε_u is the ultimate strain capacity, f_t is the tensile strength of an equivalent continuum material, \mathbf{S}° is the set of all inter-particle links elements within the PSM mesh under consideration and \mathbf{S}_{eff}° is the set of inter-particle links considered as *candidates for failure*.

For a homogeneous lattice, this was equivalent to the criterion applied by Schlangen and van Mier [80, 81, 82] who removed the beam element with the highest stress to strength ratio. Furthermore, it resembles a Rankine criterion, as noted by van Mier [59], (See Eq. 5.5.), although in terms of total strain rather than stress.

$$\sigma_{(link)} = E\varepsilon_t = \frac{F_{i(beam)}}{A_{(beam)}} \leq f_t \quad \text{Eq. 5.5.}$$

where, $\sigma_{(link)}$ is the uniaxial stress in an inter-particle link element.

As discussed above, it would not be possible to directly implement a Rankine stress criterion in the PSM due to the lack of physical cross-sectional area associated with the inter-particle links. Furthermore, it should be noted that this comparison is only in consideration of an element itself and not the equivalent continuum material as a whole.

5.5.2. Implementation of the Mark 1 Failure Criterion

Implementation of the Mark 1 failure criterion, within the basic DEM calculation cycle employed by PFC^{3D} (See Section 5.3. above), required only a simple *FISH* routine designed to check each link element of the PSM mesh in turn and determine if its uniaxial total strain exceeded its ultimate strain. Each time an element was found to have exceeded its ultimate strain, as determined by the simple constitutive model (See Fig. 5.3.), its strain was compared to that of the stored current ‘worst case’ element. If its strain was found to exceed that of the current ‘worst case’ element, it was labelled as the new ‘worst case’ element. After examination of all the inter-particle link elements, the final stored ‘worst case’ element was considered to have failed and was removed from the PSM mesh.

The *FISH* routine for the Mark 1 failure criterion can be summarised as shown in Fig. 5.4. Inspection can also be made of the actual *FISH* code, which is presented in Section AIII.5. of Appendix III and, where possible, variable names employed in the code, are shown beside the relevant process in the flow chart below.

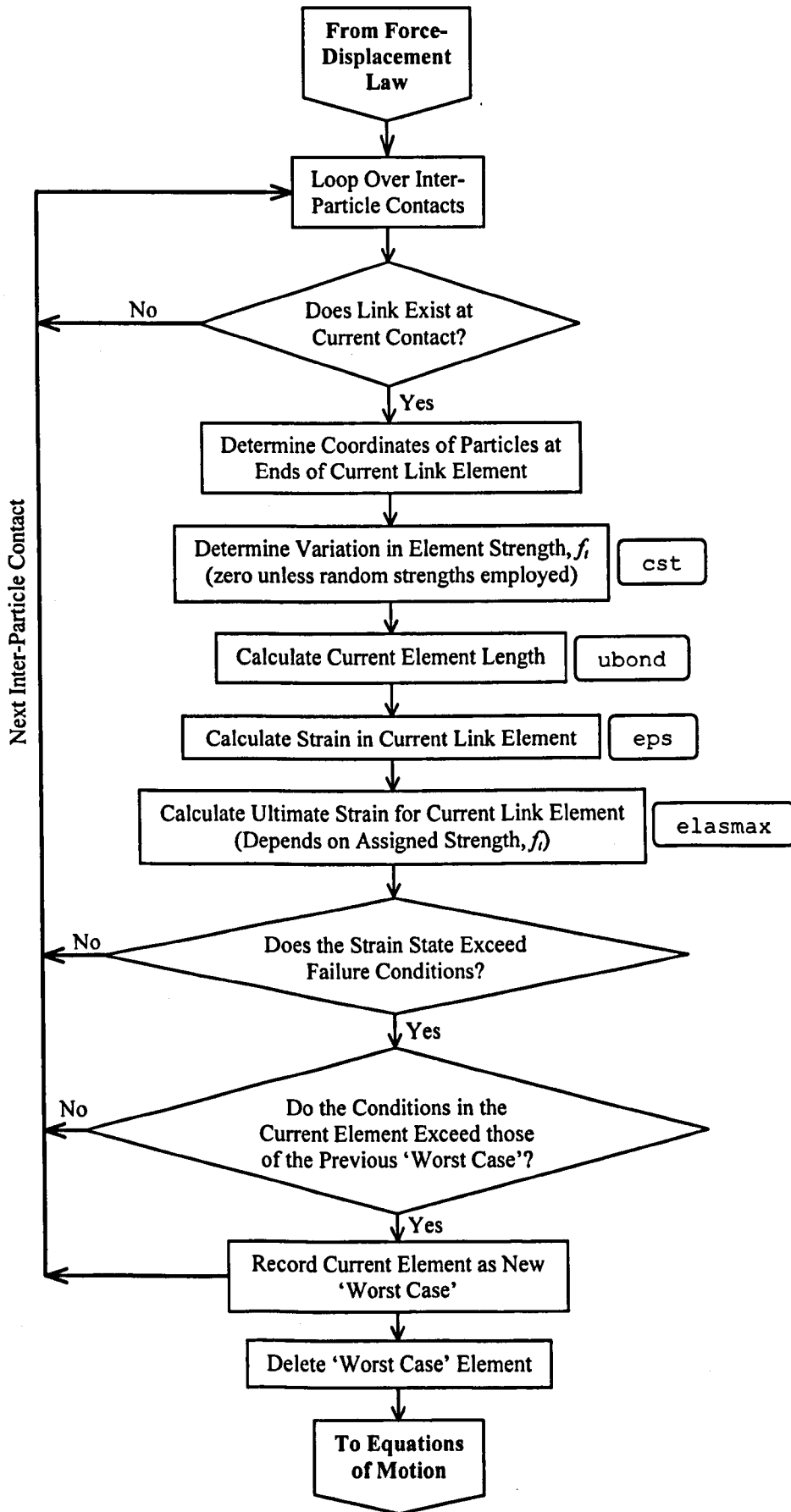


Fig. 5.4. Flow Chart Summarising FISH Code for Mark 1 Failure Criterion

5.5.3. Mark 1 Failure Criterion Benchmark Study

The Mark 1 failure criterion was applied to the Two-Dimensional Uniaxial Benchmark Model, discussed in Section 5.4. above, and the following numerical studies, detailed in Table 5.2. below, were carried out.

Displ.	Element Length h (m)	Young's Modulus E (MPa)	Poisson's Ratio ν	Material Strength f_t (N/mm ²)	Prescribed Velocity (m/s)
x	0.50	1785	0.25	0.48750	5×10^{-9}
x	0.25	1785	0.25	0.48750	5×10^{-9}
x	0.10	1785	0.25	0.48750	5×10^{-9}
y	0.50	1785	0.25	0.48750	5×10^{-9}
y	0.25	1785	0.25	0.48750	5×10^{-9}
y	0.10	1785	0.25	0.48750	5×10^{-9}

Table 5.2. Details of Two-Dimensional Uniaxial Model Studies with Mark 1 Failure Criterion

From the studies listed above, the load-displacement curves shown below, in *Fig. 5.5.* and *Fig. 5.6.*, were produced.

As can be seen from the plots below, the Mark 1 fracture criterion produced load-displacement curves generally similar to those that would be expected for an elastic-brittle criterion of this kind. There are, however, several points of note.

Firstly, the N_f lines, shown on the load-displacement curves, in both *Fig. 5.5.* and *Fig. 5.6.*, represent the applied loads at which the maximum tensile strength, f_t , of an equivalent continuum material, with properties as shown in Table 5.2. and dimensions as shown in *Fig. 5.2.*, would be reached. As can be seen from the plots, all six of the load-displacement curves show yielding of the material well above this line. Therefore, while the link elements were individually failed when f_t was reached, the Mark 1 failure criterion over predicted the strength of the material as a whole.

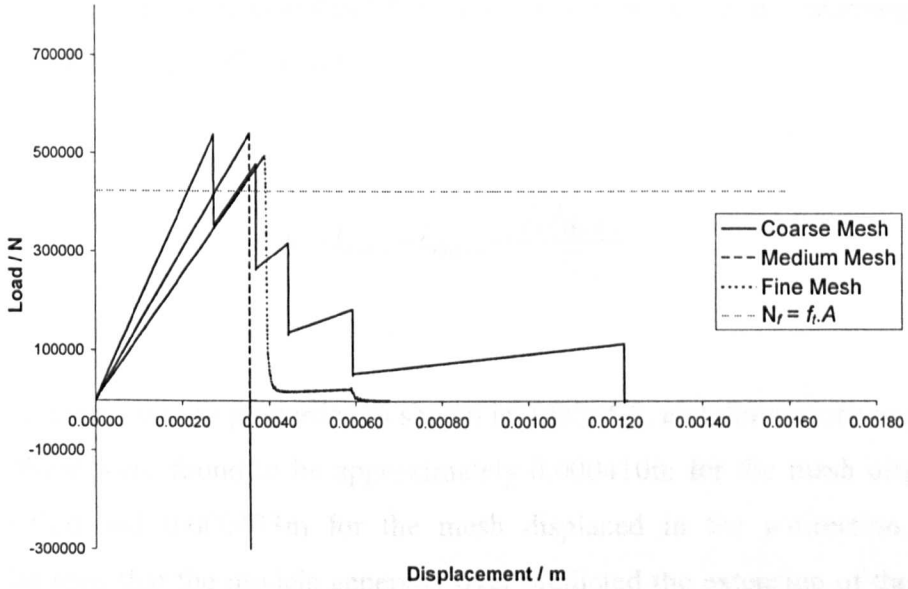


Fig. 5.5. Load-Displacement Plots for the Two-Dimensional Uniaxial Benchmark Model with the Mark 1 Failure Criterion and Prescribed Displacement in the x-direction

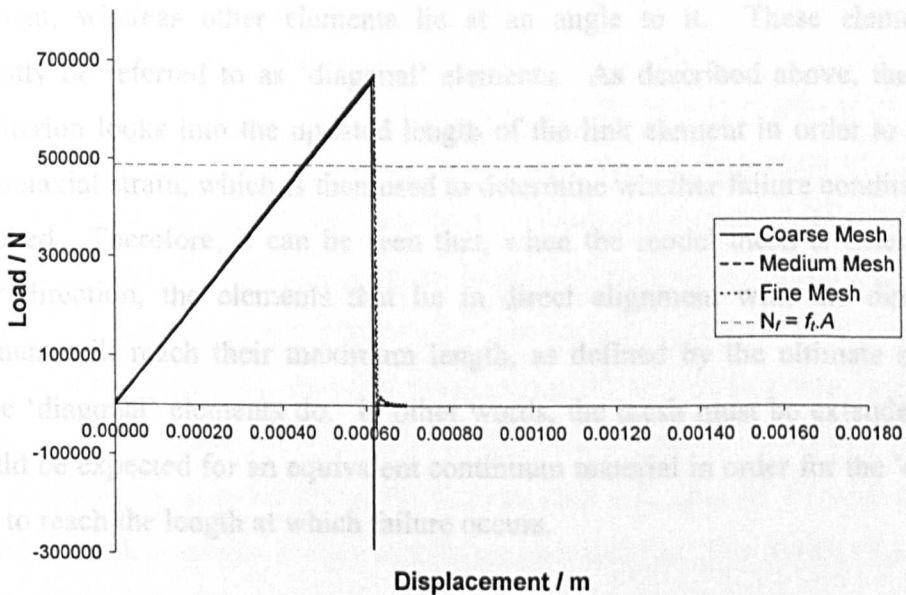


Fig. 5.6. Load-Displacement Plots for the Two-Dimensional Uniaxial Benchmark Model with the Mark 1 Failure Criterion and Prescribed Displacement in the y-direction

Additionally, for an equivalent continuum material, the displacements at which failure was expected to occur were calculated from Eq. 5.6. below, which is a rearrangement of components of Eq. 5.2. and Eq. 5.4.

$$u = l_{(link)} - l_{0(link)} = \frac{f_t \cdot l_{0(link)}}{E} \quad \text{Eq. 5.6.}$$

Again, for a material with properties as shown in Table 5.2. and dimensions as shown in Fig. 5.2., these were found to be approximately 0.000410m for the mesh displaced in the x -direction and 0.000473m for the mesh displaced in the y -direction. It can therefore be seen that the models generally over predicted the extension of the mesh as well as the strength, in comparison to the expected results for an equivalent continuum.

These effects can be explained when the Mark 1 failure criterion is examined in conjunction with the triangular configuration of the PSM mesh. As can be seen in Fig. 5.2., some of the inter-particle link elements are aligned with the direction of prescribed displacement, whereas other elements lie at an angle to it. These elements will subsequently be referred to as ‘diagonal’ elements. As described above, the Mark 1 failure criterion looks into the updated length of the link element in order to calculate the total uniaxial strain, which is then used to determine whether failure conditions have been reached. Therefore, it can be seen that, when the model mesh is extended in a particular direction, the elements that lie in direct alignment with the direction of displacement will reach their maximum length, as defined by the ultimate strain, ϵ_u , before the ‘diagonal’ elements do. In other words, the mesh must be extended further than would be expected for an equivalent continuum material in order for the ‘diagonal’ elements to reach the length at which failure occurs.

A similar effect was observed by Schlangen and Garboczi [79] (See Chapter 2, Section 2.3.1.) who noted that in a regular, triangular lattice model, of similar configuration to the PSM mesh, under uniaxial strain, elements lying in one direction carried more load than the others and therefore, these elements would be the first to fail. They also reported that a strain in the y -direction results in 33% higher stress at fracture

than a strain in the x -direction. This is very close to the behaviour shown above for the Mark 1 criterion where, the effect in the PSM can be seen, as would be expected, to reduce as the mesh discretisation increases and the difference between a 'diagonal' element and an in-line element diminishes. However, in agreement with the findings of Schlangen and Garboczi, it can also be seen to be a more significant effect in the mesh displaced in the y -direction, where there are only 'diagonal' elements, than in the mesh displaced in the x -direction, where a mixture of elements are present. In fact, it can be seen that the curves for the medium and, in particular, the fine meshes, displaced in the x -direction, are quite close to the yield and displacement predicted for an equivalent continuum.

In addition to the over predictions of length and yield strength, it can be seen in the load-displacement plot for prescribed displacement in the x -direction (*Fig. 5.5.*) that the loading slopes and consequently the elastic responses of the model are different in each of the three mesh discretisations. As discussed above, the accuracy of the results, in comparison to those that would be expected for an equivalent continuum material, improve with increasing discretisation. An explanation for this can be found in the studies conducted by van Vliet [95]. As discussed previously (See Chapter 2, Section 2.3.1. and Chapter 4, Section 4.2.3.2.), van Vliet [95] found that a mesh length to element length ratio, $L \geq 20$, was required in order for boundary effects to diminish sufficiently to allow a lattice model to accurately reproduce the behaviour of its nominal material properties. The ratio L for the coarse, medium and fine mesh discretisations of the Two-Dimensional Uniaxial Benchmark Model for prescribed x -displacement were, respectively 3, 6 and 15, in the x -direction. The lack of accuracy could therefore be expected and it can clearly be seen that the precision of the results would improve with increasing mesh discretisation. In fact, the benchmark studies conducted in Section 4.2.3.2. of Chapter 4, showed that a PSM mesh with a L ratio of 17 very accurately reproduced expected results. This would suggest that the fine mesh discretisation applied in the Two-Dimensional Uniaxial Benchmark Model would show reasonably accurate behaviour and this is indeed shown in the results. The low values of L for the Two-Dimensional Uniaxial Benchmark Model and the consequent loss of accuracy were accepted in trade off with the practicalities of required computational effort involved in running finer mesh models (See Section 5.4. above).

Similar mesh-size dependency of results, obtained from one and two force lattice models employing brittle fracture laws, were also noted by van Mier [59]. It can also be noted, however, that the load-displacement curves for prescribed displacement in the y -direction (Fig. 5.6.) did not show the same evidence of mesh-size dependency despite the fact that the ratio L for the coarse, medium and fine meshes were approximately 3.5, 6.9 and 17.3, respectively. While it might have been expected, as mentioned above, that the fine mesh model would have shown accurate behaviour, the results from the x -displacement model suggest that the results from the coarse and medium meshes would have shown more evidence of mesh-size dependency. This unexpected result is thought to be due to the ‘diagonal’ elements discussed previously and is probably also related to the cause of the stepped events visible in the post-peak sections of the load-displacement curves shown above. These intermittent drops in supported load, which are particularly noticeable in the coarse mesh curve in Fig. 5.5., can be shown to be associated with the failure of individual link elements (See Fig. 5.7. below).

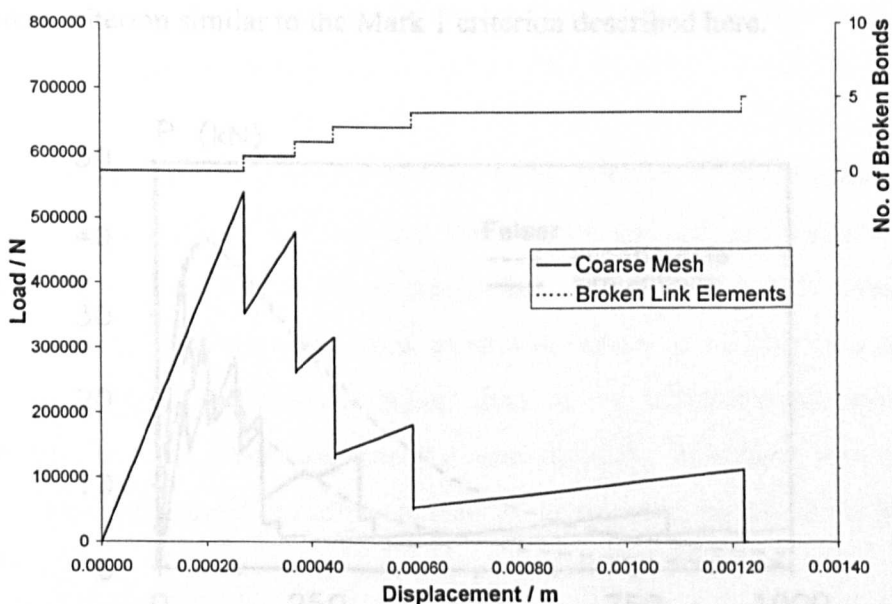


Fig. 5.7. Load-Displacement Plot for Two-Dimensional Uniaxial Benchmark Model Coarse Mesh with the Mark 1 Criterion and Prescribed Displacement in the x -direction, Overlaid with Plot of Number of Failed Elements-Displacement

Following the failure of each element the load on the mesh continues to increase but, as would be expected, the overall response is less stiff. Predictably, it is the ‘diagonal’

bonds that are last to fail, when the mesh is extended well beyond the displacement expected for an equivalent continuum material.

It is considered that these events are a consequence of the fracture localisation in the PSM meshes, which is induced by the introduction of a zone of weaker elements (See Section 5.4. and Fig. 5.2. above). As it can be seen, the triangular configuration of the mesh requires this weak zone to follow a zigzag path in the meshes to which displacement is applied in the x -direction. The coarser the mesh the more pronounced this zigzag is and in the coarsest mesh the width of the weak zone is such that the effects of strain vary along its length and consequently some elements fail before others. As would be expected, the effect and the steps in the post-peak response of the load-displacement curves reduce as the width of the weak zone reduces and more closely approximates a straight line. Similar stepped load-displacement plots to those shown above are discussed by Beranek and Hobbelman [8] and van Vliet [95] and presented by Schlangen and van Mier [80] (See Fig. 5.8. below) who were employing an elastic-brittle failure criterion similar to the Mark 1 criterion described here.

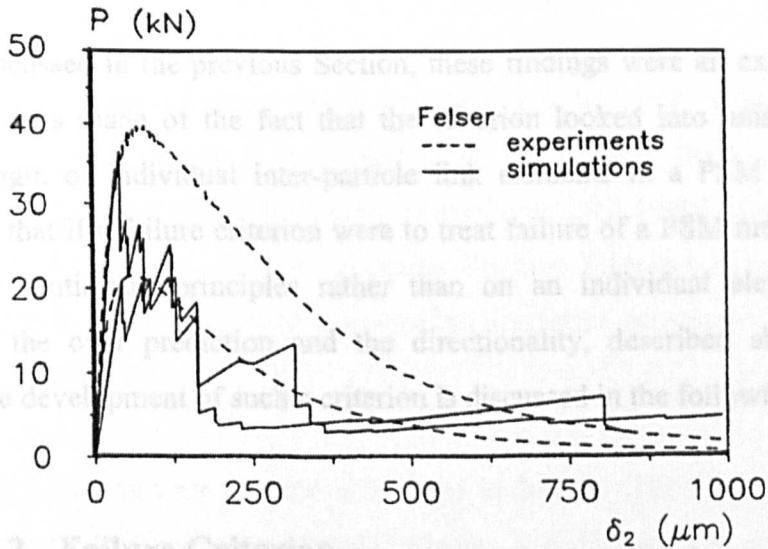


Fig. 5.8. Load-Displacement Curves for Experimental Studies and Lattice Simulations of a Felser SEN Beam Test (After Schlangen and van Mier [80])

In contrast, and again because of the mesh configuration, the zone of weak elements in the meshes to which y -displacements are applied always follows a straight path.

Consequently, the effects of strain are uniform throughout it, irrespective of the mesh discretisation. As can be seen from *Fig. 5.6*, failure occurs almost simultaneously in all of the weak zone elements, thus representing the brittle failure behaviour that would be expected.

5.5.4. Mark 1 - Conclusions

In summary, it can be said that the Mark 1 failure criterion generally produces results as would be expected for an elastic-brittle criterion. However, it displayed a clear tendency to over predict the strength and maximum extension that would be expected for an equivalent continuum material. Despite this, it was also shown capable of reasonably accurate results when given a sufficiently fine mesh discretisation and loaded in the x -direction. However, this was not the case when the mesh was loaded in the y -direction and it became clear that the Mark 1 criterion has a directional bias. Furthermore, the criterion was shown to produce results that were dependent on the size of the inter-particle link elements.

As discussed in the previous Section, these findings were all explainable when consideration was made of the fact that the criterion looked into uniaxial behaviour along the length of individual inter-particle link elements in a PSM mesh. It was therefore felt that if a failure criterion were to treat failure of a PSM mesh on the basis of piecewise continuum principles rather than on an individual element basis the problems of the over prediction and the directionality, described above, could be resolved. The development of such a criterion is discussed in the following Section.

5.6. Mark 2 - Failure Criterion

(Brittle, Rankine - Principal Stress Criterion)

5.6.1. Theory of the Mark 2 Failure Criterion

The Mark 2 criterion considers failure in the PSM from continuum principles rather than on an individual element basis. To do this, it was desirable to consider the stress field that developed in the particle assembly under prescribed displacement.

As described fully in Section 3.4.2. of Chapter 3, it is possible to calculate the average stress tensor in a DEM particle from the sum of the contributions of the contact forces acting on it, according to Eq. 3.42. repeated below.

$$\bar{\sigma}_{ij}^{(p)} = -\frac{1}{V^{(p)}} \sum_{N_c} |x_i^{(c)} - x_i^{(p)}| n_i^{(c,p)} F_j^{(c)} \quad \text{Eq. 3.42.}$$

PFC^{3D} automatically calculates the averaged stress tensor in each particle in a model and this data was therefore available for each particle in the PSM meshes at every time step. As discussed in Chapter 3, Section 3.4.2., the stress tensors that are produced by the method shown above are representative of the stress state in a granular material. Therefore, before applying these stress tensors to a failure criterion, they were converted, via the granular-continuum stress conversion factors, discussed in Chapter 3, Section 3.4.3. and Chapter 4, Section 4.2.3.2.2., to continuum stress tensors as would be expected at points coinciding with the particle centroids in an equivalent continuum material.

The components of these stress tensors could be easily adjusted with code written in the *FISH* language associated with PFC^{3D} and therefore, they could theoretically be employed in the implementation of any stress based failure criterion for the PSM. For the Mark 2 criterion, a simple Rankine Principal stress criterion was developed where it was necessary to calculate the maximum principal stress in an inter-particle link element.

Two approaches were developed in order to do this. The first of these methods initially calculated the maximum principal stresses and directions in each particle pair from the continuum stress tensors developed as described above. It was then assumed that the maximum principal stress in the link between a particle pair, $\sigma_{1(link)}$, was simply the average of those in the particles, in both magnitude and direction (See Eq. 5.7. to Eq. 5.9. and Fig. 5.9. below).

$$\begin{aligned} \bar{\sigma}_{ij}^{(A)} &\Rightarrow \sigma_1^{(A)}, \mathbf{n}_1^{(A)} \\ \bar{\sigma}_{ij}^{(B)} &\Rightarrow \sigma_1^{(B)}, \mathbf{n}_1^{(B)} \end{aligned} \quad \text{Eq. 5.7.}$$

$$\sigma_{1(link)} = \frac{1}{2}(\sigma_1^{(A)} + \sigma_1^{(B)}) \quad \text{Eq. 5.8.}$$

$$\mathbf{n}_{1(link)} = \frac{1}{2}(\mathbf{n}_1^{(A)} + \mathbf{n}_1^{(B)}) \quad \text{Eq. 5.9.}$$

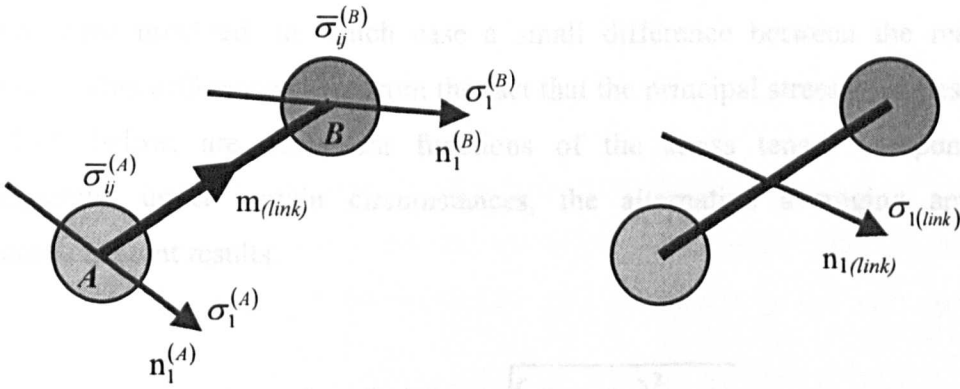


Fig. 5.9. Diagram Showing Development of Principal Stresses in the Inter-Particle Link Elements of a PSM Mesh from the Principal Stresses in Particles

The second, alternative method, developed according to a scheme suggested by Mustoe [64], assumed that the average stress tensor in an inter-particle link element, $\bar{\sigma}_{ij(link)}$, was simply the average of the continuum stress tensors in the particles that it lay between. It was then a simple matter to calculate the magnitude and direction of the maximum principal stress in the link element (See Eq. 5.10. and Fig. 5.10. below).

$$\bar{\sigma}_{ij(link)}^{(A,B)} = \frac{1}{2}(\bar{\sigma}_{ij}^{(A)} + \bar{\sigma}_{ij}^{(B)}) \Rightarrow \sigma_{1(link)}^{(A,B)}, \mathbf{n}_{1(link)}^{(A,B)} \quad \text{Eq. 5.10.}$$

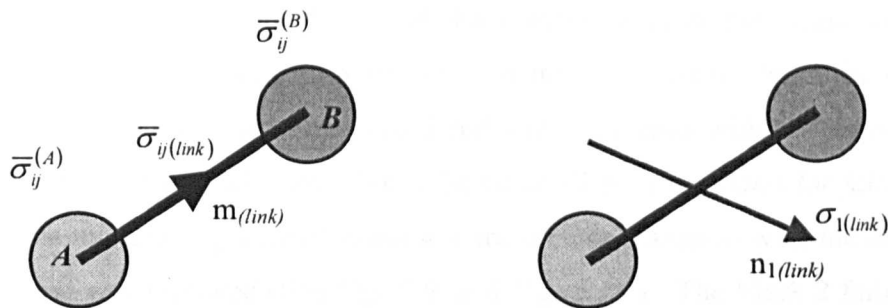


Fig. 5.10. Diagram Showing Development of Principal Stresses in the Inter-Particle Link Elements of a PSM Mesh from a Average Stress Tensor in the Link Element

It was in fact found that these two methods of calculating the maximum principal stress in an inter-particle link element produced almost identical results, unless large shear stresses were involved, in which case a small difference between the results was observed. This difference arose from the fact that the principal stresses, as described by Eq. 5.11. below, are non-linear functions of the stress tensor components and consequently, under certain circumstances, the alternative averaging approaches, produced different results.

$$\sigma_{1,2} = \frac{\sigma_x + \sigma_y}{2} \pm \sqrt{\left(\frac{\sigma_x - \sigma_y}{2}\right)^2 + \tau_{xy}^2} \quad \text{Eq. 5.11.}$$

However, it is felt that the small differences between the values produced by the two methods would not cause a significant difference in the overall fracturing behaviour of a PSM mesh. Nonetheless, in future applications it would be desirable to employ the second method since, in a number of ways, it is more versatile than the first. Firstly, it would easily allow the implementation of alternative stress based failure criteria and secondly, it can easily be modified to include a weighting function in order to calculate the stress state in a link element between particles of different volumes, as would occur in an irregular PSM mesh.

Whichever method was applied, the maximum principal stress in the link element was compared directly with the material strength, f_t , and link elements were

considered as *candidates for failure* if the maximum principal stress exceeded the material strength. The direction of the maximum principal stress, in each of the *candidates for failure*, was then considered and compared with the direction of the candidate inter-particle link itself. From the set of all the *candidates for failure*, the link in which the maximum principal stress was most closely aligned with the orientation of the link itself was removed (See Fig. 5.9. and Fig. 5.10.). The Mark 2 failure criterion can thus be stated as shown below (See Eq. 5.12. to Eq. 5.13.).

$$\max(\mathbf{n}_{1(link)}^e \cdot \mathbf{m}_{(link)}^e) \quad \text{for } \mathbf{e} \in \{\mathbf{S}_{eff}^e\} \quad \text{Eq. 5.12.}$$

$$\{\mathbf{S}_{eff}^e\} = \{\mathbf{e} : \sigma_{1(link)}^e \geq f_t\} \subset \{\mathbf{S}^e\} \quad \text{Eq. 5.13.}$$

where, $\mathbf{n}_{1(link)}$ is a unit vector in the direction of the maximum principal stress in an inter-particle link element, $\mathbf{m}_{(link)}$ is a unit vector in the direction of the inter-particle link element itself and $\sigma_{1(link)}$ is the maximum principal stress in an inter-particle link element.

As with the Mark 1 fracture criterion the Mark 2 criterion resembles a simple Rankine, Principal Stress Criterion (See Eq. 5.5.). However, in contrast to the Mark 1 criterion, which examined the uniaxial stress in an individual link element, the Mark 2 criterion considers a continuum stress state. In determining the 'worst case' link element for removal, it was considered appropriate to account for the direction of the principal stress, rather than the magnitude by which it exceeded the material strength. This was to acknowledge that, although this fracture criterion is based on continuum properties, the mesh itself is of a lattice type configuration and as such, consists of a discrete distribution of material.

5.6.2. Implementation of the Mark 2 Failure Criterion

As with the Mark 1 failure criterion the *FISH* function through which the Mark 2 failure criterion was implemented, examined each inter-particle link element in turn. In a similar fashion to the Mark 1 failure criterion, the Mark 2 criterion considered simple elastic-brittle behaviour, but was based on the equivalent continuum stress state in an element rather than the uniaxial total strain. This required a more complex *FISH* code than for the Mark 1 criterion, since manipulation of the components of the internally computed granular stress tensors was necessary for each pair of particles associated with an inter-particle link element. Once the tensors components had been retrieved, it was required to calculate the magnitude and direction of the maximum principal stress in the link element under consideration. As discussed in the previous Section two separate approaches were adopted for this purpose.

Whichever technique was applied, for each element in which the magnitude of the computed maximum principal stress was found to have exceeded the predefined element strength, the direction of the maximum principal stress was compared to the orientation of the element itself. If the included angle, between the principal direction and the element orientation, was found to be less than that of the previous 'worst case' element then the current element was recorded as the new 'worst case'. In the event that the current angle was found to be the same as that of the previous 'worst case' then the percentage by which the magnitude of the maximum principal stress exceeded the element strength was also taken into account. After examination of all the inter-particle link elements, the final stored 'worst case' element was removed from the PSM mesh.

The *FISH* routine for the Mark 2 failure criterion can be summarised as shown in *Fig. 5.11*. where both alternative routines for the calculation of the maximum principal stress in the inter-particle link element are given. Both methods are also presented in the full version of the code, which can be seen in Section AIII.6. of Appendix III. It can also be noted, particularly in the actual code, that, in addition to the benefits discussed in the previous Section, the second method is also the more efficient in terms of computational requirements.

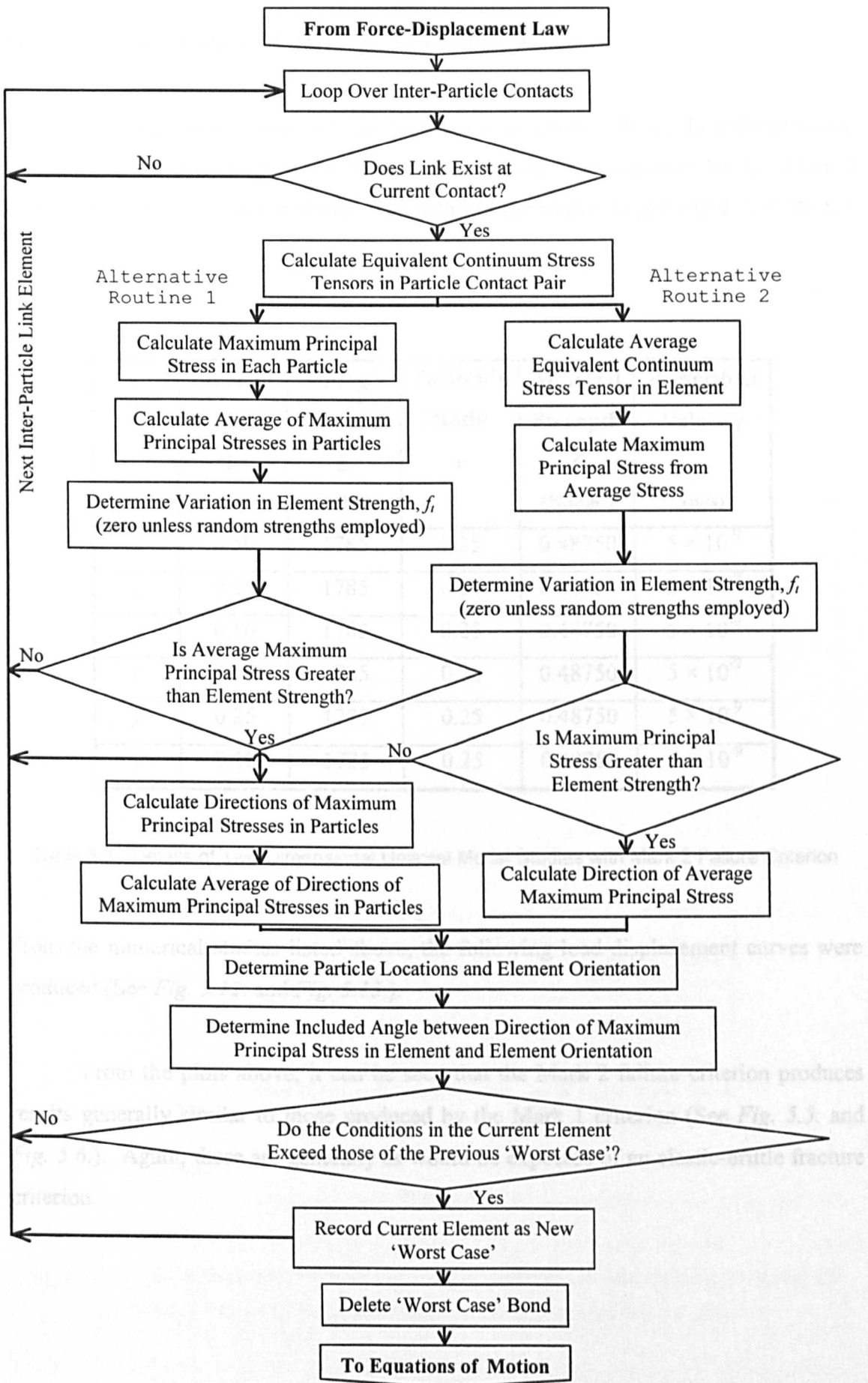


Fig. 5.11. Flow Chart Summarising FISH Code for Mark 2 Failure Criterion

5.6.3. Mark 2 Failure Criterion Benchmark Study

The numerical studies carried out for the Mark 1 criterion with the Two-Dimensional Uniaxial Benchmark Model (See Section 5.4. above) were repeated for the Mark 2 failure criterion, as discussed above. The detail of the studies is presented in Table 5.3. below.

Displ.	Element Length h (m)	Young's Modulus E (MPa)	Poisson's Ratio ν	Material Strength f_t (N/mm ²)	Prescribed Velocity (m/s)
x	0.50	1785	0.25	0.48750	5×10^{-9}
x	0.25	1785	0.25	0.48750	5×10^{-9}
x	0.10	1785	0.25	0.48750	5×10^{-9}
y	0.50	1785	0.25	0.48750	5×10^{-9}
y	0.25	1785	0.25	0.48750	5×10^{-9}
y	0.10	1785	0.25	0.48750	5×10^{-9}

Table 5.3. Details of Two-Dimensional Uniaxial Model Studies with Mark 2 Failure Criterion

From the numerical studies listed above, the following load-displacement curves were produced (See *Fig. 5.12.* and *Fig. 5.13.*).

From the plots above, it can be seen that the Mark 2 failure criterion produces results generally similar to those produced by the Mark 1 criterion (See *Fig. 5.5.* and *Fig. 5.6.*). Again, these are generally as would be expected of an elastic-brittle fracture criterion.

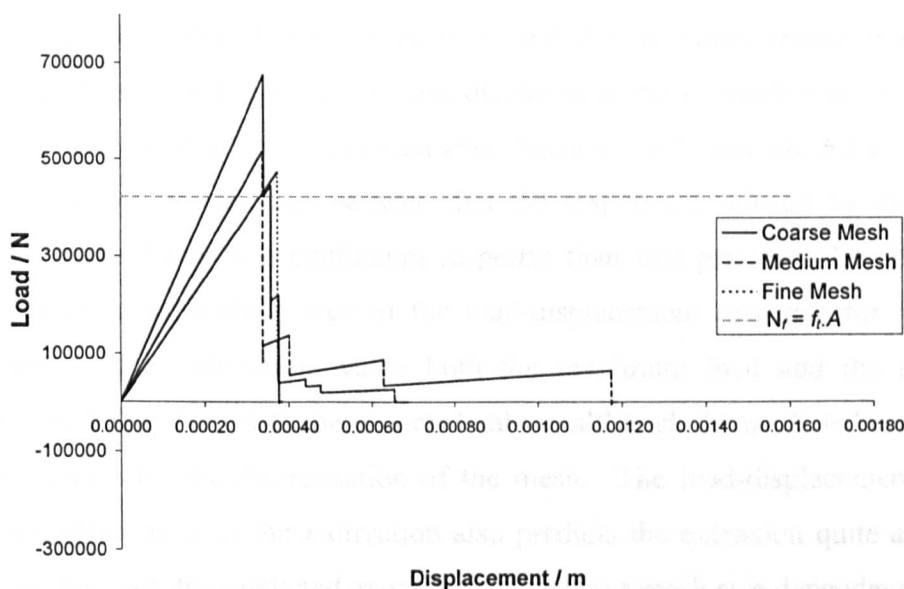


Fig. 5.12. Load-Displacement Plots for the Two-Dimensional Uniaxial Benchmark Model with the Mark 2 Failure Criterion and Prescribed Displacement in the x-direction

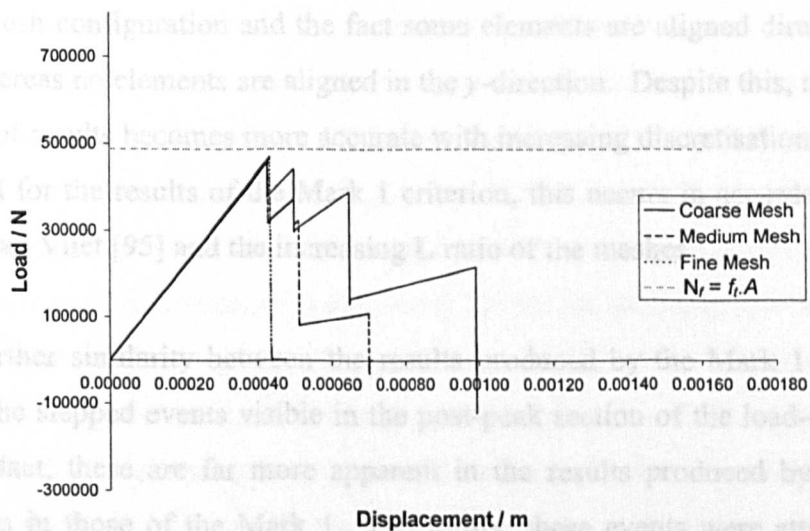


Fig. 5.13. Load-Displacement Plots for the Two-Dimensional Uniaxial Benchmark Model with the Mark 2 Failure Criterion and Prescribed Displacement in the y-direction

As before the load-displacement curves shown above can be compared with the expected response of an equivalent continuum material. Again, the expected maximum loads are indicated on the plots by the N_f lines, and the maximum predicted extensions were calculated as 0.000410m for the mesh displaced in the x -direction and 0.000473m for the mesh displaced in the y -direction (See Section 5.5.3. and Eq. 5.5). From the plots shown above, it can thus be seen that the response produced by the Mark 2 criterion is much closer to a continuum response than that produced by the Mark 1 criterion. This is particularly true of the load-displacement response for prescribed displacement in the y -direction where both the maximum load and the maximum extension match very well with the expected values, although the predicted extension of the mesh varies with the discretisation of the mesh. The load-displacement plot for prescribed displacement in the x -direction also predicts the extension quite accurately, however, in this case, the predicted maximum load shows mesh size dependency.

Therefore, it can be seen that both the Mark 1 and Mark 2 criteria produce results that are dependent on the discretisation of the mesh. In the results from both criteria, this is most clearly seen in the load-displacement plot for prescribed x -displacement. It is not immediately clear why the mesh loaded in the x -direction should be more sensitive to discretisation than the mesh loaded in the y -direction, but it may be due to the mesh configuration and the fact some elements are aligned directly in the x -direction whereas no elements are aligned in the y -direction. Despite this, the behaviour of both sets of results becomes more accurate with increasing discretisation of the mesh. As described for the results of the Mark 1 criterion, this occurs in accordance with the findings of van Vliet [95] and the increasing L ratio of the meshes.

A further similarity between the results produced by the Mark 1 and Mark 2 criteria are the stepped events visible in the post-peak section of the load-displacement curves. In fact, these are far more apparent in the results produced by the Mark 2 criterion than in those of the Mark 1. Previously, these events were attributed to an effect of mesh discretisation and this is again the case. However, rather than being related to the induced zone of weak elements in the meshes (See Section 5.5.3. above), in this case it more likely to be caused by boundary effects. In particular, these boundary effects relate to the calculation of the average stress tensors in the particles in two, separate ways. Firstly, the stress tensors are averaged over the volume of the

particles. Therefore, the larger the particles are the larger the volume over which the average is taken and consequently the less accurately the value will represent the stress state at the end of a link element. Since the stress tensor for the element itself is assumed to be the average of two particle tensors, any error will be further increased before the maximum principal stress in the bond is calculated. Secondly, as discussed above, the stress tensor is calculated from the contributions of contact forces on the particles. Consequently, the particles at the edge of a mesh, which obviously have fewer contacts than particles in the centre of a mesh, will have apparently lower values of stress than particles in the centre of a mesh. The larger the particles the further this effect will penetrate into the mesh. This effect also accounts for the long tails present in several of the load-displacement curves since the apparently lower magnitude stresses in the edge particles will require larger than expected loads and hence a larger than expected displacement in order to reach the failure stress. As would be expected, this effect also diminishes with increasing mesh discretisation.

In addition to the two problems, associated with the averaged stress tensors in the particles, discussed above, a further inaccuracy may occur due to deformation and changes in the configuration of the PSM mesh. As discussed in Chapter 3, Section 3.4.3. and Chapter 4, Section 4.2.3.2.2., the granular-continuum stress conversion factors are dependent on the mesh configuration. Therefore, the application of a constant and uniform conversion factor, throughout the mesh and in time, assumes that only small deformations take place. While this was seen to be a reasonable assumption in the benchmark tests carried out in Section 4.2.3.2.2. of Chapter 4, only elastic deformations were considered during that study. Clearly, when fracturing of the mesh is introduced the configuration of the contacts on certain particles, and in particularly those adjacent to a fracture, will change in time. This will consequently produce anomalies in the stress tensors, similar to those described above for particles at the edge of a mesh, which could subsequently lead to inaccuracies in the determination of failure conditions in the mesh. However, this was not felt to be a significant problem for the models developed in the course of this work since the areas of the mesh in which the stress state was of particular importance were those ahead of a crack tip where, by definition, the mesh was still intact and the original configuration prevailed. As mention previously, it would perhaps be necessary to develop an automatically varying set of conversion factors that would be constantly altered, for each individual particle,

on the basis of the updated local mesh configuration. However, as also discussed previously, this may be very difficult to code and would likely be computationally expensive if developed in the *FISH* language associated with PFC^{3D}. Given these potential problems it was not felt to be a worthwhile development during the course of this research.

In contrast, a difference between the two sets of results, from the Mark 1 and Mark 2 criteria, is that the results for x and y -displacements, were generally far more similar to each other under the Mark 2 criteria than they were under the Mark 1 criterion. This would suggest that the Mark 2 criterion has much less of a directional bias than the Mark 1 criterion. This is as would be expected since this criterion calculates the stress in an element irrespective of its orientation. The presence of 'diagonal' elements, as discussed previously, is therefore irrelevant.

It can further be noted that, as mentioned before, the results and behaviour seen here for the Mark 1 and Mark 2 criteria are similar to results reported by Schlangen and Garboczi [79]. As discussed in Chapter 2, Section 2.3.1. and in Section 5.5.3. above, these researchers encountered similar problems, associated with the fracture of a triangular lattice model displaced in the x -direction, to those encountered in the PSM model with the Mark 1 failure criterion, whereby all the elements aligned in the x -direction failed, leaving the 'diagonal' elements intact (See *Fig. 2.10.*). Failure of all the in-line elements in a mesh was avoided in the previous study of the Two-Dimensional Uniaxial Benchmark Model with the Mark 1 criterion due to the application of the weak zone in order to induce fracture localisation. However, it was observed, as discussed previously, that the weak zone elements aligned in the x -direction that failed first, leaving the 'diagonal' elements intact.

To overcome this problem Schlangen and Garboczi employed the 'node stress' fracture criterion (See Chapter 2, Section 2.3.1.), which can be seen to implement a stress homogenisation technique similar to that used in the Mark 2 criterion to calculate the particle stress tensors. As discussed in See Chapter 2, Section 2.3.1. and Section 5.5.3. above, the failure criterion applied in lattice models examines the stress in individual lattice elements. However, the 'node stress' criterion considered the

maximum principal force in a node, divided over the combined cross-sectional area of the beams in the associated principal direction (See Fig. 2.11. repeated below).

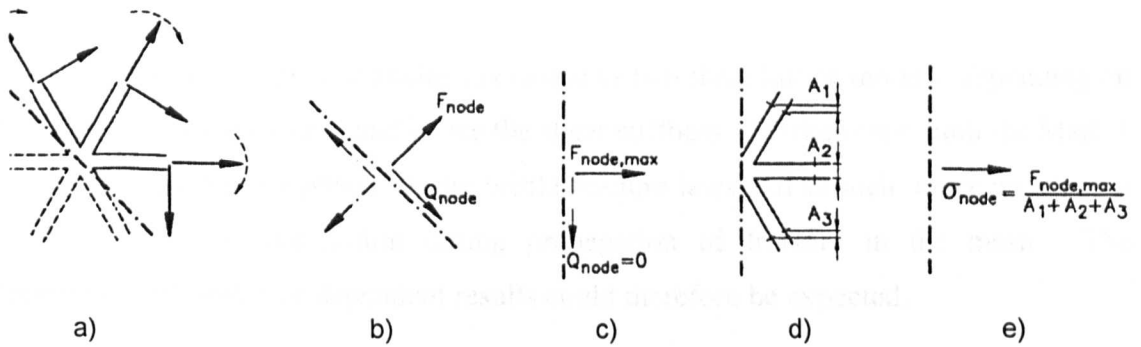


Fig. 2.11. Diagram Showing Procedure for Calculation of 'Node Stress' in a Lattice. a) Forces in Lattice Elements b) Resultant Normal and Shear Force Perpendicular to Nodal Cut c) Principal Normal Force d) Cross-Sectional Area of Lattice Elements in Principal Direction e) Nodal Stress (After Schlangen and Garboczi [79]) (repeated from page 38)

In this way, as with the Mark 2 criterion, the stress state and hence the failure conditions for a lattice element are independent of the orientation of the element.

5.6.4. Mark 2 - Conclusions

From the results discussed above, it can be concluded that the Mark 2 failure criterion showed definite improvement over the Mark 1 criterion in predicting the behaviour that would be expected of an equivalent continuum material. This can be seen in both, the predicted values of maximum load capacity and the predicted extensions of the meshes at failure. Furthermore, it can also be seen that the Mark 2 criterion overcomes the problems of directionality that were associated with the Mark 1 failure criterion.

Despite the improvements in the behaviour, described above, the results from the studies involving the Mark 2 criterion again show size dependency, as was seen in the results from the studies involving the Mark 1 criterion. Size dependent behaviour in simple one or two force lattice type models with elastic-brittle failure criteria was also noted by van Mier [59]. However, with the employment of three force lattice models,

which, as discussed in Chapter 2, Section 2.3.1., develop the behaviour of a higher order, Cosserat type material, no such size dependency is observed (van Mier [58], Schlangen and Garboczi [79], Schlangen and van Mier [80, 81, 82]).

The PSM meshes are analogous to one or two force lattice models, depending on the value of Poisson's ratio and hence the shear stiffness. Furthermore, both the Mark 1 and Mark 2 criteria are purely elastic-brittle fracture laws and as such, make no account of fracture energy dissipation during propagation of fracture in the mesh. The appearance of mesh size dependent results could therefore be expected.

It was consequently desirable, and a logical progression of this work, to develop an elastic-softening failure criterion that could be used to account for fracture energy dissipation and maintain a constant fracture energy release rate for any mesh discretisation. If modified appropriately for a particular element length, a criterion such as this would produce results that were independent of the mesh discretisation and consequently, would be a more generally applicable law.

A further advantage of an elastic-softening failure criterion is noted by Chang et al. [14] who acknowledge that, although, given a fine enough lattice model, overall softening behaviour can be produced with only a simple, brittle fracture law, with such a fine lattice, such an approach is not practical for the modelling of larger structures. They suggest that similar behaviour could be modelled if a coarser lattice were to be used in conjunction with a softening criterion, thus allowing larger structures to be modelled with less computational effort.

It was considered that the simplest type of criterion in which this behaviour could be developed was one based on the total uniaxial strain in an element in a similar fashion to the Mark 1 criterion (See Section 5.5.). The development of such a criterion, designated as the Mark 3, is described in the following Section.

5.7. Mark 3 - Failure Criterion

(Softening, Uniaxial Total Strain Criterion)

5.7.1. Theory of the Mark 3 Failure Criterion

As discussed above, it was desired to develop an elastic-softening failure criterion that would account for fracture energy dissipation during failure of the PSM mesh and hence develop results independent of the size of the inter-particle link elements, h . It was initially decided to implement this criterion on the basis of a Uniaxial Total Strain model similar to the Mark 1 criterion (See Section 5.5.1.).

One way to implement a non-linear failure criterion such as this, would be to modify the material stiffness in the model as plastic deformation is incurred. However, as discussed in Chapter 3, Section 3.3. and Chapter 4, Section 4.2.1., the normal and shear contact spring stiffnesses of the 'contact bonds', representing the inter-particle link elements, are associated with the contact stiffnesses of the PFC^{3D} particles themselves. Therefore, it would not be possible to change the stiffness of one inter-particle link element without affecting several other elements. This would not be an accurate representation of material behaviour and consequently the non-linear behaviour in the Mark 3 criterion was formulated with the so called K_0 , initial stiffness algorithm, with all non-linear effects accounted for by out of balance forces. This is discussed in more detail below.

As with the Mark 1 criterion the Mark 3 criterion compared the uniaxial total strain in each inter-particle link element, $\epsilon_{(link)}$, to a constitutive model. However, rather than the simple linear-elastic model used for the Mark 1 criterion, the comparison made here was with a piecewise linear, elastic-softening model, as shown in *Fig. 5.14.* below.

The precise shape of the constitutive model was dependent on the size of the inter-particle link elements. In order to maintain mesh size objectivity, it was necessary to keep the fracture energy release rate, G_f , which could be calculated from the area under the constitutive model multiplied by the element characteristic length, h , constant for any element size. Since the Young's Modulus, E , and material strength, f_t , were

fixed for a given material, this was done by modifying the Softening Modulus, E_s , and hence the softening slope, of the constitutive model. For the PSM the element characteristic length, h , was assumed equal to the original length of the inter-particle links, i.e. equal to twice the particle radius.

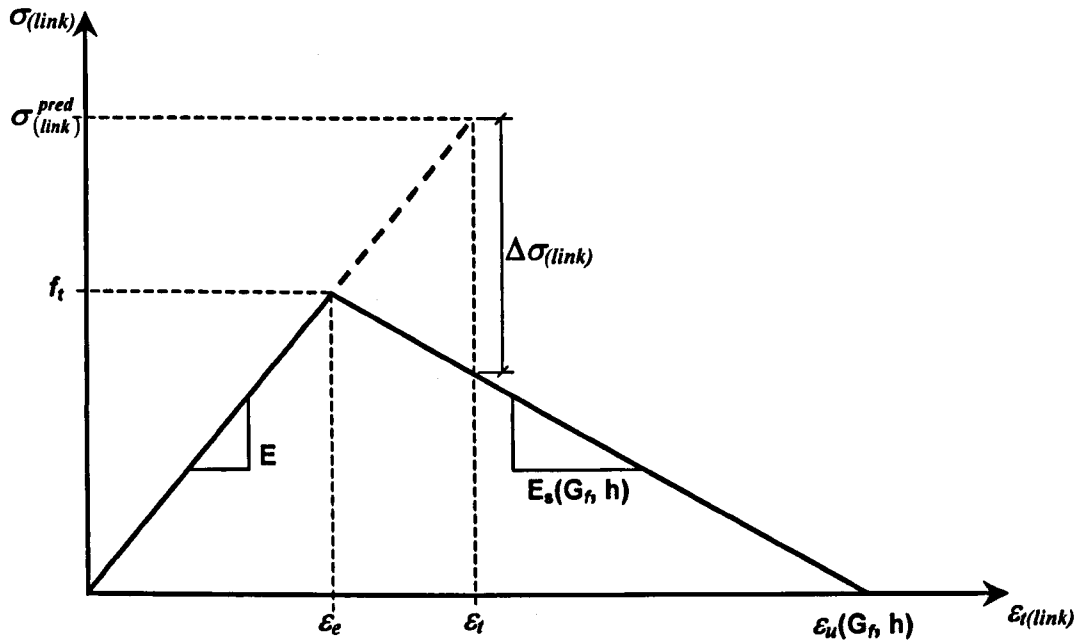


Fig. 5.14. Diagram Showing Elastic-Softening Constitutive Model for Mark 3 - Uniaxial Total Strain Failure Criterion for the PSM

By writing the fracture energy release rate in terms of the area under the constitutive model, as described above, it was then possible to rearrange the equation in terms of the required Softening Modulus, E_s , for a given element length (See Eq. 5.14. and Eq. 5.15.).

$$G_f = \left[\frac{1}{2} \left(\frac{f_t}{E} + \frac{f_t}{E_s} \right) f_t \right] \cdot h \quad \text{Eq. 5.14.}$$

$$E_s = \frac{1}{\left[\left(\frac{2G_f}{f_t^2 \cdot h} \right) - \frac{1}{E} \right]} \quad \text{Eq. 5.15.}$$

It should be noted that for a given set of material properties this formulation has a limiting value, such that, for a certain element size, h , the softening modulus tends to infinity and the elastic-softening model tends to an elastic-brittle model. Beyond this limit, the softening slope of the model becomes inverse and the model would exhibit snap back behaviour (See Fig. 5.15.). This effect is also noted by Jirásek & Bažant [40] who point out that snap back behaviour is very hard to deal with computationally. For this reason behaviour of this kind has been avoided in this work.

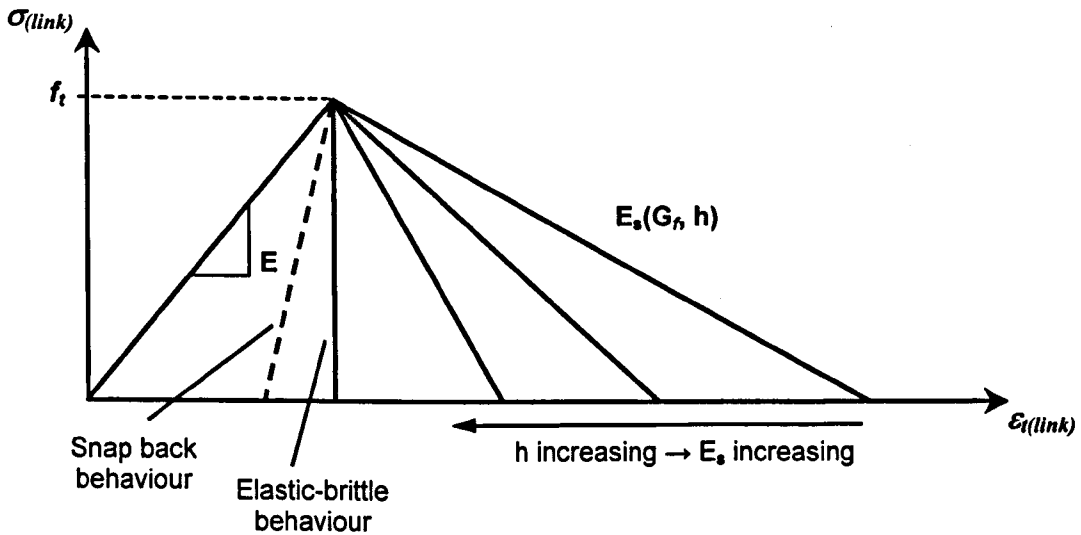


Fig. 5.15. Diagram of Elastic-Softening Constitutive Model Showing Increasing Gradient of Softening Slope with Increasing Element Length

From Eq. 5.15. and Fig. 5.15. above, it can be seen that the maximum value of element length for a given set of material properties can be calculated as shown below (See Eq. 5.16. and Eq. 5.17.).

$$\text{As } E_s \rightarrow \infty \text{ so } \left[\left(\frac{2G_f}{f_t^2 \cdot h} \right) - \frac{1}{E} \right] \rightarrow 0 \quad \text{Eq. 5.16.}$$

$$\therefore E_s \approx \infty \text{ for } h_{\max} = \frac{2G_f E}{f_t^2} \quad \text{Eq. 5.17.}$$

For the value of $G_f = 200\text{N/m}$ assumed for these studies, as discussed in Section 5.4. above, the maximum element length, h_{\max} , computed from Eq. 5.17. is 3.00m. Clearly, even the coarsest mesh of the Two-Dimensional Uniaxial Benchmark Model, with an element length of 0.5m, is well within this limit.

When comparison was made with the elastic-softening constitutive model, as shown in Fig. 5.14. above, link elements were considered as *candidates for failure*, in a similar procedure to that employed for the Mark 1 criterion, if the uniaxial total strain was found to have exceeded the ultimate strain. In this case the ultimate strain was defined by the constitutive model and was the strain at which the strength of the element reached zero. From the set of all the *candidates for failure*, the link with the highest strain was removed. This can be stated as shown below (See Eq. 5.18. and Eq. 5.19.).

$$\max \varepsilon_{i(\text{link})}^{\circ} \quad \text{for } e \in \{S_{\text{eff}}^{\circ}\} \quad \text{Eq. 5.18.}$$

$$\{S_{\text{eff}}^{\circ}\} = \left\{ e : \varepsilon_{i(\text{link})}^{\circ} \geq \varepsilon_u = f_t \left(\frac{1}{E} + \frac{1}{E_s} \right) \right\} \subset \{S^{\circ}\} \quad \text{Eq. 5.19.}$$

In addition to the set of *candidates for failure*, a second set of *softening elements* had to be considered. This consisted of elements in which the uniaxial total strain had exceeded the maximum elastic strain, ε_e , but had not exceeded the ultimate strain, ε_u (See Eq. 5.20. below).

$$\{S_{\text{se}}^{\circ}\} = \left\{ e : \frac{f_t}{E} = \varepsilon_e \leq \varepsilon_{i(\text{link})}^{\circ} < \varepsilon_u = f_t \left(\frac{1}{E} + \frac{1}{E_s} \right) \right\} \subset \{S^{\circ}\} \quad \text{Eq. 5.20.}$$

where, S_{se}° is the set of inter-particle links considered as *softening elements*.

Unlike the failure criterion, shown in Eq. 5.18., where only the 'worst case' element' from the set of *candidates for failure* was removed, all of the elements in the

set of *softening elements* were considered to experience softening behaviour and were treated as discussed below.

As indicated previously, constraints of the PFC^{3D} modelling environment required that the non-linear behaviour of the Mark 3 failure criterion be implemented in the so called K_θ initial stiffness algorithm. For this reason the uniaxial total strain in an element could always be considered in relation to the deformation of a linear elastic material. Consequently, the predicted uniaxial stress in an element, $\sigma_{(link)}^{pred}$, also described as the ‘effective stress’ (Lu and Vaziri [53]) or the ‘elastic response stress’ (Han and Chen (1986): cited by Lu and Vaziri [53]), could be simply calculated, from Young’s Modulus, E , and the uniaxial total strain, $\epsilon_t(link)$.

As can be seen from *Fig. 5.14.* above, for elements in the set of *softening elements*, this predicted stress, was larger than the maximum stress capacity of the element, as defined by the elastic-softening constitutive model. In order to implement softening behaviour the excess stress, $\Delta\sigma_{(link)}$, also know as the ‘relaxation stress’ (Lu and Vaziri [53]), which was representative of the difference between the predicted stress and the maximum stress capacity of the element, had to be redistributed, from the softening element to other areas of the bonded particle assembly. This was done by returning the stress to the element in the form of a self-equilibrating pair of out of balance forces, F_{cor} , applied to the particles at each end of the link element (See *Fig. 5.16.*).

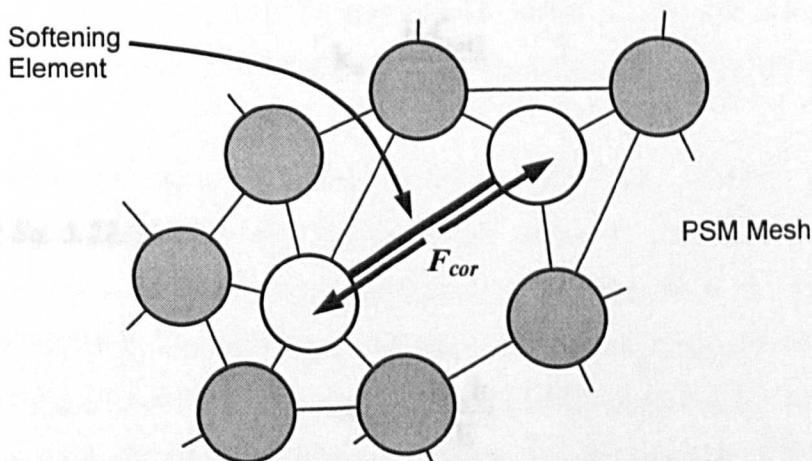


Fig. 5.16. Diagram Showing Self Equilibrating Out of Balance Corrective Forces Applied to Particle Pair to Redistribute Relaxation Stress to Other Parts of Bonded Particle Assembly

These 'corrective' forces acted to further stretch the element and redistribute the relaxation stress to other parts of the bonded particle assembly

The forces were developed, as shown below, by multiplying the relaxation stress, $\Delta\sigma_{(link)}$, over an apparent cross-sectional area for the inter-particle link element, $A_{(link)}^*$ (See Eq. 5.21.).

$$F_{cor} = \Delta\sigma_{(link)} \cdot A_{(link)}^* \quad \text{Eq. 5.21.}$$

The apparent cross-sectional area was determined by relating the normal stiffness of the link element, produced by Morikawa and Sawamoto's equation for strain energy equivalence under plane strain conditions (See Eq. 4.29. repeated below), to the material properties via a simple elastic relationship (See Eq. 5.22.). This formulation assumes that the material properties of the individual elements are the same as those of the equivalent continuum material.

$$k_n = \frac{E}{\sqrt{3}(1-2\nu)(1+\nu)} \quad \text{Eq. 4.29.}$$

$$k_n = \frac{EA_{(link)}^*}{h} \quad \text{Eq. 5.22.}$$

Rearranging Eq. 5.22. gives,

$$A_{(link)}^* = \frac{k_n h}{E} \quad \text{Eq. 5.23.}$$

Substituting Eq. 4.29. into Eq. 5.23. gives,

$$A_{(link)}^* = \frac{h}{\sqrt{3}(1-2\nu)(1-\nu)} \quad \text{Eq. 5.24.}$$

As the uniaxial total strain in the elements increased, the *softening elements* would eventually also become *candidates for failure* and be considered by the failure criterion described in Eq. 5.18. above. The application of forces, for the purposes of stress redistribution, was continued in each of the *softening elements*, as discussed above, until an element was considered to have failed and was consequently removed.

5.7.2. Implementation of the Mark 3 Failure Criterion

The *FISH* routine employed for the implementation of the Mark 3 failure criterion was very similar to that of the Mark 1 failure criterion (See Section 5.5.2.). The code again checked each link element of the PSM mesh in turn and determined if its uniaxial total strain exceeded its ultimate strain. Each time an element was found to have exceeded its ultimate strain, as determined by the constitutive model (See Fig. 5.14.), its strain was compared to that of the stored current 'worst case' element. If its strain was found to exceed that of the 'worst case' element then it was recorded as the new 'worst case' element. After examination of all the inter-particle link elements, the final stored 'worst case' element was considered to have failed and was removed from the PSM mesh.

In addition to testing for failure conditions, the Mark 3 criterion also took into account softening behaviour by modifying the states of link elements that were considered to have exceeded their elastic capacity. This was done by representing the redistribution of stress through the application of self-equilibrating, out of balance force dipoles to the particle contact pairs associated with each inter-particle link element that was found to have exceeded its maximum elastic strain (See Fig. 5.16. above). As mentioned in the previous Section, these out of balance forces, referred to as corrective forces, F_{cor} , were added to the total force acting on a particle. This subsequently

affected the acceleration of the particle, as computed in the Motion calculation directly following the execution of the failure criterion code in each time step (See Fig. 5.1.). Thus, under the Mark 3 failure criterion, Eq. 3.26. (repeated below) can be rewritten as in Eq. 5.25. below.

$$a^{(p)} = \frac{\sum F^{(p)}}{m^{(p)}} \quad \text{Eq. 3.26.}$$

$$a^{(p)} = \frac{\sum F^{(p)} + \sum F_{cor}^{(p)}}{m^{(p)}} \quad \text{Eq. 5.25.}$$

It may be noted that all other equations of the distinct element calculation remained unaltered.

The *FISH* routine through which the Mark 3 failure criterion was developed can be summarised as shown in Fig. 5.17. Detail of the actual *FISH* code can be found in Section AIII.7. of Appendix III and, where possible, variable names employed in the code, are shown beside the relevant process in the flow chart below.

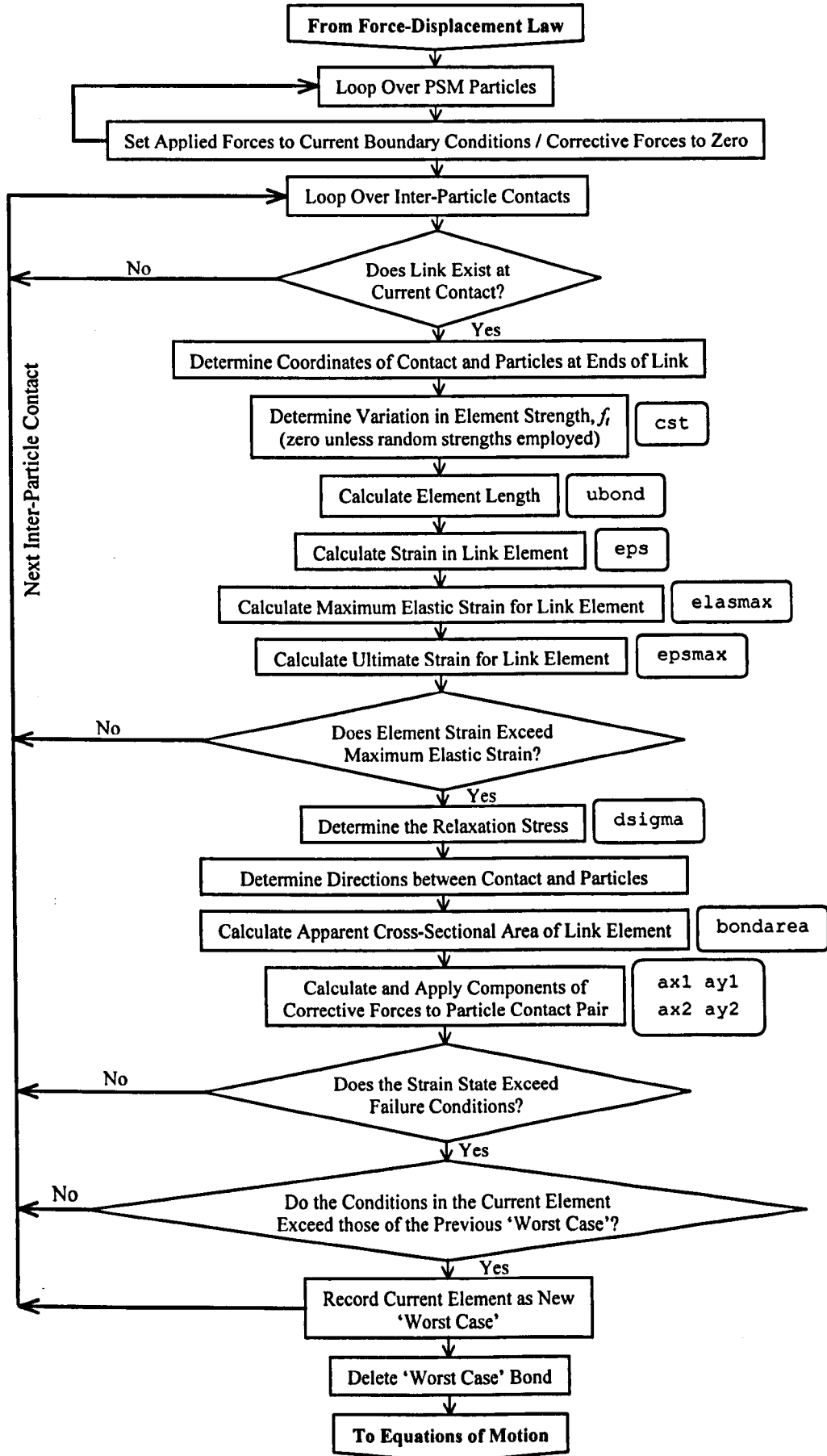


Fig. 5.17. Flow Chart Summarising FISH Code for Mark 3 Failure Criterion

5.7.3. Mark 3 Failure Criterion Benchmark Study

The Mark 3 failure criterion, as described in Section 5.7.1. above, was applied to the Two-Dimensional Uniaxial Benchmark Model, discussed in Section 5.4., and the following numerical studies, detailed in Table 5.4. below, were carried out.

Displ.	Element Length h (m)	Young's Modulus E (MPa)	Poisson's Ratio ν	Fracture Energy G_f (N/m)	Softening Modulus E_s (MPa)	Material Strength f_t (N/mm ²)	Prescribed Velocity (m/s)
x	0.50	1785	0.25	200	356.38	0.48750	5×10^{-8}
x	0.25	1785	0.25	200	162.02	0.48750	5×10^{-8}
x	0.10	1785	0.25	200	61.46	0.48750	5×10^{-8}
y	0.50	1785	0.25	200	356.38	0.48750	5×10^{-9}
y	0.25	1785	0.25	200	162.02	0.48750	5×10^{-9}
y	0.10	1785	0.25	200	61.46	0.48750	5×10^{-9}
x	0.50	1785	0.25	1000	61.46	0.48750	5×10^{-8}
x	0.25	1785	0.25	500	61.46	0.48750	5×10^{-8}
x	0.10	1785	0.25	200	61.46	0.48750	5×10^{-8}
y	0.50	1785	0.25	1000	61.46	0.48750	5×10^{-8}
y	0.25	1785	0.25	500	61.46	0.48750	5×10^{-8}
y	0.10	1785	0.25	200	61.46	0.48750	5×10^{-9}

Table 5.4. Details of Two-Dimensional Uniaxial Model Studies with Mark 3 Failure Criterion

As can be seen in table above, two groups of numerical tests were carried out. Both of these considered the prescribed displacement, in the x and y -directions, of all three discretisations of the model mesh. The first set of tests was carried out with a fixed value for the fracture energy release rate, G_f , for each of the three mesh discretisations. The second set of tests repeated the first set but applied a constant Softening Modulus, E_s , for each of the three discretisations. As discussed previously, this effectively altered

the fracture energy release rate for the various meshes. From the described studies, the following load-displacement curves were produced (See Fig. 5.18. to Fig. 5.21.).

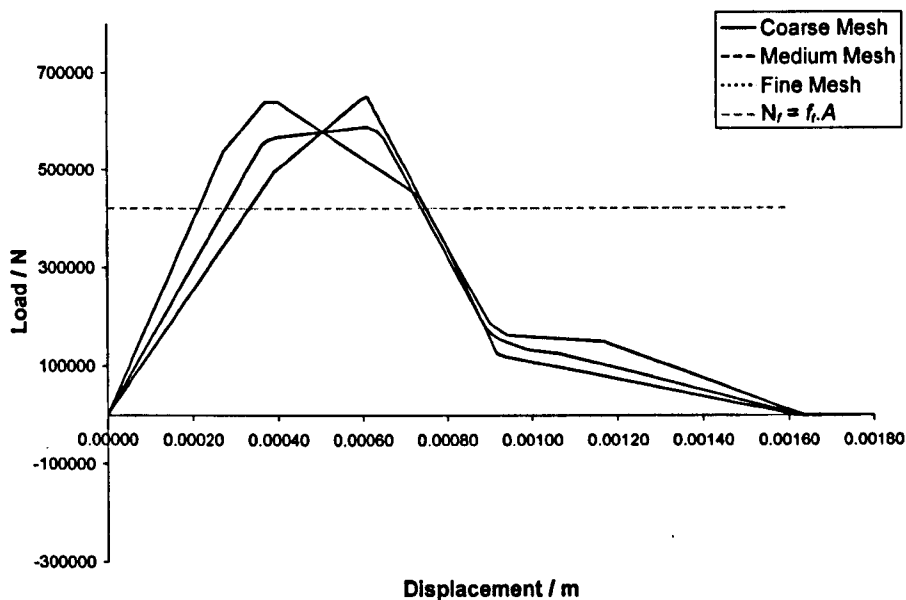


Fig. 5.18. Load-Displacement Plots for the Two-Dimensional Uniaxial Benchmark Model with the Mark 3 Failure Criterion and Prescribed Displacement in the x-direction (Modified E_s - constant G_f)

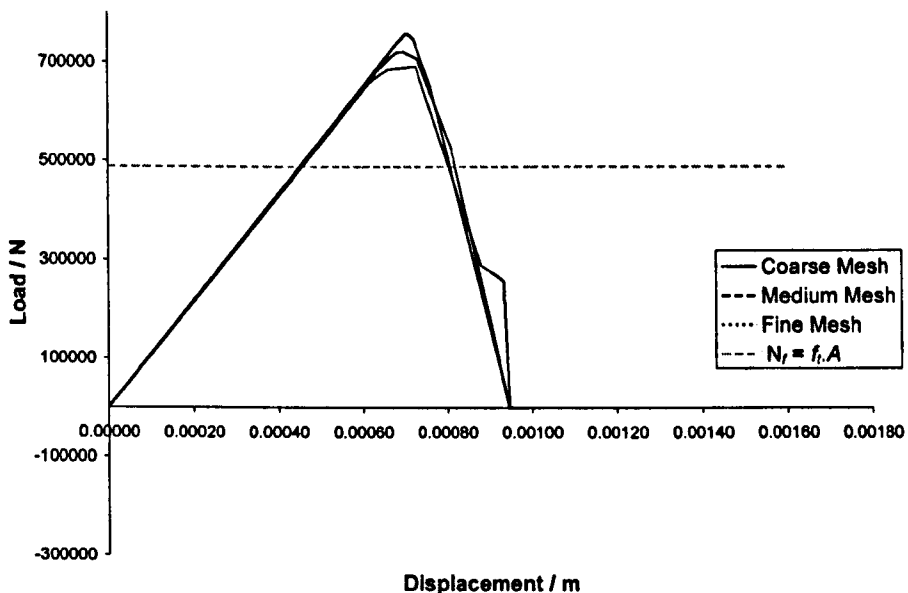


Fig. 5.19. Load-Displacement Plots for the Two-Dimensional Uniaxial Benchmark Model with the Mark 3 Failure Criterion and Prescribed Displacement in the y-direction (Modified E_s - constant G_f)

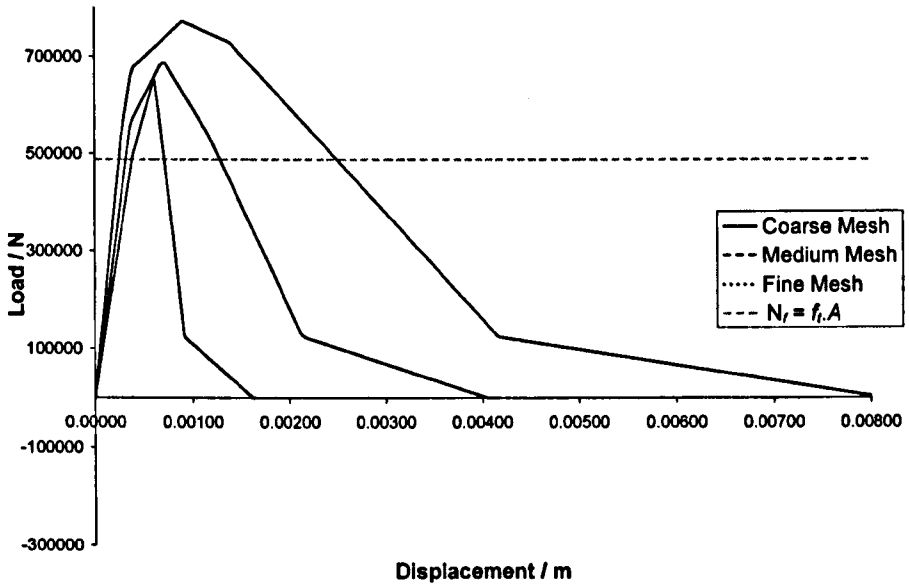


Fig. 5.20. Load-Displacement Plots for the Two-Dimensional Uniaxial Benchmark Model with the Mark 3 Failure Criterion and Prescribed Displacement in the x-direction (Constant E_s - non-constant G_f)

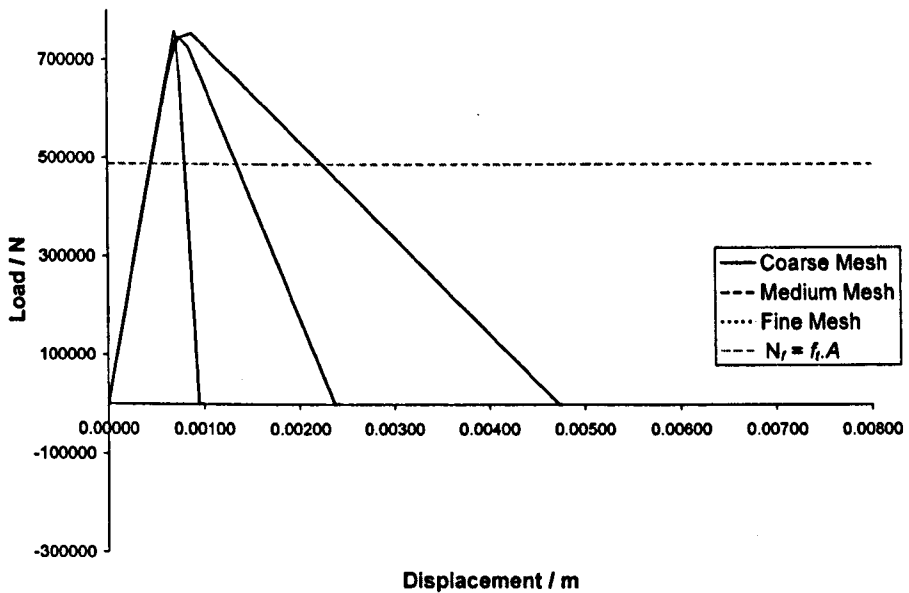


Fig. 5.21. Load-Displacement Plots for the Two-Dimensional Uniaxial Benchmark Model with the Mark 3 Failure Criterion and Prescribed Displacement in the y-direction (Constant E_s - non-constant G_f)

It is immediately obvious from the load-displacement plots shown above, that the post peak behaviour displays controlled unloading behaviour, as would generally be expected for an elastic-softening failure criterion. This is in contrast to the sudden unloading behaviour seen in the load-displacement curves from the elastic-brittle, Mark 1 and Mark 2 failure criteria.

From examination of the results of the two studies for which the fracture energy release rate, G_f , was held constant (*Fig. 5.18.* and *Fig. 5.19.*), it is also clearly seen that the load-displacement curves, for all three mesh discretisations, reach failure, as indicated by load capacity of zero, at precisely the same displacement. Thus, the Mark 3 failure criterion can be seen to show mesh size objectivity and produce results that are independent of the mesh discretisation.

This behaviour is further confirmed in the plots of the two studies for which the softening slope was held constant, where it can clearly be seen that the maximum displacements vary considerably for the three mesh discretisations. This variation was to be expected since a fixed softening slope results in an effective decrease of the fracture energy release rate with decreasing element size.

Despite the general accuracy of the results in terms of the reproduction of elastic-softening behaviour and the development of mesh size independent results there are a number of specific features to be noted from the load-displacement results.

Firstly, despite evidence of mesh size objectivity in the softening behaviour associated with the Mark 3 failure criterion, the elastic responses of the three mesh discretisations vary as they did under the Mark 1 criterion and, as before, this effect is strongest in the meshes displaced in the x -direction. As discussed in Section 5.5.3. above, the mesh size dependency of the elastic behaviour is a consequence of the low L ratios of the meshes applied in the Two-Dimensional Uniaxial Benchmark Model. As similarly observed by van Vliet [95], the accuracy of the results, in comparison to those expected for an equivalent continuum material, improved as the ratio, L , increased and the boundary effects diminished. As discussed previously, according to the findings of van Vliet and of the Uniaxial Benchmark Tests conducted in Section 4.2.3.2.1. of Chapter 4, the fine meshes applied in the Two-Dimensional Uniaxial Benchmark Model

had an L ratio sufficiently high to produce reasonably accurate results while the coarser meshes could be expected to show evidence of boundary effects. Again, the deficiencies of the coarser meshes are accepted on practical grounds due to the computational effort involved in running models with finer meshes.

Secondly, it was again desirable to compare the predictions of the load-displacement curves with the maximum load capacities and extensions as would be expected from equivalent continuum material. As in previous sets of results, the maximum expected continuum load capacity was indicated on the load-displacement curves by an f_t line. It can thus be seen that all of the tests over predicted the overall material strength and yielded well above this value. Furthermore, the maximum extensions of the meshes at failure were calculated by considering the ultimate strain defined by the elastic-softening constitutive model (See *Fig. 5.14.* and *Eq. 5.26.*). This was possible since, as described previously, failure in the meshes was localised in a weak zone of elements, the remainder of the mesh was completely unloaded when fracturing occurred and hence, the strain in the weak zone elements was equal to the strain in the whole mesh.

$$u = \left(\frac{f_t}{E} + \frac{f_t}{E_s} \right) \cdot h \quad \text{Eq. 5.26.}$$

From the equation above, the expected extensions were found to be 0.000821m for the meshes displaced in both the x and y -directions. It can therefore be seen, from the plots above, that all of the tests over predict the extension of the mesh in comparison to an equivalent continuum material. As for the Mark 1 criterion, this is clearly explainable by the presence of 'diagonal' elements that lie in a direction at an angle to the direction of prescribed displacement. In order for these elements to reach their ultimate strain the mesh as a whole must be extended beyond the maximum value that would be expected for an equivalent continuum material.

Although the constitutive model is applied to the uniaxial total strain in an individual element, it is perhaps unrealistic, given the presence of ‘diagonal’ elements, to assume that the overall extension of the meshes would be equal to the ultimate strain in an element. Perhaps a more realistic measure of overall extension would be based on a characteristic length associated with the width of the weak zone of elements (See Fig. 5.22.).

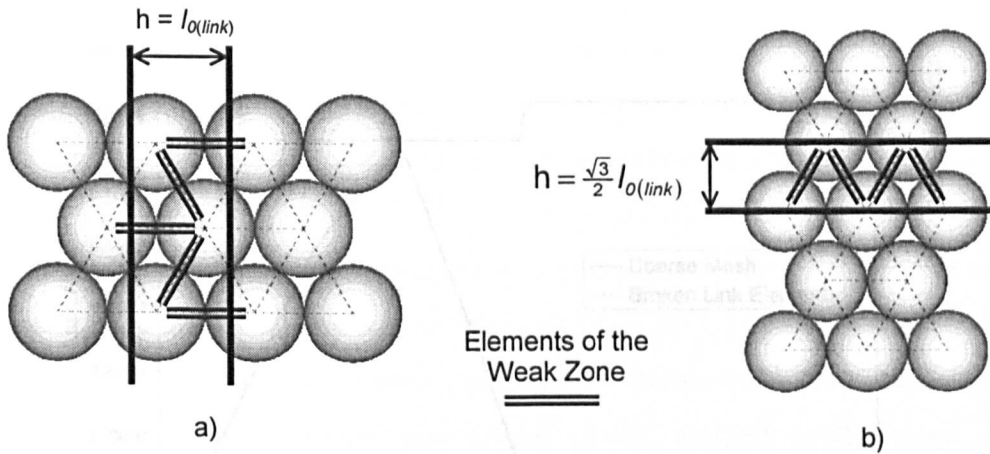


Fig. 5.22. Diagram Showing Alternative Interpretations of Characteristic Length, h , for Two-Dimensional Uniaxial Benchmark Model Meshes for displacement in a) the x -direction and b) the y -direction

As indicated above, it may be reasonable to assume a weak zone width equal to the original link element length, $l_{o(link)}$, for the meshes displaced in the x -direction. However, for the meshes displaced in the y -direction a value of $\frac{\sqrt{3}}{2} l_{o(link)}$ may be more appropriate. When these values of characteristic length are substituted into Eq. 5.26. above, the maximum mesh displacements are calculated as 0.000821m for the meshes displaced in the x -direction, as before, and 0.000711m for the meshes displaced in the y -direction. As can be seen from the load-displacement plots this alternative interpretation in fact leads to less accurate results than the assumption of the characteristic length equal to the element length.

Further evidence of the effect of ‘diagonal’ elements of the load-displacement behaviour can be seen in the results for prescribed displacement in the x -direction (See Fig. 5.18. and Fig. 5.20. above). As can be seen in all six plots, a distinct change in slope occurs in the post-peak section of the curves at approximately the same load in all cases. This change can be shown to coincide with the failure of the elements aligned in the x -direction and the consequent transfer of the load to the remaining diagonals elements (See Fig. 5.23. below).

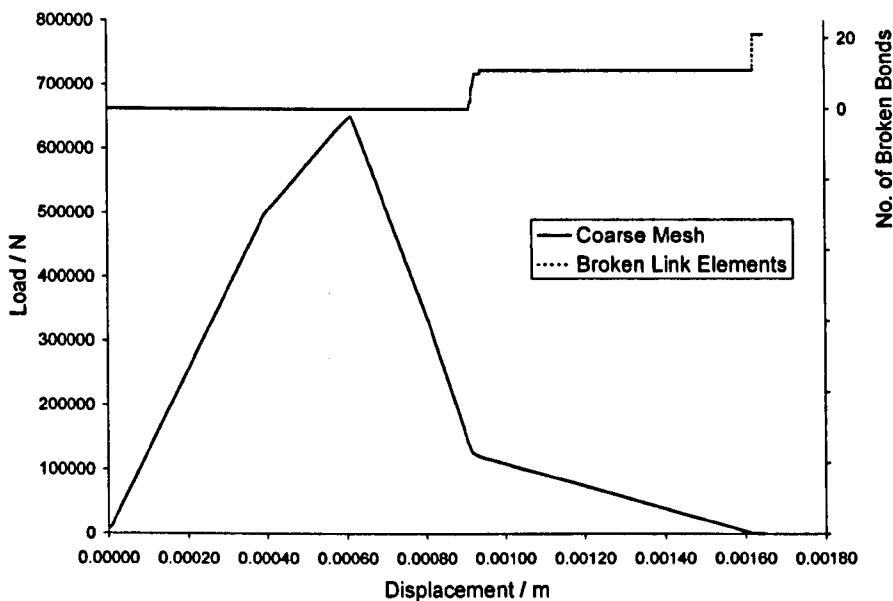


Fig. 5.23. Load-Displacement Plot for Two-Dimensional Uniaxial Benchmark Model Coarse Mesh with the Mark 3 Criterion and Prescribed Displacement in the x -direction, Overlaid with Plot of Number of Failed Elements-Displacement

Accordingly, this behaviour is not seen in the plots from prescribed displacement in the y -direction (See Fig. 5.19. and Fig. 5.21.), since in these cases, there are only ‘diagonal’ elements present and, as would be expected, these yield, soften and fail simultaneously.

It was subsequently found that Bažant et al. [7] had also developed a bonded particle assembly with an elastic-softening failure criterion, very similar to that developed in this work. In fact, they applied the same formulation, as discussed above (See Eq. 5.14. and Eq. 5.15.), in order to vary the softening slope of the constitutive model and maintain a constant fracture energy release rate. However, the model

developed by Bažant et al. employed a random particle assembly and while that would be feasible with the PSM, and possibly a desirable extension of this work, it would require the application of individual constitutive models to each element. This would require more complex coding and an increase in the computational effort. A further difference between their model and the PSM was that they considered the inter-particle link elements to consist of three sections, made up of the two particles at each end of the link and a cement material between them. In fact, it was only the cement component of the link element that experienced softening behaviour. This is probably a reasonable method of approximating the composition of a material such as concrete with a macro-scale lattice type model as opposed to the micro-scale lattice models applied to the study of concrete by authors such as Schlangen and van Mier [82]. However, this would not be easily applicable within the PFC^{3D} framework and a smeared approach to the various material properties within one link element would probably be required, especially since softening occurs over the full length of a link element. As can be seen in *Fig. 5.24.* below, the load-displacement curves presented by Bažant et al. for a model similar to the Two-Dimensional Uniaxial Benchmark Model applied in this work, showed approximately exponential softening behaviour as might generally be expected for a quasi-brittle material such as concrete.

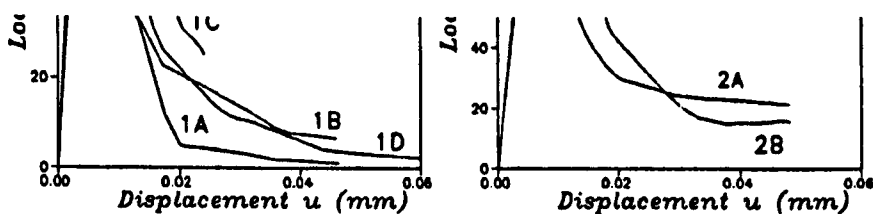


Fig. 5.24. Load-Displacement Curves for Tension Specimen Constructed with a Random Bonded Particle Assembly Model (Bažant et al. [7])

The increasing softening that occurs with increasing displacement in the post-peak behaviour of the model was probably a result of microcrack formation as elements fail in various parts of the assembly. This behaviour would consequently not be seen in the

load-displacement curves produced by the Two-Dimensional Uniaxial Model since failure is limited to a narrow weak zone in the mesh. It is unlikely however that this behaviour would be produced by these models even if a weak zone were not included in the meshes. Given the uniform configuration and strength in the PSM meshes, failure is likely to occur throughout the meshes at almost the same time. A random strength distribution in the PSM meshes might produce results similar to those shown in *Fig. 5.24.*, however, the Mark 3 failure criterion would still over predict the strength and extension of the meshes in comparison to an equivalent continuum material.

The development of the Mark 3 failure criterion can also be seen to have some similarities with work carried out by Jirásek and Bažant [40], who, as discussed in Chapter 2, Section 2.3.3., investigated the microscopic fracture characteristics of random particle systems. The inter-particle links of their models were also considered to have an elastic-softening constitutive model similar to those applied here.

In their research, Jirásek and Bažant considered two different approaches that would account for the size of the link elements with softening behaviour. Firstly, they considered maintaining a constant fracture energy release rate, G_f , in the link element, in a method similar to that which was applied in this work. Secondly, they consider maintaining a constant ratio between the ultimate strain for a link element and the maximum elastic strain for a link element. They describe this ratio as the 'microductility'. They also note that the consideration of a constant fracture energy release rate is only valid if there is only one crack in the full length of an inter-particle link element whereas, a constant 'microductility' is valid even if more than one crack is considered. As discussed previously (See Chapter 2, Section 2.3.1. and Section 5.2. above), it is usual in lattice type models to consider only one fracture per element and this is the assumption made in this work. Therefore, the consideration of a constant fracture energy release rate in the Mark 3 criterion is valid.

In the work carried out by Jirásek and Bažant, a clear distinction is made between the 'microproperties' of the particle links and the 'macroproperties' of the equivalent continuum material. Additionally, they note that the parameter having the strongest influence on the overall ductility of the continuum material is the fracture energy, G_f , of the inter-particle links. These assertions are confirmed in the results seen

above in this Section since, firstly, the overall load-displacement curves for the meshes show behaviour significantly different to that represented by the constitutive model for an individual link, and, secondly, altering the fracture energy release rate was seen to significantly affect the overall softening behaviour of the PSM meshes. However, 'microproperties' were not considered in this work and the inter-particle link elements were assumed to have the same material properties as an equivalent continuum material. This is perhaps partially responsible for the poor reproduction of equivalent continuum behaviour, by the Mark 3 failure criterion, which is based on the properties of individual link elements. It might be possible to follow the work by Jirásek and Bažant and choose various 'microproperty' values for the elements that would produce overall mesh behaviour as would be expected with the desired 'macroproperties'. However, it is not immediately clear how this would be achieved and a trial and error calibration may be required, whereby link properties are assigned and the overall material response determined by testing. Furthermore, as was seen in the previous Sections of this Chapter, there was a significant improvement in the results produced by the Mark 2 criterion, where continuum principles were applied, over those produced by the Mark 1 criterion, which considered the uniaxial strain in individual link elements. It is therefore a logical progression of this work to develop an elastic-softening model, similar to the Mark 3 criterion, but based on continuum principles in a similar fashion to the Mark 2 criterion.

A further difference between the two schemes described above and Mark 3 failure criterion is the implementation of material degradation incurred during plastic deformation of the inter-particle link elements. The models developed by Bažant et al. [7] and Jirásek and Bažant [40, 41] employ secant unloading schemes and reduce the stiffness of the link elements accordingly, however, as discussed previously, the Mark 3 failure criterion was formulated in the K_0 , initial stiffness algorithm and considers only the current uniaxial total strain in a link element. Consequently unloading and reloading of the material would follow the initial loading path. Therefore, degradation of the material stiffness is not considered by the Mark 3 criterion and in the numerical studies conducted in this work it is assumed that loading is purely monotonic. Once a link has started to soften it is assumed that it does not unload before failure. Although it is understood that some unloading may take place due to stress relaxation after a fracture propagation event, given the limitation of one element failure per time step (See Section

5.3.), this is considered to have a negligible effect on the overall behaviour of the PSM mesh.

Although it is a highly desirable development of this work to take account of material degradation due to plastic deformation, the K_θ formulation obviously, by definition, precludes the implementation of a secant stiffness algorithm. As mentioned above, the existing Mark 3 criterion considers only the current uniaxial total strain of a link element and has no knowledge of the strain history. Any unloading that takes place will be elastic and from the position of the predicted stress, $\sigma_{(link)}^{pred}$. It may be possible, however, to implement a scheme whereby an irrecoverable strain is developed in the inter-particle link elements. This would require the maximum uniaxial total strain experienced by an element to be recorded. From the position on the constitutive model, corresponding to the maximum recorded strain, a certain amount of elastic unloading, representative of the recoverable deformation in the element, would be permitted (See Fig. 5.25.).

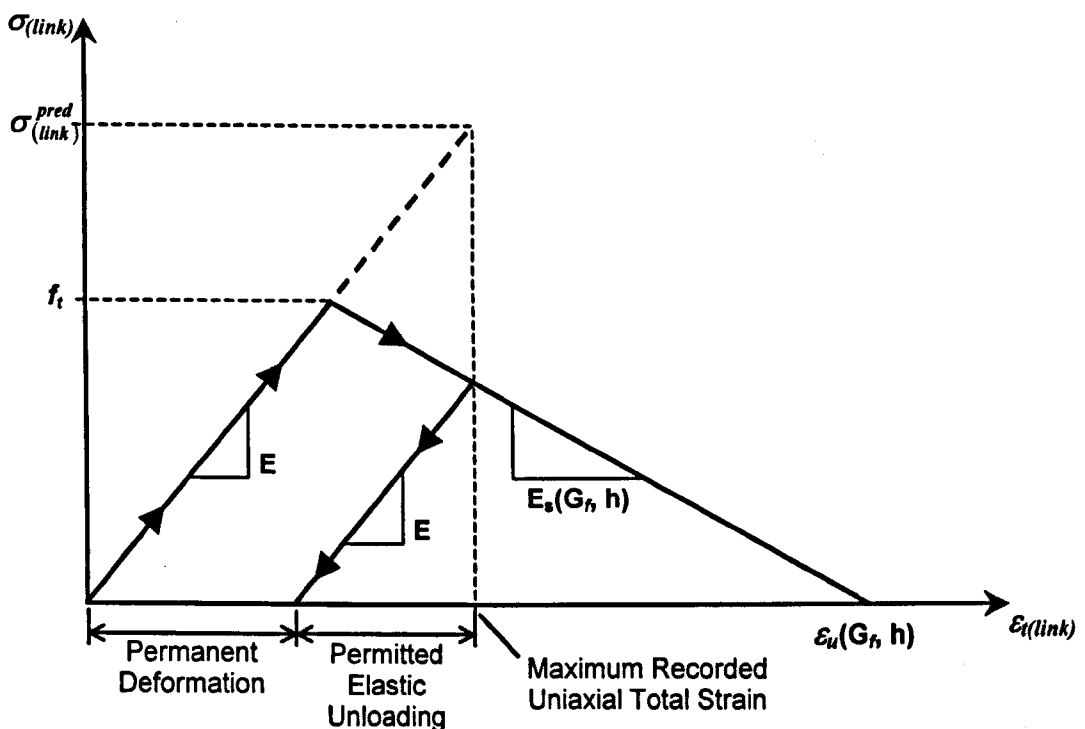


Fig. 5.25. Diagram Showing Elastic-Softening Constitutive Model for Modified Mark 3 Failure Criterion with Elastic Unloading Scheme

When the permitted elastic unloading was complete and the load capacity had reached zero, the remaining, unrecoverable, deformation could perhaps be maintained by applying appropriate forces to the particles at each end of the link, thereby preventing further shortening of the element.

No attempt to implement plastic degradation of the material was made in the course of this work, as it was desired to continue the development of a softening failure criterion that would accurately reproduce the behaviour that would be expected of an equivalent continuum material.

5.7.4. Mark 3 - Conclusions

In summary, it can be concluded that, the Mark 3 elastic-softening failure criterion is capable of producing load-displacement behaviour that is independent of the size of the inter-particle link elements.

Despite this, it can also be seen that the maximum load capacities and the extensions of the meshes at failure predicted by the Two-Dimensional Uniaxial Benchmark Model with the Mark 3 criterion applied, exceed those that would be expected for an equivalent continuum material. This is as would be expected for a model that considers the uniaxial total strain in the individual link elements of the PSM mesh and the behaviour is similar to that observed and discussed in conjunction with the Mark 1 failure criterion (See Section 5.5.3. above).

Further limitations of the Mark 3 criterion, associated with the lack of consideration of material degradation due to plastic deformation, were acknowledged and it is accepted that, in its current form, the criterion is only representative of a softening material undergoing monotonic loading. The numerical tests carried out in this work are all considered to experience this loading condition.

In Section 5.6.3. it was shown that the Mark 2 failure criterion, which was developed through continuum principles applied in the PSM mesh, showed an improvement in the reproduction of equivalent continuum behaviour over the Mark 1 criterion, which was based on the uniaxial total strain in the individual link elements of the PSM mesh. In the previous Section, it has also been shown that the Mark 3 elastic-softening criterion overcomes the problems of the size dependent results produced by both the Mark 1 and Mark 2 elastic-brittle criteria but that it suffers from the poor reproduction of equivalent continuum behaviour seen with the Mark 1 criterion. It was therefore a logical progression for this work to develop a fourth failure criterion that combined the accuracy of a model based on continuum principles and the generality of an elastic-softening model. The development of this, the Mark 4 criterion, is discussed in the following Section.

5.8. Mark 4 - Failure Criterion

(Softening, Continuum Total Strain Criterion)

5.8.1. Theory of the Mark 4 Failure Criterion

As discussed in the previous Section, the Mark 4 criterion was intended to be an elastic-softening model developed from continuum principles. It was initially hoped that this would be implemented via a combination of the converted granular stress tensors, as had been utilised for the Mark 2 criterion (See Section 5.6.1.), and the stress redistribution technique developed for the Mark 3 criterion (See Section 5.7.1.). However, it became apparent that this would not be possible. Due to the averaged nature of the stress tensors in the particles, a force applied to one side of a particle, as would occur in the stress redistribution process developed for the Mark 3 criterion (See Section 5.7.1.), increased the granular stress by only half of what would be expected for a given applied force in a continuum material. Consequently, due to the assumption that the stress tensor in the link element was the average of those in the particles between which it lay, the stress reported in the link element would also increase by only half of what would be expected.

It was therefore necessary to find an alternative approach to the measurement of continuum properties in the PSM meshes and it was decided to return to a failure criterion formulated from the total strain in an element. However, rather than considering the uniaxial strain in an element, as had been the case for the Mark 1 and Mark 3 criteria, a continuum measurement of total strain was taken. This was done by considering each link element in the PSM mesh to be representative of an equivalent continuum area of material which was defined by the two triangles on either side of it, as delineated by other link elements to which it was joined (See Fig. 5.26.).

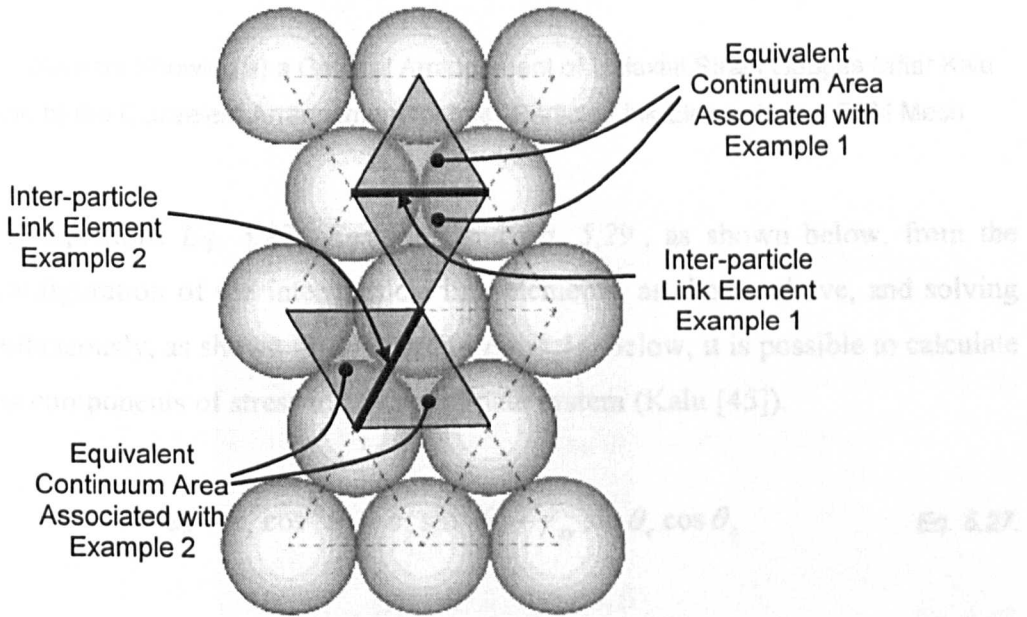


Fig. 5.26. Diagram Showing Equivalent Continuum 'Diamond' Area of PSM Mesh Associated with Individual Link Elements for Mark 4 Failure Criterion

The average strain tensors in these triangles could then be calculated from the stretches of each of the elements around its perimeter. This was done by treating the inter-particle links as simple strain gauges, as might be employed to experimentally measure the strain in a material sample (See Fig. 5.27.).

$$\begin{bmatrix} \epsilon_x \\ \epsilon_y \\ \gamma_{xy} \end{bmatrix} = [T]^T \begin{bmatrix} \epsilon_1 \\ \epsilon_2 \\ \epsilon_3 \end{bmatrix}$$

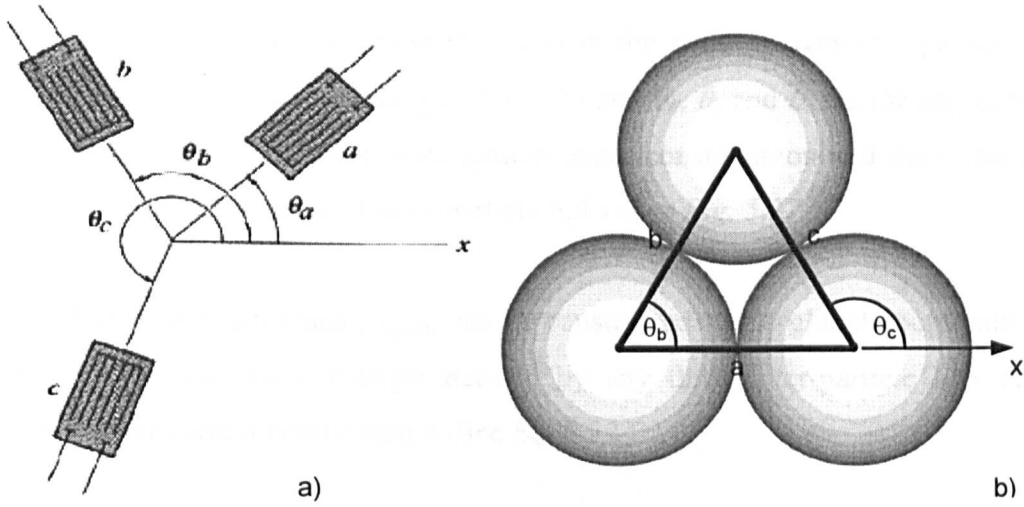


Fig. 5.27. Diagram Showing a) a General Arrangement of Uniaxial Strain Gauges (after Kalu [45]) and b) the Equivalent Arrangement for Inter-Particle Link Elements in a PSM Mesh

Developing equations Eq. 5.27., Eq. 5.28. and Eq. 5.29., as shown below, from the updated configuration of the inter-particle link elements, as shown above, and solving them simultaneously, as shown in Eq. 5.30. to Eq. 5.31. below, it is possible to calculate the various components of stress in any coordinate system (Kalu [45]).

$$\epsilon_c = \epsilon_x \cos^2 \theta_c + \epsilon_y \sin^2 \theta_c + \gamma_{xy} \sin \theta_c \cos \theta_c \quad \text{Eq. 5.27.}$$

$$\epsilon_b = \epsilon_x \cos^2 \theta_b + \epsilon_y \sin^2 \theta_b + \gamma_{xy} \sin \theta_b \cos \theta_b \quad \text{Eq. 5.28.}$$

$$\epsilon_c = \epsilon_x \cos^2 \theta_c + \epsilon_y \sin^2 \theta_c + \gamma_{xy} \sin \theta_c \cos \theta_c \quad \text{Eq. 5.29.}$$

$$\begin{bmatrix} \epsilon_a \\ \epsilon_b \\ \epsilon_c \end{bmatrix} = \begin{bmatrix} \cos^2 \theta_a & \sin^2 \theta_a & \sin \theta_a \cos \theta_a \\ \cos^2 \theta_b & \sin^2 \theta_b & \sin \theta_b \cos \theta_b \\ \cos^2 \theta_c & \sin^2 \theta_c & \sin \theta_c \cos \theta_c \end{bmatrix} \begin{bmatrix} \epsilon_x \\ \epsilon_y \\ \gamma_{xy} \end{bmatrix} = [T] \begin{bmatrix} \epsilon_x \\ \epsilon_y \\ \gamma_{xy} \end{bmatrix} \quad \text{Eq. 5.30.}$$

$$\begin{bmatrix} \epsilon_x \\ \epsilon_y \\ \gamma_{xy} \end{bmatrix} = [T]^{-1} \begin{bmatrix} \epsilon_a \\ \epsilon_b \\ \epsilon_c \end{bmatrix} \quad \text{Eq. 5.31.}$$

where, ε_a , ε_b and ε_c are the uniaxial strains in the strain gauges or equivalent inter-particle links, (calculated according to Eq. 5.2.) and θ_a , θ_b and θ_c are the angles between the positive x -axis of the coordinate system under consideration and the orientation of the strain gauges or equivalent inter-particle links (See Fig. 5.27.).

Hence, a strain tensor, $\varepsilon_{ij(\Delta)}$, can be constructed in the global coordinate system of the PSM mesh for a triangle defined by any three inter-particle link elements whatever their current configuration (See Eq. 5.32.).

$$\varepsilon_{ij(\Delta)} = \begin{bmatrix} \varepsilon_x & \gamma_{xy} \\ \gamma_{yx} & \varepsilon_y \end{bmatrix} \quad \text{Eq. 5.32.}$$

where, the shear stress components are assumed to be symmetrical such that $\gamma_{xy} = \gamma_{yx}$

The average strain tensor in a link element, $\varepsilon_{ij(link)}$, was then assumed to be the average of the strain tensors in its two associated triangles (See Eq. 5.33.)

$$\varepsilon_{ij(link)} = \frac{1}{2} \left(\varepsilon_{ij(\Delta)}^{(\text{triangle 1})} + \varepsilon_{ij(\Delta)}^{(\text{triangle 2})} \right) \quad \text{Eq. 5.33.}$$

When an element on the boundary of the mesh was considered and only one triangle was available, the strain was assumed to be symmetrical about the inter-particle link in question. Consequently, the strain measured in the one available triangle was directly representative of the average strain tensor in the link.

The process, detailed above, for the calculation of the averaged strain tensor in an inter-particle link element of the PSM, is illustrated below (See Fig. 5.28. and Eq. 5.34. to Eq. 5.36.).

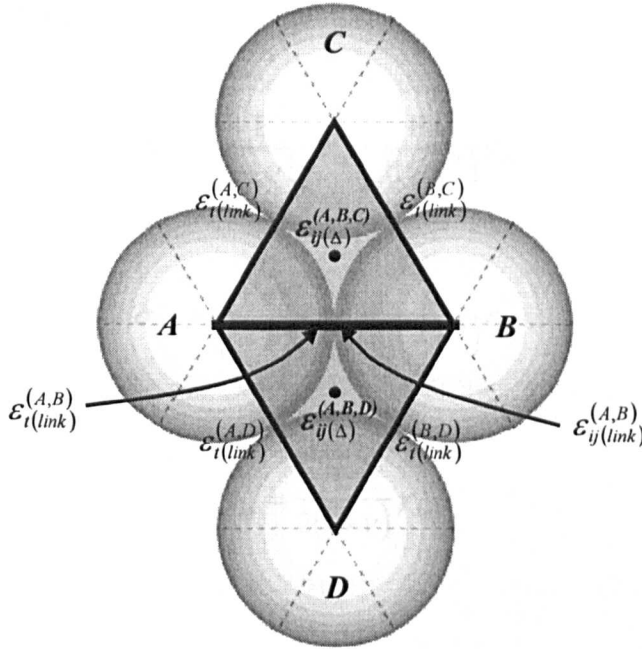


Fig. 5.28. Diagram Showing Construction of Averaged Strain Tensors in Intra-Element Triangles and Inter-Particle Link from Uniaxial Strains in Individual Inter-Particle Links

$$\begin{aligned}
 \mathcal{E}_a &\equiv \mathcal{E}_{i(link)}^{(A,B)} \\
 \mathcal{E}_b &\equiv \mathcal{E}_{i(link)}^{(A,C)} \Rightarrow \mathcal{E}_{ij(\Delta)}^{(A,B,C)} \\
 \mathcal{E}_c &\equiv \mathcal{E}_{i(link)}^{(B,C)}
 \end{aligned}
 \tag{Eq. 5.34}$$

$$\begin{aligned}
 \mathcal{E}_a &\equiv \mathcal{E}_{i(link)}^{(A,B)} \\
 \mathcal{E}_b &\equiv \mathcal{E}_{i(link)}^{(B,D)} \Rightarrow \mathcal{E}_{ij(\Delta)}^{(A,B,D)} \\
 \mathcal{E}_c &\equiv \mathcal{E}_{i(link)}^{(A,D)}
 \end{aligned}
 \tag{Eq. 5.35}$$

$$\mathcal{E}_{ij(link)}^{(A,B)} = \frac{1}{2} \left(\mathcal{E}_{ij(\Delta)}^{(A,B,C)} + \mathcal{E}_{ij(\Delta)}^{(A,B,D)} \right)
 \tag{Eq. 5.36}$$

The continuum total strain state, $\mathcal{E}_{ij(continuum)}$, is defined by the principal strains, could then be compared to an elastic softening constitutive model in a similar technique to that from the strain tensor in the inter-particle link, it was then possible to calculate principal strains, $\mathcal{E}_{1(link)}$ and $\mathcal{E}_{2(link)}$, and hence, from the classical two-dimensional plane elasticity relationships (See Eq. 4.21. to Eq. 4.26. repeated below), it was also possible to calculate the maximum principal stress in the inter-particle link, $\sigma_{1(link)}$.

Plane Stress Conditions:

$$\sigma_{xx} = \frac{E}{(1-\nu^2)} \varepsilon_{xx} + \frac{E\nu}{(1-\nu^2)} \varepsilon_{yy} \quad \text{Eq. 4.21.}$$

$$\sigma_{yy} = \frac{E\nu}{(1-\nu^2)} \varepsilon_{xx} + \frac{E}{(1-\nu^2)} \varepsilon_{yy} \quad \text{Eq. 4.22.}$$

$$\tau_{xy} = \frac{E}{2(1+\nu)} \gamma_{xy} \quad \text{Eq. 4.23.}$$

Plane Strain Conditions:

$$\sigma_{xx} = \frac{E(1-\nu)}{(1+\nu)(1-2\nu)} \varepsilon_{xx} + \frac{E\nu}{(1+\nu)(1-2\nu)} \varepsilon_{yy} \quad \text{Eq. 4.24.}$$

$$\sigma_{yy} = \frac{E\nu}{(1+\nu)(1-2\nu)} \varepsilon_{xx} + \frac{E(1-\nu)}{(1+\nu)(1-2\nu)} \varepsilon_{yy} \quad \text{Eq. 4.25.}$$

$$\tau_{xy} = \frac{E}{2(1+\nu)} \gamma_{xy} \quad \text{Eq. 4.26.}$$

The continuum total strain state, $\varepsilon_{(1,2)(link)}$, as defined by the principal strains, could then be compared to an elastic-softening constitutive model in a similar technique to that applied for the Mark 1 and Mark 3 failure criteria. However, rather than the uniaxial stress-uniaxial total strain space, $\sigma_{(link)}-\varepsilon_{(link)}$, in which the previous models had been constructed, the constitutive model for the Mark 4 criterion was constructed in principal stress - two-dimensional principal strain space, $\sigma_{1(link)}-\varepsilon_{1(link)}-\varepsilon_{2(link)}$, (See Fig. 5.29. below).

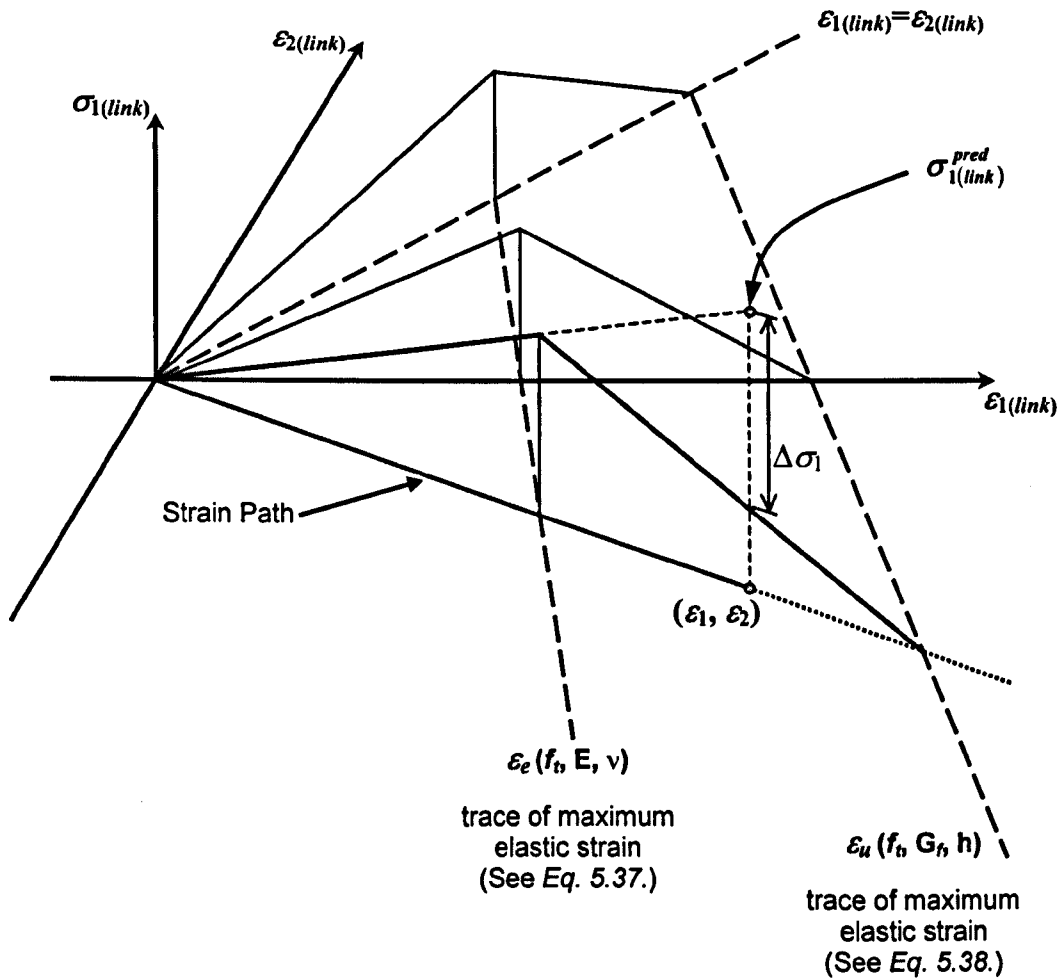


Fig. 5.29. Diagram Showing Elastic-Softening Constitutive Model for Mark 4 - Continuum Total Strain Failure Criterion for the PSM

As can be seen in the plot above, it was possible, again through the plane elasticity relationships (See Eq. 4.21. to Eq. 4.26.), to plot the trace of a maximum elastic strain state, ϵ_e , within this space (See Eq. 5.37. below). Furthermore, by applying the formulation discussed in Section 5.7.1. above (See Eq. 5.15.), to calculate the required Softening Modulus for a given fracture energy release rate, it was also possible to plot the trace of an ultimate strain state, ϵ_u (See Eq. 5.38. below).

$$\epsilon_2 = \frac{\nu - 1}{\nu} \epsilon_1 + \frac{f_t(1 + \nu)(1 - 2\nu)}{\nu E} \tag{Eq. 5.37.}$$

$$\varepsilon_2 = -\frac{1}{\sqrt{2}-1} \left(\varepsilon_1 - \frac{2G_f}{f_i h} \right) \quad \text{Eq. 5.38.}$$

Consequently, as before, in order to demonstrate mesh size objectivity in the results, the precise shape of the constitutive model is defined by the fracture energy release rate, G_f , and the length of the inter-particle link elements, h . Again, for a given fracture energy release rate, there will be a maximum element length for the model, beyond which snapback behaviour will be introduced (See Fig. 5.15. and Eq. 5.16. and Eq. 5.17.).

It can thus be seen, from Fig. 5.29., that, for any strain path, defined by the current $\varepsilon_{1(link)}-\varepsilon_{2(link)}$ total principal strain state, a specific elastic-softening constitutive model can be described, consisting of an apparent Young's Modulus, E^* , and a corresponding apparent Softening Modulus, E_s^* . Considering all possible strain paths and their associated constitutive models, the overall model can be visualised as a surface in $\sigma_{1(link)}-\varepsilon_{1(link)}-\varepsilon_{2(link)}$ space. Since the maximum principle strain is always defined as $\varepsilon_{1(link)}$ the constitutive surface is mirrored about the line defined by $\varepsilon_{1(link)}=\varepsilon_{2(link)}$. Furthermore, since failure of the inter-particle links in compression is not considered, only the quadrants of $\varepsilon_{1(link)}-\varepsilon_{2(link)}$ space where $\varepsilon_{1(link)}$ is positive need be considered.

In a process similar to that applied in the Mark 3 failure criterion, when comparison was made with the elastic-softening constitutive surface, as discussed above, link elements were considered as *candidates for failure* if the continuum total strain state, defined by $(\varepsilon_{1(link)}, \varepsilon_{2(link)})$, was outside the area enclosed by the trace of the ultimate strain state. From the set of all the *candidates for failure*, the link in which the total strain exceeded the ultimate strain by the largest amount was removed. This can be stated as shown below (See Eq. 5.39. and Eq. 5.40.).

$$\max(\varepsilon_{(1,2)(link)}^e - \varepsilon_u) \quad \text{for } e \in \{S_{eff}^e\} \quad \text{Eq. 5.39.}$$

$$\{S_{eff}^e\} = \left\{ e : \left(\sqrt{\varepsilon_1^2 + \varepsilon_2^2} \right) = \varepsilon_{(1,2)(link)}^e \geq \varepsilon_u = f_i \left(\frac{1}{E^*} + \frac{1}{E_s^*} \right) \right\} \subset \{S^e\} \quad \text{Eq. 5.40.}$$

where, $\epsilon_{(1,2)(link)}$ is the continuum total strain state in an inter-particle link element and E^* and E_s^* are the apparent Young's Modulus and apparent Softening Modulus respectively, which are dependent on the continuum total strain state.

Again, in a similar fashion to the Mark 3 criterion, a set of *softening elements* was also considered that consisted of elements in which the continuum total strain state had exceeded the maximum elastic strain, ϵ_e , but had not exceeded the ultimate strain, ϵ_u (See Eq. 5.41. below).

$$\{S_{se}^*\} = \left\{ e : \frac{f_t}{E^*} = \epsilon_e \leq \epsilon_{(1,2)(link)}^* < \epsilon_u = f_t \left(\frac{1}{E^*} + \frac{1}{E_s^*} \right) \right\} \subset \{S^*\} \quad \text{Eq. 5.41.}$$

As before, all of the elements in the set of *softening elements* were considered to experience softening behaviour. This was again dealt with in the K_0 , initial stiffness algorithm, by treating the total strain in a link element, in this case the continuum total strain as defined by the principal strains, $\epsilon_{(1,2)(link)}$, as a deformation in an elastic material. The predicted elastic response stress, in this case the maximum principal stress from the maximum principal strain, $\sigma_{1(link)}^{pred}$, was then calculated, as mention above, from the plane strain relationship shown in Eq. 4.24. to Eq. 4.26. As discussed previously, while it was possible to consider either plane stress or plane strain conditions, only the latter were investigated in these studies. Accordingly, the relaxation stress, $\Delta\sigma_1$, was then calculated from the difference between the elastic response stress, $\sigma_{1(link)}^{pred}$, and the maximum stress capacity, as defined by the constitutive model (See Fig. 5.29.).

It was intended to redistribute the excess stress in exactly the way that it had been done in the Mark 3 criterion, by returning the excess stress to the link element in the form of forces (See Eq. 5.21. to Eq. 5.24.) applied to the particles at each end of the link element (See Fig. 5.16. repeated below).

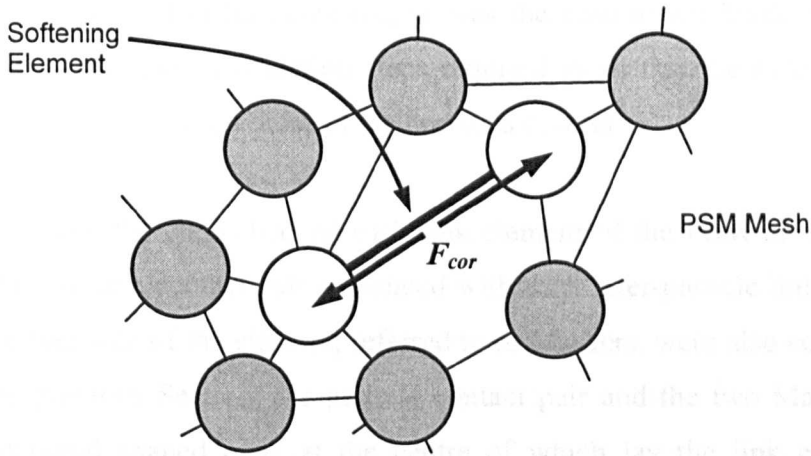


Fig. 5.16. Diagram Showing Self Equilibrating Out of Balance Corrective Forces Applied to Particle Pair to Redistribute Relaxation Stress to Other Parts of Bonded Particle Assembly
(Repeated from Page 225)

However, in the Mark 4 criterion, the relaxation stress was calculated in terms of the maximum principal stress and was therefore considered to act in the direction of the maximum principal stress. If corrective forces based on the total relaxation stress had been applied in the direction of the maximum principal stress, unless this aligned directly with the link element, a force couple would have been introduced to the mesh. This was an undesirable consequence and therefore, before redistribution could take place, it was necessary to calculate the component of the relaxation stress that acted in the direction of the inter-particle link element, $\Delta\sigma_{1(link)}^{\rightarrow}$. The corrective forces, F_{cor} , were then produced from this component and applied, as before, in the direction of the link element (See Eq. 5.42.).

$$F_{cor} = \Delta\sigma_{1(link)}^{\rightarrow} \cdot A_{(link)}^* \quad \text{Eq. 5.42.}$$

5.8.2. Implementation of the Mark 4 Failure Criterion

The Mark 4 failure criterion considered the total strain state in an equivalent continuum area associated with each inter-particle link element, rather than considering the uniaxial application of self-equilibrating, out of balance force dipoles to the particle contact pairs

total strain in an individual link element, as was the case in the Mark 1 and Mark 3 criteria. Due to numerous calculation steps required to do this the *FISH* routine was longer and more complex than those of the previous criteria.

Once again, the code checked each link element of the PSM mesh in turn. In addition to the particle contact pair associated with each inter-particle link element, the particles on either side of the element, referred to as Markers, were also considered. As shown in the previous Section, the particle contact pair and the two Marker particles defined a diamond shaped area, at the centre of which lay the link element under consideration (See *Fig. 5.26.* and *Fig. 5.28.*). In order to save computational effort the determination of the Markers particles associated with each inter-particle link element was carried with a separate *FISH* routine prior to running a model that employed the Mark 4 failure criterion. Each time a link element was checked, the stretches of the five elements making up the associated diamond area were calculated. A second separate *FISH* routine was then employed to calculate the strain tensors in the two triangles, making up the diamond area on either side of the link element under consideration, from the stretches in the appropriate elements. Once these strain tensors had been established it was possible to compute an average strain tensor and hence average principal strains for the diamond area associated with the link element under consideration. The strain state defined by the principal strains was then compared to a constitutive model in a similar manner to the Mark 3 criterion (See *Fig. 5.29.*). Each time the strain state in an element was found to lay beyond the failure surface, the amount by which the ultimate strain was exceeded, in the direction of the strain path, was compared to that noted for the stored current 'worst case' element. If the amount was found to be larger than that of the 'worst case' element then the current element was recorded as the new 'worst case' element. After examination of all the inter-particle link elements, the final stored 'worst case' element was considered to have failed and was removed from the PSM mesh.

Again, similarly to the Mark 3 criterion, the Mark 4 criterion took into account softening behaviour, in addition to testing for failure conditions. This was again done by modifying the strain states of link elements that were considered to have exceeded their elastic capacity. As before, the redistribution of stress was represented through the application of self-equilibrating, out of balance force dipoles to the particle contact pairs

associated with each inter-particle link element in which the strain state was found to lay beyond the yield surface, but inside the failure surface, as defined by the constitutive model (See *Fig. 5.29*). As discussed in Section 5.3. earlier in this Chapter and again in conjunction with the Mark 3 criterion (See Section 5.7.1.), these out of balance forces, referred to as corrective forces, F_{cor} , were added to the total force acting on a particle. This subsequently affected the acceleration of the particle, as computed in the Motion calculation directly following the execution of the failure criterion code in each time step (See *Fig. 5.1*). Thus, under the Mark 4 failure criterion, *Eq. 3.26*. can again be rewritten as in *Eq. 5.25*. (repeated below).

$$a^{(p)} = \frac{\sum F^{(p)} + \sum F_{cor}^{(p)}}{m^{(p)}} \quad \text{Eq. 5.25.}$$

Once more, it may be noted that all other equations of the distinct element calculation remained unaltered.

The *FISH* routine for the Mark 4 failure criterion can be summarised as shown in *Eq. 5.35*. The actual *FISH* code is presented in Section AIII.8. of Appendix III. and, where possible, variable names employed in the code, are shown beside the relevant process in the flow chart below.

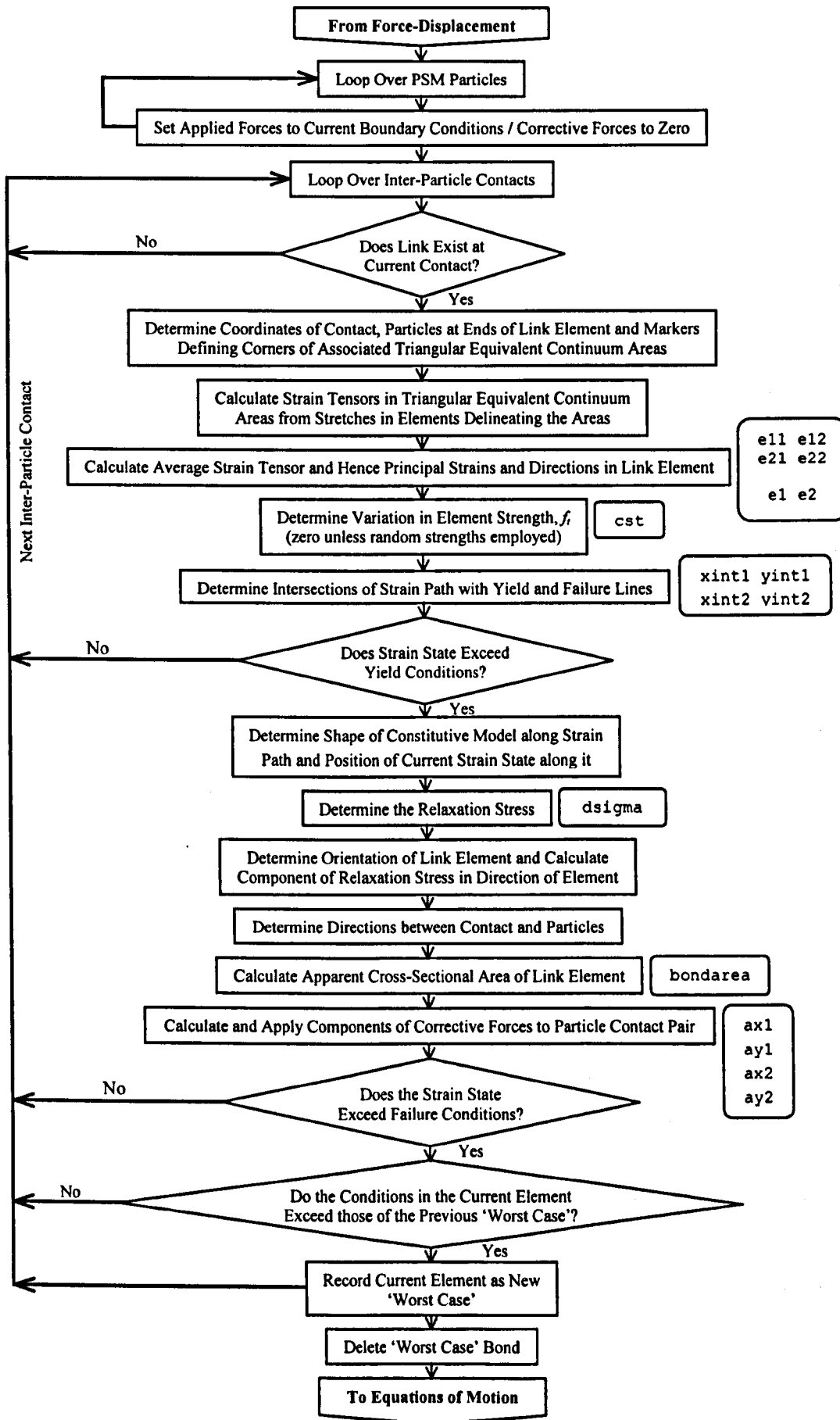


Fig. 5.30. Flow Chart Summarising FISH Code for Mark 4 Failure Criterion

5.8.3. Mark 4 Failure Criterion Benchmark Study

The Mark 4 failure criterion, as described above, was applied to the Two-Dimensional Uniaxial Benchmark Model, discussed in Section 5.4., and the following numerical studies, detailed in Table 5.5. below, were carried out.

Displ.	Element Length h (m)	Young's Modulus E (MPa)	Poisson's Ratio ν	Fracture Energy G_f (N/m)	Softening Modulus E_s (MPa)	Material Strength f_t (N/mm ²)	Prescribed Velocity (m/s)
x	0.50	1785	0.25	200	356.38	0.48750	5×10^{-8}
x	0.25	1785	0.25	200	162.02	0.48750	5×10^{-8}
x	0.10	1785	0.25	200	61.46	0.48750	5×10^{-8}
y	0.50	1785	0.25	200	356.38	0.48750	5×10^{-9}
y	0.25	1785	0.25	200	162.02	0.48750	5×10^{-8}
y	0.10	1785	0.25	200	61.46	0.48750	5×10^{-8}

Table 5.5. Details of Two-Dimensional Uniaxial Model Studies with Mark 4 Failure Criterion

From the numerical studies listed above, the following load-displacement results were obtained (See *Fig. 5.31.* and *Fig. 5.32.*).

As can be seen from the load-displacement plots shown above, there is a significant difference between the general shape of the curves developed for prescribed displacement in the x -direction and those for prescribed displacement in the y -direction. Those describing displacement in the x -direction (See *Fig. 5.31.*), once again, show results that are generally as would be expected for an elastic-softening failure criterion. As would be further expected, given the success of the Mark 3 criterion, these curves also show mesh size objectivity and all three plots reach failure at exactly the same displacement, irrespective of link element size.

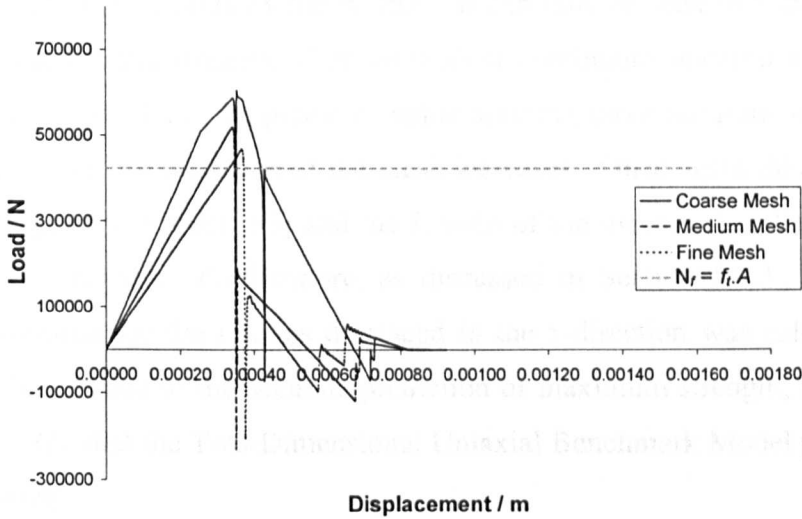


Fig. 5.31. Load-Displacement Plots for the Two-Dimensional Uniaxial Benchmark Model with the Mark 4 Failure Criterion and Prescribed Displacement in the x-direction

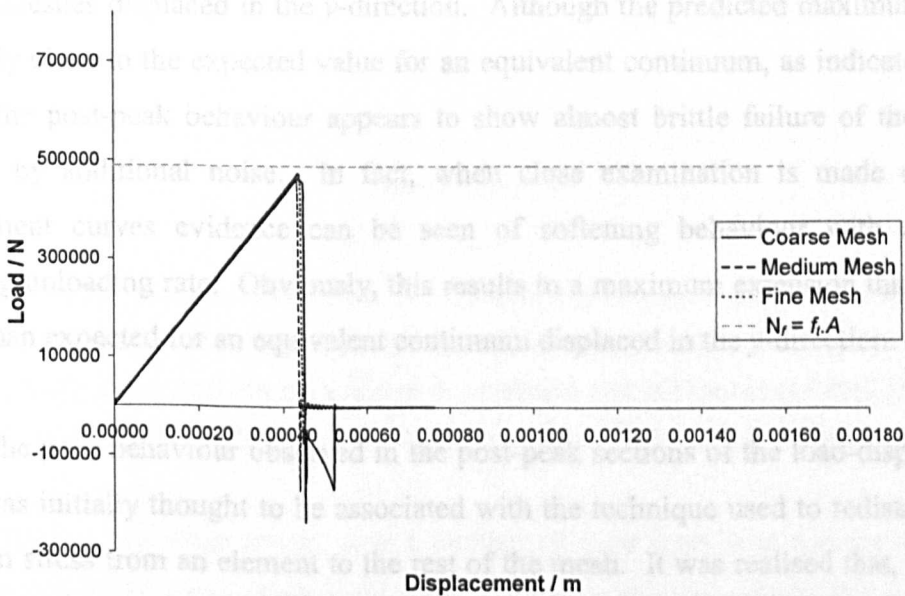


Fig. 5.32. Load-Displacement Plots for the Two-Dimensional Uniaxial Benchmark Model with the Mark 4 Failure Criterion and Prescribed Displacement in the y-direction

As with previous sets of results, these were also compared with the expected values of maximum load capacity and maximum mesh extension for an equivalent continuum material. As before, the maximum expected load capacity for the meshes is indicated

on the load-displacement plots by the N_f line. It can thus be seen that the plots for x -displacement predict the strength of an equivalent continuum material very well. In addition, it can be noted that the predicted value becomes more accurate, in comparison to the N_f line, as the discretisation of the mesh increases. Once again this is consistent with the findings of van Vliet [95] and the L ratio of the meshes (See Sections 5.5.3., 5.6.3. and 5.7.3. above). Furthermore, as discussed in Section 5.7.3., the expected maximum extension for the meshes displaced in the x -direction was calculated to be 0.000821m. In addition to the accurate prediction of maximum strength, it can also be seen, in Fig. 5.31., that the Two-Dimensional Uniaxial Benchmark Model predicted this value very closely.

Although, as described above, the results, produced with the Mark 4 failure criterion, for prescribed displacement in the x -direction, show mesh size objectivity and predict equivalent continuum behaviour very accurately it can be seen that there is considerable noise in the post-peak behaviour. This is even more apparent in the plots from the meshes displaced in the y -direction. Although the predicted maximum load is reasonably close to the expected value for an equivalent continuum, as indicated by the N_f line, the post-peak behaviour appears to show almost brittle failure of the meshes followed by additional noise. In fact, when close examination is made of the y -displacement curves evidence can be seen of softening behaviour with a rapidly increasing unloading rate. Obviously, this results in a maximum extension that is much shorter than expected for an equivalent continuum displaced in the y -direction.

The poor behaviour observed in the post-peak sections of the load-displacement curves was initially thought to be associated with the technique used to redistribute the relaxation stress from an element to the rest of the mesh. It was realised that, while the total strain state and consequently the predicted elastic response stress, were determined from continuum principles, the excess stress was redistributed on an individual element basis. Furthermore, as described above, only the component of the excess stress in the direction of the link under consideration, $\Delta\sigma_{1(\lnk)}^{\rightarrow}$, was redistributed. Consequently, if the principal strains did not align directly with the element, as was unlikely to occur, then, when the ultimate strain was exceeded and the element removed, only a portion of the total excess stress, $\Delta\sigma_1$, would have been dissipated. It was thought that the

resulting sudden release of energy, equivalent to a brittle failure, caused the noise seen in the unloading slopes of the load-displacement curves. However, closer examination of the noise events, which were characterised by sharp drops in load capacity, showed that, despite the relatively short time over which these events occurred, they developed over a number of time steps and further more the element failure, and subsequent removal from the mesh, occurred at the end of the event and not the beginning. Thus, the events were the cause and not the effect of a bond failure (See Fig. 5.33.).

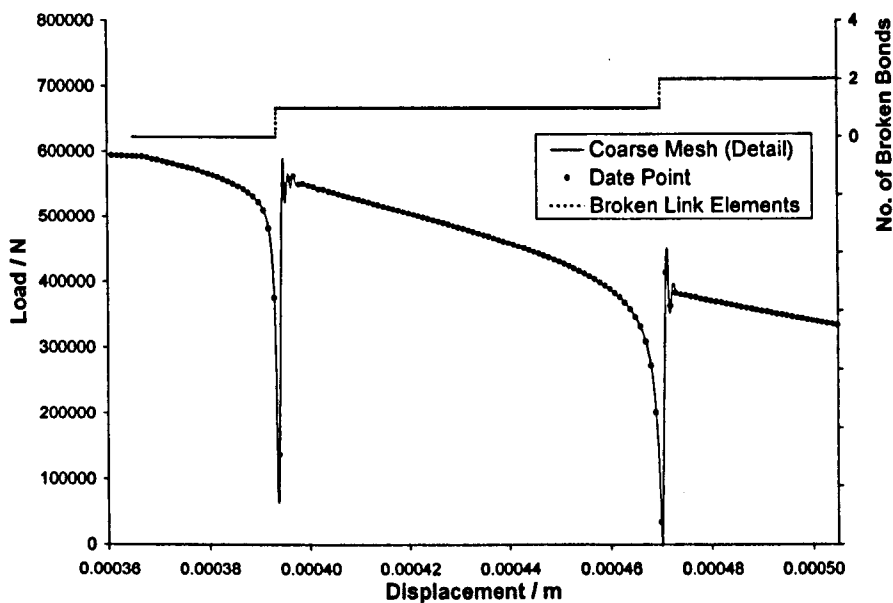


Fig. 5.33. Load-Displacement Plot for the Two-Dimensional Uniaxial Benchmark Model with the Mark 4 Failure Criterion and Prescribed Displacement in the x -direction Showing Typical Detail of Noise Events in the Post-Peak Behaviour Overlaid with Plot of Number of Failed Elements-Displacement (NB - The Data Points are Marked Every 20th Time Step)

The development of these events over a number of time steps with rapidly increasing unloading rate is the same effect seen in the curves for displacement in the y -direction, as discussed above. The difference being that the meshes displaced in the y -direction lose all of their load carrying capacity whereas the meshes displaced in the x -direction recover at least some of their strength and continue to unload. This is again probably, at least partially, an effect of the mesh configuration. As described previously, the elements in the meshes displaced in the y -direction are all 'diagonal' elements and consequently failed at the same time. The meshes displaced in the x -direction consisted of a combination of 'diagonal' elements and elements aligned in the x -direction.

Observation of the failure process of these meshes showed that the 'diagonal' elements failed first leaving the elements aligned in the x -direction. This indicated a directional bias in the Mark 4 failure criterion, which was the kind of behaviour that the continuum approach was intended to prevent.

After further consideration, it was concluded that both the noise in the load-displacement curves and the directional bias were caused by the technique that was employed to dissipate excess stress from softening link elements. This was not due to brittle failures of elements from which the excess stress had only partially been dissipated, as initially thought, but was an effect of the feedback from the corrective forces, applied in order to redistribute the excess stress, to the triangles in which strain was measured.

Evidence for this was found after further examination of the noise events where it became apparent, from the rapidly increasing unloading rates, that the corrective forces were becoming larger and larger. This implied that a cyclic effect existed between the redistribution of excess stress and the continuum total strain state whereby the corrective forces, applied to the particles at each end of the link element, further deformed the triangles associated with that link element and caused an increase in the strain, which consequently led to larger corrective forces. The speed with which this occurred implied that this was an uncontrolled feedback.

This effect seemed to become even more significant after the failure and removal of some elements. This occurred when, situations developed where the continuum total strain was measured from the separation between sets of three particles that were no longer bonded. With at least two of the particles unbonded and free to move apart, the apparent strain in the triangle could become very large. Furthermore, redistribution of the excess stress only served to increase the separation between these free particles since there were no link elements to ensure their movement as a combined unit, thereby perpetuating the situation.

This behaviour was further confirmed by the sections of the curves, noticeable in both the sets of load-displacement plots, where the load becomes negative, implying that more force was being redistributed than was being applied. Obviously, this is not a realistic situation but it is interesting to note that, at least for the meshes displaced in the

x -direction, the situation returned to normal as the link elements progressively failed and in the end, the desired result, for an equivalent continuum material, was very accurately reproduced. However, in order to develop a completely general model that could capture elastic-softening behaviour in the post-peak regime, under any loading conditions, it was necessary to solve the problems associated with redistribution of the excess stress. It was hoped to do this by considering a redistribution of stress on the basis of continuum principles, similar to those applied in order to calculate the continuum total strain in a link element, rather than on the basis of an individual link element, as was considered in the Mark 4 criterion. This is further discussed in the following Sections.

An additional note, which should be made in regard to the Mark 4 criterion, concerns the methods applied in order to calculate a continuum representation of the total strain in an inter-particle link element. As discussed previously, the strain in the triangles associated with a particular link element are computed from the current stretches of the sides of those triangles in consideration of their current geometry. It is recognised that this calculation is synonymous with an Eulerian strain measurement. It is further recognised that the calculation of stresses from these strains, via the simple, two-dimensional plane elasticity relationships, (See *Eq. 4.21. to Eq. 4.26.* above) results in a Cauchy stress regime. While this is a method consistent with the approach employed by the explicit, time stepping dynamic relaxation solver associated with the PFC^{3D} DEM code, it is only accurate for a continuum that experiences small strains. For the purposes of the work carried out for this thesis, the assumption of small strains is considered to be sufficient and while the limitations of the stress-strain measurement technique are acknowledged, it was not felt necessary to apply any alternative schemes. This topic is further explored in Chapter 7, Section 7.2.2.

It is also worth noting that the Mark 4 failure criterion has similarities to a strain based rotating crack model applicable in FE frameworks. Both the rotating crack model and the Mark 4 failure criterion evaluate the principal strains in order to determine whether failure conditions exist. However, the rotating crack model considers a fracture to open in the direction of the maximum principal strain whereas the Mark 4 failure criterion is limited to opening a fracture in the direction of the inter-particle link elements, which do not often align with the principal directions.

5.8.4. Mark 4 - Conclusion

In summary, it can be said that the Mark 4 failure criterion was generally very successful in reproducing the elastic-softening behaviour of a continuum material. This was particularly true in the case of meshes displaced in the x -direction, the studies of which produced accurate results for both predicted maximum load and predicted maximum extension. Furthermore, as was expected from the results of the studies involving the Mark 3 criterion (See Section 5.7.3.), the Mark 4 criterion produced results that were independent of the discretisation of the mesh.

As discussed in the previous Section, it was also seen, despite the overall accuracy of the results, that there was considerable noise in the post-peak behaviour of failure criterion. This was seen to be worse under y -displacement than under x -displacement. It was concluded that this noise was a consequence of the technique employed to redistribute excess stress from softening links to elsewhere in the particle assembly. While the total strain in an element was calculated from an equivalent continuum area associated each link element, the stress redistribution was carried out on an individual element basis and it was felt that these two schemes were not compatible.

Furthermore, it was seen that while the calculation of the continuum total strain in an inter-particle link was accurate under elastic conditions the process became less accurate as fractures developed and, for some elements, strain was measured across an open fracture. It was felt that the relatively large displacements associated with opening fractures led to anomalous strain calculations, which consequently resulted in anomalous stress redistributions and a self-perpetuating inaccuracy.

In order to solve these problems and improve the unloading behaviour of the Mark 4 criterion it was therefore desired to develop a method for redistributing excess stress in a link element over the whole continuum area from which the strain was calculated. The development of such a model, designated the Mark 5 failure criterion, is discussed in the following Section.

5.9. Mark 5 - Failure Criterion

(Modified Softening, Continuum Total Strain Criterion)

5.9.1. Theory of the Mark 5 Failure Criterion

As discussed above it was the objective of the Mark 5 failure criterion to overcome the problems, which were encountered with the Mark 4 failure criterion, in association with the redistribution of excess stress during softening of the link elements (See Section 5.8.3.).

The calculation of the continuum total strain in an inter-particle link element and the failure criterion itself were exactly as they were for the Mark 4 criterion (See Section 5.8.1. and *Eq. 5.39. to Eq. 5.41.*). Consequently, the calculation of the relaxation stress, $\Delta\sigma_1$, in the direction of the maximum principal stress, in a softening link element was also exactly the same as for the Mark 4 criterion. However, the strategy employed in order to dissipate the excess stress from the link was significantly modified.

Rather than returning the excess stress to the mesh via corrective forces applied in the link element itself, as was the case for the Mark 3 and Mark 4 failure criteria (See *Fig. 5.16. and Eq. 5.21. to Eq. 5.24.*), the Mark 5 criterion returned the relaxation stress via the whole equivalent continuum area defined by the two triangles associated with the link element under consideration (See *Fig. 5.26.*). To do this it was assumed, in a reversal of the procedure applied in the calculation of the continuum total strain in the link element, that the relaxation stress, $\Delta\sigma_1$, calculated in the link element, was also an averaged value acting throughout each of the associated triangles. It was then possible to treat the triangles on either side of the link element in a similar fashion to constant strain finite elements. Given this analogy, out of balance nodal forces, equivalent to the excess stress, could be calculated for both of the triangles, as shown for triangle (A,B,C) in *Eq. 5.43. to Eq. 5.47.* below.

$$\{\Delta f\}^{(A,B,C)} = [K]\{\delta u\} \quad \text{Eq. 5.43.}$$

$$\therefore \{\Delta f\}^{(A,B,C)} = \left(\int_{(A,B,C)} [B]^T [D] [B] dV \right) \{\delta u\} \quad \text{Eq. 5.44.}$$

$$\{\varepsilon\} = [B] \{\delta u\} \quad \text{Eq. 5.45.}$$

$$\{\sigma\} = [D] \{\varepsilon\} = [D] [B] \{\delta u\} \equiv \Delta \sigma_1 \quad \text{Eq. 5.46.}$$

$$\therefore \{\Delta f\}^{(A,B,C)} = \int_{(A,B,C)} [B]^T \Delta \sigma_1 dV \quad \text{Eq. 5.47.}$$

where, $\{\Delta f\}$ are the equivalent out of balance nodal forces for a triangular element, $[K]$ is the stiffness matrix for the triangular elements, $\{\delta u\}$ are the element nodal displacements, $\{\varepsilon\}$ are the element nodal strains, $\{\sigma\}$ are the element nodal stresses, $[B]$ is the element strain matrix and $[D]$ is the element elasticity matrix.

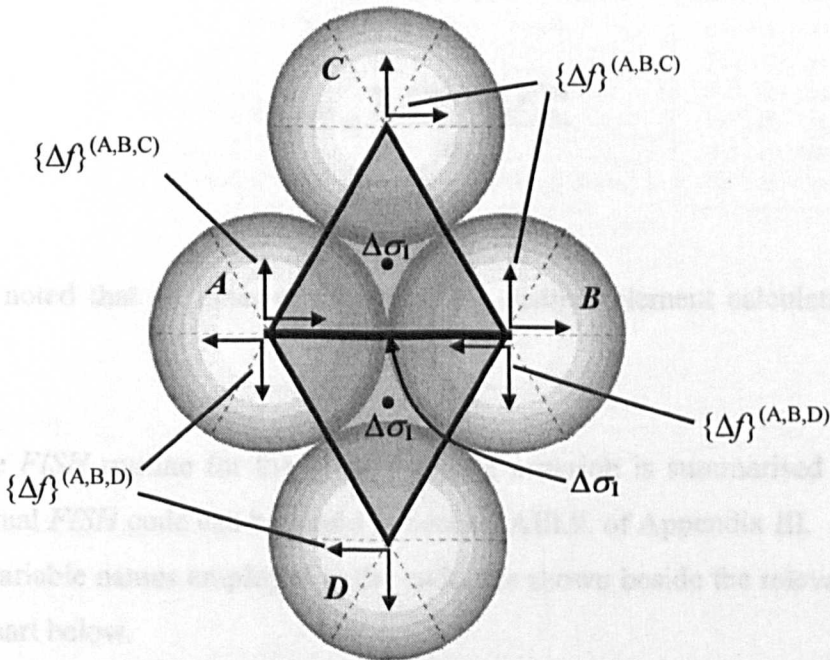


Fig. 5.34. Diagram Showing Application of Out of Balance Nodal Forces to Equivalent Continuum Triangular Elements in Order to Redistribute the Relaxation Stress

These nodal forces were then applied to the particles at the corners of the triangles under consideration (See *Fig. 5.34.* below) and in this way, the excess stress was redistributed over the whole of the equivalent continuum area associated with an inter-particle link element, to other parts of the PSM mesh.

5.9.2. Implementation of the Mark 5 Failure Criterion

The *FISH* routine employed for the implementation of the Mark 5 failure criterion was essentially the same as that of the Mark 4 failure criterion (See Section 5.8.2.). However, in accounting for element softening behaviour, redistribution of stress was represented by the application of self-equilibrating, out of balance forces, not just to the particle contact pairs but also to the Marker particles associated with each inter-particle link element that was found to have exceeded its maximum elastic strain (See *Fig. 5.34.* above). Once again, these out of balance forces were referred to as corrective forces, F_{cor} (See Section 5.7.1.), and were added to the total force acting on a particle, subsequently affecting the acceleration of the particle, as computed in the Motion calculation directly following the execution of the failure criterion code in each time step (See *Fig. 5.1.*). Therefore, *Eq. 5.25.*, rewritten from *Eq. 3.26.* and repeated below, is again applicable.

$$a^{(p)} = \frac{\sum F^{(p)} + \sum F_{cor}^{(p)}}{m^{(p)}} \quad \text{Eq. 3.26.}$$

It may be noted that all other equations of the distinct element calculation remained unaltered.

The *FISH* routine for the Mark 5 failure criterion is summarised in *Fig. 5.35.* and the actual *FISH* code can be found in Section AIII.9. of Appendix III. Again, where possible, variable names employed in the code, are shown beside the relevant process in the flow chart below.

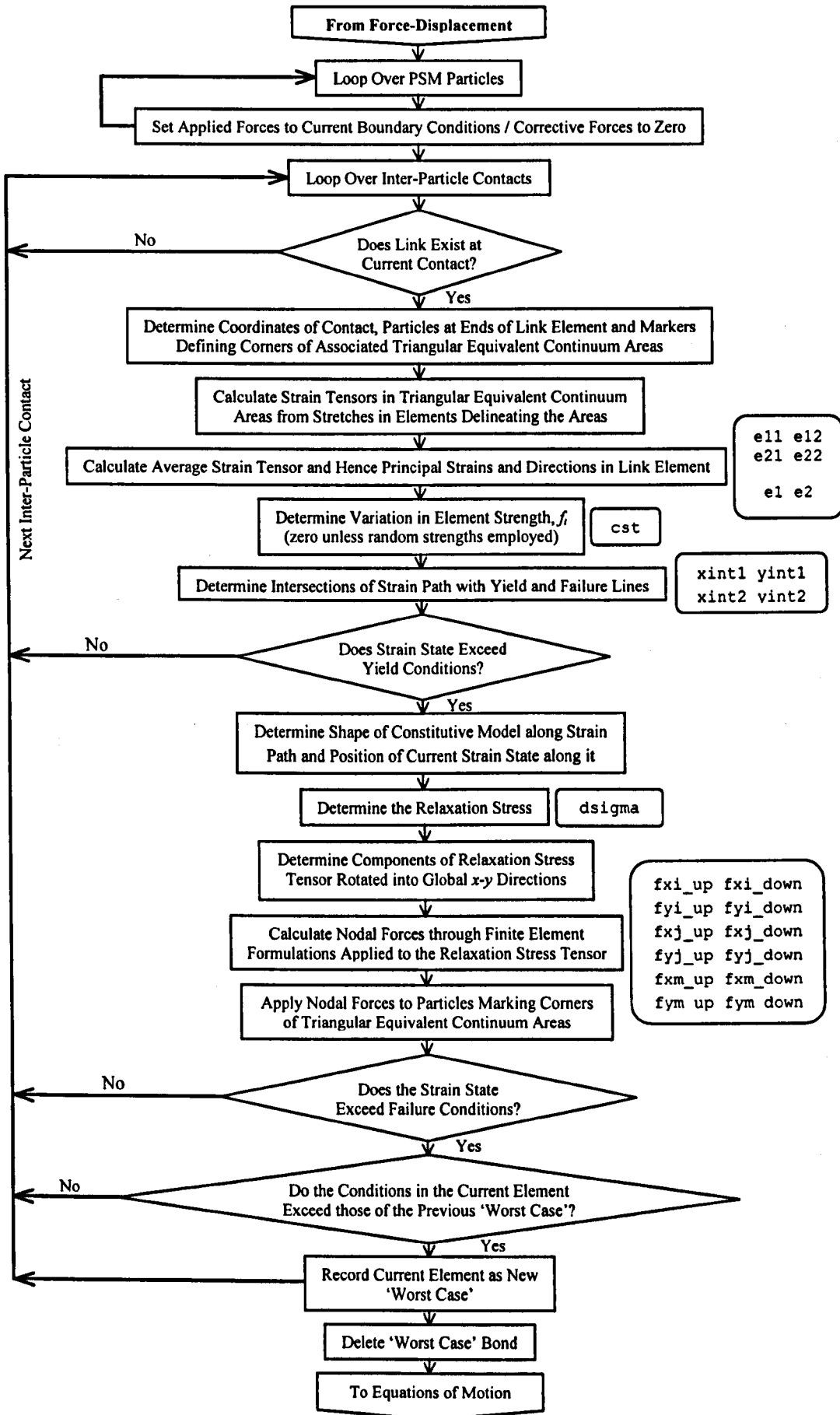


Fig. 5.35. Flow Chart Summarising FISH Code for Mark 5 Failure Criterion

5.9.3. Mark 5 Failure Criterion Benchmark Study

The Mark 5 failure criterion was then applied to the Two-Dimensional Uniaxial Benchmark Model and the numerical studies carried with the Mark 4 failure criterion were repeated. The detail of these studies is given in Table 5.6. below.

Displ.	Element Length h (m)	Young's Modulus E (MPa)	Poisson's Ratio ν	Fracture Energy G_f (N/m)	Softening Modulus E_s (MPa)	Material Strength f_t (N/mm ²)	Prescribed Velocity (m/s)
x	0.50	1785	0.25	200	356.38	0.48750	5×10^{-8}
x	0.25	1785	0.25	200	162.02	0.48750	5×10^{-8}
x	0.10	1785	0.25	200	61.46	0.48750	5×10^{-8}
y	0.50	1785	0.25	200	356.38	0.48750	5×10^{-8}
y	0.25	1785	0.25	200	162.02	0.48750	5×10^{-8}
y	0.10	1785	0.25	200	61.46	0.48750	5×10^{-8}

Table 5.6. Details of Two-Dimensional Uniaxial Model Studies with Mark 5 Failure Criterion

From the numerical studies listed above, the following load-displacement plots were produced (See *Fig. 5.36.* and *Fig. 5.37.*).

As can be seen from the load-displacement plots shown above, the general form of the curves does not as closely resemble the shape expected for elastic-softening behaviour as those from the studies with the Mark 4 failure criterion did. This is particularly the case for the plots concerning displacement in the x -direction. The plots describing displacement in the y -direction are very similar to those produced by the Mark 4 criterion, although neither criterion produced an accurate representation of elastic-softening behaviour in this direction (See *Fig. 5.31.* & *Fig. 5.32.* and *Fig. 5.36.* & *Fig. 5.37.*).

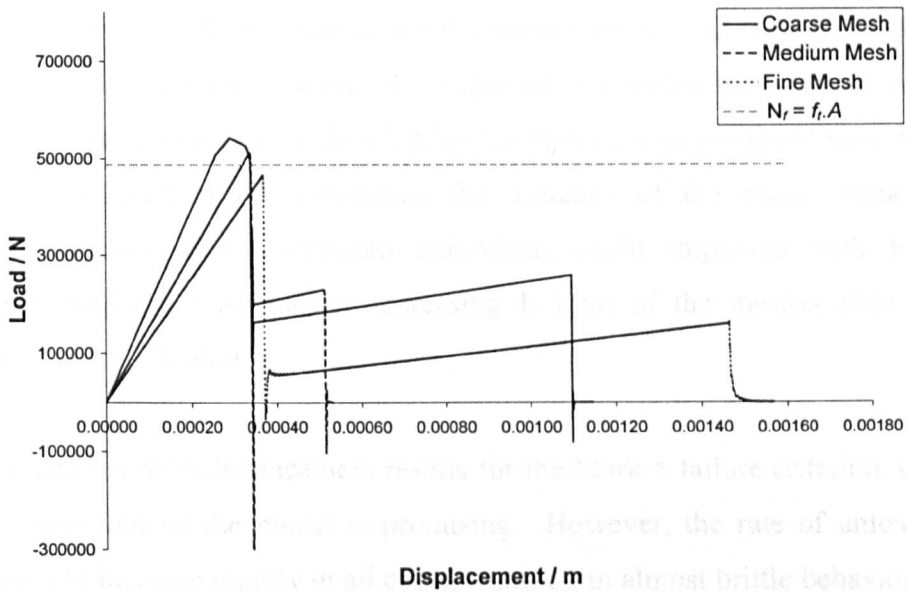


Fig. 5.36. Load-Displacement Plots for the Two-Dimensional Uniaxial Benchmark Model with the Mark 5 Failure Criterion and Prescribed Displacement in the x-direction

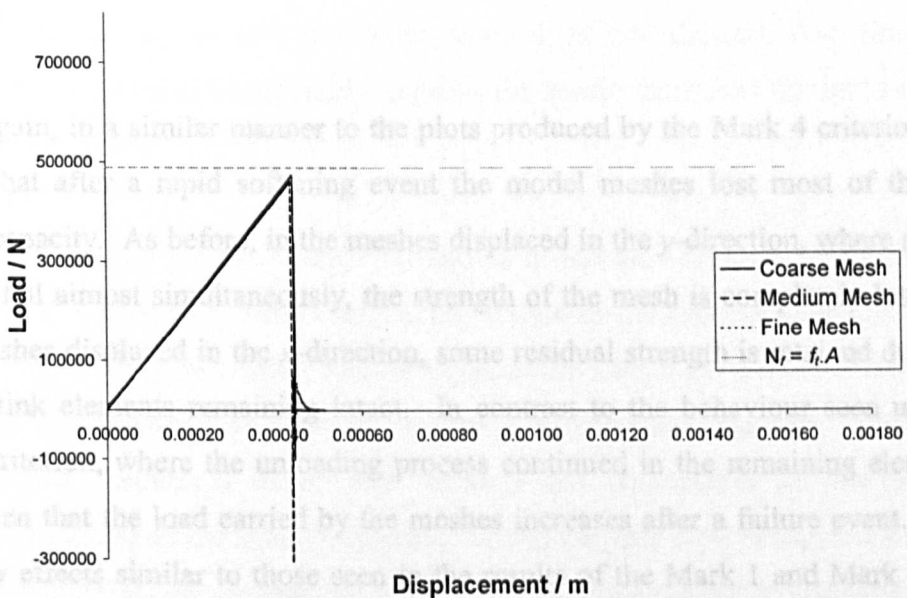


Fig. 5.37. Load-Displacement Plots for the Two-Dimensional Uniaxial Benchmark Model with the Mark 5 Failure Criterion and Prescribed Displacement in the y-direction

As in the previous studies conducted with the various failure criteria discussed in the preceding Sections, the elastic responses for displacement in both the x and y -directions show good results and furthermore, the expected maximum load for an equivalent continuum material, indicated in the plots by the N_f line, was predicted very well. For the meshes displaced in the x -direction the accuracy of the elastic behaviour, in comparison to equivalent continuum behaviour, again improves with increasing discretisation and the consequently increasing L ratio of the meshes (See Sections 5.5.3., 5.6.3. and 5.7.3. above).

As with the load-displacement results for the Mark 4 failure criterion, the initial post-peak behaviour of the model is promising. However, the rate of unloading can again be seen to increase rapidly in all cases, resulting in almost brittle behaviour. As in the previous studies, this behaviour appears to be associated with an uncontrolled feedback cycle between the corrective forces, in this case nodal forces, applied in order to redistribute the relaxation stress, and the continuum total strain measured in the inter-particle link element. It can therefore be seen that, although the results produced by the Mark 5 criterion are different to those produced by the Mark 4 criterion, the problems associated with stress redistribution during softening of the link elements have not been overcome.

Again, in a similar manner to the plots produced by the Mark 4 criterion, it can be seen that after a rapid softening event the model meshes lost most of their load carrying capacity. As before, in the meshes displaced in the y -direction, where all of the elements fail almost simultaneously, the strength of the mesh is completely lost, while, in the meshes displaced in the x -direction, some residual strength is retained due to one or more link elements remaining intact. In contrast to the behaviour seen under the Mark 4 criterion, where the unloading process continued in the remaining elements, it can be seen that the load carried by the meshes increases after a failure event. This is caused by effects similar to those seen in the results of the Mark 1 and Mark 2 failure criteria (See *Fig. 5.5.*, *Fig. 5.12.* and *Fig. 5.13.*) where, due to the method of calculating stress, or in this case the total strain, in the remaining link elements, an extension, far greater than would be expected for an equivalent continuum material, is required to fail them.

One further possible explanation that was considered for the poor unloading behaviour shown by the Mark 5 criterion was the assumed characteristic length for the PSM mesh. As mentioned previously, it was initially assumed that the characteristic length, h , would be equal to the initial inter-particle link length. However, given that the Mark 5 criterion considers an equivalent continuum 'element' consisting of the triangles on either side of an inter-particle link it was felt that it might have been more appropriate to choose a characteristic length based on this area. Clearly, this would also apply to the Mark 4 criterion since the same approach is taken for the calculation of the continuum total strain in a link element.

To test this hypothesis, a square was considered, the area of which was equal to the area of the 'diamond' formed by the two triangles associated with a link element. A characteristic length was then set equal to the length of the side of this square. This gave a value for h of $\frac{\sqrt{3}}{2}$ times the initial length of the inter-particle link. However, when the coarse mesh run for displacement in the x -direction, shown in *Fig. 5.36* above, was repeated with the new value of h no significant difference was seen in the load-displacement behaviour of the mesh. Various other choices for h are possible, such as the diameter of a circle of area equal to that of the 'diamond' element, however, given the results of the test discussed here, it is not thought that altering the characteristic length will significantly improve the results produced by the Mark 4 and Mark 5 failure criteria.

In addition to the poor behaviour shown in the load-displacement plots, it can also be noted that some dynamic effects are visible in the form of oscillations in the curves. This effect is particularly noticeable in the fine mesh curves. This is indicative that the applied velocity was too high to develop a quasi-static analysis. These effects were however considered minor and certainly not responsible for the unloading behaviour produced by the Mark 5 criterion. Given the very slow computational rate of the model caused by the complexity of the *FISH* code for the Mark 5 criterion, it was not considered necessary to repeat the numerical runs with a lower applied velocity.

5.9.4. Mark 5 - Conclusions

From the results discussed above it can be concluded that, as would be expected from the results of previous studies, the Mark 5 failure criterion produced accurate pre-peak and initially promising post-peak elastic-softening behaviour in the PSM. However, it was also clear that it made no significant improvements to the reproduction of softening behaviour over the results produced by the Mark 4 failure criterion. Furthermore, it can be seen that although the Mark 4 criterion was able to accurately predict the extension of an equivalent continuum material the Mark 5 criterion was entirely unable to do so. It was apparent that, despite the adopted continuum approach to the redistribution of the excess stress in an element, the Mark 5 criterion suffered from the same problems seen in the Mark 4 criterion, namely an uncontrolled feedback between the corrective forces and the continuum total strain in a link element, resulting in 'runaway' softening of the meshes.

As yet, no satisfactory interpretation has been found to explain this behaviour, which was seen in the results produced by both the Mark 4 and Mark 5 failure criteria. However, the problem seems to relate to the continuum total strain in a link element, as calculated from the continuum area associated with that link element. More particularly, it seems to relate to the modification of the continuum total strain by the redistribution of excess stress through the application of forces either at the nodes, as in the Mark 5 criterion, or in the element itself, as in the Mark 4 criterion. Further investigation will be required in order to establish the precise nature of this relationship and to find an appropriate solution to the redistribution of excess stress from the softening link elements, which will allow an accurate representation of elastic-softening behaviour, in an equivalent continuum material, to be modelled by the PSM.

5.10. Summary

In the preceding Sections, the development of five failure criteria for the PSM was presented in detail. Each of these criteria was applied to a simple two-dimensional, uniaxial benchmark model and the results of the studies conducted were also presented and discussed in detail.

The first criterion was developed in a total strain formulation and considered the uniaxial extension of individual link elements. As would be expected, this was shown to produce results consistent with the deformation of a lattice- or truss-like framework with purely elastic-brittle behaviour. However, the ultimate objective was to employ the PSM to model fracturing of an equivalent continuum material. In order to achieve this, the second model therefore applied continuum principles to the failure criterion by considering the internal stress in the PSM mesh. As was again to be expected, this showed behaviour much closer to that of an equivalent continuum material than that produced by the first criterion. However, both the Mark 1 and Mark 2 models were purely elastic-brittle criteria and as such showed behaviour that was dependent on the mesh discretisation.

In order to develop a completely general model, that would produce results independent of the link element size, the third criterion applied elastic-softening behaviour, where softening behaviour was dependent on the mesh element size, and thereby accounted for fracture energy dissipation during failure. For simplicity, this was constructed in the uniaxial total strain formulation in a similar way to the first criterion. This was shown to produce excellent results but, as would be expected, these were again representative of a lattice-like framework and not of an equivalent continuum material. Once again, in order to produce the desired behaviour a fourth criterion was developed that employed a continuum approach. However, rather than considering the internal stress state in the mesh, a continuum total strain approach was developed that looked into an equivalent continuum area associated with each of the inter-particle link elements. This produced some reasonable results in comparison with those expected for an equivalent continuum material but problems were encountered with the redistribution of excess stress to the PSM mesh. The Mark 5 criterion was developed in an attempt to solve this problem by redistributing the excess stress over the associated continuum area rather than in only the link element itself but this proved not to solve the problems and a solution has yet to be found.

In general, it can be said that some success was had in developing fracture criteria for the PSM and reproducing the expected behaviour for an elastic-brittle material both in the form of a lattice-like structure and of an equivalent continuum material. The criteria also successfully reproduced the more general elastic-softening

behaviour of a lattice-like structure and demonstrated mesh size objectivity. However, it proved difficult to develop this behaviour in terms of an equivalent continuum material and, despite the development and adoption of several approaches, further investigation will be required in this area.

Given the findings discussed above, the work described in the following Chapter will continue the development of the combined modelling framework and look into more realistic multi-phase fracture benchmark models where fracturing is driven by fluid pressure. The basic methods discussed in detail in Chapter 4 will be applied in conjunction with the fracture criteria discussed in this Chapter. Although consideration will be given to the Mark 4 and 5 criteria, the emphasis will be on the Mark 1, 2 and 3 criteria, which are known to give accurate results, although not always for an equivalent continuum material. The results of these combined benchmark models will be presented and discussed in detail along with any conclusions that are drawn.

Chapter 6:

Coupled Hydraulic Fracture

Benchmark Models

6.1. Introduction

The work discussed in the preceding Chapters has been concerned with the development of the Particle Solid Model (PSM) and the Particle Fluid Model (PFM) and the validation of the behaviour of these models, through simple benchmark studies. As discussed previously, these models were found to produce satisfactory results for the examined problems. The work discussed in this Chapter concerns the application of the PSM and PFM to more specific benchmark models in order to test their ability to reproduce the basic behaviour of common geomechanical problems.

Two benchmark studies will be discussed. The first of these will look at the simple propagation of a hydraulically driven fracture in a continuous rock matrix under various loading conditions and with various fracturing criteria applied. The general set-up of the model will be described before the results of the conducted parametric studies are presented and discussed in detail. Conclusions will then be drawn.

The second study will look into a coupled fracture problem where the fracturing of a continuous rock matrix, similar to that studied in the first benchmark model, will be driven by a high pressure fluid modelled with the PFM. Again, the set-up of this model will be described before the results of a limited parametric study are presented and discussed. Finally, conclusions drawn on these results will also be presented.

6.2. Hydraulic Fracture Benchmark Model (PSM)

6.2.1. Introduction and Model Set-up

As seen from the studies presented in the previous Chapters, the PSM was shown to accurately reproduce the elastic deformation behaviour of an equivalent continuum material (See Chapter 4, Section 4.2.3.). It was further shown that elastic-brittle and elastic-softening fracture behaviour could also be accurately modelled when an appropriate failure criterion was applied to a PSM mesh (See Chapter 5). However, the studies discussed previously were conducted with very simple benchmark models and in order to further test the capabilities of the PSM it was desirable to develop a more complex benchmark model of a realistic geomechanical problem. Furthermore, given the specific aim of this work to develop a combined modelling framework (See Chapter 3, Section 3.2.), it was desirable to develop a benchmark model of a multi-phase problem. For these purposes, it was decided to construct a model similar to a two-dimensional plane strain finite element model developed by Papanastasiou [69, 70, 71, 72] and applied to the study of, amongst other factors, the effects of elasto-plastic material behaviour on hydraulic fracture propagation, in a poorly consolidated sandstone.

The benchmark model was set up as shown below (See *Fig. 6.1.* and *Fig. 6.2.*) and consisted of a PSM mesh constructed as described in Chapter 4, with an inter-particle link length of 0.24m. As can be seen below, the mesh was fixed with a symmetry boundary at one end while the other three sides were considered as stress boundaries. Forces were applied to these three boundaries on a per-unit-length basis in order to simulate confining pressures. As will be further discussed in the following Sections, confinement was applied to the Hydraulic Fracture Benchmark Model mesh at two different intensities, during the course of these studies. Numerical runs were firstly carried out under zero confinement, in order to produce experimental control results and secondly under a maximum horizontal stress, $\sigma_2 = 9.0\text{MPa}$ (in the x -direction) and a minimum horizontal stress, $\sigma_3 = 3.7\text{MPa}$ (in the y -direction). The latter values were the in situ stresses applied in the FE studies, carried out by Papanastasiou [69, 70, 71, 72], as being representative of the stress field in a sandstone reservoir formation at a depth of 1500m.

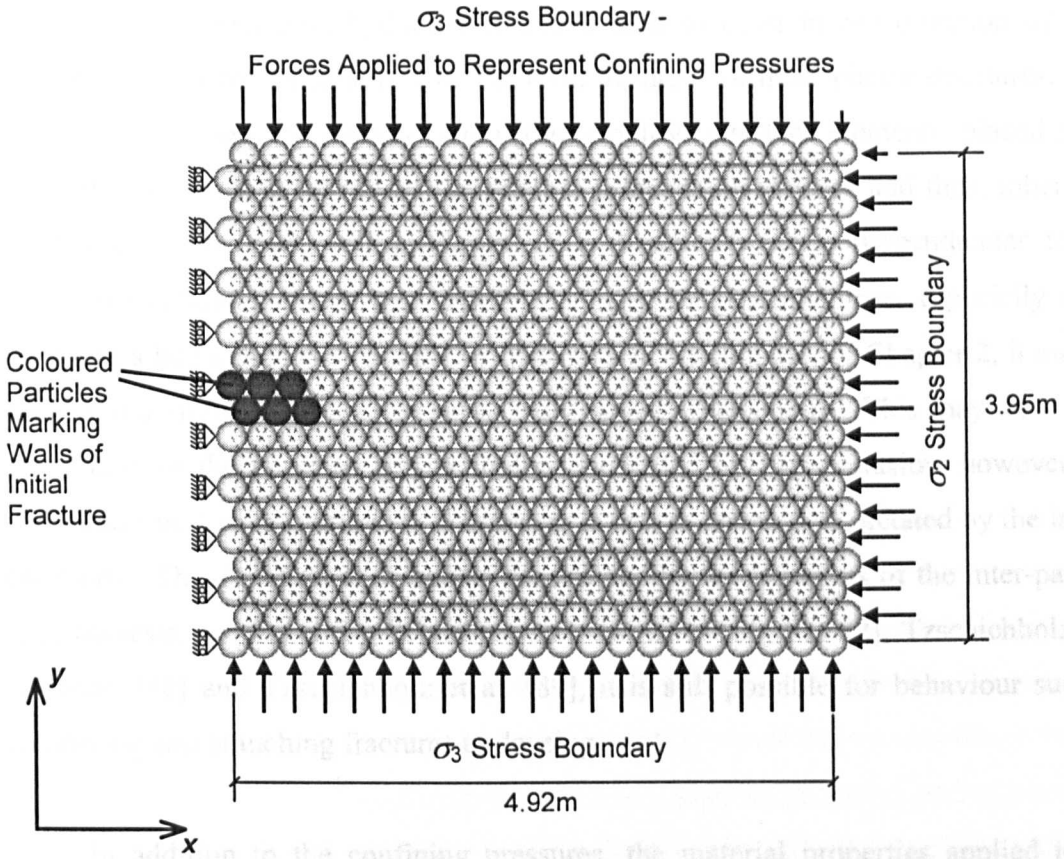


Fig. 6.1. Diagram Showing Set-up of Hydraulic Fracture Benchmark Model Mesh

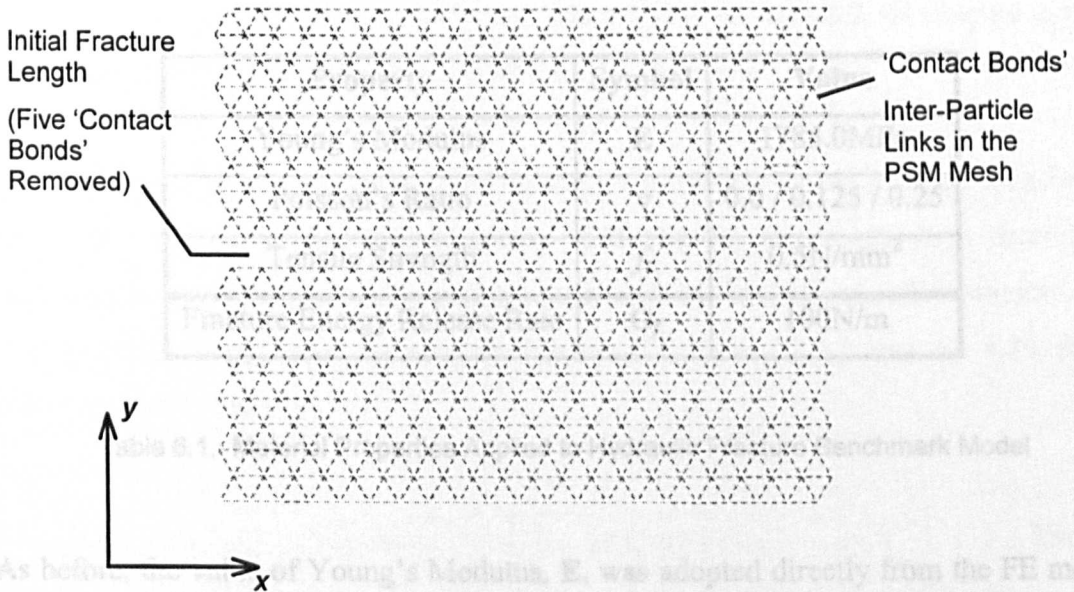


Fig. 6.2. Diagram of Initial Hydraulic Fracture Benchmark Model Mesh Showing Only Inter-Particle Link 'Contact Bonds' for Clarity

As mentioned previously, hydraulic fractures tend to open in the direction of least resistance and therefore usually take the form of large, vertical, planar structures. The FE model, developed by Papanastasiou [69], employs interface elements, placed along the centre of the mesh, to model the fracture propagation process and thus, inherently assumes that the crack will propagate in a direction exactly perpendicular to the minimum horizontal stress, σ_3 . While this may be generally true, especially for a fracture in a homogeneous material, as discussed in Section 2.2. of Chapter 2, it may be considered a simplification in terms of truly realistic behaviour. This may have been appropriate for the purposes of the studies conducted by Papanastasiou, however, the PSM makes no such assumption. Fracturing is free to develop as dictated by the in situ conditions. This freedom is of course constrained by the locations of the inter-particle links, however, as shown by Schlangen and van Mier [80, 81, 82], Tzschichholz and Herrmann [88] and Tzschichholz et al. [89], it is still possible for behaviour such as meandering and branching fractures to develop.

In addition to the confining pressures, the material properties applied to the Hydraulic Fracture Benchmark Model were also taken from the FE studies conducted by Papanastasiou [69, 70, 71, 72]. These are listed in Table 6.1. below and it can be noted that they are similar to the properties applied in the Two-Dimensional Uniaxial Benchmark Model employed in Chapter 5 (See Chapter 5, Section 5.4.).

Property	Symbol	Value
Young's Modulus	E	1785.0MPa
Poisson's Ratio	ν	0.0 / 0.125 / 0.25
Tensile Strength	f_t	0.5N/mm ²
Fracture Energy Release Rate	G_f	100N/m

Table 6.1. Material Properties Applied to Hydraulic Fracture Benchmark Model

As before, the value of Young's Modulus, E , was adopted directly from the FE model, as was the material tensile strength, f_t . Again, the value of Poisson's ratio applied by Papanastasiou's model was 0.3, however, for plane strain conditions, the equations of Morikawa and Sawamoto [63] impose a maximum value of 0.25 (See Chapter 4,

Section 4.2.2.3.). In addition, it was intended to vary the Poisson's ratio as part of the parametric studies carried out with the Hydraulic Fracture Benchmark Model and consequently values of 0.25, 0.125 and 0.0 were chosen for Poisson's ratio.

As discussed in Chapter 5, a value for the material fracture energy release rate, G_f , was also required for the elastic-softening fracture criteria. Although, for the Two-Dimensional Uniaxial Benchmark Model a compromise value of 200N/m was applied in order to satisfy problems of practicality in running test studies, it was found that a value of 100N/m, initially chosen as being representative of a quasi-brittle material such as concrete, worked well in the Hydraulic Fracture Benchmark Model.

As mentioned above, Papanastasiou's FE model was based on the plane strain fracture geometry. While this is clearly a simplification of a complex three-dimensional process, as discussed in Section 2.2. of Chapter 2, plane strain modelling can be considered an acceptable simplification for certain fracture problems and in particular for modelling short fractures, with a low length to height ratio, that can be assumed to approach a rectangular profile in the xz -plane. For a rectangular profile such as this, it is also implicitly assumed that the fracture remains within one layer of the reservoir and is prevented from growing outside this layer by the toughness of the bounding layers and the in situ stresses present within them. Consequently, only one set of material properties need be considered. As further discussed in Section 2.2. of Chapter 2, these assumptions are similar to those made by the CGDD model.

In order to ensure plane strain behaviour in the Hydraulic Fracture Benchmark Model the values of the contact spring stiffnesses in the mesh were determined according to the plane strain equations developed by Morikawa and Sawamoto [63] through strain energy equivalence (See Chapter 4, Section 4.2.2.3. and Eq. 4.29. & Eq. 4.30. repeated below).

$$k_n = \frac{E}{\sqrt{3}(1-2\nu)(1+\nu)} \quad \text{Eq. 4.29.}$$

$$k_s = \frac{E(1-4\nu)}{\sqrt{3}(1-2\nu)(1+\nu)} \quad \text{Eq. 4.30.}$$

Furthermore, the fluid driven fracturing model, employed by Papanastasiou in the FE study, required an initial fracture length from which to begin an analysis and this was typically set at 0.5m. As can be seen in *Fig. 6.1.* above, an initial fracture length of 0.6m was also included in the Hydraulic Fracture Benchmark Model. This was not specifically a requirement of the model, however in order to initiate fracturing it was necessary to apply fluid pressure to some kind of imperfection in the mesh. This initial fracture length can therefore be viewed as a stress concentration similar to a wellbore perforation.

Fluid pressure in the fracture was implemented by applying forces on a per-unit-length basis to the particles making up the walls of the fracture (See *Fig. 6.1.* and *Fig. 6.2.* above), in a similar method to that used to apply the external confining pressures, as discussed above. The ‘fluid forces’ were increased linearly in time until an inter-particle link element was failed and removed from the mesh according to whatever failure criterion was in place (See Chapter 5). The fracture fluid pressure was then reduced, according to the ratio of the new fracture volume to the old fracture volume, in an attempt to simulate the pressure variation that would be experienced under a constant pumping rate in a realistic fracture treatment (See *Eq. 6.1.*).

$$(P_f)_t = \frac{(V_f)_{t_N}}{(V_f)_{t_{N-1}}} (P_f)_{t_{N-1}} \cong \frac{(l_f)_{t_N}}{(l_f)_{t_{N-1}}} (P_f)_{t_{N-1}} \cong \frac{(N_{link})_{t_N}}{(N_{link})_{t_{N-1}}} (P_f)_{t_{N-1}} \quad \text{Eq. 6.1.}$$

where, P_f is the fracture fluid pressure, V_f is the fracture volume, l_f is the fracture length and N_{link} is the number of broken links. The subscript t refers to the time step.

As can be seen above, this simplified scheme (*Eq. 6.1.*) firstly assumed that the fracture volume was directly related to the fracture length and furthermore that each link element, that was failed and removed, represented a fixed length of fracture growth. Therefore, in order to calculate the ratio of new to old fracture ‘volume’, it was possible to simply count the number of broken link elements. This scheme also tacitly assumed that fracture propagation was always continuous and unbroken. This was considered a reasonable assumption since, as will be seen from the results shown in the following

Sections, in cases where discontinuous fracturing occurred, the overall behaviour of the model was usually not considered to be realistic for a hydraulic fracture treatment. After the failure and removal of a link element, the recalculated 'fluid forces' were applied to all particles making up the wall of the fracture, including the new pair formed as a result of the propagation event. This method of applying force dipoles in place of removed link elements was similar to a technique applied to typical lattice models by Tzschichholz and Herrmann [88] and Tzschichholz et al. [89] (See Chapter 2, Section 2.3.2.) and was chosen for the Hydraulic Fracture Benchmark Model because, as discussed previously, it was easy to precisely control the applied fluid pressure at all times.

In a further simplification, the 'fluid force' dipoles were always applied to the particles in the y -direction (See *Fig. 6.1.*), each particle in a debonded pair receiving a positive or negative force depending on their relative positions. This technique was similar to the method of fluid pressure application employed by Bruno et al. [11], although they do not appear to have considered the application of fluid pressure within the newly opened length of a propagating fracture. If, as would be suggested by the observation that hydraulic fractures generally open in the direction of least resistance, the fractures propagated in the x -direction, then this simplification would have generally applied the fluid pressure in a direction normal to the fracture walls, as would be expected in a realistic situation. However, it was understood and accepted that, if the fracture deviated in the y -direction, some inaccuracy would be incurred, as at certain locations, particles would experience loading that could not be considered normal to the fracture wall.

An alternative method for applying the 'fluid forces' would have been to apply the force dipoles in the orientation of the link element that they replaced, as was applied in the Wellbore Stability Model developed by Davie [21]. However, although this would have been more complex to implement, generally this would still not have solved the problem of accurately applying the pressure in a direction normal to the fracture surface when it deviated in the y -direction.

Ideally, the fluid pressure should be represented by a 'follower' load system so that the 'fluid forces' always acted perpendicular to the fracture surface. In order to

implement this it would have been necessary to develop a scheme by which to determine the local orientation of the fracture surface. While this may be, in principle, quite possible, by taking into account the relative locations of neighbouring particles, it would be algorithmically very complex to implement in a freely propagating system of branching fractures. The limitations of PFC^{3D} and the associated *FISH* coding language would have made this even more difficult and very computationally expensive. Therefore, for the purposes of these studies, ‘fluid forces’ were only applied in the *y*-direction.

For the purposes of the parametric studies carried out with the Hydraulic Fracture Benchmark Model, it was assumed that the fracture fluid pressure profile was constant along the whole length of the fracture, although it was understood that this was a further, perhaps significant, simplification of the fluid behaviour. Although there are many different assumptions that can be made for the fluid pressure profile in a fracture, ranging from constant, through piecewise linear and linear drop off, to parabolic distributions and more complex polynomial profiles, (Valkó and Economides [91]), these would again be very difficult to implement in a meandering or branched fracture system in a PSM mesh. Furthermore, on examination of the fracture pressure profiles produced by Papanastasiou, with a reasonably complex fluid model, (See Fig. 6.3. below) it can be seen that the pressure is relatively constant over most of the fracture length.

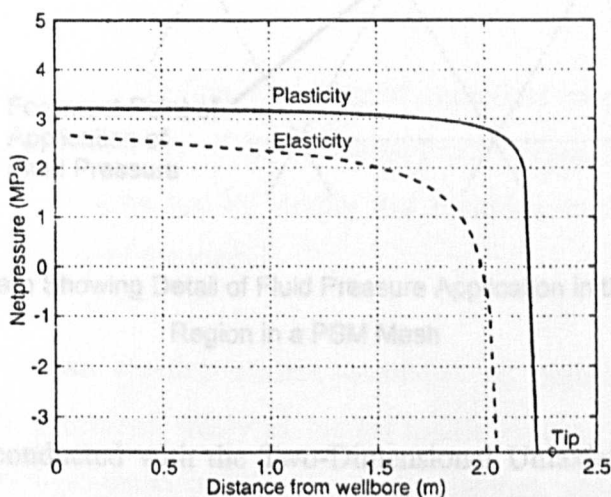


Fig. 6.3. Plot Showing Net Pressure Profiles along the Length of a Fracture

(After Papanastasiou [69])

It is therefore argued that a constant fracture pressure profile was reasonable for the purposes of this work. Despite this, a further concern would be the, generally agreed on, phenomenon known as fluid lag, whereby the fluid flowing into the fracture never reaches the tip before fracture propagation occurs, thereby resulting in a complete drop in pressure near to but not at the fracture tip. This effect can clearly be seen in Fig. 6.3. above, however, for the Hydraulic Fracture Benchmark Model it was felt that the fluid lag region could at least partially be accounted for within the length between the foremost point at which ‘fluid forces’ are applied and the actual fracture tip (See Fig. 6.4. below) and would therefore not be ‘visible’ within the applied pressure profile. The assumption of a constant pressure profile in the Hydraulic Fracture Benchmark Model can still therefore be considered valid, although, obviously, if a higher mesh discretisation were to be applied then this assumption might have to be rethought, especially in regard to the near tip zone.

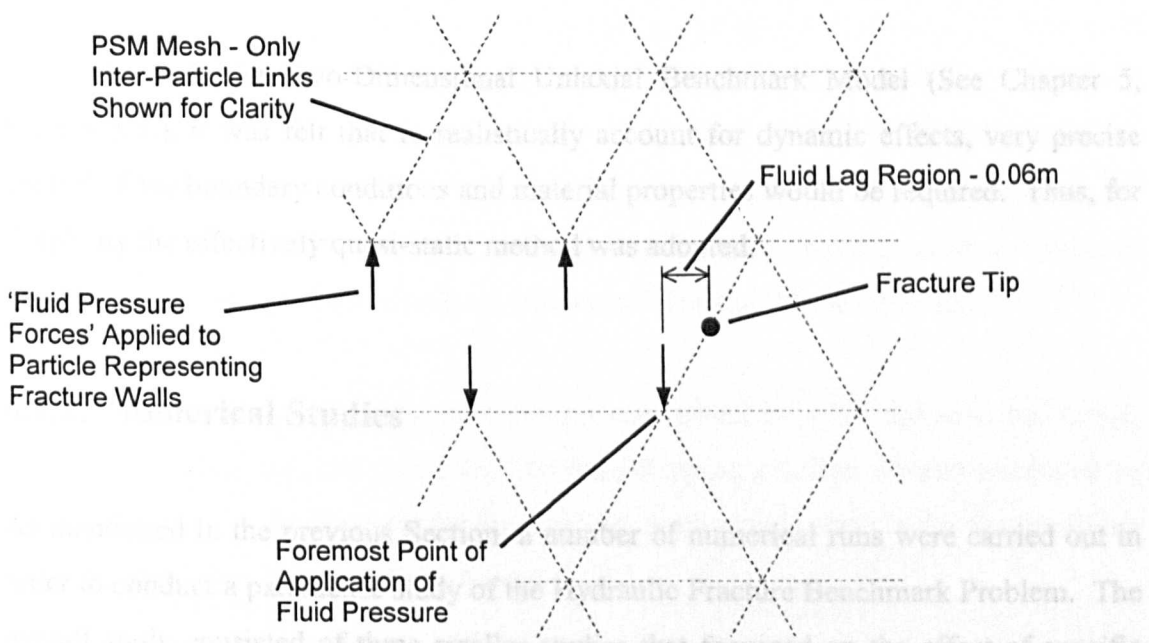


Fig. 6.4. Diagram Showing Detail of Fluid Pressure Application in the Fracture Tip Region in a PSM Mesh

As for the studies conducted with the Two-Dimensional Uniaxial Benchmark Model discussed in Chapter 5, the numerical studies run with the Hydraulic Fracture Benchmark Model were carried out as quasi-static analyses. Quasi-static behaviour was again ensured by invoking the differential density scaling function, integral to PFC^{3D},

and by applying a sufficiently slow loading rate so as to eliminate most of the dynamic effects in the mesh.

Although fracturing may be considered a dynamic process, it can be argued that it is acceptable to model hydraulic fracturing quasi-statically, since the fluid and solid phases work on very different time scales, where the fluid transport is much slower than the fracturing of the rock. The quasi-static nature of the problem modelled by the Hydraulic Fracture Benchmark Model was further implied by the assumption of complete stress redistribution between time steps, as inferred by the restriction of fracture propagation to one link element per time step. This was previously discussed in Chapter 2, Section 2.3.1. and Chapter 5, Section 5.3. In addition, the assumption of instantaneous fluid flow in the fracture, as implied by the immediate application of a 'fluid force' dipole as soon as a link element was removed, was also suggestive of a quasi-static problem.

As with the Two-Dimensional Uniaxial Benchmark Model (See Chapter 5, Section 5.4.), it was felt that to realistically account for dynamic effects, very precise control of the boundary conditions and material properties would be required. Thus, for simplicity the effectively quasi-static method was adopted.

6.2.2. Numerical Studies

As mentioned in the previous Section, a number of numerical runs were carried out in order to conduct a parametric study of the Hydraulic Fracture Benchmark Problem. The overall study consisted of three smaller studies that focussed on the effect of specific parameters on the behaviour of the model.

The first of these smaller studies consisted of eighteen numerical runs constituting a general parametric study of the Hydraulic Fracture Benchmark Model. The varied parameters were the Poisson's ratio of the material, which was equivalent to varying the ratio of normal to shear stiffness in the PSM mesh (See *Eq. 4.29.* and *Eq.*

4.30.), the confining pressure and the fracture criterion, which was chosen from the Mark 1, 2 and 3 criteria.

The second study was a more limited investigation that repeated six of the tests from the first study, several times each, while also considering the effects of a heterogeneous material by randomising the material strength throughout the PSM mesh.

The final study again consisted of numerical tests similar to those carried out in the first study but was intended to specifically investigate the capabilities of the Mark 4 and 5 failure criteria in a realistic benchmark problem.

It was the intention in each case, to run the models until a given number of inter-particle link elements, N_{fail} , had failed. N_{fail} was chosen as nineteen, assuming the fractures would propagate in the x -direction, as would be the case if the fracture opened exclusively in the direction of least resistance (See Section 6.2.1. above), in which case fractures of similar length to those in the results presented by Papanastasiou [69] would have been produced. While this was appropriate in many of the tests, as will be seen in the following Sections, some runs were stopped prior to N_{fail} link element failures as the fracture approached the boundary of the mesh. Furthermore, some runs were continued past N_{fail} element failures in order to further develop the failure behaviour.

In addition to the time taken to reach a state where N_{fail} link elements had failed, it should be noted that, due to the explicit time stepping solution scheme employed by PFC^{3D}, time had to be allowed for the mesh to reach steady state under the confining pressure before fracturing could be begun.

The numerical runs carried out for the various parametric studies, as discussed above, are listed in detail below (See Table 6.2. and Table 6.3.).

Test Group	Run No.	Fracture Model	Young's Modulus E MPa	Poisson's Ratio ν	Fracture Energy G _f N/m	Softening Modulus E _s MPa	Tensile Strength f _t N/mm ²	% Variation of Tensile Strength	In situ Stress MPa	
									σ_2	σ_3
A	001	Mark 1	1785.0	0.00	-	∞	0.5	0.00	0.0	0.0
	002	Mark 2	1785.0	0.00	-	∞	0.5	0.00	0.0	0.0
	003	Mark 3	1785.0	0.00	100.0	360.61	0.5	0.00	0.0	0.0
B	004	Mark 1	1785.0	0.125	-	∞	0.5	0.00	0.0	0.0
	005	Mark 2	1785.0	0.125	-	∞	0.5	0.00	0.0	0.0
	006	Mark 3	1785.0	0.125	100.0	360.61	0.5	0.00	0.0	0.0
C	007	Mark 1	1785.0	0.25	-	∞	0.5	0.00	0.0	0.0
	008	Mark 2	1785.0	0.25	-	∞	0.5	0.00	0.0	0.0
	009	Mark 3	1785.0	0.25	100.0	360.61	0.5	0.00	0.0	0.0
D	010	Mark 1	1785.0	0.00	-	∞	0.5	0.00	9.0	3.7
	011	Mark 2	1785.0	0.00	-	∞	0.5	0.00	9.0	3.7
	012	Mark 3	1785.0	0.00	100.0	360.61	0.5	0.00	9.0	3.7
E	013	Mark 1	1785.0	0.125	-	∞	0.5	0.00	9.0	3.7
	014	Mark 2	1785.0	0.125	-	∞	0.5	0.00	9.0	3.7
	015	Mark 3	1785.0	0.125	100.0	360.61	0.5	0.00	9.0	3.7
F	016	Mark 1	1785.0	0.25	-	∞	0.5	0.00	9.0	3.7
	017	Mark 2	1785.0	0.25	-	∞	0.5	0.00	9.0	3.7
	018	Mark 3	1785.0	0.25	100.0	360.61	0.5	0.00	9.0	3.7

Table 6.2. Details of Numerical Runs Carried Out for the First, General Parametric Study of Hydraulic Fracture Benchmark Model

Test Group	Run No.	Fracture Model	Young's Modulus E MPa	Poisson's Ratio ν	Fracture Energy G_f N/m	Softening Modulus E_s MPa	Tensile Strength f_t N/mm ²	% Variation of Tensile Strength	In situ Stress MPa	
									σ_2	σ_3
G	019	Mark 1	1785.0	0.00	-	∞	0.5	5.00	0.0	0.0
	020	Mark 2	1785.0	0.00	-	∞	0.5	5.00	0.0	0.0
	021	Mark 3	1785.0	0.00	100.0	360.61	0.5	5.00	0.0	0.0
H	022	Mark 1	1785.0	0.25	-	∞	0.5	5.00	0.0	0.0
	023	Mark 2	1785.0	0.25	-	∞	0.5	5.00	0.0	0.0

a)

Test Group	Run No.	Fracture Model	Young's Modulus E MPa	Poisson's Ratio ν	Fracture Energy G_f N/m	Softening Modulus E_s MPa	Tensile Strength f_t N/mm ²	% Variation of Tensile Strength	In situ Stress MPa	
									σ_2	σ_3
I	024	Mark 4	1785.0	0.25	100.0	360.61	0.5	0.00	0.0	0.0
	025	Mark 5	1785.0	0.25	100.0	360.61	0.5	0.00	0.0	0.0
J	026	Mark 4	1785.0	0.00	100.0	360.61	0.5	0.00	0.0	0.0
	027	Mark 5	1785.0	0.00	100.0	360.61	0.5	0.00	0.0	0.0
K	028	Mark 4	1785.0	0.00	100.0	360.61	0.5	0.00	9.0	3.7
	029	Mark 5	1785.0	0.00	100.0	360.61	0.5	0.00	9.0	3.7

b)

Table 6.3. Details of Numerical Runs Carried Out for the a) Second and b) Third, Specific Parametric Studies of Hydraulic Fracture Benchmark Model

6.2.3. Discussion of Results

6.2.3.1. Introduction

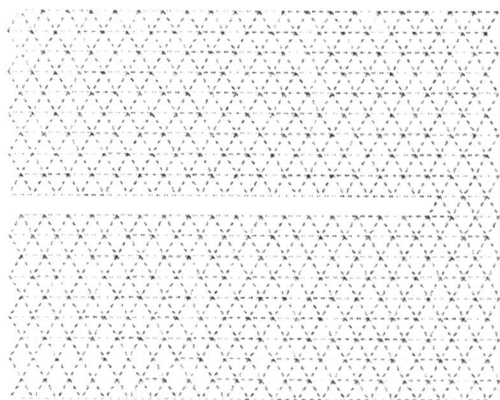
In the following pages presentation and discussion is made of the results from the studies described in the previous Sections. As discussed above, for each of the runs listed in Table 6.2. and Table 6.3., a fracture system was developed in the Hydraulic Fracture Benchmark PSM mesh. Many of these followed a straight path, propagating in the x -direction, along the centreline of the mesh and thereby opening in the direction of least resistance, as would be expected for fractures of this type. However, various other, deviated fracture patterns were also produced. Table 6.4. below, lists a summary of the fracture patterns produced by each numerical run and indicates the figure which best illustrates the fracture behaviour. Since there was considerable repetition within the results, only a representative sample of fracture shapes are shown (*Fig. 6.5. to Fig. 6.8.*), however, where a unique fracture pattern developed a plot has been included. For ease of comparison, the summary table and the fracture patterns themselves are presented collectively in Section 6.2.3.2., before a detailed discussion given in Section 6.2.3.3.

For the fractures that developed along the centreline of the mesh it was also possible to produce comparative results of the fracture width profiles, the failure of the inter-particle link elements in the mesh during propagation of the fractures and the net applied pressure at the point of failure for each link element. Since the pressure in the fracture was constant, the latter was equivalent to a plot of the net pressure at the wellbore. Plots of this kind, from the results of Test Groups A to E, as defined in Table 6.2., are shown below in *Fig. 6.12. to Fig. 6.16.* before a detailed discussion is presented, in which comparison is made with the results given by Papanastasiou [69] and reproduced in *Fig. 6.11.* For fractures that deviated from the centreline of the mesh, it was not feasible to produce meaningful comparative plots of fractures width profiles, however, in some instances, where a distinct fracture was judged to have formed, and meaningful results were available, plots of link element failure and net wellbore pressure have been included. Where no distinct fracture developed, results of this form were not found to be appropriate. Similarly to the general fracture shape results, the detailed profile plots are presented collectively, for ease of comparison, in Section 6.2.3.4., ahead of their detailed discussion in Section 6.2.3.5.

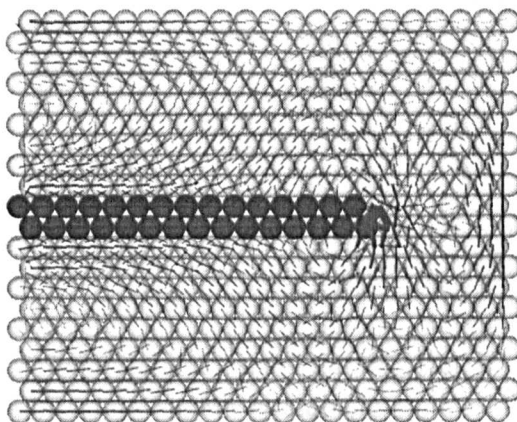
6.2.3.2. Figures Showing General Fracture Patterns

Test Group	Run No.	General Fracture Shape	Representative Figures
A	001	Straight Fracture (in x -direction)	<i>Fig. 6.5. a) & b)</i>
	002	Straight Fracture (in x -direction)	<i>Fig. 6.5. a) & b)</i>
	003	Straight Fracture (in x -direction)	<i>Fig. 6.5. a) & b)</i>
B	004	Straight Fracture (in x -direction)	<i>Fig. 6.5. a) & c)</i>
	005	Straight Fracture (in x -direction)	<i>Fig. 6.5. a) & c)</i>
	006	Deviated Fracture (in $-y$ -direction)	<i>Fig. 6.5. e)</i>
C	007	Straight Fracture (in x -direction)	<i>Fig. 6.5. a) & d)</i>
	008	Straight Fracture (in x -direction)	<i>Fig. 6.5. a) & d)</i>
	009	Deviated Fracture (in $+y$ -direction)	<i>Fig. 6.5. f)</i>
D	010	Straight Fracture (in x -direction)	<i>Fig. 6.5. a)</i>
	011	Deviated Fracture (in $+y$ -direction)	<i>Fig. 6.6. d)</i>
	012	Straight Fracture (in x -direction)	<i>Fig. 6.5. a)</i>
E	013	Straight Fracture (in x -direction)	<i>Fig. 6.5. a)</i>
	014	Straight Fracture (in x -direction)	<i>Fig. 6.5</i>
	015	Straight Fracture (in x -direction)	<i>Fig. 6.5. a)</i>
F	016	Deviated Fracture (in $+y$ -direction)	<i>Fig. 6.6. a)</i>
	017	Deviated Fracture (in $+y$ -direction)	<i>Fig. 6.6. b)</i>
	018	Deviated Fracture (in $+y$ -direction)	<i>Fig. 6.6. c)</i>
G	019	Straight Fracture (in x -direction)	<i>Fig. 6.5. a) & b)</i>
	020	Straight Fracture (in x -direction)	<i>Fig. 6.5. a) & b)</i>
	021	Straight Fracture (in x -direction)	<i>Fig. 6.5. a) & b)</i>
H	022	Straight Fracture (in x -direction)	<i>Fig. 6.5. a) & d)</i>
	023	Variable Deviation (in $+y$ -direction)	<i>Fig. 6.7. a) & b)</i>
I	024	Deviated Fracture (in $-y$ -direction)	<i>Fig. 6.8. c)</i>
	025	No Defined Fracture	<i>Fig. 6.8. e) & f)</i>
J	026	Deviated Fracture (in $-y$ -direction)	<i>Fig. 6.8. a)</i>
	027	Deviated Fracture (in $\pm y$ -direction)	<i>Fig. 6.8. d)</i>
K	028	No Defined Fracture Crack Bridging	<i>Fig. 6.8. b)</i>
	029	Deviated Fracture (in $\pm y$ -direction) Crack Bridging	<i>Fig. 6.8. b)</i>

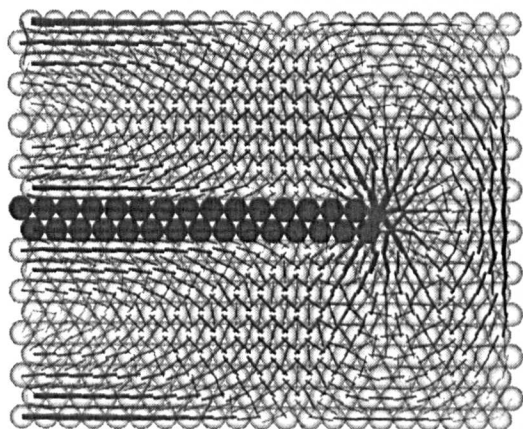
Table 6.4. Summary of General Fracture Patterns Produced in Listed Numerical Runs During Parametric Studies on Hydraulic Fracture Benchmark Model



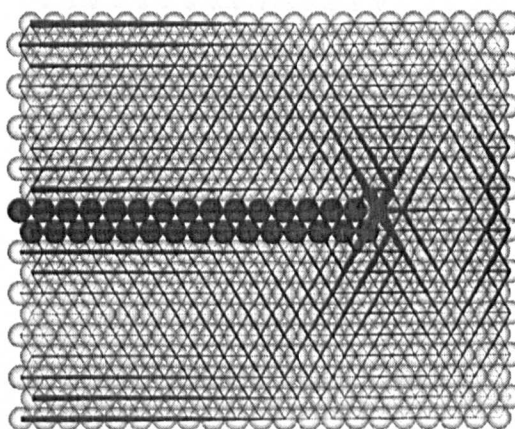
a) Typical Straight Fracture Pattern, Any Failure Criteria, any value of ν



b) Typical Contact Force Pattern for Straight Frac., Unconfined, $\nu = 0.00$

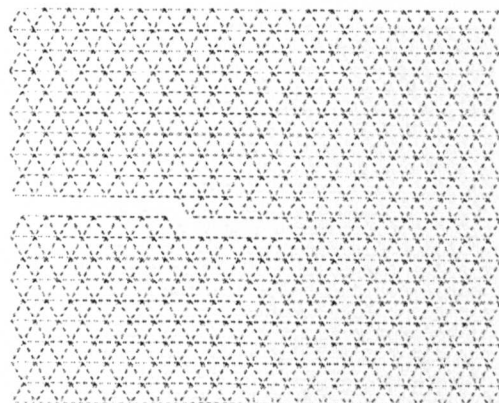


c) Typical Contact Force Pattern for Straight Frac., Unconfined, $\nu = 0.125$

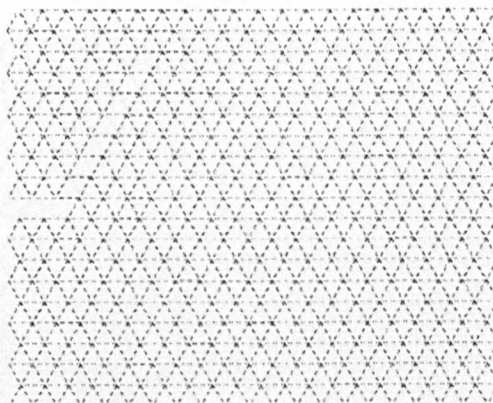


d) Typical Contact Force Pattern for Straight Frac., Unconfined, $\nu = 0.25$

Figure 6.5: Typical Fracture Patterns Produced by Numerical Runs during 1st Parametric Study (Test Groups D, E & F) on Hydraulic Fracture Benchmark Model

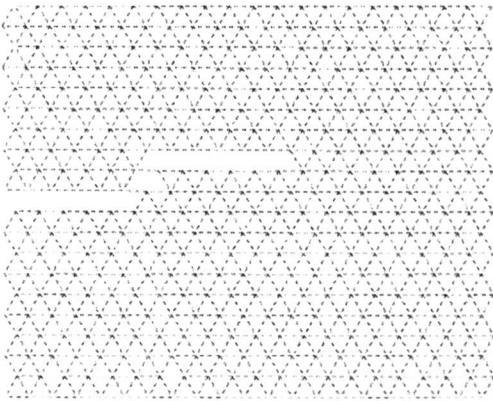


e) Deviated Fracture Pattern for Mark 3 Failure Criterion, $\nu = 0.125$, Unconfined

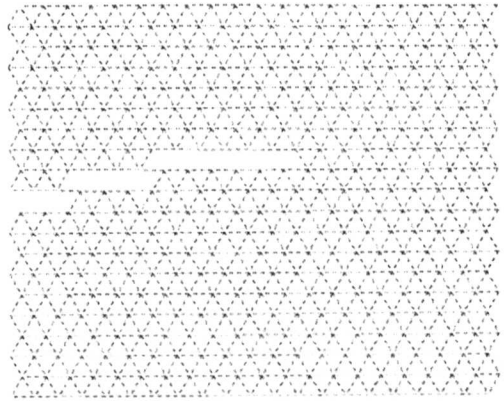


f) Deviated Fracture Pattern for Mark 3 Failure Criterion, $\nu = 0.25$, Unconfined

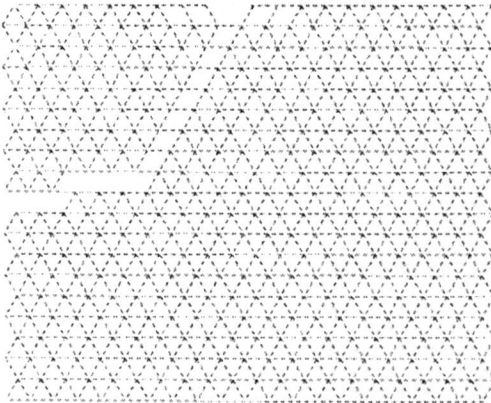
Fig. 6.5. Diagrams of Various Fracture and Contact Force Patterns Produced by Numerical Runs during 1st Parametric Study (Test Groups A, B & C) on Hydraulic Fracture Benchmark Model



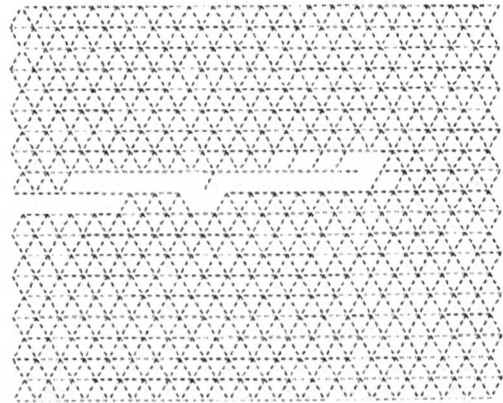
a) Fracture Pattern for Mark 1 Failure Criterion, $\nu = 0.25$, Confined



b) Fracture Pattern for Mark 2 Failure Criterion, $\nu = 0.25$, Confined

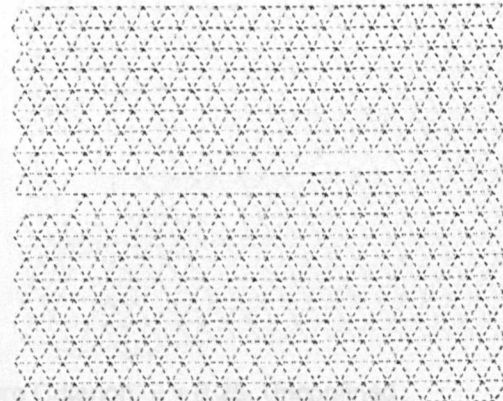
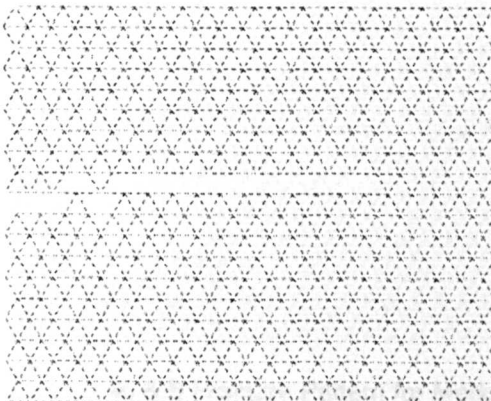


c) Fracture Pattern for Mark 3 Failure Criterion, $\nu = 0.25$, Confined



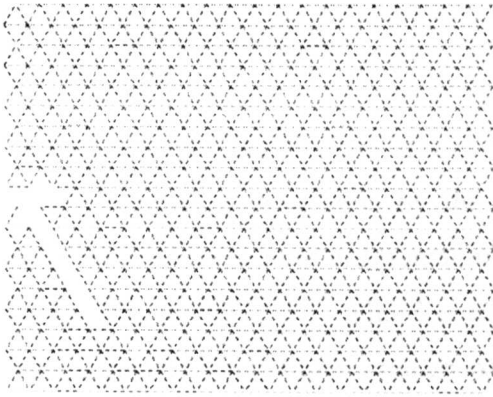
d) Fracture Pattern for Mark 2 Failure Criterion, $\nu = 0.0$, Confined

Fig. 6.6. Diagrams of Various Fracture Patterns Produced by Numerical Runs during 1st Parametric Study (Test Groups D, E & F) on Hydraulic Fracture Benchmark Model

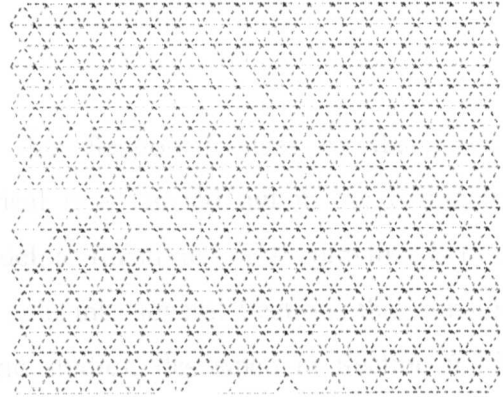


a) & b) Fracture Pattern for Mark 2 Failure Criterion, $\nu = 0.25$, Unconfined, Random Strength Distribution

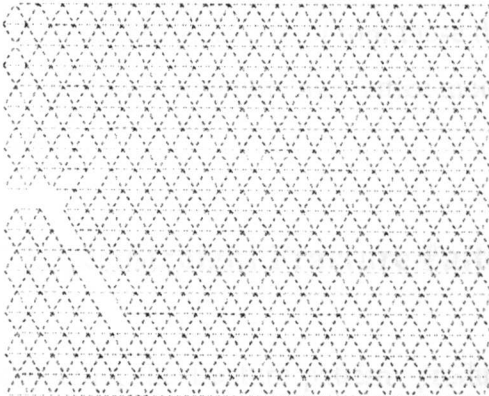
Fig. 6.7. Diagrams of Various Fracture Patterns Produced by Numerical Runs during 3rd Parametric Study (Test Groups G & H) on Hydraulic Fracture Benchmark Model



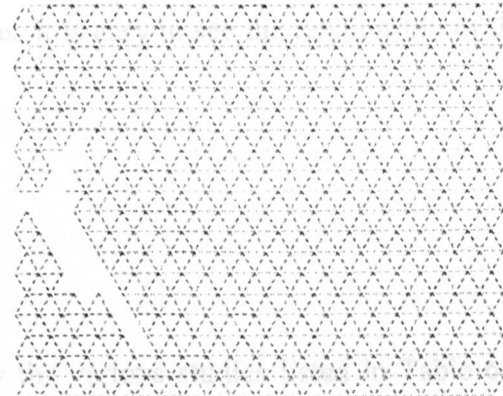
a) Fracture Pattern for Mark 4 Failure Criterion, $\nu = 0.0$, Unconfined



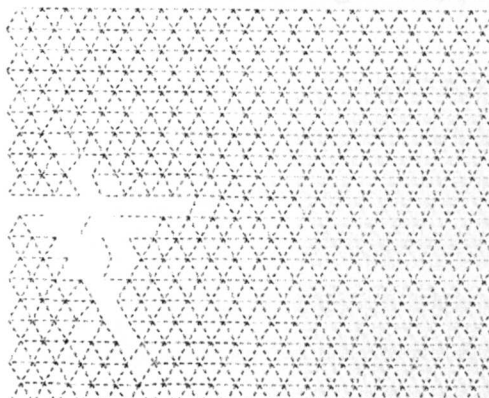
b) Fracture Pattern for Mark 4 Failure Criterion, $\nu = 0.125$, Confined



c) Fracture Pattern for Mark 4 Failure Criterion, $\nu = 0.25$, Unconfined



d) Fracture Pattern for Mark 5 Failure Criterion, $\nu = 0.0$, Unconfined



e) & f) Fracture Pattern for Mark 5 Failure Criterion, $\nu = 0.25$, Unconfined

Fig. 6.8. Diagrams of Various Fracture Patterns Produced by Numerical Runs during 3rd Parametric Study (Test Groups I, J & K) on Hydraulic Fracture Benchmark Model

6.2.3.3. Discussion of General Fracture Patterns

6.2.3.3.1. Introduction

As mentioned previously, the discussion in this Section focuses on the general fracturing behaviour developed by the numerical runs carried out in the parametric study of the Hydraulic Fracture Benchmark Model, as illustrated in the previous Section (See *Fig. 6.5.* to *Fig. 6.8.*). The discussion is split into several Sections that consider various aspects of the three smaller parametric studies, described in Section 6.2.2., which made up the overall parametric study of the Hydraulic Fracture Benchmark Model. As can be seen in the figures presented in the previous Section, for clarity, most of the plots show only the ‘contact bonds’ acting as the inter-particle links in the PSM bonded particle assembly. From these diagrams, it is easy to see the relationship of the bonded particle assembly to a lattice model.

6.2.3.3.2. Straight Fracture Patterns

Considering the fracture patterns produced by the various studies listed in Table 6.2. and Table 6.3., it can be seen, from the summary of results given in Table 6.4., that most of the numerical runs produced straight fractures that propagated down the centreline of the mesh, as illustrated in *Fig. 6.5. a)* (repeated below).

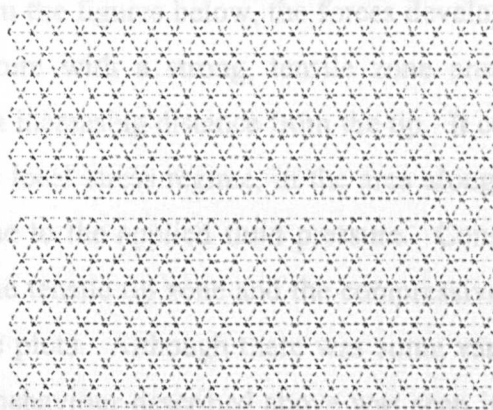


Fig. 6.5. a) Typical Straight Fracture Pattern

(repeated from Section 6.2.3.2. above)

This was the expected behaviour for the Hydraulic Fracture Benchmark Model since, as mentioned previously, a fracture of this type tends to open in the direction of least resistance (See Section 6.2.1. and *Fig. 6.1.* above). However, an additional influence may have been the orientation of the applied ‘fluid pressure forces’, which, as described in detail in Section 6.2.1., always acted in the y -direction, thereby tending to open a fracture in this orientation. Nonetheless, based on these results, it was considered clear that the PSM could be applied to realistic geomechanical problems and develop the generally expected behaviour. A specific and detailed comparative study of the precise behaviour of the numerical runs that produced these straight fractures is carried out in Sections 6.2.3.4. and 6.2.3.5. below.

6.2.3.3.3. Contact Force Patterns for Straight Fractures

While, due to the development of a straight fracture in most of the numerical runs, the general behaviour of the model was considered to be acceptable, further aspects of the model behaviour can be noted on examination of plots showing the contact forces acting between the particles in the PSM mesh (See *Fig. 6.5.* b), c) and d) repeated below). In these plots, the dark lines indicate compressive forces, the light grey lines indicate tensile forces and the force magnitude is indicated by the relative line thicknesses.

As can be seen in the figures below, the forces developed as would be expected for a propagating fracture with a strong, tensile zone around the fracture tip that dissipated, radially, with increasing distance from the tip. It can also be seen that as the fracture propagated, the local stress regime, in the area along the walls of the fracture, became compressive due to the applied fluid pressure. Consequently, a neutral stress zone existed between the tensile tip zone and the compressive wall zones although this is not easily seen in the plots. Although there was some variation due to the material properties, the general behaviour described above was seen in the results of all studies in which a straight fracture pattern was produced.

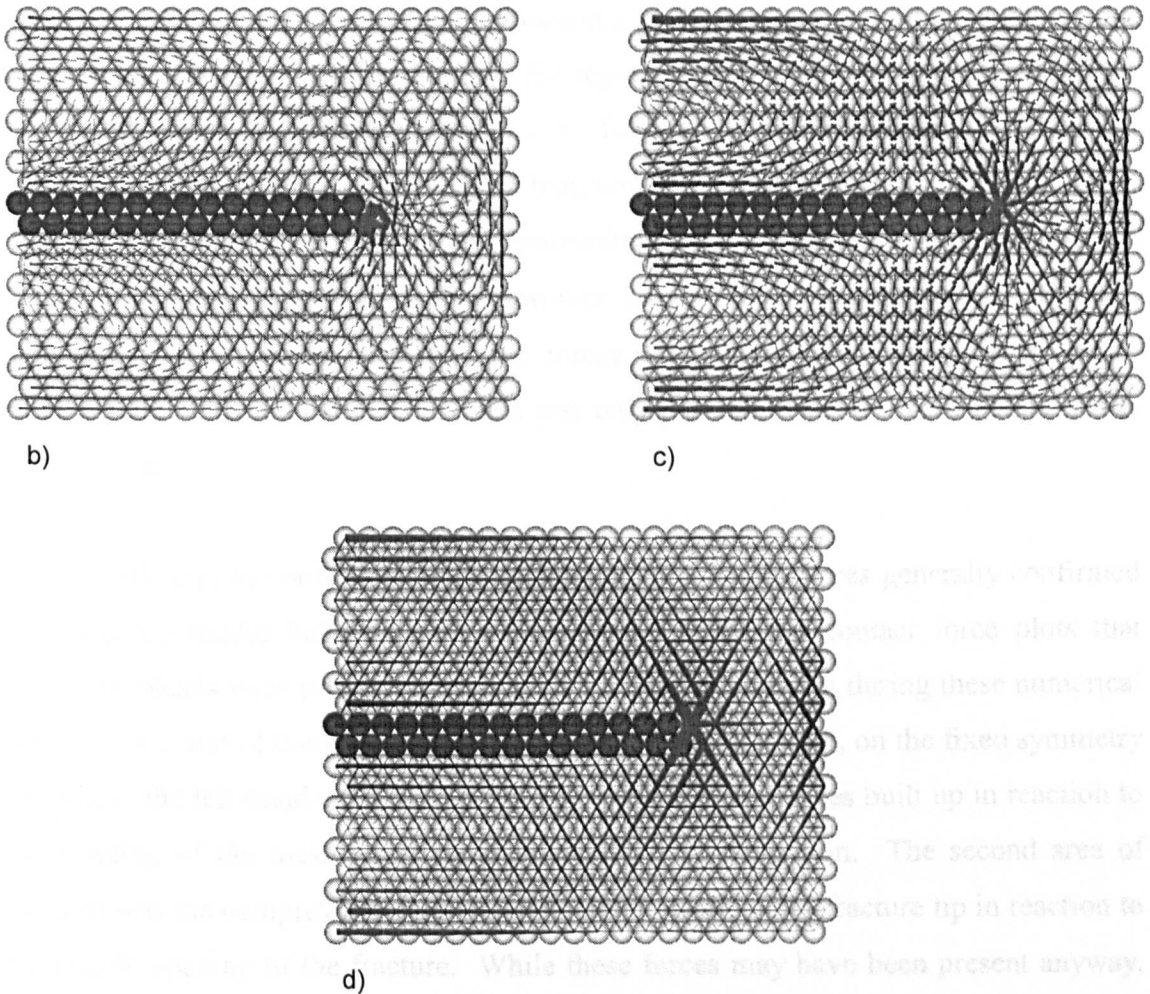


Fig. 6.5. Typical Contact Force Pattern for Straight Fracture Pattern under Zero Confining Pressure with b) $\nu = 0.00$ c) $\nu = 0.125$ and d) $\nu = 0.25$

(repeated from Section 6.2.3.2. above)

However, on further examination of *Fig. 6.5. b), c) and d)*, it can also be seen that the precise configuration of the contact force distribution apparently changed considerably with Poisson's ratio. This was in fact due to the direct relationship between the Poisson's ratio of the particle assembly and the ratio of the normal and shear contact spring stiffnesses, as described by the equations of Morikawa and Sawamoto [63] (See *Fig. 4.29.* and *Fig. 4.30.*). Thus, when the Poisson's ratio of the mesh was 0.25, the shear stiffness was zero and only normal forces could be transmitted between the particles, thereby resulting in a distinct hexagonal pattern of force distribution (See *Fig. 6.5. d)*). As Poisson's ratio decreased and the ratio of normal to shear stiffness increased, more and more of the contact forces could be transmitted in shear. In *Fig.*

6.5. b), c) and d), this effect is most noticeable in the regions around the fracture tip, where tensile loads are highest, and in the region ahead of the fracture tip, where, as mentioned above, a compressive zone is formed. Taking, as an example, the compression zone, it can be clearly seen that, with a Poisson's ratio, $\nu = 0.25$ ($k_s = 0.0$) (Fig. 6.5. d)), the compression was transmitted in a diamond pattern, with forces normal to the inter-particle contacts. However, with a Poisson's ratio, $\nu = 0.0$ ($k_s = k_n$) (Fig. 6.5. b)), it can be seen that the forces were transmitted vertically (in the y -direction) between the particles and this was only possible because of the action of the shear springs.

Although the observed configurations of the contact forces generally confirmed the expected model behaviour, it was also clear from the contact force plots that boundary effects were present in three areas of the PSM meshes during these numerical studies. The first of these can be seen at the corners of the mesh, on the fixed symmetry boundary (the left-hand corners of the plots), where tensile forces built up in reaction to the bending of the mesh as it was displaced in the y -direction. The second area of concern was the compressive zone that developed ahead of the fracture tip in reaction to the tensile opening of the fracture. While these forces may have been present anyway, they were clearly concentrated by the presence of the mesh boundary. The third noticeable effect, observed particularly in Fig. 6.5. c), was the concentration of forces near the boundaries directly lateral to the fracture tip, where the natural force distribution paths were intersected by the edges of the mesh. After examination of the plots, it was concluded that all of these boundary effects occurred far enough from the centreline of the mesh so as not to be a significant influence on the fracture propagation over the length of interest in this work. However, if the fractures propagated too far or deviated in the y -direction, as was the case in several of the numerical runs, then it was considered that the boundary effects might have influenced the results. Where these situations arose during this benchmark testing, as mentioned previously, the runs were stopped when it was felt that the fracture was approaching to close to the mesh boundary.

6.2.3.3.4. Deviated Fracture Patterns

First Parametric Study - (Test Groups A to F)

As stated previously, from the observations of the development of the straight fractures produced by the majority of the benchmark tests and the associated contact force patterns, the general behaviour of the Hydraulic Fracture Benchmark Model was considered satisfactory. However, in addition to the straight fractures, several of the numerical runs also produced fracture patterns that deviated from the centreline of the mesh (See *Fig. 6.5. e) & f)* and *Fig. 6.6. a) to d)* repeated below).

In considering these results, which developed under various applied material properties and fracturing criteria, several points are notable. The first point of note is that, in the results that produced deviated fracture patterns, there was a general tendency for the deviation to take place in the positive y -direction (the upwards direction in *Fig. 6.5. to Fig. 6.7.*). A trend such as this is indicative of an artificial influence acting within the model since, in a real material, a randomly distributed deviation would be expected.

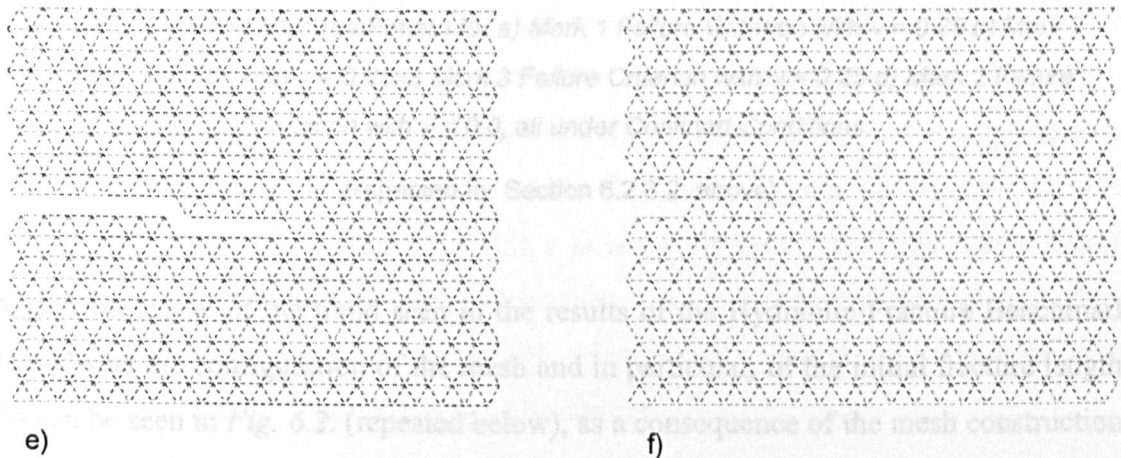


Fig. 6.5. Deviated Fracture Pattern for Mark 3 Failure Criterion with e) $\nu = 0.125$ and Zero Confining Pressure f) $\nu = 0.25$ and Zero Confining Pressure

(repeated for Section 6.2.3.2. above)

The referenced 'upper' and 'lower' sides of the Hydraulic Fracture Model mesh refer to the orientation in which all figures are presented in Sections 6.2.3.1. and 6.2.3.3.

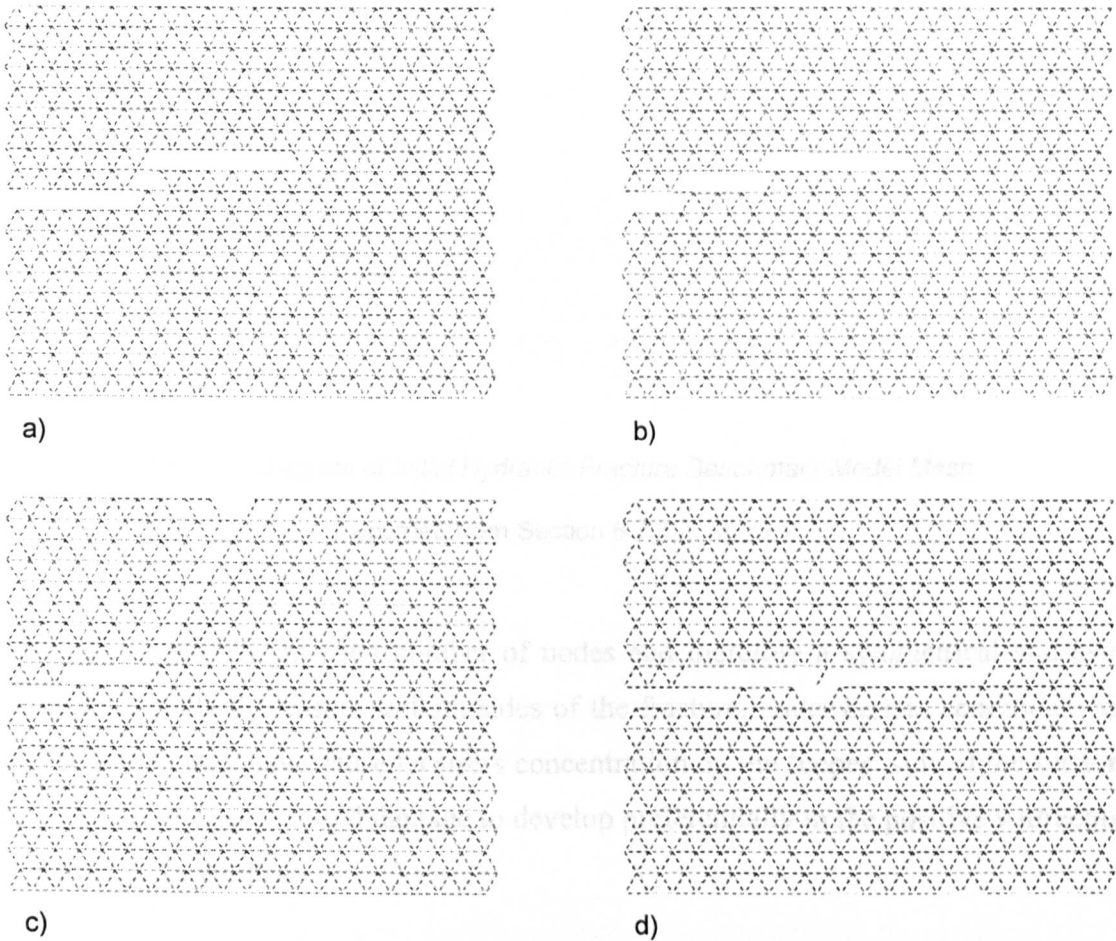


Fig. 6.6. Deviated Fracture Pattern for a) Mark 1 Failure Criterion with $\nu = 0.25$ b) Mark 2 Failure Criterion with $\nu = 0.25$ c) Mark 3 Failure Criterion with $\nu = 0.25$ d) Mark 2 Failure Criterion with $\nu = 0.0$, all under Confined Conditions

(repeated for Section 6.2.3.2. above)

A possible cause of the trend seen in the results of the Hydraulic Fracture Benchmark Model was the configuration of the mesh and in particular, of the initial fracture length. As can be seen in *Fig. 6.2.* (repeated below), as a consequence of the mesh construction, the sides of the initial fracture consisted of three inter-particle link elements on the ‘upper’ side and two elements on the ‘lower’ side[†].

[†] The referenced ‘upper’ and ‘lower’ sides of the Hydraulic Fracture Model mesh refer to the orientation in which all figures are presented in Sections 6.2.3.2. and 6.2.3.3.

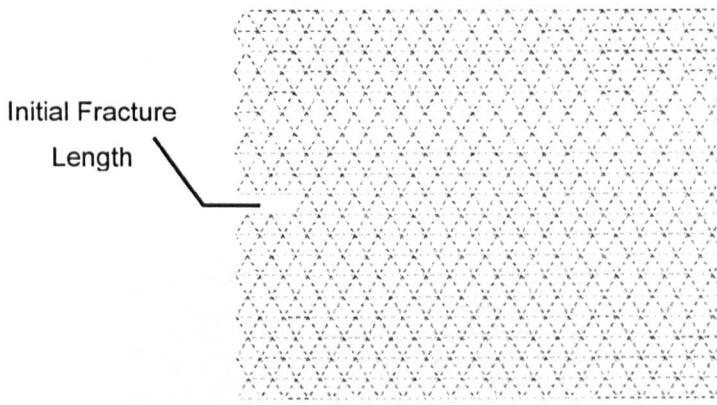


Fig. 6.2. *Diagram of Initial Hydraulic Fracture Benchmark Model Mesh*

(repeated from Section 6.2.3.2. above)

Although this led to an even number of nodes and therefore a symmetrical and even application of fluid pressure to both sides of the fracture, under certain conditions, the uneven length may have caused a stress concentration on the ‘upper’ side of the fracture tip. This would have caused damage to develop preferentially in the positive y -direction as shown in the results.

In order to test this theory, it would be possible to set-up a similar model in which the initial fracture was configured in the opposite way, with the longer wall on the lower side. If the uneven length of the fracture walls was the cause of the trend in fracture deviation then the trend should be reversed when the fracture configuration is reversed. Repeating the numerical studies that were shown to develop deviated fractures would then confirm this. This was not attempted during the course of this work since the majority of the results were not affected by this problem and furthermore, the deviated fracture results were not considered an entirely accurate representation of the expected fracturing behaviour.

A further possible explanation for the deviated fracture patterns discussed above, was the presence of minor numerical imbalances in the loads applied to the mesh in order to represent both in situ stresses and fluid pressure (See Section 6.2.1. above and *Fig. 6.1.*). Given the single symmetry boundary, fixed against displacement in the x -direction, and the application of the fluid pressures forces in the y -direction, it was

expected that the mesh would displace laterally, to either side the fracture, as propagation progressed, and this behaviour was observed during most of the numerical runs (See Fig. 6.9. a)).

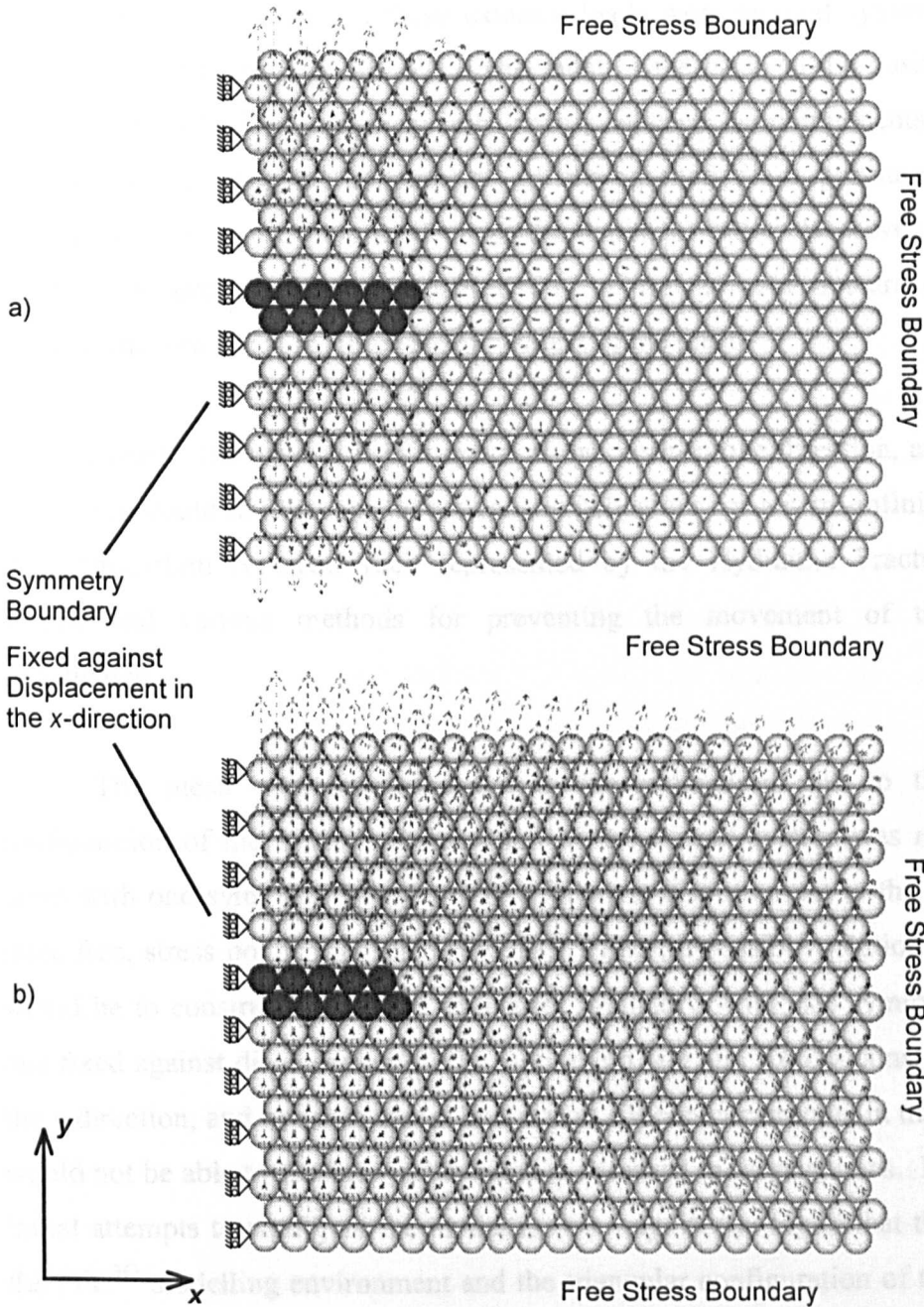


Fig. 6.9. Diagram Showing Typical Displacement of Hydraulic Fracture Benchmark Model Mesh
 a) Under Symmetrically Applied Fluid Pressure Forces and Confining Loads b) Under
 Unbalanced Fluid Pressure Forces and Confining Loads (Arrows Indicate Particle Velocities)

However, it was also noticed that there was a tendency for the whole mesh to displace in the positive y -direction (See *Fig. 6.9. b*), resulting in very large distortions. This effect was particularly evident in the numerical runs in which the mesh was subjected to confinement and consequently high fluid pressure loads were required in order to initiate fracturing. Although these external loads were applied symmetrically to the model, it was felt that the overall displacement of the mesh in the positive y -direction was the result of slight numerical imbalances, between the components of the applied confining loads and the components of the applied fluid pressure loads, which developed as the mesh deformed under the action of both. However, it is not clear whether the forces became unbalanced due to the deviated fracture or whether the deviated fracture was a result of the movement of the mesh.

Clearly, the overall displacement of the mesh in one direction, and the resulting distortions, could not be considered realistic behaviour for a semi-infinite body such as the hydrocarbon reservoir rock represented by the Hydraulic Fracture Benchmark Model, and various methods for preventing the movement of the mesh were investigated.

The mesh was free to move in the y -direction due to the symmetrical configuration of the model, whereby half of the overall system was represented by a mesh with one symmetry boundary, fixed against displacement in the x -direction, and three free, stress boundaries (See *Fig. 6.1.*). Thus, a possible solution to this problem would be to construct the model in quarter symmetry, with two symmetry boundaries, one fixed against displacement in the x -direction and one fixed against displacement in the y -direction, and two free, stress boundaries. When constrained in this way, the mesh would not be able to displace in the manner observed in these studies. However, during initial attempts to configure the model in this way, it was found that the constraints of the PFC^{3D} modelling environment and the triangular configuration of the mesh, caused difficulties in propagating a fracture along a symmetry boundary. Furthermore, it is clear that a model constructed in this way would not allow for inherently non-symmetrical behaviour such as meandering or branching fracture patterns as may occur in a heterogeneous material. It was therefore decided to continue with the half symmetry model as was applied in this study.

In an alternative effort to prevent displacement, the mesh was 'anchored' at its corners, however this was found to affect the fracturing behaviour. Consequently, although not entirely satisfactory, minor displacements of the mesh were accepted. Where large displacements occurred, the results were generally disregarded, since they were also usually accompanied by a deviated fracture pattern.

A noticeable feature of nearly all the deviated fracture patterns shown in *Fig. 6.5.* to *Fig. 6.7.* is crack bridging, whereby link elements, separate from the initial fracture length, failed and were removed from the mesh. Since a 'fluid force' dipole was inserted, as discussed previously, to replace a failed link element, irrespective of its relative position, these bridged fractures continued to propagate without connecting to the main fracture. Obviously, this is not wholly realistic behaviour since a fracture fluid would not be able to flow from the wellbore into unconnected lengths of fracture. This effect could have been corrected if the 'fluid pressure forces' were only applied in continuous fractures that were directly connected to the initial fracture length and not in place of remote failed elements. However, a program routine capable of discerning between connected and remote fractures in a PSM mesh would be very complex to code and it was not felt necessary for the purposes of this study since a single, straight, connected fracture was the desired and expected behaviour.

Additionally, it can be noticed that in most cases where crack bridging occurs it is horizontal elements (those orientated in x -direction) that remain intact while other elements fail. This phenomenon can be attributed to a combination of the applied loading conditions, the configuration of the mesh and the failure criterion. Due to the applied fluid pressure loading in the y -direction the elements aligned in the x -direction tended not to go into tension, which would lead to a violation of the Mark 1, and 3 failure criteria as described in Chapter 5. Furthermore, the effect is also seen in runs where the Mark 2 criterion was applied and this is because, despite its consideration of the maximum principal stress in an element, the Mark 2 criterion also takes into account the orientation of the element relative to the direction of the of the maximum principal stress. In the Hydraulic Fracture Benchmark Model the direction of the maximum principal stress, developed under the pressure applied in the y -direction, was almost perpendicular to the elements orientated in the x -direction. Consequently, elements more closely aligned with the y -direction were preferred for failure over those aligned in

the x -direction. Conversely, it can be seen that the crack bridging effect is less prominent in the runs in which the Mark 4 and 5 criteria were applied. This is, however, as would be expected since these criteria consider strain in an equivalent continuum area associated with each link element and take no account of the directions of either the principal strains or of the link element itself when considering failure.

It may also be noticed that the effect described above is similar to a problem encountered by Schlangen and Garboczi [79] whereby, in a lattice model subjected to uniaxial loading, elements of a particular orientation failed in preference to those in other orientations. In order to solve this problem Schlangen and Garboczi developed a failure criterion that considered a homogenised stress state at the nodes of the lattice. This is a similar approach to that of the Mark 4 and 5 criteria, mentioned above, but based on nodal stresses rather than elemental strains. The effect observed by Schlangen and Garboczi is discussed in detail in Chapter 2, Section 2.3.1. and also in Section 5.5.3. and Section 5.6.3. of Chapter 5, in conjunction with the Mark 1 and Mark 2 failure criteria.

Thus, although, these problems were not addressed further during the course of this work, it is clear from the points noted above that, in order to prevent their occurrence within a regular, triangular PSM mesh, a failure criterion based on continuum principles should be employed rather than one that considers the behaviour of individual link elements.

In addition to the mechanisms discussed above, it has also been suggested by Schlangen and Garboczi [79] that the fracturing behaviour of a lattice type model is dependent on the type of element employed and particularly on the number of degrees of freedom considered in each element. As discussed previously, the number of degrees of freedom considered for the inter-particle link elements of the PSM is related to the Poisson's ratio of the mesh. When Poisson's ratio is greater than or equal to zero but less than the maximum value of 0.25^\dagger , two force components, a normal and a shear

[†] As discussed in Section 4.2.2.3. of Chapter 4, 0.25 is the maximum value of Poisson's ratio according to the equations of strain energy equivalence derived for plane strain conditions (*Eq. 4.29.* and *Eq. 4.30.*) (Morikawa and Sawamoto [63], Griffiths and Mustoe [32]).

force, are considered in each element of a PSM mesh. However, when Poisson's ratio is equal to the maximum value of 0.25 the shear spring stiffness goes to zero and hence only one force component, an axial force, is considered.

A comparative study of three lattice models, conducted by Schlangen and Garboczi [79], considered lattices constructed of elements capable of transmitting normal (one force lattice), normal and shear (two force lattice), and normal, shear and bending forces (three force lattice). The results showed that, in general, the accuracy of the lattice fracture patterns, in comparison to experimental results, increased with increasing number of force components in the elements. While it is difficult to directly compare the results of Schlangen and Garboczi [79] with the studies carried out in this work, due to the different tests carried out, further examination of the results presented above, shows that there are more occurrences of deviated fracture patterns when only one force component is considered ($\nu = 0.25$) than when two are considered ($0.0 \leq \nu < 0.25$). This effect is more evident when in situ stresses are applied to the mesh than under conditions of zero confinement, but it can be seen that there is general agreement between the results of Schlangen and Garboczi and the results of the Hydraulic Fracture Benchmark Model. This finding suggests that the accuracy of the fracturing behaviour produced by the PSM might decrease with increasing values of Poisson's ratio and this should be taken into account when considering the results of a fracture study. However, little difference was seen between the results produced with a Poisson's ratio of 0.0 and of 0.125. This implies that fracturing behaviour may be modelled accurately as long as two force components are maintained, in which case only an application of the maximum value of Poisson's ratio will lead to a reduction in the accuracy of the results. In fact, it can be argued, from the results shown in Table 6.4., that the choice of failure criteria may be more significant to the propagated fracture shape than the ratio of normal to shear spring stiffness as long as a two force lattice model is employed.

A further study by Schlangen and Garboczi [79] investigated the influence of the mesh configuration on the fracturing behaviour of a lattice model. They concluded that the fracture patterns developed in a regular lattice were always influenced, to some extent, by the dominant directions of the mesh. However, they found the regular triangular mesh able to produce more realistic fracture patterns, in comparison to

experimental results, than an equivalent square lattice. This is a finding confirmed by Schlangen and van Mier [82], who applied a triangular lattice on the basis that it provides the least opportunity for a preferential fracture direction to develop. However, it can be said that to a certain extent the propagation of a fracture in a lattice type model is always influenced by the mesh configuration since a failure of the model material can only occur where a lattice element exists. While in the limiting case a fine lattice approaches a continuous material, the failure of a lattice element may not occur exactly as the failure of an equivalent continuum material would. Despite this many examples can be found of fracture patterns developed in lattice type models that very accurately reproduce the patterns observed in experimental results (Schlangen and Garboczi [79], Schlangen and van Mier [80, 81, 82], Tzschichholz and Herrmann [88], Tzschichholz et al. [89], van Vliet [95]).

From the results of the benchmark tests shown above, it can be seen, as discussed previously, that the majority of the numerical runs produced straight fractures that propagated down the centre of the mesh. While this was the expected result for the benchmark model, it could be argued that these fractures propagated along a preferential direction in the mesh. Furthermore, it is clear that some of the deviated fracture patterns, such as those produced by runs 006 and 009 (See Fig. 6.5. e) and f) repeated below), did propagate along a preferred line of fracture in the mesh.

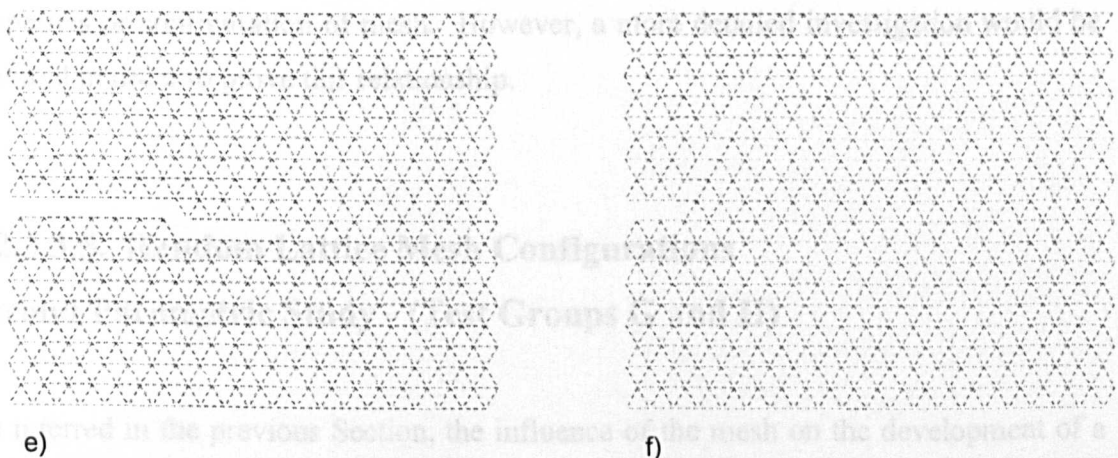


Fig. 6.5. Deviated Fracture Pattern for Mark 3 Failure Criterion with e) $\nu = 0.125$ and Zero Confining Pressure f) $\nu = 0.25$ and Zero Confining Pressure

(Repeated from Section 6.2.3.2. above)

Conversely, it can be argued that that runs such as 017 (See Fig. 6.6. b) repeated below), although producing results that were not considered accurate behaviour for the Hydraulic Fracture Benchmark Model, developed fracture patterns that propagated across the preferential lines of fracture in the mesh.

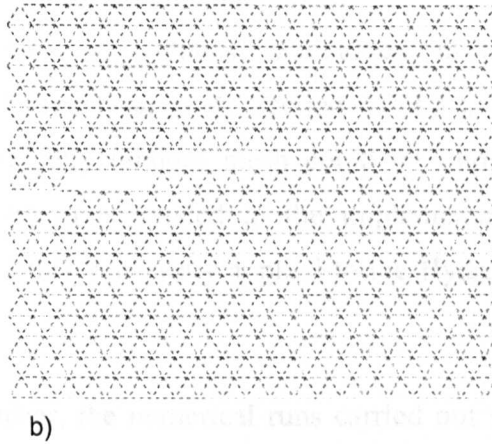


Fig. 6.6. b) Mark 2 Failure Criterion with $\nu = 0.25$ under Confined Conditions

(Repeated from Section 6.2.3.2. above)

The fact that runs 006 and 009 both employed the Mark 3 fracture criterion and run 017 employed the Mark 2 fracture criterion lends weight to the premise that, as mentioned above, the fracture pattern is influenced more by the chosen failure criterion than by the properties or configuration of mesh. However, a more detailed investigation would be required in order to prove this relationship.

6.2.3.3.5. Random Lattice Mesh Configurations

Second Parametric Study - (Test Groups G and H)

As inferred in the previous Section, the influence of the mesh on the development of a fracture pattern is largely irrelevant in the case on the Hydraulic Fracture Benchmark Model since the desired fracture path lies along a preferential direction in the PSM mesh. However, in order to overcome the general problems associated with the influence of the mesh configuration on fracture propagation, Schlangen and Garboczi

[79] advocate the use of random lattice configurations. For ease of implementation, they also note that a suitably fine regular lattice mesh, given random element properties, will produce the same effect and will successfully reproduce fracture patterns similar to those observed in experimental results for fracture in heterogeneous materials such as concrete.

There are a number of technical difficulties, in particular an appropriate calibration of the model (See Chapter 4, Section 4.2.2.3.), which would need to be overcome before a completely random mesh could be implemented with the PSM. However, no such complexities existed in the implementation of random element strengths in the PSM and this was easily applied to the Hydraulic Fracture Benchmark Model mesh.

As mentioned earlier, the numerical runs carried out with the random strength distribution ($\pm 5\%$ deviation from the mean value), from groups G and H (See Table 6.3.), were repeated several times each. However, it was found that, in all cases, runs 019, 020, 021 and 022 always produced a straight fracture that propagated down the centreline of the mesh. While this was the expected behaviour for the propagation of a hydraulic fracture in a homogeneous material, it was hoped that with a random strength distribution some meandering or branching behaviour would be observed. In fact, only run 023 could be shown to produce this kind of behaviour, examples of which can be seen in *Fig. 6.7.* (repeated below).

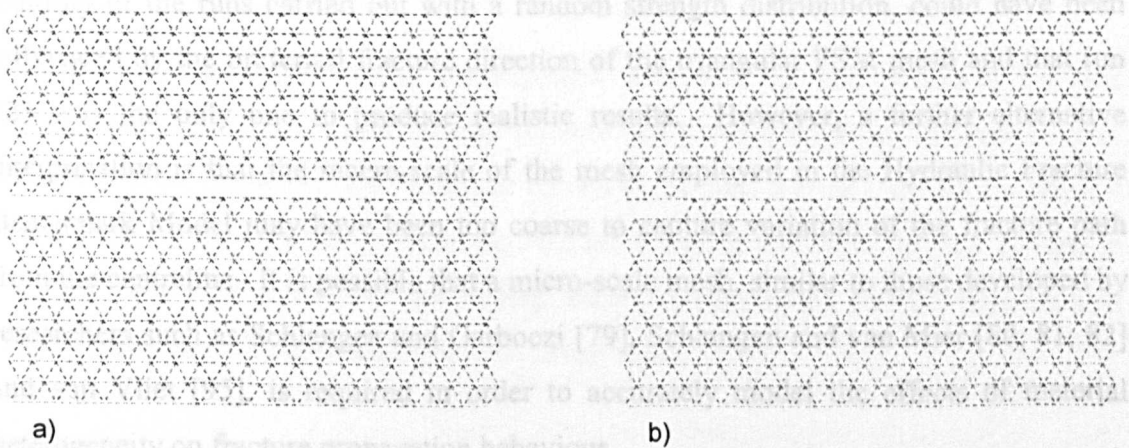


Fig. 6.7. Typical Fracture Patterns for Mark 2 Failure Criterion, $\nu = 0.25$, Unconfined, Random Strength Distribution

(Repeated from Section 6.2.3.2. above)

Several possible explanations can be offered for these results. Firstly, run 023 employed the Mark 2 criterion, which, as discussed in Chapter 5, Section 5.6.1., is formulated in terms of the maximum principal stress in an element rather than the total strain, as is the case for the other failure criteria developed for the PSM. For this reason it is possible that the Mark 2 criterion was more sensitive to random variations of the material strength than those criteria that considered the deformation of the inter-particle link elements and that it was therefore more able to capture the meandering fracture behaviour that would be associated with a heterogeneous material. However, it can also be noted that run 023 considered a mesh with Poisson's ratio, $\nu = 0.25$. As discussed previously, a PSM mesh with this property is reduced to a single force component in each element, which may lead to an inherent inaccuracy in the results. Thus, the meandering nature of the fracture produced by run 023 may in fact be an inaccurate result, similar to that produced by run 017 (See Fig. 6.6. b). It is further noticeable that where deviation of the fractures produced by run 023 occurred it was always in the positive y -direction as was the case for most of the deviated fracture patterns seen in the results of the Hydraulic Fracture Benchmark studies. As stated above, this may have been related to numerical imbalances and overall deformation of the Hydraulic Fracture Benchmark Model mesh rather than an accurate representation of meandering fracture behaviour in a heterogeneous material.

Alternatively, it could also be argued that the straight fractures, produced by the majority of the runs carried out with a random strength distribution, could have been influenced by the preferred fracture direction of the triangular PSM mesh and that run 023 was the only one to produce realistic results. However, a further alternative interpretation is that the macro-scale of the mesh employed in the Hydraulic Fracture Benchmark Model may have been too coarse to capture variation of the fracture path from the centreline. It is possible that a micro-scale mesh, similar to those developed by researchers such as Schlangen and Garboczi [79], Schlangen and van Mier [80, 81, 82] and van Vliet [95], is required in order to accurately model the effects of material heterogeneity on fracture propagation behaviour.

Clearly, the results of these tests are inconclusive and further investigation would be required in order to determine the behaviour of fracture propagation in a PSM mesh with a random strength distribution. In addition, after further investigation, it may be possible and, as indicated by Schlangen and Garboczi [79], desirable, to develop and test a randomly configured PSM mesh for the purposes of modelling heterogeneous materials. Such a model could consider variations of stiffness and strength on an individual element basis, as might be appropriate for a micro-scale model considering material variation on the grain scale, or, alternatively, material properties could be varied over regions of the mesh, as may be more appropriate in the study of large rock masses with a macro-scale model.

6.2.3.3.6. Application of the Mark 4 and Mark 5 Failure Criteria Third Parametric Study - (Test Groups I, J and K)

In addition to the work discussed so far in this Section, the third and final benchmark study, consisting of Test Groups I, J and K, as defined in Table 6.3. above, consisted of numerical tests employing the Mark 4 and Mark 5 failure criteria, as described in Chapter 5. Given the disappointing behaviour developed by these criteria with the Two-Dimensional Uniaxial Benchmark Model (See Section 5.8.3. and Section 5.9.3. of Chapter 5), the tests carried out in these studies simply serve to further investigate and illustrate their poor performance.

As described previously, the expected behaviour for the Hydraulic Fracture Benchmark Model was a single straight fracture that propagated down the centreline of the PSM mesh. As can be seen from the results of the runs carried out with the Mark 4 and 5 criteria (See *Fig. 6.8.* repeated below), the fractures tended to initially deviate in the negative y -direction before developing extensive distributed fracture patterns that finally resulted in very large deformations of the mesh.

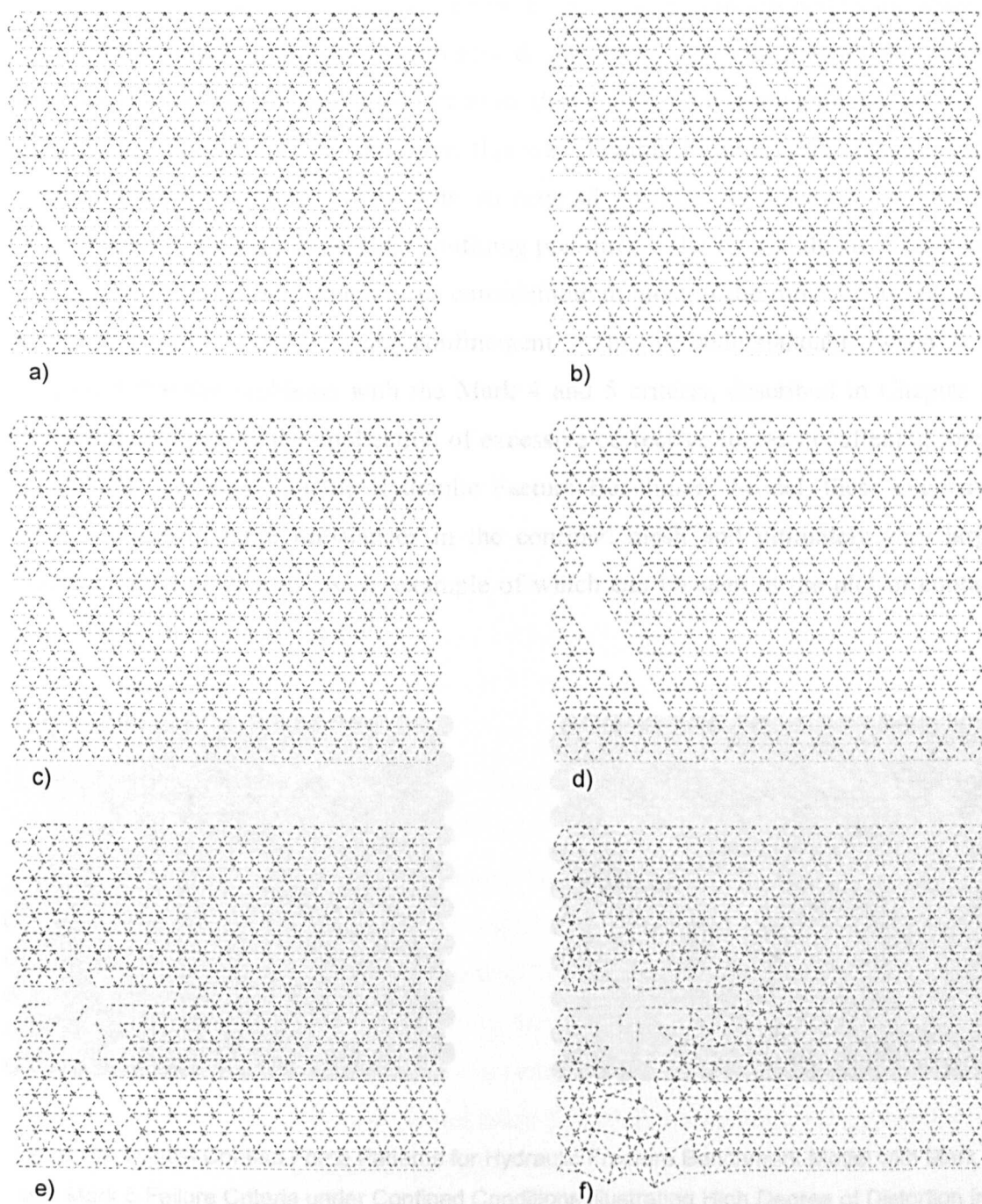


Fig. 6.8. Deviated Fracture Patterns for a) Mark 4 Failure Criterion with $\nu = 0.0$ under Zero Confinement b) Mark 4 Failure Criterion with $\nu = 0.0$ under Confined Conditions c) Mark 4 Failure Criterion with $\nu = 0.25$ under Zero Confinement d) Mark 5 Failure Criterion with $\nu = 0.0$ under Zero Confinement e) & f) Mark 5 Failure Criterion with $\nu = 0.25$ under Zero Confinement (Repeated from Section 6.2.3.2. above)

In contrast to the results of the studies conducted with the Mark 1, 2 and 3 failure criteria, little difference was seen between the fracture patterns developed by the Mark 4 and 5 criteria under confined or unconfined conditions. It was noticed that under confinement the fracturing tended to be more distributed, with more evidence of crack bridging (See *Fig. 6.8. b*). However, this was possibly more a consequence of the overall displacement of the mesh from its original position, as discussed in Section 6.2.3.3.4. above, than of the applied confining pressures. The overall displacement and distortion of the mesh was found to be considerable in most of the runs conducted with the Mark 4 and 5 criteria under confinement. This is understandable when it is considered that the problems with the Mark 4 and 5 criteria, described in Chapter 5, were a consequence of the application of excessive corrective forces in softening inter-particle link elements. In the Hydraulic Fracture Benchmark Model, these excessive forces resulted in large imbalances in the confined mesh and ultimately very large displacements and distortions, an example of which can be seen in the plot of contact forces shown in *Fig. 6.10.* below.

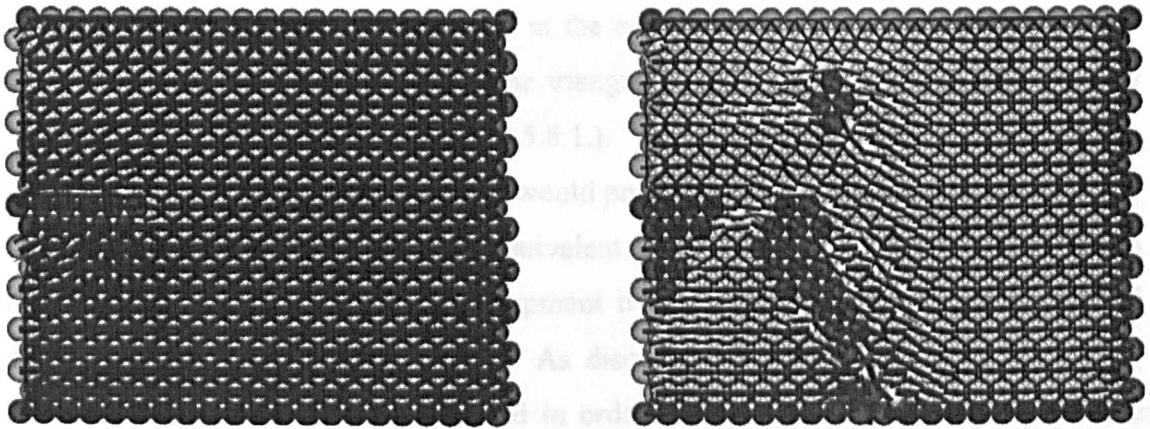


Fig. 6.10. Typical Contact Force Patterns for Hydraulic Fracture Benchmark Model with Mark 4 and Mark 5 Failure Criteria under Confined Conditions Illustrating High Degree of Distortion in the Mesh Resulting from Overall Displacement in the y-direction

Clearly, the behaviour described above and illustrated in *Fig. 6.8.* and *Fig. 6.10.* was not considered accurate for the Hydraulic Fracture Benchmark Model. However, as mentioned previously, the continuum principles, on which these failure criteria are based, resulted in the development of more continuous fractures and less crack bridging than was developed by other failure criteria.

A further point of note that can be seen in the results developed by the Mark 4 and 5 failure criteria in the Hydraulic Fracture Benchmark Model was the failure of the horizontal elements (aligned in the x -direction) on either side of the initial fracture length in preference to the elements at the fracture tip. This occurred as a consequence of the measure of the total strain, which was developed from the relative displacements in the 'diamond' of equivalent continuum material associated with each link element in the mesh. For the link elements in the wall of the initial fracture length, the associated 'diamond' spanned the fracture. Consequently, as the fracture opened under the influence of the applied fluid pressure, very large strains were measured in these 'diamonds'. These strains were subsequently related to the continuum total strain in these elements, thereby resulting in their failure. This behaviour was also noticed and discussed in Chapter 5, in conjunction with the Two-Dimensional Uniaxial Benchmark Model. In order to solve this problem it would be desirable to develop coding in order to determine if a particular link element is next to a fracture. This could be done by checking whether all of the link elements forming an equivalent continuum 'diamond' are intact. If an element was found to be at the edge of a fracture, then it could be treated in the same way as an element at the edge of a mesh and its continuum total strain state could be calculated from the triangular equivalent continuum area on only one side of it (See Chapter 5, Section 5.8.1.). As in previous examples, code of this kind would be complex to develop and would probably be computationally expensive to execute. Furthermore, should the equivalent continuum area on both sides of an element be affected by fracture development it is not clear how the continuum total strain state would then be measured. As discussed in Section 5.9.4. of Chapter 5, further investigation would be required in order to determine the exact nature of the problems associated with the Mark 4 and Mark 5 failure criteria and in order to develop them into robust failure criteria for the PSM.

6.2.3.4. Figures Showing Comparative Fracture Propagation Results

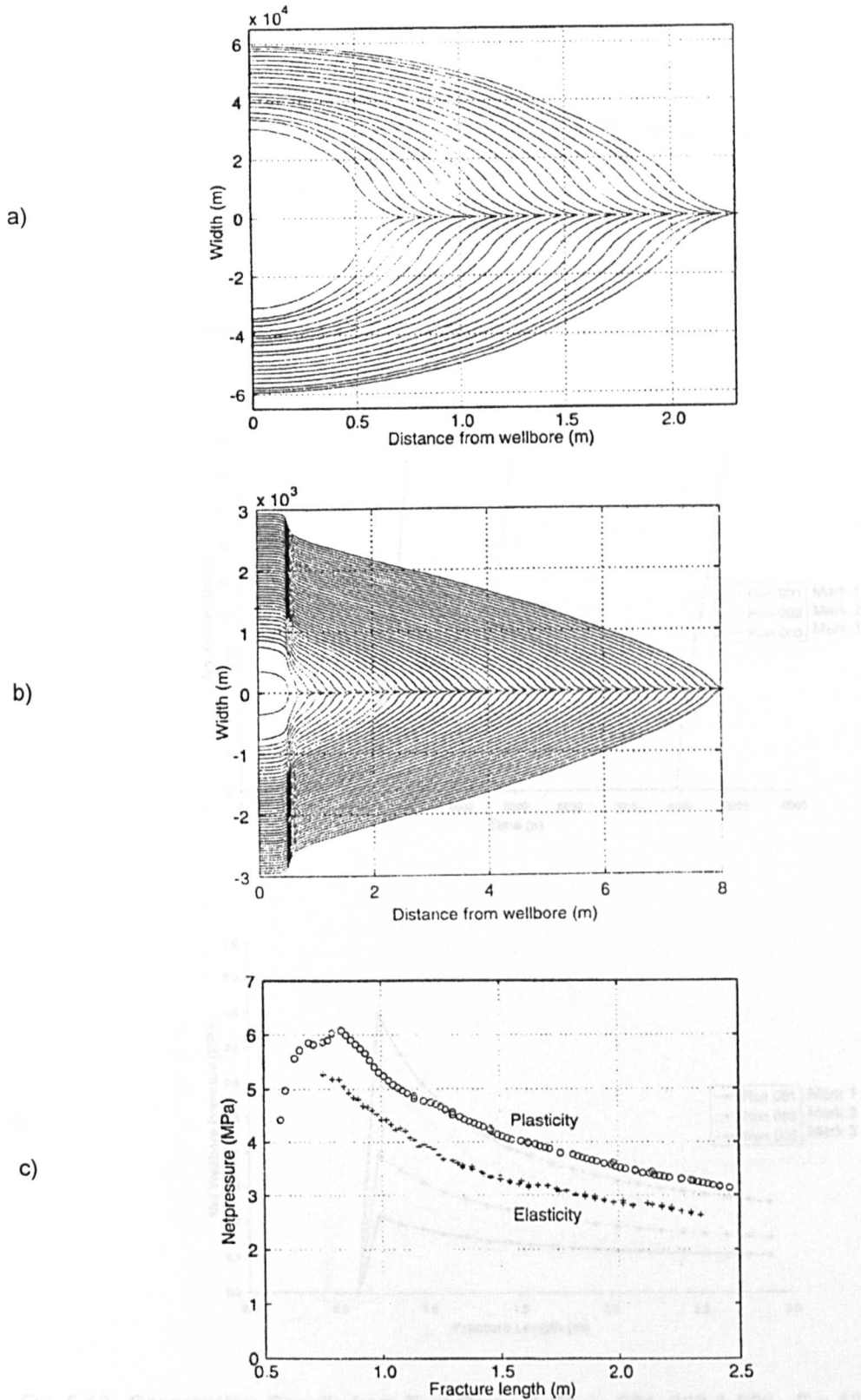


Fig. 6.12. Comparative Results from Test Group 1 (E = 1785 GPa, $\nu = 0.01$, $\sigma_{01} = 0.02$ & $\sigma_{03} = -E \times 1785$ MPa)

Fig. 6.11. Plotted Results from FE Study by Papanastasiou [69] Showing a) Propagating Fracture Width Profiles in an Elastic Medium, b) Propagating Fracture Width Profiles in and Elasto-Plastic Medium & c) Plots of Net Pressure in Wellbore during Fracture Propagation

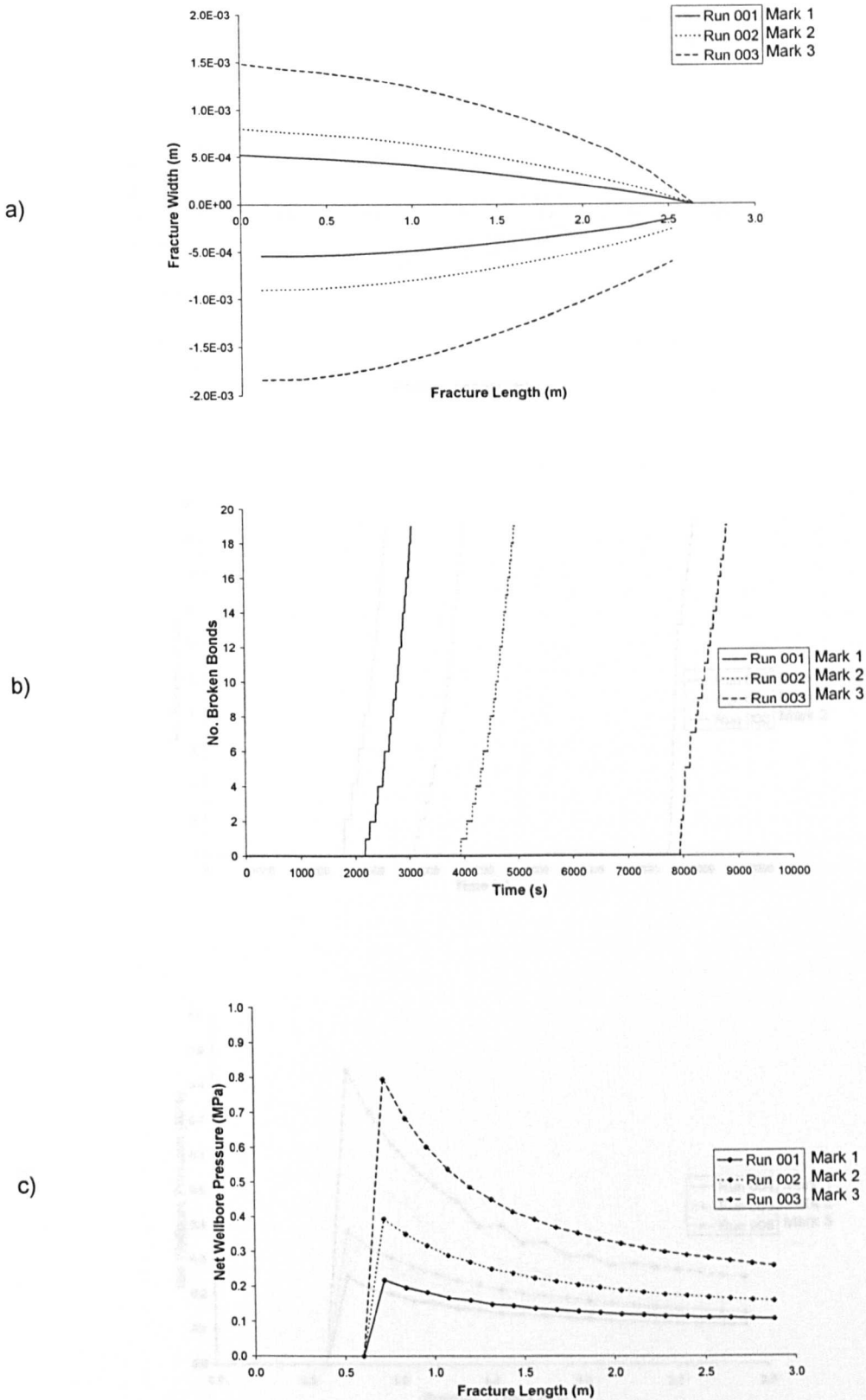


Fig. 6.12. Comparative Results from Test Group A (Runs 001, 002 & 003 - $E = 1785.0\text{MPa}$, $\nu = 0.00$, $\sigma_2 = 0.0\text{MPa}$, $\sigma_3 = 0.0\text{MPa}$) Showing a) Final Fracture Width Profiles, b) Number of Failed Inter-Particle Link Elements in Time during Fracture Propagation and c) Net Wellbore Pressure against Propagating Fracture Length

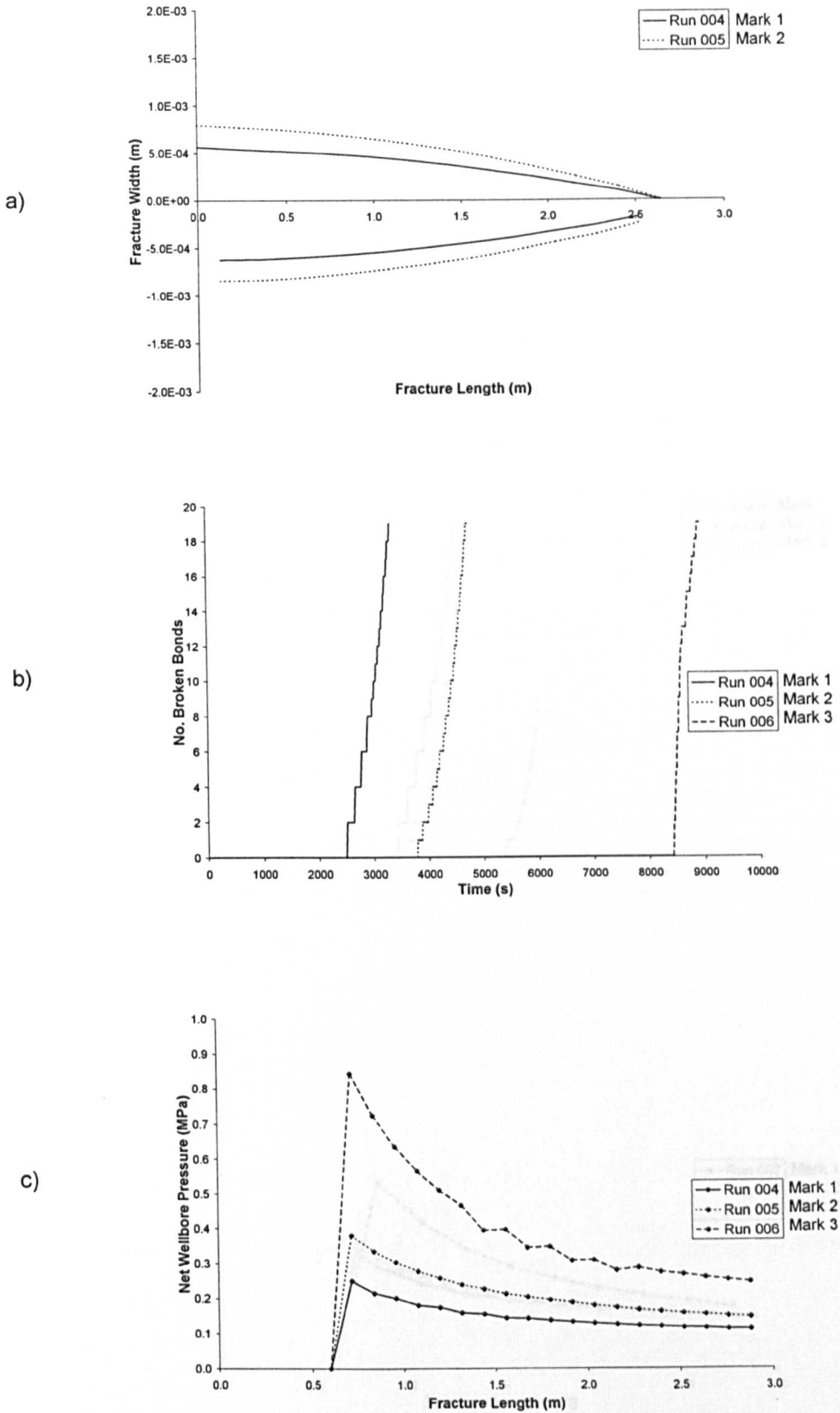


Fig. 6.13. Comparative Results from Test Group B (Runs 004, 005 & 006 - $E = 1785.0\text{MPa}$, $\nu = 0.125$, $\sigma_2 = 0.0\text{MPa}$, $\sigma_3 = 0.0\text{MPa}$) Showing a) Final Fracture Width Profiles, b) Number of Failed Inter-Particle Link Elements in Time during Fracture Propagation and c) Net Wellbore Pressure against Propagating Fracture Length

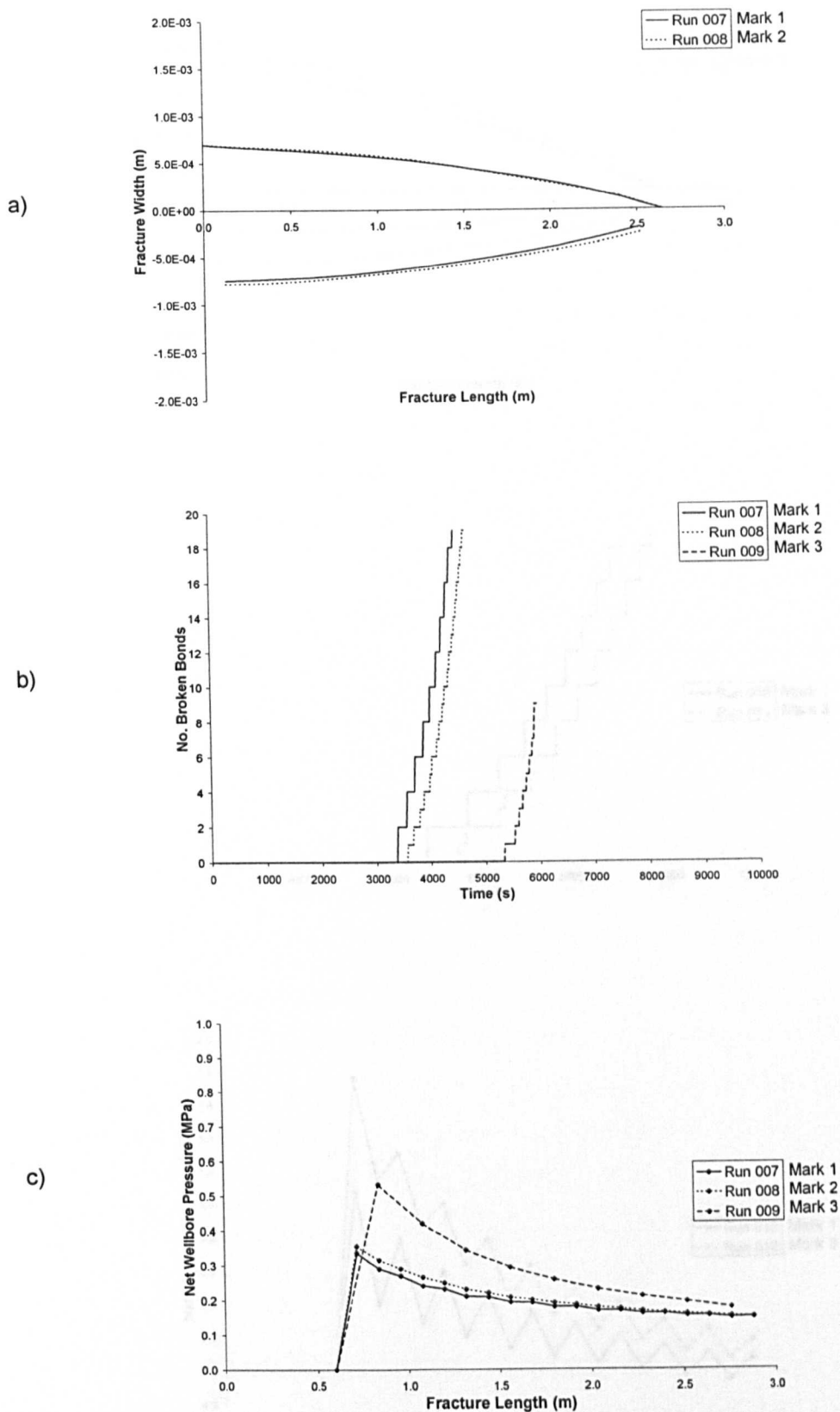


Fig. 6.14. Comparative Results from Test Group C (Runs 007, 008 & 009 - $E = 1785.0\text{MPa}$, $\nu = 0.25$, $\sigma_2 = 0.0\text{MPa}$, $\sigma_3 = 0.0\text{MPa}$) Showing a) Final Fracture Width Profiles, b) Number of Failed Inter-Particle Link Elements in Time during Fracture Propagation and c) Net Wellbore Pressure against Propagating Fracture Length

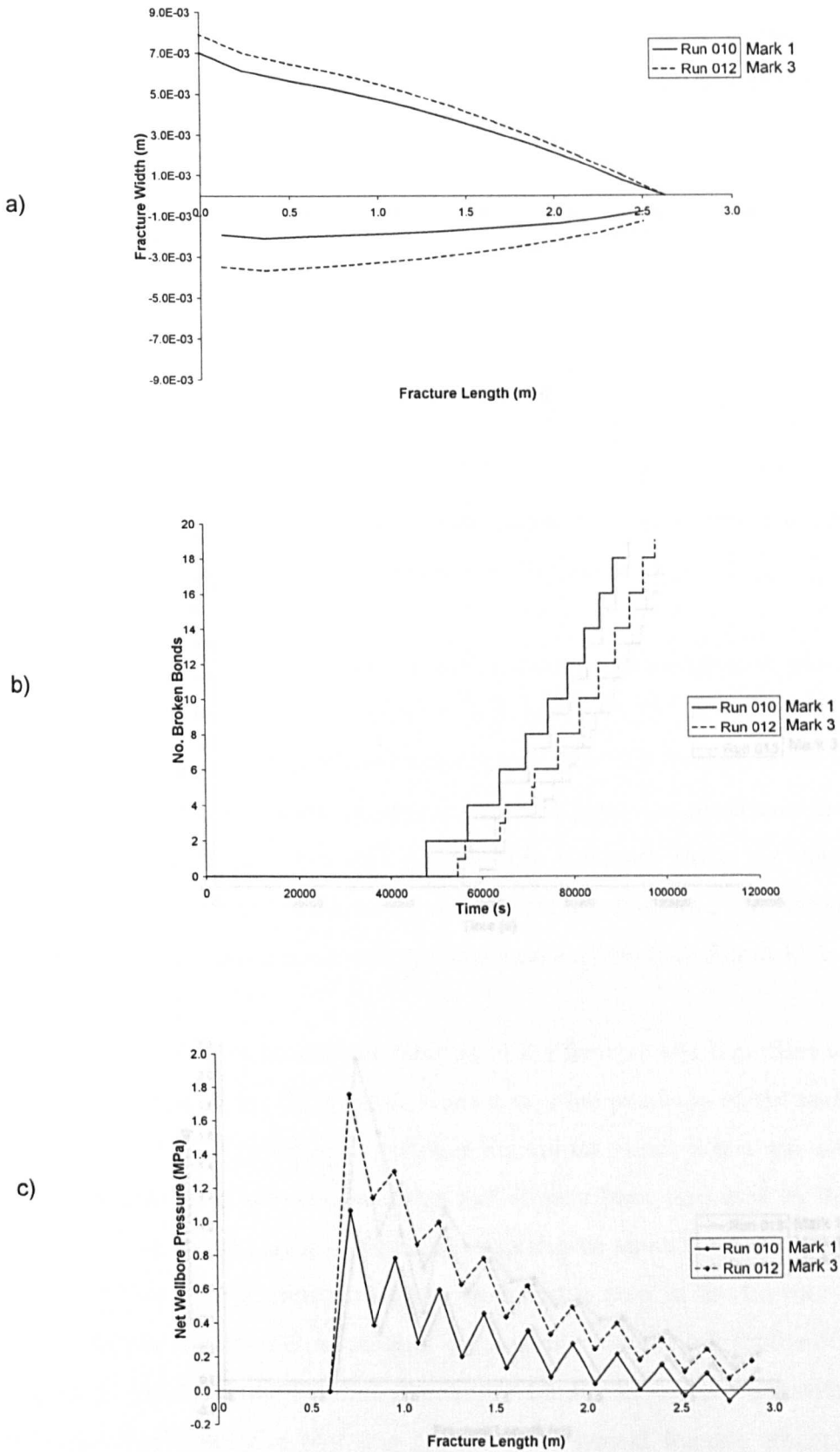


Fig. 6.15. Comparative Results from Test Group D (Runs 010, 011 & 012 - $E = 1785.0\text{MPa}$, $\nu = 0.00$, $\sigma_2 = 9.0\text{MPa}$, $\sigma_3 = 3.7\text{MPa}$) Showing a) Final Fracture Width Profiles, b) Number of Failed Inter-Particle Link Elements in Time during Fracture Propagation and c) Net Wellbore Pressure against Propagating Fracture Length

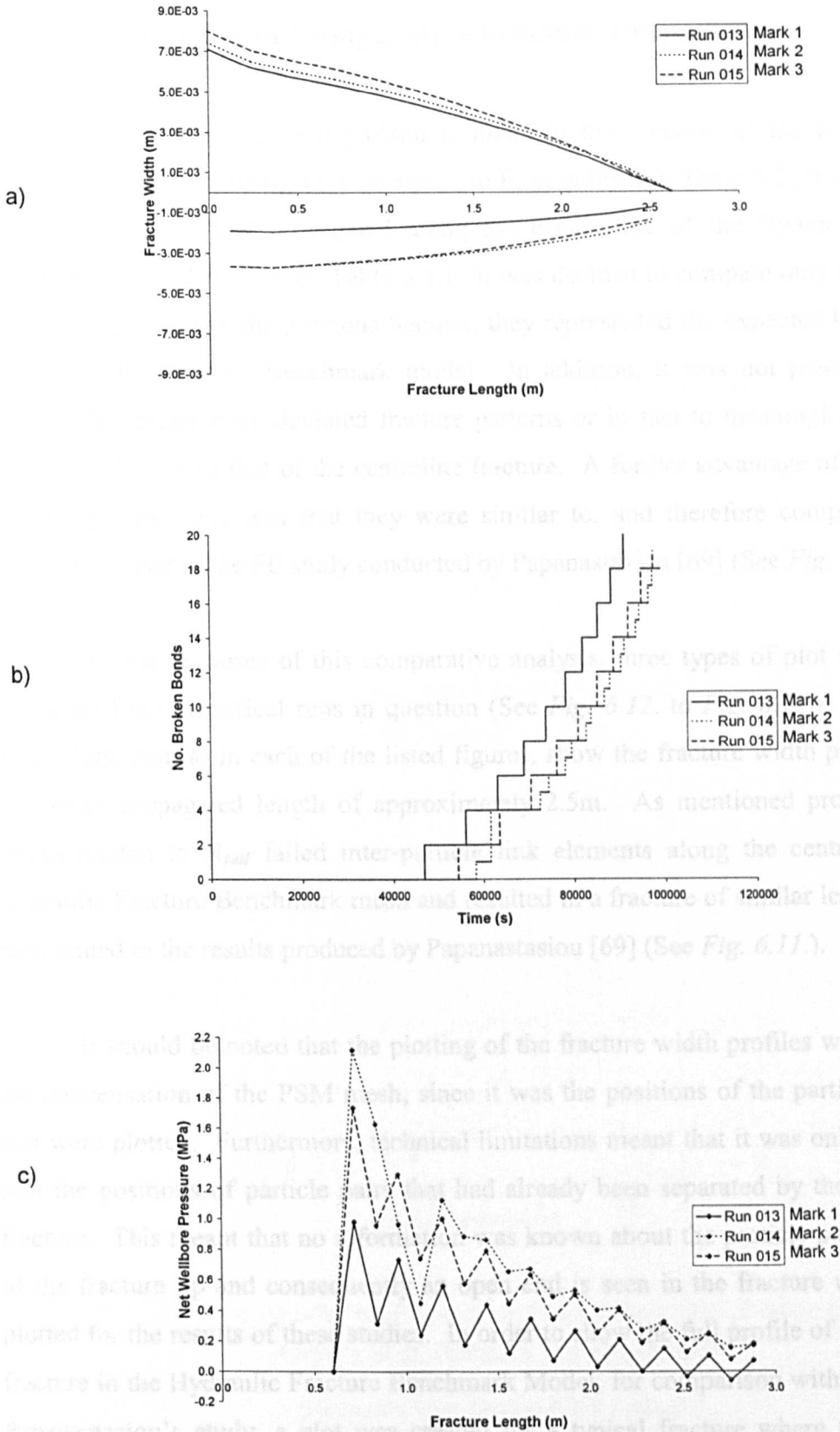


Fig. 6.16. Comparative Results from Test Group E (Runs 013, 014 & 015 - $E = 1785.0\text{MPa}$, $\nu = 0.125$, $\sigma_2 = 9.0\text{MPa}$, $\sigma_3 = 3.7\text{MPa}$) Showing a) Final Fracture Width Profiles, b) Number of Failed Inter-Particle Link Elements in Time during Fracture Propagation and c) Net Wellbore Pressure against Propagating Fracture Length

6.2.3.5. Discussion of Comparative Fracture Propagations

As mentioned previously, comparison is made in this Section of the results of the numerical runs, comprising Test Groups A to E, as defined in Table 6.2., that resulted in a straight fracture that propagated along the centre line of the Hydraulic Fracture Benchmark Model mesh (See Table 6.4.). It was decided to compare only these results since, as discussed in the previous Section, they represented the expected behaviour of the Hydraulic Fracture Benchmark model. In addition, it was not practical to plot meaningful results from deviated fracture patterns or in fact to meaningfully compare their behaviour with that of the centreline fracture. A further advantage of considering the straight fractures was that they were similar to, and therefore comparable with, results produced in the FE study conducted by Papanastasiou [69] (See Fig. 6.11.).

For the purposes of this comparative analysis, three types of plot were created for each of the numerical runs in question (See Fig. 6.12. to Fig. 6.16.). The first of these plots, item a) in each of the listed figures, show the fracture width profiles at the maximum propagated length of approximately 2.5m. As mentioned previously, this length related to N_{fail} failed inter-particle link elements along the centreline of the Hydraulic Fracture Benchmark mesh and resulted in a fracture of similar length to those represented in the results produced by Papanastasiou [69] (See Fig. 6.11.).

It should be noted that the plotting of the fracture width profiles was limited by the discretisation of the PSM mesh, since it was the positions of the particle centroids that were plotted. Furthermore, technical limitations meant that it was only possible to plot the positions of particle pairs that had already been separated by the propagating fracture. This meant that no information was known about the particle positions ahead of the fracture tip and consequently an open end is seen in the fracture width profiles plotted for the results of these studies. In order to show the full profile of a propagating fracture in the Hydraulic Fracture Benchmark Model, for comparison with the results of Papanastasiou's study, a plot was created for a typical fracture where the centreline propagation path was known beforehand. This plot is shown in Fig. 6.17. below and it can clearly be seen that the general shape of the propagating fracture profiles match very well with those of the fractures produced in FE study conducted by Papanastasiou

(See Fig. 6.11. a) repeated below). For the remainder of the fracture width profiles shown in Fig. 6.12. to Fig. 6.16., it is assumed that the shape, beyond the foremost plotted position, is similar to that shown below.

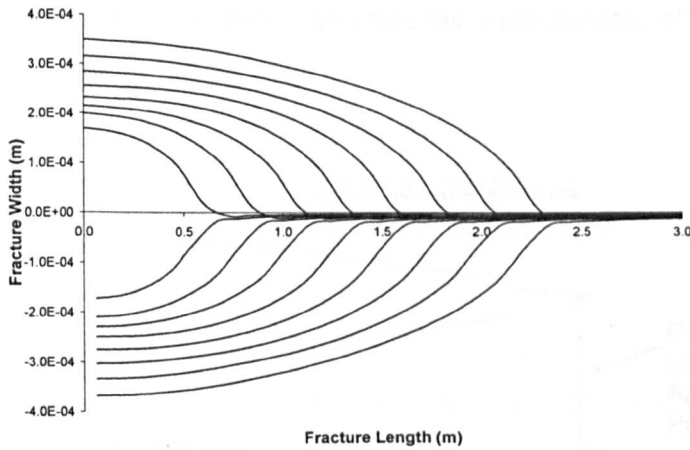


Fig. 6.17. Diagram Showing Typical Fracture Width Profiles for a Propagating Hydraulic Fracture in a PSM mesh

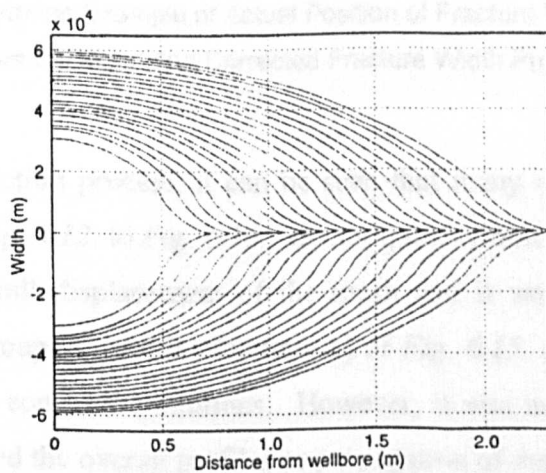


Fig. 6.11. a) Plotted Results from FE Study by Papanastasiou [69] Showing Propagating Fracture Width Profiles in an Elastic Medium

(Repeated from Section 6.2.3.4. above)

It should also be noted that, as discussed in Section 6.2.3.3.4. above, an overall displacement of the PSM mesh in the y -direction was experienced, due to slight imbalances in the total applied forces, during some of the numerical runs carried out in

these studies. It was consequently found that some of the fracture width profiles were offset from their original positions. For the purposes of this work, it was therefore necessary to re-centre these fracture profiles in order to overlay them in a comparative manner as shown in *Fig. 6.12.* to *Fig. 6.16.* This was done simply by deleting the amount by which the mesh had displaced from the y -coordinates of the plotted particle centroids (See *Fig. 6.18.* below).

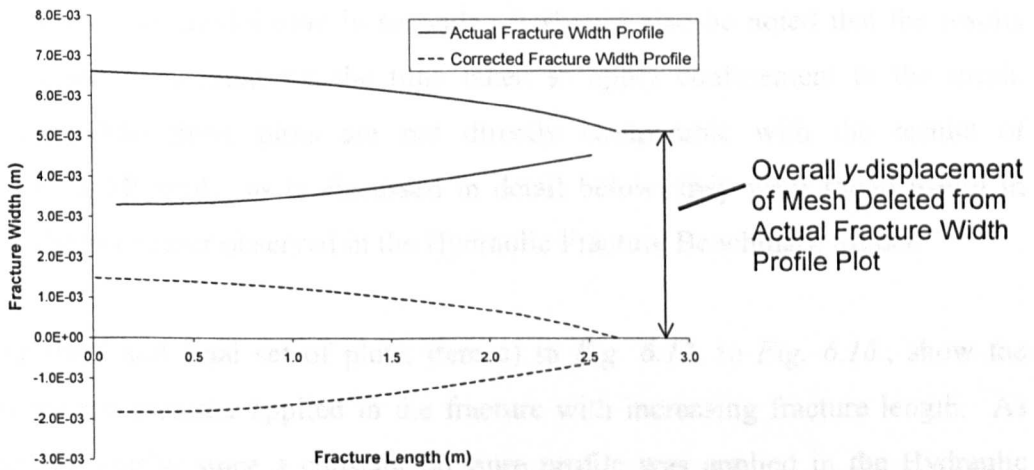


Fig. 6.18. Plot Showing Example of Actual Position of Fracture Width Profile Resulting from Overall Displacement of Mesh and Corrected Fracture Width Profile for Comparative Overlay

Despite this correction process, it can be seen that many of the fracture width profile plots, shown in *Fig. 6.12.* to *Fig. 6.16.*, are not quite symmetrical. This effect is again a result of the overall displacement of the mesh and it was particularly noticeable in results of Test Groups D and E (See item a) of *Fig. 6.15.* and *Fig. 6.16.*), which were carried out under confined conditions. However, it was not felt that this deformation significantly altered the overall profiles or propagation of the fractures.

An additional feature noticeable in most of the fracture width profiles is an anomalous change in the curve of the fracture walls, either into or out of the fracture, at the end nearest the wellbore. Again, this effect was partially due to the overall movement of the PSM mesh but it was also thought to be associated with a combination of the symmetry boundary conditions and the applied fluid pressure load on the PFC^{3D} particle at the edge of the PSM mesh. Nonetheless, as with the previous examples, this

effect was not considered to have a significant influence on the overall shape of the fracture profiles.

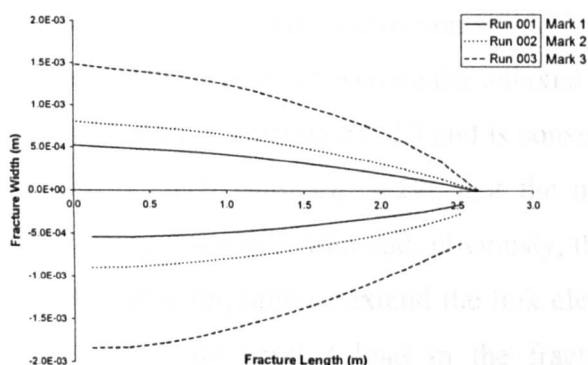
The second set of plots, item b) in *Fig. 6.12.* to *Fig. 6.16.*, show the number of broken inter-particle link elements against the number of model time steps. Since the application of the differential density scaling function, in order to develop quasi-static behaviour (See Section 6.2.1.), results in a unit time step, the *x*-axis of these plots actually represent the model time in seconds. It should also be noted that the results were normalised to account for the time taken to apply confinement to the mesh. Furthermore, while these plots are not directly comparable with the results of Papanastasiou's FE study, as is discussed in detail below, they were found useful in confirming the behaviour observed in the Hydraulic Fracture Benchmark Model.

The third and final set of plots, item c) in *Fig. 6.12.* to *Fig. 6.16.*, show the change in the net pressure applied in the fracture with increasing fracture length. As mentioned previously, since a constant pressure profile was applied in the Hydraulic Fracture Benchmark Model, the net fracture pressure was equivalent to the net pressure at the wellbore. These plots were then directly comparable with the net pressure plots produced by Papanastasiou [69] for the FE study (See *Fig. 6.11. c*).

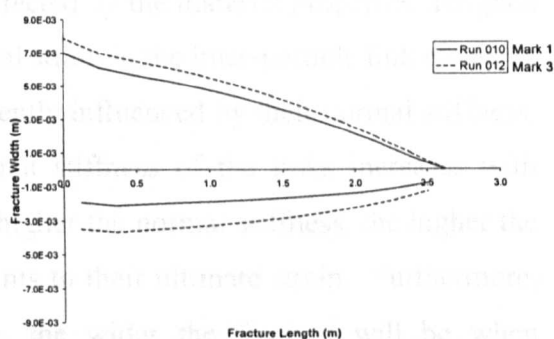
It should be noted that these plots show the net fracture pressures at which the inter-particle link elements failed. The curves do not represent the actual pressure in the fracture at all times. Due to the algorithm employed in the Hydraulic Fracture Benchmark Model to apply the 'fluid pressure forces' (See Section 6.2.1. and *Eq. 6.1.*), the actual fracture pressure dropped considerably after each fracturing event before it increased linearly again, at the same rate as the initial pressure increase.

Considering firstly the plotted fracture width profiles for each of the five Test Groups under consideration (See item a) in *Fig. 6.12.* to *Fig. 6.16.* repeated below), several points of note can be made. Firstly, it can be seen that, in all cases, although the fracture profiles within each individual plot are generally of the similar shape, the actual width is greater under the Mark 2 failure criterion than under the Mark 1, and is greater yet under the Mark 3 criterion. It can also be seen in *Fig. 6.12.*, *Fig. 6.13.* and *Fig. 6.14.*, that the profile of the fractures developed under the Mark 2 criterion varies very

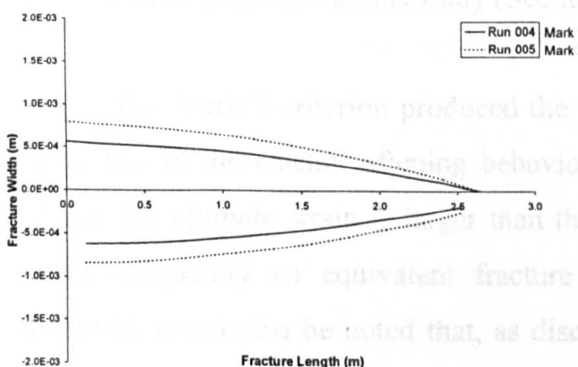
little while the profile of the fractures developed under the Mark 1 criterion widens with increasing Poisson's ratio. In Fig. 6.14., with a Poisson's ratio, $\nu = 0.25$, it can be seen that the profiles of the Mark 1 and Mark 2 fractures are virtually identical.



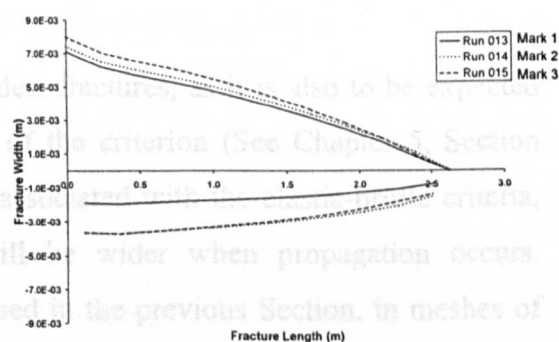
i)



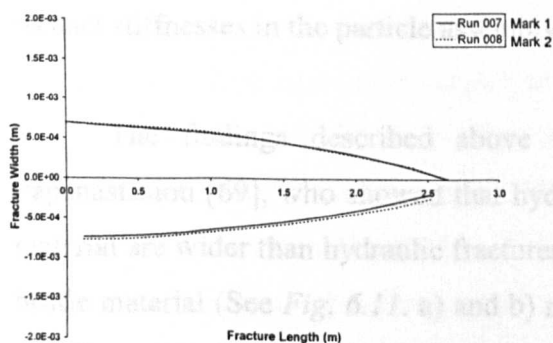
iv)



ii)



v)



iii)

Fracture Width Profiles from i) (Fig. 6.12.) Runs 001, 002 and 003, $\nu = 0.00$, Zero Confining Pressure ii) (Fig. 6.13.) Runs 004 and 005, $\nu = 0.125$, Zero Confining Pressure iii) (Fig. 6.14.) Runs 007 and 008, $\nu = 0.25$, Zero Confining Pressure iv) (Fig. 6.15.) Runs 010 and 012, $\nu = 0.00$, $\sigma_2 = 9.0\text{MPa}$, $\sigma_3 = 3.7\text{MPa}$ v) (Fig. 6.16.) Runs 013, 014 and 015, $\nu = 0.125$, $\sigma_2 = 9.0\text{MPa}$, $\sigma_3 = 3.7\text{MPa}$
(Repeated from Section 6.2.3.4. above)

The finding that the Mark 2 criterion was unaffected by varying Poisson's ratio is as would be expected since the criterion is based on the stress tensors in the PFC^{3D} DEM particles (See Chapter 5, Section 5.6.1.) and, as discussed previously, these tensors are only dependent on the external loading conditions. Furthermore, it is also to be expected that the Mark 1 criterion would be affected by the material properties assigned to the mesh since it is based on the uniaxial total strain in the inter-particle link elements (See Chapter 5, Section 5.5.1.) and is consequently influenced by their normal stiffness. It can be seen from *Eq. 4.29.*, that the normal stiffness of the links increases with increasing Poisson's ratio and, obviously, the higher the normal stiffness, the higher the force that is required to extend the link elements to their ultimate strain. Furthermore, the higher the applied load in the fracture, the wider the fracture will be when propagation occurs and, indeed, this is the behaviour that can be observed in the fracture width profiles produced in this study (See item a) in *Fig. 6.12.* to *Fig. 6.14.*).

The Mark 3 criterion produced the widest fractures, as it is also to be expected since, due to the elastic-softening behaviour of the criterion (See Chapter 5, Section 5.7.1.), the ultimate strain is larger than that associated with the elastic-brittle criteria, and consequently an equivalent fracture will be wider when propagation occurs. However, it can also be noted that, as discussed in the previous Section, in meshes of Poisson's ratio, $\nu = 0.125$ and 0.25 , the Mark 3 criterion produces a deviated fracture pattern, thus indicating that it is most sensitive to changes in the ratio of normal to shear contact stiffnesses in the particle assembly.

The findings described above are also generally confirmed by those of Papanastasiou [69], who showed that hydraulic fractures developed in an elasto-plastic material are wider than hydraulic fractures, of the same length, propagated in an elastic-brittle material (See *Fig. 6.11.* a) and b) repeated below). However, it can also be seen that Papanastasiou showed the profiles of elasto-plastic fractures to be of a different shape to those of an elastic-brittle fracture and this feature is not very well represented in the results of the studies presented here. A slightly different fracture shape is seen under confined conditions than under zero confinement (See *Fig. 6.12.* and *Fig. 6.15.*) but again no significant difference is seen between the shapes of the elastic-brittle and elastic-softening fractures under the same conditions.

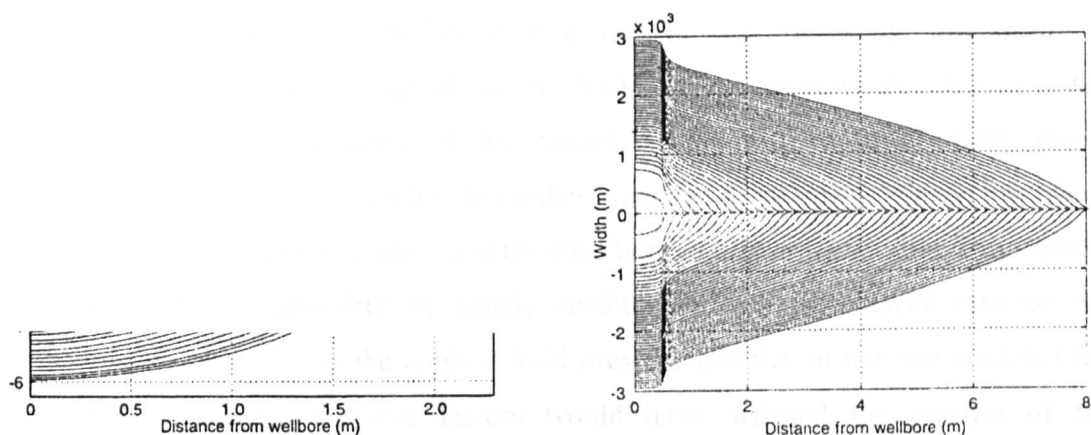


Fig. 6.11. a) *Plotted Results from FE Study by Papanastasiou [69] Showing a) Propagating Fracture Width Profiles in an Elastic Medium, b) Propagating Fracture Width Profiles in and Elasto-Plastic Medium*

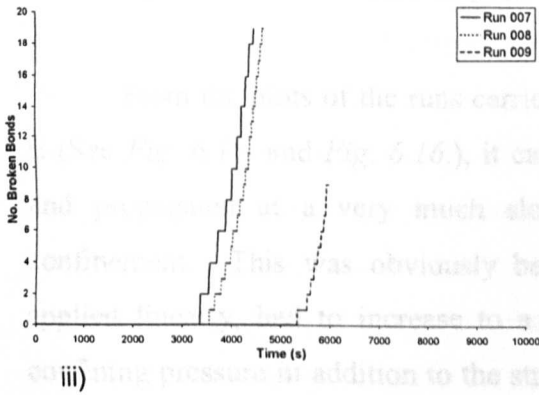
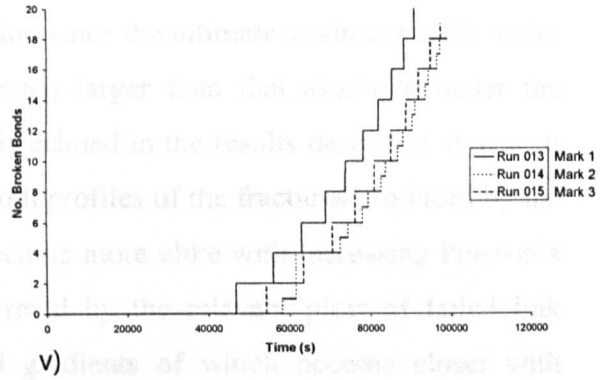
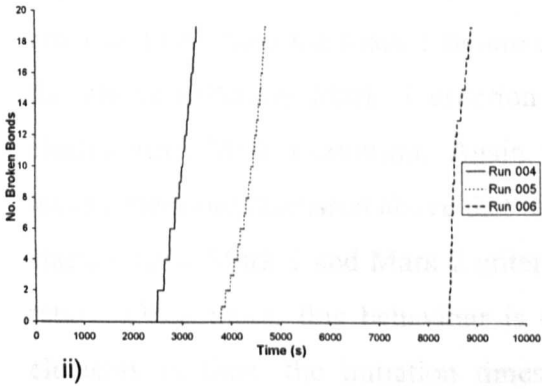
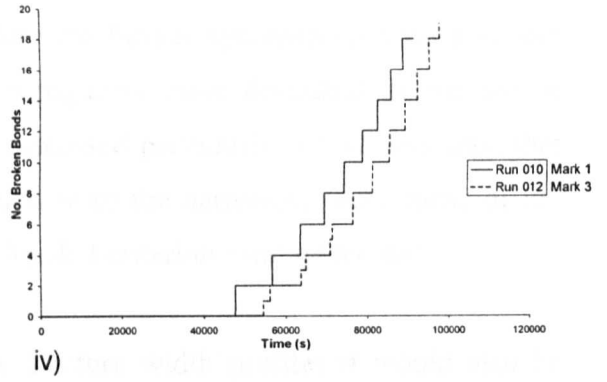
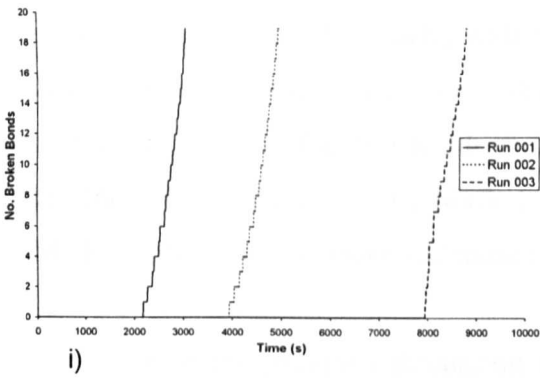
(Repeated from Section 6.2.3.4. above)

In considering the actual fracture widths produced in these studies and comparing them to the results of the FE study carried out by Papanastasiou [69] it can be seen that the fracture widths produced by the Mark 1 and Mark 2 criteria, as shown in *Fig. 6.12.* to *Fig. 6.14.*, are very similar to those presented by Papanastasiou [69] (See *Fig. 6.11. a)*). However, it is believed that this similarity is largely coincidental since, as shown in Chapter 5, the Mark 1 and Mark 2 criteria are elastic-brittle criteria and as such produce results that are dependent on the characteristic length of the mesh elements. Furthermore, these tests were carried out under zero confinement whereas those for which the results are shown in *Fig. 6.11. a)* were conducted under the confined conditions described in Section 6.2.1. above. For the tests conducted under confined conditions, as shown in *Fig. 6.15.* and *Fig. 6.16.*, the fractures produced by the Mark 1 criterion can be seen to be very much wider than the elastic-brittle fracture profiles shown by Papanastasiou (See *Fig. 6.11. a)*). This pattern is repeated with the elasto-plastic fractures developed by the Mark 3 criterion, however, the actual fracture widths shown in *Fig. 6.15.* and *Fig. 6.16.* are of a similar magnitude to those presented by Papanastasiou (See *Fig. 6.11. b)*).

As indicate above, a direct quantitative comparison cannot be made between the results of the elastic-brittle studies carried out in the FE study conducted by Papanastasiou [69] and those carried out for the Hydraulic Fracture Benchmark Study due to the inherent dependency of the results on the discretisation of the mesh. However, the quantitative results for the studies conducted with elasto-plastic behaviour should be directly comparable and the difference between the results of the two studies, described above, can probably be largely attributed to the differences between the ductility of the material and the applied fluid pressure profiles in the two models (See Section 6.2.1.). Both of these factors would have affected the profiles of the propagating fractures.

As mentioned previously, the fracture propagation behaviour inferred from the fracture profiles discussed above can be further verified by examination of the plots showing the progression of link element failure in time (See item b) in *Fig. 6.12.* to *Fig. 6.16.* repeated below). The information most obviously displayed by these figures is the time of fracture initiation and the subsequent rate of propagation of the fractures, as represented by the gradient of the curves, under the varying conditions applied in the tests.

For Test Groups A, B and C, in which the runs were carried out under zero confining pressure (See *Fig. 6.12.* to *Fig. 6.14.*), it can be seen that, of the three plotted curves in each figure, those produced by the Mark 1 criterion are first to initiate and furthermore they have slightly steeper gradients than the curves produced by the other failure criteria. Thus, it can be seen that the Mark 1 criterion produces the fastest fracture propagation. It can also be seen that the fractures produced by the Mark 2 criterion are next to be initiated and have only a slightly shallower gradient than the curves for the Mark 1 criterion. Finally, the fractures produced by the Mark 3 criterion clearly take much longer to initiate than those of the other two criteria. While these curves eventually become shallower than the others are, they start at a much steeper gradient.



Number of Failed Inter-Particle Link Elements in Time during Fracture Propagation from i) (Fig. 6.12.) Runs 001, 002 and 003, $\nu = 0.00$, Zero Confining Pressure ii) (Fig. 6.13.) Runs 004, 005 and 006, $\nu = 0.125$, Zero Confining Pressure iii) (Fig. 6.14.) Runs 007, 008 and 009, $\nu = 0.25$, Zero Confining Pressure iv) (Fig. 6.15.) Runs 010 and 012, $\nu = 0.00$, $\sigma_2 = 9.0\text{MPa}$, $\sigma_3 = 3.7\text{MPa}$ v) (Fig. 6.16.) Runs 013, 014 and 015, $\nu = 0.125$, $\sigma_2 = 9.0\text{MPa}$, $\sigma_3 = 3.7\text{MPa}$

(Repeated from Section 6.2.3.4. above)

When considering the fracture width profiles discussed above it is clear that wider fractures are synonymous with higher applied fluid pressures and since the fluid steeper in time. This is indicative that the fractures become easier to propagate as their

pressure was increased linearly, wider fracture are further synonymous with a slower rate of propagation. Thus the relative propagation rates described above are in agreement with the fracture width profiles, discussed previously, which indicated that the fractures produced by the Mark 1 criterion were the narrowest while those of the Mark 2 criterion were wider and those of the Mark 3 criterion were wider still.

From the previous discussion of the fracture width profiles it would also be expected that it would take longer for a fracture to initiate under the Mark 3 failure criterion than under the Mark 1 failure criterion since the ultimate strain available under the elastic-softening Mark 3 criterion is much larger than that available under the elastic-brittle Mark 1 criterion. Again, this is echoed in the results described above. It was furthermore discussed above that the width profiles of the fractures produced by the elastic-brittle Mark 1 and Mark 2 criteria become more alike with increasing Poisson's ratio. Once more, this behaviour is confirmed by the relevant plots of failed link elements in time, the initiation times and gradients of which become closer with increasing Poisson's ratio until they are very similar under a Poisson's ratio of 0.25.

From the plots of the runs carried out under confinement, in Test Groups D and E (See *Fig. 6.15.* and *Fig. 6.16.*), it can be seen that the fractures initiated much later and propagated at a very much slower rate than those carried out under zero confinement. This was obviously because the fracture pressure, which was again applied linearly, had to increase to a much higher value, in order to overcome the confining pressure in addition to the strength of the material, before a fracture could be initiated. This is reflected in the plots of the fracture width profiles, discussed above, which showed the fractures created under confined conditions to be very much wider than those created under zero confinement. Furthermore, it can be seen that these plots show very similar initiation times and fracture propagation rates for all three failure criteria under confined conditions. Again, this was a reflection of the fracture width profiles, which showed the fractures produced by these criteria to have very similar dimensions.

It can also be noted that, for the majority of the plots of inter-particle link failure in time and particularly for the unconfined runs, the gradient of the curves becomes steeper in time. This is indicative that the fractures become easier to propagate as their

length increases, an effect that is discussed further, below. The exceptions to this observation are the plots, shown in *Fig. 6.12.* and *Fig. 6.13.*, for the runs carried out with the Mark 3 criterion under zero confinement. As mentioned previously, these curves start steeply and then slow significantly before gradually steepening again in the manner described for the other curves. The exact reason for this is not completely clear, however it is probably an effect of the redistribution of stress in the PSM mesh ahead of the fracture tip due to the elastic-softening behaviour of the Mark 3 failure criterion as described in Section 5.7.1. of Chapter 5. The exaggeration of this effect in the results of the run carried out with a Poisson's ratio of 0.125 (See *Fig. 6.13.*) is probably a consequence of the deviation that occurs approximately halfway through the propagation process.

Additionally, it can be seen, in the various plots described above, that while in most cases, as would be expected, single bond failures occur at quite regular intervals, instances can be seen where two bonds fail in close succession. This is particularly evident in the runs carried out under confinement. It was initially thought that this might be a dynamic effect resulting from too high a load rate, however a test run showed that a reduced load rate in fact increased the occurrence of this phenomenon. For the runs carried out under zero confinement it can also be seen that the incidence of this phenomenon increases with increasing Poisson's ratio. It is therefore thought possible that this was associated with the change in the PSM from considering two force components to considering only one force component in each link element, as discussed in the previous Section. However, under confined conditions, the phenomenon occurred equally with Poisson's ratio 0.0 and 0.25. It can further be noticed that, for all cases, the phenomenon is most evident in runs conducted with the Mark 1 criterion and so a third possible interpretation was that the phenomenon might be an effect of the elastic-brittle behaviour associated with the Mark 1 criterion. However, this again does not hold universally true, since the behaviour is less evident in the runs conducted with the Mark 2 criterion, which is also elastic-brittle. A further observation that can be made is that since the fracture fluid pressure drops after each element failure and increases again linearly, the second failure in the rapid succession events, occurs at a lower pressure than the first. In all cases, the second element to fail is orientated such that it is angled

downwards towards the free boundary at the 'right-hand end'[†] of the Hydraulic Fracture Benchmark Model mesh (See *Fig. 6.2*). Thus, elements orientated in this way are apparently easier to fail than those orientated such that they are angled upwards towards the 'right-hand end' of the mesh. It is not clear why this is, since the link elements in these studies have uniform strength. However, it is possible that it is a consequence of the overall movement of the mesh, as described previously, having a particular affect on elements orientated in this way and resulting their over extension and premature failure.

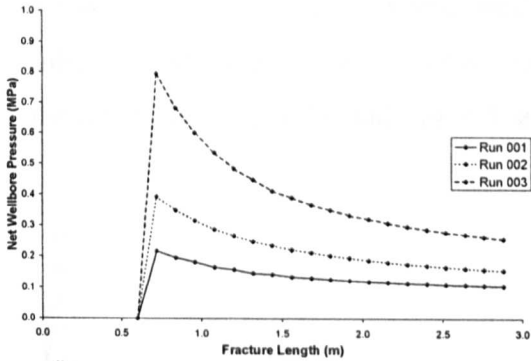
Despite the various interpretations presented above, no conclusive explanation has yet been found for the rapid succession of element failures. Whatever the cause of this phenomenon, after examination of the plots and consideration of the drop in applied fracture pressure after each element failure (See *Eq. 6.1*), it is not thought to have a significant affect on the overall fracture propagation rate. However, further consequences of this phenomenon will be discussed below, in conjunction with the variation of the net wellbore pressure during propagation of the fractures.

As mentioned, the final set of results presented in *Fig. 6.12*. to *Fig. 6.16*. are the plots of Net Wellbore Pressure against Propagating Fracture Length (repeated below). To reiterate, it should be noted that these profiles plot the net pressure in the wellbore at the time of a link element failure.

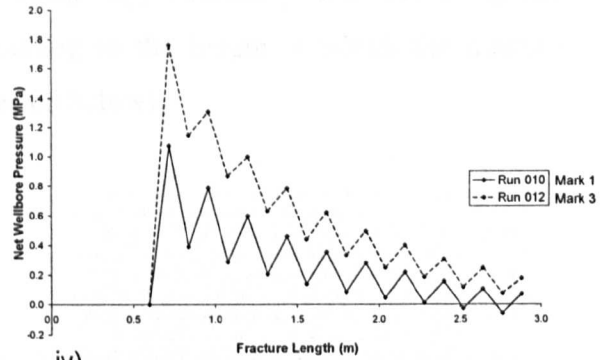
As can be seen from the plots shown below, the relative behaviour represented is as would be expected from the fracture width and element failure results discussed previously. For the tests carried out under zero confinement (See *Fig. 6.12*. to *Fig. 6.14*.), this can particularly be seen in the pressure profiles from the runs carried out with the Mark 1 criterion, which increase in magnitude with increasing Poisson's ratio. A result that concurs with the associated fracture width profiles that widen with increasing Poisson's ratio (See item a) of *Fig. 6.12*. to *Fig. 6.14*.) and with the fracture initiation times which become longer with increasing Poisson's ratio (See item b) of *Fig. 6.12*. to *Fig. 6.14*. and previous discussion). A further feature of the Mark 1 fracture width profiles discussed above was that they became more like those of the

[†] The referenced 'right-hand end' of the Hydraulic Fracture Model mesh refers to the orientation in which all figures are presented in this Section.

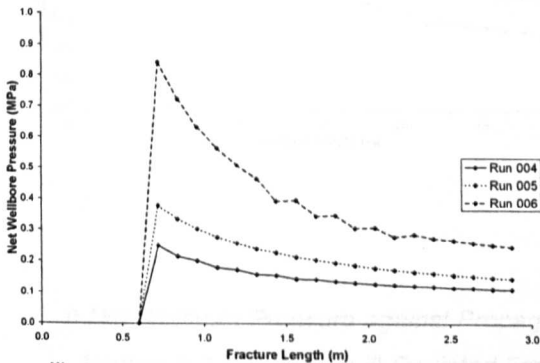
Mark 2 criterion with increasing Poisson's ratio. This is again mirrored in the pressure profiles, which are seen to match very closely in Fig. 6.14, c).



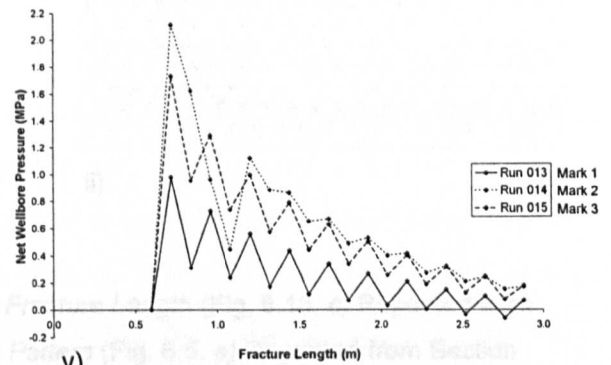
i)



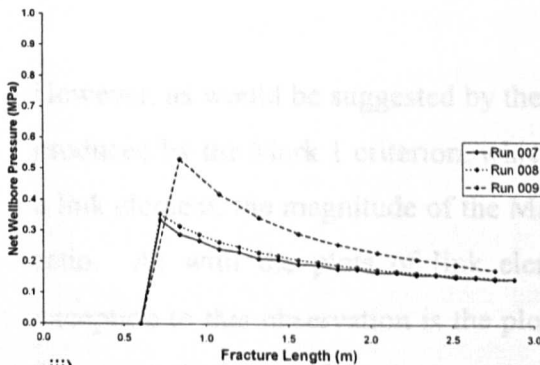
iv)



ii)



v)

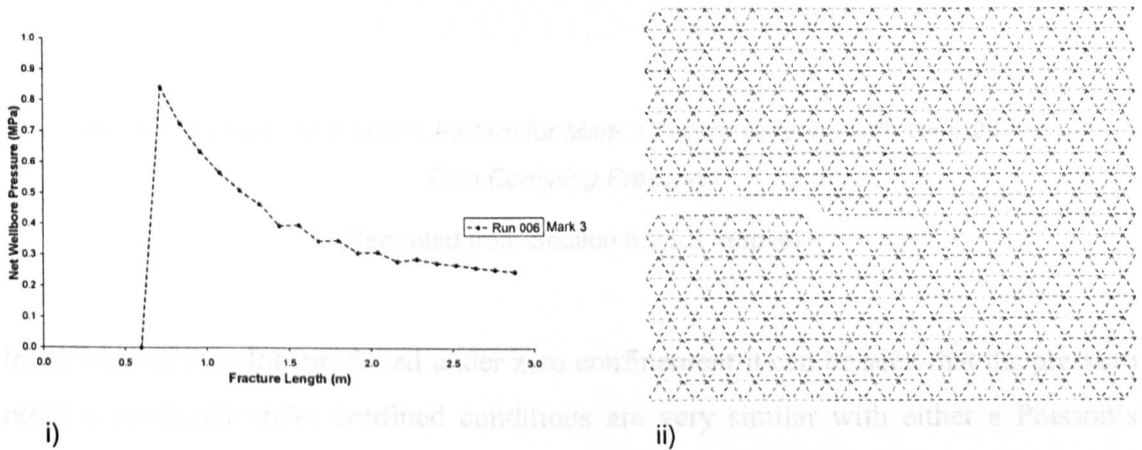


iii)

Net Wellbore Pressure against Propagating Fracture Length from i) (Fig. 6.12.) Runs 001, 002 and 003, $\nu = 0.00$, Zero Confining Pressure ii) (Fig. 6.13.) Runs 004, 005 and 006, $\nu = 0.125$, Zero Confining Pressure iii) (Fig. 6.14.) Runs 007, 008 and 009, $\nu = 0.25$, Zero Confining Pressure iv) (Fig. 6.15.) Runs 010 and 011, $\nu = 0.00$, $\sigma_2 = 9.0\text{MPa}$, $\sigma_3 = 3.7\text{MPa}$ v) (Fig. 6.16.) Runs 013, 014 and 015, $\nu = 0.125$, $\sigma_2 = 9.0\text{MPa}$, $\sigma_3 = 3.7\text{MPa}$

(Repeated from Section 6.2.3.4. above)

The pressure profiles associated with the Mark 3 criterion are not completely comparable since, as mention above, those shown in *Fig. 6.13.* and *Fig. 6.14.* are for deviated fracture patterns. Evidence of this can be seen in the plot produced with a Poisson's ratio of 0.125, where oscillation occurs approximately half way along the otherwise smooth pressure profile, corresponding to the length at which the fracture deviated (See *Fig. 6.13.* and *Fig. 6.5. e*) repeated below).



i) Net Wellbore Pressure against Propagating Fracture Length (Fig. 6.13. c) Repeated from Section 6.2.3.4. above ii) Deviated Fracture Pattern (Fig. 6.5. e) Repeated from Section 6.2.3.2. above) for Run 006, $\nu = 0.125$, Zero Confining Pressure

However, as would be suggested by the previous results and comparison with the results produced by the Mark 1 criterion, which is similarly based on the total uniaxial strain in a link element, the magnitude of the Mark 3 profiles increases with increasing Poisson's ratio. As with the plots of link element failure in time, described previously, the exception to this observation is the plot produced for Poisson's ratio, $\nu = 0.25$. Due to the severe deviation of the fracture (See *Fig. 6.5. f*) repeated below), it is seen to initiate fracturing at a very much lower pressure than the other runs conducted with the Mark 3 criterion. It can be noted however, that this profile still has a higher magnitude than those of either of the equivalent Mark 1 or Mark 2 pressure profiles.

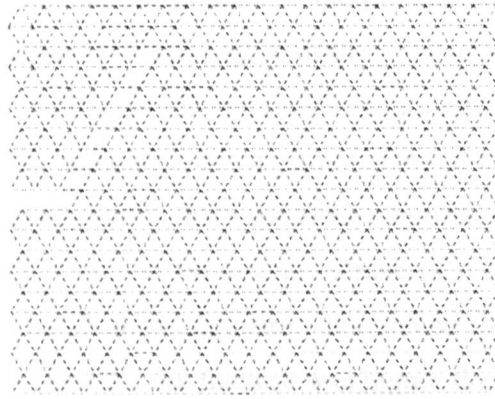


Fig. 6.5. f) *Deviated Fracture Pattern for Mark 3 Failure Criterion with $\nu = 0.25$ and Zero Confining Pressure*

(Repeated from Section 6.2.3.2. above)

In addition to the plots produced under zero confinement it can be seen that the pressure profiles produced under confined conditions are very similar with either a Poisson's ratio of 0.0 or 0.125. This is again consistent with both the associated fracture width profiles and the plots of element failure in time as discussed previously. The most obvious features of these pressure profiles are the large oscillations seen in the magnitude of the wellbore pressure during successive element failure events. These variations are directly associated with the rapid succession of link element failures discussed above. As suggested previously, it is clear from these results that the second element to fail in these rapid succession events fails at a much lower pressure than the first. In the results produced by the Mark 1 criterion it can be seen that the effect is so strong that the second element fails at a net pressure value less than zero i.e. when the pressure in the fracture is less than the confining pressure, an occurrence which should not be possible. Despite the presence of rapid succession failure events in some of the unconfined runs, as described previously, it can be noted that there is only a small amount of oscillation in the associated pressure profiles. This implies that the phenomenon is greatly enhanced by the presence of confining pressures and this would further suggest a relationship with the overall displacement of the Hydraulic Fracture Model mesh in the y -direction, which, as discussed in Section 6.2.3.3.4., is known to be more pronounced under confined conditions.

In addition to the regular oscillations in the pressure curves, a single large drop in pressure is noticeable in the pressure profile of the run carried out with Mark 2 failure criterion under confined conditions and with a Poisson's ratio of 0.25 (See Fig. 6.16.). This event can also be seen in the equivalent plot of element failure in time, where three elements failed in quick succession. It is not clear why this event occurred but it may have been a dynamic effect due to the brittle release of a large amount of potential energy associated with a build up of pressure. It is noted that, prior to the event, the critical pressure required to initiate the fracture was higher than would be expected from the previous results since it was greater than the critical pressure for the comparable Mark 3 run. The cause of the overly high critical pressure is also unclear but again it may have been a result of the overall mesh displacements discussed in the previous Section.

Despite the problems discussed above, it can be seen that the general shape of all of the net wellbore pressure profiles matches very well with those produced by Papanastasiou [69] (See Fig. 6.11. c) repeated below), with the net wellbore pressure decreasing as the fracture length increases.

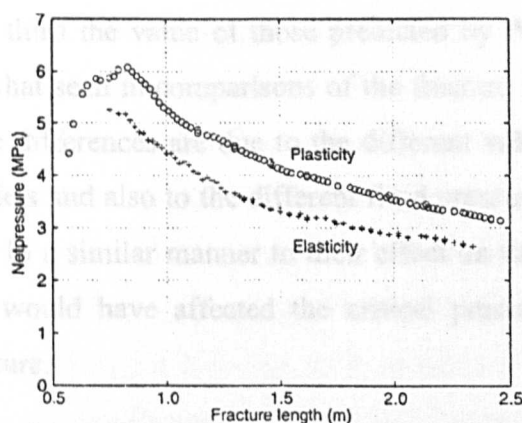


Fig. 6.11. c) Plotted Results from FE Study by Papanastasiou [69] Showing Plots of Net Pressure in Wellbore during Fracture Propagation

(Repeated from Section 6.2.3.4. above)

It can be noted that this decrease in pressure over time corresponds to the increasing fracture propagation rates noted above in conjunction with the gradient of the plotted curves of element failures in time.

Furthermore, it may also be noted that this behaviour is similar to that predicted by existing plane strain hydraulic fracture models such as the CGDD model (See Chapter 2, Section 2.2.). Additionally, similar results were also reported by Tzschichholz and Herrmann [88] for analyses carried with a lattice model representation of hydraulic fracturing that has various similarities to the Hydraulic Fracture Benchmark Model.

Thus, it can be said that the PSM model generally produces qualitatively accurate behaviour in comparison with what would be expected for a plane strain representation of a hydraulically driven propagating fracture. However, it can also be noted that the actual values of pressure predicted by this model are significantly lower than those predicted by Papanastasiou [69] (See *Fig. 6.11. c*). As with previous data the results from the analyses carried out under zero confinement are not directly comparable with those of Papanastasiou, however, the runs carried out under confined conditions are generally alike and would be expected to produce quantitatively similar numerical results. As can be seen from comparison of *Fig. 6.11. c*) with *Fig. 6.15. c*) and *Fig. 6.16. c*), the pressures predicted by the Hydraulic Fracture Benchmark Model are approximately one third the value of those predicted by Papanastasiou. This is a similar discrepancy to that seen in comparisons of the fracture width profiles and again it is possible that these differences are due to the different values of material ductility applied in the two models and also to the different fluid pressure profiles applied to the walls of the fractures. In a similar manner to their effect on the shape of the fractures, both of these factors would have affected the critical pressures required to initiate propagation of the fracture.

6.2.4. Conclusions

From the results discussed in the previous two Sections, it can be concluded that the general behaviour developed by the Hydraulic Fracture Benchmark Model was reasonably satisfactory. This assertion is made on the basis that the majority of the numerical runs produced the straight fracture patterns that would be expected for a

propagating hydraulically driven fracture in a homogeneous material. As discussed above, the accuracy of the behaviour was further verified by the contact force distribution observed in the PSM mesh.

Although the results were largely acceptable, it was also found that several of the numerical runs produced deviated fracture patterns. It was felt that this behaviour was not representative of the realistic fracture propagation behaviour in a homogeneous material. These deviated fracture patterns were thought to have been a result of the overall displacement of the mesh, which in turn was thought to be a consequence of numerical imbalances in the externally applied forces. Since the mesh was bounded by three free, stress boundaries, any out of balance forces resulting from the applied 'fluid forces' and the applied confining pressures led to overall displacements of the mesh and during the course of this work, no suitable way was found of restraining the mesh without affecting the fracture propagation behaviour. It is possible that the application of periodic boundary conditions would solve these problems, however, it is immediately not clear how these could be implemented in PFC^{3D}.

In addition to the overall displacement of the PSM mesh, it was implied by Schlangen and van Mier [82] that the regular configuration of the PSM mesh might lead to preferential directions of fracture growth. It was further implied, by Schlangen and Garboczi [79], that this effect would be exaggerated by the type of element employed in the construction of the model. Analysis of the results produced during the Hydraulic Fracture Benchmark Study showed some evidence that the regular configuration of the mesh guided the direction of fracture propagation. However, it was not conclusive and some of the results shown in *Fig. 6.5.* to *Fig. 6.11.* could be presented as evidence that any influence that the mesh configuration exerted was not strong and would be easily overcome. Evidence was also found to suggest that the type of lattice element employed did affect the fracture pattern and, as contested by Schlangen and Garboczi, it was found that PSM meshes consisting of elements with only one force component produced less accurate results than those consisting of elements with two force components. However, it should be noted that this conclusion was based on a very limited set of test results and in order to verify the findings it would be desirable to carry out further studies. Additionally, it should be noted that it was in fact found difficult to compare the results of the Hydraulic Fracture Benchmark Model with those

for the model employed by Schlangen and Garboczi since the expected fracture pattern, for the studies conducted in this work, followed what could be considered a preferential direction in the mesh. In order to find conclusive evidence that either of the mechanisms discussed above affected the behaviour developed by a PSM mesh, it would be desirable to reproduce and test the model employed by Schlangen and Garboczi [79]. It can be further noted that there was observable evidence in the fracture patterns to suggest that the choice of failure criterion was as at least as significant as either the mesh configuration or the lattice element type.

In order to prevent the influence of the mesh configuration on the fracture growth Schlangen and Garboczi [79] suggest that a randomly configured lattice is employed. However, they also note that a regular lattice is given a random strength distribution will reasonably accurately reproduce the behaviour of a propagating fracture in a heterogeneous material. When a random strength distribution was applied to the Hydraulic Fracture Model mesh it was found to have little affect on the propagating fracture behaviour. As discussed previously, it was not clear why this was the case and various possible explanations were considered. It seems most likely that the random strength variation applied ($\pm 5\%$) was not a strong enough influence to overcome the natural behaviour of the model, which was to open a straight fracture along the centreline of the mesh. It is felt that this may also have been a consequence of the scale of the Hydraulic Fracture Model and that the macro-scale PSM mesh was not sufficiently discretised in order to capture the meandering behaviour of the propagating fracture that would be expected in a heterogeneous material. It may be that a micro-scale lattice model, such as those employed by Schlangen and van Mier [80, 81, 82] and Schlangen and Garboczi [79] would have produced such behaviour. It is furthermore considered questionable whether it is reasonable to model material heterogeneity on the meso- or macro-scales represented by the PSM mesh in the models employed in this work.

Additionally, it would also be desirable to test models in which both random strengths and random stiffnesses were applied to the inter-particle link elements and in which the configuration was randomised, in order to determine whether they would be capable of producing better representations of fracture growth behaviour in a heterogeneous material. However, as mentioned previously it is not feasible to apply a

random variation of element stiffness due to the constraints of the modelling environment (PFC^{3D}) employed for this work and further investigation will be required before it is possible to develop a calibrated, randomly configured PSM mesh.

A further feature of the deviated fracture patterns discussed above was the preferential failure of elements according to their orientation. It was found that under certain loading conditions particular elements remained intact while their direct neighbours, with different orientations, were removed, resulting in the development of discontinuous fractures (See *Fig. 6.6*). It was concluded that this effect was a consequence of the failure criteria that primarily considered uniaxial tensile behaviour in the individual link elements (See Chapter 5). Thus, elements that were not caused to elongate by the externally applied loads could not be considered as candidates for failure. This is behaviour that would be expected of lattice or truss frameworks rather than a continuum material and it was further concluded that in order to prevent its occurrence it would be necessary to employ failure criteria, such as the Mark 2, Mark 4 or Mark 5 (See Chapter 5), that are based non-local, continuum principles.

It was noted however that the Mark 2 criterion also allowed elements to remain intact during propagation of the fracture despite its consideration of the equivalent continuum stress state. This was because it took into account both the direction of the maximum principal stress and the orientation of the link elements when considering failure conditions. It was felt, however, that a more complex and less directional failure criterion, such as the Mohr-Coulomb criterion, could be developed in the same way as the simple Rankine criterion applied in this work (See Chapter 5, Section 5.6.1.) and that this might, more realistically, represent continuum failure behaviour. It was further noted that the Mark 4 and 5 criteria were the least likely of the five failure criteria to leave elements intact and develop discontinuous fracture patterns since they did not consider the orientation of the inter-particle link elements when considering failure. It should therefore follow that these criteria would develop the best representation of fracturing behaviour in a continuous material. However, while they would very accurately deal with elastic-brittle behaviour, various problems were encountered when dealing with softening plasticity which is required in order to resolve mesh size dependency. The Mark 4 and 5 criteria were also shown to have difficulty dealing with link elements situated at the edge of a fracture. These issues are discussed in detail in

Chapter 5 but it can be seen that they are confirmed by the behaviour observed in the Hydraulic Fracture Benchmark Study.

In addition to the accuracy of the general behaviour developed by the Hydraulic Fracture Benchmark Model discussed above, it could also be said that the Fracture Width Profiles and the Net Wellbore Pressure Profiles, developed during the course of various fracture propagations, matched reasonably well with similar results presented by Papanastasiou [69]. It was felt that the minor differences seen between the results of the Finite Element study carried out by Papanastasiou and the results of the Hydraulic Fracture Benchmark Study, were due to minor differences between the models themselves. It was further noted that the trend in behaviour developed by the Hydraulic Fracture Benchmark Model was comparable to that which would be developed by existing plane strain hydraulic fracture models such as the CGDD (See Chapter 2, Section 2.2.) and this further verified the potential of the Multi-Phase Particulate Modelling Framework to accurately model geomechanical problems.

However, it was also noted that various modelling factors, and in particular effects resulting from the mesh boundary conditions, adversely affected the results of the fracture propagation behaviour, especially under confined conditions. Before a robust and reliable model representation can be constructed for any geomechanical problem, including the hydraulic fracture problem considered in this Chapter, it would be necessary to overcome these difficulties. Despite these problems, it is still considered that great potential for the particulate modelling framework is indicated by the results presented and discussed in the previous Sections.

6.3. Coupled Hydraulic Fracture Benchmark Model (PSM + PFM)

6.3.1. Introduction and Model Set-up

As discussed previously, it was a main aim of this work to develop a single software, multi-phase, particulate mechanics framework for modelling geomechanical problems. While the Hydraulic Fracture Benchmark Model, discussed in the previous Section, could be considered a multi-phase model, the fluid behaviour was only considered in a very basic manner, by applying forces, representative of fluid pressure, to a PSM mesh.

In order to assess the full potential of the modelling framework another benchmark model was developed, corresponding to a realistic problem, in which complex, combined behaviour of the solid and fluid phases would be considered.

A combined solid/fluid benchmark model, representative of fluid flow into a wellbore perforation, had previously been developed, as described in Section 4.4.1. of Chapter 4, in order to test the capacity of the framework to develop accurate behaviour with an integrated solid/fluid (PSM + PFM) model under primarily static conditions. By applying any of the fracture criteria developed in Chapter 5, to the PSM mesh component of this model, it was relatively easy to modify the Pressurised Notch Coupled Benchmark Problem and produce a Coupled Hydraulic Fracture Benchmark Problem.

The model itself was set up in exactly the same configuration as had been applied to the Pressurised Notch Coupled Benchmark Problem (See Fig. 4.34. and Fig. 6.19. & Fig. 6.20. below). Moreover, in a similar fashion to those employed in the Hydraulic Fracture Benchmark Model (See Section 6.2.1. above), additional forces were applied, when necessary, to the free boundaries, in order to represent confining pressures. The material properties applied to the PSM component of this benchmark model were also similar to those applied in the Hydraulic Fracture Benchmark Model and other benchmark models previously discussed (See Table 6.5. below). However, given the complexities described in Section 4.4. of Chapter 4, no attempt was made to calibrate the PFM component of this benchmark model and properties applied in the benchmark models discussed in Chapter 4 were used again.

Property	Symbol	Value
Young's Modulus	E	1785.0MPa
Poisson's Ratio	v	0.25
Tensile Strength	f_t	0.5N/mm ²
Fracture Energy Release Rate	G_f	200N/m

Table 6.5. Material Properties Applied to the PSM Component of the Coupled Hydraulic Fracture Benchmark Model

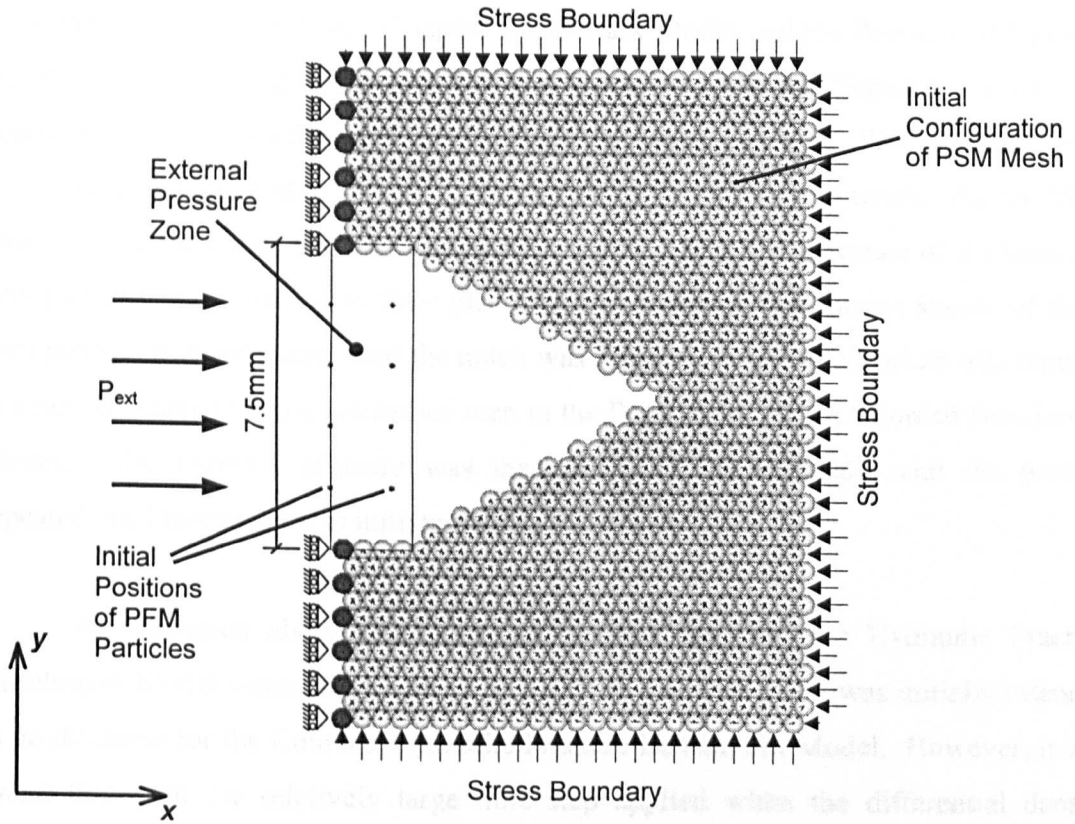


Fig. 6.19. Diagram Showing Set-up of the Coupled Hydraulic Fracture Benchmark Model

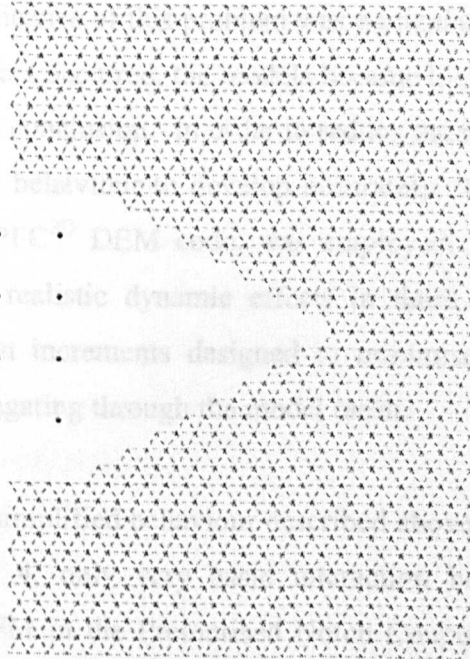


Fig. 6.20. Diagram of the Coupled Hydraulic Fracture Benchmark Model Mesh Showing Only Inter-Particle Link 'Contact Bonds' and 'Fluid Particles' for Clarity

As with the Pressurised Notch Coupled Benchmark Model and the Pressurised Cylinder Benchmark Model (See Section 4.3.4.1. and Section 4.3.4.2. of Chapter 4), an External Pressure Zone was developed at the mouth of the notch, in which ‘fluid particles’ were generated and subjected to forces representative of the external pressure. As the ‘fluid particles’ moved out of the zone and into the notch, under the influence of the pressure, new particles were created in their place, thus providing a continuous source of fluid. This process was continued until the notch was filled and static equilibrium was reached in a similar manner to the behaviour seen in the Pressurised Notch Coupled Benchmark Model. The external pressure was then increased incrementally and the process repeated until fracturing was initiated in the PSM mesh.

As discussed above, the numerical studies run with the Hydraulic Fracture Benchmark Model were carried out as quasi-static analyses and it was initially intended to do the same for the Coupled Hydraulic Fracture Benchmark Model. However, it was found that with the relatively large time step applied when the differential density scaling function is employed in PFC^{3D}, it was not possible to capture the interaction behaviour of the PSM and PFM components. This resulted in physical contact between the ‘fluid’ and ‘solid’ particles, which as discussed in Section 4.3.2. of Chapter 4 is not acceptable for the purposes of developing an accurate representation of fluid behaviour with the PFM. The significance of this problem was particularly illustrated in this study since, when physical contact occurred, the models became highly unstable and it proved impossible to run them to conclusion. In order to reduce the model time step and allow the solid/fluid interaction behaviour to develop accurately, the fully dynamic solution scheme, integral to the PFC^{3D} DEM code, was employed. Despite this, it was not intended to account for realistic dynamic effects in these studies and the external pressure was increased in increments designed to minimise the effects of stress or displacement waves propagating through the model mesh.

In addition to the simplified behaviour described above, it can also be noted that, as discussed in Chapter 4, only very basic interaction behaviour was considered between the PSM and PFM in the Pressurised Notch Coupled Benchmark Model. It was concluded that, although the static behaviour could be considered accurate, hence implying the accuracy of the dynamic behaviour, and the integrated behaviour was

considered satisfactory, further investigation would be required in order to develop rigorous solid/fluid interaction with a combined PSM + PFM model.

Thus, it was the intention of the studies carried out with the Coupled Hydraulic Fracture Benchmark Model to qualitatively assess the capabilities of the single software multi-phase modelling framework to model complex, multi-phase geomechanical problems. As will be seen in the following Sections, this will be done by comparing the results of these studies with those of the Hydraulic Fracture Benchmark Model, discussed in the preceding Sections, and with the behaviour expected for a problem of this kind in the field. It is not however expected that this model will simulate a realistic hydraulic fracture treatment.

Despite the simplicity of the model, it was hoped that, as mentioned above, it would demonstrate the potential of the combined particulate modelling framework. It was furthermore hoped that the model would demonstrate the potential of a combined PSM + PFM to eliminate the need for simplifications of one or both of the model phases as is often the case in a coupled or combined model. This ability was demonstrated by this benchmark model when it was considered that, unlike the Hydraulic Fracture Benchmark Model presented in the first part of this Chapter, there was no requirement for simplifying assumptions for the fluid behaviour, such as a constant pressure profile in the fracture or the limitation of applied fluid pressures to the y -direction only (See Section 6.2.1. above). The pressure profile and the application of fluid pressure to the solid mesh developed naturally as a result of the interaction of the PSM and PFM in the manner described in Section 4.4. of Chapter 4. It was further anticipated that phenomena such as fluid lag at the fracture tip would also be naturally dealt with by the combined model and furthermore, problems that occurred in the Hydraulic Fracture Benchmark Model, such as the development of fluid pressure in discontinuous and remote fractures would simply not occur.

6.3.2. Numerical Studies

The parametric study carried out with the Coupled Hydraulic Fracture Benchmark Model was limited to four numerical runs designed to briefly investigate the qualitative behaviour of the combined model in comparison with the findings of the Hydraulic Fracture Benchmark Model, discussed earlier in this Chapter, and realistic hydraulic fracture treatments. As mentioned above, during each of the numerical runs the applied external pressure was increased incrementally in steps designed to maintain the quasi-static nature of the analyses. This was repeated until the failure criterion under consideration was exceeded and a fracture was initiated. Since the pressure was maintained constantly by the external pressure field, once fracturing started it continued until it had propagated all the way through the PSM mesh.

During the course of these numerical runs the external pressure was controlled and the critical value, at which fracturing was initiated, was recorded. Once fracturing had begun the rate at which propagation occurred was monitored by recording the number of link element failures in time, as was done for the Hydraulic Fracture Benchmark Model described in the preceding Sections. The details of the numerical runs carried out for this study are presented in Table 6.6. below.

Run No.	Fracture Criterion	Young's Modulus E MPa	Poisson's Ratio ν	Tensile Strength f_t N/mm ²	Fracture Energy G_f N/m	Softening Modulus E_s MPa	In situ Stress	
							kPa	
							σ_2	σ_3
001	Mark 1	1785.0	0.25	0.5	-	∞	0.0	0.0
002	Mark 2	1785.0	0.25	0.5	-	∞	0.0	0.0
003	Mark 3	1785.0	0.25	0.5	200.0	0.30	0.0	0.0
004	Mark 1	1785.0	0.25	0.5	-	∞	75.0	75.0

Table 6.6. Details of Numerical Runs Carried Out for the Qualitative Parametric Study of the Coupled Hydraulic Fracture Benchmark Model

6.3.3. Discussion of Results

In this Section presentation and discussion is made of the results produced by the numerical runs carried out in the parametric study of the Coupled Hydraulic Fracture Benchmark Model. For each of the runs listed in Table 6.6. above, a fracture, driven by the applied fluid pressure component of the model, developed with the PFM, was propagated through the solid component of the model, as represented by the PSM. In each case fracturing initiated at the notch tip where, as would be expected, the stress concentration was highest. Once fracturing had begun it continued to propagate until the mesh was fractured through.

The values of the critical pressures, at which fracturing was initiated in each of the numerical runs, are listed in Table 6.7. below. In the following discussion relative comparison is made between these values, however, it should be remembered that, due to the simplified behaviour considered by the Coupled Hydraulic Fracture Benchmark Model, it was only intended to make a qualitative comparison. In addition to the critical pressure values, plots illustrating the development of each of the propagating fractures patterns in time are considered (See *Fig. 6.21.* to *Fig. 6.24.*). Furthermore, in order to verify the conclusions reached after examination of these results, plots of link element failures in time, similar to those produced for the results of the Hydraulic Fracture Benchmark Model, are discussed (See *Fig. 6.27.*).

Run No.	Critical Pressure kPa
001	66
002	56
003	129
004	190

Table 6.7. Summary of Critical Pressures Determined in the Numerical Runs Carried out for the Parametric Study of the Coupled Hydraulic Fracture Benchmark Model

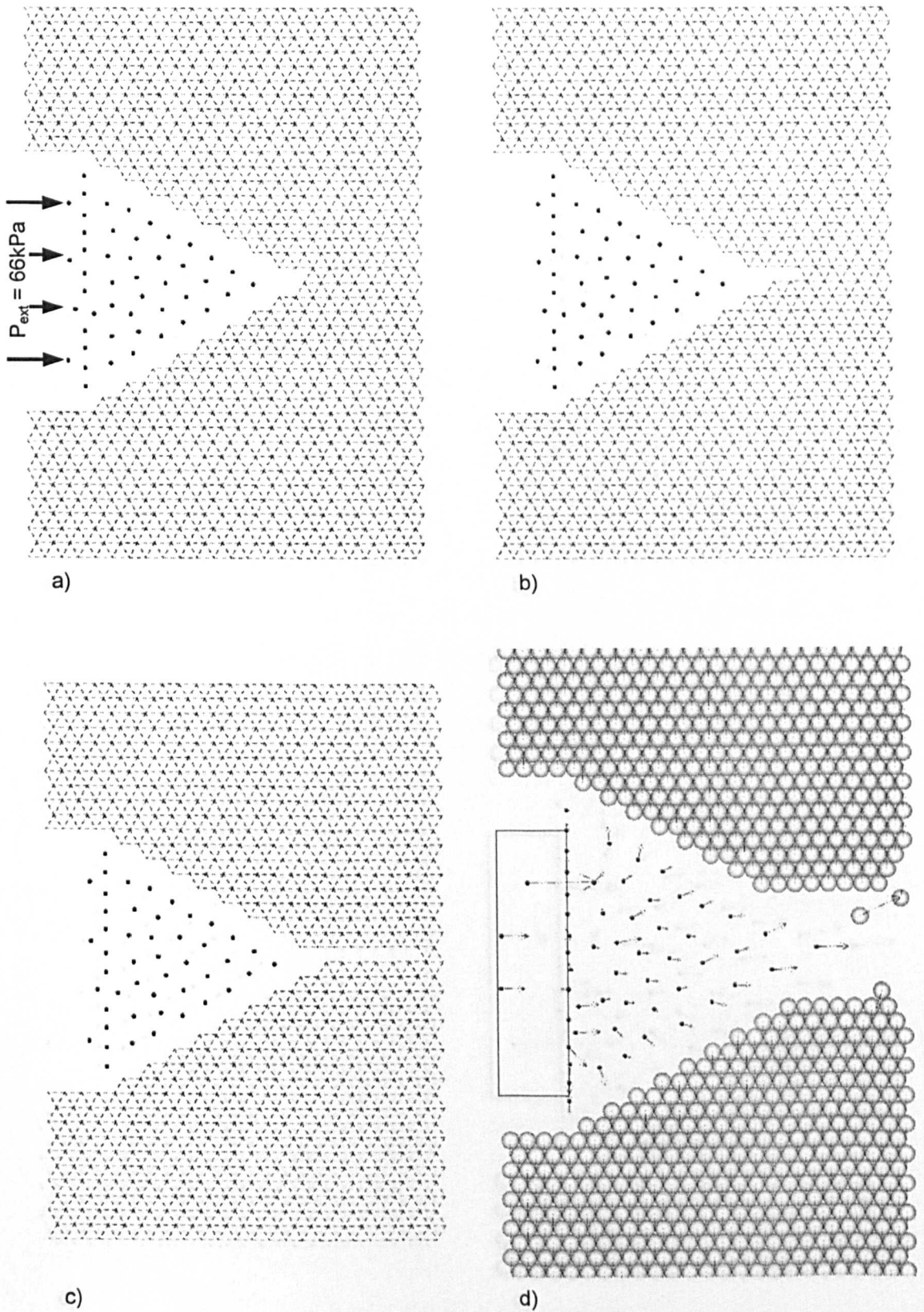


Fig. 6.21. Diagrams of Various Stages of Fracture Propagation Produced during Run 001 of the Parametric Study on the Coupled Hydraulic Fracture Benchmark Model (Mark 1 Failure Criterion, Zero Confining Pressure, Critical Pressure of 66kPa)

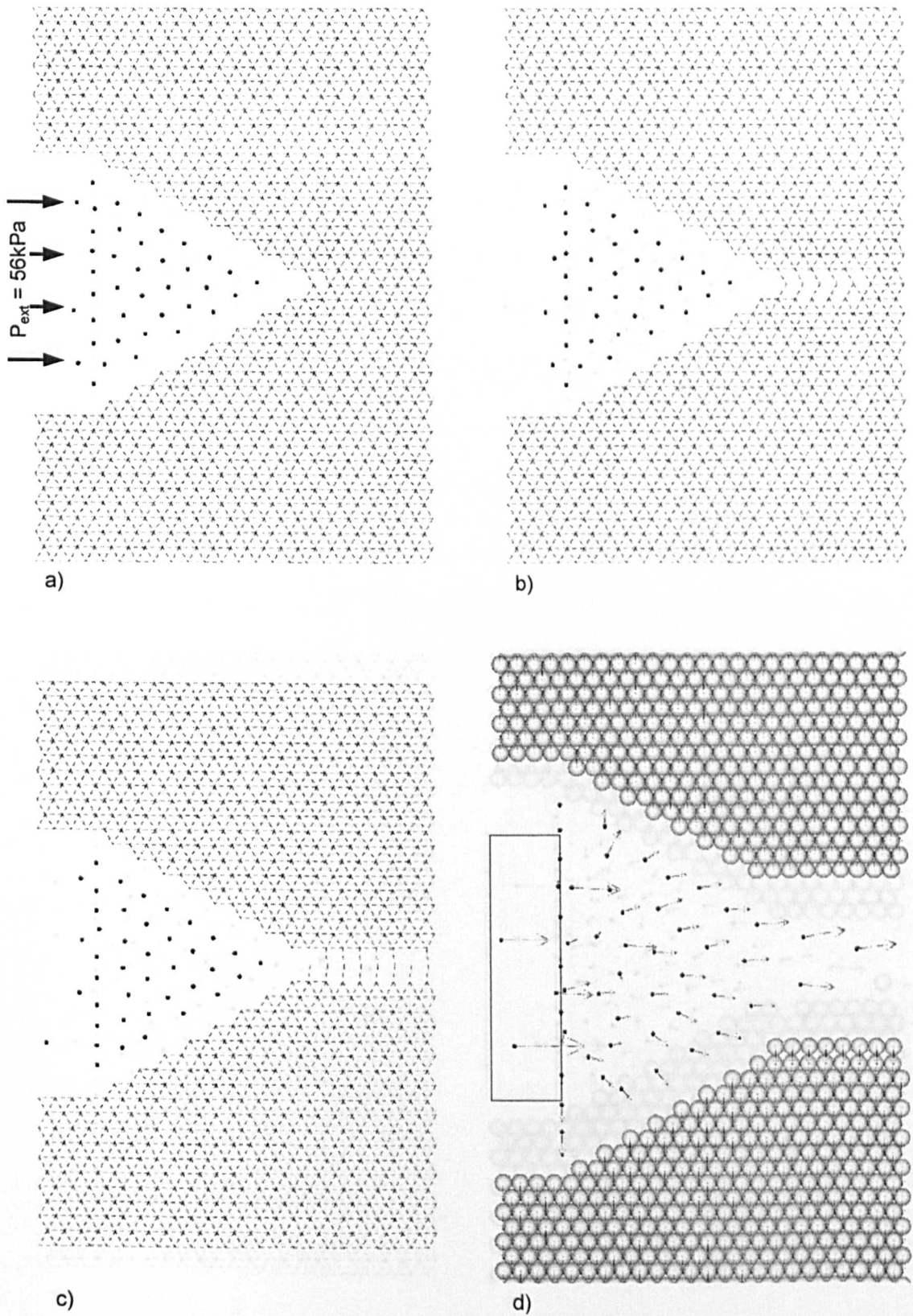


Fig. 6.22. Diagrams of Various Stages of Fracture Propagation Produced during Run 002 of the Parametric Study on the Coupled Hydraulic Fracture Benchmark Model (Mark 2 Failure Criterion, Zero Confining Pressure, Critical Pressure of 56kPa)

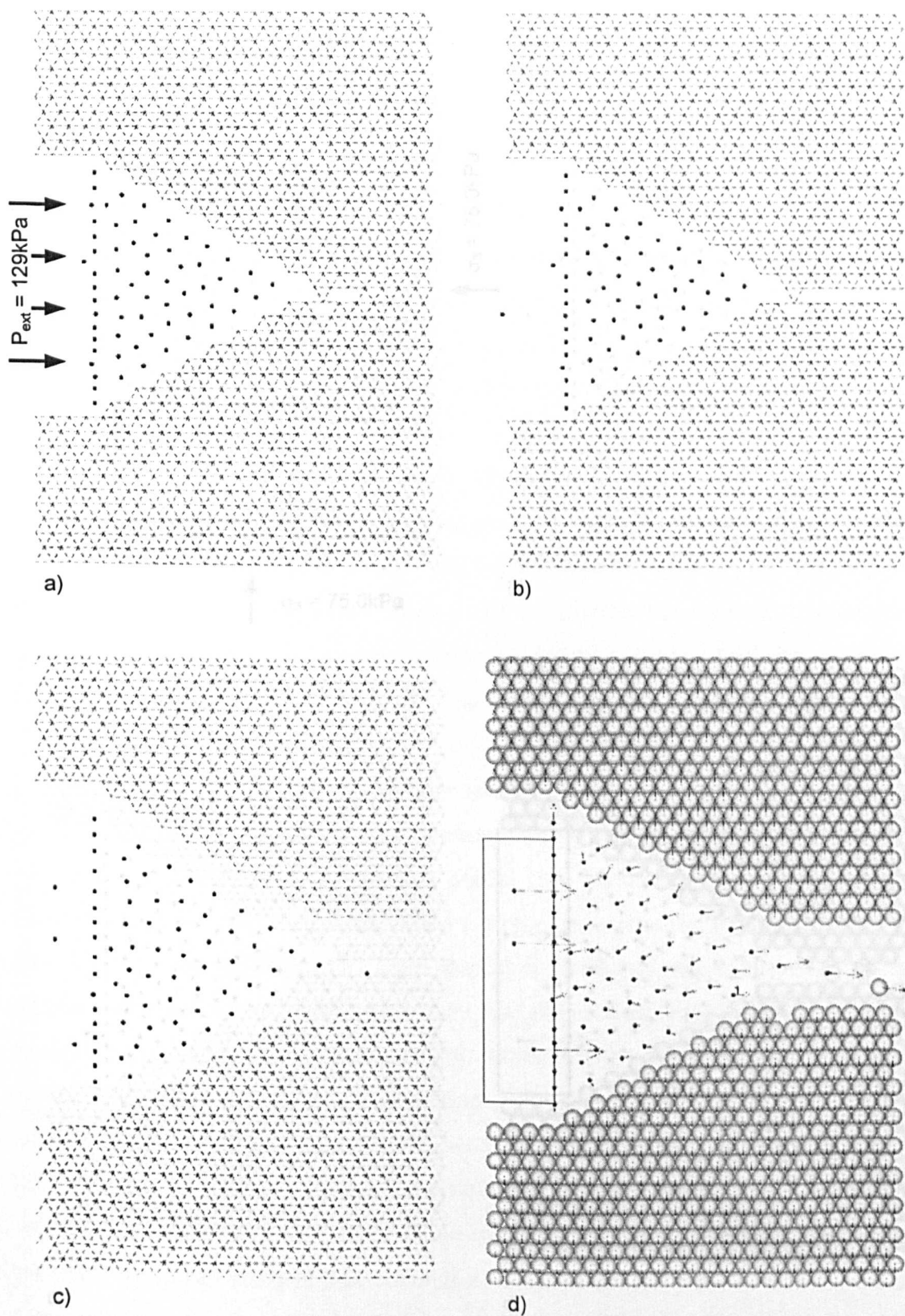


Fig. 6.23. Diagrams of Various Stages of Fracture Propagation Produced during Run 003 of the Parametric Study on the Coupled Hydraulic Fracture Benchmark Model (Mark 3 Failure Criterion, Zero Confining Pressure, Critical Pressure of 129kPa)

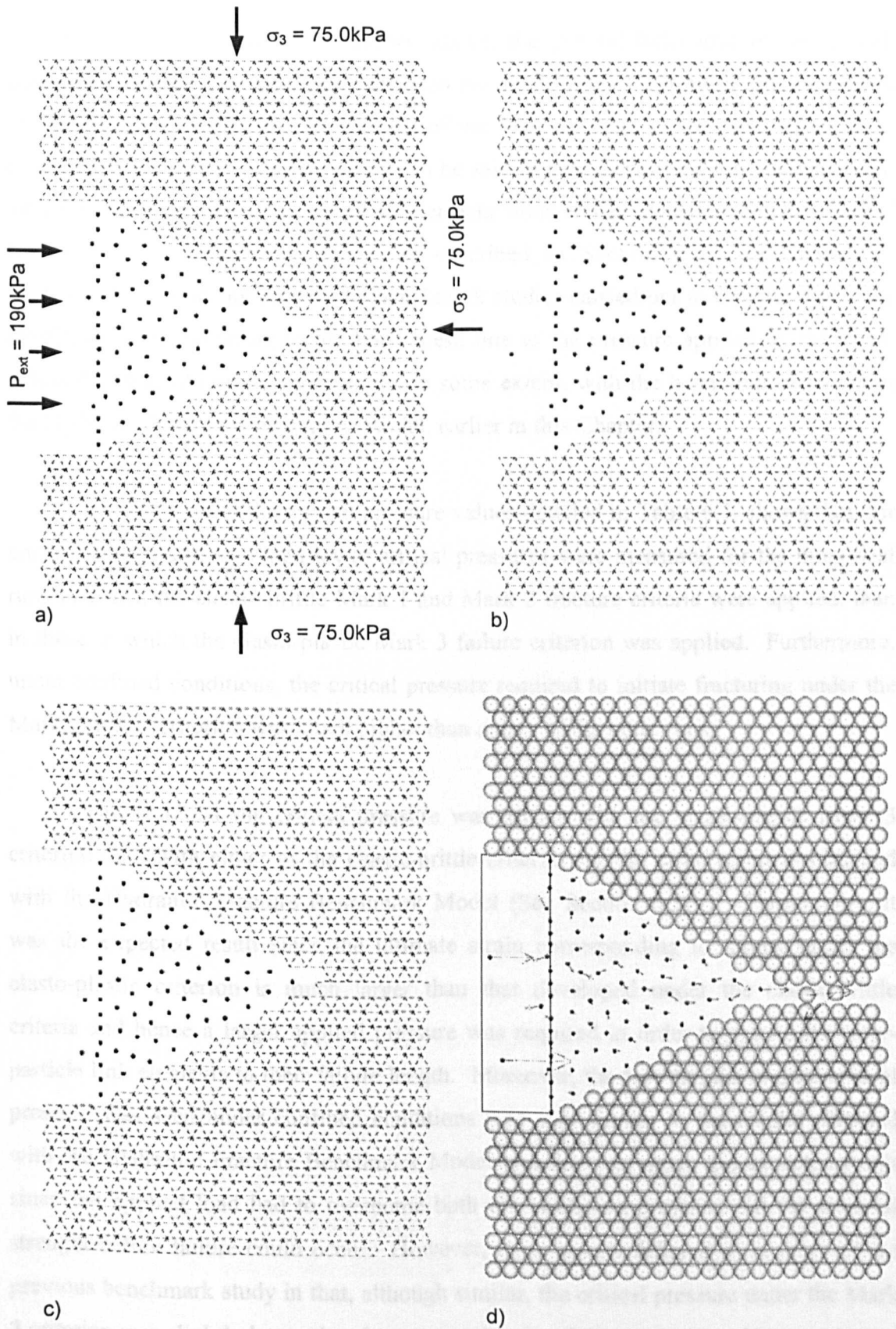


Fig. 6.24. Diagrams of Various Stages of Fracture Propagation Produced during Run 004 of the Parametric Study on the Coupled Hydraulic Fracture Benchmark Model (Mark 1 Failure Criterion, $\sigma_2 = 75.0\text{kPa}$, $\sigma_3 = 75.0\text{kPa}$, Critical Pressure of 190kPa)

As can be seen from the plots shown above, the general behaviour of the model, comprising the flow of 'fluid particles' into the notch in the PSM mesh, the interaction of the PSM and PFM, and the transfer of the fluid pressure to the solid material, is considered satisfactory and the model can be said to have performed qualitatively well. This was to be expected since very similar behaviour was produced by the Pressurised Notch Coupled Benchmark Model as described in Section 4.4.2. of Chapter 4. However, behaviour not seen in the benchmark studies carried out in Chapter 4 was the development of fracturing in the PSM mesh due to the pressure applied by the PFM, although it was obviously comparable, to some extent, with the behaviour observed in the Hydraulic Fracture Benchmark Model, earlier in this Chapter.

Examination of the critical pressure values detailed in Table 6.7. shows that, for unconfined conditions, much lower critical pressures were measured for the numerical runs in which the elastic-brittle Mark 1 and Mark 2 fracture criteria were applied, than in those in which the elasto-plastic Mark 3 failure criterion was applied. Furthermore, under confined conditions, the critical pressure required to initiate fracturing under the Mark 1 failure criterion was much higher than in any of the other runs.'

The fact that the critical pressure was higher with the elasto-plastic Mark 3 criterion than with either of the elastic-brittle criteria was the same result as obtained with the Hydraulic Fracture Benchmark Model (See Section 6.2.3.). Furthermore, it was the expected result since the ultimate strain corresponding to failure under the elasto-plastic criterion is much larger than that developed under the elastic-brittle criteria and hence a larger applied pressure was required in order to extend the inter-particle link elements to their failure length. Moreover, the fact that the highest critical pressure was seen under confined conditions was also similar to the results obtained with the Hydraulic Fracture Benchmark Model and this was again the expected result since the applied load had to overcome both the confining pressure and the material strength before failure could occur. However, these results differed from those of the previous benchmark study in that, although similar, the critical pressure under the Mark 2 criterion was slightly lower than that seen under the Mark 1 criterion. This was in fact a reversal of the situation seen with the Hydraulic Fracture Benchmark Model and it was felt that it was most likely an effect of the mesh configuration, which is an issue that is discussed in more detail below.

Although from the results discussed above the behaviour of the Coupled Hydraulic Fracture Benchmark Model may be considered relatively simple, subtle but significant variations in the fracturing process can be observed when the fracture patterns are examined in detail.

As can be seen in *Fig. 6.21. a) to c)* (repeated below) the fracture pattern developed under the Mark 1 criterion was a simple, straight fracture through the narrowest part of the mesh.

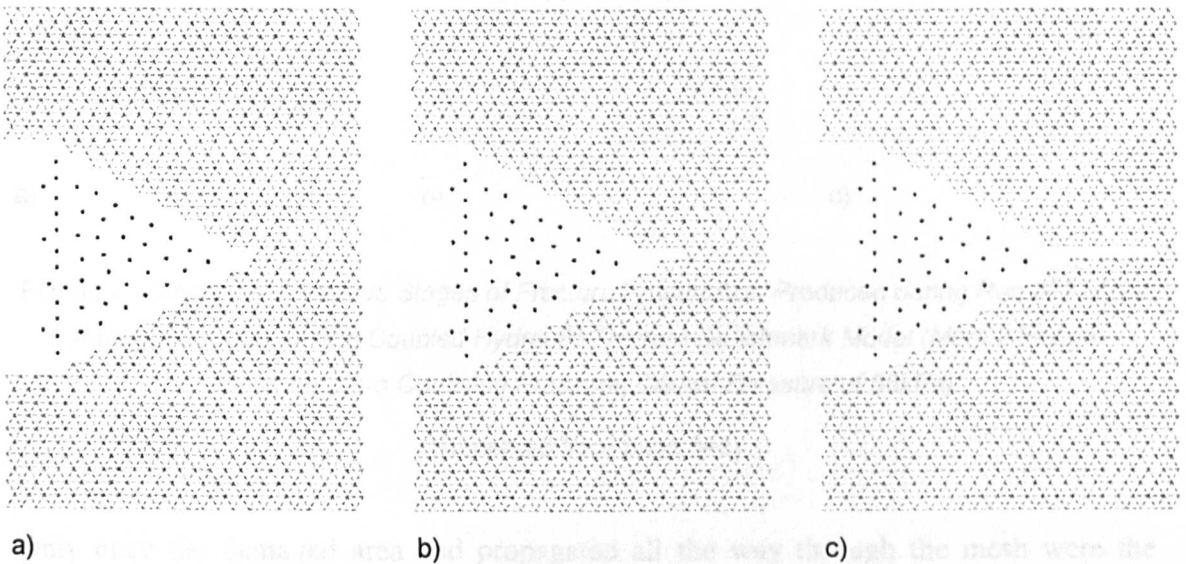


Fig. 6.21. Diagrams of Various Stages of Fracture Propagation Produced during Run 001 of the Parametric Study on the Coupled Hydraulic Fracture Benchmark Model (Mark 1 Failure Criterion, Zero Confining Pressure, Critical Pressure of 66kPa)

(Repeated from page 344)

This is a satisfactory and acceptable result for the problem, although it should be noted that, as discussed in Section 5.5.3. of Chapter 5, the deformation of the PSM mesh at failure was likely to have been larger than would be expected for an equivalent continuum material due to the method by which the Mark 1 criterion determines a failure condition.

In contrast to the straight fracture developed by the Mark 1 criterion, it can be seen in *Fig. 6.22. a) to c)* (repeated below) that, under the Mark 2 criterion, a ‘fish bone’

fracture pattern developed in which a wide but discontinuous area of damage was formed.

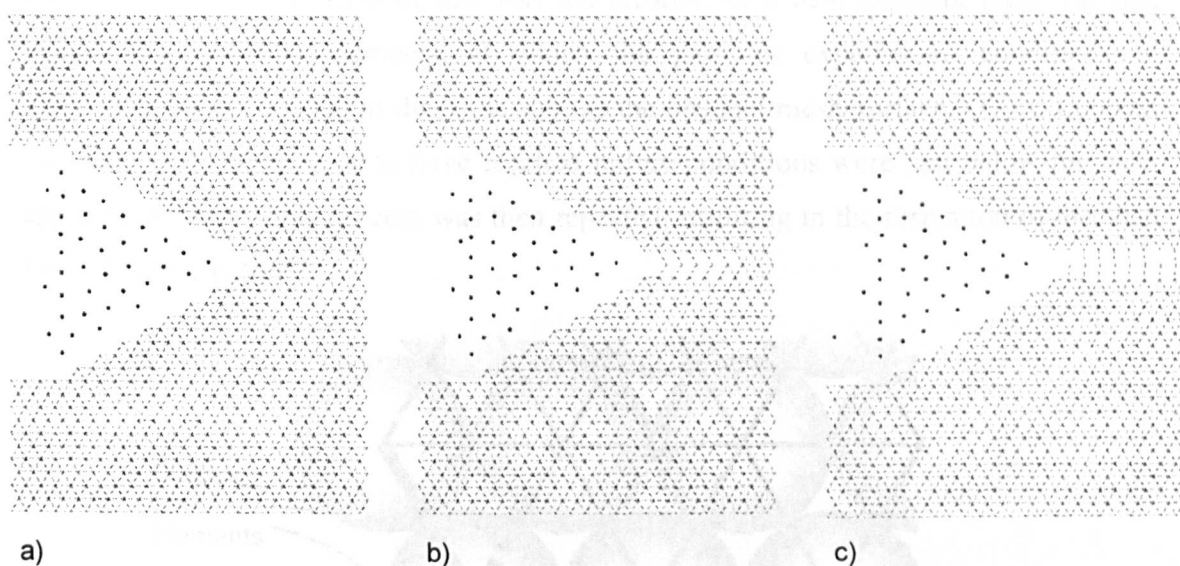


Fig. 6.22. *Diagrams of Various Stages of Fracture Propagation Produced during Run 002 of the Parametric Study on the Coupled Hydraulic Fracture Benchmark Model (Mark 2 Failure Criterion, Zero Confining Pressure, Critical Pressure of 56kPa)*

(Repeated from page 345)

Only once the damaged area had propagated all the way through the mesh were the remaining link elements failed, thereby forming a continuous fracture. Additionally, as can be seen, relatively large deformation of the mesh was required in order for these elements to reach critical conditions. It is possible that, in an infinite mesh, these ‘second choice’ link elements, left intact after the first pass of the propagating fracture pattern, would never fail.

The development of this distinctive fracture pattern was a consequence of the Mark 2 criterion’s consideration of the stress states calculated in each of the PFC^{3D} DEM particles from the contributions of contact forces acting on them (See Chapter 3, Section 3.4.2.). As described in Chapter 5, Section 5.6.3., the particles at the edge of the PSM mesh had fewer contacts, and thus apparently lower stresses, than the particles internal to the mesh. Since the stress state in the link elements was determined from the average of the stress states in the particles between which they lay, link elements attached to particles wholly within the mesh were deemed to reach failure conditions

before those attached only to surface particles. Consequently, the first elements to fail and be removed were just below the surface of the mesh. As illustrated in Fig. 6.25, below, the knock on effect of this was the creation of a new apparent mesh surface, behind the removed elements, at which the particles experienced conditions of apparently lower stresses in the same way as the original mesh surface. Thus, the next elements to be considered to have reached failure conditions were just below this new apparent surface. This process was then repeated, resulting in the formation of the ‘fish bone’ fracture pattern.

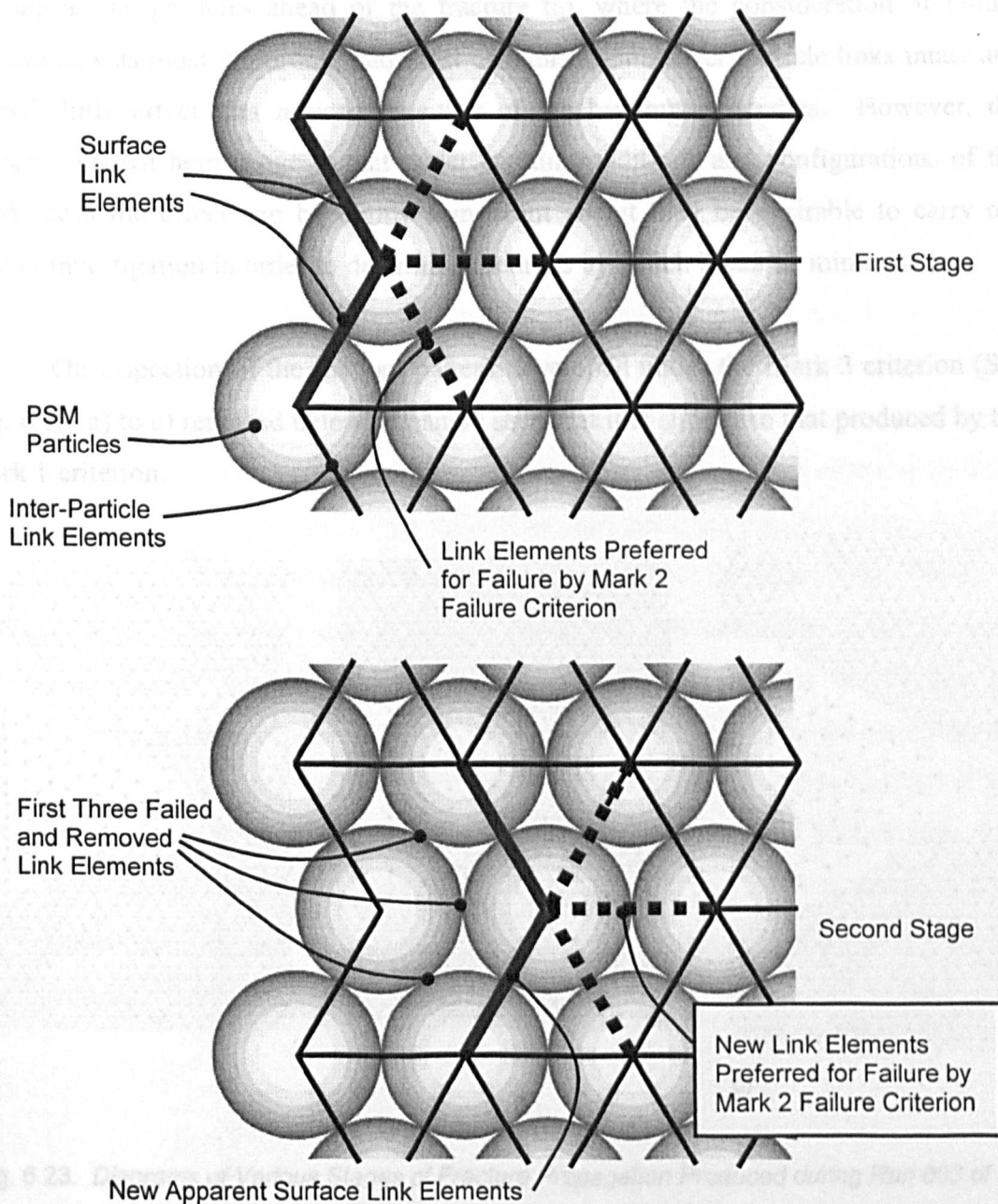


Fig. 6.25. Diagram Illustrating Progression of Fracture Development in Coupled Hydraulic Fracture Benchmark Model under Mark 2 Failure Criterion

It is possible that this effect was particularly emphasised and exaggerated by the configuration of the PSM mesh employed in the Coupled Hydraulic Fracture Benchmark Model however, it is likely that a similar effect would occur in the edge regions of any PSM mesh. The possibility of the occurrence of this phenomenon was discussed previously in conjunction with the Two-Dimensional Uniaxial Benchmark Model, employed in Chapter 5 to test the various failure criteria developed for the PSM, and also in conjunction with the Hydraulic Fracture Benchmark Model presented earlier in this Chapter. In these cases, it was concluded that the effect would not be significant as long as the particles ahead of the fracture tip, where the consideration of failure conditions was most important, had most of their original inter-particle links intact and indeed, little effect was noticed in either of the benchmark studies. However, the evidence shown here suggests that under certain conditions and configurations of the PSM mesh the effect can be highly significant and it may be desirable to carry out further investigation in order to determine methods by which it can be minimised.

On inspection of the fracture pattern developed under the Mark 3 criterion (See Fig. 6.23. a) to c) repeated below) it can be seen that it is similar to that produced by the Mark 1 criterion.

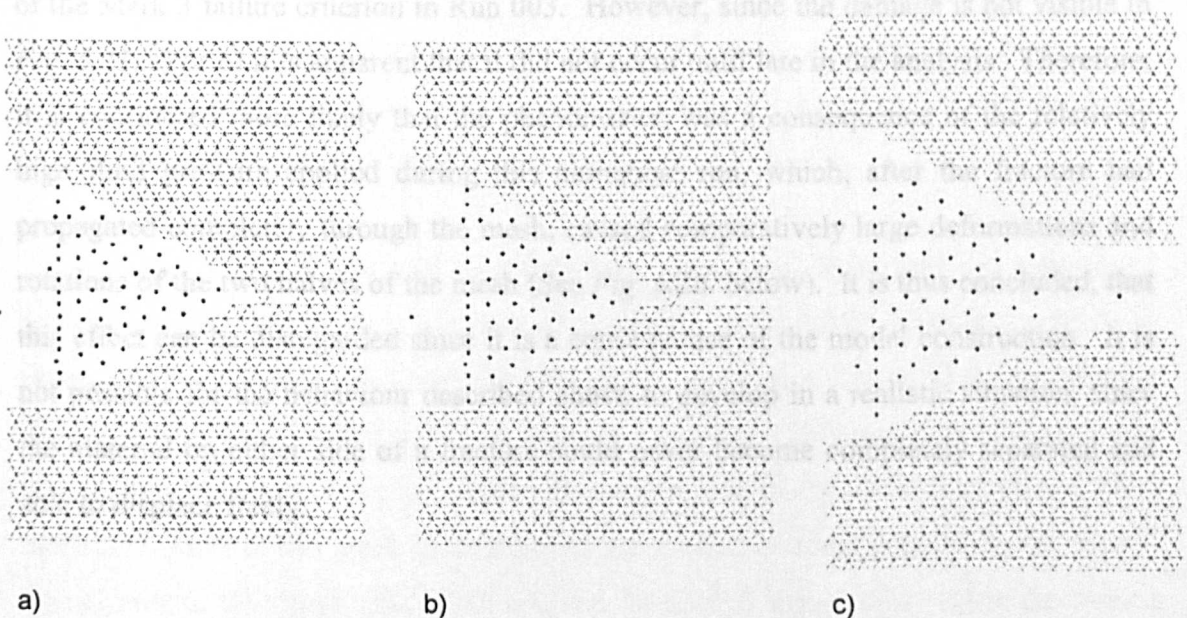


Fig. 6.23. Diagrams of Various Stages of Fracture Propagation Produced during Run 003 of the Parametric Study on the Coupled Hydraulic Fracture Benchmark Model (Mark 3 Failure Criterion, Zero Confining Pressure, Critical Pressure of 129kPa)

(Repeated from page 346)

This is an expected result given that the criteria both consider the uniaxial total strain in the inter-particle link elements in order to determine failure conditions (See Chapter 5, Section 5.5.1. and Section 5.7.1.). However, a difference between the two fracture patterns is that, although the Mark 3 fracture is generally straight and well defined, a small deviation took place shortly after initiation. The reason for this is not clear but it can be noted that in the parametric studies carried out with the Hydraulic Fracture Benchmark Model (See Section 6.2.3.), tests combining the Mark 3 criterion and a Poisson's ratio of 0.25, as applied in this test, were shown most likely to produce deviated fracture patterns. As discussed in Section 6.2.3.3.4. above, this may have been an inaccuracy associated with the analysis of a model consisting of elements in which only a single force component was considered, as is the case for a PSM mesh with a Poisson's ratio of 0.25.

In addition to the small deviation of the fracture, it can be noted that a large number of elements were failed and removed from the areas of the mesh near the fixed boundaries (See *Fig. 6.23. c*) and *Fig. 6.19.*). Since this phenomenon did not occur in either Run 001 or Run 002, this may have been a direct consequence of the application of the Mark 3 failure criterion in Run 003. However, since the damage is not visible in *Fig. 6.23. a*) or *b*) it is apparent that it did not occur until late in the analysis. Therefore, it is considered more likely that the phenomenon was a consequence of the relatively high fluid pressure applied during this numerical run, which, after the fracture had propagated completely through the mesh, caused comparatively large deformations and rotations of the two halves of the mesh (See *Fig. 6.26.* below). It is thus concluded, that this effect can be disregarded since it is a consequence of the model construction. It is not possible for the behaviour described above to develop in a realistic situation, since the material on either side of a fracture could never become completely separated and able to displace freely.

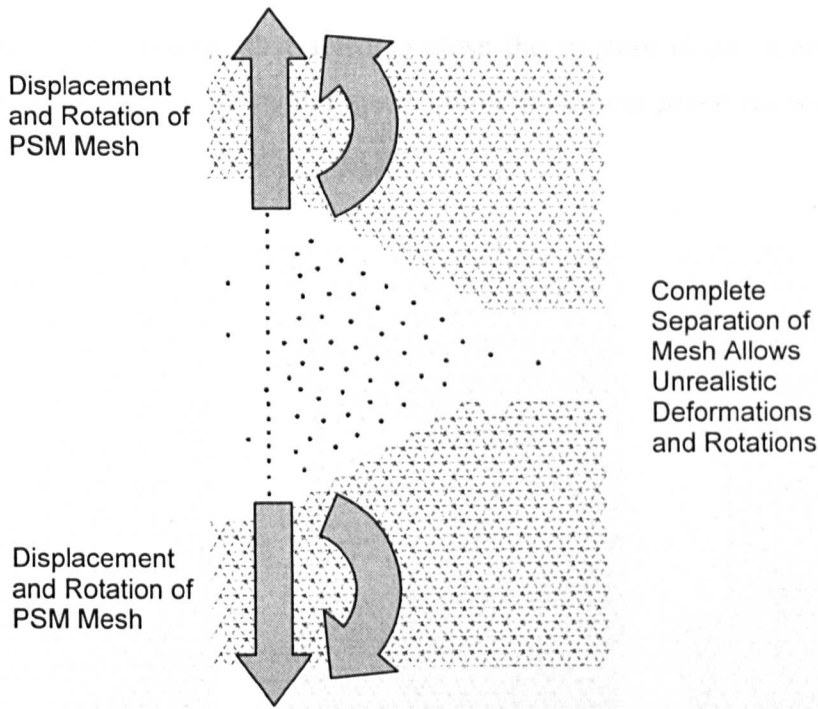


Fig. 6.26. Diagram Showing Deformation of Coupled Hydraulic Fracture Model Mesh after Complete Fracture Propagation

Fig. 6.27. Diagrams of Various Stages of Fracture Propagation Produced during Run 004 of the Benchmark Study on the Coupled Hydraulic Fracture Benchmark Model (Mark 1 Failure)

The final fracture pattern to be considered is that developed under confined conditions with the Mark 1 failure criterion in Run 004. As can be seen in Fig. 6.24. a) to c) (repeated below), the developed fracture pattern was again generally straight and well defined in a similar manner to those developed in Run 001 and Run 003 with the Mark 1 and Mark 3 failure criteria respectively.

It can be noted, however, that before the main, straight fracture was established several link elements failed in a dispersed pattern round the tip of the notch in the PSM mesh. This may have been a result of the build up and concentration of stresses around the notch due to the applied confining pressure. However, it is also possible that it was caused by a stress wave or similar dynamic effect, propagating through the PSM mesh as a result of too rapid an increase of the applied external pressure in the model. Irrespective of the cause, this effect was not thought to significantly affect the overall fracturing behaviour since it was subsequently dominated by a clearly defined, straight fracture, as mentioned above. Despite the similarity of the fracture shape to those developed in the previous numerical runs, it is also notable that this fracture remained much narrower than those seen before. This was obviously a direct consequence of the

applied confining pressures that acted to close the fracture at all times and this was representative of realistic behaviour since similar confining pressures would always be present in the field.

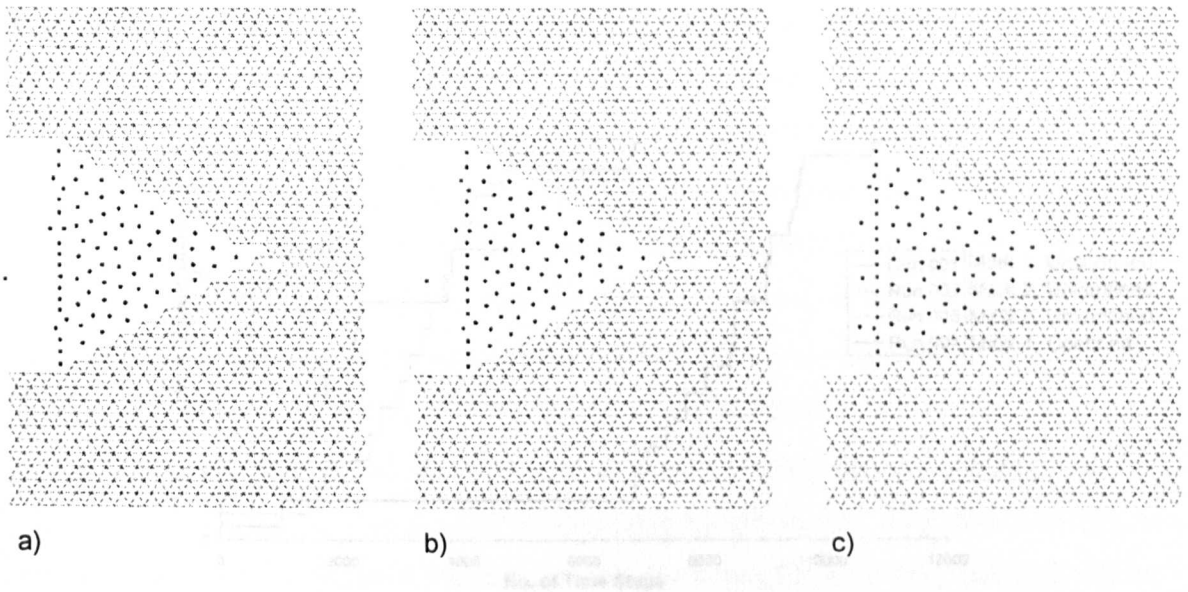


Fig. 6.24. Diagrams of Various Stages of Fracture Propagation Produced during Run 004 of the Parametric Study on the Coupled Hydraulic Fracture Benchmark Model (Mark 1 Failure Criterion, $\sigma_2 = 75.0\text{kPa}$, $\sigma_3 = 75.0\text{kPa}$, Critical Pressure of 190kPa)

(Repeated from page 347)

In addition to the fracture propagation behaviour described above, it can also be seen, in Fig. 6.24. c), that a considerable number of link elements failed near the fixed boundaries of the model. This was very similar behaviour to that observed in Fig. 6.23. c) and discussed above in conjunction with Run 003. The fact that a relatively high critical pressure was recorded for this run, as listed in Table 6.7. above, substantiates the hypothesis that the damage in both of these tests was related to the distortion of the mesh associated with large displacements after the mesh had been fractured through (See Fig. 6.26.). Despite the noted damage, the overall behaviour observed for Run 004 was generally comparable to that observed in tests carried out under confined conditions with the Hydraulic Fracture Benchmark Model (See Section 6.2.3.).

The behaviour inferred by the development of the four fracture patterns over time, as illustrated in *Fig. 6.21.* to *Fig. 6.24.*, was further verified by the examination of the progress of element failures over time for each of the numerical runs (See *Fig. 6.27.* below).

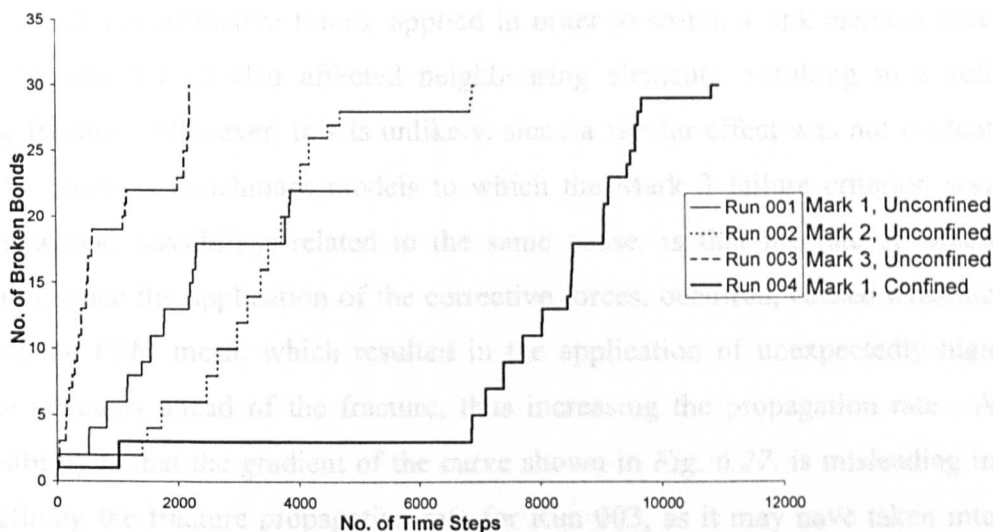


Fig. 6.27. Plots of Number of Failed Inter-Particle Link Elements in Time for the Numerical Runs of the Parametric Study of the Coupled Hydraulic Fracture Benchmark Model

As can be seen, the fracture propagation rates, as indicated by the gradients of the curves plotted in the figure above, are quite similar for the Mark 1 and Mark 2 criteria. This matches very well with the results of the Hydraulic Fracture Benchmark Model, which showed that fracture propagation behaviour under the two elastic-brittle criteria was most similar in a PSM mesh of Poisson's ratio 0.25, as was the case in these tests. It may be noted however, that after initiation of the fracture, propagation 'paused' for a short time in Run 002, under the Mark 2 criterion, whereas propagation continued at a steady rate in Run 001, under the Mark 1 criterion. The precise reason for this 'pause' is not clear, however it may have been a consequence of the 'fish bone' fracture pattern that developed under the Mark 2 criterion, as illustrated in *Fig. 6.25.* above.

In the studies conducted with the Hydraulic Fracture Benchmark Model the Mark 3 criterion was shown to produce the slowest propagation rates (See *Fig. 6.12.* to *Fig. 6.16.*). It was concluded that this was because more time was required for the elements to reach the ultimate strains associated with the elasto-plastic failure criterion

which were larger than those associated with elastic-brittle criteria. However, it can be seen in *Fig. 6.27.* that the fracture propagation rate in Run 003, under the elasto-plastic Mark 3 failure criterion, was much faster than those recorded for the elastic-brittle criteria. Again, the reason for this is not clear, although there are several possible explanations. Firstly, it is possible that it was due to a problem with the Mark 3 failure criterion in which the corrective forces, applied in order to soften a link element (See Chapter 5, Section 5.7.1.) also affected neighbouring elements, resulting in a self-perpetuating fracture. However, this is unlikely, since a similar effect was not evident in any of the previous benchmark models to which the Mark 3 failure criterion was applied. A second possibility, related to the same cause, is that the rate at which softening, and hence the application of the corrective forces, occurred, caused dynamic behaviour of the PSM mesh, which resulted in the application of unexpectedly high loads to the elements ahead of the fracture, thus increasing the propagation rate. A further possibility is that the gradient of the curve shown in *Fig. 6.27.* is misleading in terms of defining the fracture propagation rate for Run 003, as it may have taken into account the failure of elements near the boundaries of the mesh, which cannot be associated with the true fracture propagation behaviour for the model. Again, this is unlikely however, as the damage that occurred around the fixed boundaries of the mesh has been shown not to have occurred until most of the main fracture had developed. It is felt that the most likely cause of the high rate of fracture propagation was a dynamic effect associated with the application of corrective forces and, although further investigation of this will be required, the best solution would probably be to reduce the increment by which the applied external pressure was increased prior to the initiation of a fracture.

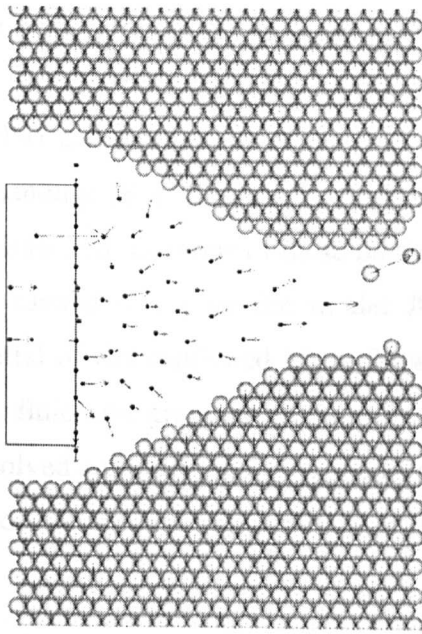
From the fracture propagation rates recorded in the Hydraulic Fracture Benchmark Model (See *Fig. 6.12.* to *Fig. 6.16.*), it would be expected that the propagation rate of a fracture produced under confined conditions would be slower than for an equivalent fracture produced under zero confinement. Thus, it was expected that the propagation rate of the fracture produced in Run 004, under the Mark 1 criterion, would have been slower than that of the fracture produced in Run 001, also under the Mark 1 criterion. However, in *Fig. 6.27.* it can be seen that the rates of propagation of these two fractures were very similar and this was probably due to the relatively low confining pressures applied in this study, in comparison to those applied earlier in the

Hydraulic Fracture Benchmark Study, having relatively little affect on the fracture growth rate. It may further be noted that after initiation of the fracture in Run 004 there was a long 'pause' before fracturing resumed at a reasonably constant rate, similar to that recorded for Run 001. It is possible that this effect was related to the applied confining pressures, but it is considered more likely that the initial element failure event, prior to the 'pause', was due to a dynamic effect caused by too rapid an increase in the applied external pressure. This conclusion is in agreement with that reached previously after consideration of the dispersed pattern of the failed elements.

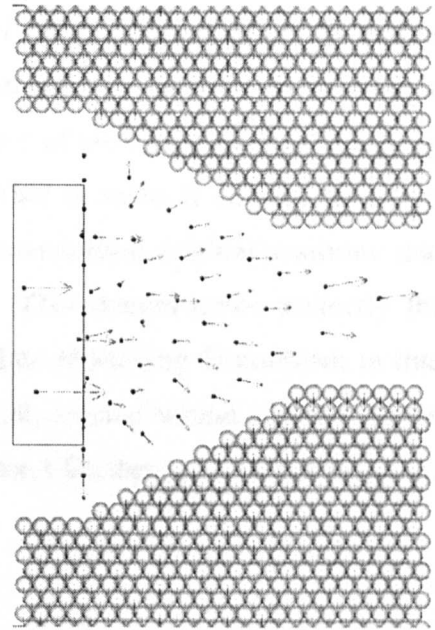
Lastly, in all of the curves shown in *Fig. 6.27*. it can be seen that after an initially steady fracture propagation rate the gradient of the curves becomes more variable. The steep steps and long 'pauses' can be attributed to boundary effects, as the fractures reached the outside boundary of the mesh, and, in the cases of Run 003 and Run 004, the failure of link elements in the areas of the mesh near the fixed boundaries. Both of these effects can be ignored as they occur in isolation of the realistic hydraulically driven fracture growth behaviour and in a model employing a sufficiently large mesh, fracturing could be halted before they were encountered.

Further to the diagrams illustrating the development of the fracture patterns in time, item d) in *Fig. 6.21*. to *Fig. 6.24*. (repeated below) shows the configuration of both the PSM and PFM particles at a late stage in the numerical runs.

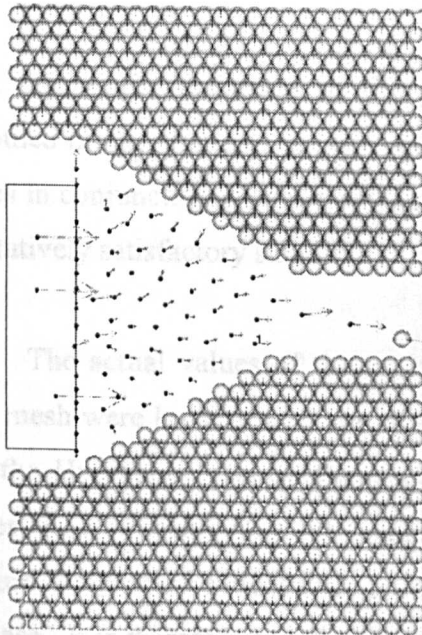
As can be seen from the positions of the particles and their velocities, as indicated by the arrows, the fractures in the PSM meshes have opened wide and the PFM 'fluid particles' have flowed into the gap. While, as mentioned previously, the complete separation of the PSM mesh cannot be considered a realistic representation of hydraulic fracturing behaviour, the plots are intended to demonstrate the potential of the combined model to represent fluid flow in a propagating fracture. Although it was not practical in the present circumstances, it is hoped that in the future it will be possible to employ a large enough mesh so that sporadic fracture propagation events, accompanied by the flow of fluid into the newly opened fracture, can be modelled with this framework.



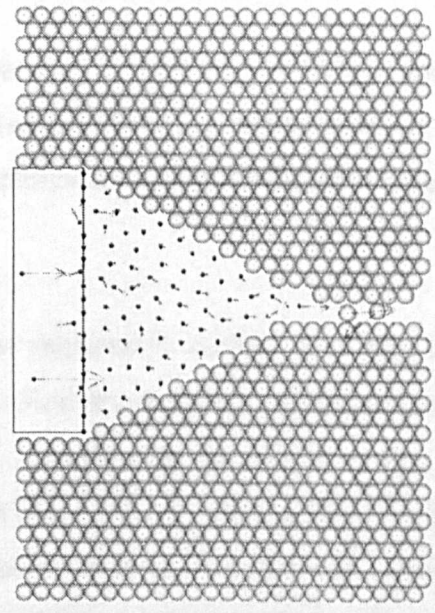
i)



ii)



iii)



iv)

Diagrams Showing PSM and PFM Particles in Final Stages of Fracture Propagations Produced in the Parametric Study on the Coupled Hydraulic Fracture Benchmark Model from i) (Fig. 6.21. d)) Run 001 (Mark 1 Failure Criterion, Zero Confining Pressure, Critical Pressure of 66kPa) ii) (Fig. 6.22. d)) Run 002 (Mark 2 Failure Criterion, Zero Confining Pressure, Critical Pressure of 56kPa) iii) (Fig. 6.23. d)) Run 003 (Mark 3 Failure Criterion, Zero Confining Pressure, Critical Pressure of 129kPa) iv) (Fig. 6.24. d)) Run 004 (Mark 1 Failure Criterion, $\sigma_2 = 75.0\text{kPa}$, $\sigma_3 = 75.0\text{kPa}$, Critical Pressure of 190kPa)

(Repeated from pages 344, 345, 346 & 347)

Additionally, it can be seen in item d) of *Fig. 6.21.*, *Fig. 6.23.* and *Fig. 6.24.* that several PSM particles became detached from the main mesh due to the fluid pressure applied by the PFM and this can be considered representative of processes such as disaggregation and sanding (See Chapter 2, Section 2.5.). What is more it can be seen from the velocities and positions of these particles, in relation to their original positions, that they were carried along by the model fluid flow. This demonstrates perfectly the full potential of the combined Multi-Physics Particulate Modelling Framework to integrate solid, fluid and granular phases within one model, created within a single framework and solved simultaneously, as proposed, in Chapter 3 Section 3.2., for the long term aim for a computational framework such as this.

6.3.4. Conclusions

From the results discussed in the previous Section, it can be concluded that the combined model was able to reproduce the interaction behaviour of the solid and fluid phases in conjunction with the propagation of fractures driven by the fluid pressure, to a qualitatively satisfactory standard.

The actual values of the critical pressures required to initiate fracturing in the PSM mesh were lower than those observed under similar conditions in tests carried out with the Hydraulic Fracture Benchmark Model. Considering the results of the those studies, it is probable that the critical pressures recorded for the Coupled Hydraulic Fracture Benchmark Model were much lower than would be expected for an equivalent real case. It is therefore concluded that further investigation is required in order to fully understand and improve the interaction behaviour of the PSM and PFM components of the modelling framework and to thereby to accurately reproduce realistic behaviour. This conclusion is in agreement with the findings of the Pressurised Notch Coupled Benchmark Problem discussed in Section 4.4.2. of Chapter 4. Despite these findings, it is felt that the Coupled Hydraulic Fracture Benchmark Model showed considerable promise and demonstrated, very well, the potential of the combined multi-phase modelling framework.

It is further considered possible that in order to accurately reproduce the behaviour of fluid flow in a propagating fracture it may be necessary to account for fully dynamic behaviour in the model. Although, it can be considered acceptable, given the differing times scales involved in fracture propagation and fluid flow, to model hydraulic fracturing as a quasi-static process, this may not be sufficient for the combined PSM + PFM framework in order to accurately capture the solid/fluid interaction and fracturing behaviour. It would therefore be desirable to consider dynamic behaviour in the future although it is accepted that this would require very accurate control of the model parameters and boundary conditions.

Although the small benchmark models considered in this study were able to illustrate the possibilities available with a multi-phase particulate modelling framework, it should be noted that they were quite computationally expensive due to the number of particles required and the complex *FISH* routines running concurrently during each time step of the PFC^{3D} model. It should also be noted that these models were only representative of a few square millimetres of material and while it is desired, in the future, to create a large enough mesh to model realistic hydraulic fracture treatments, combining fracture propagation and fluid flow, this will require far more computing power and, ideally, an optimised and perhaps purpose written code, rather than a general DEM framework with only limited flexibility for user defined changes, as was the case here.

In addition to the promising general behaviour, it can also be noted that the results of the numerical tests conducted with the Coupled Hydraulic Fracture Benchmark Model illustrated several problems concerning the Mark 2 and Mark 3 failure criteria. While these effects had been previously highlighted as potential problems, they were not manifested until the criteria were applied to the PSM mesh employed in this study, thus indicating their relationship to the mesh configuration. Further investigation will be required in order to determine the precise cause of these manifestations and to develop possible modifications to these models.

6.4. Summary

In this Chapter, two benchmark studies, conducted with the purpose of testing the capabilities of the Particulate Mechanics Modelling Framework to represent realistic multi-phase geomechanical problems, were presented and discussed in detail. Both benchmark models considered pseudo-realistic representations of propagating hydraulically driven fractures.

The first benchmark model employed a PSM mesh in order to represent the solid phase hydrocarbon reservoir rock and a simplified force representation for the pressure applied to the walls of the fracture by the fracture fluid. Extensive parametric testing was carried out with this model to determine the effects, on the fracture growth behaviour, of varying the Poisson's ratio of the solid material, varying the confining pressure, different failure criteria and randomising the material strength in order to represent a heterogeneous material.

It was found that the model generally produced the straight fracture pattern expected for a hydraulic fracture treatment in a homogeneous material and also produced the behaviour expected under the parametric variations, to a reasonable standard. The model was furthermore found to be capable of reproducing the results of previous numerical studies to a satisfactory degree. However, not all of the numerical studies produce results that were considered representative of the realistic hydraulic fracture behaviour and problems were specifically related to the constraints and boundary conditions applied to the PSM mesh. It was additionally noted that the force representation of the fluid pressure, employed by this model, was limiting and resulted in highly simplified fluid behaviour. Moreover, it is felt that very complex coding would be required in order to develop a more rigorous fluid model and to accurately reproduce multi-phase behaviour using this technique.

The second benchmark model again employed a PSM mesh in order to represent the solid phase material, however, rather than the force representation considered in the first model, the fluid phase material was directly represented with the PFM. Given the complexities and known limitations of the interaction behaviour between the Particle

Solid Model and the Particle Fluid Model (See Chapter 4, Section 4.4.), the brief parametric studies conducted with this model were intended only for a qualitative assessment of the capabilities of the Particulate Modelling Framework in representing complex multi-phase behaviour.

It was found that the combined model generally produced the expected trends in behaviour for a hydraulic fracture problem and was able to reproduce the interaction behaviour of the solid and fluid phases in conjunction with the propagation of fractures driven by the fluid pressure, to a qualitatively satisfactory standard. It was furthermore noted that the model was able to demonstrate the full potential of the single software Particulate Mechanics Framework to combine the modelling of granular phase material with the solid and fluid phases, without further development or modification of the modelling framework.

Although the model was generally found to produce qualitatively acceptable results, it is accepted that a considerable amount of work will be required before a realistic representation of a problem, such as a hydraulic fracture treatment, can be modelled. It is further accepted that a large model, as will be required for a realistic problem such as this, would be very computationally expensive and an optimised code, running on a powerful machine will be required to make it feasible. It is hoped, however, that with the development of computing power this type of modelling framework will become practical for everyday use.

In the next Chapter, the work presented during the course of this thesis will be summarised in conjunction with the main conclusions reached. Additionally, suggestions will be made for the direct continuation and enhancement of the studies carried out for this thesis. An overall assessment will then be made of the Single Software Multi-Phase Particulate Modelling Framework and the various modelling techniques applied within it. Finally, discussion will be made of the overall implications of the work considered and the conclusions drawn in this thesis, for the future application of particulate frameworks and lattice type models in various fields to which computational modelling is applicable.

Chapter 7:

Conclusions and Further Work

7.1. Introduction

The research conducted for this thesis was concerned with the development of a particulate mechanics framework for modelling multi-phase processes in fracturing geomaterials, as is commonly required for geomechanical problems encountered in disciplines such as petroleum, civil and geotechnical engineering. The framework was developed within the existing commercial geotechnical DEM code, Particle Flow Code in Three Dimension (PFC^{3D}), with the aim that all material phases could be modelled within a single software environment and solved simultaneously by the existing dynamic relaxation solver.

The first part of this Chapter is divided into Sections concerning the development of the solid phase *Particle Solid Model (PSM)*, the fluid phase *Particle Fluid Model (PFM)* and combined *Solid/Fluid Models (PSM + PFM)*. In each of the Sections, a brief review of the work undertaken will be given in conjunction with a statement of the main conclusions reached after consideration of the work presented in the preceding Chapters. Additionally, suggestions and recommendations will be made for the direct extension and continuation of this research. Following these three sections, an overview and assessment will be made, of the particulate mechanics framework and its capabilities and potential as an environment in which generally applicable multi-phase models of geomechanical problems can be developed.

In the second part of this Chapter, discussion will be made of the wider implications of this work for the future application of particulate and lattice type modelling in various fields to which computational analysis is applicable.

7.2. Particle Solid Model (PSM)

7.2.1. Summary and Conclusions

The Particle Solid Model (PSM) was developed to allow the creation of model representations of continuous, solid materials, in the form of two-dimensional regularly configured, bonded particle assemblies, thus producing models comparable to lattice type representations. The particles in the assemblies interacted through normal and shear contact springs inherent in the PFC^{3D} modelling environment and continuum equivalence was established via equations developed by Morikawa and Sawamoto [63] from the strain energy equivalence in regular triangular cells of closely packed particles. The assemblies were bonded together by means of inter-particle links, realised through 'contact bonds', also inherent in the PFC^{3D} modelling environment, which allowed contact interactions to develop under tensile loading conditions. These links could be removed from the assembly, as desired, in order to represent fracturing of the solid material.

The initial work carried out with the PSM for this thesis considered the reproduction of simple benchmark tests developed by Griffiths and Mustoe [32] for a discrete element model similar to the PSM. These tests considered the deformation of a square sample of material and a cantilever beam under prescribed loading conditions and were designed to determine the capability of the PSM to reproduce the elastic behaviour that would be expected of an equivalent continuum material. The results of these tests showed that the PSM could very accurately reproduce the deformations that would be expected for an equivalent continuum material and that as would be expected, from the results of other numerical studies (van Vliet [95]), the accuracy of the predictions increased with increasing discretisation of the PSM mesh. However, it was also noted that the accuracy of the predicted deformations, decreased with increasing Poisson's ratio. This was particularly noticeable in the lateral displacements, occurring perpendicular to the direction of applied loading in the tests concerning the square sample of material. It was concluded, however, that with a suitably fine mesh, the accuracy of the PSM in reproducing the deformation behaviour of an elastic material was more than sufficient for most requirements.

The second area of investigation conducted with the PSM considered the development of five failure criteria, which were used to develop fracturing behaviour in the PSM mesh through the controlled removal of inter-particle links. The criteria were tested in a simple benchmark model, which considered the development of a fracture in a rectangular model mesh, subjected to uniaxial loading conditions.

The Mark 1 failure criterion considered elastic-brittle behaviour based on the uniaxial total strain in individual inter-particle link elements. The criterion was found to over predict both the ultimate load capacity and ultimate extension of the material sample in comparison to the results that were expected for an equivalent continuum material. It was concluded that this behaviour was to be expected since, due to the triangular configuration of the particle assembly, the PSM mesh had to be over extended in order for inter-particle links orientated diagonally to the direction of loading to reach their ultimate strain. This effect was further confirmed by a directional bias that was noted in the results, which could be related to the alignment of the inter-particle links in comparison to the direction of loading. It was additionally concluded that a failure criterion based on continuum principles, rather than the uniaxial behaviour of individual inter-particle links, would be required in order to accurately reproduce equivalent continuum behaviour in a meso- or macro-scale lattice type model such as the PSM. It was noted however, that similar investigations, conducted by other researches (Schlangen and Garboczi [79], Schlangen and van Mier [80, 81, 82], Tzschichholz and Herrmann [88], Tzschichholz et al. [89], van Vliet [95]), applying simple elastic-brittle failure criteria to micro-scale lattice models, produced accurate results in comparison to those expected for an equivalent continuum material. This tendency was also noted in these studies as the results approached those expected for an equivalent continuum with an increasing discretisation of the PSM mesh. In addition to the behaviour discussed above, evidence was also seen of mesh size dependency in the results produced by the Mark 1 criterion. This effect could be attributed to the fact that the Mark 1 failure criterion was a purely elastic-brittle model and as such made no account of fracture energy dissipation during failure of the inter-particle links.

The Mark 2 failure criterion also considered elastic-brittle behaviour. However, inter-particle link failure was based on the Rankine principal stress criterion that considered the continuum stress state, calculated in the particles of the PSM mesh,

rather than the uniaxial total strain of individual links. In confirmation of the conclusions reached after the tests conducted with the Mark 1 criterion, this failure criterion was found to produce a more accurate prediction of expected equivalent continuum behaviour. Furthermore, much less evidence of a directional bias was seen in these results than in those of the Mark 1 tests. However, as observed in the results produced by the Mark 1 criterion, the results produced by the Mark 2 criterion showed evidence of mesh size dependency. Again, this was attributed to the purely elastic-brittle behaviour considered by the model. Given the limitations of the PFC^{3D} modelling environment, it was concluded that, in order for a failure criterion for the PSM to show mesh size objectivity, it would be required to maintain a constant fracture energy release rate, independent of the mesh discretisation.

The Mark 3 failure criterion was an elastic-softening model designed specifically to vary the softening behaviour in relation to the inter-particle link length and the fracture energy release rate. Similarly to the Mark 1 criterion, the Mark 3 considered the uniaxial total strain in individual inter-particle links. It was found that this criterion was highly proficient at developing mesh size objectivity under uniaxial loading in any direction, however, as would be expected from the results of the tests conducted with the Mark 1 criterion, the Mark 3 criterion over predicted both the ultimate strength and ultimate extension of the model mesh in comparison to the expected results for an equivalent continuum material. This further substantiated the hypothesis that a failure criterion based on continuum principles, rather than the uniaxial behaviour of individual inter-particle links, would be required in order to accurately reproduce equivalent continuum behaviour in a meso- or macro-scale lattice type model such as the PSM.

The Mark 4 failure criterion again considered elastic-softening behaviour but was based on a continuum measure of the total strain in an equivalent continuum area surrounding an inter-particle link element. This criterion also showed mesh size objectivity and was furthermore found to produce far more accurate predictions of ultimate strength and ultimate extension, in comparison to those expected for an equivalent continuum, than the Mark 3 criterion, thus confirming the benefit of a continuum based failure criterion for the PSM. However, considerable noise was observed in the post-peak regions of the load-displacement curves plotted for these

tests. It was considered that this behaviour was a consequence of the technique employed to redistribute excess stress from softening links, which, in contrast to the equivalent continuum measure of the total strain state, was carried out on an individual element basis.

The Mark 5 failure criterion was a modified version of the Mark 4 criterion and employed the same technique to calculate the continuum total strain state in the inter-particle links. However, rather than redistributing the excess stress from a softening inter-particle link through the link itself, redistribution was also spread over the whole of the associated equivalent continuum area. Given the similarity of the two criteria the results produced by the Mark 5 criterion were initially very similar to those produced by the Mark 4 criterion in terms of the ultimate strength and extension of the model mesh in comparison to the results expected for an equivalent continuum material. However, the altered redistribution technique failed to solve the problem of noise in the unloading phase of the numerical solution and in fact the overall behaviour produced by the Mark 5 criterion was considered to be generally worse than that of the Mark 4 criterion. Although it is felt likely that the problem is related to an uncontrolled feedback between the corrective forces, developed in order to redistribute excess stress from softening inter-particle links, and the continuum total strain state, as yet no satisfactory explanation or solution can be given for the noise produced in the load-displacement behaviour of both the Mark 4 and Mark 5 criteria.

7.2.2. Suggestions for Further Work

Given that the elastic behaviour of the PSM, and hence the applied continuum equivalence technique, were found to be very accurate, the main area in which it would be desirable to extend the development of the PSM is with the failure criteria. As mentioned above, it was concluded that a continuum based failure criterion was required in order to accurately reproduce equivalent continuum behaviour in a meso- or macro-scale lattice type model such as the PSM. Thus, it would seem most appropriate to continue the development of the Mark 2, Mark 4 and Mark 5 criteria.

In respect of the Mark 2 criterion, although only the simple Rankine principal stress criterion was applied in this work, it is theoretically possible to develop any stress based failure criterion through manipulation of the continuum stress tensors calculated for each particle in a PSM mesh. Thus, there is scope to develop more complex failure criteria, such as the Mohr-Coulomb criterion, that may more accurately model the fracture behaviour of a geomaterial. It should be noted however that, as with the Mark 2 Rankine criterion, this again would probably be restricted to an elastic-brittle analysis unless a method can be found of developing softening behaviour through this approach.

For the Mark 4 and Mark 5 failure criteria, it is obviously desirable to determine and solve the cause of the considerable noise observed in the post-peak load-displacement behaviour and further investigation is required to this end. In addition to these problems, it was also observed that the measurement of total strain employed in the Mark 4 and 5 failure criteria was limited to an Eulerian approach, whereby simple stretches of the link elements were calculated, irrespective of the current orientation or location. Furthermore, the associated stress states were calculated via a simple Hookean relationship, thus developing the Cauchy stress formulation. This technique was consistent with the approach employed by the explicit, time stepping dynamic relaxation solver, associated with the PFC^{3D} distinct element code, which determines contact forces and particle velocities based on only the current configuration of the particle assembly. Obviously, the Eulerian formulation was dependent on the assumption that only small strains took place, although it was equally applicable under either large or small overall displacements. Under certain conditions, it may be desirable to accurately model large strains with the PSM, in which case a Lagrangian formulation would be preferable, taking into account the change in length and orientation of the mesh. Under a Lagrangian formulation the stress could no longer be directly related to the strain state through Hooke's law and an alternative formulation, such as Piola-Kirchhoff, would be required. It would then also be required to map the stress-strain state between the current and original mesh configurations. Obviously, the rigorous treatment of large strains in a lattice type model would not be a simple procedure. However, although it was not attempted during the course of this work to apply a large strain formulation to the PSM, it is clear that there is significant scope to do so. Furthermore, this would not be limited just to the PSM but would also be applicable in a general lattice type setting and a large area of research could be opened up from this simple proposal.

7.3. Particle Fluid Model (PFM)

7.3.1. Summary and Conclusions

The Particle Fluid Model (PFM) was developed to allow the modelling of fluid like materials through a particle representation. The particles carried mass, position and velocity information, and interacted with other particles, which came within certain radii of influence, through drag and repulsion forces, representative of pressure and viscosity fields. The DEM particles themselves were thus prevented from ever coming into physical contact. The properties of the model fluid were dependent on five model parameters; a coefficient of repulsion, a coefficient of drag, the radius of influence of repulsion, the radius of influence of drag and the coefficient of mechanical damping which is a parameter inherent to the PFC^{3D} modelling environment.

In order to test the capacity of the PFM to develop simple fluid behaviour, two benchmark models were created. The first considered static behaviour through the development of a uniform pressure field in a closed cylinder subjected to an externally applied pressure. The second model considered dynamic behaviour through the development of a simple lubrication flow regime, representative of incompressible, one-dimensional, steady, uniform, laminar flow between two parallel plates.

The results of the first benchmark model showed that the PFM was capable of accurately developing a uniform pressure field under static conditions as, under various applied pressures, the reaction measured on the walls of the cylinder matched very closely the magnitude of the externally pressure field. Furthermore, it was seen from the results of the second benchmark model that the PFM was also capable of accurately producing dynamic fluid behaviour, since the expected parabolic velocity profile, associated with lubrication flow, was successfully reproduced under various combinations of the model parameters. It was also noted however, that the flow developed with the PFM was prone to considerable noise in the solution, although this was not found to significantly affect the development of simple dynamic behaviour.

Furthermore, despite the qualitative accuracy of the results seen in the benchmark models it is also concluded that the relationships governing the effects of the

five main model parameters on the behaviour of the PFM are extremely complex and are far from fully understood. During the course of the work carried out for this thesis it was only possible to determine the properties of the model fluid by comparing the behaviour produced by the benchmark model with the lubrication flow theory. It was not possible to calibrate the fluid properties prior to an analysis. Nonetheless, on the basis of the results produced by the benchmark models, it is felt that the PFM shows great promise and has the potential to be developed into a rigorous fluid modelling tool.

7.3.2. Suggestions for Further Work

There is still much work required in order to develop the PFM into a rigorous and robust fluid model. The first priority will be to develop an understanding of the relationships between the five main model parameters and the model fluid behaviour. This may be attempted by empirical means but may prove extremely difficult to achieve in the five parameter space. Thus, a more efficient and accurate approach may be to develop an analytical relationship between the parameters of the PFM and the Navier-Stokes equation for a fluid continuum. It may also prove useful to further investigate the techniques applied to modelling fluids with the Particle-and-Force (PAF) model (Johnson [43]) and furthermore, the relationship of this method to the PFM. Study of the PAF, and particularly into recent advances made in discrete macroscopic modelling of fluids and in improving the stability and efficiency of the solution scheme, may also prove useful in reducing the noise observed in the flow developed by the PFM.

7.4. Combined Model (PSM + PFM)

7.4.1. Summary and Conclusions

Two types of multi-phase benchmark model were developed in order to test the capabilities of the particulate mechanics framework in modelling combined solid/fluid interaction behaviour. The first of these benchmark models considered the propagation of a hydraulically driven fracture through a solid, rock like material. The solid phase

was represented by a PSM mesh and the fluid phase was represented simply by forces, corresponding to fluid pressures, applied to the walls of the fracture.

Under most conditions this benchmark model was shown to produce the generally expected behaviour for a propagating hydraulically driven fracture in a homogeneous material. It was also shown that the fracture profiles and associated fracture pressures, measured during the propagation of the model fractures, matched reasonably well with similar results presented by Papanastasiou [69]. Furthermore, the general behaviour was comparable to that which would be expected from existing plane strain hydraulic fracture models.

Although the results were largely acceptable, it was also found that under certain parametric combinations, and in particular when confining pressures were applied, inaccurate or unexpected behaviour was observed. This was attributed mainly to the boundary conditions and fixity of the model mesh constructed for this benchmark model, which caused the model to become unstable when imbalances developed in the externally applied forces. During the course of this work, no method was found of solving this problem without affecting the fracture propagation behaviour.

Although it will be required to resolve this problem, it is concluded, from the behaviour observed in this benchmark study, that the particulate modelling framework is capable of reproducing combined solid/fluid behaviour and that great potential was shown for the future development of the framework for modelling multi-phase problems. It may be noted however, that, while the representation of the fluid phase through the application of forces representing pressure allowed easy control over the boundary conditions of the model problem, it would be very difficult to describe complex flow and pressure distributions using this method.

The second benchmark model also considered hydraulically driven fracture growth behaviour in a solid material represented by a PSM mesh, however, rather than a simple force representation, the fracture fluid was directly modelled with the PFM. In simple parametric studies, it was found that the combined PSM/PFM model was qualitatively able to reproduce both static and dynamic solid/fluid interaction behaviour, as well as fluid driven fracture propagation behaviour, to a satisfactory standard.

However, the measured critical pressures, required to initiate fracturing in the PSM mesh, were, quantitatively, lower than those expected from the results of previous studies.

It is thus concluded that the particulate modelling framework showed considerable promise and potential for the modelling of multi-phase problems with combined PSM/PFM models, although, clearly, further investigation is required in order to fully understand and improve the interaction behaviour of the separate phase models in order to accurately reproduce coupled solid/fluid behaviour. Once this is achieved, it is hoped that the combined PSM and PFM framework will naturally reproduce complex flow and pressure distributions that it would be difficult to model with the force representation employed in the first benchmark model.

7.4.2. Suggestions for Further Work

It would initially be desirable to continue and extend the investigations carried out with the first benchmark model. These would firstly carry on the studies carried out for this thesis, with the aim of reaching clearer conclusions regarding the effects of the various model parameters on fracture growth behaviour. Investigation would secondly extend the work carried out for this thesis in order to explore the capacity of the particulate modelling framework to deal with various model and problem parameters that may influence fracture growth behaviour. These may include the presence of planes of weakness or existing discontinuities, varying conditions of confinement and the mesh discretisation. In addition to this suggested work, a main priority would be to resolve the problems encountered during the course of the studies carried out for this thesis, that were associated with the boundary conditions and the fixity of the PSM mesh.

However, it is also felt that it may prove more productive to focus future investigation on the development of combined PSM/PFM models, as considered in the second benchmark model. It is considered that if this type of model could be improved in order to produce quantitatively accurate results, it would naturally overcome most of the difficulties encountered in the first benchmark study. In order to accurately model

multi-phase problems in this way it will be required to more thoroughly investigate the results produced by the combined benchmark model and furthermore, it will be desirable to reconsider the precise mechanism by which 'solid' particles interact with 'fluid' particles.

Although the multi-phase models investigated during the course of these studies were all considered to exhibit quasi-static behaviour it may also be desirable in the future to consider fully dynamic behaviour in order to develop the most accurate representation possible. It is however acknowledged that this will require a very detailed understanding and accurate control of the model parameters and boundary conditions.

7.5. Overall Assessment and Conclusions

The overall aim of this project was to develop a particulate mechanics framework for modelling multi-physics processes for particular application to geomechanical problems that may involve fracturing. From the work presented in this thesis, it can be concluded that in general this type of framework has considerable potential to deal with a wide range of material combinations, undergoing complex interactions and developing complex behaviour, in almost any conceivable configuration. Furthermore, the particulate mechanics framework was shown to have many advantages over multi-phase continuum mechanics modelling schemes, although clearly, within such a framework, numerous methods and techniques are applicable to the modelling of the various material phases and each would have their own particular advantages and disadvantages. The particulate mechanics framework developed during the course of this work and the techniques applied therein, are examined in more detail below, along with their specific pros and cons, and some possible alternatives.

Considering firstly the modelling of the solid phase, it was shown in benchmark testing, that the PSM very accurately reproduced the behaviour of an elastic solid material and this additionally implies the suitability of the strain energy equivalence technique used to calibrate the PSM mesh. It was furthermore shown that the PSM

dealt reasonably well with softening behaviour and the development of fracturing, although the results were dependent on the particular failure criterion employed. During this benchmark testing, the advantages of a particulate mechanics framework over a continuum framework were also clearly demonstrated, since it could be seen that the PSM dealt naturally with the break up of an initially continuous material into discrete pieces. It can furthermore be noted that, in contrast to a continuum framework in which fracturing behaviour is developed, there was no requirement to remesh or redefine elements or boundaries in the PSM mesh. Additionally, while the development of a discrete fracture pattern in a solid mechanics framework may be limited to predefined paths, the freedom of a fracture pattern to propagate naturally in a particulate mechanics framework, developing meandering and branching behaviour, was also demonstrated with the PSM.

In order to promote this realistic fracture growth behaviour, to allow the modelling of fracturing in heterogeneous materials and to eliminate the possibility of fracture growth being controlled by the configuration of the particle assembly, it is suggested, by Schlangen and Garboczi [79], that a randomly configured assembly is considered. This would thus be an appropriate extension of the work carried out for this thesis, which was limited to the study of regular particle assemblies. Random variation of the material strength in a PSM mesh was briefly considered in this work, although it was seen to have little affect on the behaviour of the benchmark model. It is felt however, that implementation of a random arrangement of particles with the PSM will encounter several difficulties. Firstly, limitations of the PFC^{3D} modelling environment, in which the particulate mechanics framework was developed during the course of this work, make it difficult to vary the stiffness of the inter-particle links in the PSM mesh. Secondly, the strain energy equivalence technique developed by Morikawa and Sawamoto [63] would no longer be directly applicable to a randomly configured particle assembly. While similar techniques have been employed in order to establish continuum equivalence in randomly configured lattice models, it is likely that it will be difficult to do the same in a particle assembly, such as those created with the PSM, in which the inter-particle links have no cross-sectional area. Further investigation will be required in this area.

The second main area of investigation considered during this work was the modelling of the fluid phase. While it was concluded, from the results of benchmark testing, that the PFM has significant potential, it was also acknowledged that a considerable amount of work must be undertaken before it will be possible to accurately model the behaviour of a specific fluid, especially in combination with a solid phase material. The two main difficulties encountered with the application of the PFM were, firstly, a lack of stability in the flow systems developed with the model and, secondly, in the capacity to calibrate the model for particular fluid properties. Given these problems, the possibility of employing an entirely different type of fluid model, in conjunction with the particulate representation of a solid material, is considered.

During the course of this work, as an alternative technique to the PFM, it was attempted to represent fluid behaviour through the application of simple forces corresponding to fluid pressures. It was concluded, however, that, while it worked for a simple case, it would be very difficult to model complex fluid behaviour in an irregular fracture pattern with this technique. It was further noted that several, simplifying assumptions had to be made for the fluid behaviour before the technique could practically be implemented. In contrast, it is hoped that, once refined, the PFM will naturally model complex fluid flow in any situation, without the need for any simplifications or assumptions.

A further possible method of implementing fluid behaviour would be to utilise a dedicated fluid modelling code, acting in combination with the particulate mechanics framework. This would determine the fluid flow behaviour according to the current configuration of the particle assembly and calculate the appropriate fluid pressures to be applied to the solid material. Techniques of this kind have previously been shown to work well in various schemes (Bruno et al. [11], Rouainia et al. [78].) However, it is felt that such a technique would defeat the purpose of the single software particulate mechanics framework, since separate codes are required and information must be transferred back and forwards between them in a staggered analysis. The more efficient single software scheme would solve both the solid and fluid models simultaneously with a single solver.

It is thus concluded that it remains worthwhile to pursue the concept of a particle fluid representation, such as the PFM, that can interact with a particulate representation of a solid material, such as the PSM, within a single modelling framework. Alternatively, a further possibility may be the development of other forms of particle representation for the fluid phase, such as Smooth Particle Hydrodynamics (SPH), within the particulate mechanics framework. However, this would again require the use of separate solvers for the solid and fluid phases and, for the purposes of the framework developed during this project, even if SPH could be realised through code written in the *FISH* language associated with PFC^{3D}, it is likely that it would be extremely computationally expensive.

The final material phase considered in this work is that of granular material. Given the particulate mechanics basis of the modelling framework a granular material is naturally modelled, however, where granular materials occur in geomechanical problems they are likely to interact with solid and fluid materials. While these combinations were not specifically tested, the potential for the particulate mechanics framework to handle the simultaneous interaction of solid, fluid and granular phases was illustrated in the course of benchmark testing of the combined solid and fluid (PSM + PFM) models, during which individual particles, dislodged from the solid material, were carried along by the fluid. As before, it can be seen that all of these phases can be dealt with in a single framework employing one solver. Furthermore, the partial conversion of a continuous solid material to a discrete, particulate material is naturally captured and again this is achieved without the need for complex remeshing. This is behaviour that it would certainly be difficult to model in a continuum mechanics framework.

It may be noted that, in order to realistically represent granular material, such as sand or proppant, in a combined model such as that discussed above, it would be necessary to employ a very large number of small particles. A consequence of large numbers of particles is increasing computational expense and it was noted, even with the relatively small benchmark models developed during the course of these studies, that some of the analyses were reasonably slow to run. It is conceded however that these benchmark studies were conducted on what may now be considered a slow machine. It is further acknowledged that the code, developed in the *FISH* language

associated with PFC^{3D}, was not maximally efficient. It is felt that with an optimised and perhaps purpose written particulate mechanics code, running on a powerful computer, this modelling framework could be practically applied to modelling realistic, large-scale geomechanical problems. The available possibilities can only increase as computer power develops.

In overall assessment of the particulate modelling framework, it is thus concluded that, although the capabilities are currently limited, there is significant potential for the development of a simple and robust framework that can model complex, multi-phase problems, and has the ability to combine various material scales and can furthermore naturally capture complex processes such as fracturing.

As an ultimate aim for the particulate mechanics framework, it would be highly desirable, given the nature of geomechanical problems such as hydraulic fracture treatments, to develop a fully three-dimensional framework. Although this may be a considerable advance from what is currently feasible, it would seem to be a reasonable goal since some investigation of three-dimensional lattice type models have already been conducted (Beranek and Hobbelman [8]) and the particulate mechanics environment is readily applicable in three dimensions. However, before a three-dimensional framework can be developed, various problems, such as the calibration of the various phase models in three dimensions, would have to be addressed. As mentioned previously, this has not yet been achieved for all cases in two dimensions. Furthermore, it is probable that one of the largest problems encountered will be the computational requirement associated with the huge numbers of particles required to construct a fully three-dimensional model on a realistic scale. Even considering these potential problems it is concluded that the particulate mechanics framework holds significant promise as a versatile, alternative modelling framework for many applications and particularly those concerning fracturing geomaterials.

7.6. The Wider Implications for Lattice Type Modelling

The particulate mechanics framework and specifically the Particle Solid Model (PSM), developed during the course of this work, is essentially equivalent to a lattice model. The concept behind a lattice type model is to replace a continuous material with a framework of simple beam- or truss-like elements that individually develop simple behaviour, and are consequently simple to analyse, while the overall lattice develops behaviour equivalent to the continuum material which it has replaced.

Typically, lattice models have been applied at the micro-scale, with elements on the order of millimetres in length, in order to capture grain scale phenomena (D'Addetta et al. [20]), and there are many examples of studies in which this type of application has been shown to produce excellent results (Bolander et al. [9], Chang et al. [14], Herrmann et al. [34], Hrennikoff [36], van Mier [59], Schlangen and Garboczi [79], Schlangen and van Mier [80, 81, 82], Tzschichholz [87], Tzschichholz and Herrmann [88], Tzschichholz et al. [89], van Vliet [95]). However, when considering large-scale structures, it becomes impractical to apply a lattice type model, given the numbers of elements that would be required. In these cases, when phenomena associated with the material grains become less important and the material can be regarded as essentially homogeneous, it is most efficient to employ continuum mechanics models. A disadvantage of continuum mechanics models is that, if it is desirable to introduce discontinuous processes such as fracture, it is necessary to consider some kind of material length scale. A length scale is also accounted for when considering higher order continua, such as Cosserat type media, as rotational degrees of freedom and consequently moments, are taken into account. In contrast, it is to situations such as this that lattice type models are particularly suited. Since a lattice type model consists of individual linear elements, joined at their ends by nodes, a length scale is inherently available. Thus, a lattice type model provides a simple framework that can be naturally applied to the analysis of both continuous and discrete processes within the same model. During the course of this work, it has been attempted to exploit this characteristic of lattice type models in modelling large-scale structures and, rather than their typical micro-scale application, meso- and macro-scale lattice type models were developed, with elements on the order of tens of centimetres in length.

Although micro-scale lattice models have been shown to develop the expected overall behaviour of reasonably large bodies of material while considering only simple behaviour in the individual lattice elements, it was found that in order to accurately develop overall material behaviour with meso-/macro-scale lattice type models, it was necessary to consider element behaviour based on equivalent continuum principles. This is a similar concept to the application of continuum mechanics models that employ phenomenological laws in order to reproduce the overall behaviour of large-scale structures, although it may be noted that the inherent length scale and consequent natural ability to capture discrete behaviour remained available in the meso-/macro-scale lattice type models.

During the course of this work, application of continuum principles to the lattice type model was made to work well under conditions of simple elastic behaviour however difficulties were encountered in implementing more complex softening behaviour. It is hoped that in the future, the development of more rigorous integrations of lattice type model meshes and continuum mechanics principles may allow these problems to be overcome, thus leading to the creation of a highly robust particulate modelling framework in which discrete behaviour can be readily modelled in large-scale structures.

A possible avenue for this development is the notable similarity between lattice type models and micro-plane models. In its simplest form, the micro-plane/lattice analogy relates the limited number of failure planes, considered by a micro-plane model to pass through a particular material point, to the limited number of discrete inter-particle link or lattice elements, in which failure can occur, around a particular node of a lattice mesh. The equivalence of micro-plane models and particulate models, of the type employed in the creation of the PSM, has been examined in detail by Kuhl et al. [46] who compared the normal and shear stiffnesses, acting at an inter-particle contact, to the normal and tangential elastic moduli, considered on a micro-plane. They found that both model types produced very similar behaviour and further proposed that, given their natural abilities to deal with grain scale behaviour but their consequent computational expense for large-scale applications, particle models could be used to carry out microstructural analyses in order to determine micromechanical properties which could subsequently be entered into micro-plane based finite element models.

This kind of application certainly warrants further investigation, however, it is felt that it may also be possible to apply micro-plane formulations directly to meso-/macro-scale lattice type models. In order to implement such a scheme an equivalent micro-plane could be considered for each inter-particle link or lattice element. As in the comparative study conducted by Kuhl et al. [46], the normal and shear contact forces developed by the interaction of particle contact pairs, via contact springs, could be related to the normal and shear components of tractions acting on each plane considered by a micro-plane model. Consequently, any failure criterion that can be developed for a micro-plane model could also be applied to lattice type model. It is anticipated that softening behaviour, as determined by the micro-plane formulation, could be realised in the lattice type model in much the same way as was realised in the elastic-softening criteria developed during the course of this work (See Chapter 5).

In addition to the determination of failure conditions, it should also be possible to use the information gathered from micro-plane analyses, carried out on planes equivalent to inter-particle links or lattice elements, to determine the continuum stress-strain state at points in an equivalent continuum, coincident with the particle centroids or lattice nodes. This would result in a non-local measurement of the stress-strain state similar to the granular stress measurements described earlier in this thesis (See Chapter 3, Section 3.4.2.). However, in contrast to the granular stress tensors, there would be no requirement to employ granular-continuum stress conversion factors. Hence, this system would seem to be potentially more readily applicable to deforming and irregular particle assemblies and should furthermore be applicable under conditions of softening behaviour.

If a rigorous system to apply equivalent continuum principles to lattice type models, such as that described above, can be developed, it will allow meso- and macro-scale lattice type models to be readily employed in the modelling of large-scale structures. However, it may also be noted that lattice type models are equally applicable on scales smaller than the micro-scale to which they are typically applied. In fact, if we consider nano-scale or even molecular- and atomic-scale problems, then lattice type models become highly representative of the material structure and continuum concepts, such as stress, become unworkable in bonds that cannot reasonably be considered to have measurable cross-sectional areas. It may be argued that the purest and most

realistic material model that can be constructed would consider material structure on the atomic level, where only simple laws would be required to determine if an atomic bond was intact or not. Clearly, with current technology, it is not feasible to model even small machine components at this level, however, in the future this kind of model may become practical for all scales of engineering.

In conclusion, it can be seen that while lattice type models are highly suited to modelling material at extremely small scales they are equally applicable over a wide range of modelling levels. This has been demonstrated during the course of this work where it has been shown that, as long as behavioural principles appropriate to the scale of the problem are applied, lattice type models can be utilised where other, less versatile types of model are more typically employed. Thus, advantage can be taken of the simple implementation of lattice type models and their inherent ability to capture both continuous and discrete behaviour simultaneously, in any scale of problem. Once the behaviour of a lattice type model developed for a specific type of problem is understood, it is largely applicable to any scale of problem and it is thus concluded that considerable potential exists in the development of lattice type modelling frameworks. The work carried out for this thesis has also demonstrated the potential of lattice type models and particularly particulate mechanics models for the implementation of multi-physics problems, an area of modelling for which there is much demand and opportunity. In summary, it can therefore be concluded that extensive further investigation in this field will be extremely valuable and highly worthwhile for all fields in which computational analysis is applicable.

Appendix IA:

References

1. Advani, S. H., Lee, T. S., Dean, R. H., Pak, C. K. & Avasthi, J. M., Consequences of Fluid Lag in Three Dimensional Hydraulic Fractures, International Journal for Numerical and Analytical Methods in Geomechanics, Vol. 21, No. 4, pp 229 - 240, 1997.
2. Advani, S. H., Lee, T. S. & Lee, J. K., Three dimensional Modeling of Hydraulic Fractures in Layered Media., Part I - Finite Element Formulations., Journal of Energy Resources Technology, Transactions of the ASME, Vol. 112, No. 1, pp 1 - 9, 1990.
3. Advani, S. H., Lee, T. S. & Lee, J. K., Three dimensional Modeling of Hydraulic Fractures in Layered Media., Part II - Calibrations, parametric sensitivity and field simulations, Journal of Energy Resources Technology, Transactions of the ASME, Vol. 112, No. 1, pp 10 - 19, 1990.
4. Amadei, B. & Illangasekare, T., A Mathematical Model for Flow and Solute Transport in Non - Homogeneous Rock Fractures, International Journal of Rock Mechanics, Mining Sciences & Geomechanics, Vol. 31, No. 6, pp 719 - 731, 1994.
5. Asgian, M. I., Cundall, P. A. & Brady, B. H., Mechanical Stability of Propped Hydraulic Fractures: A Numerical Study, SPE 28510, Society of Petroleum Engineers - Annual Technical Conference & Exhibition, 1995.
6. Bale, A., Owren, K. & Smith, M. B., Propped Fracturing as a Tool for Sand Control and Reservoir Management, SPE Production & Facilities, pp 19 - 28, 1994.

-
7. Bažant, Z. P., Tabbara, M. R., Kazemi, M. T. & Pijaudier-Cabot, G., Random Particle Model for Fracture of Aggregate or Fiber Composites, *Journal of Engineering Mechanics - ASCE*, Vol. 116, No. 8, pp 1686 - 1705, 1990.
 8. Beranek, W. J. & Hobbelman, G. J., Constitutive Modeling of Structural Concrete as an Assemblage of Spheres, In: *Computational Modeling of concrete Structures*, Proc. Int. Con. EURO-C 94, 1994, ISBN 0 906674 84 0.
 9. Bolander, Jr., J. E., Shiraishi, T., & Isogawa, Y., An Adaptive Procedure for Fracture Simulation in Extensive Lattice Networks, *Engineering Fracture Mechanics*, Vol. 54, No. 3, pp 325 - 334, 1996.
 10. Bonet, J., Kulasegaram, S. & Lok, T-S. L., Corrected Smooth Particle Hydrodynamics Methods for Fluid and Solid Mechanics Computations, *European Conference on Computational Mechanics*, Munchen, Germany, 1999.
 11. Bruno, M.S., Dorfmann, L., Lao, K. & Honeger, C., Coupled Particle and Fluid Flow Modelling of Fracture and Slurry Injection in Weakly Consolidated Granular Media - Wall, *Trends in Computational Structural Mechanics W.A.*, Bletzinger, K-U. & Schweizerhof, K. (Eds.), pp 647 - 659, CIMNE, Barcelona, 2001.
 12. Chang, C. S. & Liao, C. L., Constitutive Relation for a Particulate Medium with the Effect of Particle Rotation, *International Journal for Solids and Structures*, Vol. 26, No. 4, pp 437 - 453, Pergamon, 1990.
 13. Chang, C. S. & Ma, L., Modeling of Discrete Granulates as Micropolar Continua, *Journal of Engineering Mechanics*, Vol. 116, No. 12, pp 2703 - 2721, 1990.
 14. Chang, C. S., Wang, T. K., Sluys, L. J. & van Mier, J. G. M., Fracture Modelling with a Microstructural Mechanics Approach, *Fracture Mechanics of Concrete Structures - de Borst et al. (Eds.)*, pp 231 - 238, Swets & Zeitlinger, Lisse, 2001, ISBN 90 2651 825 0.
-

-
15. Christoffersen, J., Mehrabadi, M. M. & Nemat-Nasser, S., A Micromechanical Description of Granular Material Behaviour, *Journal of Applied Mechanics*, Vol. 48, pp 339 - 344, June, 1981.
 16. Clifford, P. J., Simulations of Waterflood Fracture Growth with Coupled Fluid Flow, Temperature and Elasticity., In: *The Mathematics of Oil Recovery*, King, P. R. (Editor), pp 23, Clarendon Press, Oxford, 1992.
 17. Commonwealth Scientific and Industrial Research Organisation (CSIRO) - Mathematical and Information Sciences (CMIS), Computational Fluid Dynamics, Smooth Particle Hydrodynamics, <<http://www.cmis.csiro.au/CFD/sph/>>, (25th July 2002)
 18. Cundall, P. A. & Strack, O. D. L., A Discrete Numerical Model for Granular Assemblies., *Geotechnique*, Vol. 29, pp 47 - 65, 1979.
 19. Cundall, P. A. & Strack, O. D. L., Modeling of Microscopic Mechanisms in Granular Material, In: *Mechanics of Granular Material: New Models and Constitutive Relations*, Jenkins, J. T. & Satake, M. (Eds.), pp 137 - 149, Elsevier Science, Amsterdam, 1983.
 20. D'Addetta, G. A., Kun, F., Ramm, E., & Herrmann, H. J., From Solids to Granulates - Discrete Element Simulations of Fracture and Fragmentation Processes in Geomaterials, In: Vermeer, P. A. et al. (Eds.), *Continuous and Discontinuous Modelling of Cohesive-Frictional Materials*, Springer, 2001, ISBN 3 540 41525 4.
 21. Davie, C. T., Computational Modelling of Well Bore Phenomena, MSc Thesis, Department of Civil Engineering, University of Glasgow, Glasgow, 1999.
 22. Desroches, J., Detournay, E., Lenoach, B., Papanastasiou, P., Pearson, J. R. A., Thiercelin, M. & Cheng, A., The Crack Tip Region in Hydraulic Fracturing, *Proceedings of the Royal Society of London A*, Vol. 447, pp 39 - 48, The Royal Society, Great Britain, 1994.
-

-
23. Douglas, J. F. & Swaffield, J. A. & Gasiorek, J. M., Fluid Mechanics, 3rd Ed., Longman, 1995, ISBN 0 582 23408 5.
 24. Drescher, A. & De Josselin De Jong, G., Photoelastic Verification of a Mechanical Model for the Flow of a Granular Material, Journal for the Mechanics and Physics of Solids, Vol. 20, pp 337 - 351, 1972.
 25. Dugdale, D. S., Elements of Elasticity, 1st Ed., Pergamon Press, Edinburgh, 1968, ISBN 08 103495 4.
 26. Economides, M. J. & Nolte, K. G., Reservoir Stimulation, 3rd Ed., John Wiley and Sons Ltd, 2000, ISBN 0471491926.
 27. Ercolessi, F., A Molecular Dynamics Primer, Spring College in Computational Physics, ICTP, Trieste, Italy, 1997.
 28. Ercolessi, F., MDBNCH: A molecular dynamics benchmark, Dipartimento di Fisica, Università di Udine, <<http://www.fisica.uniud.it/~ercolessi/mdbnch.html>> (25th July 2002).
 29. Feng, S., Thorpe, M. F. & Garboczi, E., Effective-medium Theory of Percolation on Central-Force Elastic Networks, Physical Review B, Vol. 31, No. 1, pp 276 - 280, 1985.
 30. Fung, Y. C., A First Course in Continuum Mechanics: for Physical and Biological Engineers and Scientists, 3rd Ed., Prentice-Hall, 1994, ISBN 0 13 061524 2.
 31. Goel, N. & Shah, S. N., Investigation of Proppant Flowback by Use of a Large Scale Fracturing Simulator, Journal of Petroleum Technology, 2000, Synopsis of: Experimental Investigation of Proppant-Flowback Phenomena Using a Large Scale Fracturing Simulator, Society of Petroleum Engineers, SPE 56880, 1999.
-

32. Griffiths, D. V. & Mustoe, G. G. W., Modeling of Elastic Continua using a Grillage of Structural Elements Based on Discrete Element Concepts, *International Journal for Numerical Methods in Engineering*, Vol. 50, No. 7, pp 1759 - 1775, 2001.
 33. Gu, H. & Leung, K. H., 3D Numerical Simulation of Hydraulic Fracture Closure with Application to Minifracture Analysis, *Journal of Petroleum Technology*, Vol. 45, pp 206 - 211, 1993.
 34. Herrmann, H. J., Hansen, A. & Roux, S., Fracture of Disordered Elastic Lattices in Two Dimensions, *Physical Review B*, Vol. 39, No. 1, 1989.
 35. Hopkins, C., Real-Time 3D Hydraulic Fracture Models, *Petro Systems World*, May/June, pp 12 - 17, 1996.
 36. Hrennikoff, A., Solution of Problems of elasticity by the Framework Method., *Journal of Applied Mechanics*, Vol. 8, pp A 169 - A 175, 1941.
 37. Itasca Consulting Group Inc., Particle Flow Code in Three-Dimensions, Version 1.1, Users Manual, Minneapolis, Minnesota, 1995.
 38. Itasca Consulting Group Inc., Minneapolis, Minnesota , UDEC Software, <<http://www.itascacg.com/udec.html>> (25th July 2002)
 39. Jankovic, D., Küntz, M. & van Mier, J. G. M., Numerical Analysis of Moisture Flow and Concrete Cracking by Means of Lattice Type Models, *Fracture Mechanics of Concrete Structures - de Borst et al. (Eds.)*, pp 231 - 238, Swets & Zeitlinger, Lisse, 2001, ISBN 90 2651 825 0.
 40. Jirásek, M. & Bažant, Z. P., Macroscopic Fracture Characteristics of Random Particle Systems, *International Journal of Fracture*, No. 69, pp 201 - 228, Kluwer Academic, Netherlands, 1995.
 41. Jirásek, M. & Bažant, Z. P., Particle Model for Quasibrittle Fracture and Application of Sea Ice, *Journal of Engineering Mechanics*, pp 1016 - 1025, 1995.
-

42. Johnson, D., *Advanced Structural Mechanics*, Collins, London, 1986, ISBN 0 00 383165 5.
43. Johnson, N. L., *The Legacy and Future of CFD at Los Alamos*, Canadian CFD Conference, Ottawa, 1996.
44. Kafritsas, J., *Coupled Flow/Deformation Analysis with the Distinct Element Method.*, MIT, Cambridge, 1987.
45. Kalu, P., Online lecture notes, *Strain and Tensor Transformations*, Florida State University, <<http://www.eng.fsu.edu/~kalu/ema4225/00/topics/chap7/sld001.htm>>, (25th July 2002)
46. Kuhl, E., D'Addetta, G. A., Leukart, M. & Ramm, E., *Microplane Modelling and Particle Modelling of Cohesive-Frictional Materials*, In: Vermeer, P. A. et al. (Eds.), *Continuous and Discontinuous Modelling of Cohesive-Frictional Materials*, Springer, 2001, ISBN 3 540 41525 4.
47. Lenoach, B., *The Crack Tip Solution for Hydraulic Fracturing in a Permeable Solid*, *Journal of the Mechanics and Physics of Solids*, Vol. 43, No. 7, pp 1025 - 1043, 1995.
48. Liao, C. L., Chan, T. C., Sucker, A. S. J. and Chang, C. S., *Pressure-Dependent Elastic Moduli of Granular Assemblies*, *International Journal for Numerical and Analytical Methods in Geomechanics*, Vol. 24, pp 265 - 279, 2000.
49. Libersky, L. D., Putsches, A. G., Carney, T. C., Hip, J. P. R. & Alidade, F. A., *High Strain Lagrangian Hydrodynamics, A Three-Dimensional SPH Code for Dynamic Material Response.*, *Journal of Computational Physics*, Vol. 109, pp 67 - 75, 1993.
50. Lister, J. R., *Buoyancy-Driven Fluid Fracture: the Effects of Material Toughness and of Low-Viscosity Precursors*, *Journal of Fluid Mechanics*, Vol. 210, pp 263 - 280, 1990.

51. Lister, J. R., Buoyancy-Driven Fluid Fracture: Similarity Solutions for the Horizontal and Vertical Propagation of Fluid-Filled Cracks, *Journal of Fluid Mechanics*, Vol. 217, pp 213 - 239, 1990.
52. Lowenstein, M. & Mathews, W. G., Adiabatic Particle Hydrodynamics in Three Dimensions, *Journal of Computational Physics*, Vol. 62, pp 414 - 428, 1986.
53. Lu, P. F. & Vaziri, R., The Equivalence of Stress- and Strain-Based Plasticity Theories, *Computer Methods in Applied Mechanics and Engineering*, Vol. 147, pp 125 - 138, 1997.
54. Luding, S., Lätzel, M., Volk, W., Diebels, S. & Herrmann, H. J., From Discrete Element Simulations to a Continuum Model, *Computer Methods in Applied Mechanics and Engineering*, Vol. 191, pp 21 - 28, 2001.
55. Masson, S. & Martinez, J., Effect of Particle Mechanical Properties on Silo Flow and Stresses from Distinct Element Simulations, *Powder Technology*, Vol. 109, pp 164 - 178, 2000.
56. Mendelsohn, D. A., A Review of Hydraulic Fracture Modeling. - Part I: General Concepts, 2D Models, Motivation for 3D Modeling, *Journal of Energy Resources Technology*, Transactions of the ASME, Vol. 106, pp 369 - 376, 1984.
57. Mendelsohn, D. A., A Review of Hydraulic Fracture Modeling. - Part II: 3D Modeling and Vertical Growth in Layered Rock, *Journal of Energy Resources Technology*, Transactions of the ASME, Vol. 106, 1984.
58. van Mier, J. G. M., *Fracture Processes of Concrete: Assessment of Material Parameters for Fracture Models*, CRC Press, London, 1997, ISBN 0 8493 9123 7.
59. van Mier, J. G. M., Lattice Type Modeling for Fracture: Methodology and Future Prospects, *Fracture Mechanics of Concrete Structures*, Proceedings of FRAMCOS-3, AEDIFICATIO, Freiburg.

60. Milton-Taylor, D., Stephenson, C. & Asgian, M. I., Factors Affecting the Stability of Proppant in Propped Fractures: Results of a Laboratory Study, SPE 24821, Society of Petroleum Engineers - 67th Annual Technical Conference & Exhibition, 1992.
61. Monaghan, J. J., An Introduction to SPH, Computational Physics Communications, Vol. 48, pp 89 - 96, 1988.
62. Monaghan, J. J., Simulating Free Surface Flow with SPH, Journal of Computational Physics, Vol. 110, pp 399 - 406, 1994.
63. Morikawa, H. & Sawamoto, Y., Local Fracture Analysis of a Reinforced Concrete Slab by the Discrete Element Method, Proceedings of the 2nd International Conference on the Discrete Element Method, MIT, 1993.
64. Mustoe, G. and Williams, J., Short Course on Discrete Element Analysis, Fourth International Conference on Analysis of Discontinuous Deformation, Department of Civil Engineering, University of Glasgow, 2001.
65. Nguyen, P. D., Duterhoft, R. G., Dewprashad, B. T. & Weaver, J. D., New Guidelines for Applying Curable Resin-Coated Proppants, From SPE 39582, Journal of Petroleum Technology, 1998.
66. Noorishad, J., Tsang, C. F. & Witherspoon, P. A., A Coupled Thermal-Hydraulic-Mechanical Finite Element Model for Saturated, Fractured, Porous Rocks, Journal of Geophysical Research, Vol. 89, No. B12, pp 10365-10373, 1984.
67. Ouyang, S., Carey, G. F. & Yew, C. H., Adaptive Finite Element Scheme for Hydraulic Fracturing with Proppant Transport, International Journal for Numerical Methods in Fluids, Vol. 24, No. 7, 645 - 670, 1997.
68. Papamichos, E., Sand Production and Well Productivity in Conventional Reservoirs, Proceedings of the 37th U.S. Rock Mechanics Symposium. - Rock Mechanics for

-
- Industry., Amadei, B., Kranz, R.L., Scott, G.A. & Smeallie, P.H. (Eds.), Vol. 1, pp 209 - 216, Balkema, Rotterdam, 1999, ISBN 90 5809 052 3.
69. Papanastasiou, P., An Efficient Algorithm for Propagating Fluid-Driven Fractures, Computational Mechanics, Vol. 24, pp 258 - 267, Springer-Verlag, 1999.
70. Papanastasiou, P., Formation Stability After Hydraulic Fracturing, International Journal for Numerical and Analytical Methods in Geomechanics, Vol. 23, pp 1927 - 1944, John Wiley & Sons, 1999.
71. Papanastasiou, P., Influence of Rock Plastic Deformation in Hydraulic Fracturing, Colorado Hydraulic Fracture Workshop, Schlumberger, Cambridge, 1999.
72. Papanastasiou, P., The Effective Fracture Toughness in Hydraulic Fracturing, International Journal of Fracture, Vol. 96, pp 127 - 147, Kluwer Academic Publishers, Netherlands, 1999.
73. Preece, D.S., Jensen, R.P., Perkins, E.D. & Williams, J.R., Sand Production Modeling Using Superquadric Discrete Elements and Coupling of Fluid Flow and Particle Motion, Proceedings of the 37th U.S. Rock Mechanics Symposium. - Rock Mechanics for Industry., Amadei, B., Kranz, R.L., Scott, G.A. & Smeallie, P.H. (Eds.), Vol. 1, pp 161 - 167, Balkema, Rotterdam, 1999, ISBN 90 5809 052 3.
74. Ramakrishnan, S., Budhu, M. & Frantziskonis, G., Deformation and Failure of Granular Media a Lattice Type Model, In: Salami, M. and Banks, D. (Eds.), Proceedings of the First International Forum on Discontinuous Deformation Analysis (DDA) and Simulations of Discontinuous Media, Berkeley, USA, 1996, ISBN 0 9627451 07.
75. Randles, P. W., Libersky, L. D. & Petschek, A. G., On Neighbors, Derivatives and Viscosity in Particle Codes.
76. Rodriguez-Paz, M. X., Bonet, J., Kulasegaram, S. & Lok, T-S. L., Mesh-Free Numerical Simulations of Debris Flow Avalanches, Proceedings of the 8th Annual
-

- Conference of the Association for Computational Mechanics in Engineering, University of Greenwich, 2000.
77. Rothenburg, L. & Selvadurai, A. P. S., A Micromechanical Definition of the Cauchy Stress Tensor for Particulate Media, In: Mechanics of Structured Media, Proceedings of the International Symposium on the Mechanical Behaviour of Structured Media, Selvadurai, A. P. S. (Ed.), Elsevier Scientific, Amsterdam, 1981, ISBN 0 444 41983 7.
78. Rouainia, M., Pearce, C. & Bićanić, N., HYDRO-DDA Modelling of Fractured Mudrock Seals, Fourth International Conference on Analysis of Discontinuous Deformation, Department of Civil Engineering, University of Glasgow, 2001, ISBN 0 85261 735 6.
79. Schlangen, E. & Garboczi, E. J., Fracture Simulations of Concrete Using Lattice Models: Computational Aspects, Engineering Fracture Mechanics, Vol. 57, No. 2/3, pp 319 - 322, Elsevier Science, 1997.
80. Schlangen, E. & van Mier, J. G. M., Crack Propagation in Sandstone: Combined Experimental and Numerical Approach, Rock Mechanics and Rock Engineering, Vol. 28, No. 2, pp 93 - 110, 1995.
81. Schlangen, E. & van Mier, J. G. M., Micromechanical Analysis of Fracture in Concrete, Journal of Damage Mechanics, Vol. 1, pp 435 - 454, 1992.
82. Schlangen, E. & van Mier, J. G. M., Simple Lattice Model for Numerical Simulation of Fracture of Concrete Materials and Structures, Materials and Structures, Vol. 25, pp 534 - 542, 1992.
83. Smooth Particle Hydrodynamics Group at George Mason University (GMU), <<http://www.science.gmu.edu/~jwallin/sph.html>>, (25th July 2002)
-

84. Swenson, D. & Hardeman, B., The Effects of Thermal Deformation on Flow in a jointed Geothermal Reservoir., *International Journal of Rock Mechanics and Mining Science*, Vol. 34, No. 3/4, pp 445, 1997.
85. Thallak, S. G., Holder, J. & Gray, K. E., *Physical Mechanisms of Solids Production*, Center for Earth Sciences and Engineering, University of Texas, Austin, Texas, 1992.
86. Trent, B., The Effect of Micro-Structure on Macroscopic Behaviour of Cemented Granular Material., Thesis LA-11169-T, Los Alamos National Laboratory, New Mexico, 1988.
87. Tzschichholz, F., Peeling Instability in Cosserat - like Media, *Physical Review B*, Vol. 45, No. 22, pp 12691 - 12698, 1992.
88. Tzschichholz, F. & Herrmann, H. J., Simulations of Pressure Fluctuations and Acoustic Emission in Hydraulic Fracturing, *Physical Review E*, Vol. 51, pp 1961 - 1970, 1995.
89. Tzschichholz, F., Herrmann, H. J., Roman, H. E & Pfuff, M., Beam Model for Hydraulic Fracturing, *Physical Review B*, Vol. 49, pp 7056 - 7059, 1994.
90. Unwin, A. T. & Hammond, P. S., Computer Simulations of Proppant Transport in a Hydraulic Fracture, SPE 29649, Society of Petroleum Engineers, circa 1994.
91. Valkó, P. & Economides, M. J., *Hydraulic Fracture Mechanics*, Wiley, Chichester, 1995, ISBN 0 471 95664 3.
92. Vangelsten, B. V., Numerical Simulations of Installation of Skirt Foundations, Doctoral Thesis, Department of Geotechnical Engineering, The Norwegian University of Science and Technology, 1997.

93. Visser J. H. M. & van Mier, J. G. M., Hydraulic Fracturing of Concrete and Rock, Fracture and Damage of Concrete and Rock - FDCR-2, Rossmann H. P. (Ed.), E & FN Spon, 1993, ISBN 0419 18470 8.
94. Visser, J. H. M. & van Mier, J. G. M., The Mechanical Behaviour of Hydraulically Fractured, Possibly Saturated Materials., Fracture Mechanics of Concrete Structures, Proceedings of FRAMCOS-3, AEDIFICATIO, Freiburg.
95. van Vliet, M. R. A., Size Effects in Tensile Fracture of Concrete and Rock, Delft University Press, Delft, The Netherlands, 2000, ISBN 90 407 1994 2.
96. Wilcock, P, Generic Study of Coupled T-H-M Processes in the Near Field (BMT3), Coupled Thermo - Hydro - Mechanical Processes of Fracture Material, Vol. 79, Elsevier Science, 1996.
97. Zhai, E. D., Miyajima, M. & Kitaura, M., DEM Simulation of Rise of Excess Pore Water Pressure of Saturated Sands Under Vertical Ground Motion, Computer Methods and Advances in Geomechanics, Yuan (Ed.), Balkema, Rotterdam, 1997, ISBN 90 5410 904 1.
98. Zhang, R., Mustoe, G. G. W. & Nelson, K. R., Simulation of Hydraulic Phenomena using the Discrete Element Method, Proceedings of the 2nd International Conference on Discrete Element Methods, Williams, J. R. & Mustoe, G. W. (Ed.), Massachusetts Institute of Technology, 1993, ISBN 0 918062 88 8.

Appendix IB:

Bibliography

1. Ameen, M. S. (Editor), *Fractography: fracture topography as a tool in fracture mechanics and stress analysis* (Geological Society Special Publication No. 92), Geological Society, London, 1995, ISBN 1 897799 32 2.
2. Anderson, T. L., *Fracture Mechanics Fundamentals and Applications*, Ed. 2, CRC Press, London, 1995, ISBN 0 8493 8974 7.
3. Atkinson, B. K. (Editor), *Fracture Mechanics of Rock*, Academic Press Inc., London, 1987, ISBN 0 12 066265 5.
4. Blyth, F. G. H. & de Freitas, M. H., *A Geology for Engineers*, 6th Ed., Arnold, Bath, 1974, ISBN 0 7131 2441 5.
5. Brebbia, C. A. & Ferrante, A. J., *Computational Methods for the Solution of Engineering Problems*, 2nd Ed., Pentech Press, Plymouth, 1979.
6. Cafiero, R., Luding, S. & Herrmann, H. J., *Two-Dimensional Granular Gas of Inelastic Spheres with Multiplicative Driving*, *Physical Review Letters*, Vol. 84, No. 26, pp 6014 - 6017, 2000.
7. Committee on Fracture Characterisation & Fluid Flow, *Rock Fractures and Fluid Flow: Contemporary Understanding and Applications*, National Academy, Washington D.C., 1996, ISBN 0 309 04996 2.
8. Cornell Fracture Group (CFG), <<http://www.cfg.cornell.edu/>>, (25th July 2002)

9. Cundall, P. A., Distinct Element Models of Rock and Soil Structure, In: Analytical and Computational Methods in Engineering Rock Mechanics, Brown, E. T. (Ed.), Allen & Unwin, London, 1987, ISBN 0 04 620020 7.
10. D'Addetta, G. A., Kun, F., Herrmann, H. J. & Ramm, E., Application of Discrete Model to Fracture Process of Cohesive Frictional Materials, Continuous and Discontinuous Modelling of Cohesive Frictional Materials Symposium, Stuttgart, 2000.
11. Davie, C. T. and Bićanić, N., Failure Criteria for Quasi Brittle Materials in Lattice Models, Proceedings of 10th Annual Conference of the Association for Computational Mechanics in Engineering, University of Swansea, 2002, ISBN 0 9542544 0 6.
12. Davie, C. T. and Bićanić, N., Progressive Fracturing Using Lattice Models, Proceedings of 9th Annual Conference of the Association for Computational Mechanics in Engineering, University of Birmingham, 2001, ISBN 0 70442 302 2.
13. Davie, C. T. and Bićanić, N., Progressive Fracturing Using Lattice Models, Proceedings of Fourth International Conference on Analysis of Discontinuous Deformation, University of Glasgow, 2001, ISBN 0 85261 735 6.
14. Gramberg, J., A Non-Conventional View on Rock Mechanics and Fracture Mechanics, A. A. Balkema, Rotterdam, 1989, ISBN 90 6191 806 5.
15. Gu, H. & Yew, C. H., Finite Element Solutions of a Boundary Integral Equation for Mode I Embedded 3D Fractures., International Journal for Numerical Methods in Engineering, Vol. 26, pp 1525 - 1540, 1988.
16. Hardeman, B. & Swenson, D., A Geometric Modelling Framework for the Numerical Analysis of Geothermal Reservoirs., Proceedings of the 23rd Workshop on Geothermal Reservoir Engineering, Stanford University, Stanford University, 1998.

17. Herrmann, H. J., Fracture Patterns and Scaling Laws, *Physica A*, Vol. 163, pp 359 - 372, 1990.
18. Herrmann, H., Fractures, In: *Fractals and Disordered Systems.*, Bunde, A & Havlin, S. (Editors), 2nd Ed., Springer, London, 1996, ISBN 3 540 56219 2.
19. Herrmann, H. J. & Kertesz, J., Stability Analysis of Crack Propagation, *Physica A*, Vol. 178, pp 227 - 235, 1991.
20. Hill, R., Elastic Properties of Reinforced Solids: Some Theoretical Principles, *Journal of the Mechanics and Physics of Solids*, Vol. 11, pp 357 - 372, 1963.
21. Hinton, E. (Ed.), *NAFEMS Introduction to Nonlinear Finite Element Analysis.*
22. Hockney, R. W. & Eastwood, J. W., *Computer Simulation Using Particles*, McGraw-Hill, 1981, ISBN 0 07 029108 X.
23. Knoll, J. F., *Fundamentals of Fracture Mechanics.*, Butterworths, London, 1973, ISBN 0 408 70529 9.
24. Kun, F. & Herrmann, H. J., A Study of Fragmentation Processes Using a Discrete Element Method, *Computer Methods in Applied Mechanics and Engineering*, Vol. 138, pp 3 - 18, 1996.
25. Ladanyi, B. & Dague, K. M., Effect of Confinement on the Bursting of Thick-Walled Rock Cylinders Under Internal Pressure., *Proceedings of the 37th U.S. Rock Mechanics Symposium. - Rock Mechanics for Industry.*, Amadei, B., Kranz, R.L., Scott, G.A. & Smeallie, P.H. (Eds.), 1999.
26. Lätzel, M., Luding, S. & Herrmann, H. J., From Discontinuous Models Towards a Continuum Description, *Continuous and Discontinuous Modelling of Cohesive Frictional Materials Symposium*, Stuttgart, 2000.

27. Lee, J. S., Bang, C-S. & Choi, I-Y., Analysis of Borehole Instability Due to Grouting Pressure, Proceedings of the 37th U.S. Rock Mechanics Symposium - Rock Mechanics for Industry, Amadei, B., Kranz, R.L., Scott, G.A. & Smeallie, P.H. (Eds.), Vol. 1, pp 217 - 223, Balkema, Rotterdam, 1999, ISBN 90 5809 052 3.
28. Lewis, R. W. & Masters, I., Modelling of Well Stability in Chalk Reservoirs - Case for Support.
29. Love, A. E. H., A Treatise on the Mathematical Theory of Elasticity, 4th Ed., Dover Publications, New York, 1944.
30. Massey, B. S., Mechanics of Fluids, 3rd Ed., Van Nostrand Reinhold, 1975, ISBN 0 442 30037 5.
31. Morvan, H., Graded Sediment Transport: The use of the Discrete Element Method in Modeling Particle Infiltration and the Segregation Process under the Influence of Vibration., Department of Civil Engineering, University of Glasgow, Glasgow, 1997.
32. Mühlhaus, H.-B. & Oka, F., Dispersion and Wave Propagation in Discrete and Continuous Models for Granular Materials, International Journal of Solids and Structures, Vol. 33, No. 19, pp 2841 - 2858, 1996.
33. Papanastasiou, P. C. & Vardoulakis, I. G., Numerical Analysis of Borehole Stability Problem (Chapter 19) In: Soil-Structure Interaction: Numerical Analysis and Modelling, Bull, J. W. (Ed.), pp 673 - 711, E & FN Spon, 1994.
34. Papanastasiou, P., Cook, J. & Durban, D., Modes of Fracture Initiation in Thick-Walled Cylinder Experiments, Proceedings of the 37th U.S. Rock Mechanics Symposium. - Rock Mechanics for Industry., Amadei, B., Kranz, R.L., Scott, G.A. & Smeallie, P.H. (Eds.), Vol. 1, pp 333 - 340, Balkema, Rotterdam, 1999, ISBN 90 5809 052 3.

35. Papanastasiou, P. & Durban, D., Bifurcation of Elastoplastic Pressure-Sensitive Hollow Cylinders, *Journal of Applied Mechanics*, Vol. 66, pp 117 - 123, ASME, 1999.
36. Rocha, M. & Franciss, F., Determination of Permeability in Anisotropic Rock Masses from Integral Samples, *Rock Mechanics*, Vol. 9, pp 67 - 93, 1977.
37. Stagg, K. G. & Zienkiewicz, O. C. (Eds.), *Rock Mechanics in Engineering Practice*, Wiley, London, 1968, ISBN 471 81965 4.
38. Swenson, D., Hardeman, B., Kilkarni, S. & Liu, T., Modeling Production/Injection Strategies in Fracture-Dominated Geothermal Reservoirs, Quarterly Progress Reports for April - June 1998 to July - September 1999, Mechanical & Nuclear Engineering Department, Kansas State University.
39. Timoshenko, S., *Theory of Elasticity*, McGraw-Hill, New York, 1934.
40. Wang, Y., Shen, S. S. & Cheng, H., Evolution of the Plastic Zone Near a Microfracture: a Numerical Simulation and its Implications on In Situ Stress Measurement, *Canadian Journal Geotechnical*, Vol. 31, No. 5, pp 779 - 787, 1994.
41. Weaver, J., Three dimensional Crack Analysis, *International Journal of Solids and Structures*, Vol. 13, pp 321-330, 1977.

Appendix II:

Granular-Continuum Stress Conversion Factors

This Appendix contains the individual derivations of the four granular-continuum stress conversion factors, $\alpha(x,x)^{G-C}$, $\alpha(x,y)^{G-C}$, $\alpha(y,x)^{G-C}$ and $\alpha(y,y)^{G-C}$, required to convert the components of a granular stress tensor, as developed in the particles of the regular hexagonally packed bonded particle assembly employed by the Particle Solid Model (PSM) (See *Fig. AII.1.* below), to the components of an equivalent continuum stress tensor. The technique applied in this Appendix is taken directly from that described in Section 3.4.2. of Chapter 3.

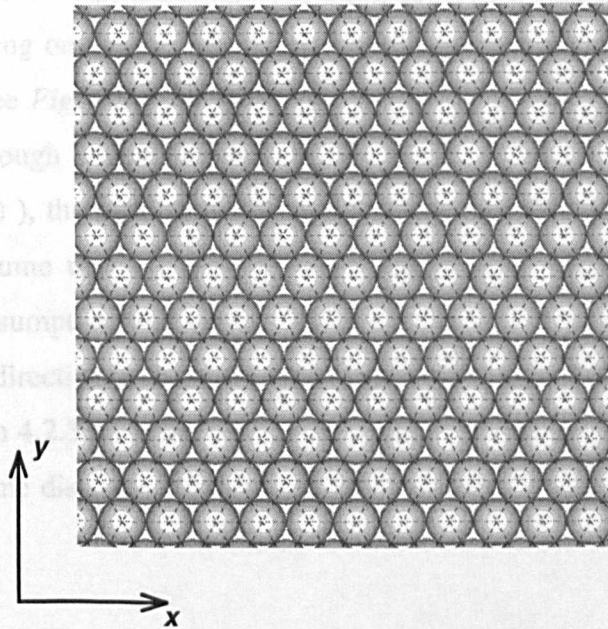


Fig. AII.1. Typical Example of Regular Hexagonally Packed Particle Assembly Employed by the Particle Solid Model

$\alpha_{(x,x)}^{G-C}$:- Conversion Factor for granular stress, σ_{xx}^G , to continuum stress, σ_{xx} .

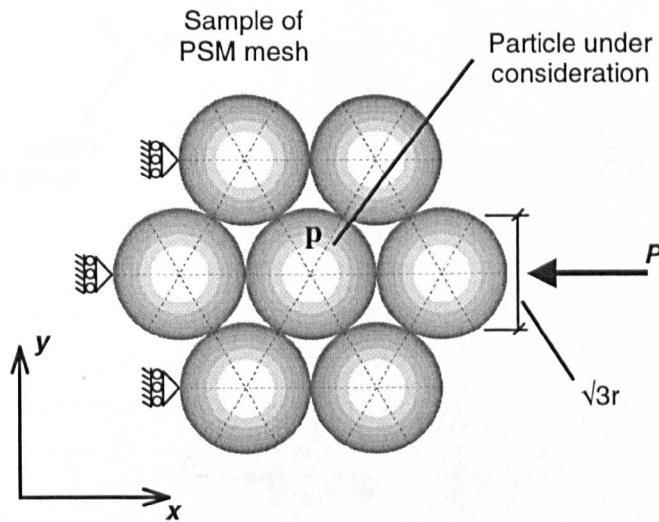


Fig. AII.2. Diagram of Simple Loading Case Considered in Order to Derive Granular - Continuum Conversion Factor for Normal Stress in the x -direction

From examination of the controlled loading case, shown in Fig. AII.2. above, the contact forces acting on the particle 'p', as a result of the external applied load, P , can be determined (See Fig. AII.3. below). It may be noted that, although there are three contact points through which the load, P , applied in the x -direction could be resisted (See Fig. AII.3. a), the lack of confinement in the y -direction suggests that it is most reasonable to assume that the load is transferred directly through the particle. The validity of this assumption was confirmed by observation of a PSM mesh subjected to loading in the x -direction as was the case for the Uniaxial Benchmark Problem (See Chapter 4, Section 4.2.3.2.). The resulting contact forces on a particle at the centre of a PSM mesh, at some distance from the externally applied load, are shown in Fig. AII.3. b).

Hence, from examination of Fig. AII.2. above, the contact forces acting on the particle 'p', as a result of the external applied load, P , can be determined (See Fig. AII.3. below). It may be noted that, although there are three contact points through which the load, P , applied in the x -direction could be resisted (See Fig. AII.3. a), the lack of confinement in the y -direction suggests that it is most reasonable to assume that the load is transferred directly through the particle. The validity of this assumption was confirmed by observation of a PSM mesh subjected to loading in the x -direction as was the case for the Uniaxial Benchmark Problem (See Chapter 4, Section 4.2.3.2.). The resulting contact forces on a particle at the centre of a PSM mesh, at some distance from the externally applied load, are shown in Fig. AII.3. b).

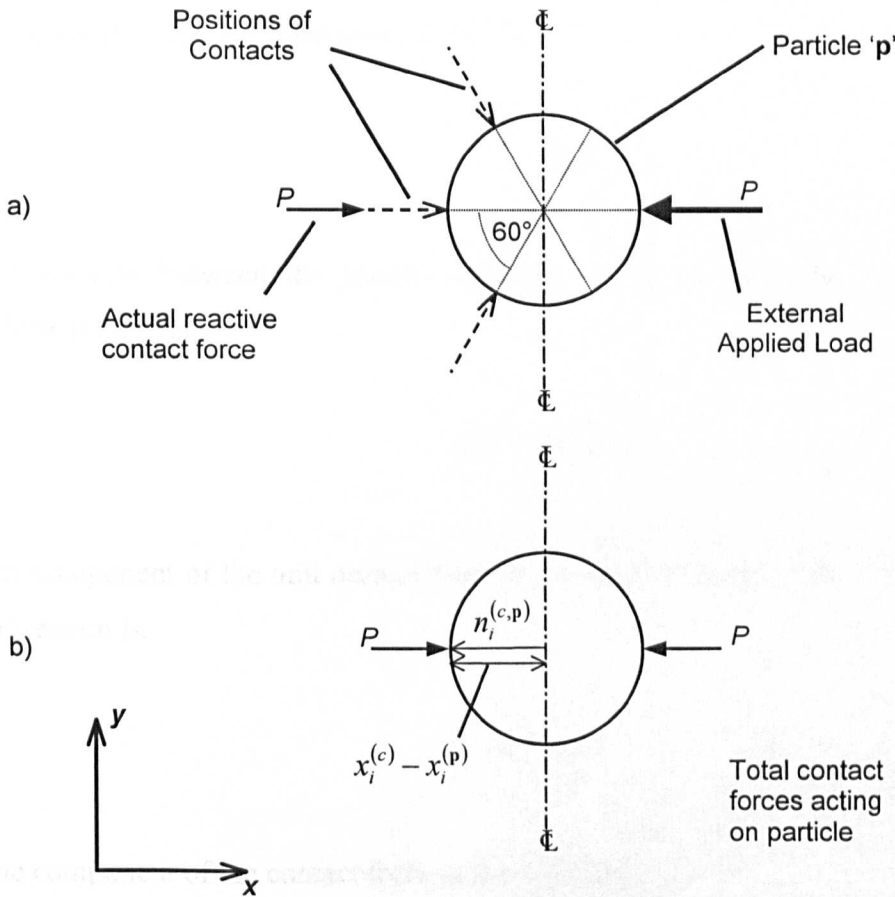


Fig. AII.3. Diagram of Development of Contact Forces on the Particle 'p' Experiencing Normal Stress in the x-direction Showing a) the reaction to external loading and b) the total resulting contact forces on the particle

As derived in Section 3.4.2. of Chapter 3, the granular-continuum stress conversion factor for the σ_{xx} stress component, $\alpha(x, x)^{G-C}$, can be written as shown in Eq. 3.46., (repeated below).

$$\alpha(x, x)^{G-C} = \frac{P_x V^{(p)}}{A_x \sum_{N_c} |x_i^{(c)} - x_i^{(p)}| n_x^{(c,p)} F_x^{(c)}} \tag{Eq. 3.46.}$$

Hence, from examination of Fig. AII.3. it can be seen that the following values can be substituted into Eq. 3.46. in order to calculate the granular continuum stress conversion factor for the normal stress component in the x-direction, $\alpha(x, x)^{G-C}$.

The volume of the spherical particle, 'p', is,

$$V^{(p)} = \frac{4}{3} \pi r^3 \quad \text{Eq. All.1}$$

The distance between the particle centroid and the contact points, assuming small deformations[†], is,

$$|x_i^{(c)} - x_i^{(p)}| \approx r \quad \text{Eq. All.2.}$$

The component of the unit normal from the particle centroid to the contact point, in the x -direction is,

$$n_x = \pm 1 \quad \text{Eq. All.3.}$$

The component of the contact force in the x -direction is,

$$F_x = \pm P \quad \text{Eq. All.4.}$$

The equivalent continuum area associated with the external load acting on a unit thickness continuum, as shown in *Fig. AII.2.*, is,

$$A = \sqrt{3}r.1 \quad \text{Eq. All.5.}$$

Substituting these values into *Eq. 3.46.* for the two contact forces acting on the particle, as shown in *Fig. AII.3. b)*, gives the following solution for the granular-continuum conversion factor for the component of normal stress in the x -direction,

[†] Although the initial distance between the centroid of a particle and a contact on the surface of that particle will be equal to the particle radius, this distance will change when the particle assembly deforms. In order to maintain a constant value for the conversion factor it can be assumed that only small deformations occur and that, consequently, the separation between the particle centroid and the contacts remains approximately equal to the particle radius.

$$\alpha_{(x,x)}^{G-C} = \frac{-P \frac{4}{3} \pi r^3}{\sqrt{3}r \cdot ((r \cdot -1 \cdot P) + (r \cdot 1 \cdot -P))} \quad \text{Eq. All.6.}$$

which simplifies to give,

$$\alpha_{(x,x)}^{G-C} = \frac{2\pi r}{3\sqrt{3}} \quad \text{Eq. All.7.}$$

$\alpha_{(y,y)}^{G-C}$:- Conversion Factor for granular stress, σ_{yy}^G , to continuum stress, σ_{yy} .

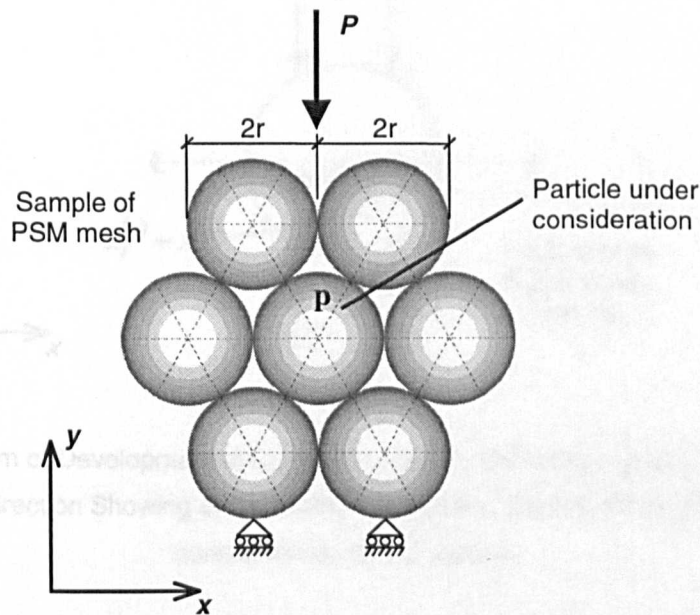


Fig. All.4. Diagram of Simple Loading Case Considered in Order to Derive Granular - Continuum Conversion Factor for Normal Stress in the y-direction

From examination of the controlled loading case, shown in Fig. All.4. above, the contact forces acting on the particle 'p', as a result of the external applied load, P, can be determined (See Fig. All.5. below).

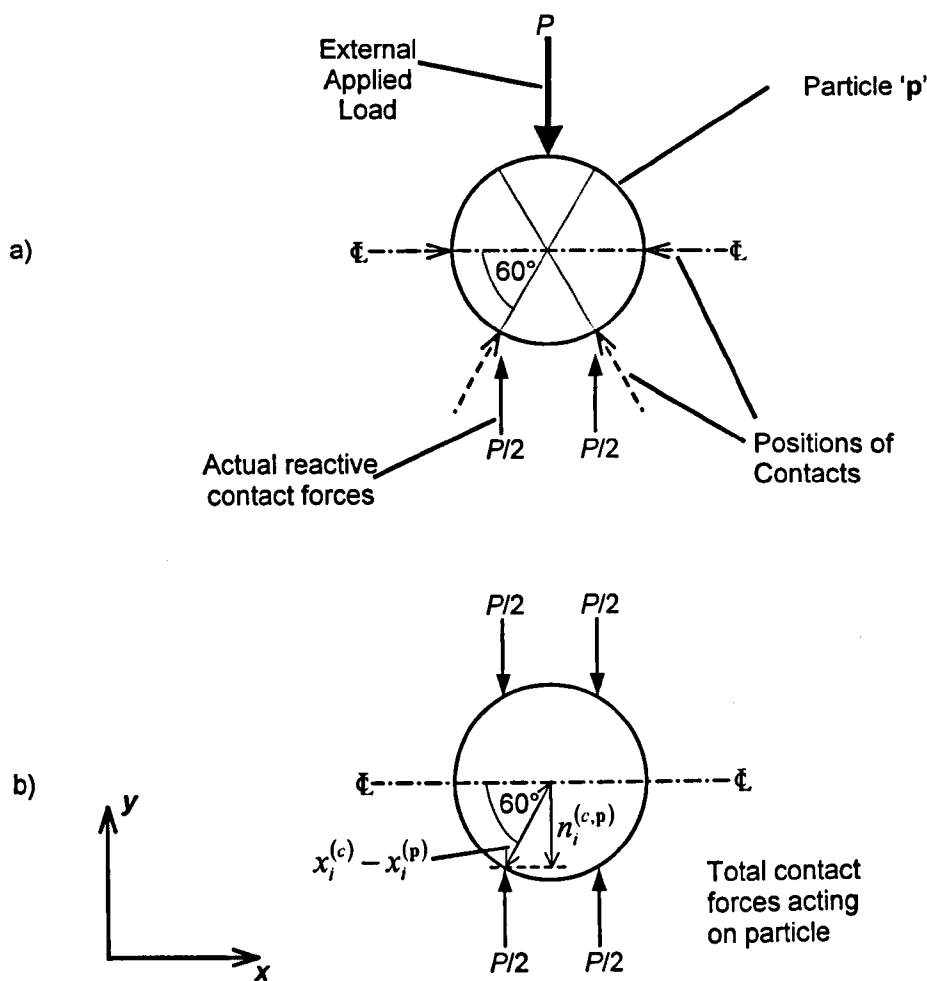


Fig. AII.5. Diagram of Development of Contact Forces on the Particle 'p' Experiencing Normal Stress in the y -direction Showing a) the reaction to external loading and b) the total resulting contact forces on the particle

Although there are four contact points that can be considered to act on one half of the particle two of these contacts are aligned exactly in the x -direction and are assumed not to resist any load in the y -direction (See Fig. AII.5. a)). Therefore, the entire applied load is resisted by the remaining two contact points as shown above. The resulting contact forces on a particle at the centre of a PSM mesh, at some distance from the externally applied load, are shown in Fig. AII.5. b).

In a similar fashion to the equation describing the granular-continuum stress conversion factor for the σ_{xx} stress component (See Eq. 3.46. and Section 3.4.2. of Chapter 3), an equation can be derived for the granular-continuum stress conversion factor for the σ_{yy} stress component, $\alpha_{(y,y)}^{G-C}$ (See Eq. AII.8.).

$$\alpha_{(y,y)}^{G-C} = \frac{P_y V^{(p)}}{A_y \sum_{N_c} |x_i^{(c)} - x_i^{(p)}| n_y^{(c,p)} F_y^{(c)}} \quad \text{Eq. All.8.}$$

From examination of *Fig. All.5.* it can be seen that the following values can be substituted into *Eq. All.8.* in relation to the calculation of the granular continuum stress conversion factor for the normal stress component in the *y*-direction, $\alpha_{(y,y)}^{G-C}$.

The volume of the spherical particle, 'p', is,

$$V^{(p)} = \frac{4}{3} \pi r^3 \quad \text{Eq. All.9.}$$

The distance between the particle centroid and the contact points, assuming small deformations (See † on page 403), is,

$$|x_i^{(c)} - x_i^{(p)}| \approx r \quad \text{Eq. All.10.}$$

The component of the unit normal from the particle centroid to the contact point, in the *y*-direction is,

$$n_y = \pm \frac{\sqrt{3}}{2} \quad \text{Eq. All.11.}$$

The component of the contact force in the *y*-direction is,

$$F_y = \pm \frac{P}{2} \quad \text{Eq. All.12.}$$

The equivalent continuum area associated with the external load acting on a unit thickness continuum, as shown in *Fig. All.4.*, is,

$$A = 2r.1 \quad \text{Eq. All.13.}$$

Substituting these values into Eq. AII.8. for the four contact forces acting on the particle, as shown in Fig. AII.5. b), gives the following solution for the granular-continuum conversion factor for the component of normal stress in the y-direction,

$$\alpha_{(y,y)}^{G-C} = \frac{-P \frac{4}{3} \pi r^3}{2r \left(\left(r \cdot \frac{\sqrt{3}}{2} \cdot -\frac{P}{2} \right) + \left(r \cdot \frac{\sqrt{3}}{2} \cdot -\frac{P}{2} \right) + \left(r \cdot -\frac{\sqrt{3}}{2} \cdot \frac{P}{2} \right) + \left(r \cdot -\frac{\sqrt{3}}{2} \cdot \frac{P}{2} \right) \right)} \quad \text{Eq. AII.14.}$$

which simplifies to give,

$$\alpha_{(y,y)}^{G-C} = \frac{2\pi r}{3\sqrt{3}} \quad \text{Eq. AII.15.}$$

$\alpha_{(y,x)}^{G-C}$:- Conversion Factor for granular stress, σ_{yx}^G , to continuum stress, σ_{yx} .

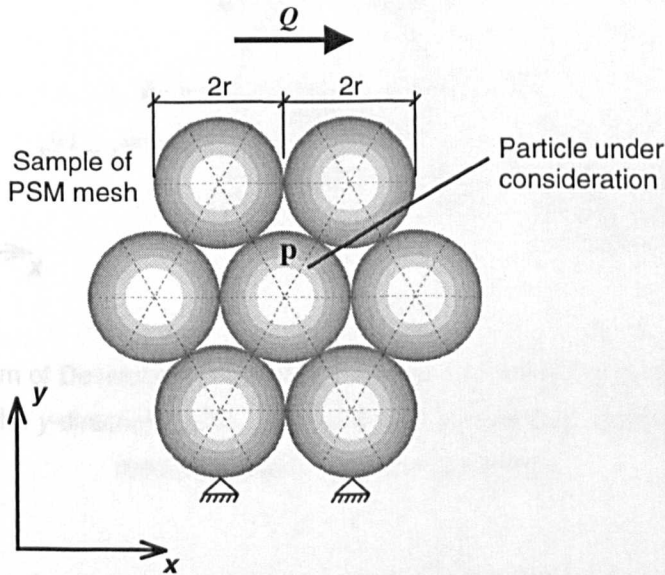


Fig. AII.6. Diagram of Simple Loading Case Considered in Order to Derive Granular - Continuum Conversion Factor for Shear Stress across the y-direction

From examination of the controlled loading case, shown in *Fig. AII.6.* above, the contact forces acting on the particle 'p', as a result of the external applied load, Q , can be determined (See *Fig. AII.7.* below).

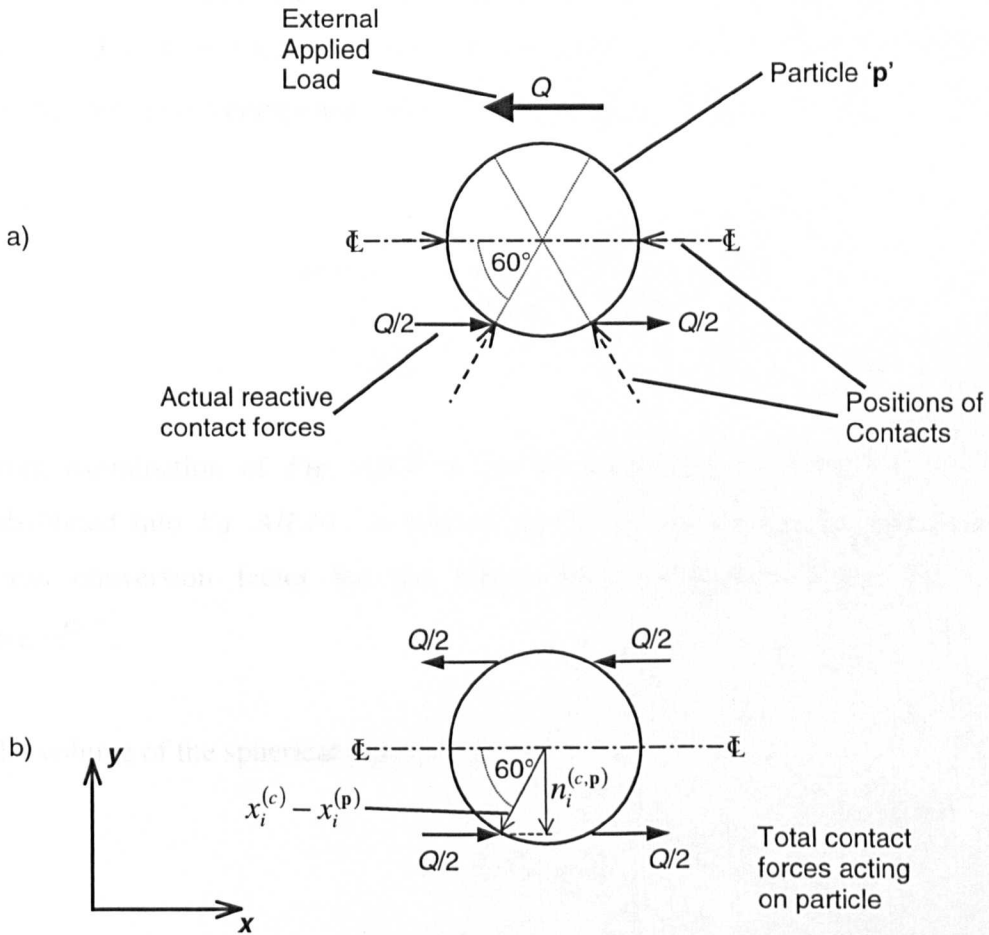


Fig. AII.7. Diagram of Development of Contact Forces on the Particle 'p' Experiencing Shear Stress across the y -direction Showing a) the reaction to external loading and b) the total resulting contact forces on the particle

Although there are four contact points that can be considered to act on one half of the particle two of these contacts are aligned exactly in the x -direction and are assumed to experience no displacement relative to their neighbouring particles. Consequently, they will not develop contact forces under the shear loading conditions applied in the controlled loading case shown in *Fig. AII.6.* The validity of this assumption was confirmed by observation of a PSM mesh subjected to shear loading conditions. The

resulting contact forces on a particle at the centre of a PSM mesh, at some distance from the externally applied load, are shown in *Fig. AII.7. b*).

An equation similar to those derived for the granular-continuum stress conversion factors for the normal components of the stress tensor (See *Eq. 3.46. & Eq. AII.8.* and Section 3.4.2. of Chapter 3), can be developed for the conversion factor for the σ_{yx} shear stress component, $\alpha_{(y,x)}^{G-C}$ (See *Eq. AII.16.*).

$$\alpha_{(y,x)}^{G-C} = \frac{QV^{(p)}}{A_y \sum_{N_c} |x_i^{(c)} - x_i^{(p)}| n_y^{(c,p)} F_x^{(c)}} \quad \text{Eq. AII.16.}$$

From examination of *Fig. AII.7.* it can be seen that the following values can be substituted into *Eq. AII.16.* in relation to the calculation of the granular continuum stress conversion factor for the shear stress component across the y-direction, $\alpha_{(y,x)}^{G-C}$.

The volume of the spherical particle, 'p', is,

$$V^{(p)} = \frac{4}{3} \pi r^3 \quad \text{Eq. AII.17.}$$

The distance between the particle centroid and the contact points, assuming small deformations (See [†] on page 403), is,

$$|x_i^{(c)} - x_i^{(p)}| \approx r \quad \text{Eq. AII.18.}$$

The component of the unit normal from the particle centroid to the contact point, in the y-direction is,

$$n_y = \pm \frac{\sqrt{3}}{2} \quad \text{Eq. AII.19.}$$

The component of the contact force in the x -direction is,

$$F_x = \pm \frac{Q}{2} \quad \text{Eq. AII.20.}$$

The equivalent continuum area associated with the external load acting on a unit thickness continuum, as shown in *Fig. AII.6.*, is,

$$A = 2r.1 \quad \text{Eq. AII.21.}$$

Substituting these values into *Eq. AII.16.* for the four contact forces acting on the particle, as shown in *Fig. AII.7. b)*, gives the following solution for the granular-continuum conversion factor for the component of shear stress across the y -direction,

$$\alpha_{(y,x)}^{G-C} = \frac{-Q \frac{4}{3} \pi r^3}{2r \left(\left(r \cdot \frac{\sqrt{3}}{2} - \frac{Q}{2} \right) + \left(r \cdot \frac{\sqrt{3}}{2} - \frac{Q}{2} \right) + \left(r - \frac{\sqrt{3}}{2} \cdot \frac{Q}{2} \right) + \left(r - \frac{\sqrt{3}}{2} \cdot \frac{Q}{2} \right) \right)} \quad \text{Eq. AII.22.}$$

which simplifies to give,

$$\alpha_{(y,x)}^{G-C} = \frac{2\pi r}{3\sqrt{3}} \quad \text{Eq. AII.23.}$$

$\alpha_{(x,y)}^{G-C}$:- Conversion Factor for granular stress, σ_{xy}^{G-C} , to continuum stress, σ_{xy} .

Given that the shear components of the granular stress tensors computed by PFC^{3D} are equal, such that $\sigma_{yx}^G = \sigma_{xy}^G$, it may be assumed that the granular-continuum stress conversion factors for the shear stress components are also equal, such that $\alpha_{(y,x)}^{G-C} = \alpha_{(x,y)}^{G-C}$. However, this may be confirmed numerically by considering equilibrium conditions for a particle under shear loading conditions (See *Fig. AII.8.* below).

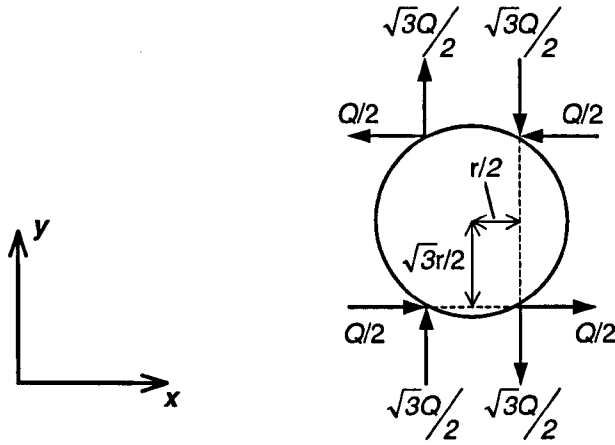


Fig. AII.8. Diagram Showing Equilibrium Conditions for Particle under Shear Loading
Conditions as Shown in Fig. AII.7. b)

In order for equilibrium conditions to exist for a particle subjected to the horizontal contact forces developed under the applied shear load, Q , as described in Fig. AII.7., a corresponding set of vertical contact force couples are indicated. Due to the difference in the length of the vertical and horizontal lever arms, measured between the particle centroid and the positions of the contacts, the vertical contact forces must have a value $\sqrt{3}$ times those of the horizontal contact forces (See Fig. AII.8. above).

The procedure used to derive the granular-continuum stress conversion factor, $\alpha(y, x)^{G-C}$, can then be applied to the derivation of the conversion factor $\alpha(x, y)^{G-C}$. From Eq. AII.16. it follows that a similar equation can be written for $\alpha(x, y)^{G-C}$ as shown below.

$$\alpha(x, y)^{G-C} = \frac{QV^{(p)}}{A_x \sum_{N_c} |x_i^{(c)} - x_i^{(p)}| n_x^{(c,p)} F_y^{(c)}} \quad \text{Eq. AII.24.}$$

From examination of Fig. AII.7. and Fig. AII.8. it can be seen that the component of the unit normal from the particle centroid to the contact point, in the x -direction is,

$$n_x = \pm \frac{1}{2} \quad \text{Eq. AII.25.}$$

It can further be seen that the component of the contact force in the y-direction is,

$$F_y = \pm \frac{\sqrt{3}Q}{2} \quad \text{Eq. AII.26.}$$

With the exception of these, the values of the variables applicable in the calculation of the conversion factor $\alpha_{(x,y)}^{G-C}$ (See Eq. AII.24.) are the same as those applicable to the calculation of $\alpha_{(y,x)}^{G-C}$ (See Eq. AII.16. to Eq. AII.21.). Substituting into Eq. AII.24. for the four vertical contact forces, as shown in Fig. AII.8., gives the following solution for the granular-continuum conversion factor for the component of shear stress across the x-direction,

$$\alpha_{(x,y)}^{G-C} = \frac{-Q \frac{4}{3} \pi r^3}{2r \left(\left(r - \frac{1}{2} \cdot \frac{\sqrt{3}Q}{2} \right) + \left(r - \frac{1}{2} \cdot \frac{\sqrt{3}Q}{2} \right) + \left(r - \frac{1}{2} \cdot \frac{\sqrt{3}Q}{2} \right) + \left(r - \frac{1}{2} \cdot \frac{\sqrt{3}Q}{2} \right) \right)} \quad \text{Eq. AII.27.}$$

which simplifies to give,

$$\alpha_{(x,y)}^{G-C} = \frac{2\pi r}{3\sqrt{3}} \quad \text{Eq. AII.28.}$$

Appendix III:

FISH Code

AIII.1. Introduction

This Appendix contains routines written in *FISH* code with the purpose of supplementing the behaviour of the distinct element method applied in PFC^{3D} in order to implement fluid behaviour with the PFM (See Chapter 4, Section 4.3.) and the failure criteria for the PSM (See Chapter 5). The codes are presented in full and comments are shown in bold type. Where it was felt appropriate further information has been given concerning the User Defined Variables and User Defined Functions in the Glossaries at the beginning of the Chapter. It may be noted that many more, smaller routines were developed in *FISH* for the purposes of creating the models, collating data and processing results, some of which are referred to in the following. However, the precise details of those routines were not considered critical to the work carried for this thesis and it was thus felt unnecessary to list them here.

AIII.2. Glossary of User Defined Variables

<code>bondarea</code>	the apparent cross-sectional area of the inter-particle link elements derived from the equations of normal stiffness for the link elements and employed in the redistribution of stresses as forces (See Chapter 5, Section 5.7.1.).
<code>broken_bonds</code>	simple total of number of link elements removed from the PSM mesh through any of the failure criteria.
<code>cst</code>	used to store the variation in strength of an element from the mean value when random elements strengths were employed. The actual

	strength of the PFC ^{3D} 'contact bond' was set unbreakably high (1×10^{21} N) and assigned a random variation of plus or minus 1×10^{20} N. The size of the variation was then interpreted in the FISH code as the variation from the mean material strength, f_t , up to a maximum percentage variation defined with the variable <code>maxmin</code> .
<code>dragfor</code>	the coefficient of drag required for the PFM (See Chapter 4, Section 4.3.2.).
<code>dsigma</code>	the excess or relaxation stress (See Chapter 5, Section 5.7.1.).
<code>dwght</code>	weighting function used to resolve problems with drag forces in interactions between PSM and PFM particles (See Chapter 4, Section 4.4.1.).
<code>elamax</code>	maximum elastic strain in and inter-particle link element.
<code>eps</code>	measured uniaxial strain in an inter-particle link element.
<code>fracend1</code>	model specific identifier for particle at the junction of the mesh boundary and a fracture wall.
<code>fracendpresup</code>	force representative of fracture fluid pressure applied to particle at the junction of the mesh boundary and a fracture wall.
<code>fracpresdown</code>	force representative of fracture fluid pressure applied to particles in a fracture wall (opposite to <code>fracpresup</code>).
<code>fracpresup</code>	force representative of fracture fluid pressure applied to particles in a fracture wall (opposite to <code>fracpresdown</code>).
<code>ft</code>	predefined mean material strength.
<code>Gsubf</code>	predefined fracture energy release rate.

marker1id, marker2id	element specific identifiers for Marker particles delineating diamond shaped equivalent continuum areas considered by Mark 4 and Mark 5 failure criteria. During execution of the failure criteria, these identity numbers are read from tables constructed by a separate <i>FISH</i> routine prior to the running the fracture analysis.
maxmin	maximum percentage variation of material strength above and below mean value. Used in conjunction with <i>cost</i> .
poissons	predefined Poisson's ratio of equivalent continuum material.
radinfdrag	radius of influence of drag required for the PFM (See Chapter 4, Section 4.3.2.).
radinfrep	radius of influence of repulsion required for the PFM (See Chapter 4, Section 4.3.2.).
radius	PSM particle radius used in construction of PSM mesh and determination of uniaxial strains.
repfor	the coefficient of repulsion required for the PFM (See Chapter 4, Section 4.3.2.).
stresscoeff	granular-continuum stress conversion factors (See Chapter 3, Section 3.4.3., Chapter 4, Section 4.2.3.2.2. and Chapter 5, Section 5.6.1.).
ubond	measured length of an inter-particle link element.
upstrmpres	force representing external fluid pressure acting in PFM. The magnitude of this force is calculated by the separate <i>FISH</i> routine <i>updownpresfield</i> .
youngs	predefined Young's Modulus of equivalent continuum material.

AIII.3. Glossary of User Defined Functions

- fracshape** function used to determine and record the positions of the particles in the wall of a fracture so that fracture width profiles can be plotted (See Chapter 6, Section 6.2.3.).
- fracsurface** function that flags particles making up walls of fracture during crack propagation so that the appropriate fluid pressure forces can be applied in subsequent time steps.
- fractime** simple function to determine and record the model time at which a fracture propagation event occurs.
- rosette_solver** function used to analytically solve simultaneous equations in order to calculate normal and shear stresses in terms of the global coordinate system from simple uniaxial strains equivalent to strain gauge measurements (See Chapter 5, Section 5.8.1.). The function makes use of the variables `straina`, `strainb`, `strainc`, `anglea`, `angleb` and `anglec`.
- updownpresfield** function used to calculate the force to applied to a PFM particle in order to represent a predefined external fluid pressure.

hard· ware (*hård'wâr'*) The physical, touchable, material parts of a computer or other system.

<<http://www.dictionary.com>> (25th June 2002)

soft· ware (*sôft'wâr', sôft'-*) The stuff you can only swear at!

Bitter experience

AIII.4. Particle Fluid Model Code

```

def attractrepulse
  repfor = 1e4
  dragfor = 1e3
  radinfdrag = 2.2
  radinfrep = 1.5
  radinfdrag2 = (radinfdrag * radinfdrag)
  radinfrep2 = (radinfrep * radinfrep)
  updownpresfield
; ===== MAIN PARTICLE LOOP =====
bp1 = ball_head ;                loop over all particles
loop while bp1 # null ;
  bid1 = b_id(bp1) ;                determine particle identity
  if b_ex(bp1) = 1 ;                checks if particle is 'fluid' particle
    bx1 = b_x(bp1) ;                determine particle location
    by1 = b_y(bp1) ;
    bxv1 = b_xvel(bp1) ;            determine particle velocity
    byv1 = b_yvel(bp1) ;
    xdrag = 0.0 ;                    reset all applied forces to zero
    ydrag = 0.0
    xrep = 0.0
    yrep = 0.0
    xwdrag = 0.0
    ywdrag = 0.0
    xwrep = 0.0
    ywrep = 0.0
; ===== NESTED PARTICLE LOOP =====
  dwght = 0 ;                        reset weighting function
  bp2 = ball_head ;                loop over all particles
  loop while bp2 # null
    bid2 = b_id(bp2) ;                determine particle identity
    section
    if b_ex(bp2) = 0 ;                checks if particle is 'fluid' particle
      exit section
    else
      endif
    if bid1 > 19999 ; check if particles are both 'solid' particles
      if bid2 > 19999 ;                NB particle id numbers model specific
        exit section ;
      else
        endif
    else
      endif
    if bid1 = bid2
      exit section
    else
      endif

```

```

bx2 = b_x(bp2) ; determine 2nd particle location
by2 = b_y(bp2)
bxv2 = b_xvel(bp2) ; determine 2nd particle velocity
byv2 = b_yvel(bp2)
; determine separation between particles and rejects
; particle outwith radius of influence of repulsion
xdist = bx2 - bx1
modxdist = abs(xdist)
if modxdist < radinfrep
  ydist = by2 - by1
  modydist = abs(ydist)
  if modydist < radinfrep
    resdist = ((modxdist*modxdist) + (modydist*modydist))
    if resdist < radinfrep2
; determines repulsive force acting between particles
    repulsive = (-1.0*repfor)/resdist
; determine and sum components of repulsive force in global x and y
    if xdist = 0.0
      xdist = 0.00000001
    else
      endif
    if xdist < 0 then
      repangle = atan(ydist/xdist) + (pi)
    else
      repangle = atan(ydist/xdist)
    endif
    xrep = xrep + (repulsive * cos(repangle))
    yrep = yrep + (repulsive * sin(repangle))
  else
    endif
  else
    endif
else
  endif
endif
; determine separation between particles and rejects
; particle outwith radius of influence of drag
if modxdist < radinfdrag
  ydist = by2 - by1
  modydist = abs(ydist)
  if modydist < radinfdrag
    resdist = ((modxdist*modxdist) + (modydist*modydist))
    if resdist # 0.0
      if resdist < radinfdrag2
; determine relative velocity of particles
        relxvel = bxv1 - bxv2
        relyvel = byv1 - byv2
        trelvel2 = ((relxvel * relxvel) + (relyvel * relyvel))
        if bxv2 > -15/tdel
; determines drag force acting between particles

```

```

        drag = (-1.0*dragfor*trelvel2)/resdist
;   determine and sum components of drag force in global x and y
        if relxvel = 0.0
            relxvel = 0.00000001
        else
            endif
        if relxvel < 0 then
            dragangle = atan(relyvel/relxvel) + (pi)
        else
            dragangle = atan(relyvel/relxvel)
        endif
        xdrag = xdrag + (drag * cos(dragangle))
        ydrag = ydrag + (drag * sin(dragangle))
        dwght = dwght + 1
    else
        endif
    else
        endif
    else
        endif
    else
        endif
endsection
bp2 = b_next(bp2)
endloop
;===== NESTED WALL LOOP ===
if bx1 < 0.0 ;                               model specific
wp3 = wall_head ;                             loop over all walls
loop while wp3 # null
    wx3 = b_x(wp3) ;                           determine wall location
    wy3 = b_y(wp3)
    wxv3 = b_xvel(wp3) ;                       determine wall velocity
    wyv3 = b_yvel(wp3)
;   determine x separation between particle and wall and rejects
;   particle outwith radius of influence of repulsion
    wxdist = wx3 - bx1
    modwxdist = abs(wxdist)
    if modwxdist # 0
        if modwxdist < radinfrep
;   determine and sum x component of repulsive
;   force acting between particle and wall
            wxrepulsive = ((-1.0 * repfor) / (modwxdist * modwxdist))
            if wxdist < 0 then
                modifier = -1.0
            else
                modifier = 1.0
            endif

```

```

    xwrep = xwrep + (modifier * wxrepulsive)
  else
  endif
else
endif
;   determine y separation between particle and wall and rejects
;   particle outwith radius of influence of repulsion
wydist = wy3 - by1
modwydist = abs(wydist)
if modwydist # 0
  if modwydist < radinfrep
;   determine and sum y component of repulsive
;   force acting between particles and wall
wyrepulsive = ((-1.0 * repfor) / (modwydist * modwydist))
if wydist < 0 then
  modifier = -1.0
else
  modifier = 1.0
endif
ywrep = ywrep + (modifier * wyrepulsive)
else
endif
else
endif
;   determine x relative velocity of particle and wall and
;   rejects particle outwith radius of influence of drag
if modwxdist < radinfdrag
;   determine relative velocity of particle and wall

relwxvel = bxv1 - wxv3
relwyvel = byv1 - wyv3
trelwvelx2 = ((relwxvel * relwxvel) + (relwyvel * relwyvel))
;   determine and sum components of drag force in global x and y
wdragx = (-1.0*dragfor*trelwvelx2)/(modwxdist*modwxdist)
if relwxvel = 0.0
  relwxvel = 0.00000001
else
endif
if relwxvel < 0 then
  wdragangle = atan(relwyvel/relwxvel) + (pi)
else
  wdragangle = atan(relwyvel/relwxvel)
endif
xwdrag = xwdrag + (wdragx * cos(wdragangle))
ywdrag = ywdrag + (wdragx * sin(wdragangle))
else
endif
;   determine y separation between particle and wall and
;   rejects particles outwith radius of influence of drag

```

```

modwydist = abs(wydist)
if modwydist < radinfdrag
;           determine relative velocity of particle and wall
relwxvel = bxv1 - wxv3
relwyvel = byv1 - wyv3
trelwvely2 = ((relwxvel * relwxvel) + (relwyvel * relwyvel))
;           determine and sum components of drag force in global x and y
wdragy = (-1.0*dragfor*trelwvely2)/(modwydist*modwydist)
if relwxvel = 0.0
relwxvel = 0.00000001
else
endif
if relwxvel < 0 then
wdragangle = atan(relwyvel/relwxvel) + (pi)
else
wdragangle = atan(relwyvel/relwxvel)
endif
xwdrag = xwdrag + (wdragy * cos(wdragangle))
ywdrag = ywdrag + (wdragy * sin(wdragangle))
else
endif
wp3 = b_next(wp3)
endloop
else
endif
; ===== END OF NESTED LOOPS =====
if b_x(bp1) < 0.0 ;           application of upstream fluid pressure
if bid1 < 20000 ;           NB model specific parameters
upstrm = upstrmpres
else
endif
else
upstrm = 0
endif
if b_x(bp1) > 50.0 ;           application of downstream fluid pressure
if bid1 < 20000 ;           NB model specific parameters
dwnstrm = downstrmpres
else
endif
else
upstrm = 0
endif
if dwght = 0
dwght = 1
else
endif
;           application of totalled repulsion and drag forces
b_xfap(bp1)=(xdrag/dwght)+xrep+upstrm+dwnstrm+xwdrag+xwrep
b_yfap(bp1)=(ydrag/dwght)+yrep+ywrep+ywdrag

```

```

    else
    endif
    bp1 = b_next(bp1)
  endloop
end

```

AIII.5. Mark 1 Failure Criterion

```

def uniaxial_B
  maxmin = 0.05
  laststepsmax = 0.0
  rbmin = 1000
  rb = contact_head ;           loop over all inter-particle contacts
  loop while rb # null
  section
  if c_bflag(rb) = 1 ;           check if link exists at contact
    cb1 = c_ball1(rb) ;         determine particle locations
    cb2 = c_ball2(rb)
    cb1id = b_id(cb1)
    cb2id = b_id(cb2)
    cb1x = b_x(cb1)
    cb1y = b_y(cb1)
    cb2x = b_x(cb2)
    cb2y = b_y(cb2)
                                ; determine variation of element strength
    cst = (((c_nstrength(rb)/1e20)-10)*maxmin*ft)
    ubond=(sqrt(((cb2x-cb1x)^2)+((cb2y-cb1y)^2))) ; element length
    eps = (ubond - (2*radius))/(2*radius) ; uniaxial element strain
    elasmx = (ft+cst)/(youngs*1e6) ; element ultimate strain
    if eps < elasmx ;           check if element strain less than ultimate
      exit section
    else
    endif
    if eps > elasmx ;           check if element strain greater than
      if eps > laststepsmax ;   previous maximum
        laststepsmax = eps ;     record new 'worst case' strain
        rbmin = rb ;             record new 'worst case' element
      else
      endif
    else
    endif
  else
  endif
  endsection
  rb = c_next(rb)
endloop

```

```

if type(rbmin) = 4
  cpmin = rbmin
  c_bflag(cpmin) = 0 ; delete 'worst case' element
  broken_bonds = broken_bonds + 1
  fracshape
  fractime
  fracsurface
else
endif
end

```

AIII.6. Mark 2 Failure Criterion

```

def rankine_C2
  maxmin = 0.05
  strdiff = 0.0
  rbmin = 1000
  minsepangle = 1000
  rb = contact_head ; loop over all inter-particle contacts

  loop while rb # null
  section
  if c_bflag(rb) = 1 ; check if link exists at contact
    cb1 = c_ball1(rb) ; determine particle identities
    cb2 = c_ball2(rb)
    cb1id = b_id(cb1)
    cb2id = b_id(cb2)
  ; determine equivalent continuum stress tensors
  ; in contact particle pair

  cb1sp = b_stress(cb1) ;
  cb1sp11 = cb1sp ;
  cb1sp12 = cb1sp + 1
  cb1sp21 = cb1sp + 3
  cb1sp22 = cb1sp + 4
  cb1s11 = mem(cb1sp11) * stresscoeff ; 1st particle stress tensor
  cb1s12 = mem(cb1sp12) * stresscoeff
  cb1s21 = mem(cb1sp21) * stresscoeff
  cb1s22 = mem(cb1sp22) * stresscoeff
  cb2sp = b_stress(cb2)
  cb2sp11 = cb2sp
  cb2sp12 = cb2sp + 1
  cb2sp21 = cb2sp + 3
  cb2sp22 = cb2sp + 4
  cb2s11 = mem(cb2sp11) * stresscoeff ; 2nd particle stress tensor
  cb2s12 = mem(cb2sp12) * stresscoeff
  cb2s21 = mem(cb2sp21) * stresscoeff

```

```

cb2s22 = mem(cb2sp22) * stresscoeff

; ----- ALTERNATIVE METHOD 1
;           Principal Stress in Element from Average of
;           Principal Stresses in Particles
;           determine principal stresses from particle stress tensors
cb1smax=(((cb1s11+cb1s22)/2)+(sqrt((((cb1s11-cb1s22)/2)^2)+
(cb1s12^2))))
cb2smax=(((cb2s11+cb2s22)/2)+(sqrt((((cb2s11-cb2s22)/2)^2)+
(cb2s12^2))))
if cb1smax < (ft - (maxmin * ft)) ;           check if failure
if cb2smax < (ft - (maxmin * ft)) ;           conditions probable
  exit section
else
endif
else
endif

;           ; average of max principal stresses in particles
avsmax = (cb1smax + cb2smax)/2
;           ; determine variation of element strength
cst = (((c_nstrength(rb)/1e20)-10)*maxmin*ft)
if avsmax < (ft + cst) ;           check if average maximum principal
  exit section ;           stress greater than element strength
else ;           NOTE: DISALLOWS COMPRESSION FAILURE
endif

;           ; calculate directions of maximum
;           ; principal stresses in particles
if cb1s11 = cb1s22 then
  theta1 = (45*degrad) ;
else
  theta1 = (atan(((2*cb1s12)/(cb1s11-cb1s22))))/2
endif
tta21 = 2 * theta1
cb1sx=(((cb1s11+cb1s22)/2)+(((cb1s11-cb1s22)/2)*cos(tta21))+
(cb1s12*sin(tta21))
cb1sy=(((cb1s11+cb1s22)/2)-(((cb1s11-cb1s22)/2)*cos(tta21))-
(cb1s12*sin(tta21))
if cb1smax = cb1sx then
  smaxangle1 = theta1
else
  if cb1smax = cb1sy then
    smaxangle1 = theta1 + (90*degrad)
  else
  endif
endif
if cb2s11 = cb2s22 then
  theta2 = (45*degrad)
else
  theta2 = (atan(((2*cb2s12)/(cb2s11-cb2s22))))/2

```

```

endif
tta22 = 2 * theta2
cb2sx=((cb2s11+cb2s22)/2)+(((cb2s11-cb2s22)/2)*cos(tta22))+
(cb2s12*sin(tta22))
cb2sy=((cb2s11+cb2s22)/2)-(((cb2s11-cb2s22)/2)*cos(tta22))-
(cb2s12*sin(tta22))
if cb2smax = cb2sx then
  smaxangle2 = theta2
else
  if cb2smax = cb2sy then
    smaxangle2 = theta2 + (90*degrad)
  else
    endif
endif
;       average direction of maximum principal stresses in particles
avsmaxangle = (smaxangle1 + smaxangle2)/2

; ----- ALTERNATIVE METHOD 2
;
;       Principal Stress in Element from Average
;
;       Stress Tensor in Element
;
;       calculate averaged equivalent continuum stress tensor in element
avs11 = ((cb1s11+cb2s11)/2) * stresscoeff
avs12 = ((cb1s12+cb2s12)/2) * stresscoeff
avs21 = ((cb1s21+cb2s21)/2) * stresscoeff
avs22 = ((cb1s22+cb2s22)/2) * stresscoeff
; calculate maximum principal stress in element from averaged tensor
avsmax=(((avs11+avs22)/2)+(sqrt((((avs11-avs22)/2)^2+ (avs12^2))))
; determine variation of element strength
cst = (((c_nstrength(rb)/1e20 )-10)*maxmin*ft)
if avsmax < (ft + cst) ;       check if average maximum principal
  if avsmin < (ft + cst) ;       stress greater than element strength
    exit section ;       NOTE: DISALLOWS COMPRESSION FAILURE
  else
    endif
else
  endif
if avs11 = avs22 then;       calculate direction of maximum
  theta = (45*degrad) ;       principal stress in element
else
  theta = (atan(((2*avs12)/(avs11-avs22))))/2
endif
tta21 = 2 * theta
avsx=(((avs11+avs22)/2)+(((avs11-avs22)/2)*cos(tta21))+
(avs12*sin(tta21))
avsy=(((avs11+avs22)/2)-(((avs11-avs22)/2)*cos(tta21))-
(avs12*sin(tta21))
if avsmax = avsx then
  avsmaxangle = theta
else

```

```

    if avsmax = avsy then
        avsmaxangle = theta + (90*degrad)
    else
        endif
    endif
; =====

    cb1x = b_x(cb1) ; determine particle locations
    cb1y = b_y(cb1)
    cb2x = b_x(cb2)
    cb2y = b_y(cb2)
    if cb2x = cb1x ; determine orientation of element
        bondangle = (90*degrad)
    else
        bondangle = atan((cb2y-cb1y)/(cb2x-cb1x))
    endif
; determine angle of separation between direction of average
; maximum principal stresses and element orientation
    rotangle = abs(avsmaxangle - bondangle)
    if rotangle > (pi/2)
        sepangle = pi - rotangle
    else
        sepangle = rotangle
    endif
    if sepangle < minsepangle ; check if angle of separation
        minsepangle = sepangle ; less than previous 'worst case'
        newstrdiff = (avsmax - (-1.0*(ft + cst)))/(-1.0*(ft + cst))
        strdiff = newstrdiff
        rbmin = rb
    else
        if sepangle = minsepangle
            if newstrdiff > strdiff
                strdiff = newstrdiff
                rbmin = rb
            else
                endif
        else
            minsepangle = minsepangle
            rbmin = rbmin
        endif
    endif
    endsection
    rb = c_next(rb)
endloop
if type(rbmin) = 4
    cpmin = rbmin
    c_bflag(cpmin) = 0 ; delete 'worst case' element

```

```

broken_bonds = broken_bonds + 1
fracshape
fractime
fracsurface
else
endif
end

```

AIII.7. Mark 3 Failure Criterion

```

def uniaxial_D
maxmin = 0.05
lastepsmax = 0.0
rbmin = 1000
baf = ball_head ;
loop while baf # null ;
  if b_ex(baf) = 3 ;
    b_xfap(baf) = b_xfap(baf) ;
    b_yfap(baf) = b_yfap(baf) ;
  else
    if b_ex(baf) = 2
      b_xfap(baf) = 0.0
      b_yfap(baf) = fracpresdown
    else
      if b_ex(baf) = 1
        if b_id(baf) = fracendl
          b_xfap(baf) = 0.0
          b_yfap(baf) = fracendpresup
        else
          b_xfap(baf) = 0.0
          b_yfap(baf) = fracpresup
        endif
      else
        b_xfap(baf) = 0.0
        b_yfap(baf) = 0.0
      endif
    endif
  endif
  baf = b_next(baf)
endloop
rb = contact_head ;
loop while rb # null
  section
    if c_bflag(rb) = 1 ;
      cb1 = c_ball1(rb) ;
      cb2 = c_ball2(rb)

```

**loop over all particles to
reset applied forces to
current boundary conditions
(corrective forces set to zero
before each calculation)**

loop over all inter-particle contacts

**check if link exists at contact
determine locations of particles**

```

cb1id = b_id(cb1)
cb2id = b_id(cb2)
cb1x = b_x(cb1)
cb1y = b_y(cb1)
cb2x = b_x(cb2)
cb2y = b_y(cb2)
cx = c_x(rb) ; determine location of contact
cy = c_y(rb)

; determine variation of element strength
cst = ((c_nstrength(rb)/1e20 )-10 )*maxmin*ft)
ubond=(sqrt(((cb2x-cb1x)^2)+((cb2y-cb1y)^2))) ; element length
eps = (ubond - (2*radius))/(2*radius) ; uniaxial element strain
elasmax = (ft+cst)/(youngs*1e6) ; max. elastic strain
; ultimate element strain
epsmax=((ft+cst)/(youngs*1e6))+((ft+cst)/(softening*1e6))
; check if element strain less than max. elastic strain
; in order to determine relaxation stress
if eps < elasmax
  dsigma = 0.0
  exit section
else
  epsplas = eps - elasmax
  dsigma=(eps*(youngs*1e6))-(ft+cst)+(epsplas*(softening*1e6))
endif
; determine orientation of line between contact and 1st particle
if cy = cb1y
  if cx > cb1x
    plasang1 = 0.0
  else
    plasang1 = (180 * degrad)
  endif
else
  if cx = cb1x
    if cy > cb1y
      plasang1 = (90*degrad)
    else
      plasang1 = (-90*degrad)
    endif
  else
    if cx < cb1x then
      if cy < cb1y
        oa = ((cy-cb1y)/(cx-cb1x))
        plasang1 = atan(oa)-(180*degrad)
      else
        oa = ((cy-cb1y)/(cx-cb1x))
        plasang1 = atan(oa)+(180*degrad)
      endif
    else
      if cy < cb1y

```

```

    oa = ((cy-cb1y)/(cx-cb1x))
    plasang1 = atan(oa)
  else
    oa = ((cy-cb1y)/(cx-cb1x))
    plasang1 = atan(oa)
  endif
endif
endif
endif
;   determine orientation of line between contact and 2nd particle
if cy = cb2y
  if cx > cb2x
    plasang2 = 0.0
  else
    plasang2 = (180 * degrad)
  endif
else
  if cx = cb2x
    if cy > cb2y
      plasang2 = (90*degrad)
    else
      plasang2 = (-90*degrad)
    endif
  else
    if cx < cb2x then
      if cy < cb2y
        oa = ((cy-cb2y)/(cx-cb2x))
        plasang2 = atan(oa)-(180*degrad)
      else
        oa = ((cy-cb2y)/(cx-cb2x))
        plasang2 = atan(oa)+(180*degrad)
      endif
    else
      if cy < cb2y
        oa = ((cy-cb2y)/(cx-cb2x))
        plasang2 = atan(oa)
      else
        oa = ((cy-cb2y)/(cx-cb2x))
        plasang2 = atan(oa)
      endif
    endif
  endif
endif
endif
;   calculate apparent cross-sectional area of element
bondarea = (2*radius)/sqrt(3.0)/(1-(2*poissons))/(1+poissons)
;   calculate and apply x and y components of
;   corrective forces to particle pair
ax1 = -1.0*(dsigma*cos(plasang1)*bondarea)
ay1 = -1.0*(dsigma*sin(plasang1)*bondarea)

```

```

ax2 = -1.0*(dsigma*cos(plasang2)*bondarea)
ay2 = -1.0*(dsigma*sin(plasang2)*bondarea)
b_xfap(cb1)= b_xfap(cb1) + ax1
b_yfap(cb1)= b_yfap(cb1) + ay1
b_xfap(cb2)= b_xfap(cb2) + ax2
b_yfap(cb2)= b_yfap(cb2) + ay2
if eps > epsmax ;      check if element strain exceeds ultimate
  if eps > lastepsmax ; check if greater than previous maximum
    lastepsmax = eps ;      record new 'worst case' strain
    rbmin = rb ;          record new 'worst case' element
  else
  endif
else
endif
else
endif
endif
endsection
rb = c_next(rb)
endloop
if type(rbmin) = 4
  cpmin = rbmin
  c_bflag(cpmin) = 0 ;      delete 'worst case' element
  broken_bonds = broken_bonds + 1
  fracshape
  fractime
  fracsurface
else
endif
end

```

AIII.8. Mark 4 Failure Criterion

```

def rankine_E
  maxmin = 0.05
  rbmin = 1000.0
  laste_exceed = 0.0
  baf = ball_head ;      loop over all particles to
  loop while baf # null ; reset applied forces to
    if b_ex(baf) = 3 ;      current boundary conditions
      b_xfap(baf) = b_xfap(baf) ; (corrective forces set to zero
      b_yfap(baf) = b_yfap(baf) ; before each calculation)
    else
      if b_ex(baf) = 2
        b_xfap(baf) = 0.0
        b_yfap(baf) = fracpresdown
      else

```

```

if b_ex(baf) = 1
  if b_id(baf) = fracend1
    b_xfap(baf) = 0.0
    b_yfap(baf) = fracendpresup
  else
    b_xfap(baf) = 0.0
    b_yfap(baf) = fracpresup
  endif
else
  b_xfap(baf) = 0.0
  b_yfap(baf) = 0.0
endif
endif
endif
baf = b_next(baf)
endloop
rb = contact_head ;           loop over all inter-particle contacts
loop while rb # null
  section
  if c_bflag(rb) = 1 ;           check if link exists at contact
    cb1 = c_ball1(rb) ;         determine locations of particles
    cb2 = c_ball2(rb)
    cb1id = b_id(cb1)
    cb2id = b_id(cb2)
    cb1x = b_x(cb1)
    cb1y = b_y(cb1)
    cb2x = b_x(cb2)
    cb2y = b_y(cb2)
    cx = c_x(rb) ;             determine location of contact
    cy = c_y(rb)
    marker1id = 0 ;            determine marker balls associated with
    marker2id = 0 ;            current link element from predefined tables
    retnum = c_ex(rb)
    marker1id = table(1,retnum)
    marker2id = table(2,retnum)
    if marker2id = 0 ;         finds pointers of marker balls
      bp10 = ball_head ;       & mirror marker balls at edges
      loop while bp10 # null
        if b_id(bp10) = marker1id
          marker1add = bp10
          marker2add = bp10
        endif
        bp10 = b_next(bp10)
      endloop
    else
      if marker1id = 0
        bp10 = ball_head
        loop while bp10 # null
          if b_id(bp10) = marker2id

```

```

        marker1add = bp10
        marker2add = bp10
    endif
    bp10 = b_next(bp10)
endloop
else
    bp10 = ball_head
    loop while bp10 # null
        if b_id(bp10) = marker1id
            marker1add = bp10
        endif
        if b_id(bp10) = marker2id
            marker2add = bp10
        endif
        bp10 = b_next(bp10)
    endloop
endif
endif
; ***** STRAIN FROM equivalent continuum DIAMOND AREA
;                                     (BALL1, BALL2, MARKER1, MARKER2)
if b_x(cb1) > b_x(cb2) ;    assign numbering for force calculations
    b1x = cb1x
    b1y = cb1y
    b2x = cb2x
    b2y = cb2y
else
    b1x = cb2x
    b1y = cb2y
    b2x = cb1x
    b2y = cb1y
endif
m1x = b_x(marker1add) ;    coordinates of marker balls
m1y = b_y(marker1add)
m2x = b_x(marker2add)
m2y = b_y(marker2add)
;    strains of link elements forming triangles/diamond
epsa=(((sqrt(((b1x-b2x)^2)+(b1y-b2y)^2)))-(2*radius))/(2*radius)
ebup=(((sqrt(((b2x-m1x)^2)+(b2y-m1y)^2)))-(2*radius))/(2*radius)
ecup=(((sqrt(((b1x-m1x)^2)+(b1y-m1y)^2)))-(2*radius))/(2*radius)
ebdown=(((sqrt(((b1x-m2x)^2)+(b1y-m2y)^2)))-(2*radius))/(2*radius)
ecdowm=(((sqrt(((b2x-m2x)^2)+(b2y-m2y)^2)))-(2*radius))/(2*radius)
if b1x = b2x ;    orientations of elements forming triangles/diamond
    anga = pi/2
else
    anga = atan((b1y-b2y)/(b1x-b2x))
endif
if m1x = b2x
    angbup = pi/2
else

```

```

    angbup = atan((m1y-b2y)/(m1x-b2x))
endif
if m1x = b1x
    angcup = pi/2
else
    angcup = atan((m1y-b1y)/(m1x-b1x))
endif
if m2x = b1x
    angbdown = pi/2
else
    angbdown = atan((m2y-b1y)/(m2x-b1x))
endif
if m2x = b2x
    angcdown = pi/2
else
    angcdown = atan((m2y-b2y)/(m2x-b2x))
endif
straina = epsa    ;    calculation of strain tensor in upper triangle
strainb = ebus
strainc = ecup
anglea = anga
angleb = angbup
anglec = angcup
rosette_solver
eupperx = xxx
euppery = yyy
eupperxy = zzz
straina = epsa    ;    calculation of strain tensor in lower triangle
strainb = ebdown
strainc = ecdown
anglea = anga
angleb = angbdown
anglec = angcdown
rosette_solver
elowerx = xxx
elowery = yyy
elowerxy = zzz
e11 = (eupperx + elowerx)/2    ;    calculate strain tensor in bond
e12 = (eupperxy + elowerxy)/2
e21 = e12
e22 = (euppery + elowery)/2
;D1 = poissons    ;    D matrix variables
;D2 = (1-poissons)
;D3 = (1-(2*poissons))/2
D5 = ((youngs*1e6)/((1+poissons)*(1-(2*poissons))))
;s11 = D5*((D2*e11)+(D1*e22))    ;    stress tensor from strain tensor
;s12 = D5*(D3*e12)
;s21 = s12
;s22 = D5*((D1*e11)+(D2*e22))

```

```

;smax=((s11+s22)/2)+(sqrt((((s11-s22)/2)^2)+(s12^2)))
;smin=((s11+s22)/2)-(sqrt((((s11-s22)/2)^2)-(s12^2)))
;
principal strains from strain tensor in bond
e1=((e11+e22)/2)+(sqrt((((e11-e22)/2)^2)+(e12^2)))
e2=((e11+e22)/2)-(sqrt((((e11-e22)/2)^2)+(e12^2)))
if e2 > e1 ;
    e1 = e2 ;
    e2 = e1
else
    e1 = e1
    e2 = e2
endif
if e1 <= 0.0
    if e2 <= 0.0
        exit section
    else
        endif
else
    endif
endif
;
determine variation of element strength
cst = (((c_nstrength(rb)/1e20)-10)*maxmin*ft)
if cst > (ft * 0.05)
    exit section
else
    endif
endif
emax = max(e1,e2)
if e11 = e22 then ;
    theta = (45*degrad)
else
    theta = (atan(((2*e12)/(e11-e22))))/2
endif
ex=((e11+e22)/2)+(((e11-e22)/2)*cos(2*theta))+(e12*sin(2*theta))
ey=((e11+e22)/2)-(((e11-e22)/2)*cos(2*theta))-(e12*sin(2*theta))
if emax = ex then
    emaxangle = theta
else
    if emax = ey
        emaxangle = theta + (90.0*degrad)
    else
        endif
endif
endif
; determine intersections of strain path with yield and failure lines
;
terms A-E come from components of equations
;
defining yield and failure lines
A_term = (e2/e1)
B_term = ((poissons - 1)/poissons)
C_term = (((ft + cst)/poissons)*(1/D5))
D_term = (-1.0/(sqrt(2.0)-1))
E_term = ((2*Gsubf)/((ft + cst)*(2*radius)))

```

```

xint1 = (C_term/(A_term - B_term))
yint1 = (A_term*xint1)
xint2 = ((D_term*E_term)/(D_term-A_term))
yint2 = (A_term*xint2)
elgth = sqrt(((xint1)^2)+((yint1)^2))
ecurrent = sqrt(((e1)^2)+((e2)^2))
if ecurrent < elgth ;                               check if strain state exceeds
  exit section ;                                     yield surface
else
endif
;           determine shape of constitutive model along strain path
;           and determine position of current strain state along it
tlgth = sqrt(((xint1-xint2)^2)+((yint1-yint2)^2))
slgth = sqrt(((xint1-e1)^2)+((yint1-e2)^2))
Eapp = (ft + cst)/elgth ;           determine apparent Young's Modulus
Esapp = (ft + cst)/tlgth ;         determine apparent Softening Modulus
dsigma = (ecurrent-elgth)*(Eapp+Esapp) ; determine relaxation stress
if cb2x = cb1x ;                     determine orientation of link element
  bondangle = (90.0*degrad)
else
  bondangle = atan((cb2y-cb1y)/(cb2x-cb1x))
endif
rotangle = abs(bondangle - emaxangle)
;determine component of relaxation stress in direction of link element
dsigmabond = dsigma * abs(cos(rotangle))
;           determine orientation of line between contact and 1st particle
if cy = cb1y
  if cx > cb1x
    plasang1 = 0.0
  else
    plasang1 = (180 * degrad)
  endif
else
  if cx = cb1x
    if cy > cb1y
      plasang1 = (90*degrad)
    else
      plasang1 = (-90*degrad)
    endif
  else
    if cx < cb1x then
      if cy < cb1y
        oa = ((cy-cb1y)/(cx-cb1x))
        plasang1 = atan(oa)-(180*degrad)
      else
        oa = ((cy-cb1y)/(cx-cb1x))
        plasang1 = atan(oa)+(180*degrad)
      endif
    else

```

```

if cy < cb1y
  oa = ((cy-cb1y)/(cx-cb1x))
  plasang1 = atan(oa)
else
  oa = ((cy-cb1y)/(cx-cb1x))
  plasang1 = atan(oa)
endif
endif
endif
endif
;      determine orientation of line between contact and 2nd particle
if cy = cb2y
  if cx > cb2x
    plasang2 = 0.0
  else
    plasang2 = (180 * degrad)
  endif
else
  if cx = cb2x
    if cy > cb2y
      plasang2 = (90*degrad)
    else
      plasang2 = (-90*degrad)
    endif
  else
    if cx < cb2x then
      if cy < cb2y
        oa = ((cy-cb2y)/(cx-cb2x))
        plasang2 = atan(oa)-(180*degrad)
      else
        oa = ((cy-cb2y)/(cx-cb2x))
        plasang2 = atan(oa)+(180*degrad)
      endif
    else
      if cy < cb2y
        oa = ((cy-cb2y)/(cx-cb2x))
        plasang2 = atan(oa)
      else
        oa = ((cy-cb2y)/(cx-cb2x))
        plasang2 = atan(oa)
      endif
    endif
  endif
endif
endif
;      calculate apparent cross-sectional area of element
bondarea=(D5*(2*radius))/sqrt(3.0)/Eapp
;      calculate and apply x and y components of
;      corrective forces to particle pair
ax1 = -1.0*(dsigmabond*cos(plasang1)*bondarea)

```

```

ay1 = -1.0*(dsigmabond*sin(plasang1)*bondarea)
ax2 = -1.0*(dsigmabond*cos(plasang2)*bondarea)
ay2 = -1.0*(dsigmabond*sin(plasang2)*bondarea)
b_xfap(cb1)= b_xfap(cb1) + ax1
b_yfap(cb1)= b_yfap(cb1) + ay1
b_xfap(cb2)= b_xfap(cb2) + ax2
b_yfap(cb2)= b_yfap(cb2) + ay2
if slgth > tlgth ;      check if strain state exceeds failure surface
  if (slgth-tlgth)>laste_exceed ; check if greater than previous max.
    laste_exceed = (slgth - tlgth) ; record new 'worst case' strain
    rbmin = rb ; record new 'worst case' element
  else
    laste_exceed = laste_exceed
    rbmin = rbmin
  endif
else
endif
else
endif
endsection
rb = c_next(rb)
endloop
if type(rbmin) = 4
  cpmin = rbmin
  c_bflag(cpmin) = 0 ; delete 'worst case' element
  broken_bonds = broken_bonds + 1
  fracshape
  fractime
  fracsurface
else
endif
end

```

AIII.9. Mark 5 Failure Criterion

```

def rankine_F
  maxmin = 0.05
  rbmin = 1000.0
  laste_exceed = 0.0
  baf = ball_head ; loop over all particles to
  loop while baf # null ; reset applied forces to
    if b_ex(baf) = 3 ; current boundary conditions
      b_xfap(baf) = b_xfap(baf) ; (corrective forces set to zero
      b_yfap(baf) = b_yfap(baf) ; before each calculation)
    else
      if b_ex(baf) = 2

```

```

    b_xfap(baf) = 0.0
    b_yfap(baf) = fracpresdown
else
    if b_ex(baf) = 1
        if b_id(baf) = fracend1
            b_xfap(baf) = 0.0
            b_yfap(baf) = fracendpresup
        else
            b_xfap(baf) = 0.0
            b_yfap(baf) = fracpresup
        endif
    else
        b_xfap(baf) = 0.0
        b_yfap(baf) = 0.0
    endif
endif
endif
endif
baf = b_next(baf)
endloop
rb = contact_head ;           loop over all inter-particle contacts
loop while rb # null
    section
    if c_bflag(rb) = 1 ;           check if link exists at contact
        cb1 = c_ball1(rb) ;       determine locations of particles
        cb2 = c_ball2(rb)
        cb1id = b_id(cb1)
        cb2id = b_id(cb2)
        cb1x = b_x(cb1)
        cb1y = b_y(cb1)
        cb2x = b_x(cb2)
        cb2y = b_y(cb2)
        cx = c_x(rb) ;           determine location of contact
        cy = c_y(rb)
        marker1id = 0 ;           determine marker balls associated with
        marker2id = 0 ;           current link element from predefined tables
        retnum = c_ex(rb)
        marker1id = table(1,retnum)
        marker2id = table(2,retnum)
        if marker2id = 0 ;           finds pointers of marker balls
            bp10 = ball_head ;       & mirror marker balls at edges
            loop while bp10 # null
                if b_id(bp10) = marker1id
                    marker1add = bp10
                    marker2add = bp10
                endif
                bp10 = b_next(bp10)
            endloop
        else
            if marker1id = 0

```

```

    bp10 = ball_head
    loop while bp10 # null
        if b_id(bp10) = marker2id
            marker1add = bp10
            marker2add = bp10
        endif
        bp10 = b_next(bp10)
    endloop
else
    bp10 = ball_head
    loop while bp10 # null
        if b_id(bp10) = marker1id
            marker1add = bp10
        endif
        if b_id(bp10) = marker2id
            marker2add = bp10
        endif
        bp10 = b_next(bp10)
    endloop
endif
endif
; ***** STRAIN FROM equivalent continuum DIAMOND AREA
;                                     (BALL1, BALL2, MARKER1, MARKER2)
if b_x(cb1) > b_x(cb2) ;      assign numbering for force calculations
    b1x = cb1x
    b1y = cb1y
    b2x = cb2x
    b2y = cb2y
else
    b1x = cb2x
    b1y = cb2y
    b2x = cb1x
    b2y = cb1y
endif
m1x = b_x(marker1add) ;      coordinates of marker balls
m1y = b_y(marker1add)
m2x = b_x(marker2add)
m2y = b_y(marker2add)
;      strains of link elements forming triangles/diamond
epsa=(((sqrt(((b1x-b2x)^2)+((b1y-b2y)^2)))-(2*radius))/(2*radius))
ebup=(((sqrt(((b2x-m1x)^2)+((b2y-m1y)^2)))-(2*radius))/(2*radius))
ecup=(((sqrt(((b1x-m1x)^2)+((b1y-m1y)^2)))-(2*radius))/(2*radius))
ebdown=(((sqrt(((b1x-m2x)^2)+((b1y-m2y)^2)))-(2*radius))/(2*radius))
ecdowm=(((sqrt(((b2x-m2x)^2)+((b2y-m2y)^2)))-(2*radius))/(2*radius))
if b1x = b2x ;      orientations of elements forming triangles/diamond
    anga = pi/2
else
    anga = atan((b1y-b2y)/(b1x-b2x))
endif

```

```

if m1x = b2x
  angbup = pi/2
else
  angbup = atan((m1y-b2y)/(m1x-b2x))
endif
if m1x = b1x
  angcup = pi/2
else
  angcup = atan((m1y-b1y)/(m1x-b1x))
endif
if m2x = b1x
  angbdown = pi/2
else
  angbdown = atan((m2y-b1y)/(m2x-b1x))
endif
if m2x = b2x
  angcdown = pi/2
else
  angcdown = atan((m2y-b2y)/(m2x-b2x))
endif
straina = epsa      ;    calculation of strain tensor in upper triangle
strainb = ebup
strainc = ecup
anglea = anga
angleb = angbup
anglec = angcup
rosette_solver
eupperx = xxx
euppery = yyy
eupperxy = zzz
straina = epsa      ;    calculation of strain from lower triangle
strainb = ebdown
strainc = ecdown
anglea = anga
angleb = angbdown
anglec = angcdown
rosette_solver
elowerx = xxx
elowery = yyy
elowerxy = zzz
e11 = (eupperx + elowerx)/2      ;    calculate strain tensor in bond
e12 = (eupperxy + elowerxy)/2
e21 = e12
e22 = (euppery + elowery)/2
;D1 = poissons      ;    D matrix variables
;D2 = (1-poissons)
;D3 = (1-(2*poissons))/2
D5 = ((youngs*1e6)/((1+poissons)*(1-(2*poissons))))
;s11 = D5*((D2*e11)+(D1*e22))    ;    stress tensor from strain tensor

```

```

;s12 = D5*(D3*e12)
;s21 = s12
;s22 = D5*((D1*e11)+(D2*e22))
;smax=((s11+s22)/2)+(sqrt((((s11-s22)/2)^2)+(s12^2)))
;smin((((s11+s22)/2)-(sqrt((((s11-s22)/2)^2)-(s12^2))))
;
;           principal strains from strain tensor in bond
e1=(((e11+e22)/2)+(sqrt((((e11-e22)/2)^2)+(e12^2))))
e2=(((e11+e22)/2)-(sqrt((((e11-e22)/2)^2)+(e12^2))))
if e2 > e1 ;           establish strain state in positive
  e1 = e2 ;           quadrants of e1-e2 space
  e2 = e1
else
  e1 = e1
  e2 = e2
endif
if e1 <= 0.0
  if e2 <= 0.0
    exit section
  else
    endif
else
  endif
endif
;           determine variation of element strength
cst = (((c_nstrength(rb)/1e20)-10)*maxmin*ft)
if cst > (ft * 0.05)
  exit section
else
  endif
emax = max(e1,e2)
if e11 = e22 then ;           calculate principal directions
  theta = (45*degrad)
else
  theta = (atan(((2*e12)/(e11-e22))))/2
endif
ex=(((e11+e22)/2)+(((e11-e22)/2)*cos(2*theta))+(e12*sin(2*theta))
ey=(((e11+e22)/2)-(((e11-e22)/2)*cos(2*theta))-(e12*sin(2*theta))
if emax = ex then
  emaxangle = theta
else
  if emax = ey
    emaxangle = theta + (90.0*degrad)
  else
    endif
endif
; determine intersections of strain path with yield and failure lines
;           terms A-E come from components of equations
;           defining yield and failure lines
A_term = (e2/e1)
B_term = ((poissons - 1)/poissons)

```

```

C_term = ((ft + cst)/poissons)*(1/D5)
D_term = (-1.0/(sqrt(2.0)-1))
E_term = ((2*Gsubf)/((ft + cst)*(2*radius)))
xint1 = (C_term/(A_term - B_term))
yint1 = (A_term*xint1)
xint2 = ((D_term*E_term)/(D_term-A_term))
yint2 = (A_term*xint2)
elgth = sqrt(((xint1)^2)+((yint1)^2))
ecurrent = sqrt(((e1)^2)+((e2)^2))
if ecurrent < elgth ;                               check if strain state exceeds
    exit section ;                                   yield surface
else
endif
tlgth = sqrt(((xint1-xint2)^2)+((yint1-yint2)^2))
slgth = sqrt(((xint1-e1)^2)+((yint1-e2)^2))
Eapp = (ft + cst)/elgth ;                               apparent Young's Modulus
Esapp = (ft + cst)/tlgth ;                               apparent Softening Modulus
;                                                       determine relaxation stress& components of relaxation
;                                                       stress tensor rotated into global x,y
dsigma = slgth*(Eapp+Esapp)
dsigmax = (dsigma/2) + ((dsigma/2)*cos(-2.0*emaxangle))
dsigmay = (dsigma/2) - ((dsigma/2)*cos(-2.0*emaxangle))
dsigmaxy = (-1.0*(dsigma/2)*sin(-2.0*emaxangle))
;                                                       determine nodal forces for first triangle
;                                                       i = b2    j = b1    m = m1    See Johnson [42]
if marker1id = 0
    fxi_up = 0.0
    fyi_up = 0.0
    fxj_up = 0.0
    fyj_up = 0.0
    fxm_up = 0.0
    fym_up = 0.0
else
    fxi_up = ((1.0/2.0)*(((b1y-m1y)*dsigmax)+((m1x-b1x)*dsigmaxy)))
    fyi_up = ((1.0/2.0)*(((m1x-b1x)*dsigmay)+((b1y-m1y)*dsigmaxy)))
    fxj_up = ((1.0/2.0)*(((m1y-b2y)*dsigmax)+((b2x-m1x)*dsigmaxy)))
    fyj_up = ((1.0/2.0)*(((b2x-m1x)*dsigmay)+((m1y-b2y)*dsigmaxy)))
    fxm_up = ((1.0/2.0)*(((b2y-b1y)*dsigmax)+((b1x-b2x)*dsigmaxy)))
    fym_up = ((1.0/2.0)*(((b1x-b2x)*dsigmay)+((b2y-b1y)*dsigmaxy)))
endif
;                                                       determine nodal forces for second triangle
;                                                       i = b1    j = b2    m = m2    See Johnson [42]
if marker2id = 0
    fxi_down = 0.0
    fyi_down = 0.0
    fxj_down = 0.0
    fyj_down = 0.0
    fxm_down = 0.0
    fym_down = 0.0

```

```

else
  fxi_down = ((1.0/2.0)*(((b2y-m2y)*dsigmax)+((m2x-b2x)*dsigmaxy)))
  fyi_down = ((1.0/2.0)*(((m2x-b2x)*dsigmay)+((b2y-m2y)*dsigmaxy)))
  fxj_down = ((1.0/2.0)*(((m2y-b1y)*dsigmax)+((b1x-m2x)*dsigmaxy)))
  fyj_down = ((1.0/2.0)*(((b1x-m2x)*dsigmay)+((m2y-b1y)*dsigmaxy)))
  fxm_down = ((1.0/2.0)*(((b1y-b2y)*dsigmax)+((b2x-b1x)*dsigmaxy)))
  fym_down = ((1.0/2.0)*(((b2x-b1x)*dsigmay)+((b1y-b2y)*dsigmaxy)))
endif
if b_x(cb1) > b_x(cb2) ; sum and apply nodal forces
  b_xfap(cb1)= b_xfap(cb1) + fxj_up + fxi_down
  b_yfap(cb1)= b_yfap(cb1) + fyj_up + fyi_down
  b_xfap(cb2)= b_xfap(cb2) + fxi_up + fxj_down
  b_yfap(cb2)= b_yfap(cb2) + fyi_up + fyj_down
else
  b_xfap(cb1)= b_xfap(cb1) + fxi_up + fxj_down
  b_yfap(cb1)= b_yfap(cb1) + fyi_up + fyj_down
  b_xfap(cb2)= b_xfap(cb2) + fxj_up + fxi_down
  b_yfap(cb2)= b_yfap(cb2) + fyj_up + fyi_down
endif
b_xfap(marker1add) = b_xfap(marker1add) + fxm_up
b_yfap(marker1add) = b_yfap(marker1add) + fym_up
b_xfap(marker2add) = b_xfap(marker2add) + fxm_down
b_yfap(marker2add) = b_yfap(marker2add) + fym_down

if slgth > tlgth ; check if strain state exceeds failure surface
  if (slgth-tlgth)>laste_exceed ; check if greater than previous max.
    laste_exceed = (slgth - tlgth) ; record new 'worst case' strain
    rbmin = rb ; record new 'worst case' element
  else
    laste_exceed = laste_exceed
    rbmin = rbmin
  endif
else
endif
else
endif
endsection
rb = c_next(rb)
endloop
if type(rbmin) = 4
  cpmin = rbmin
  c_bflag(cpmin) = 0 ; delete 'worst case' element
  broken_bonds = broken_bonds + 1
  fracshape
  fractime
  fracsurface
else
endif
end

```

Appendix IV:

Publications

This Appendix contains additional papers produced from the work carried out for this thesis and published during the course of this research.

1. Davie, C. T. and Bićanić, N., *Progressive Fracturing Using Lattice Models*, Proceedings of Fourth International Conference on Analysis of Discontinuous Deformation, University of Glasgow, 2001, ISBN 0 85261 735 6.

It may be noted that a very similar paper of the same title was also published in:

Proceedings of 9th Annual Conference of the Association for Computational Mechanics in Engineering, University of Birmingham, 2001, ISBN 0 70442 302 2.

To avoid repetition, this is not included here.

2. Davie, C. T. and Bićanić, N., *Failure Criteria for Quasi Brittle Materials in Lattice Models*, Proceedings of 10th Annual Conference of the Association for Computational Mechanics in Engineering, University of Swansea, 2002, ISBN 0 9542544 0 6.

Progressive Fracturing Using Lattice Models

C. Davie and N. Bićanić

Department of Civil Engineering, University of Glasgow, Glasgow, G12 8LT

Introduction

Potential of the lattice modelling framework is explored in the study of hydraulically driven fractures in which propagation is initiated by the action of a high pressure fluid. A good understanding of hydraulic fracturing is of primary interest to the oil industry where the deliberate inducement of hydraulic fractures in oil bearing rock units is a technique employed to increase oil production rates by creating high permeability pathways from the reservoir to the well bore. However, the same physical phenomenon is also of interest to civil engineers concerned with unlined water carrying tunnels and dam foundations.

Lattice models comprise assemblies of truss or beam elements and the principal intention behind a lattice model is to replace a continuum domain by a simpler analogue of equivalent line elements. One of the first people to utilise this method was Hrennikoff [4] in the early 1940s. Since then, lattice model investigations have been carried out on various problems, notably by Schlangen & van Mier [6] into fracture of concrete, and by Tzschichholz et al. [7] into basic hydraulic fracture models. There are various strategies to arrive at equivalent lattice properties, with the aim to adequately replace the continuum domain - such strategies depend on the form and regularity of lattice configuration, ranging from highly regular assemblies to fully randomised lattice configurations.

Model Construction

All lattice models used here were formulated in the discrete element modelling (DEM) environment Particle Flow Code in Three Dimensions (PFC^{3D})[1], which nominally deals with transient dynamics of particulate media. The same modelling environment also deals with bonded particulate media, where bonds may be of different types – either so called *contact* bonds (with axial and shear stiffness and limited axial and shear strength) or *parallel* bonds, where the local transfer of moments between particles is possible. The normal contact bond model is adopted here and the dynamic relaxation solver was used to arrive at static solutions to the problem. In such situations the system response is governed by bond stiffness and strength only and the PFC^{3D} framework represents a lattice modelling framework, with a specific type of lattice element, with a normal and shear spring. A built-in coding language, known as *FISH*, allows additional functions to be written that can act in conjunction with any model constructed in the PFC^{3D} modelling environment.

The elastic deformability equivalence between the continuum and the lattice model was achieved using a technique recently proposed by Griffiths & Mustoe [3] for a model of lattice type configuration very similar to those used here. The technique is based on the equivalence of strain energy density for two frameworks for a basic triangular shape unit of three lattice elements. For a material with a given Young's modulus and Poisson ratio under plane strain conditions, the equivalent axial and shear stiffness of the contact bonds are defined as

$$k_n = \frac{E}{\sqrt{3}(1-2\nu)(1+\nu)}$$

$$k_s = \frac{E(1-4\nu)}{\sqrt{3}(1-2\nu)(1+\nu)}$$

Stress State and Failure Criterion in Lattice Framework

Formulation of any strength criterion to initiate material failure requires the knowledge of the state of stress within the domain of interest. Although the lattice modelling framework is best suited to formulate failure criteria based on critical values of normal or shear forces, here a strategy of an equivalent continuum failure criterion is adopted. In the lattice framework the average stress tensor at a given point can be defined from contributions from all contact forces acting on a particle

$$\bar{\sigma}_{ij}^{(p)} = \frac{1}{V^{(p)}} \sum_{N_c} |x_i^{(c)} - x_i^{(p)}| n_i^{(c,p)} F_j^{(c)}$$

where $\bar{\sigma}$ is the average stress tensor at the particle point, V is the volume of the particle, x is the location of the contact force or of the particle centroid, n is the unit normal from the centroid towards the location of the contact force, F is the magnitude of the contact force and the superscripts c and p indicate contact and particle respectively.

The Rankine principal stress criterion $\sigma_1 \geq f_t$ is adopted here. The algorithm considers each lattice element (contact bond) in turn and determines the pair of end particles involved. Maximum principal stresses are calculated in both end particles using the respective averaged stress tensors. It is then assumed that the magnitude of the maximum principal stress in the bond is the average of the two end values. If this stress exceeds the predefined tensile strength of the bond, the bond is considered as a candidate for failure. The direction of the principal stress in the bond is also determined as the average of the principal stress directions associated with the end particles. This direction is then compared to the orientation of the bond. From all the "candidates for failure" the worst case bond is subsequently removed - i.e. the bond in which the maximum principal stress has exceeded its tensile strength and whose direction is closest to that of the principal stress. In the event that two bonds have failed and are inclined at the same angle with respect to the direction of the principal stress the percentage by which stress exceeds strength is taken into consideration for the removal of bond.

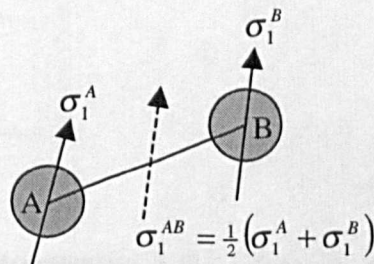


Fig. 3(c) Plot Showing Normal Stress in Bond
Showing Not-precise

Numerical Example using Rankine Failure Criterion

The numerical example shown below was implemented using the Rankine criterion described above. A lattice model was constructed (See Fig. 1 below) that was similar to the plane strain finite element model developed by Papanastasiou [5].

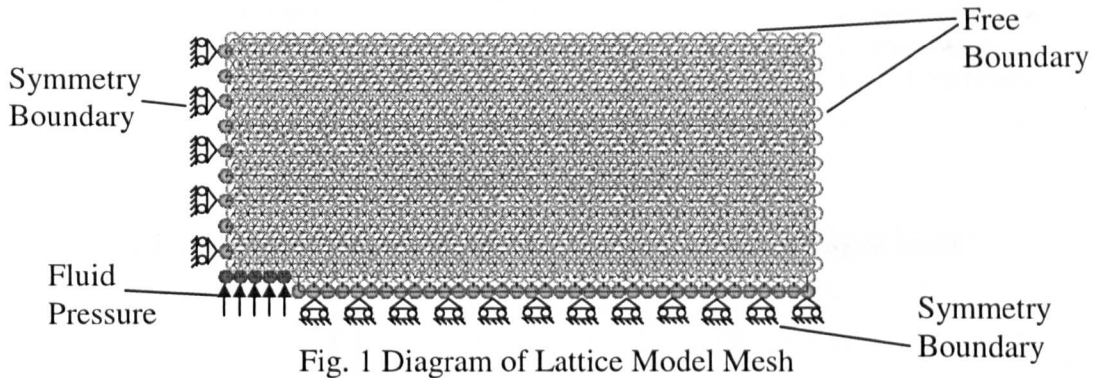


Fig. 1 Diagram of Lattice Model Mesh

Forces were applied to the fracture walls to represent fluid pressures. These increased linearly until the failure criterion is reached and the bond removed, representing a propagated fracture. The associated drop of the fluid pressure was then accounted for by recalculating the new pressures by the ratio of the new fracture length to the old. For simplicity, fluid pressures were assumed to be constant over the length of the fracture. As the fracture extended the deformed shapes of its walls were recorded and compared to the fracture shape obtained by Papanastasiou [5]. The pressure at which fracturing occurred was also noted. The comparative results are shown below (See Fig. 2a & Fig. 2b and Fig. 3a & Fig. 3b).

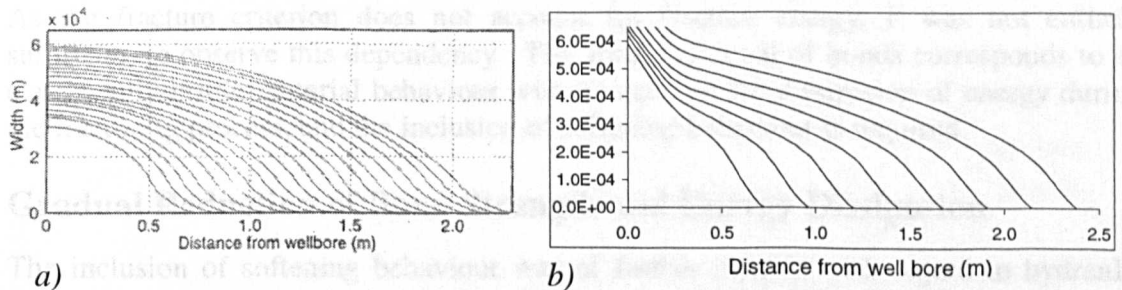


Fig. 2 a) Plotted Fracture Shapes (after Papanastasiou [5]), b) Plotted Fracture Shapes from PFC^{3D} Lattice Models

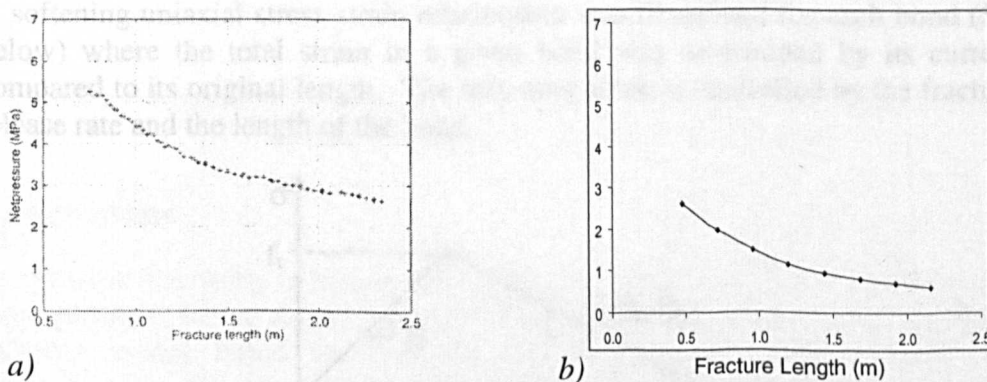


Fig. 3 a) Plot Showing Net-pressures at Well Bore (after Papanastasiou [5]), b) Plot Showing Net-pressures at Well Bore from PFC^{3D} Lattice Models

Configuration sensitivity tests subsequently showed the lattice fracture shapes to be clearly dependent on lattice element size (See Fig. 4 & Fig. 5 below).

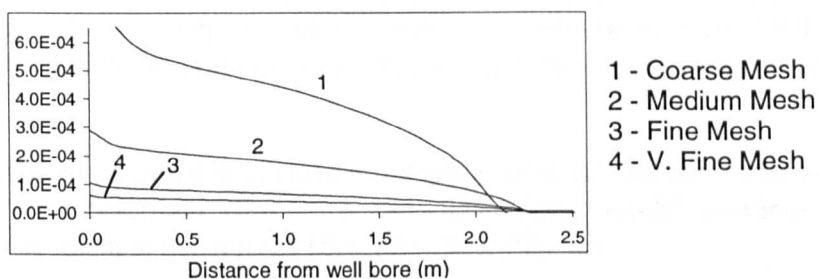


Fig. 4 Plotted Fracture Shapes for Varying Lattice Element Sizes

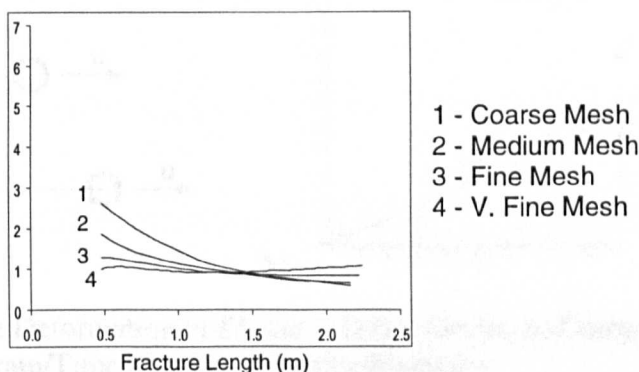


Fig. 5 Plot Showing Net-pressures at Well Bore for Varying Lattice Element Sizes

As the fracture criterion does not account for fracture energy, it was not entirely surprising to observe this dependency. The abrupt removal of bonds corresponds to an elastic-fully-brittle material behaviour with no account for dissipation of energy during the fracturing process, and the inclusion of softening behaviour is required.

Gradual Reduction of Bond Strength and Energy Dissipation

The inclusion of softening behaviour was of further interest with regard to hydraulic fracturing as Papanastasiou [5] had shown that elasto-plastic behaviour has very significant influence on fracture propagation and shape.

A softening uniaxial stress-strain relationship was developed for each bond (See Fig. 6 below) where the total strain in a given bond was determined by its current length compared to its original length. The softening slope is controlled by the fracture energy release rate and the length of the bond.

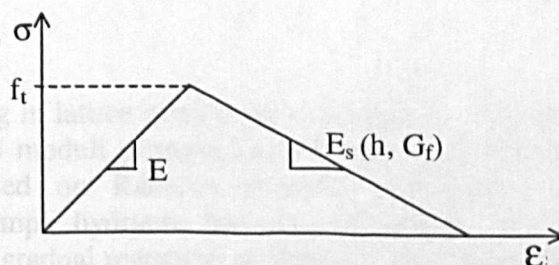


Fig. 6 Diagram of Typical Loading/Unloading Model for Lattice Element

At every step, each bond was taken in turn and the available stress capacity, evaluated from the total strain, was calculated according to the constitutive model. Any out of balance residual force was then taken into account for the subsequent deformation of the lattice model. Once the stress capacity of the bond was reduced to zero (total strain equal to the ultimate strain) the bond is considered to have failed and is removed from the model.

An illustrative numerical example was carried out using both the elastic-brittle and the elastic-softening model described above. A one-dimensional model problem under prescribed end displacement is considered (See Fig. 7a & Fig. 7b).

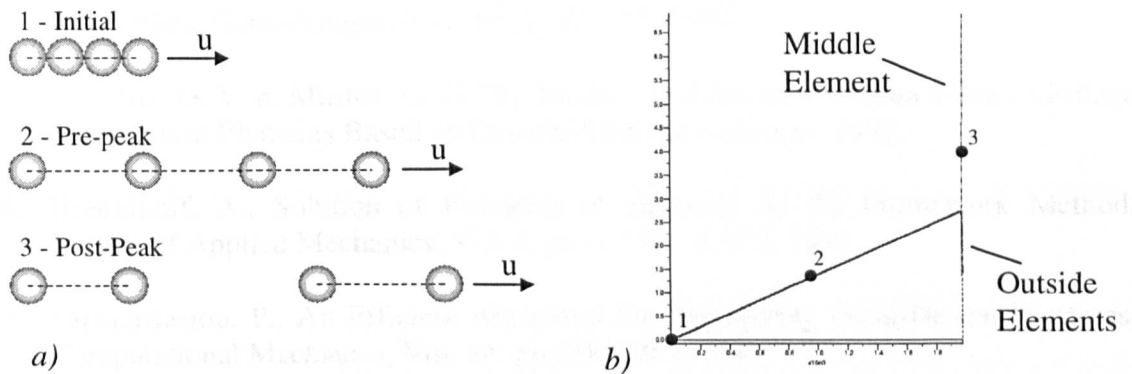


Fig. 7 a) Progressive Deformation of Elastic 1-D Bar Model, b) Comparative Strain/Time Plot for all Lattice Elements

The middle bond is given a tensile strength slightly lower than that of the outside two to ensure strain localisation solution. As above, total strain histories for the three bonds are shown below (See Fig. 8a & Fig. 8b below).

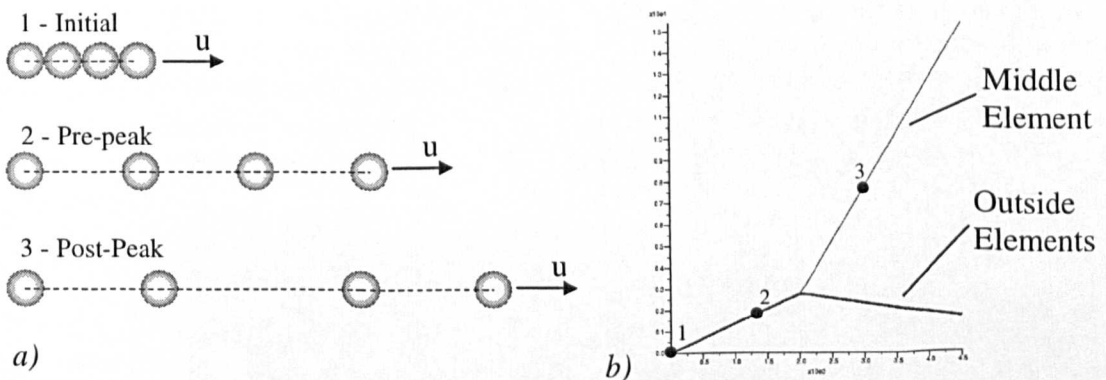


Fig. 8 a) Progressive Deformation of Elasto-plastic 1-D Bar Model, b) Comparative Strain/Time Plot for all Lattice Elements

Conclusions

Progressive fracturing in lattice models was considered. The deformability is based on the equivalent lattice moduli proposed by Griffiths and Mustoe and an elastic-brittle material model based on Rankine criterion produced a reasonable, qualitative representation of a simple hydraulic fracture propagation. The inclusion of a softening model to represent a gradual reduction of strength and the associated energy dissipation was illustrated on the one dimensional model problem. Further work will include the

incorporation of softening for a general state of stress in order to study the influence of material plasticity on hydraulic fracturing and to eliminate lattice element size dependency.

References

1. Particle Flow Code in Three Dimensions, Version 1.1, Users Manual, Itasca Consulting Group Inc., Minnesota, 1995.
2. Cundall, P. A. & Strack, O. D. L., A Discrete Numerical Model for Granular Assemblies, *Geotechnique*, Vol. 29, pp 47 – 65, 1979.
3. Griffiths, D. V. & Mustoe, G. G. W., Modeling of Elastic Continua using a Grillage of Structural Elements Based on Discrete Element Concepts, 1999.
4. Hrennikoff, A., Solution of Problems of elasticity by the Framework Method, *Journal of Applied Mechanics*, Vol. 8, pp A 169 - A 175, 1941.
5. Papanastasiou, P., An Efficient Algorithm for Propagating Fluid-Driven Fractures, *Computational Mechanics*, Vol. 24, pp 258 – 267, 1999.
6. Schlangen, E. & van Mier, J. G. M., Micromechanical Analysis of Fracture of Concrete, *International Journal of Damage Mechanics*, Vol. 1, 1992.
7. Tzschichholz, F., Herrmann, H. J., Roman, H. E. & Pfuff, M., Beam Model for Hydraulic Fracturing, *Physical Review B*, Vol. 49, No. 10, pp 7056 – 7059, 1994.

Failure Criteria for Quasi Brittle Materials in Lattice Models

C. Davie and N. Bićanić

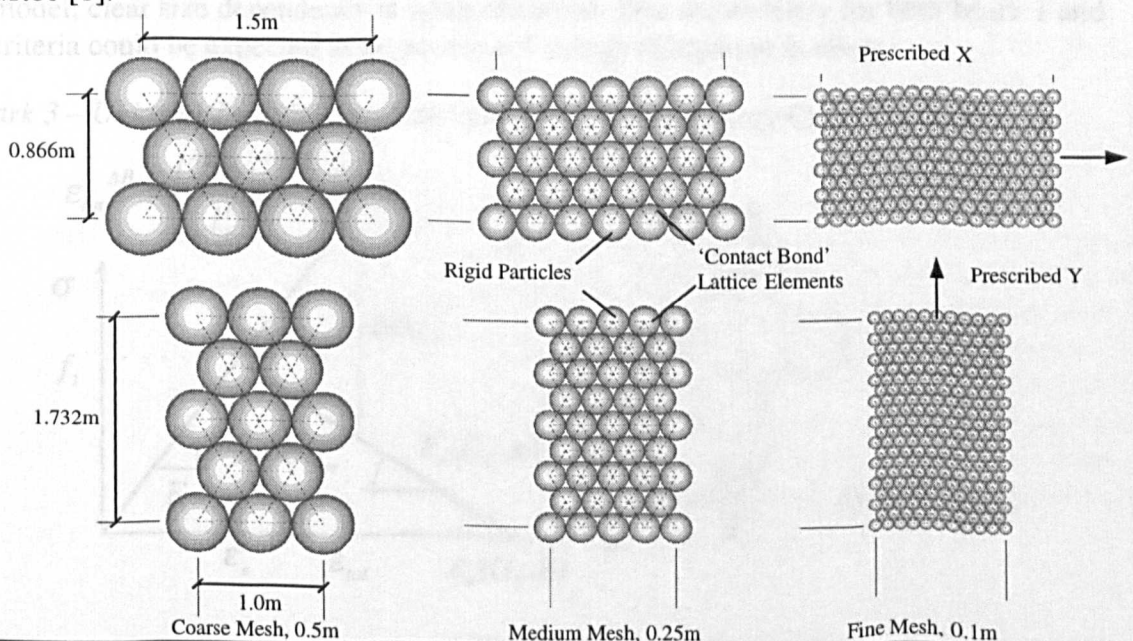
Department of Civil Engineering, University of Glasgow, Glasgow, G12 8LT

Various lattice models exist to simulate behaviour of simple and higher order continua. Lattice members are assigned equivalent elastic properties and lattice configurations range from regular patterns to random lattices. Such models have also been extended to include modelling of material failure, where the removal of individual lattices is usually controlled by some strength based criterion.

Lattice based models have also been adopted for modelling of quasi brittle materials, e.g. concrete and rock, where the experimental evidence suggests softening behaviour under displacement control and a gradual reduction of strength is observed. Very fine random lattice configurations are adopted and some researchers have argued that the simple removal of lattice members after a strength criterion is reached is adequate whereas others have suggested that the inclusion of softening into the lattice failure models is needed [3,7].

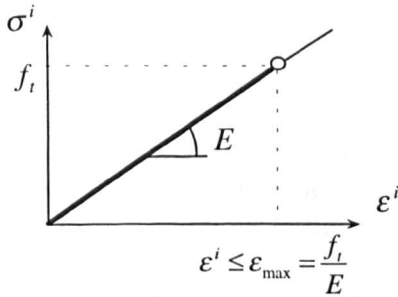
In the following, several simple strategies to implement failure criteria for quasi brittle materials in lattice models based on the gradual reduction of strength are explored. The implementation of these strategies is conducted in the lattice modelling environment, realised within the DEM code PFC^{3D}, where a static solution is obtained through dynamic relaxation, using an explicit time stepping scheme. Failure criteria were implemented through code developed in the *FISH* language associated with PFC^{3D}. For simplicity and for reasons of PFC^{3D} constraints, the nonlinear solution scheme employs the \mathbf{K}_0 initial stiffness algorithm.

Two simple configurations (plane strain panels under prescribed extension) are considered, using six regular lattice meshes. Lattice members, realised through normal and shear contact springs, \mathbf{k}_n and \mathbf{k}_s can transfer axial and shear forces only. Values for \mathbf{k}_n and \mathbf{k}_s are determined by relating the strain energy density of a typical triangular unit of lattice elements to an equivalent continuum with \mathbf{E} and ν . This approach was proposed by Morikawa and Sawamoto [5] and further developed by Griffiths and Mustoe [1].



Five failure criteria were implemented and examined for the two model problems.

Mark 1 - Limit Total Strain Criterion (Brittle)



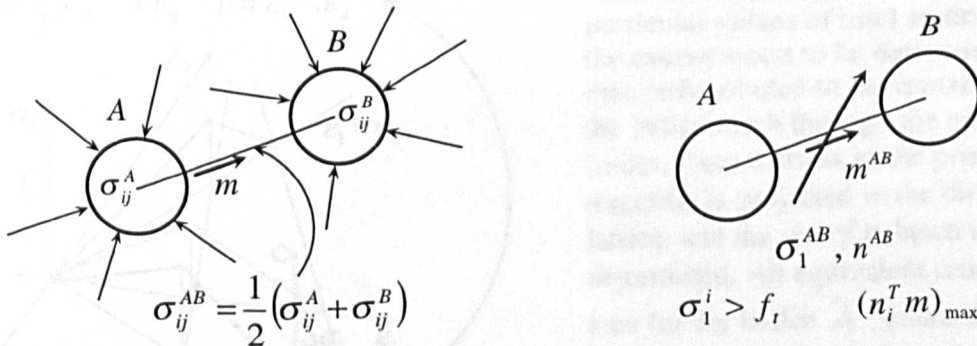
$$\epsilon^i = \frac{l^i - l_0^i}{l_0^i} \leq \epsilon_{\max} = \frac{f_t}{E}$$

where a lattice element is removed from the mesh when its strain is larger than the critical value. No softening is considered.

Mesh size dependency and a directionality bias are observed.

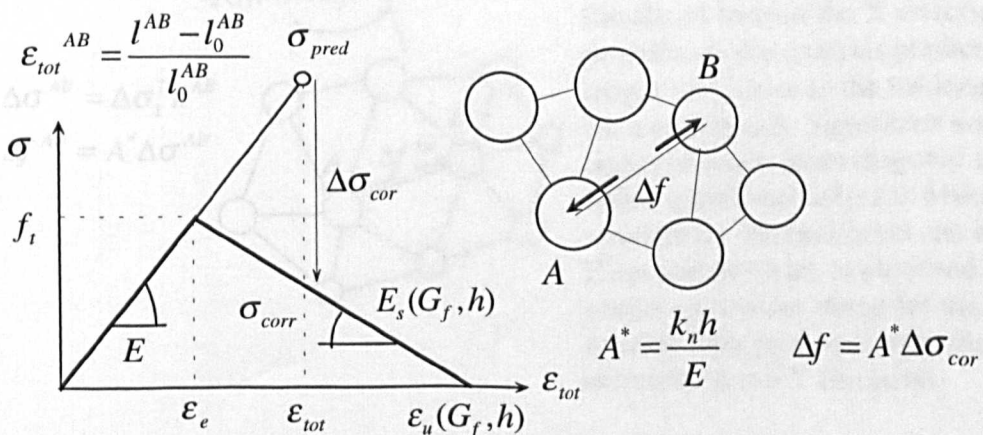
Mark 2 - Principal Stress Criterion (Rankine, Brittle)

The average stress tensor in a discrete particle can be calculated from the contributions of the contact forces acting on the particle. The stress tensor in the ‘contact bond’/lattice element between two particles is approximated as the average of the tensors in the particle pair. As the components of the average stresses refer to “granular” stresses, conversion factors were derived to obtain stress tensor in an equivalent continuum of unit thickness. Lattice elements were then removed when the Rankine principal stress criterion was violated. No softening is considered. If more than one lattice had a stress state exceeding f_t , the bond in which the maximum principal stress was most closely aligned to the bond orientation was removed.



Although a better prediction of the failure length was obtained as compared to the Mark 1 model, clear size dependency is again observed. Size dependency for both Mark 1 and 2 criteria could be expected as no account of energy dissipation is taken.

Mark 3 – Uniaxial Total Strain Criterion with Fracture Energy Controlled Softening

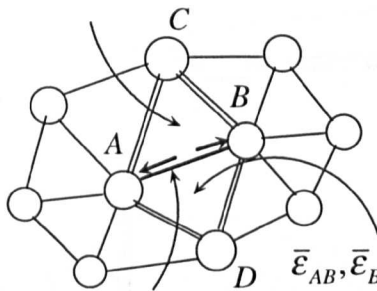


This elasto softening plasticity model, based on the total strain model accounts for the fracture energy dissipation in an element, hence the softening slope is mesh size dependent to ensure mesh objectivity. Any excess stress during softening is applied as a self equilibrating set of out of balance forces to the lattice ends. Lattice elements were removed from the mesh, once the ultimate total strain has been reached.

Results showed objectivity with respect to the mesh size, although a directionality bias is present (diagonal lattices in y-direction). Conversely, when a constant softening slope was used for various lattice sizes, mesh sensitivity was noticed, as expected.

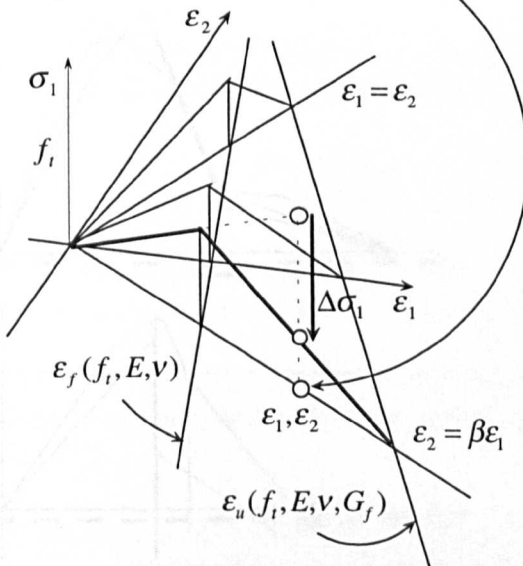
Mark 4 - Total Continuum Strain Model with Fracture Energy Controlled Softening (A)

$$\bar{\epsilon}_{AB}, \bar{\epsilon}_{BC}, \bar{\epsilon}_{CA} \Rightarrow \epsilon_{ij}^{ABC}$$



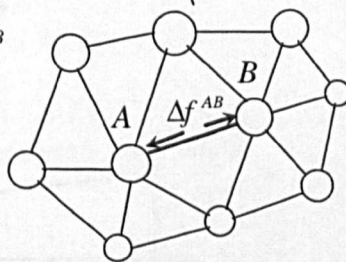
$$\bar{\epsilon}_{AB}, \bar{\epsilon}_{BD}, \bar{\epsilon}_{DA} \Rightarrow \epsilon_{ij}^{ABD}$$

$$\epsilon_{ij}^{AB} = \frac{1}{2} (\epsilon_{ij}^{ABC} + \epsilon_{ij}^{ABD}) \Rightarrow \epsilon_1^{AB}, \epsilon_2^{AB}, n^{AB}$$



$$\Delta \sigma^{AB} = \Delta \sigma_1^T n^{AB}$$

$$\Delta f^{AB} = A^* \Delta \sigma^{AB}$$



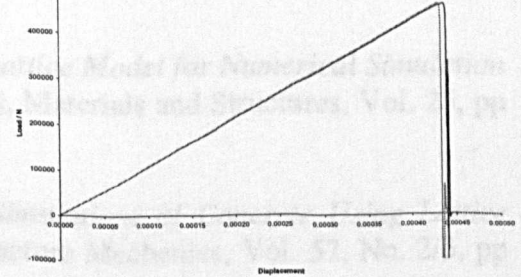
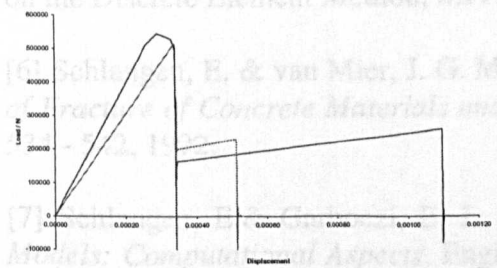
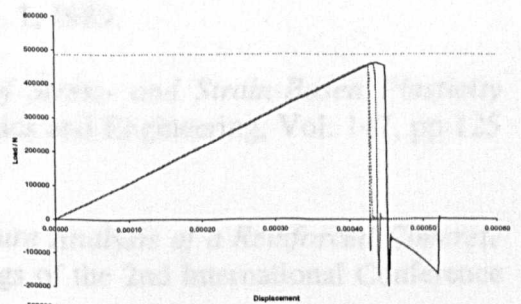
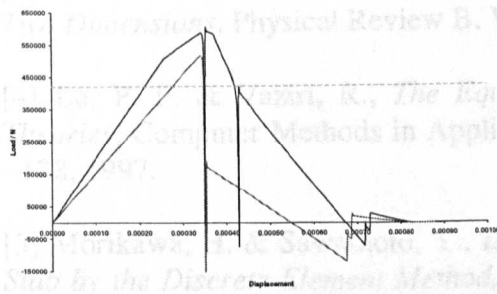
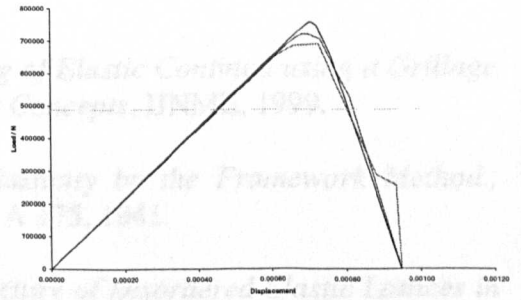
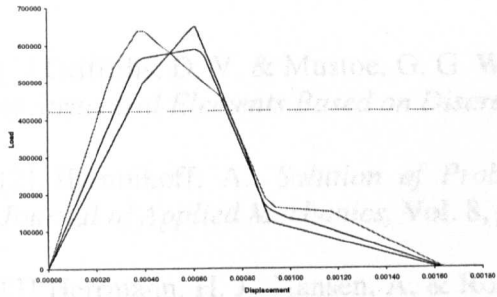
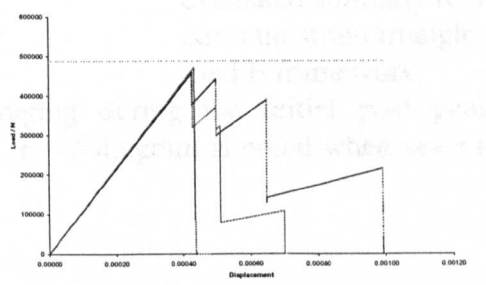
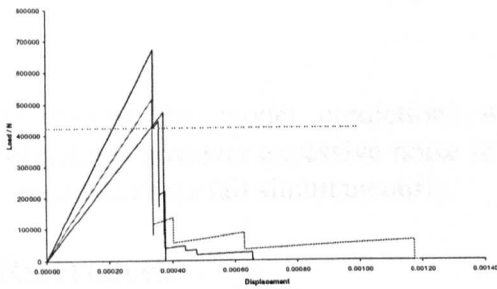
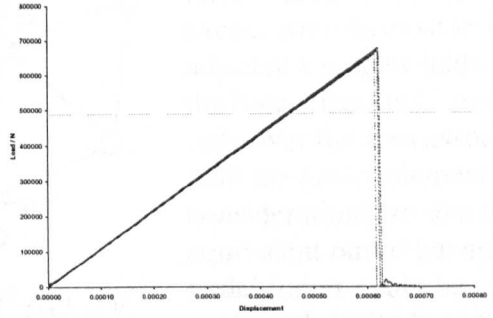
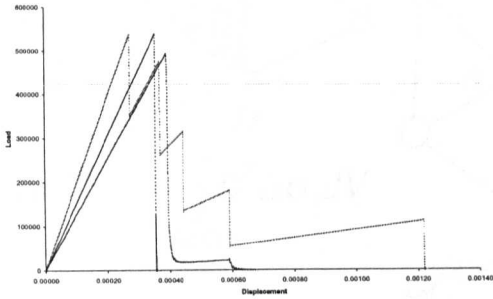
Strain tensors in the two triangles adjacent to the lattice element were evaluated from simple stretches of the three sides. The strain tensor in the lattice was then assumed to be the average of the strain tensors reported for the two triangles, and the two principal strains in the lattice are subsequently computed. Softening Rankine principal stress criterion is then considered in the principal total strain space. The reduction of strength associated with particular values of total strains allows for the excess stress to be determined, which is then redistributed to the remaining part of the lattice mesh through the out of balance forces. Excess stress in the principal direction is projected in the direction of the lattice, and the out of balance forces are determined. An equivalent cross section area for the lattice A^* , emanating from the k_n spring equivalence, was adopted, similarly to the Mark 3 model. Lattice elements were removed from the mesh, when the ultimate state of total strains ϵ_1, ϵ_2 was reached.

Results of tests in the X direction showed promise, as the analysis predicted failure length very close to the solution expected for a continuum. Significant solution noise occurred when more diagonal lattices failed simultaneously, for which no satisfactory interpretation can be given. Directionality bias is observed again, and poorer results are noted for the model meshes with predominantly diagonal elements in the Y direction.

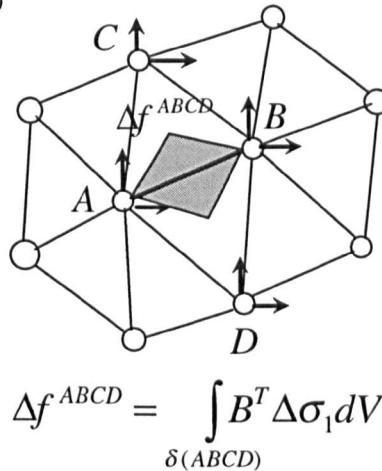
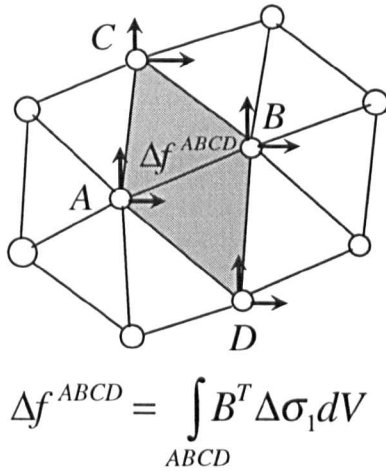
P- δ diagrams for model problems using the five failure criteria (Mark 1-5)

Prescribed Displacement X

Prescribed Displacement Y



Mark 5 - Total Continuum Strain Model with Fracture Energy Controlled Softening (B)



The model is essentially identical to the *Mark 4* model, except for the excess stress redistribution strategy. Here it is assumed that the excess stresses exist in both adjacent triangles (either over the hole “diamond” area, or only over the area associated with the lattice element under consideration), so that the equivalent out of balance nodal forces could be evaluated similarly to the constant strain triangles in the FE framework.

As before, the model predictions were encouraging during the initial post peak behaviour, however excessive noise in the overall $P - \delta$ diagram is noted when several lattice members fail simultaneously.

References

- [1] Griffiths, D. V. & Mustoe, G. G. W., *Modeling of Elastic Continua using a Grillage of Structural Elements Based on Discrete Element Concepts*, IJNME, 1999.
- [2] Hrennikoff, A., *Solution of Problems of elasticity by the Framework Method.*, *Journal of Applied Mechanics*, Vol. 8, pp A 169 - A 175, 1941.
- [3] Herrmann, H. J., Hansen, A. & Roux, S., *Fracture of Disordered Elastic Lattices in Two Dimensions*, *Physical Review B*, Vol. 39, No. 1, 1989.
- [4] Lu, P. F. & Vaziri, R., *The Equivalence of Stress- and Strain-Based Plasticity Theories*, *Computer Methods in Applied Mechanics and Engineering*, Vol. 147, pp 125 - 138, 1997.
- [5] Morikawa, H. & Sawamoto, Y., *Local Fracture Analysis of a Reinforced Concrete Slab by the Discrete Element Method*, *Proceedings of the 2nd International Conference on the Discrete Element Method*, MIT, 1993.
- [6] Schlangen, E. & van Mier, J. G. M., *Simple Lattice Model for Numerical Simulation of Fracture of Concrete Materials and Structures*, *Materials and Structures*, Vol. 25, pp 534 - 542, 1992.
- [7] Schlangen, E. & Garboczi, E. J., *Fracture Simulations of Concrete Using Lattice Models: Computational Aspects*, *Engineering Fracture Mechanics*, Vol. 57, No. 2/3, pp 319 - 322, Elsevier Science, 1997.